THESE

Pour l'obtention du Grade de

DOCTEUR DE L'UNIVERSITÉ DE POITIERS

École Nationale Supérieure d'Ingénieurs de Poitiers
(Diplôme National - Arrêté du 25 mai 2016)

École doctorale : Sciences et Ingénierie des Matériaux, Mécanique, Énergétique - SIMME (Poitiers)
Secteur de Recherche : Acoustique et Aéroacoustique

Présentée par
Wagner José Gonçalves da Silva Pinto

Modélisation du bruit d'origine aérodynamique : influence de la géométrie dans le bruit de forme

Modelling airframe noise: from aerodynamic topology to acoustic efficiency

Directeur de thèse: Yves Gervais
Co-directeur de thèse: Florent Margnat

Soutenue le 24 octobre de 2019
devant la Commission d'Examen

JURY

Phillip Joseph	Professeur, University of Southampton	Président
Manfred Kaltenbacher	Professeur, Vienna University of Technology	Rapporteur
Marc Jacob	Professeur, ISAE-SUPAERO	Rapporteur
Éric Manoha	Ingénieur de Recherche, ONERA	Examinateur
Véronique Fortuné	Maître de conférences, Université de Poitiers	Examinateur
Andreas Spohn	Maître de conférences, ISAE-ENSMA	Examinateur
Yves Gervais	Professeur, Université de Poitiers	Examinateur
Florent Margnat	Maître de conférences, Université de Poitiers	Examinateur

Acknowledgements

I am grateful to the students and interns that I had the pleasure to work with and that contributed directly or indirectly to this project (in chronological order): Iyer Periyapattana Manasa Srinivas, Swapnil Kharche, Rasmus Schlander, Alejandro Benitez de la Riva, Ismaël Wittke, Mathias Guillet, Rodrigo Vicente Cruz, Alexis Mousseau and Antoine Severin.

Thank you to the members of the Fluid, Thermal and Combustion Sciences department, from researches to students, whom I have had the pleasure to present and discuss my work with in several occasions. The advice of Laurent Cordier, Peter Jordan and Andreas Spohn are particularly appreciated.

I also wish to thank my fellow colleagues Yoann Beausse, Woodlens Chery, Zhiping Qiu, Robin Sebastian, Yinshi Zhou and Christian Zumi Doli for their presence on this long journey and the great ambiance we shared.

The administrative support from Bouba El Harchi and Marlène Martin and the assistance I received from Jean-Christophe Vergez in all IT related matters are greatly appreciated.

I owe my deepest gratitude to Pascal Biais, Janick Laumonier and Laurent Phillipon for their endeavor to prepare and perform the experiments presented herein.

I would like to greatly acknowledge my advisors Yves Gervais and Florent Margnat for their guidance. They nurtured an open and fruitful environment on all the duration of this work.

The jury members Phillip Joseph, Manfred Kaltenbacher, Marc Jacob, Éric Manoha, Véronique Fortuné and Andreas Spohn are acknowledged for accepting this duty and engaging their time and knowledge for appreciating my work.

Last but not least, I would like to thank my wife Isabela Iuriko Campos Maruo for all the love and support throughout this journey.

Columbus being at a party with many noble Spaniards, where, as was customary, the subject of conversation was the Indies: one of them undertook to say: —"Mr. Christopher, even if you had not found the Indies, we should not have been devoid of a man who would have attempted the same that you did, here in our own country of Spain, as it is full of great men clever in cosmography and literature." Columbus said nothing in answer to these words, but having desired an egg to be brought to him, he placed it on the table saying: "Gentlemen, I will lay a wager with any of you, that you will not make this egg stand up as I will, naked and without anything at all." They all tried, and no one succeeded in making it stand up. When the egg came round to the hands of Columbus, by beating it down on the table he fixed it, having thus crushed a little of one end; wherefore all remained confused, understanding what he would have said: that after the deed is done, everybody knows how to do it; that they ought first to have sought for the Indies, and not laugh at him who had sought for it first, while they for some time had been laughing, and wondered at it as an impossibility.

History of the New World by Girolamo Benzoni, Hakluyt Society, London, 1857, p. 17.

Contents

List of Figures

List of Tables

List of Symbols

Greek symbols

α, β, γ	real coefficients
$\epsilon(y)$	IBM solid domain array
$\varepsilon = (\mathrm{Re} - \mathrm{Re}_c)/\mathrm{Re}_c$	distance to critical Reynolds number
$\eta = \Delta y_3/d$	normalized spanwise distance
δ_{ij}	Kronecker's delta
Γ	spanwise coherence
ι	imaginary number, $\iota^2 = -1$
λ	wave length
Λ	spanwise integral one-sided correlation length
∇	gradient operator
ν	kinematic viscosity, taken as $\nu = 1.5 \times 10^{-5}$ m/s^2 for air
Ω	angular frequency
ω_n	natural frequency of the IBM forcing term
ω_3	flow vorticity in the spanwise direction
Π	population of agents in the optimization
ρ	flow density, taken as $\rho = 1.225$ kg/m^3 for air
ζ	damping coefficient of the IBM forcing term
τ	time
τ_{ij}	viscous stress tensor
τ_c	turbulence time scale parameter
$\boldsymbol{\Theta}$	vector of shape optimization parameters
θ	vector of particles velocity

Roman symbols

$\mathrm{AR} = b/d$	sectional aspect ratio
b	sectional breadth
c	sound speed, taken as $c = 340$ m/s for air
C	contour, perimeter of a cross-section
c_w	inertia factor of the optimization routine
c_1	social factor of the optimization routine
c_2	cognitive factor of the optimization routine
$\lvert C_L \rvert, C_L'$	average and RMS lift coefficients
$\lvert C_D \rvert, C_D'$	average and RMS drag coefficients
d	cylinder's diameter, sectional height
D	aerodynamic drag
e	residual
f	frequency
f_{peak}	lift/vortex shedding frequency
$f(\boldsymbol{\Theta})$	objective/cost function

$\hat{f}(\mathbf{\Theta})$	modeled objective/cost function
F_i	aerodynamic force components
h	geometrical thickness measurement
i, j, k	indexing variables with no exclusive application
L	aerodynamic lift
L_r	recirculation length
L_f	formation length
ℓ	cylinder's total spanwise extent
ℓ_c	spanwise one-sided coherence length
ℓ_g	spanwise gaussian one-sided coherence length
ℓ_s	cylinder's segment spanwise extent
Ma	Mach number
N_s	number of segments of a cylinder
p	pressure
P_1, P_2, P_3, P_4	points in space
P	acoustic pressure
$\overline{P}$	average Fourier transform of the acoustic pressure
P_{ref}	reference acoustic pressure, 20 μPa
Q_{ij}	source terms in the wave equation
r	source-observer distance
R	spanwise correlation
Re	Reynolds number
Re_c	critical Reynolds number for the transition from steady to unsteady flow
$\text{Re}_{2D\to3D}$	critical Reynolds number for the transition from 2D to 3D flow
S	smooth surface moving in space
St	Strouhal number
St_{peak}	Strouhal number of the vortex shedding frequency
t	time
T_{ij}	Lighthill's tensor
u, v, w	flow velocity in the cartesian axis (streamwise, crosswise and spanwise, respectively)
U_∞	inlet velocity
V	control volume
W	acoustic power
$W_a = W/\rho_0 U_\infty^3 d$	acoustic efficiency
x_1, x_2, x_3	cartesian coordinates in the observer frame
y_1, y_2, y_3	cartesian coordinates in the source frame
Y_1, Y_2	auxiliary cartesian coordinates in the source frame
Y_1Y_2	plan normal to the cylinder's axis

List of Acronyms

2D	two-dimensional
3D	three-dimensional
ANN	**A**rtificial **N**eural **N**etworks
BSPL	**B**and **S**ound **P**ressure **L**evel
dB	**d**eci**B**el
DNC	**D**irect **N**oise **C**omputation
DNS	**D**irect **N**avier-**S**tokes
DoF	**D**egrees of **F**reedom
DoE	**D**esign of **E**xperiment
GPU	**G**raphics **P**rocessing **U**nit
IBM	**I**mmersed **B**oundary **M**ethod
IRLS	**I**teratively **R**eweighted **L**east **S**quares
LDA	**L**aser **D**oppler **A**nemometry
LDV	**L**aser **D**oppler **V**elocimetry
LHS	**L**atin **H**ypercube **S**ampling
MPI	**M**essage **P**assing **I**nterface standard
OASPL	**O**ver**A**ll **S**ound **P**ressure **L**evel
PDF	**P**robability **D**ensity **F**unction
PIP	**P**oint-in-**P**olygon
PIV	**P**article **I**mage **V**elocimetry
PSPL	**P**eak **S**ound **P**ressure **L**evel
PSD	**P**ower **S**pectral **D**ensity
PSO	**P**article **S**warm **O**ptimization
QCCQBC	**Q**uadratic **C**ubic **C**ubic **Q**uadratic **B**ézier **C**urves
RANS	**R**eynolds-**A**veraged **N**avier–**S**tokes equations
RMS	**R**oot **M**ean **S**quare
RSM	**R**esponse **S**urface **M**odel
SPL	**S**ound **P**resssure **L**evel
SSP	**S**caled **S**ound **P**ressure

Introduction

A lot of things have changed in the world since Curle, von Kármán, Lighthill, Prandtl, Rayleigh, Reynolds, Stokes, Strouhal and others established the sciences of Fluid Mechanics and Aeroacoustics. The tools available for the study of the vast set of flow phenomena have become extremely precise, and at the same time robust and versatile. The use of numerical methods represents an immense expansion of the possibilities of cases and regimes that can be studied, while simultaneously giving an enormous knowledge of the flow. From the onset of the scientific field until the later decades of the previous century, this could only be achieved with thousands to millions of probes, in a completely utopic experimental setup.

However, two important parts in the equation are rather unchanged: the flow dynamics and human beings. At the same time that several questions remain unanswered in terms of fluids behavior, our physiology remains susceptible to noise, even if society has accepted it as a fundamental brick of the progress. Thus, the necessity and difficulties of comprehending the flow and noise dynamics remain as intriguing, with the complexity of having faster vehicles, more concentrated urban areas and a more sensible and fuel scarce environment.

In this context, sound generated aerodynamically is a prominent problem that raises scientific interest and social concern. As an intrinsically unsteady phenomenon, it combines the complex dynamics of the organization of the flow in wakes and jets with a part of the energy generating acoustic wakes. Besides the direct benefit of mitigating the noise pollution, reducing the noise production of the vehicles opens the possibility to operate at more efficient regimes, reducing fuel consumption.

This document reports a study of the shape influence on the aeroacoustic emission of the flow around bluff bodies. The context, pertinence, philosophy and nuances of the current study are presented next.

Context of the laboratory

This works is performed at the PPRIME Institute, located at Poitiers, France. It is a research unit affiliated to the CNRS (National Center for Scientific Research) linked with the University of Poitiers and the National Higher School of Mechanics and Aeroengineering (ISAE-ENSMA). The staff accounts about 600 people, with around 200 researchers and 200 PhD students. The unit is constituted by three departments: Department of Physics and Materials Mechanics (DPMM, D1), Department of Fluid, Thermal and Combustion Sciences (DFTC, D2) and Department of Mechanical Engineering and Complex Systems (DGMSC, D3). This investigation is developed in 2AT team (Acoustics, Aerodynamics and Turbulence) of the DFTC. The principal activities of the team are the numerical and experimental analysis of turbulent flows, thermoacoustics, jet and channel flow noise.

The team disposes of powerful tools for the numerical and experimental study of aeroacoustic phenomena, such as the solver incompact3d and immersed boundary methods (used in this work), developed and enhanced within the team on many years, emphasis is given to the thesis by Lardeau [126], Parnaudeau [182], Laizet [123] and Margnat [144]. Experimentally, many studies are performed in the anechoic wind-tunnels EOLE and BETI (where the experimental results presented here have been performed), with the extensive use of microphones, beamforming [54, 179], hot-wire and PIV [289] for the description of aerodynamic and aeroacoustic signature

of diverse obstacles such as facing-steps [127], cavities and aerodynamic profiles [21]. Attention must also be given to the study of automotive aeroacoustic sources such as the rear-mirror [128] and the transmission of sound to the vehicle's interior [19].

Impact and motivation

Aerodynamics makes up an important part of the sound emission of modern transportation. At higher speeds, it is the major sound source for both automotive ($U_\infty > 100$ km/h) and railroad noise ($U_\infty > 300$ km/h), as illustrated next. Moreover, the aerodynamic sound sources emerge as the component to tackle with the increase of electrical motorization, much quieter than combustion based engines.

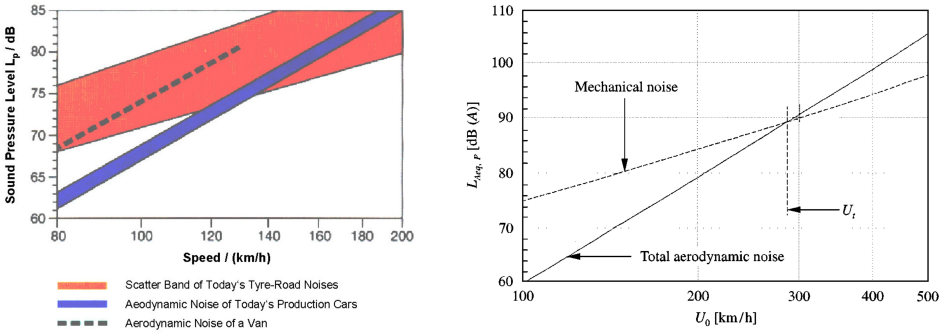

Figure: Evolution of the contribution of the aerodynamics sources in the sound emission of cars (left, reproduced from [74]) and trains (right, reproduced from [254]) with the vehicles' speed.

For these examples and in many other cases in external aerodynamics, the acoustical signature is formed by broadband and tonal components. While the first is associated with turbulence, the latter is a result of hydrodynamic modes. The presence of bluffly elements on the body of the vehicles, such as antennas and supporting beams, result in the production of such tonal factor, defined by the periodic vortex shedding in the wake of these geometrical features. Examples of components that produce tonal noise in modern vehicles are illustrated next.

Current work focuses on the influence of the shape of the obstacle that generates that type of noise, also known as "aeolian tone". Naturally, a modification of the shape of the obstacle induces a change of its sound emission properties. Recent studies concerning pantographs [83, 84] and automotive roof crossbars [149], where the shape of the cross-sections is a key aspect of the spectral distribution and amplitude of the noise perceived by both on the interior of those vehicles and on the surroundings, are clear examples of the interest and positive impact of investigating the aeolian tone generation.

From a constructor point of view, taking account of the aerodynamic sound production in the moment of defining the format of a product represents hundreds of hours of computation and engineer work. Often, once the project is constrained by multiple aspects, the aeroacoustics is neglected or considered solely based on low fidelity simulations or empirical models. Great interest in the aeroacoustics community is given into the development and enhancement of experimental and numerical methods for the prediction of the acoustic signature, with successful applications supported by the recent advances in computational power and the use of GPUs (Graphics Processing Units).

In a different, but complementary direction, this work is not aimed at designing any of those vehicles/devices or proposing technical advances for the solution of the numerical equations. In a more fundamental approach, the objective of the current project is to understand the changes in the aerodynamic and acoustic signature of bluff bodies that are inherited from a modification of their forms. This also means that there is no compromise in respecting geometrical or dynamical similitudes. Despite this relative distance, once the discussion is focused on the flow mechanisms, it pertinent not only in academia.

Figure: Photographs of sources of aiframe tonal noise in vehicles: rear mirror and antennas present in automobiles, photos from (a) to (c), representing almost canonical bluff bodies with large recirculation zones; the pantographs (devices that connect the vehicle to the electric line) of trains and trolleys, composed by cylindrical bodies, as illustrated from a lateral and frontal views in (d) and (e); and the landing gear of airplanes presented on (f) and (g), also reducible to a combination of round cylinders in an aeroacoustic point of view. Attributions: (a) "truck driver mirror", by Ted Gresham (CC BY 2.0, cropped), (b) "parked car", by Peter Heeling (CC0, cropped), (c) "The Nissan Leaf", by Tom Raftery (CC BY-NC-SA 2.0, cropped), (d) "High speed train at Poitiers' train station, France", by the current author, (e) DBAG Class 146 electric locomotive, unknown author (CC0, cropped), (f) "A Korean Air Airbus A330 is landing at Vienna International Airport", by Ulrich Latzenhofer (CC BY-SA 2.0, cropped) and (g) "Main landing gear of a Boeing 747-8F prototype", by Olivier Cleynen (CC BY-SA 3.0, cropped).

Bluff body flow and aeroacoustics

As stated earlier, this thesis is aimed at the study of the influence of the shape of bluff bodies in the aerodynamic noise production. Thus, the base configuration studied in this work is a cylinder immersed in a uniform flow. Beyond a given flow velocity, a vortex wake is generated of periodical, counter-rotating vortices, known as the von Kármán wake. The generation of these vortices, associated with flow interactions with the surface of the cylinder, is responsible for the production of tonal noise.

For this configuration, the tonal component is associated with the vortex-shedding, which means that the flow topology must be considered in the analysis. Consequently, the principal scope of this work is to describe the aerodynamic behavior of prismatic bluff bodies and the influence of the cross-section on it. The objective being the aeroacoustic efficiency, it is fundamental to consider unsteady aerodynamics and second order statistics, in this sense, the proposed aerodynamic study is placed one step further the classical analysis focused on the average behavior of such category of geometries.

The analysis is restrained to low Mach number and compact sources, that is, configurations where the effects of the flow compressibility and of the shape in the acoustic field are negligible.

Nevertheless, recall that the description of the bluff body flow dynamics also has an application in civil engineering and architecture, notable for large buildings and structural design, specially in what concerns the reduction of static and dynamic loads [44, 282] and the design of heat exchangers (for instance, the investigation of Vijaybabu et al. [270]).

Philosophy of the study and methodology

Rather than a detailed description of a single configuration, this study is based on the comparison of multiple shapes. This means that there is a privilege to performing an elevated number of simulations with reduced precision and comparing them, with the help of optimization and statistical tools. Same is performed in the experimental work, focusing on the comparison of the obtained results and the values and conclusions present in the literature.

I share the vision of Roshko [222] that the simulations are not different from the experiments in the point of view of a scientific result. Taking a high-order, validated solver and numerical setups, the simulations are going to work, in the limits of the respect of all the hypotheses in the model, the same as a measurement performed with a large number of probes. I agree that in this way, the scientist has a lot of information concerning the flow, for example, the rates of changes in flow quantities, the energetic content of the flow and the dimensions of the topological features, however, there is no information regarding the principles of the phenomenon. A small set of simulations represents only a small range of possibilities in terms of flow regimes, and even if the knowledge of that specific configuration of boundary conditions and flow regime are enormous, the simulation alone has no advantage in terms of dissecting the physics. This is only achieved by the production of models that encapsulate the state of art in terms of the comprehension of the physical phenomenon.

In its essence, this work can be compared to the extensive experimental campaigns performed worldwide in the first decades of the 20^{th} century, notable from Roshko [218, 219], that measured the behavior of the flow around different shapes of geometries, producing an incredible amount of information around the bluff body noise. This work is not aimed at producing a database, despite also being the case. Looking at unsteady flow statistics and noise, using numerical tools to enlarge the possibilities with the use of statistics and optimization in order to highlight the trends.

The two pillars of the work are: the 2D, low Reynolds number ($\mathrm{Re} = 20 - 200$) incompressible simulations using Direct Navier-Stokes solver and an Immersed Boundary Method (IBM), associated with a compact tonal noise emission model; and the measurements performed in the anechoic wind-tunnel BETI at Reynolds number range of about $\mathrm{Re} = 10^3$ to 5×10^4. Even if the flow regimes studied by each one of these means are not coincident at any moment, the

universality of the phenomenon of periodic vortex shedding is evoked as to justify such disparity in methodology.

This work leaves a lot of doors open and possible directions of expansion. In terms of laminar, 2D flow and the general description of bluff bodies flow dynamics, the study and proposition of new criteria for quantifying the flow regime, as a complement of the Reynolds number is a clear way. The analysis of the transition between wake modes, naturally attached to the first one, is also an interesting point to be clarified and universalized. Close to acoustic studies, the scattering properties of the shapes may be addressed through the concept of tailored Green's function.

Organization of the document

The manuscript is organized as follows:

Chapter 1 contains the description of the scientific context. First, the phenomenon of vortex shedding at the wake of bluff bodies is described in Section 1.1. Second, in Section 1.2, the principles of aeroacoustics are presented, with a focus on the sound produced by boundaries. Airframe noise and the presence of cylinder noise in the literature are discussed next, in Section 1.3. A synthesis of the major shape-dependent quantities of the phenomenon and the principle of the current approach are presented in Section 1.4;

Chapter 2 contains the study of the flow around a large set of geometries using 2D, low Reynolds simulations. The solver and the IBM implementation are presented in Section 2.1. In Section 2.2, the considered geometries and topological and integral features of the modeled flows are discussed, with a discussion and quantification of the distance to the onset of unsteadiness. The obtained values are analyzed in a regression study in Section 2.3, where global and geometry exclusive relationships are highlighted. Parametric studies inspired on the tested shapes and observed behaviors are reported in Section 2.4. Conclusions under the shape influence on low Reynolds number close the chapter in Section 2.5;

In **Chapter 3**, the analysis of canonical shapes reported in the previous chapter is expanded through shape optimization. Analysis is performed in 2D, low Reynolds for compact cylinders (same setup as in Chapter 2). The elements of a shape optimization routine are presented in Section 3.1. The concepts and the implementation of a Particle Swarm Optimization (PSO) algorithm are described in Section 3.2. In Section 3.3, optimal shapes and the associated flow topologies are presented for 3 distinct parametrizations. Section 3.4 is dedicated to the final discussion on the pertinence of the proposed implementation and the conclusions about the shape influence on the noise emission;

The experimental work is reported in **Chapter 4**. Hot-wire anemometry and microphones were used for the aerodynamic (in both streamwise and spanwise directions) and acoustic description of a set of different shapes, both techniques and setups are presented in Section 4.1. In terms of results, an analysis of the velocity signals of flows around circular and rectangular cylinders is presented in Section 4.2. Next, sn Section 4.3, the results of the quantification of the spanwise correlation and coherence of the flow are presented, also focusing on the difference in behavior associated with the different cross-sections. Further, in Section 4.4, the acoustic signature of a variety of of cylinders is presented. Both results (coherence length and sound emission) are combined in Section 4.5, where a methodology designed to correct the sound pressure levels of short cylinders is reversed in order to estimate the sectional RMS lift coefficient and to compare the mechanisms that provoke the differences in the sound emission. In Section 4.6, the influence of the length of the cylinder on the amplitude of the sound emission is investigated. Finally, conclusions and criticisms close the chapter in Section 4.7;

Chapter 5 contains the presentation of the main conclusions and the perspectives of the project. The disparities and similarities noted in the aeroacoustic signatures obtained in 2D and 3D are presented in Section 5.1. A global vision of the shape influence on noise and vortex shedding dynamics, derived from the current analysis, is presented on Section 5.2. Section 5.3 contains the final comments and perspectives, closing the document.

Communications

The majority of the work that constitutes this document has been communicated in different occasions, listed next. Also, the author has participated in the scientific communication competition 3 Minute Thesis, organized by the Coimbra Group, and its french equivalent "Ma These dans 180 secondes", organized by the CNRS. The work has been exposed in a poster and an oral presentation on the institute internal events for the PhD students as well.

- Conferences:
  - Margnat, F. and da Silva Pinto, W. J. G. (2018). Contribution à l'optimisation de forme pour le bruit d'origine aérodynamique. In *14ème Congrès Français d'Acoustique (CFA18 - Le Havre)*
  - Pinto, W. J. G. S. and Margnat, F. (2018). Shape optimisation for the noise induced by the flow over compact bluff bodies. In *International Conference on Computational Fluid Dynamics (ICCFD10), July 9th-13th, Barcelona, Spain*
  - Pinto, W. J., Margnat, F., and Gervais, Y. (2019b). Influence of cross-section on the aeolian tone: a numerical study in the laminar regime. In *25th AIAA/CEAS Aeroacoustics Conference*, Aeroacoustics Conferences. American Institute of Aeronautics and Astronautics
  - Pinto, W. J., Margnat, F., and Gervais, Y. (2019a). Effect of cross-section on flow three-dimensionality for prismatic bodies and the associated noise emission. In *25th AIAA/CEAS Aeroacoustics Conference*, Aeroacoustics Conferences. American Institute of Aeronautics and Astronautics
- Articles:
  - da Silva Pinto, W. J. G. and Margnat, F. (2019). A shape optimization procedure for cylinders aeolian tone. *Computers & Fluids*, 182:37 – 51
  - Pinto, W. J. G. S. and Margnat, F. (2019b). Influence of bluff body sectional breadth and shape on the onset of flow unsteadiness. *submitted to Physics of Fluids*
  - Pinto, W. J. G. S. and Margnat, F. (2019a). Experimental study of the influence of cross section shape on spanwise coherence length in flow around cylinders. *under consideration for publication*
  - Pinto, W. J. G. S. and Margnat, F. (2019c). Shape optimisation for the noise induced by the flow over compact bluff bodies. *submitted to Computer & Fluids - ICCFD special issue*

Chapter 1

Scientific context of bluff body noise

The noise production by cylinders is a complex phenomenon associated with multiple energy interactions. First step is the spatial and temporal change from the incoming, uniform flow, to the perturbed wake and the second, also in time and space, is the transformation of the flow perturbations present in the wake into acoustic waves. This section is dedicated to introduce the basis of the principal phenomena associated to both those passages and present the relevant works available in the literature.

Section 1.1 contains the description of the mechanisms behind the vortex shedding. Next, in Section 1.2, the basis of the science of aeroacoustics are presented, with a focus on the sound emission by cylinders. A description of the airframe noise, focusing on investigations of the effect of the geometry compose Section 1.3. Finally, the open questions and the current approach are discussed in Section 1.4.

1.1 Bluff body flow

The easiest way to define a bluff body is by opposition. A streamlined body is a shape that has a small impact on the flow. Its edges are parallel to the flow direction as much as possible, what results in small perturbations of the flow. By having been elongated in the streamwise direction, streamlined shapes allow (depending on the regime) the flow to re-organize before arriving at its further downstream limits, forming less disturbed wakes. A bluff body is the opposite. As defined by Roshko [220], *the main feature of flow past a bluff body is its separation from the body surface, well ahead of the rear stagnation point, and the formation of a large wake.* Such properties are associated with strong mean and fluctuating aerodynamic efforts and, consequently, sound emission.

Naturally, as for any other flow, the analysis of bluff body flows is based on the flow regime. The characterization is condensed in the Reynolds number, a rate between inertia and diffusion effects:

$$\mathrm{Re} = \frac{U_\infty d}{\nu} \tag{1.1.1}$$

where U_∞ is the flow incoming velocity, ν is the fluids dynamic viscosity and d is an characteristic length of the problem. In the case of cylindrical bodies d is taken as the cylinder blockage (its diameter in the case of a circular cross-section). As a fundamental quantity in fluid mechanics, it conjugates, on this specific application, the flow capacity to decrease amplification rates and to stabilize the shear layers [222], modifying the dynamics of the wake hydrodynamic modes. The major instability in the case of cylindrical bodies, the focus on this study, is the von-Karman vortex-shedding, further discussed next.

1.1.1 The von Kármán vortex shedding

The phenomenon of vortex shedding was first established by Theodore von Kármán in 1911 [121], author that gives its modern name, in his proposition of a model for the spacing of the vortices.

It consists in the periodic generation of vortices of opposite direction behind an obstacle, also generating a periodic wake, as exemplified in Figure 1.1.

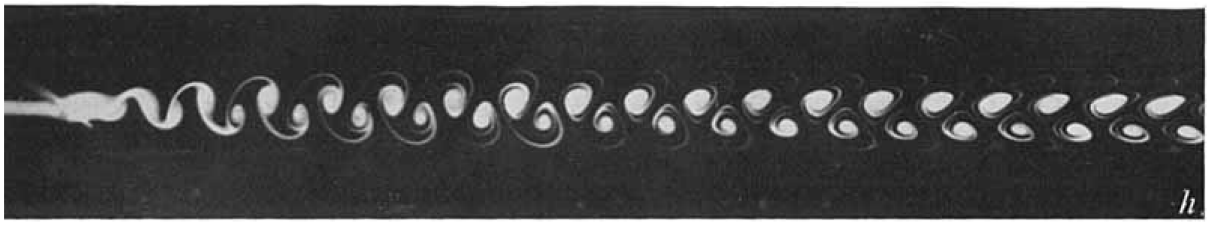

Figure 1.1: Smoke visualization of the von Kármán vortex street at the wake of a circular cylinder, Re = 90. Reproduced from [284].

A scaling law of the vortex shedding frequency was defined some decades earlier, on the article by Strouhal in 1878 [247]. By observing the relationship between the flow velocity, the diameter and the frequency of the produced tone, the following non-dimensional number was defined:

$$\mathrm{St} = \frac{fd}{U_\infty} \tag{1.1.2}$$

where f is the frequency and d a characteristic length. In the case of vortex shedding by a circular cylinder, where d is the diameter, the Strouhal number is of about 0.2. Naturally, this value also fluctuates with the Reynolds number. Since the work of the latter two scientists, tremendous advances have been made and our comprehension of the phenomenon has been enlarged.

For fluids at very reduced velocity (small Reynolds number), where the viscous dissipation is the major outlet of fluids energy, the wake of the body is steady and symmetrical. With further increase of the flow speed and the consequential reduction of the relative influence of the dissipation, there is the formation of the unsteady flow, both regimes are further illustrated on Figure 1.2. A classical view, as described by Strykowski & Sreenivasan [249] is that *as the flow Reynolds number increases, viscous diffusion alone cannot keep up with the increased vorticity production in the upstream boundary layers, and vortices break away at regular intervals, constituting "vortex shedding".*

Topologically, such flow is composed by two shear layers, on the upper and lower portions of the body, and associated boundary layers at the walls. The vortices are feed by the reverse flow issued from the opposite hemisphere of the body [58]. The mechanism of generation of the vortices (not the vortex shedding as a whole) is independent of vortex diffusion [187], what arguments in favor of the existence of the von Kármán vortex street for a wide range of Reynolds number and flow regimes.

1.1.1.1 Brief description of the instability mode

In a different description, the vortex shedding is categorized as a globally unstable mode [150, 248], what means that the instability is of the entire flow field. A short and light description of some observations concerning the stability aspect of the vortex shedding are presented next, the reader is invited to check the review articles by Huerre & Monkewitz [79] and Chomaz [32] for complete discussions on the matter of flow instabilities.

Close to the onset of the unsteadiness it is defined as a Hopf bifurcation that obeys Stuart-Landau equation [150], with the Reynolds number as the control parameter, defined by the change from a steady to a periodic solution (see Figure 1.2), what is mathematically defined as the eigenvalues crossing the imaginary axis (from negative to positive), being the imaginary part of that eigenvalue the angular frequency of the mode. The Reynolds number where the transition occurs is referred to as critical Reynolds number, $\mathrm{Re_c}$.

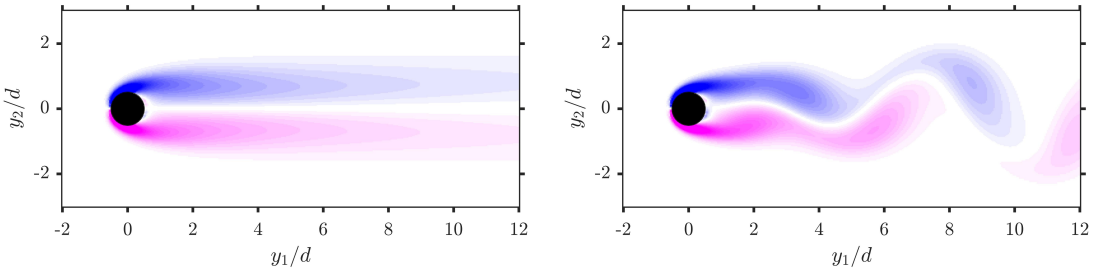

Figure 1.2: Spanwise vorticity fields for the steady (left, Re = 40) and unsteady (right, Re = 60) wakes of a circular cylinder.

At the vicinity of $\mathrm{Re_c}$, the saturation amplitude is found to be proportional to the "distance" in terms of the flow regime [79]:

$$A_{sat} \propto (\mathrm{Re} - \mathrm{Re_c})^{1/2}, \quad \mathrm{Re} > \mathrm{Re_c} \tag{1.1.3}$$

where A_{sat} indicates a real coefficient that quantifies a saturation amplitude.

It is a global instability mode that may be analyzed in terms of linear instability concepts before the non-linear terms become important [119]. For instance, the frequency of the vortex shedding may be predicted by local instability analyses [192]. Nonetheless, the non-linearities have a strong influence on the amplitudes [204], justifying why the relation presented on Equation (1.1.3) is valid only close to the transition.

As discussed by many authors [2, 113, 249], for the wake stability analysis, it is not necessary to consider the body for performing the analysis, only the effective flow field. The characteristics of the wake and the velocity profiles that define the instability may be modeled using synthetic wakes as done by Koch [113]. The importance of the shear layer distribution is exemplified by the classical experiment by Strykowski & Sreenivasan [249], where the presence of an additional, smaller control cylinder (ratio of diameter of about 1/10) placed at the wake at a few diameters of the center is capable of extinguishing the vortex shedding by diffusing the vorticity of one of the shear layers, thus, destabilizing the wake.

Even if, in terms of wake dynamics, the shape may be neglected, it does not answer the question concerning the noise production, that is, in the case of cylinders, directly related to the magnitude and phase of wall pressure fluctuations. Since the shape is the only origin of the modifications of the mean field here, thus the definer of the flow dynamics, it is fundamental to be considered in this work. In this sense, some works present in the literature which focus on the differences noted on the hydrodynamic modes for different sets of cross-sections are presented as follows.

1.1.1.2 Instability studies for different cross-sections

Some studies may be highlighted in what concerns the investigation of the influence of the cross-section on the flow stability. These studies are not focusing on the principle and mechanisms of the stability, that are the same for all bluff body wakes [220], but the differences in terms of the response when the flow around different shapes is considered.

In a study more focused on the presentation of a methodology, Jackson [93] calculated the critical Reynolds for elliptical, triangular and flat plates. The importance of domain and boundary conditions in these results is reinforced. Using an Immersed Boundary Method (IBM) formalism, Paul et al. [185] studied the flow transitions from fully attached to the laminar separation and from steady to unsteady for elliptical cylinders of different aspect ratios and angles of attack, concluding that an increase of the angle of attack induces the tendency to detachment and to unsteadiness (lower $\mathrm{Re_c}$). Also using IBM, Yoon et al. [281] investigated the effect of the angle of incidence of a square cylinder on the flow instability. They proposed a relationship between the growth rate of the recirculation length of the flow and the critical Reynolds number and highlighted the influence of symmetry in three-dimensional flows. Thompson et al.

[261] investigated the transition and wakes of different elliptical sections (multiple aspect ratio) using linear and Floquet stability analysis. In a study of triangular sections, Ng et al. [164] also discussed that the changes in the critical Reynolds number are due to modifications in the distribution of the wake vorticity. For their configuration, it was mostly due to the generation of a leading edge recirculation bubble originating from inclination of the triangle.

Similarly to the conclusions performed on the control cylinder study by Strykowski & Sreenivasan [249], major conclusions concern the influence of the shape on the distribution of the vorticity in the wake, thus, on its instability. Thompson et al. [261] justify an increase of flow perturbation when comparing the flow around elliptical sections of decreasing aspect ratio at a fixed Reynolds number, to the increase of vorticity flux for the smaller-aspect-ratio cases.

Despite the important insights contained in those articles, the descriptions are focused on a limited number of shapes and have no intention to provide any form of global representation of the phenomenon. As stated by Johnson et. al [101] in their study of the frequencies of the wake of elliptical cylinders, other shapes should be considered in order to fully understand the flow dynamics. Despite not using instability analysis, the current study is believed to contribute in this sense by analyzing a large scope of geometries and also performing the estimation of the critical Reynolds number (Section 2.2.3) for a part of them and proposing geometry-independent empirical relationships.

1.1.2 Evolution of the flow with the Reynolds number

The evolution of the flow with the Reynolds number is an important part of the problem. The changes in the relative dissipation rates imply a modification of the average and instantaneous flow topology by replacing and resizing the boundary and shear layers. Such modifications are associated with the onset and supression of the vortex shedding. A general description of the different regimes associated with the change of Re is provided next, for the circular and square cylinder. The reader is invited to check the reviews by Williamson [276] and Zdravkovich [283] for deeper discussion around the flow around the circular cylinder.

1.1.2.1 Circular cylinder

1.1.2.1.1 Evolution of the base pressure The response of the flow around a circular cylinder to a change in regime is represented by the graph of the base pressure (pressure coefficient for the furthest downstream point of the section) versus Reynolds number on Figure 1.3. The different regions are discussed next.

At really low Reynolds ($Re < 6.5$, [185], not in the graph), the flow is completely attached to the walls. As Re increases, there is a detachment and the generation of a steady recirculation bubble. The flow remains steady, with a growing recirculation length, until Reynolds number reaches a value of about 47. After that, the wake is unstable and the vortex shedding is established, with an increase of the base suction with the Reynolds number, associated with the amplification of the instability (discussed on Section 1.1.1) and of the Reynolds stresses at the vicinity of the cylinder [222].

From $Re = 47$ to around 150, the flow is unsteady but completely 2D, that is, structures are unchanged in the spanwise direction, flow is completely phased. After that, transitions take place in the spanwise direction, with the establishment of three dimensional instability modes, known as Mode A (generation of vortex loops, dominant for $Re = 140 - 194$ [276]), and Mode B (composed by small streamwise vortices, dominant for $Re = 230 - 250$ [100]), with a transition range at approximately $Re = 230 - 260$. If the flow velocity is increased, the structures are further degenerated and disorganization increases.

From about $Re = 10^3$ to 10^5, there is a gradual increase of the base pressure, associated also with an increase of the RMS lift coefficient, simultaneously with a shortening of the wake provoked by the increase of the Reynolds stresses in the shear layers [222]. At Reynolds number higher than 10^5, the boundary layer is reinvigorated by the formation of a separation-reattachment bubble [222], pushing the separation point further downstream, what results in a

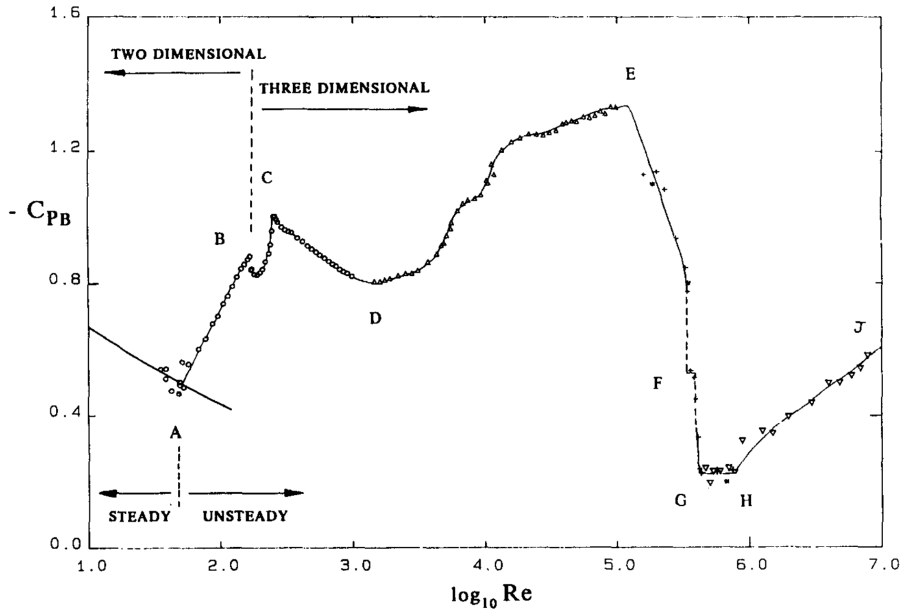

Figure 1.3: Evolution of the base pressure with the Reynolds number for the flow around a circular cylinder, reproduced from the review paper by Williamson [276].

strong decrease in the drag (the "drag crisis"). For a range of $5 \times 10^5 - 10^6$, flow is symmetric and there is no vortex shedding. At Reynolds number higher than 10^6, the boundary layers transition to turbulence is pushed upstream and vortex shedding is re-established [221].

1.1.2.1.2 Evolution of the fluctuating lift Naturally, the different flow regimes also affect the fluctuating lift, a fundamental ingredient of the noise emission (see Section 1.2.3.2). A short description is presented further. The reader is invited to check the articles by Norberg [171, 172] for a deeper discussion around the evolution of the fluctuating efforts with the Reynolds number and the discussion around the different methods for measuring them. Results from the latter reference are reproduced on Figure 1.4.

From the onset of the vortex shedding to about 150 (start of threedimensionality), there is a monotonic increase of the RMS lift coefficient C_L'. It is followed by a decrease due to the disorganization and distancing of the structures until the Re reaches about 10^3. This is followed by an increase with a plateau of $C_L' \approx 0.5$, and a further decrease associated with the boundary layer transition and the drag crisis, as discussed on previous section.

A similarity in the shape of the curves is also noted for the evolution of both the base pressure and the RMS lift coefficients. A quantification of such relationship is proposed by the comparison of the averaged drag and RMS lift coefficient of multiple geometries at Re = 150 further in the document (Section 2.3.3.4).

1.1.2.2 Square cylinder

The evolution of the flow around square cylinders is also discussed in literature. The current description is based on the results and compilation performed by Bai [10], illustrated by the evolution of the average drag reproduced on Figure 1.5. To the author's knowledge, despite graphs with the evolution of the Strouhal number with the Reynolds number, no similar descriptions are available for any other different cylinder geometry.

For the flow around a square cylinder, the unsteady, 2D, laminar flow is in the range of Re = $45 - 160$. Transition to 3D (de-correlation in the spanwise direction), takes places for a range of approximately Re = $160 - 220$ [10]. For larger Reynolds number, the vortex shedding is turbulent and the transition of the shear layer to turbulence may happen downstream ($220 < \text{Re} < 1,000$) or upstream ($\text{Re} > 1,000$) of the trailing corner, the latter being associated

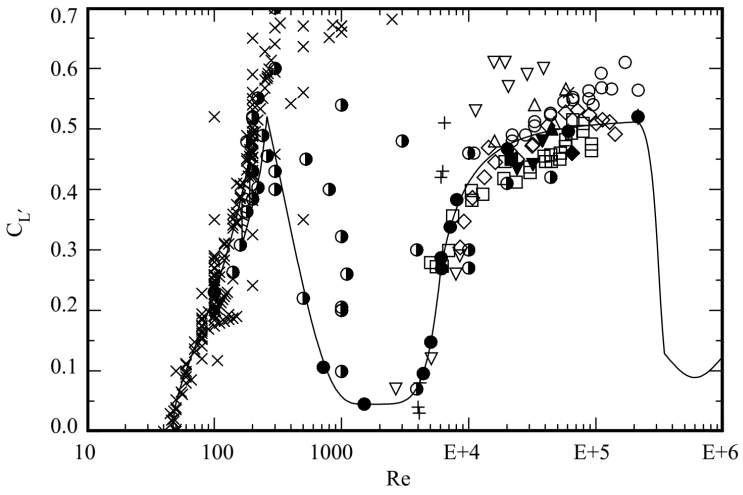

Figure 1.4: Evolution of the sectional RMS lift coefficient with the Reynolds number for the flow around a circular cylinder, reproduced from the review paper by Norberg [172].

with a reattachment of the boundary layer to the edges.

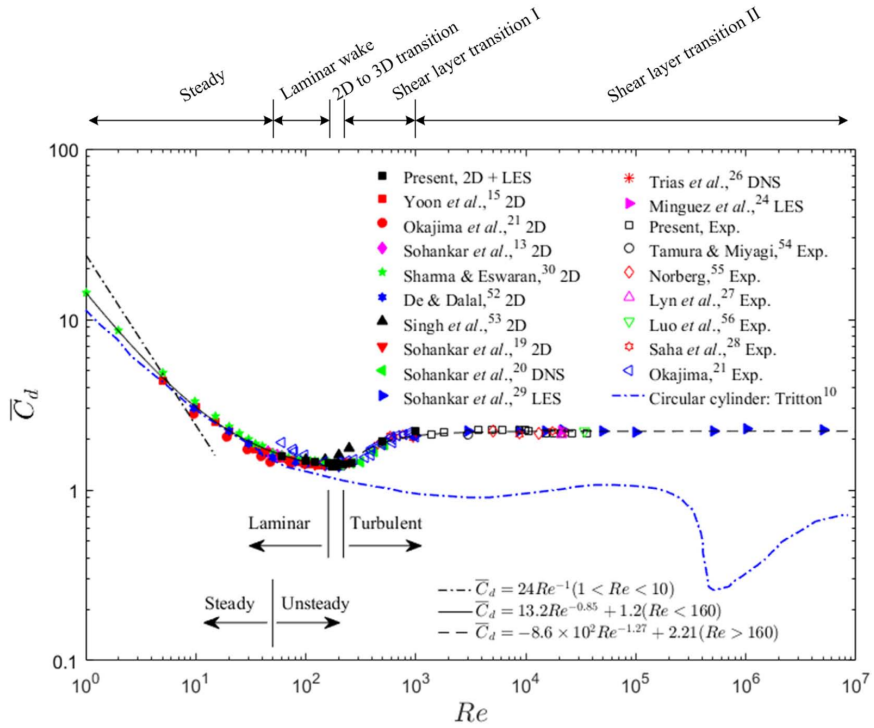

Figure 1.5: Evolution of the base pressure with the Reynolds number for the flow around a square cylinder, reproduced from the paper by Bai & Alam [10].

Differently from the circular section, there is no drag crisis. By having sharp-edges, the flow around the square cylinder has a strongly reduced possibility in terms of detachment points. Thus, the evolution of the flow is rather simplified. This behavior is partially reproduced for rectangular sections. The presence of longer edges increases the variability of the flow topology by enlarging the possibilities of detachment, what results in the existence of supplementary vortex shedding modes [138, 238].

Those two cases (circular and square cylinder) exemplify the simultaneous difference and similarity of the flows around bluff bodies with distinct cross-sections. While the dynamics of the flow are intrinsically related to the similarly evolving energy exchanges between the wake, shear and boundary layers, in a manner quantified by the Reynolds number, those relations vary

in terms of amplitudes of flow quantities, size and localization of the structures in the wake and the position where the transitions take place in the Re scale.

The presented robustness of the vortex shedding in terms of the change in the geometry naturally leads some attempts to create a universal model, discussed next.

1.1.3 Attempts of a universal description

As claimed by Roshko [219], *because of the similarity in all bluff-cylinder wakes, one would expect to find a parameter to compare the wakes of different cylinders.* Since the von Kármán's model [121], which described the vortex street with an idealized potential flow model using point-vortex approximations [14], many other insviscid models of the vortex shedding have been proposed. For instance, the articles by Schaefer & Eskinazi [229] and Saffman & Schatzman [224]. Other remarkable examples of universal descriptions are more empirically inspired, such as the wake Strouhal number by Roshko [14, 219], the universal Strouhal number proposed by Griffin [70] and the laws based on the separation angle by Xu et al. [278]. Another distinctive example is the wake model by Ahlborn [3, 4], author who made analytic developments based on the momentum equations and the representation of the dynamics of vortex shedding as a periodic oscillator. Despite its tremendous grounding on the physics of the problem, it still resides in empirical constants.

Despite the insights those descriptions contain, they are applicable to a global description, specially in terms of the shape influence on the bluff body noise. By being most of the times insviscid, they are based on strong hypotheses and generalizations around the mechanism of the generation of the vortices, strictly related to wall stress and viscous dissipation. Even if the mechanism is well described for the wake, it fails to predict the effect near the obstacle, and is thus not adapted to a description of the sound emission of boundaries. Another restriction concerning these models is the fact that they are mostly focused on describing the frequency of the shedding and the average drag. As described by Saffman & Schatzman [224] to be pointed by Roshko, the relationship between the properties of a vortex street and the fluctuating lift (fundamental ingredient of the cylinder noise, see Section 1.2.3.2) cannot exist in an inviscid description since a flat plate normal to such flow has no lift but a developed vortex-street. Finally, it is observed that, up to date, these descriptions are still related to some sort of geometry related empiricism. Preliminary tests performed in the current work, not presented in this manuscript, have shown that the proposed constants (such as the energy mode and the vortex diffusion parameter) that serve as closure fail to be compatible to the full set of tested shapes simulated herein.

In conclusion, despite the various attempts, there are still no consistent models of the vortex shedding, as claimed by Roshko a few decades earlier [222]. This question remains unanswered, according to the author's knowledge. On the other way, there is a growing effort to describe the vortex shedding around different shapes and to expose the influence of the geometry. Some of the studies found in the literature that compare the geometrical features of different shapes by associating them with the observed changes in flow response are presented next.

1.1.4 Discussion on the vortex shedding around different geometries

Rather then proposing universal laws some studies evaluated the flow around different geometries and make conjectures concerning the shape influence. For instance, from the observations of the response of numerous shapes, Roshko proposed the concept of "bluffness" [220]. Considering geometries with the same blockage, the body that diverges the flow more is considered "bluffer". By creating a wider wake, it has a higher drag and lower Strouhal number.

Gerrard [59] evaluated experimentally the low Reynolds number flow transitions (transition to unsteadiness and from 2D to 3D) for the circular cylinder and also the effect of the shape by considering 7 geometries (including a circular cylinder with 3 configurations of splitter plates). The study is entirely performed by flow visualization using dye. He observed that the flows around square and diamond sections are more organized than those around circular cylinders.

He also claims that the mechanism of changing the interaction of the shear layers by the splitter plate is similar to the effect of changing the Reynolds number of the flow.

Luo et al. [140] performed the visualization and measured the aerodynamic efforts for the flow around for 4 different cylinders (Re = 3.4×10^4): a back-pointing triangle, a square and two trapeziums of intermediary inclination of the lateral edge, at different angles of incidence. Their main conclusion regards the role of the influence of the lateral direction in the vortex shedding. By increasing the inward tendency of the shear layers (considering a scale that starts at the square and finishes at the triangle), the interaction between them is increased and the Strouhal number is reduced, also affecting the mean and fluctuating pressure loads on the surface. They introduce the concept of "interference" for qualitatively describing the amount of interaction between the shear layers and the solid body (for example, the square is more interfering than the triangle). An increase on the "interfering" properties of the geometry (by a change of either the shape or the angle of incidence) results in an increased interaction between the shear layers and their consequential straightening, followed by a reduction of the base pressure and the drag coefficient.

Cheng & Liu [31] studied similar geometries numerically (2D incompressible flow, Re = 250) by varying the ratio of the upstream edge divided by the downstream edge (equals 1 for square and 0 for the back-pointing triangle). Similarly to [140], they associate the contraction of downstream portion of the body (from square to triangular cross-section) with an increase of the interaction of the shear layers. In their simulations, this resulted in an amplification of the pressure fluctuation and, for a downstream edge smaller than 0.5, an increase of the fluctuating lift.

The evaluation of the cross-section influence on the flow is also present in the studies by Becker et al. [16] (experimental work, Re = 12.5×10^4 and 37.6×10^4) and Uffinger et al. [265] (experimental and numerical, Re = $12,800$), performed on the same facility and employing laser Doppler anemometry (LDA). They compared the effect of the shape with a base square cylinder and elliptical and triangular (wedge) forebodies/afterbodies (that is, upstream and downstream of the square section, respectively). It was observed that the addition of the bodies has an impact on the height of the wake and on the base pressure, consequently, on the drag and sound emission (only present in the first work). The leading wedge is associated with the creation of a more unstable flow. Most of the mechanisms of the changes noted in the wake are associated with the modification of the detachment point. By performing an analysis of a short-span cylinder (length/diameter of 6), their conclusion is likely submitted to end-effects.

In a series of experiments using hot-wire anemometry, Particle Image Velocimetry (PIV) and measurements of the aerodynamic efforts Xu et al. [278] evaluated the flow around a set of polygonal prisms for a range of Re = $10^4 - 10^5$. They highlighted the influence of the orientation of the cylinders in the aerodynamic response observed in the body in terms of aerodynamic efforts. Also, they concluded that above a number of 12 faces, an increase in the number of faces of the cross-section act as roughness. Moreover, they presented empirical relationships that found significant correlation between the separation angle and the average drag.

1.2 Theoretical foundations of aeroacoustics and cylinder noise

Aeroacoustics is the science that investigates the mechanisms of generation and dissipation of the sound that is produced by the unsteady fluctuations of flows. The field can be considered as being founded in the 1950's with the work of Sir James Lighthill [132]. The nature of his analysis is to deduce a wave equation from the laws describing the flow dynamics.

As any other acoustic phenomenona, the sound production of aerodynamic sources is a thermodynamic problem, where complex energy transmission between pressure and velocity takes place. As such, a key parameter is the Mach number:

$$\mathrm{Ma} = \frac{U_\infty}{c} \tag{1.2.1}$$

where c is the speed of sound in the medium. It represents a criterion for considering the

effects of compressibility on flow and sound analysis. This study considers only small velocities (Ma < 0.3), so the nuances of the energy transfer dynamics are condensed in the hypotheses of an incompressible flow.

In this section, the Lightill tensor is deduced. The discussion is extended to the integral solutions focusing on the sound generated by static boundaries, the configuration analyzed in this work. Many other possibilities and developments exist in the field, such as the Kirchoff formalism, not discussed here for conciseness.

1.2.1 Flow equations

From the Reynolds transport theorem, the mass, momentum and energy fluxes are used to derive the flow equations, presented next:

- Continuity:

$$\frac{\partial \rho}{\partial t} + \frac{\partial}{\partial x_i}(\rho u_i) = 0 \tag{1.2.2}$$

- Momentum equation:

$$\frac{\partial}{\partial t}(\rho u_i) + \frac{\partial}{\partial x_j}(\rho u_i u_j) = -\frac{\partial}{\partial x_j}(p\delta_{ij} - \tau_{ij}) + \rho g_i \tag{1.2.3}$$

- Energy equation:

$$\frac{\partial}{\partial t}(\rho E) + \frac{\partial}{\partial x_j}(\rho E u_j) = -\frac{\partial}{\partial x_j} q_i - \frac{\partial}{\partial x_j}(p\delta_{ij} u_j) + \frac{\partial}{\partial x_j}(\tau_{ij} u_i) + \rho g_i u_i \tag{1.2.4}$$

  where ρ is the density, t is the time, x_i is the space coordinate, u_i is the fluid velocity component, p is the pressure, δ_{ij} is the Kronecker delta (1 if $i = j$, null elsewhere), τ_{ij} is the viscous stress sensor, g_i is the external forces component (such as the gravity), E is the total energy $E = e + 1/2u^2$, and q_i is the heat-flux component.

The closure of the system relies in the use of constitutive equations, for example, the perfect gas hypothesis. For incompressible flows, the energy equation reduces to a linear combination of the mass and momentum equations, so the flow is described by only the first 2 differential equations.

1.2.2 Acoustic analogies

By the solution of the complete form of the flow equations presented on Section 1.2.1, both the hydrodynamic and acoustic fields are represented. This is achieved by using DNS compressible solvers, also known as Direct Noise Computation (DNC). The solution of the complete flow equations is expensive and complex.

The principle of Lighthill's development is to obtain the acoustic field from the fluctuation of flow quantities. That is, with only mathematical manipulation, the Navier-Stokes equations are transformed into an inhomogeneous wave equation, where the derivatives of the flow quantities are formally analogous to acoustic sources. Such formalism is a substantial step in any aeroacoustics study as it suggests the origins of aeroacoustic noise and defines the hybrid approach to investigate the aerodynamic noise.

The hybrid approach, employed in this work, consists in solving the aeroacoustic problem in two steps: first the hydrodynamic field is determined, and later this result is used for building the forcing term to the wave equation. Thus, the present development is not only of scientific importance but also technically meaningful as it allows a cheaper modeling of the acoustic field.

Next, the derivation of the Lighthill equation is presented, with an interpretation of each term the of Lightill's tensor. A different formulation based on flow vorticity, the vortex sound theory proposed by Powell [202], is also discussed.

1.2.2.1 Lightill's equation

First, the time derivative of the mass conservation equation - Equation (1.2.2) - is calculated:

$$\frac{\partial^2 \rho}{\partial t^2} + \frac{\partial^2}{\partial t \partial x_i}(\rho u_i) = 0 \tag{1.2.5}$$

Also, the space derivative (divergent) of the mass conservation - Equation (1.2.3) - is performed:

$$\begin{aligned} \frac{\partial^2}{\partial t \partial x_i}(\rho u_i) + \frac{\partial^2}{\partial x_j \partial x_i}(\rho u_i u_j) &= -\frac{\partial^2}{\partial x_j \partial x_i}(p\delta_{ij} - \tau_{ij}) \\ \frac{\partial^2}{\partial t \partial x_i}(\rho u_i) &= -\frac{\partial^2}{\partial x_j \partial x_i}(\rho u_i u_j + p\delta_{ij} - \tau_{ij}) \end{aligned} \tag{1.2.6}$$

Replacing the right side of (1.2.6) in (1.2.5), we get:

$$\frac{\partial^2 \rho}{\partial t^2} = \frac{\partial^2}{\partial x_j \partial x_i}(\rho u_i u_j + p\delta_{ij} - \tau_{ij}) \tag{1.2.7}$$

Subtracting the term $c_0^2 \nabla \rho$, that represents the dissipation of a density wave at the sound speed, in both sides of the equality, we get:

$$\frac{\partial^2 \rho}{\partial t^2} - c_0^2 \frac{\partial^2}{\partial x_j \partial x_i}\rho = \frac{\partial^2}{\partial x_j \partial x_i}(\rho u_i u_j + p\delta_{ij} - \tau_{ij}) - c_0^2 \frac{\partial^2}{\partial x_j \partial x_i}\rho \tag{1.2.8}$$

Finally, Equation (1.2.8) reduces to the famous Lighthill equation:

$$\frac{\partial^2 \rho}{\partial t^2} - c_0^2 \frac{\partial^2}{\partial x_j \partial x_i}\rho = \frac{\partial^2}{\partial x_j \partial x_i}[\rho u_i u_j + (p - c_0^2 \rho)\delta_{ij} - \tau_{ij}] \tag{1.2.9}$$

that is a non-homogeneous wave equation. The forcing term, hereafter referred to as the Lighthill tensor T_{ij}, is thus defined as:

$$T_{ij} = \rho u_i u_j + (p - c_0^2)\delta_{ij} - \tau_{ij} \tag{1.2.10}$$

Lighthill's tensor is a sum of different contributions associated to flow that produce noise. From the left to the right, we have the flow convection, the propagation of sound with variable speed and the gradual dissipation by conduction (summed by the deviation from the initial pressure-density condition) and the dissipation by viscosity, that is, the attenuation of the sound or noise due to unsteady friction.

Equation reduces to:

$$\left(\frac{\partial^2}{\partial t^2} - c_0^2 \nabla^2\right)\rho = \frac{\partial T_{ij}}{\partial x_i \partial x_j} \tag{1.2.11}$$

The double space derivative indicates that the pressure fluctuations within the flow (issued from the different phenomena discussed in the previous paragraph) act analogously as quadrupoles. This equation is able to model the sound production of any aerodynamic source such as jets and cavities. Nonetheless, by separating the hydrodynamic from the acoustic field, the acoustic feedback, that may act as a frequency selector of the hydrodynamic mode for instance, is not present. This is the main drawback of the formalism.

Considering the acoustic ($\lambda = f/c_0$), flow time (d/U_∞) and spatial derivative ($U_\infty/(c_0 d)$) scales, the acoustic power scales to $W \propto U_\infty^8$.

1.2.2.2 Vortex sound

Introduced by Powell in 1964 [202] and expanded by Howe [76], the vortex sound theory considers the fluctuations in the vorticity field for building its forcing term. The flow equations are transformed to vorticity equations by using vector identities such as the following:

$$\nabla\left(\frac{1}{2}|\mathbf{v}|^2\right) = \mathbf{v}\times\omega + \mathbf{v}\cdot\mathbf{v} \tag{1.2.12}$$

where $\mathbf{v} = \mathbf{u} + \nabla\phi$, with ϕ being the scalar potential that describes the compressible motions.

Once the equations are transformed, the formalism used to obtain the Lighthill's tensor, presented earlier, is applied. The following inhomogeneous wave equation is obtained:

$$\frac{\partial^2\rho}{\partial t^2} - c_0^2\nabla^2\rho = c_0^2\nabla\left[\rho(\omega\times\mathbf{v}) + \nabla\left(\frac{1}{2}\rho|\mathbf{v}|^2\right) - \mathbf{v}\frac{\partial\rho}{\partial t} - \frac{1}{2}|\mathbf{v}|^2\nabla\rho\right] + \frac{\partial}{\partial t}(p - \rho c_0^2) \tag{1.2.13}$$

For the case of an isentropic flow, such that any pressure change must be accompanied by a density change, $\partial(p - \rho c_0^2)/\partial t$ is null. For low speed flows (Ma $\ll 1$), the last three remaining terms are negligible, thus, the equation is reduced to:

$$\left(\frac{\partial^2}{\partial t^2} - c_0^2\nabla^2\right)\rho = c_0^2\nabla\rho(\omega\times\mathbf{v}) \tag{1.2.14}$$

Now, the forcing term is presented as the divergent of the vector product between the vorticity and the flow velocity, and as such, a dipolar source. Main principle of this formulation is to be able to separate the sound generating regions by the distribution of vorticity, vanishing in irrotational regions. Even if not being directly applied to this work, the principle of thinking of the aeroacoustic sources as transformations of the vortices and of the vorticity field was an inspiration for some parts of the analysis employed here.

1.2.3 The effect of boundaries and integral solutions

Further historical development considers the separation between the sound emitted by the flow eddies (the quadrupole sources in the Lighthill's equation) and the sources associated with walls. Deduction here will be performed in the reverse of what was chronologically defined. First, the development by Ffwocs Williams & Hawkings [275] will be described, and later simplified into the Curle's analogy. The acoustic notation, with the source at $\mathbf{y}$ and the observer at $\mathbf{x}$, as represented on Figure 1.6, is considered on this work.

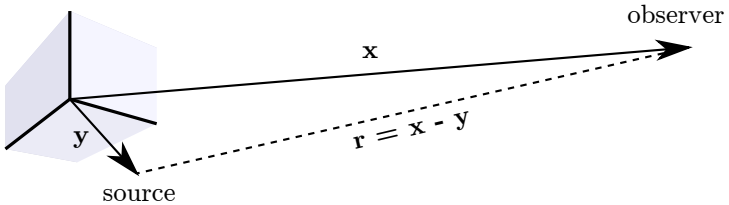

Figure 1.6: Diagram representing the location of source and observer.

The derivation of the Ffowcs Williams-Hawkings equation starts by the definition of an arbitrary control volume V enclosed by a surface $\sum$ and a moving boundary defined by the surface S, with velocity $\mathbf{v}$. A Heaviside-like variable s is defined as 0 at the surface S, $s < 0$ at the interior and $s > 0$ at the exterior. After some rearrangements, the source term is separated into 3 terms (considering the x_i axis system to represent the observer):

$$\left(\frac{\partial^2}{\partial^2 t} - c_0^2\nabla^2\right)\rho = \frac{\partial^2 T_{ij}}{\partial x_i\partial x_j} - \frac{\partial}{\partial x_i}\left(p_{ij}\delta(s)\frac{\partial s}{\partial x_j}\right) + \frac{\partial}{\partial t}\left(\rho_0 v_i\delta(s)\frac{\partial s}{\partial x_i}\right) \tag{1.2.15}$$

where δ is the Dirac delta function and $p_{ij} = (p - c_0^2)\delta_{ij} - \tau_{ij}$ is the compressive stress tensor, v_i is the velocity component of the surface and T_{ij} equals the Lighthill's stress (Equation (1.2.10)). Outside any surfaces, the analogous sound sources are the quadrupoles as in Lighthill's equation, the second term is the source distribution of acoustic dipoles associated with the presence of the boundary S and the third element are surface distributions of monopole sources representing the volume displacement effect. That is, the volume displacement of the movement surface is analogous to a dipole of strength proportional to the acceleration of the surface and a quadruple proportional to $v_i v_j$ [69].

Different formulations are possible based on the definition of the control volume, each one with different advantages and drawbacks, specially in terms of the numerical solution of the equations. For example, when considering all the regions as a static control volume, the surface sources are null such as to return to Lightill's equation.

Consider then a generalized non-homogeneous wave equation and Q_{ij} sources:

$$\left(\frac{\partial^2}{\partial^2 t} - c^2 \nabla^2\right)\Phi = \frac{\partial^n Q_{ij} \cdots}{\partial x_i \partial x_j \cdots} \tag{1.2.16}$$

The integral solution by using the free space Green's functions is of the form:

$$\Phi(x,t) = \frac{1}{4\pi c_0^2}\int_{-\infty}^{+\infty} \frac{\partial^n Q_{ij} \cdots (y,\tau)}{\partial y_i y_j \cdots} \frac{\delta(\tau - t + r/c_0)}{r} dy d\tau \tag{1.2.17}$$

where $r = |\mathbf{x} - \mathbf{y}|$ is the distance between the source and the observer. When considering the sources indicated on Equation (1.2.15), one obtains the following formulation for the acoustic pressure, also known as Curle's equation:

$$4\pi c_0^2 P(x,t) = \frac{\partial^2}{\partial x_i \partial x_j}\left[\int_V \frac{T_{ij}}{r} dV\right] - \frac{\partial}{\partial x_i}\left[\int_S \frac{(p_{ij} n_j + \rho u_j u_n)}{r} dS\right] + \frac{\partial}{\partial t}\left[\int_S \frac{\rho u_n}{r} dS\right] \tag{1.2.18}$$

where u_n is the outward normal velocity of the boundary of the control volume S and P is the acoustic pressure $P = p - p_0$. All the elements are evaluated at the retarded time $t - r/c_0$.

1.2.3.1 Curle's model

By setting the surface to be placed at the walls of the cylinder of null velocity ($u_n = 0$), as considered by Curle [37], Equation (1.2.18) is reduced to:

$$4\pi c_0^2 P(x,t) = \frac{\partial^2}{\partial x_i \partial x_j}\left[\int_V \frac{T_{ij}}{r} dV\right] - \frac{\partial}{\partial x_i}\left[\int_S \frac{p_{ij} n_j}{r} dS\right] \tag{1.2.19}$$

By neglecting the quadrupoles at the control volume, significantly less noise than the surface terms at low Mach [37], the following formulation is obtained:

$$4\pi c_0^2 P(x,t) = -\frac{\partial}{\partial x_i}\left[\int_S \frac{p_{ij} n_j}{r} dS\right] \tag{1.2.20}$$

The equation is simplified by some hypothesis concerning the observer position and the source properties:

- **Far-field approximation**: at a point far enough of the flow and the acoustic sources, the space derivatives can be approximated by the time derivatives:

$$\frac{\partial}{\partial x_i} \approx \frac{x_i}{c_0 |\mathbf{x}|}\frac{\partial}{\partial t} \tag{1.2.21}$$

- **Compactness**: if the dimensions of the source, in this case the diameter of the cylinder, are negligible in comparison to a sound emission characteristic length (normally the wave length of a mode of interest [77], $|x| \gg \lambda$), the differences in retarded time for the different instances of the body are negligible and the body may be considered as a point source. Also, the source-to-observer distance may considered approximately the distance from the observe to the origin of the source:

$$\frac{1}{r} = \frac{1}{|\mathbf{x} - \mathbf{y}|} \approx \frac{1}{|\mathbf{x}|} \tag{1.2.22}$$

After applying those hypothesis, changing from space to time derivative and evidencing the retarded time, following formulation is obtained:

$$4\pi c_0^2 P(x,t) = -\frac{\partial}{\partial x_i}\left[\int_S \frac{p_{ij} n_j}{r} dS\right] = -\frac{x_i}{c_0 r}\frac{\partial}{\partial t}\left[\int_S \frac{p_{ij}(t - r/c_0) n_j}{r} dS\right] \tag{1.2.23}$$

1.2.3.2 Sound radiated by a cylinder at its shedding frequency

The surface integral of $p_{ij} n_j$ around the cylinder's wall equals, by definition, to the opposite of aerodynamic force around the cylinder $-F_i(t - r/c_0)$. For an observer at a distance r of the source, orthogonal to the incoming flow, the sound pressure radiated from an acoustically compact solid surface reduces to:

$$P(r,t) = \frac{1}{4\pi c_0}\frac{x_i}{r^2}\frac{\partial F_i(t - r/c)}{\partial t} \tag{1.2.24}$$

Under this condition (observer at a freestream location and a compact source), the sound intensity grows with the velocity to an exponent 6, while the acoustic efficiency follows a U_∞^3 proportionality. This correlates with the performed hypothesis that at low Mach the sound emitted by the eddies (represented by the Lighthill's tensor) are negligible (U_∞^8 versus U_∞^6) when compared to surface sources for low Mach flows.

Further simplifications can be performed. By neglecting the retarded time (compact, far-field), and dividing the aerodynamic effort lift and drag, one arrives to:

$$\frac{\partial F_i(t - r/c)}{\partial t} \approx \frac{(\partial L(t) + D(t))}{\partial t} = \frac{\partial L(t)}{\partial t} + \frac{\partial D(t)}{\partial t} \tag{1.2.25}$$

Neglecting the fluctuating drag ($\partial D(t)/\partial t \approx 0$), and considering a lift effort defined by its lift coefficient C_L (the lift divided by the dynamic pressure multiplied by the lifting surface $\ell \times d$) and assuming that the lift does not depend on the spanwise location, equation is transformed to:

$$\frac{\partial F_i(t - r/c)}{\partial t} \approx \frac{\partial C_L(t)}{\partial t}(1/2\rho_0 U_\infty^2 d\ell) \tag{1.2.26}$$

where ℓ is the length of the cylinder, its spanwise extent. Further assuming the lift as a perfect sinusoidal wave of angular velocity ω, the time derivative is simplified into:

$$\frac{\partial C_L(t)}{\partial t} = \omega C_L(t) \tag{1.2.27}$$

Since the lift oscillates at the vortex shedding frequency, $\omega = 2\pi \mathrm{St} U_\infty / d$, we may replace (1.2.27) in (1.2.24):

$$P(r,t) = \frac{1}{4\pi c_0}\frac{r_i}{r^2}\omega C_L(t)(1/2\rho_0 U_\infty^2 d\ell) = \frac{1}{4\pi c_0}\frac{x_i}{r^2}\rho_0 U_\infty^3 \mathrm{St}\ell C_L(t) \tag{1.2.28}$$

Applying the mean square operation for a complete vortex shedding cycle, and considering that the geometry is geometrically compact ($\ell \ll r$) and for an observer at the axial center of the cylinder so that $x_i \approx r$, we get:

$$\overline{P}^2(r) = \frac{\rho_0^2 U_\infty^6 \mathrm{St}^2 \ell^2 C_L'^2}{16 c_0^2 r^2} \tag{1.2.29}$$

where C_L' is the RMS lift coefficient of the cylinder.

Although its multiple hypotheses, this formulation remains an important tool for the description of the cylinder noise be highlighting the principal ingredients that are: the incoming flow properties (ρ_0, U_∞, c_0), evidencing the exponent 6 for the incoming velocity; the position of the observer (r); the span of the cylinder (ℓ) and the characteristics of the vortex shedding (St, C_L'). This work is interested in the later two, naturally influenced by both the regime (Re) and the shape of the cross-section.

Nevertheless, the presented formulation is based on the hypothesis that the flow can be represented by a single, spatially continuous, fluctuating effort. In other words, that the aerodynamic effort is completely phased in the axial direction. For flow at larger Reynolds numbers (Re > 150 for the circular cylinder, as discussed in Section 1.1.2.1), the flow is 3D, so considering that the cylinder is in its totality submitted to the same pressure fluctuations is erroneous. Some propositions to correct this inconsistency found in the literature are described next.

1.2.3.3 Accounting for the effect of the spanwise decorrelation

Equation (1.2.29) is derived from the hypothesis that the aerodynamic effort is two-dimensional, that is, the flow and forces at the different spanwise sections of the cylinder are completely phased. This results in an overestimation of the sound emission, since it considers that the full extent of the cylinder is producing, simultaneously, the same forcing term the acoustic field. Different approaches are used to describe and get around this problem, some of them presented next. Note that such issues are also present in the models of sound emission by aerodynamic profiles, for instance, in the formulations proposed by Amiet [6].

1.2.3.3.1 Correction using indicators of the flow spanwise distribution Two similar formulations are found for quantifying the flow's axial de-correlation: the spanwise correlation and spanwise coherence. Here, a brief introduction of those quantities in the context of a cylinder's sound emission is given. Further development is found in Section 4.3, where the mathematical formalism, the experimental procedure and the results are presented.

From the development of the integral of the surface elements into a lift effort that vary axially (in y_3), starting from Equation (1.2.20), Phillips [191] introduces the parameter of spanwise correlation (or axial correlation), Λ, that equals the integral of the spanwise lift correlation. The correlation is a measurement of the similarity of the flow's response at different locations. It measures the causal linear link between two signals of a flow quantity (normally the lift or the surface pressure) measured simultaneously at two distinct axial coordinates (same y_1 and y_2, distinct y_3). That way, a quantification of the de-correlation is performed. This principle is also present in the work of Keefe [109], that used a definition based on the centroid of the area formed by the spanwise distribution of correlation as the representative quantity, retaken by Leehey & Hanson [130]. Finally, Equation (1.2.29) is actually transformed in:

$$\overline{P}^2(r) = \frac{\rho_0^2 U_\infty^6 \mathrm{St}^2 \ell \Lambda C_L'^2}{16 c_0^2 r^2} \tag{1.2.30}$$

In a more refined analysis, the coherence (spectral evaluation of the correlation) may be considered and the coherence length ℓ_c employed as the indicator to quantify the de-correlation. The coherence is a measure of similarity of the signals evaluated using their spectral distribution, thus, accounts for the difference in behavior associated with the distinct hydrodynamic modes that exist in the wake and even extends to the broadband part of the flow. Multiple definitions

of the coherence length exist, such as the integral of the coherence (similar to what is performed for the correlation) or the coefficient of the fitting function [30]. Finally, the formulation is similar as the one presented earlier for the Aeolian tone and an observer normal to the incoming flow. The only difference is the coherence length (for a Strouhal number and coherence length evaluated at the vortex shedding frequency):

$$\overline{P}^2(r) = \frac{\rho_0^2 U_\infty^6 \mathrm{St}^2 \ell \ell_c C_L'^2}{16 c_0^2 r^2} \tag{1.2.31}$$

Equation (1.2.32) is a reference for the experimental work performed here, only evaluated considering the frequency and coherence at the vortex shedding. Fujita [57] adds a term to account for the near-field contributions, presented next, not considered in the analyzes performed here but used to validate the experimental setup.

$$\overline{P}^2(r) = \frac{\rho_0^2 U_\infty^6 \mathrm{St}^2 \ell \ell_c C_L'^2}{16 c_0^2 r^2} \left[1 + \left(\frac{\lambda}{2\pi r} \right)^2 \right] \tag{1.2.32}$$

where $\lambda = c/f$ is the wave length.

Both corrections are rather crude approximations. Even so, they clarify even further the key ingredients of the sound emission of cylinders. Focusing on the shape dependent ones, St, ℓ_c and C_L' are evidenced. Also, it has to be stated that even for a fixed shape, these elements are strongly dependent on the Reynolds number, cylinder end-conditions, upstream turbulence and cylinder vibration [130].

1.2.3.3.2 Spanwise statistical model Casalino & Jacob [30] proposed a statistical model of the lift efforts which considers the spanwise perturbation of the flow, notably end effects and vortex displacement, as a stochastic term. This randomness is associated with reduction of the sound amplitude and also with the peak broadening. The aerodynamic effort is considered as:

$$C_L(y_3, t) = C_{L,\max} \exp\{-i(2\pi \mathrm{St} t + \Upsilon(y_3))\} \tag{1.2.33}$$

where $C_{L,\max}$ is the maximal lift coefficient, Υ is a variable representing the random phase shift. From the central limit theorem, this random variation is approximated to a Gaussian distribution. This description is important by its focus on the random nature of turbulence and by evidencing the role of such effects on the vortex shedding and sound emission. Also, it is used as the basis of some methods proposed to correct the span of 2D/short-span simulation, discussed further.

1.2.3.4 Span effect and methods for span correction

As depicted on the derived equations, the magnitude of the sound emission is directly affected by the length of the cylinder. As discussed in [106, 111, 158] and in others articles, the length of the cylinder has an important effect on the aerodynamic field mostly by its influence on the role of end-effects (tip and/or joint vortices) in the vortex shedding. Even if ignoring these aspects, the sound emission is still going to be influenced by the inevitable de-phasing at higher Reynolds numbers. Based on this intrinsic condition and motivated by the difficulty to perform simulations and experiments with long cylinders, some studies have been performed in order to propose methods to compensate the obtained result to approximate the estimation to what would be generated by a body with a longer span.

A rudimentary approach is to virtually increase the span by considering the forcing term in the acoustic analogy as copies, axially displaced and completely phased, of the flow around the short-span cylinder that was simulated, as performed by Cox et al. [35] and later reproduced by Orselli et al. [177] and Du et al. [48]. Depending on the size of the initial segment, the de-correlation effect is not accounted for.

More complex methods think the total emission as partitioned by different sub-segments of a longer cylinder. Introduced by Kato [108], the principle is to define a span length (ℓ_s) within

which the flow is completely phased and radiates an acoustic emission of amplitude $\overline{P}_s^2$, and later separating the cylinder into N_s sub-segments of that given length ($N_s = \ell/\ell_s$). Making the hypothesis that all the segments have an identical acoustic response and that are only lagged, it is possible to make a simplified formulation of the sum of their individual contributions, as illustrated on Figure 1.7.

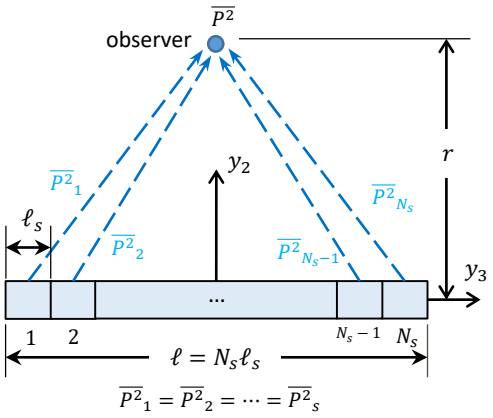

Figure 1.7: Cylinder spanwise segmentation, based on Figure 1 in [233].

Seo & Moon [233] arrived to the following formulation for the sum of the contributions of the segments to be equivalent to the sound emission $\overline{P}^2$ of a long-span de-correlated flow (the coherence function and the coherence length arises from the mathematical development, not shown here):

$$\overline{P}^2(\Omega) = \overline{P}_s^2(\Omega)\left\{\sum_{i=1}^{N_s}\sum_{j=1}^{N_s}\exp\left[-(i-j)^2\left(\frac{\ell_s}{\ell_c(\Omega)}\right)^2\right]\right\} \tag{1.2.34}$$

where Ω is a frequency quantity.

Following the same principle, Perot et al. [206] proposed a different formulation that accounts for the differences in retarded time due to the varying observer-source distance for each segment. Doolan [46] expanded the principle by considering a 2D simulation of the forcing term and performing a correction of the peak broadening based on the signature of the flow turbulence.

In terms of practical applications, the use of these formulations can be problematic for two reasons. First, the absence of the retarded time can cause wrong estimations for longer cylinders. Second, in a real application or even in a controlled environment such as a wind-tunnel measurement, it is impossible to obtain a flow that can be separated in segments which radiate the exact same acoustic intensity only de-phased. Both points are further developed in Section 4.5 and 4.6, where these models are used for the deduction of the RMS lift and the relationship between the length and the sound emission is checked experimentally, respectively.

1.2.4 Compact tonal sectional model

From the solution of the Curle's equation with a 2D free-field convected Green function, neglecting the quadrupoles and maintaining only the first modes of the Fourier expansion, Margnat [145] arrived to the following scaling law for the tonal (at the lift fluctuation frequency) sound emission of a compact cylinder:

$$W = \frac{\pi}{16}\rho_0 U_\infty^3 d\ \mathrm{St}_{\mathrm{peak}}\ \mathrm{Ma}^2(2C_D'^2 + C_L'^2) \tag{1.2.35}$$

where W is the acoustic power (integral of the acoustic intensity at an arbitrary radius) and $\mathrm{St}_{\mathrm{peak}}$ is the Strouhal number corresponding to the vortex shedding frequency. The acoustic power is shown to be directly proportional to the incoming flow properties, the square of the Mach number, the Strouhal number and a sum of the square of the RMS lift and drag coefficients

(factor 2 for the drag coefficient comes from the fact that the drag oscillate at twice the frequency of the lift). Since $\rho_0 U_\infty^3 d$ represents the reference power (by unit length) supplied by the incoming flow, all results presented on this article are for the non-dimensional acoustical power W_a, quantifying an acoustic efficiency:

$$W_a = \frac{W}{\rho_0 U_\infty^3 d} = \frac{\pi}{16}\ \mathrm{St}_{\mathrm{peak}}\ \mathrm{Ma}^2(2{C'_D}^2 + {C'_L}^2) \tag{1.2.36}$$

An important merit of this almost analytic solution is to condense the key elements of the sound emission of compact bodies in 2D. The acoustic efficiency is evidenced to be directly equivalent to a combination of 3 shape-and-Reynolds number dependent quantities: $\mathrm{St}_{\mathrm{peak}}$, C'_D, and C'_L. In the current study, since the totality of the hypothesis and considerations are respected, this is the methodology used to quantify and compare the acoustic signature of the different shapes and flow regimes, with negligible loss of precision.

1.3 Airframe noise and context of the current work

Airframe noise is the sound produced by the interaction of the flow with an object, by the mechanisms explained earlier. Unlike other sound radiation sources encountered in moving vehicles, these sources are not related to propulsion or jets, but simply to the flow perturbations that are found when the fluid adapts to the imposed boundaries and the associated flow dynamics. As described earlier, the presence of an obstacle is responsible for a sound emission that is proportional to U_∞^6. The airframe noise is not, in most cases, the most important source of noise. Since the 1980's, the aiframe noise is an important element in the design of airplanes once the sound emission levels demanded in the certification could not be reached only by power-plant noise control alone [36].

From all the possible sources of aiframe noise, such as cavities and aerodynamic profiles, this work is restricted to cylinder noise. Nevertheless, many studies are devoted to its mechanism in the literature, mostly focusing on the description of a given shape and the mitigation of the radiated sound. For instance, a significant attention is given to the study of pantograph noise, illustrated in the Introduction, focused on the reduction of its amplitude and the definition of low order models and scaling laws that represent the expected noise signature [84, 87, 88, 212, 251]. In those cases and in any other application related study, the geometrical simplification of the tested product can be problematic by its possible changes in the dynamics of the flow interactions.

More academic and physical oriented works may be narrowed down to a simple setup of a uniform incoming flow and a fixed, undeformable cylinder with no incidence. By engaging in describing the effect of the cross-section, this work is strongly funded in previous studies. A discussion around what is found in the literature is presented next.

1.3.1 Previous studies of the influence of the cross-section on cylinder noise

Different studies focused on the description of the shape influence on the cylinder noise production are presented next.

1.3.1.1 Numerical

Naturally, the simulation of the sound emission of cylinders of canonical shapes is more present in the literature. These studies are more focused on the mathematical and computational development of the technique to solve the problem of the sound emission of obstacles. There is, for instance, the direct solution of the two-dimensional unsteady compressible Navier-Stokes equations by Inoue & Hatakeyama [90] and the study of the separation of the sound emission between direct and scattered components by Gloerfelt et al. [66].

Nevertheless, some studies focused on comparing the flow and sound emission produced by different geometries can also be found, most of them in 2D. Some of them are listed next:

the article by Aoki & Ishihara [7] with the 2D simulation of the sound emission by circular, square and lozenge cross-sections at Re = 20,000; the 3D investigation of the sound emission of rectangular sections of multiple aspect ratios using LES by Rokugou et al. [217], Re = 10,000; the quantification of the influence of the aspect ratio on the sound emission of rectangular sections at low Reynolds (Re = 150) by Inasawa et al. [89] using a DNS compressible solution in 2D; the study of Margnat [145] of the influence of the angle of incidence in the noise radiated by rectangular sections using a hybrid acoustic analogy and an incompressible DNS solver at Re = 150; and the 2D analysis of the effect of a downstream wedge on the sound emission of a square cylinder performed by Samion et al. [228] at Re = 22,000, using OpenFOAM.

Despite the greater range of cross-sectional shapes, they remain somehow as simple transformations of canonical geometries (in incidence, extended, etc). Even so, the results and conclusions present on these works contributed to the understanding of the phenomena and the analysis performed here.

1.3.1.2 Experimental

By the difficulty to perform experiments with different shapes, the number of experimental studies of the shape influence on the sound emission is smaller than the number of those that employ numerical tools. Nonetheless, while many studies are exclusively focused on the circular cylinder, some works that evaluated the noise emission of different prismatic bodies can be found: the wind tunnel testing of two rectangular cylinders at incidence by Nakato et al. [160]; the study of wall-mounted geometries performed by Becker et al. [16], who used a square cylinder combined with elliptical and triangular wedges and afterbodies; King & Pfizenmaier [111], who studied a set of different cross-sections (circular, elliptical, rectangular) and cylinder lengths; Moreau & Doolan [158], who evaluated the flow and noise emission of wall-mounted circular and square cylinders of multiple lengths; Iglesias et al. [83], also for elliptical and rectangular prisms, and mostly focused on the influence of the yaw angles, aiming at the application to pantographs noise prediction [84]; and more recently, Octavianty et al. [174], who studied different rectangular sections and also performed the measurements of the spanwise flow distribution.

For such studies, there is a discrepancy in the amount of knowledge that is gathered about the flow. In general, while the topology is exhaustively described in the study of short cylinders (span/diameter lower than 10), a rather poor description of the flow is found on the remain studies (long-span cylinders). The argument for such difference in description is evident when thinking about the richness of the flow in the two contexts. Since the latter is less influenced by end-effects, discussions and conclusions are mostly based on hypothesis of spanwise homogeneity of the flow. Consequently, the knowledge of the influence of the cross-section on the flow and the noise emission, simultaneously, is poor, point discussed on this document.

1.3.2 Current trends

The problem of the sound emission of a circular cylinder is considered rather established, being used as benchmark for simulations (for example [18, 257]). Nonetheless, some developments such as the investigation of the effect of the yaw angle [83], of surface roughness [5], multiple rod configurations (combinations of cylinders, spanwise devices such as wires, finns and collars) [8, 81], active control by using plasma actuators [116], rotation [48] and other techniques, the study of the length influence on wall-mounted cylinders [200], for instance.

In the sense of mitigating the fluctuating efforts and the sound emission, the use of porous surfaces (for example, [9, 61, 136, 157, 250]) is one of the passive strategies that has been widely investigated. The addition of layers of permeable materials around the cylinders has been proven to efficiently reduce the tonal and broadband noise of a cylinder by affecting the flow field and suppressing the vortex-shedding. Similar results are is also obtained with the use of hairy flaps [105]. A similar principle is being largely studied for airframe noise in general, notable with the use of porous and/or serrated edges for aerodynamic profiles, as discussed, for example, in [60] and [97]. The sound reduction is associated with the decreasing of the spanwise correlation of

the flow.

Both strategies - looking for a further understanding of the flow and noise production of canonical cylinders and proposing devices and techniques for the reduction of their sound emission - are important and may provide interesting solutions for the current application of these geometries in industrial contexts. Current work, by focusing on the description of the shape-flow-noise relationship, is a complement of such studies.

1.4 Principal questions and current approach

The core of this investigation is to answer the following question: how does the shape of the cross-section affects the sound emission? This is fundamentally a multidisciplinary question, that involves the flow's instability, the aerodynamic field and the acoustic phenomenology, all briefly discussed in this chapter. Globally, the problem can be condensed in 3 ingredients (illustrated on Figure 1.8): the fluctuating aerodynamic efforts, the spanwise flow distribution and the frequency of the vortex shedding.

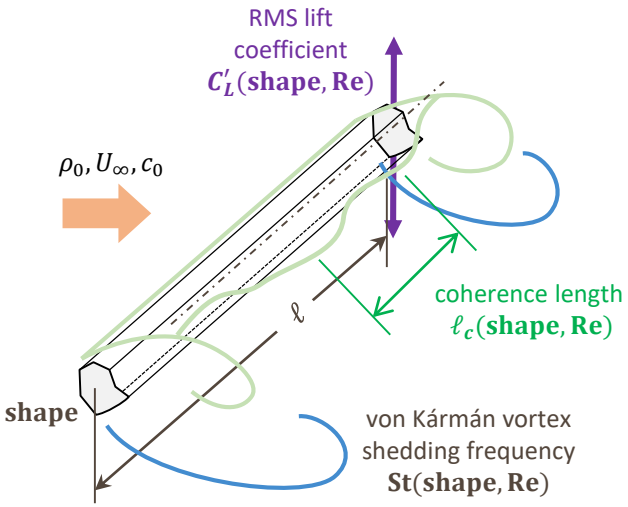

Figure 1.8: Representation of the principal ingredients for the cylinder noise.

The shape influences, simultaneously, the amplitudes and frequencies of the hydrodynamic mode, the details of the flow topology and its acoustic signature, changing the 3 parameters. By being limited to a restricted set of geometries, much of the accumulated knowledge on these subjects cannot be easily extrapolated, especially in what concerns modeling and prediction of the response of different shapes.

The principle of current investigation is to extract knowledge of the influence of the geometrical features by expanding the catalog of bluff bodies that are investigated. Two different approaches are considered in this work: the simulation of the flow in 2D and measurements in an anechoic wind tunnel.

The simulations are performed using an incompressible Direct Navier-Stokes (DNS) solver, for low-Reynolds flows. Such setup is relatively cheap, with the complete flow solution being reached within a few hours. This allowed the use of several cases of canonical shapes at multiple Reynolds numbers (see Section 2.2), to perform parametric studies (Section 2.4) and to optimize the geometry for different shape parametrizations (Chapter 3). Despite the obvious limitations due to the absence of the axial dimension, important relationships and empirical laws are derived. Equation (1.2.35) with the formula for the acoustic power of sound emitted by compact cylinders is used in the numerical work.

For the experimental part, reported in Chapter 4, the focus was also to study a different set of geometries. The number of tested shapes was of about 20. The acoustic field is simply evaluated using far-field microphones. As discussed earlier, there is poor knowledge of the flow

for any geometry other than the circular and square cylinder, point investigated by hot-wire anemometry measurements. Measurements of the spanwise correlation and coherence, scarce even for canonical shapes, are as well performed.

The two techniques are not only complementary in a physical point of view, since the basic mechanism of vortex shedding is the same in both low and high-Reynolds flows [187], but also in the analysis perspective. The absence of the third dimension on the first part allows a cleaner examination of the results, while the experiments expand the observations in 2D, low Reynolds number to a regime close to application.

Chapter 2

The shape influence on two-dimensional laminar flow noise

The study of the shape influence on the sound emission is performed by simulating the flow around several cross-sections. The discussion about the noise production of bluff bodies fluctuates around the frequency (tone), its level and the directivity. Naturally, these 3 elements are modified with the magnitude of the incoming velocity, that is, the flow Reynolds number. However, as discussed in Chapter 1, the von Kármán instability is a phenomenon that exists in a large range of regimes, both in 2D and 3D. In order to study the shape influence, it is necessary to model the flow for a large set of forms, thus, 2 choices are made concerning the range of operation of the study: to work in 2D and at low Reynolds number.

Any analysis in 2D is naturally deficient. The absence of the third dimension results in ignoring part of the complexity of the phenomenon and restraining the applicability of the results. Nevertheless, the analysis of such regime has the benefit of allowing performing simulations that are completely defined without the need to model the viscous dissipation (DNS) and the computational limitations present in a study where the spanwise direction is present.

In order to have a 2D simulation that is physically meaningful, most of the studied flows are at Reynolds numbers below Re = 150, considering the height of the body d as the reference length. At such Re, the flow around circular and square sections is completely in phase in the spanwise direction [10, 28, 98]. Even if there is no guarantee that the same happens for all the shapes tested here (point discussed further in the chapter), the analysis at such regime in 2D may be considered representative of the physics of the flow. At such regime, the use of the aeolian tone model presented in Section 1.2.4 is possible without any loss of physical accuracy of the solution [145].

The combination of these two conditions results in an extremely cheap and robust framework that makes it possible hundreds to thousands of simulations (about 70,000 within the 3 years of this work). When looking at the influence of the shape, the reliability of the generalization of the trends and the universality of the behaviors is a direct function of the number of cases that are studied. For the main goal of this work, the use of several cases (combination of geometry and Reynolds number) is a fundamental brick in the construction of the conclusions that are drawn.

This first part of results in the manuscript consists in the simulation and analysis of several canonical shapes. The conclusions are derived principally from the observations of the fields and the performance of a statistical analysis for the definition of empirical laws, accompanied by discussions around the physics of the vortex-shedding in 2D.

The chapter is started (Section 2.1) with the description of the numerical solver and setup, with a short introduction of the IBM's principle and current formulation. The description of the methodology is followed by Section 2.2 with the presentation and general description of the tested shapes and the observed integral and topological features of the flows. Empirical relationships based on the obtained results for the canonical shapes come next in Section 2.3, with a distinction between topology and shape based laws. Some parametric tests are presented in Section 2.4,

with further discussions about the geometrical features that influence the vortex shedding and noise generation. Finally, Section 2.5, contains a summary of the observed behaviors and a discussion regarding the outcome of results in the face of the project's objective.

This work was performed in its most part in parallel to the optimization analysis described in Chapter 3. As such, some of the conclusions and directions taken in the analysis are derived from the observations that were made possible by the optimal shapes. A large part of this chapter is being published in [194] and [197].

2.1 Methodology

The numerical tools used to model the aerodynamic and acoustic behaviors of the flow around bluff bodies are presented in this section.

The analysis is restricted to 2D, laminar flows. The application is also aimed to low Mach cases without any acoustic feedback, consequently the aerodynamic solution may be incompressible with negligible losses in terms of fidelity of the solution. Due to its relative simplicity, the solution can be performed using a DNS solver without prohibitive computational costs.

In order to obtain the acoustic signature of the different shapes, the incompressible aerodynamic field is analyzed using a hybrid aeroacoustical procedure. The focus is given to the total acoustic efficiency so the tonal model presented on Section 1.2.4 is the only acoustical evaluation performed on this part of the work. This formalism is completely compatible with the other properties of the flow (compact, 2D, laminar, low Mach). For the evaluation of the acoustic power, the Mach number (undefined in the simulation) is chosen arbitrarily as Ma = 0.1 (acoustic results scale with Ma^2).

The solver and the numerical setup are detailed next. The acoustics notation with x_i for the observer axis system and y_i for the source is used.

2.1.1 Solver

The flow is numerically predicted using the code Incompact3d in 2D. It is a high-order solver with a 6^{th}-order, compact centered finite difference scheme for the evaluation of space derivatives, and a 3^{rd}-order Runge–Kutta time-marching scheme.

Flow's incompressibility is assured in a fractional step method, with the solution of a Poisson equation in the spectral domain using the FFTW3 library [56]. For a better numerical behavior, the mesh is staggered for the pressure field. The grid is uniform streamwise (y_1) and stretched in the transverse direction (y_2). The stretching is considered in the solver such as to have the exact evaluation of the spatial derivatives. More details are available in [124].

In order to allow the evaluation of a large set of different geometries, the description of the obstacles is applied with the use of a virtual solid domain, described next.

2.1.2 Immersed Boundary Method (IBM)

The non-slip conditions associated towith an obstacle are implemented using an Immersed Boundary Method (IBM). It consists in applying a modification in the flow equation in order to account for the presence of walls with a grid that is non-conformal to the obstacle. Current use profits from that property, since the simulation of multiple shapes is possible without re-meshing. This advantage is fundamental in the optimization studies presented further in Chapter 3.

Since the walls are virtual, information on wall quantities (such as surface pressure or skin friction) is not directly available. An extrapolation method based on the nodes neighboring the artificial contour is implemented, but its validity is not confirmed. Due to that limitation, despite its importance on the comprehension of the flow dynamics, such quantities are mostly absent in this work. In the spirit of highlighting tendencies rather than performing refined descriptions, their absence does not reduce the pertinence of discussions and conclusions presented herein, even if the performed observations could benefit from their presence.

The principle of the method is presented next, with a description of the version that is implemented in the solver used in current work.

2.1.2.1 Principle and background

Initially proposed by Peskin [188], it was originally intended for the simulation of flow in the presence of complex, deformable shapes such as the human heart. The principle is that the presence of the bodies is not accounted from a deformation of the elements but by a modification of the equations such as to perform the correction in the flow quantities due to the presence of the solid object. The main advantage concerns the capability to be applied to any complex geometry without the need to perform complex meshing steps and mesh adaptation (notable in fluid-structure simulations) [155], since its implementation is extremely compatible with finite difference codes.

An extensive list of examples of applications of the IBM formalism can be found in [189]. Most of them deal with complex or deforming shapes. While the current use for the simulation of simple, rigid cylinders is rather marginal and mostly presented as a benchmark (for instance, [122, 125, 131]), applications of the IBM to similar configurations can be found in flow stability studies [185, 192, 281].

There are two methods for applying the forcing approach [155]: a continuous approach, where the forcing is implemented to the flow equations; and a discrete approach, where the forcing is added at the grid points after the discretization of the domain, performed by ghost cells or using the cut-cell methodology. In this case, there is an interpolation of the quantities to implicitly impose the boundary condition (for example, [142]).

For the continuous forcing approach, the flow equations are mathematically the same for all the grid points. Considering an incompressible flow, the forced momentum equation is as follow:

$$\frac{\partial \mathbf{u}}{\partial t} + \mathbf{u}_j \frac{\partial \mathbf{u}_i}{\partial y_j} = -\frac{\partial}{\partial y_j}[p\delta_{ij} - \tau_{ij}] + \mathbf{f} \tag{2.1.1}$$

where $\mathbf{f}$ is the forcing term. Multiple methods exist based on how $\mathbf{f}$ is defined, for instance, the explicit feedback forcing, the semi-implicit feedback forcing, and the direct forcing studied by Lamballais & Silvestrini [125]. The explicit feedback forcing, considered as the most efficient and realistic method in the latter work, is used in this work and presented next.

One important drawback of this technique is the difficulty to employ it at high Reynolds numbers [155]: the refinement imposed by the increase of the Reynolds number must also be applied to the solid domain, resulting in an elevated number of grid points; the smoothing provoked by the forcing term results in a poor representation of sharp edges. For the current range of study ($\mathrm{Re} = 30 - 200$), both issues are irrelevant.

2.1.2.2 Implementation

Current application employs the principle of the forcing model proposed by Goldstein et al. [68] for the simulation of rigid bodies, that defines the forcing term by a feedback loop derived from the linear control theory:

$$\mathbf{f}(\mathbf{y}, t) = \alpha \int_0^t \mathbf{u}(\mathbf{y}, t)dt + \beta \mathbf{u}(\mathbf{y}, t) \tag{2.1.2}$$

where α and β are negative constants that characterize the system. They work analogously to spring and damping coefficients, thus, control the amplitude and establishment time of the response and consequently the convergence properties of the formulation.

The principle is applied via the formulation proposed by Margnat & Morinière [147], where the second order behavior is explicited:

$$\mathbf{f}(\mathbf{y}, t) = -\epsilon(\mathbf{y}) \left[\omega_n^2 \int_0^t \mathbf{u}(\mathbf{y}, t)dt + 2\zeta\omega_n \mathbf{u}(\mathbf{y}, t) \right] \tag{2.1.3}$$

where, ω_n is the natural frequency and ζ is the damping coefficient (both positive) of the second order controller that forces a null velocity everywhere ϵ is non null. The time integration of the forcing term is performed using a left rectangle quadrature of the Runge Kutta sub-timestep. A detailed description of the time marching for the code is present at [125]. In this work, the IBM coefficients are $\omega_n = 50$ and $\zeta = 1$, based on [147].

Selection of the solid and fluid domains is based on the position of each velocity node: $\epsilon = 1$ (forced grid points) if the node is inside the analytic contour and $\epsilon = 0$ elsewhere. There are no interpolation of the forcing term or refinement close to the boundaries. By the integration of the momentum equation around the solid domain, the aerodynamic forces are directly available by the sum of the forcing terms [145], since the flow is frozen at the walls and in the solid domain.

As described in previous paragraphs, the use of the IBM formalism is extremely advantageous in regards of the simplicity to simulate different shapes without the need to reshape. Despite the easy use, this implementation imposes a limitation in the geometrical precision of the curves as big as the cells size as can be seen on Figure 2.2, discussed later, and there is a lack of information regarding the boundaries of such shapes, once the walls are modeled by a forcing term, and not really accounted for as a boundary condition.

It must also be reinforced that, as damped harmonic oscillators, the elements in the solid domain have their own dynamics of vibration and response to excitation and are subjected to instabilities [129], clearly more restrictive than the flow numerical stability conditions on current implementation [125]. Further discussions about this issue for the current solver and IBM implementation can be found in [147].

2.1.3 Numerical setup

Regarding the grid and the domain, a careful convergence study has been conducted for a generic shape, in order to obtain a fruitful trade-off between low estimation time of the unsteady flow statistics and errors. Based on the tests reported in Appendix A, the domain, illustrated on Figure 2.1 is set $25d$ long in the streamwise and $20d$ in the crosswise direction, and discretized in 649×257 nodes. The center of the geometry is at $11d$ from the inflow boundary, at the middle of the transverse direction. The boundaries are defined as follows: inlet velocity of U_∞, convective condition at the outlet and free slip for the lateral boundaries.

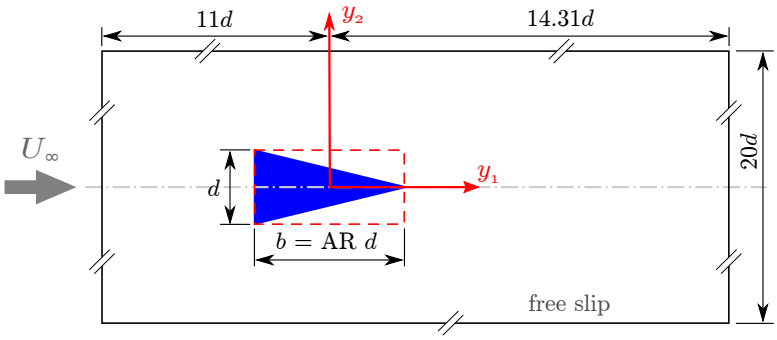

Figure 2.1: Representation of the numerical setup.

Due to the use of an IBM formalism with no wall treatment or interpolation, the geometrical precision is limited to the grid size, as illustrated by the solid and fluid domains presented on Figure 2.2. For the chosen refinement (mesh 2 in Appendix A), there are about 26 cells in a distance of length $1d$. Results obtained with a refined version of the grid (mesh 4, with the double of nodes in both directions) are also present on parts of the work, notably in validation. It is observed that for the investigated regime and quantities of interest, the coarser mesh represents a good compromise in terms of fidelity and computation costs. More details and examples can be found in Appendix A.1.2.

Next, the results for the simulation of several cross-sections are presented. For all of them, the numerical setup is exactly the same.

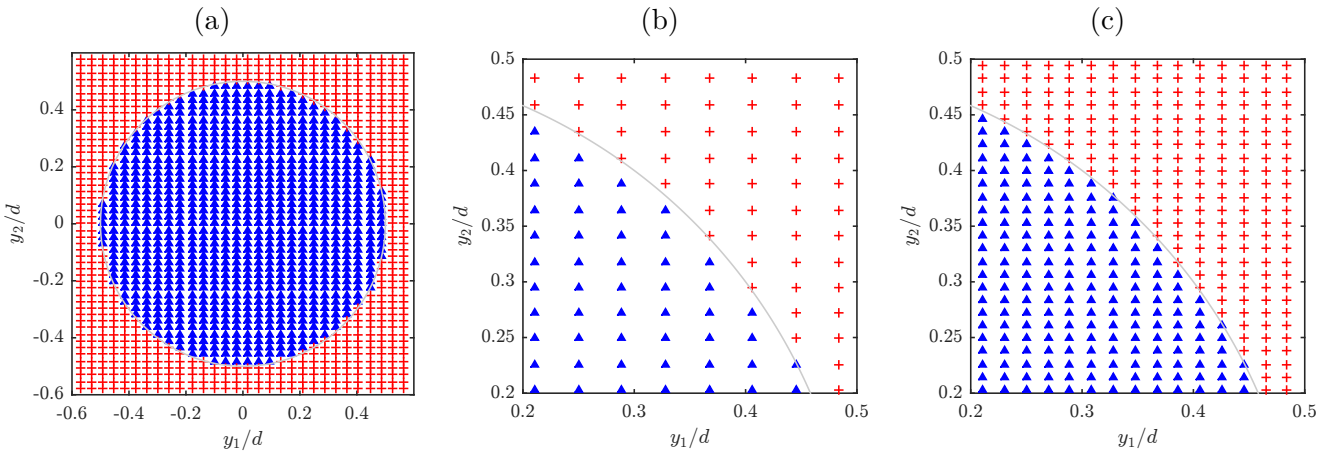

Figure 2.2: Representation of the discrete IBM representation of circular section with solid triangles for the elements at the solid domain ($\epsilon = 1$) and crosses for the fluid domain ($\epsilon = 0$). Represented grids are the base mesh - mesh 2 - in (a), focused on boundary in (b) and more refined mesh - mesh 4 - used in parts of the work in (c).

2.2 Study of canonical geometries

The simulation of the flow for a large set of different cross-sections is performed in 2D. The use of canonical shapes is privileged such as to benefit from their presence in the literature, allowing validation and providing technical and conceptual elements for the current discussions. Also, it places the study closer to industrial applications, even if not at the same regime (except when quantifying the onset of unsteadiness in Section 2.2.3, all the simulations are performed at Re = 150).

It is aimed at a general description of the results with a discussion around the shape influence on the behaviors. Both aspects are explored further in Section 2.3 where correlation between quantities and empirical laws are presented.

First, the tested shapes are presented. Second, a general description of the obtained flows in terms of integral quantities and flow topology is presented. Finally, the study concerning the transition to unsteadiness for a part of the geometries closes the section.

2.2.1 Tested geometries

In order to investigate the shape influence on the aeolian tone, several cross-sections of fixed height d are simulated (see Figure 2.3, noting that the half ellipsoids are not included in the whole study). Besides the construction paradigm (rectangle, front-pointing and back-pointing triangle, lozenge, ellipse, front-pointing and back-pointing half ellipse), the sectional breadth b, condensed in the non-dimensional parameter aspect ratio AR = b/d, is also modified. In total, 104 cases (combination of geometry and aspect ratio) are simulated. The model shown in the diagram of the numerical setup Figure 2.1 is the back-pointing triangle (trib) of aspect ratio AR = 2.0.

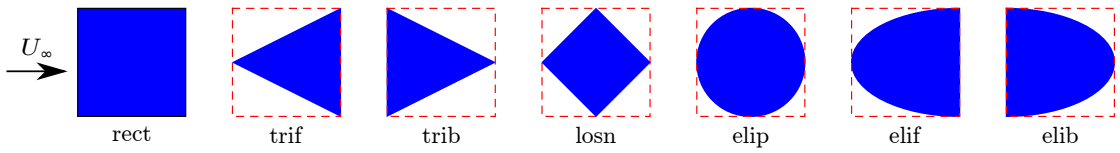

Figure 2.3: Set of tested geometries, at unitary aspect ratio, from left to right: rectangle (rect), front-pointing triangle (trif) and back-pointing triangle (trib), lozenge (losn), ellipse (elip), front-pointing half ellipse (elif), back-pointing half ellipse (elib).

Note that the use of the geometrical paradigms illustrated in Figure 2.3 is an artifice for having several geometries that share common features. That is, each individual case (geometrical paradigm + aspect ratio) is an independent shape by itself, however the fact that only the aspect ratio is modified allows for an analysis based on those subgroups and to check tendencies associated with the breadth of the obstacle.

2.2.2 General flow description

This section is dedicated to the general description of the flow from integral quantities to topological features, focusing on the differences and similarities that are obtained when modifying the shape and the aspect ratio. The discussion is based on the integral quantities (mean and RMS drag coefficients, RMS lift coefficient - mean lift is null due to symmetry - and Strouhal number), flow topology and two associated quantities (recirculation length and formation length).

2.2.2.1 Integral quantities

2.2.2.1.1 General trends Figure 2.4 presents the evolution of integral quantities (average drag coefficient, RMS lift and drag coefficients and Strouhal number) with the aspect ratio. For all the geometries, the response to an increase of AR is similar: a reduction of RMS and average drag coefficients and a rapid increase followed by a peak and a slow decrease of C_L' and St; the change of tendency (from growing to decreasing) noted for the last 2 variables is discussed later in the document (Section 2.2.2.2).

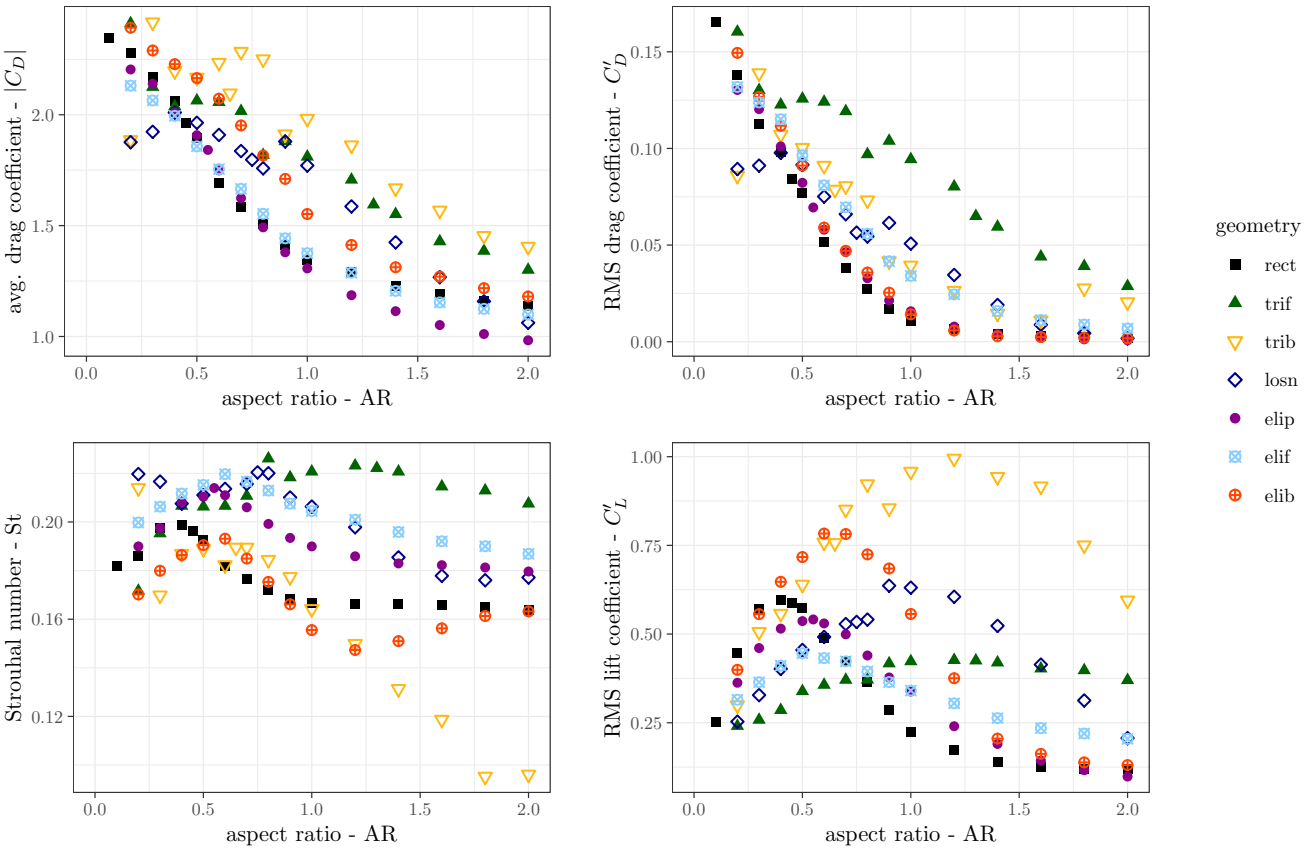

Figure 2.4: Evolution of the mean and RMS drag coefficients, Strouhal number and RMS lift coefficient with the aspect ratio for all tested shapes, Re = 150.

In terms of noise production, the estimation of the acoustic efficiency provided by Equation (1.2.35) and (1.2.36) is applied and the results are illustrated on Figure 2.5. The considered acoustic analogy based model indicates that $W_a = f(\mathrm{St}, C_D'^2, C_L'^2)$, where all the variables are shape dependent. The relationship between the acoustic efficiency and the square of the lift

coefficient fluctuation is as well presented in Figure 2.5. The fact that a linear trend is noted indicates that among the 3 terms the $C_L^{'}$ is the major factor in the construction of the tonal noise.

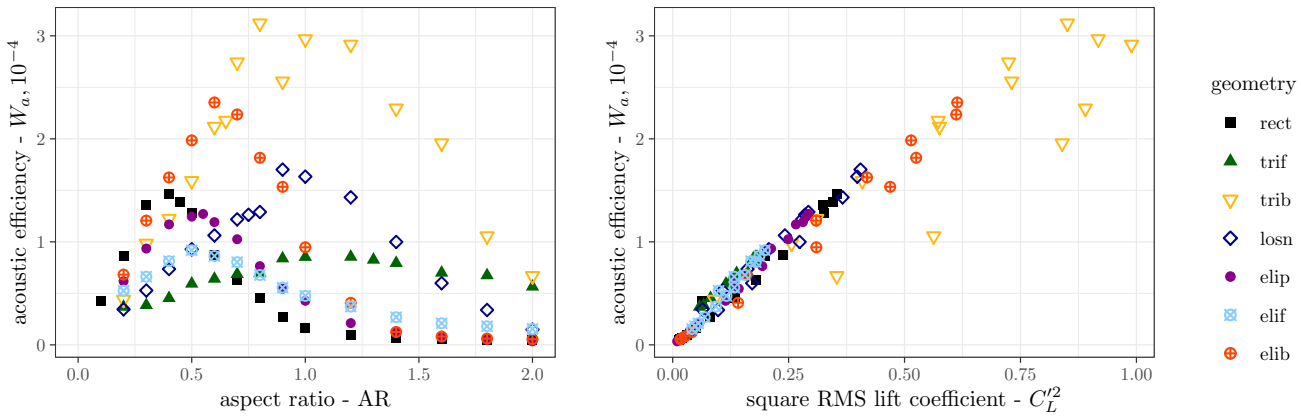

Figure 2.5: Evolution of the acoustic efficiency with the aspect ratio (left) and the relationship of the acoustic efficiency and the RMS lift coefficient (right), Re = 150.

It is observed that the fluctuating lift is the most relevant quantity not only in terms of magnitude but also in its dependency to shape. While the other two parameters (St,$C_D^{'}$) are only slightly modified when comparing different geometries (Strouhal number values lies in the range of 0.12 to 0.22 and the fluctuating drag is about 1/10 of the fluctuating lift), the $C_L^{'}$ is the quantity that has a more scattered distribution considering the tested geometries. In the same direction, previous optimization studies performed by the author under the same hypothesis and tonal noise formulation for 2 distinct shape parametrizations [38, 195] found that the geometries that have extreme behavior (minimum or maximum) in terms of acoustic efficiency and RMS lift coefficient are practically the same.

2.2.2.1.2 Influence of shape Globally, the elliptical and square sections can be taken as shapes that minimize the average and fluctuating efforts. On the other hand, the back-pointing triangle is the shape that has the biggest drag and the highest RMS lift coefficient. The front-pointing triangles are the obstacles with the biggest Strouhal numbers and RMS drag coefficients. The dichotomy between the two triangles is an interesting result that correlates to the concept of "bluffness" introduced by Roshko [220]. When considering the St, those shapes represent the extrema (trif the maximum and trib the minimum). This can be justified by the difference in the orientation of the lateral boundaries: while for the front-pointing triangle the shear layers are pushed away form each other, the walls of the back-pointing triangle induce to an approach of these layers. Distant layers correspond to wider wakes, thus, higher Strouhal numbers [51, 215, 220]. Even if not as extreme, same conclusion is noted when comparing the half-elliptical sections elif and elip. More details are provided with the quantification of flow topology features, presented next.

2.2.2.2 Flow topology

In terms of flow topology, the typical unsteady von Kármán wake is present for all the geometries with a periodic vortex shedding. Overall, for the average flow, there is a flow acceleration on the laterals sides of the body, marked by negative spanwise (y_3) vorticity (defined as $\omega_3 = \partial v/\partial y_1 - \partial u/\partial y_2$) on the upper and positive on the lower hemispheres of the section; u reaches up to 1.5 the inlet velocity and the maximum magnitude of v is of about 0.5 U_∞; the pressure is increased upstream and a base value is encountered in the downstream part of the body where a recirculation region is present in the averaged flow. The described flow is exemplified on Figure 2.6, where mean fields of the flow around the square section are presented.

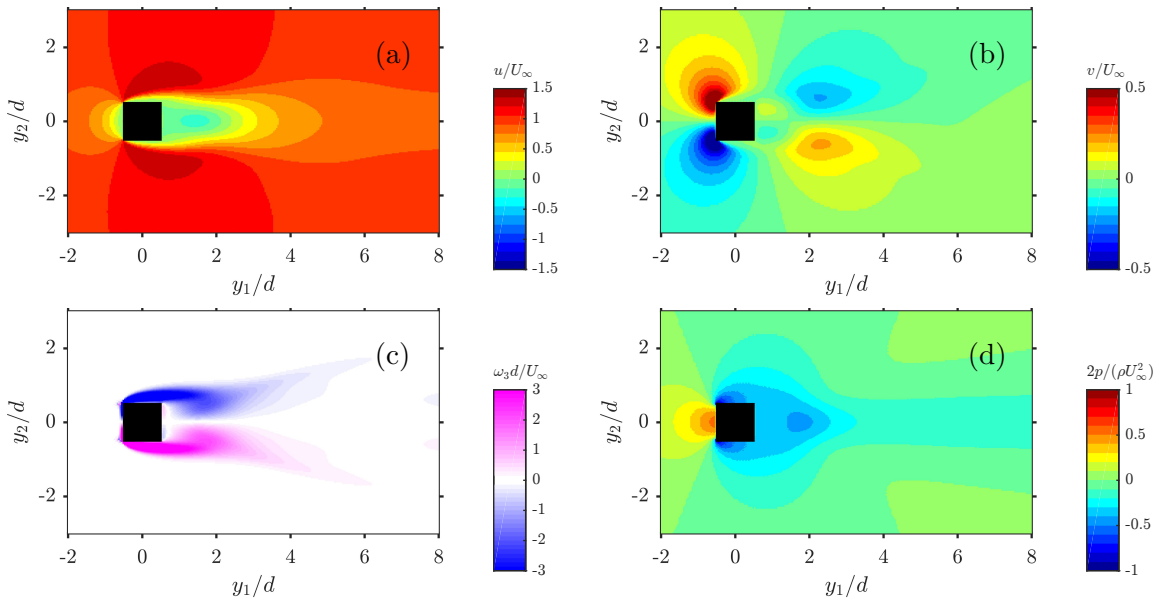

Figure 2.6: Mean flow fields for the square section (rect, AR = 1.0): (a) streamwise velocity; (b) crosswise velocity; (c) spanwise vorticity ω_3; and (d) pressure p. Re = 150.

As far as the far-wake vortex distribution is concerned, two regimes are noted and shown in Figure 2.7. At regime I, all vortices that are shed are kept aligned in a single row that has its center coincident to the axis of symmetry of the obstacle. For regime II, the initial single row wake transforms into 2 rows of vortices of equal vorticity sign. For all the tested geometries there is a clear distinction between the aspect ratios that generates each one of these two vortex arrangements, and the change from geometries with initially single and further downstream double (regime II, for "small" AR, generally speaking) to and completely single row (regime I, "big" AR) is associated with the peaks of RMS lift and Strouhal highlighted previously in Section 2.2.2.1.1.

The existence of these two very distinguishable wake regimes is studied further and presented in Section 2.2.3.4.

2.2.2.3 Formation length and recirculation length

Two variables are evaluated in order to quantify the flow distribution in the near body wake: the recirculation length L_r, taken as the size of the average flow recirculation bubble in the streamwise direction and defined by the furthest downstream node that has null average y_1-velocity; and the formation length L_f, a measurement of the distance between the body and the region of maximal flow perturbation that is analogous to the region where the vortices are shed. The interest in quantifying these values resides in the fact that these parameters are related to the vortex shedding by the characterization of the mean flow topology and the position where the vortices are shed, thus, representative of the noise production mechanism.

Different definitions are found in the literature for the formation length [33]. In this manuscript, it is based on the position of the point where the RMS of the streamwise velocity fluctuation (u') is maximal. The formation length is then defined as the distance between the downstream limit of the body and this position:

$$L_f = y_1 \text{ of } \max(u') - \frac{\text{AR}}{2} \tag{2.2.1}$$

Figure 2.8 shows three examples of recirculation and formation lengths by superinposing the u' field and the mean flow streamlines.

As exemplified in Figure 2.8, for small AR, the formation length is smaller than L_r. For extended bodies, $L_f > L_r$. The evolution of the two quantities with the aspect ratio is presented in Fig. 2.9.

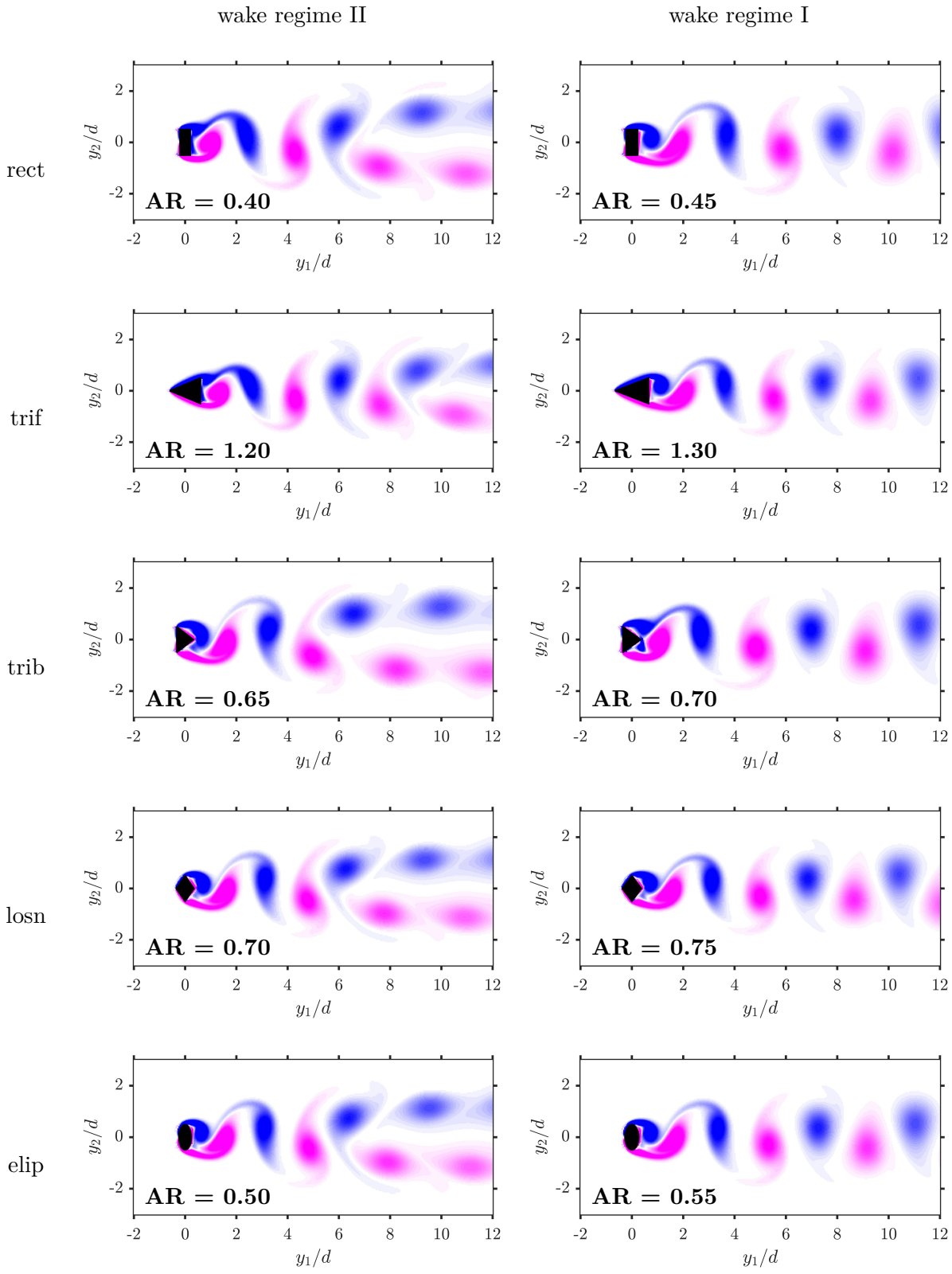

Figure 2.7: Instantaneous vorticity contour for the two wake regimes, multiple geometries. Vorticity scale is of $\omega_3 = [-3d/U_\infty, +3d/U_\infty]$, same as in Figure 2.6. Re = 150.

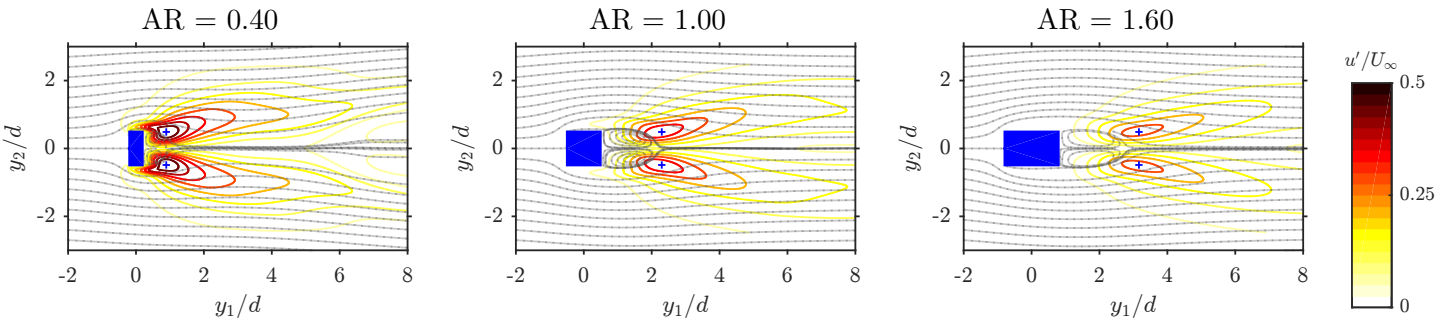

Figure 2.8: Field of RMS streamwise velocity (u') superinposed on the mean flow streamlines for rectangular sections (rect) of multiple AR, Re = 150. Crosses represent the position of maximum u'.

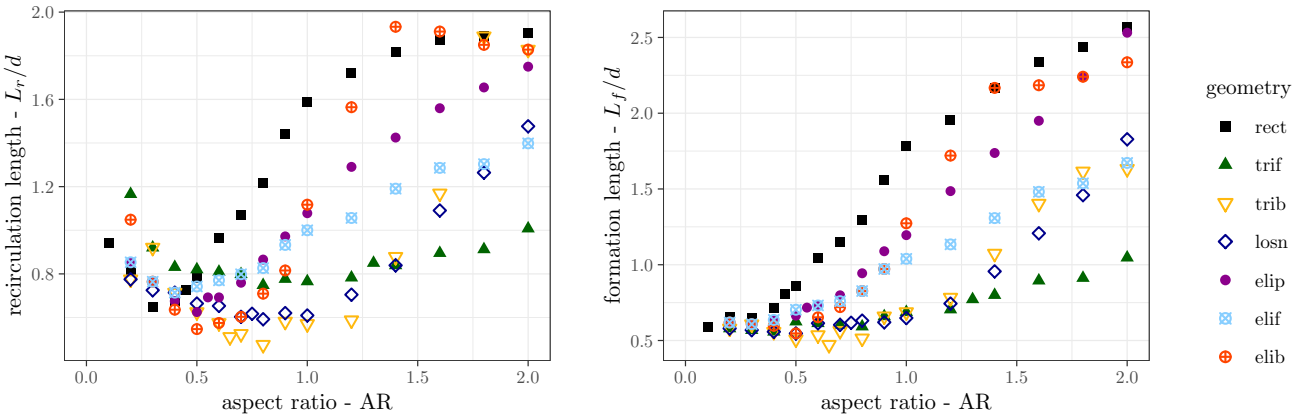

Figure 2.9: Evolution of the recirculation length (left) and formation length (right) with the aspect ratio, Re = 150.

The formation length undergoes a monotonic growth with the increase of the aspect ratio. For the recirculation length, from AR = 0.1 to 2.0, there is an initial decrease followed by an increase. For the elliptical section, for example, this change in tendency is observed at AR = 0.55. This is believed to be provoked by flow non-linearities around the shorter sections, as discussed by Pier [192]. It can also be noted that there is a lower limit $\min(L_r) \approx 0.6d$, also present for the formation length $\min(L_f) \approx 0.6$. This behavior is the exact opposite of what is noted in the curves of C_L' and St (Figure 2.4) that have peaks, as pointed out by Islam et al. [91] and Inasawa et al. [89].

For longer geometries, both recirculation and formation lengths are increased, what synthesizes the fact that the longer the geometry, the more dissipation takes place at the walls. That means that the wake is less energetic (noted by the reduction of the magnitudes at the RMS velocity fields in Fig. 2.8), and the flow instability is pushed downstream. Aiming at a quantification of that energetic state, a discussion about the distance of the flow to the onset of unsteadiness is presented next.

2.2.3 Quantification of the distance to the onset of unsteadiness

The change of cross-section shape is fundamentally a modification of how a corresponding excitation is going to take place in the fluid. However, as the body is the origin of that excitation, it is also an alteration of the "forcing" condition that leads the flow to behave differently. In this sense, an energetic based parameter must also be considered when comparing flow around different geometries.

Although being intuitive, the relationship between the velocity and force fluctuations has not yet been well investigated [172]. One of the strategies to characterize the shape influence

on noise is then an analysis based on flow instability principles, once the perturbations in the wake are directly associated with the instability modes for both the frequencies and amplitudes [192, 232, 288]. Based on the fact that, close to the steady to unsteady flow transition, the velocity fluctuations may be proportional to the corresponding distance to transition, the following parameter is used [165, 171, 232]:

$$\varepsilon = \frac{\mathrm{Re} - \mathrm{Re}_c}{\mathrm{Re}_c} \tag{2.2.2}$$

where Re_c is the critical Reynolds number that marks the transition from steady to unsteady flow.

It is a rather global criterion, representing the distance to the onset of unsteadiness for each shape, being closer to account for the geometrical specificities than the Reynolds number itself. In that sense, ε may be taken as a parameter that quantifies a given flow position in a geometry independent scale, being more associated with an universal change in the flow response mechanism with the increase of flow inertia and less with the response of the flow to the geometry change itself.

Apart from the circular and square cylinders and a few publications on the flow transition for elliptical sections [93, 185, 261], studies of the flow transition for other shapes are scarce in the literature. Consequently, in order to quantify the parameter ε for each shape studied here, it was necessary to define the critical Reynolds number. A methodology based on the current numerical setup is proposed and presented next together with the results in terms of the critical Reynolds nunber and a comparison between the behavior noted for the different geometrical paradigms that are tested. Results presented here have been previously communicated in [197].

2.2.3.1 Methodology for obtaining the critical Reynolds number

Due to the facility of performing multiple simulations in a short time, the chosen strategy for defining the critical Reynolds number is applying a bisection method for each geometry, starting with lower and upper limits of Re = 30.0 and Re = 90.0, respectively, and stopping when the difference between the steps is smaller than 0.25. That means that the error is of $\pm$ 0.25.

Rather than considering the force coefficients as an indicator of the flow unsteadiness, the flow quantities themselves are preferred due to the intrinsically different behavior of the solid domain for different geometries issued from the chosen numerical formalism. Indeed, since the wake is less perturbed by geometrical modifications than the aerodynamic efforts, that means, it has a more universal trend. Therefore considering the wake quantities is a more robust procedure to quantify the physics.

The transition between steady and unsteady flow is more evident from the fields of fluctuating variables, as presented on Figure 2.10. It is a confirmed fact that the flow around a circular cylinder transitions between Re = 45 and Re = 50, which could not be found by simply observing the vorticity field. After several tests, the RMS y_2-velocity (used to illustrate the transition in Figure 2.10) is chosen as the variable of interest for its unanimity in describing the transition in terms of magnitude (fluctuations are bigger than the other flow quantities) and location.

Since the definition of steady or unsteady flow is performed in the algorithm, an objective criterion must be defined; 8 probes are thus placed in the wake and the values of the y_2-velocity are recorded at all simulated timesteps (see Figure 2.11). For the quantification of the unsteadiness, the maximal deviation between the y_2-velocity at all times and the average velocity of it for a sub-set of timesteps is considered. For the probe k:

$$\hat{v}(k) = \frac{1}{n}\sum_{t=1}^{n} v(k, N-t) \tag{2.2.3}$$

$$\Delta v = \max|v(k, N-t) - \hat{v}(k)| \tag{2.2.4}$$

where n is the frame size, selected as 2250 (physical time of about 15 d/U_∞), and N is the last timestep that has been simulated. Probe positions are presented on Figure 2.11. The magnitude

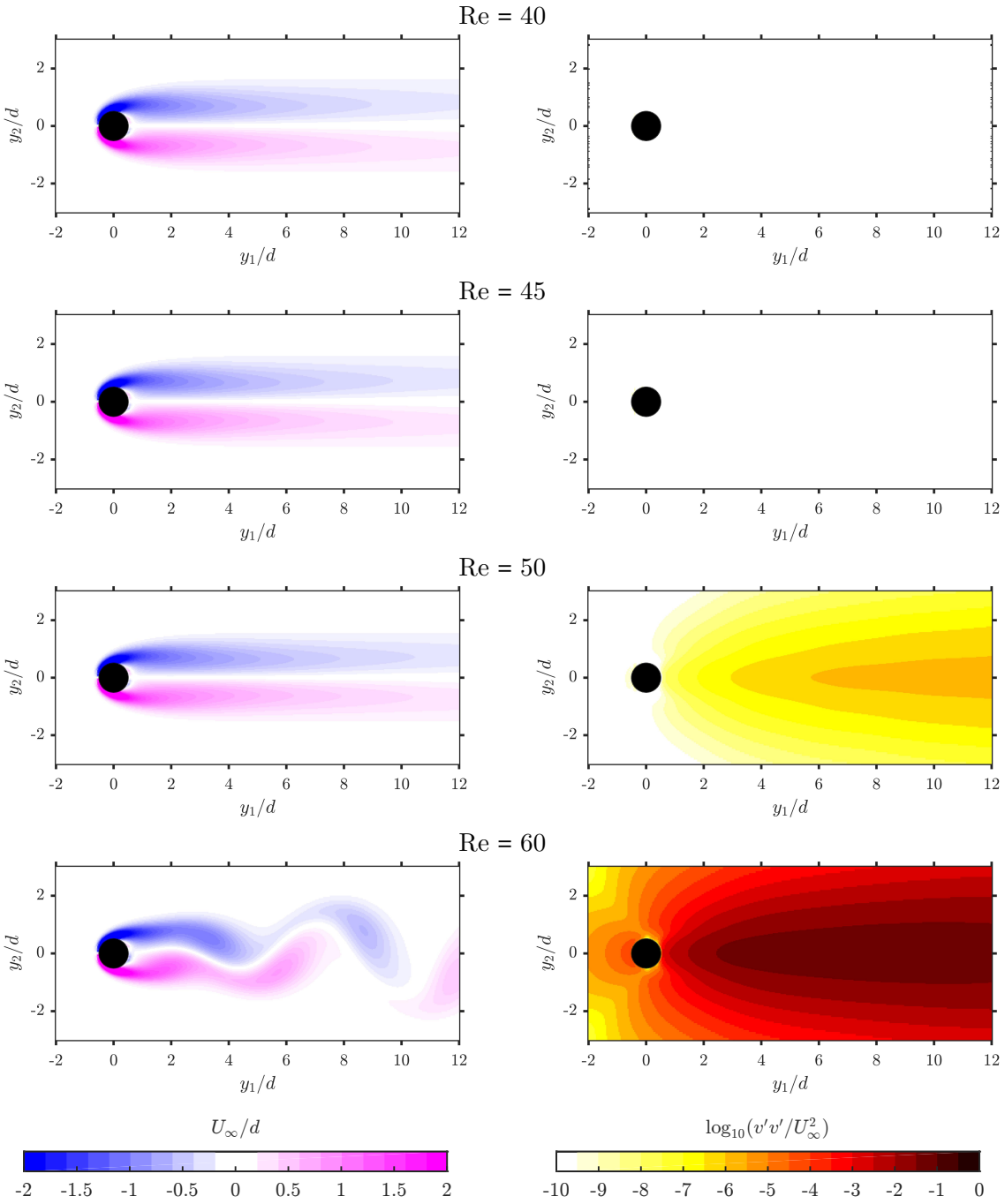

Figure 2.10: Evolution of the instantaneous vorticity ω_3 (left) and mean square of the y_2-velocity fluctuation (right) fields with the Reynolds number for the circular section (elip, AR = 1.00).

of the oscillation of the y_2-velocity remains high further away from the obstacle. After testing, probe #7 is selected due to its universality, meaning that flow fluctuations for unsteady flows were analogous at that position. The fact that it is far from the solid domain is advantageous since the near wake variances, intrinsic to each shape, are not important and also it is not influenced by the fluctuations due to the use of an IBM formalism.

The curves on Figure 2.12 illustrate the behavior of the y_2-velocity for different geometries (elip, rect and trif) at AR = 1.0. The proposed criterion represents well the evolution of the amplitude of the fluctuations, without any knowledge of the mean flow and no risk of wrong interpretation due to instantaneous low value. Naturally, the magnitude is not null in any occasion, since there are numerical errors and the solution comes from a perturbed state due to the flow initialization and the settling of the nodes in the solid domains through the IBM.

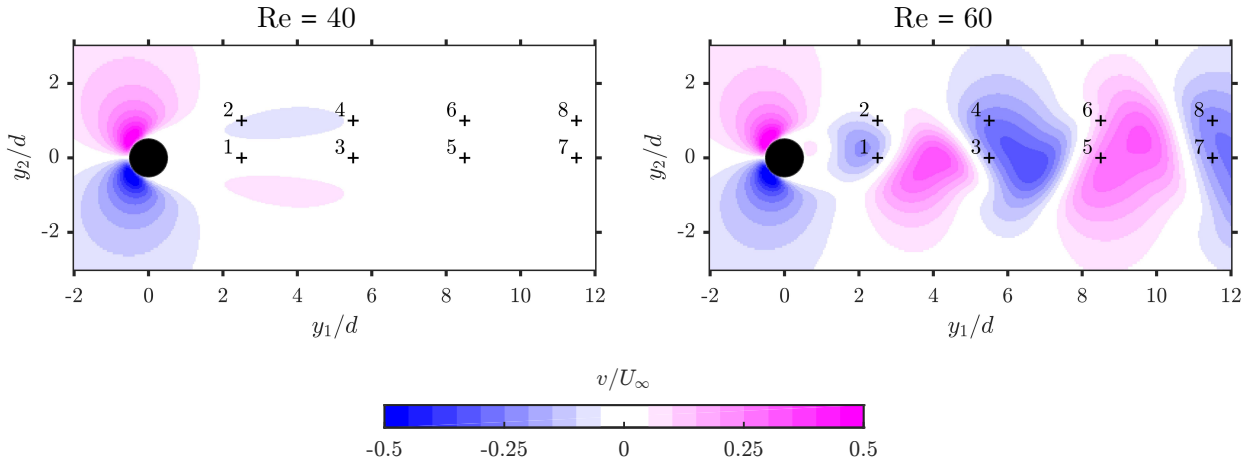

Figure 2.11: Illustration of the instantaneous y_2-velocity fields with the tested probes for a steady (upper) and unsteady (lower) flow, circular cylinder (elip, AR = 1.00). Probes start from $y_2 = 2.5d$ and finish at $y_1 = 11.5d$, uniformly spaced; odd probes are on the symmetry axis while the even probes are located at $y_2 = 1d$.

However, it is clear that, for the steady regimes, the deviation decreases. Based on what is observed for the circular cylinder, the criteria for defining the unsteadiness is $\Delta v > 10^{-4}$. This could also be performed looking at the time trend of the Δv criteria, but due to possible local deviations, the saturation at the end and the necessity to follow the evolution of the parameter $\hat{v}$, the simplest option of using the value of the last frame is selected. Considering that the time used in the computations is of 180 td/U_∞ (that equals to 25,000 timesteps with the base timestep duration), there is a safe margin associated with the given value.

Compared to the procedures used by Paul et al. [185], the current technique seems more appropriate since it does not rely on any continuity regarding the behavior of the instability. Since the flow is directly simulated, the present definition of the critical Reynolds number lies on what is observed in the simulations and not based on extrapolations of values observed on neighboring points.

2.2.3.2 Estimated critical Reynolds numbers and validation

Obtained critical Reynolds numbers are presented on Figure 2.13 for the tested shapes. For all the tested geometries, an increase of the aspect ratio is associated with an increase of the critical Reynolds number. A discussion about the aspect ratio and the geometry influence on the critical Reynolds number is presented on Section 2.2.3.3.

Values obtained in the current work are compared to reported Re_c for circular, square and front-pointing triangle (trif) sections, AR = 1.0, listed on tables 2.1 to 2.3. Results are within literature values, and despite the relatively poor precision, are well representative of the dynamics encountered in more recent works. The fact that a good result is observed for different geometries argues in favor of the use of the IBM technique and the current bisection procedure and the threshold.

However, it must be reinforced that the selected threshold of 10^{-4} is completely arbitrary and based solely on observation of the flow. Consequently, it is possible that it is not adapted to the full set of tested geometries, thus, adding an uncertainty in the results. Also, this means that such value may not be applicable to other configurations and numerical setups. Nonetheless, such facts are not in discordance with the philosophy of the analysis, because of the foregrounding of the differences in behavior associated with the shape, and not an elevated precision in the definition of the critical Reynolds number, is envisaged in this investigation.

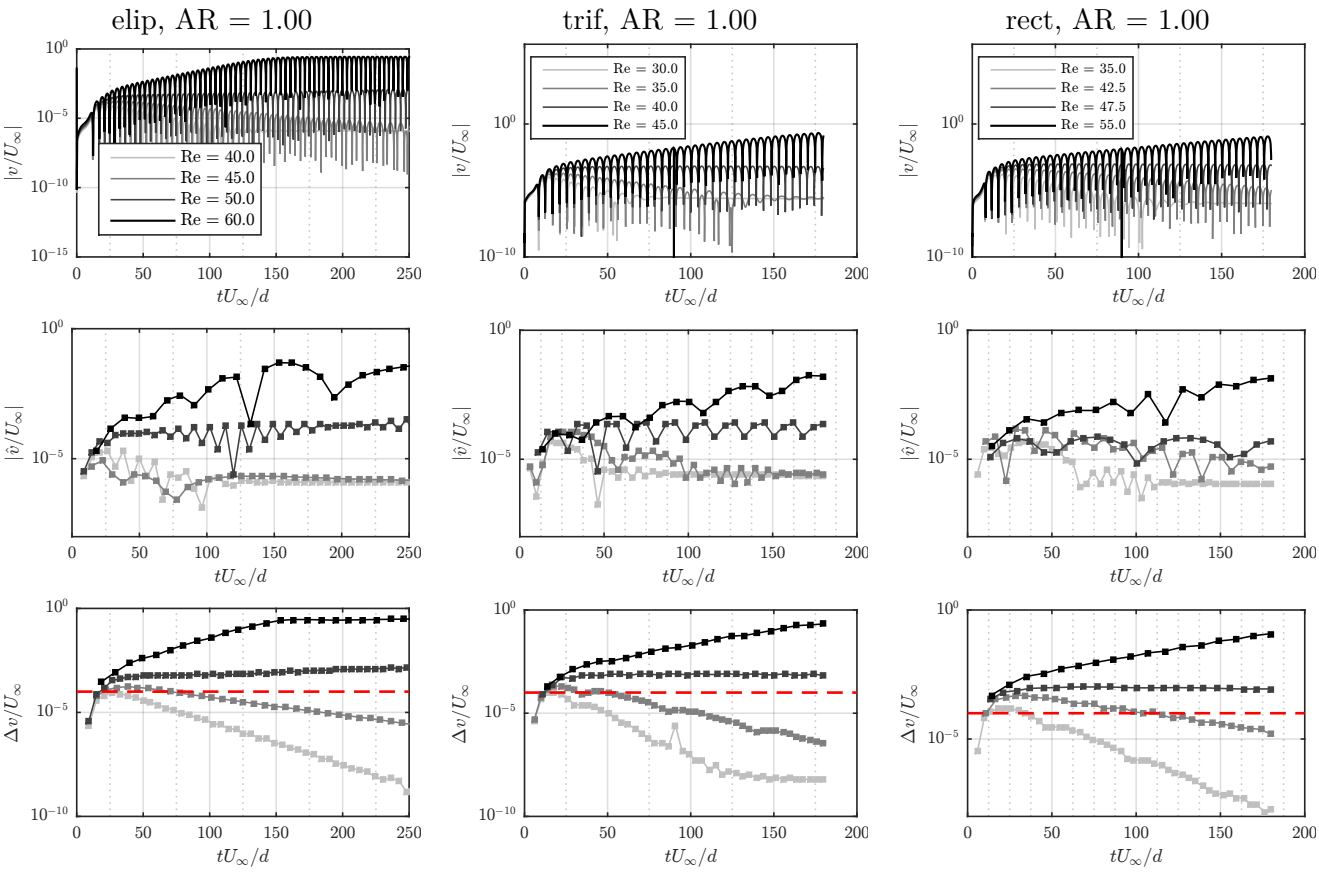

Figure 2.12: Evolution of the y_2-velocity absolute value (top), moving average (center) and deviation (bottom) with time for the probe 7, circular section (elip, AR = 1.00), front-pointing triangular section (trif, AR = 1.00) and square section (rect, AR = 1.00). Dashed line represents the selected criteriaon.

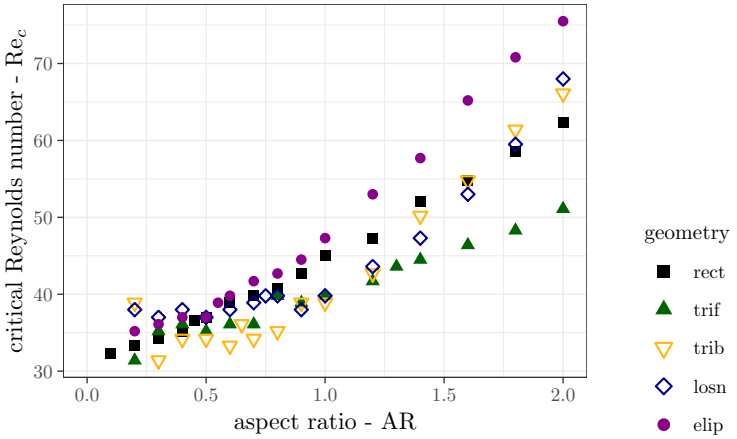

Figure 2.13: Evolution of the critical Reynolds number (Re_c) with the aspect ratio (AR) for the tested cross-sections.

2.2.3.3 Effect of the cross-section on the critical Reynolds

Current results are consistent with the concept of "bluffness" from Roshko [220] and the similar concept of "interference" proposed by Luo et al. [140], discussed in Section 1.1.4. When the body is extended in the streamwise direction, the interaction between the mixing layers is reduced, independently of the shape, thus, the transition for unsteadiness demands for a bigger amount of energy, which justifies the increase in the critical Reynolds number. The phenomenon is

Table 2.1: Literature values of Re_c (transition from steady to unsteady flow) for the circular cylinder (elip, AR = 1.00).

	reference	Re_c
	current work	47.3 ± 0.25
[285]	Zebib (1987)	45
[93]	Jackson (1987)	46.136
[204]	Provansal et al. (1987)	47
[249]	Strykowski & Sreenivasan (1990)	46
[119]	Kumar & Mittal (2006)	47.045-47.3181
[185]	Paul et al. (2014)	48.325
[261]	Thompson et al. (2014)	47.2
[33]	Chopra & Mittal (2019)	46.985

Table 2.2: Literature values of Re_c (transition from steady to unsteady flow) for the square cylinder (rect, AR = 1.00).

	reference	Re_c
	current work	45.0 ± 0.25
[242]	Sohankar et al. (1997)	47 ± 2
[243]	Sohankar et al. (1998)	51.2
[226]	Saha et al. (2000)	> 45
[281]	Yoon et al. (2010)	45
[10]	Bai & Alam (2018)	~ 50
[98]	Jiang & Cheng (2018)	~ 46

Table 2.3: Literature values of Re_c (transition from steady to unsteady flow) for the front-pointing triangular cylinder (trif, AR = 1.00).

	reference	Re_c
	current work	39.8 ± 0.25
[288]	Zielinska & Wesfreid (1995)	39.6
[41]	De & Dalal (2006)	39.9
[203]	Prhashanna et al. (2011)	40 ± 0.5
[164]	Ng et al. (2016)	40.45

quantified by the smaller vorticity flux related to big AR in [261].

For a fixed aspect ratio the analysis is not so direct. It is proposed by Luo et al. [140] that a cross-section that reduces its blockage from upstream to downstream (such as the back-pointing triangle) imposes an inward curvature of the shear layers and provokes an increase in the interaction, hence, a wake with higher Strouhal number and weaker vortices due to circulation annihilation. When group II is considered, the layers curving argument seem reasonable since both geometries (trib and losn) are similar in terms of the shape of their downstream segment and give virtually the same critical Reynolds number. What is noted in the group I (elip, rect and trib) sounds, on a first look, to be in the opposite direction of that description: the geometry that has diverged the shear layers (trif) is the one that transitions sooner.

However, the front-pointing triangle is the shape that provokes less perturbation to the flow before the detachment since the flow blockage is the least abrupt one and has an extended boundary layer, especially with the increase of the aspect ratio. This means that, at the time the shear layers will interact, at the downstream end of the section, the gradients are less important, thus, weaker vortices are generated when compared to the other shapes with the same AR, at the same regime. Hence, the size of the recirculation bubble has to be bigger to achieve an equal dissipation, as is illustrated on Figure 2.14, where the mean flow streamlines are presented for the elip and trif, AR = 1.0, below, at and beyond the critical Reynolds number. For Re < Re_c, the momentum balance for the triangular section is achieved with an extended recirculation; at Re = Re_c, the wake organizations are practically the same, that is equal recirculation length and streamlines (also noticed for the 3 other geometries at this AR); at Re > Re_c, the tendency is reversed: the recirculation is bigger for the circular cylinder.

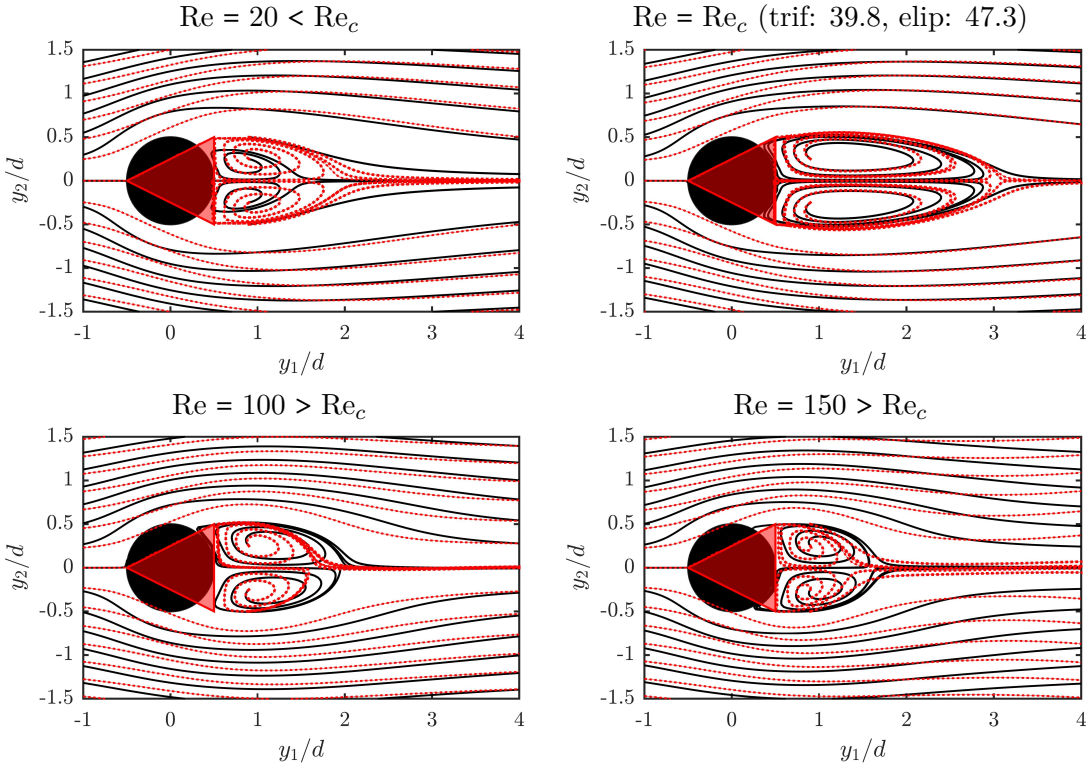

Figure 2.14: Mean flow streamlines for the circular and front-pointing triangle (elip and trif, respectively), AR = 1.00. Solid lines for elip and dotted for trif.

In terms of flow transition, this results in the fact that the transition for unsteadiness for the front-pointing triangle has to take place earlier in the Reynolds scale. The fact the recirculation for trif at Re = 150 is smaller is associated to a regime that is actually already transitioned to 3D, naturally not correctly represented in a 2D simulation. In accordance with the conclusion presented for the steady to unsteady transition, 2D to 3D transition happens much sooner for the triangular sections ($\mathrm{Re}_{2D\to3D} \sim 100 - 130$, [165]) when compared to the circular cylinder ($\mathrm{Re}_{2D\to3D} \sim 200$, [276]).

The same conclusion can be derived when the analysis is performed in an energetic point of view. For an incoming flow at a given velocity, the generation of vorticity is due to the necessity of the flow to overcome an obstacle. For a fixed blockage d, this process will be similar for all the shapes. However, how this vorticity dissipates is fundamentally a matter of all geometrical features that compose the body. Analyzing the flow close to the walls, there is a smaller perturbation and weaker gradients for the front-pointing triangle, thus, less energy can be dissipated at the body instance. So, for an amount of equal incoming energy (fixed U_∞, fixed Re), the front-pointing triangle has to dissipate more in the wake than the ellipse. This leads to the observed result of an earlier transition to unsteadiness that is also extrapolated to an earlier

transition to 3D (not verified here).

2.2.3.4 Remarks on the transition to unsteadiness and the wake regime

2.2.3.5 Consequence of performing the study at a fixed Reynolds number

The relative distance to the transition defined in Equation (2.2.2) is calculated for the tested shapes, considering the base simulation at Re = 150. As stated earlier, the increase of the critical Reynolds number with the increase of the sectional breadth can be associated with the increase of diffusion of energy at the body instance with the enlargement of the walls, thus, reducing the amount of energy available in the wake at a given Reynolds number, what correlates in the increase of the formation length discussed in previous section. Therefore, the transition is delayed in the Reynolds number scale. Considering the flow at a fixed Reynolds number of Re = 150, this represents a decrease of ε with an increase of the aspect ratio, as represented on Figure 2.15.

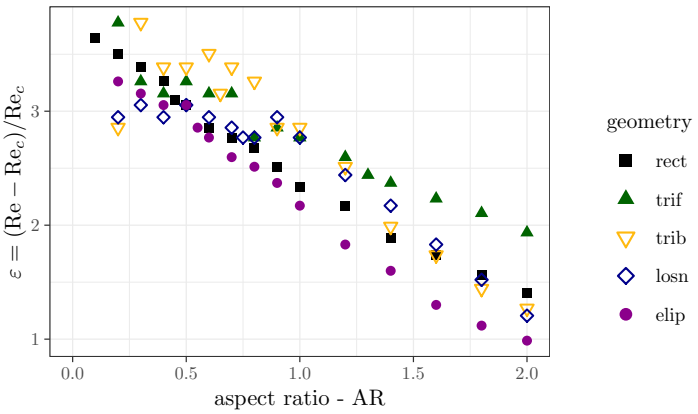

Figure 2.15: Evolution of ε with the aspect ratio for Re = 150.

On Table 2.4, the aspect ratios corresponding to before and after the apparition of the regime II are presented as well as the corresponding ε for each one of them at Re = 150. This transition takes place at the peaks of Strouhal number and fluctuating lift. It can also be deduced that the second wake regime is observed at $\varepsilon \sim 3$.

Table 2.4: Properties at the regime transition, Re = 150.

	rect	trif	trib	losn	elip
AR of regime transition	0.40-0.45	1.20-1.30	0.65-0.70	0.70-0.75	0.50-0.55
AR of peak St	0.40	1.20	0.65-0.70*	0.75	0.55
AR of peak C_L'			1.00	0.90	
ε of transition	3.26-3.10	2.60-2.44	3.16-3.39	2.86-2.77	3.05-2.86

*: both AR present the same vortex shedding Strouhal number.

As discussed in [164], the existence of multiple regimes can be actually a sign of transition to a 3D flow. The comparison to literature values indicates that the transition to 3D is around ε = 2, see Table 2.5.

Comparison of ε values on Table 2.4 and 2.5 together with an extrapolation of the results to all tested aspect ratios leads to the conclusion that the regime II is actually a wake disposition that is only made possible by the absence of the third dimension. In other terms, the fact that the flow cannot dissipate energy in the form of spanwise flow deformation results in the existence of the 2nd von Kármán instability that may be analogous to the appearance of Mode A [276]

Table 2.5: Transition Reynolds number and corresponding ε for 2D to 3D flow transition, AR = 1.0.

	rect	trif	trib	losn	elip
steady to unsteady transition - Re_c	45.0	39.8	38.9	39.8	47.3
2D to 3D transition - $Re_{2D\to3D}$ [165, 235, 261]	164	100.2	126.3	116	190.3
$\varepsilon_{2D\to3D}$	2.64	1.52	2.25	1.91	3.02

in a 3D simulation. This statement is reinforced by the fact that there is a clear distinction between the behavior of the flow quantities when analyzing wake regimes I and II.

2.2.3.5.1 Further look into the correspondence between the change of regimes and transition to 3D Additional simulations for different Reynolds numbers were performed in order to analyze the relationship between the different wake modes and the distance to the onset of transition to unsteadiness summarized by the variable ϵ. Another mode where there is the generation of a secondary instability with the deformation of the two parallel lines of vortices, exemplified on Figure 2.16, is found. Within a single time frame, the visualization of the phenomenon is rather difficult due to the streamwise truncation of the domain. This behavior, herein designated by mode III, was previously reported in the literature [101, 164, 261]. The definition of the mode is only visual, based on the solution snapshot of the last iteration that is simulated for each shape.

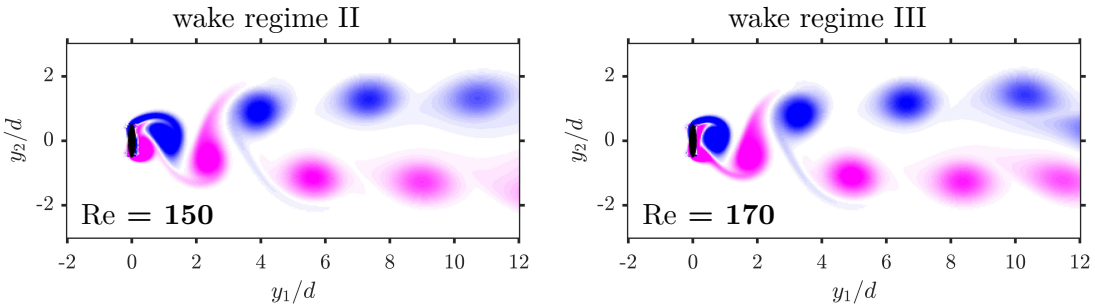

Figure 2.16: Vorticity snapshot for the elliptical section, AR = 0.20, at different Reynolds numbers representing the modes II (left) and III (right).

A diagram representing the observed wake modes is presented on Figure 2.17 for the elliptical, rectangular and front-pointing triangular sections. For the construction of the contour lines of iso-ε, empirical laws deduced for the critical Reynolds number as a function of the aspect ratio and presented further on the document (Section 2.3.3.1) were used.

For short shapes (AR < 0.5), the distance to the steady condition condensed in the value of ε is less important in the determination of the wake mode. However, for the long cross-section, modes II and III can only be found for ε at least 2. Even if the relationship is not direct (for example, for all geometries, it can not be stated that for $\varepsilon > 2$ - or any other constant value - there will be a mode II wake), there seems to be a link between the two properties.

The observations performed here are handicapped by the use of a rather small domain. The development of different wake modes might already be possible at smaller Reynolds numbers, but would not be detected due to the absence of enough downstream spanwise extent of the domain for its development. Also, the definition of the mode is only visual. This lack of precision of the analysis prohibits any strong argumentation.

The conclusion of the analysis is that there is a relationship between the distance to the onset of unsteadiness and the wake modes and transition to three-dimensionality. However, what this preliminary analysis has also shown is that this link is not solely presented by the variable ε.

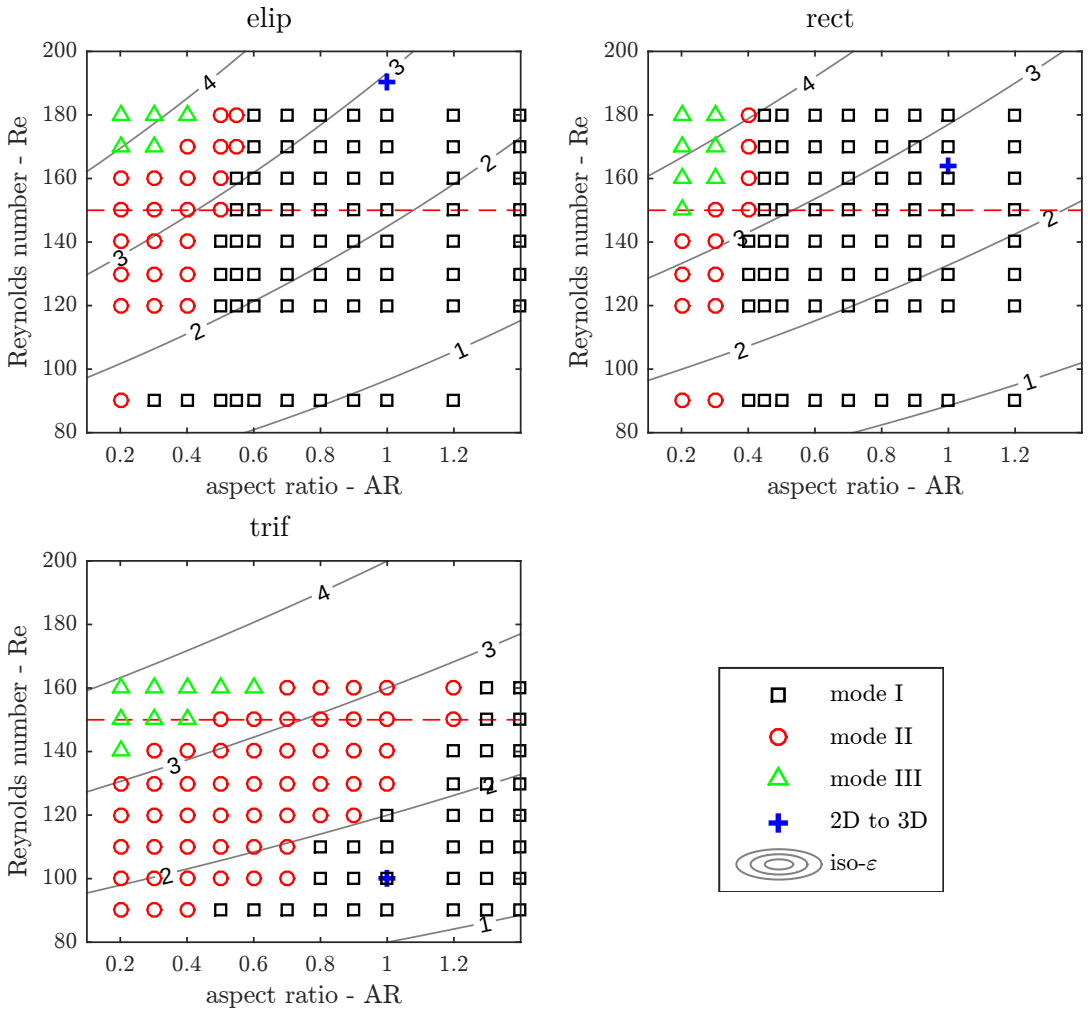

Figure 2.17: Diagram of the observed wake modes for the ellipse (elip), rectangular (rect) and front-pointing triangular (trif) sections. Mode I is for a single axis of vortices of opposite sign; Mode II is for 2 parallel lines of vortices each one of them composed by vortices of the same sign; and Mode III has presents the oscillation of the parallel line of vortices. The points indicating the transition to from 2D to 3D flow are from the literature [165, 235, 261].

Further conclusion can only be performed with more data, notably by estimating the Reynolds number of the 2D to 3D transition for more geometries.

2.3 Empirical relationships

Several relationships between flow quantities and the associated models are presented next. Such results may contribute to the production of bluff body wake models and yield insights over the physics of the phenomenon. Since this work is concentrated in the study of airframe noise, focus is given to the relation of integral and flow topology quantities to the fluctuating efforts, directly associated with the noise emission.

Some of the relationships presented here have already been hypothesized or evaluated in the literature (for instance, [78]). Regardless, the contribution of this work remains in the expansion and quantification of those laws for a large set of geometries. Also, each empirical law is associated with an interpretation of the physics of the vortex shedding and rises important conclusions regarding the shape influence on the phenomenon.

As previously presented, at Re = 150 there are 2 wake regimes, being regime II probably an artificial solution of a flow that would be actually 3D (see Section 2.2.2.2). Based on that, most of the current results are presented simultaneously for two groups: regime I only and regime

II/all points. Several relations are noted to be spoiled when this aspect is neglected. It is thus recommended that, when analyzing different shapes or flow regimes, to perform individualized analysis based on the flow dynamics, since a modification in the vortex distribution may respect a different law and hide important trends.

This section is introduced by a description of the procedure used to obtain the models (Section 2.3.1). The empirical laws are presented next, separated by their explanatory variables: Section 2.3.2 is dedicated to the laws that correlate the RMS force coefficients to flow quantities, such as the recirculation length; the integral quantities, such as the average drag coefficient, are considered the explanatory variables on Section 2.3.3.

2.3.1 Methodology and discussion over model selection

The statistical analysis presented here is a regression analysis. It consists in expressing the relationship between a response variable Y and an explanatory/predictor variable X. The major purposes of a regression analysis are description, control and prediction [120]. They mean, respectively, to understand a phenomenon, to adjust in order to get a given result and to estimate a response from a known state. The three objectives often concomitate.

In this application, the focus is on the description of the phenomenon of vortex shedding and bluff body noise production. This means that there is less focus on the precision of the models and the obtained coefficients and more attention to the physical meaning contained in the relationship that is evidenced. Since correlation does not imply causality, there is no attempt to deduce a cause and effect link in this part of the analysis.

The majority of the statistical work presented here is performed in software `R` [208], an environment for statistical computing. Despite not being exclusively for statistics, it contains all the tools necessary for the manipulation of the database, performing regressions and statistical testings. For the plots, package `ggplot2` [274] is used.

Some concepts of a regression analysis are presented next. Even if some of these were not strictly applied in current work, this review is important to provide a background and to serve as a starting point for more refined analysis and possible future works.

2.3.1.1 Normality of the residuals

For Y_i the observed values and $\hat{Y}_i$ the modeled values, the residuals $\hat{e}_i$ are defined as the difference between them $\hat{e}_i = Y_i - \hat{Y}_i$. Considering that the proposed model reproduces perfectly the relationship between the predictor and response variables, the residuals originate from the errors in the procedure used to obtain these variables (in this case, simulation errors). From the central limit theorem, the residuals must them be random, normally distributed variables with null mean and constant variance.

Thus, residuals which present a deviation from these properties are likely to be a result of a regression that is incorrect. Consequently, the analysis of the residuals is a tool for the diagnostics of errors in the model. In [120], Section 3.3, common errors visible in the analysis of residuals (such as the non-linearity of the relationship being presented by clear tendencies in the plot of the residuals) and the associated corrections are presented. Some of them are used in this work, the reader is invited to check the latter reference for more details on the procedure.

2.3.1.2 Model selection

The selection of a model consists in diagnosing the possible relationships between the variables and to propose functions that relate them and to find the coefficients. After this initial step, the model consistency is tested. When there are problems in the functional law (for example, non-normal residuals), correction techniques known as "remedial measures" (for instance, the transformation of the response or explanatory variables using the log function, more examples on [120], Chapter 3) can be applied. The test of new models continues until the behavior is considered satisfactory.

The procedure is represented on Figure 2.18. A short presentation of the elements in the routine to select the models can be found next.

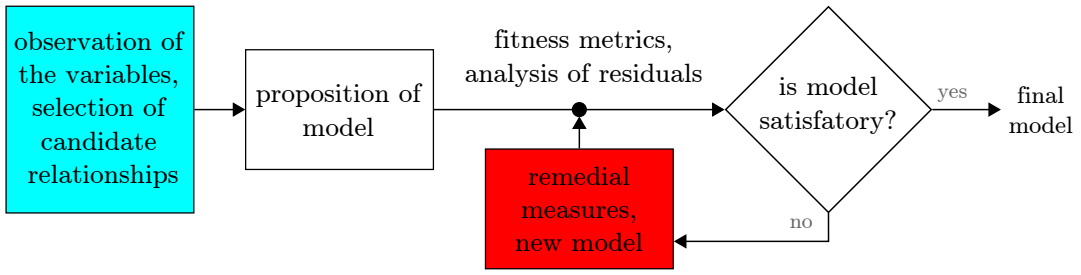

Figure 2.18: Diagram representing the steps followed for the proposition of the regression models. Adapted from [120].

2.3.1.2.1 Linear and non-linear regression The definition of the regression coefficients is normally based on the set of coefficients that minimize the residual sums of squares:

$$\sum_{i=1}^{n} (Y_i - \hat{Y}_i)^2 \tag{2.3.1}$$

Differences on how to obtain these coefficients is a mater of the type of regression model that is tested. When the function is linear, basically $Y_i = \alpha + \beta X_i + e_i$, the coefficients that provide the minimum sum of residuals is exact and can be defined mathematically (the least-squares fit). For non-linear functions, where there are exponents on the response or combination of explanatory variables, the solution is not exact. The discussion on the procedures used to define the coefficients on these two conditions is expanded next.

Linear regression model - Least-squares fit The coefficients are obtained in least squares fit by taking the derivative of the residual sum of squares with respect to the regression coefficients. When the partial derivatives are equal to zero (what represents a minimum), an exact algebraic formulation of the coefficients as a function of the explanatory and response variables is defined. The simplest procedure gives an equal weight for all the data points.

There are several techniques that aim to perform a regression accounting for the presence of outliers that may spoil the results. For instance, the Iteratively Reweighted Least Squares (IRLS), that consists in a weighted least squares regression that uses the inverse of the residuals as the weighting factors so outliers are less influential on the result, or the Theil-Sen estimator [260], that defines a confidence region for the performance of the regression. More examples can be found in [52, 120].

The dispersion of the data points around the laws obtained in this work can be high. However, this dispersion must not be considered as noise. Naturally, there are deviations associated with both the numerical method and the discretization, but they are small compared to the shape influence on the quantities being analyzed (discussion about the precision of the calculations is available on Appendix A). Consequently, robust regression techniques are not used in this study.

Non-linear regression model For several conditions the functions can be linearized, for example by applying a root, power or log transformation. However, there are laws in which this is not possible, and at least one of the derivatives of the model depends on one of the parameters [13] consisting in a non-linear regression model. In those cases, the exact solution is not available and different techniques must be employed to obtain the coefficients that minimize the residuals. Common options are the use of optimization routines and neural networks [120] to obtain the set of best coefficients.

By using optimization routines, the definition of the non-linear regression coefficients can be problematic: the convergence is not guaranteed, it may return a local instead of a global

minimum, the starting point influences the final result. These issues are discussed further in a different part of the work (Chapter 3 and Appendix D), where optimization was used in the scope of shape optimization for noise and drag.

Despite some initial testing, the implemented optimization algorithm presented in Section 3.2 is not used for the non-linear regression. The analysis is maintained in the R environment, with the use of the model fitting function `nls` [12]; an extensive discussion on the use of the function can be found in [214]. The use of a gradient based optimization was problematic in terms of starting values that would lead to invertible matrices. This issue was later overcome by the use of linear coefficients derived from a similar law as the starting point.

Independently of the type of the regression function, there are metrics to measure the quality of a model. Some of them are presented next.

2.3.1.2.2 Measurement of the goodness-of-fit

Coefficient of Determination The most diffused estimation of the quality of the fit is the determination coefficient R^2, that measures how much the variation of the response variable is explained by the tested explanatory variable. It is calculated as follows:

$$R^2 = \frac{\sum_{i=1}^{n}(\hat{Y}_i - \overline{Y})^2}{\sum_{i=1}^{n}(Y_i - \overline{Y})^2} = 1 - \frac{\sum_{i=1}^{n}\hat{e}_i^2}{\sum_{i=1}^{n}(Y_i - \overline{Y})^2} \tag{2.3.2}$$

where n is the number of observations, $\overline{Y}$ is the mean of the response variable. When R^2 equals one, it means that the residuals are null and that there is a perfect fit. A null R^2 implies that the sum of the differences between the mean and the model is null, thus, that there is an independence between the variables X and Y. In the case of a simple linear regression, the determination coefficient is the square of the correlation coefficient between the observations Y and the estimations $\hat{Y}$.

For non-linear regression, the use of the determination coefficient is not recommended. The meaning of such metric is lost since the sum of the squares of the regression $(\hat{Y}_i - \overline{Y})^2$ can be larger than the total sum of the squares $(Y_i - \overline{Y})^2$, resulting in R^2 bigger than 1.

Adjusted Coefficient of Determination The regular definition of the coefficient of determination does not account for the number of parameters in the model. Since the coefficient of determination can only increase with the addition of new parameters [52, 120], an adjusted version also exists:

$$R^2 = 1 - \left(\frac{n-1}{n-p}\right)\frac{\sum_{i=1}^{n}\hat{e}_i^2}{\sum_{i=1}^{n}(Y_i - \overline{Y})^2} \tag{2.3.3}$$

where p is the number of parameters in the model.

It must be emphasized that the determination coefficient (adjusted or not) alone does not guarantees the quality of the regression. Supplementary steps such as the analysis of the residuals are necessary to confirm that there is a good fit and that the model captures correctly the relationship between the variables.

If the contrary is not explicitly stated, all the R^2 values presented here are the adjusted version of the coefficient of determination.

Other criteria Many other criteria are available in the literature [120], such as the Mallow's C_p Criterion, Akiake's Information Criterion (AIC_p) and Prediction Sum of Squares Criterion (PRESS_p). Despite being more adapted to the comparison of models, they are not used in this manuscript. The description of the fitness quality is assessed only by the previously described metric (R^2) given its widespread and common understanding.

Note that, with the use of fitness metrics, one could perform automatic procedures to pick the "best" model, such as the Best Subsets Algorithms and the Stepwise Regression Methods (more

on previously cited reference [120]). These techniques are normally employed in multivariable regressions, where the number of possible models is very large.

Since the objective is to obtain relationships that have a physical meaning and provide conclusions about the dynamics of the vortex shedding, automatic procedures are not employed. The use of such techniques could lead to functions that, despite their good statistical properties, are physically inconsistent or asymptotically incorrect. Further discussion on the followed procedure for the selection of the models is presented next.

2.3.1.3 Current procedure for the model selection

Two principal methods were employed to search for relationships in the data and propose the models. The basic, yet fundamental, procedure of observing the flows and trying to extract the trends is the main approach. It is also largely based on the physical knowledge of the phenomenon and on trends present in the literature. The other technique is based on the visualization of a scatter plot matrix such as the sample presented on Figure 2.19, that allows to check the relationship between the variables.

The proposed laws are issued from simple combinations of canonical functions, such as exponential, log and polynomial. Their simplicity is more adapted to physical problems. Also, there is a constant concern about the asymptotic behavior of the curves to avoid, for example, a law of lift in terms of the aspect ratio that does not return 0 when AR is null.

The choice of the models is based on the determination coefficient (even if not completely adapted to it [52]), analysis of the residuals and of the F-Test (test the hypothesis that the regression coefficient is non-null). Normality of the residuals is checked mostly visually, using the plot of the residuals against the fitted values, and with the normality test of $\hat{e}_i$. The choice of the models is mostly defined by what is noted geometrically-wise in detriment of the general relationship. Obtained individual curves (for each geometry) are presented on Appendix B.

Despite the effort to obtain statistically meaningful laws (with normal residuals), since the aim is the description of the relationships, the respect of the global behavior is prioritized. In a larger sense, this means that some of the proposed regression functions knowingly present issues in the residuals (clear trends, non normality). The strategy is to avoid overly complicated models, that would naturally result in a better fit [52], and focus on general relationships.

The use of multivariate statistics was tried, notably with the combination of the aspect ratio and the distance to the transition represented by the parameter ε. However, due to the complexity of the analysis and the lack of representative results, these procedures are not formalized in this document.

All linear regression coefficients are obtained using the least-squares formalism and the non-linear regression is performed using the `nls` function in `R`. Only the final regression laws are presented, no discussion about the path to obtain the given models is presented.

2.3.1.4 Database

The main database is composed of the canonical geometries of Section 2.2, at Re = 150, with a total of 104 observations of 47 variables. The addition of different cases such simulations at a different Reynolds number or the subtraction of some geometries (for instance, elif and elib), varies the number of observations for some of the analysis.

2.3.2 Flow topology based relations

This section is dedicated to the relations found between the RMS force coefficients and flow topology quantities: recirculation (Section 2.3.2.1) and formation (Section 2.3.2.2) lengths and the vertical displacement of the vortex (Section 2.3.2.3).

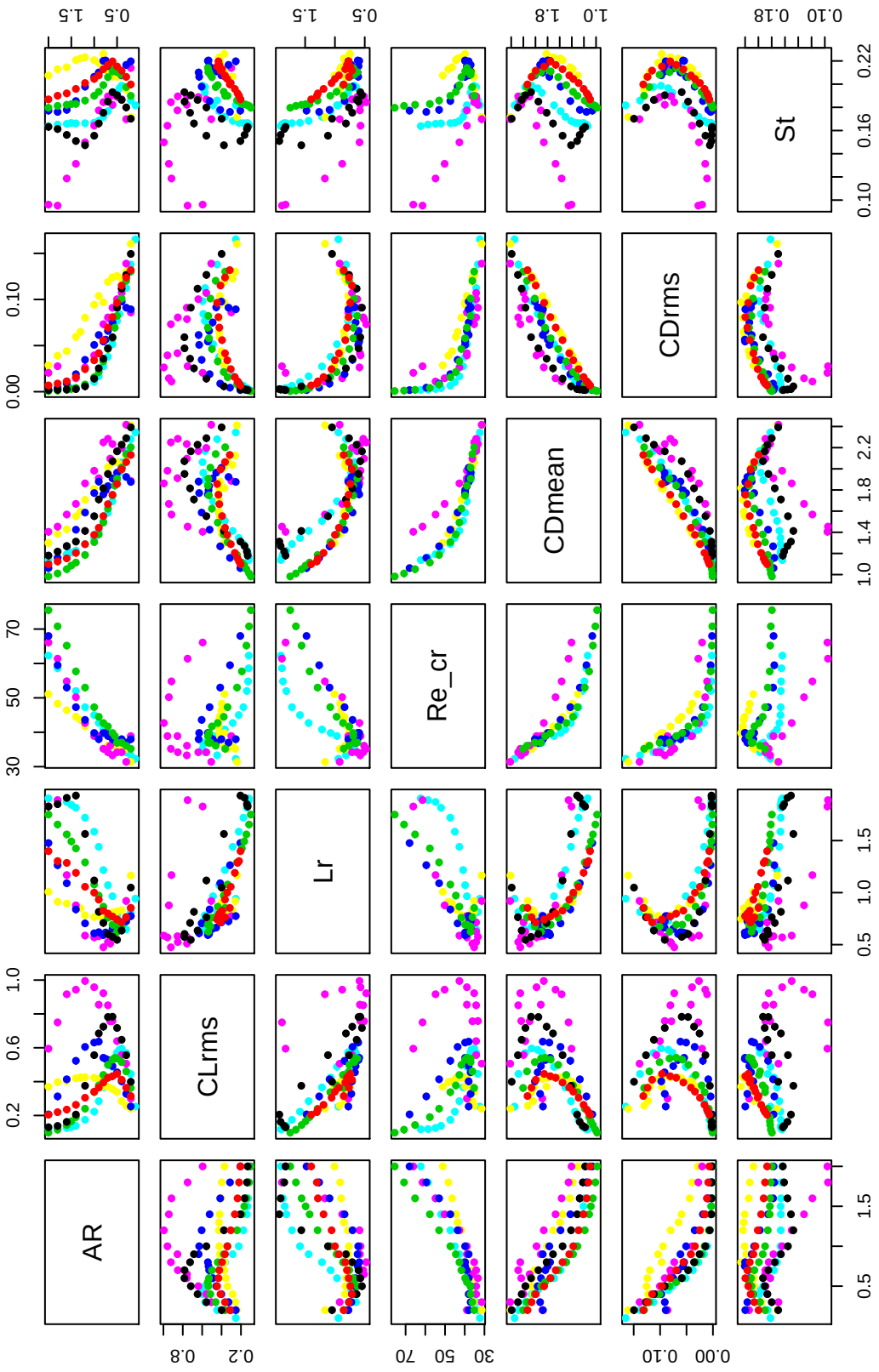

Figure 2.19: Example of scatter plot matrix with the aspect ratio, RMS lift coefficient, recirculation length, critical Reynolds number, mean and RMS drag coefficients and Strouhal number. Data for Re = 150, colored by geometry.

2.3.2.1 RMS lift coefficient vs. recirculation length

Analysis of the curves of the RMS lift coefficient and recirculation length leads to the following linear model:

$$C_L' = \alpha + \beta \frac{L_r}{d} \tag{2.3.4}$$

Results are presented in Figure 2.20, note that the distinction between the regimes is necessary for this analysis. The fit considering all the geometries is rather poor (determination coefficient of 0.5132 for regime I and 0.5499 for regime II), however, for each geometry, the linear law is very representative of the points (see Figure B.1 in Appendix B). An exponential law could be envisaged for fitting the complete data set, but due to the good individual behavior (for each geometry) only the linear model is considered.

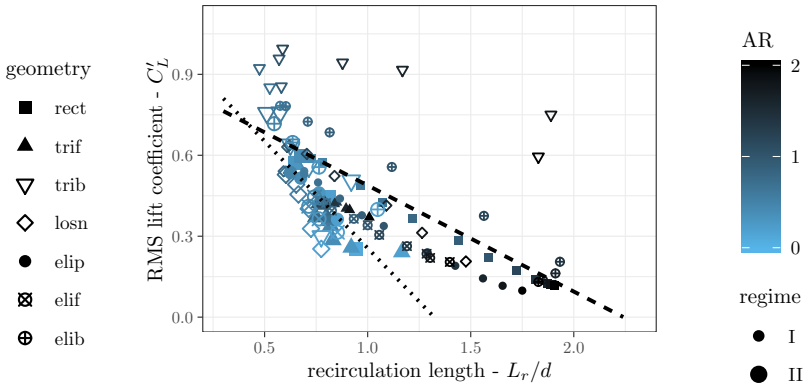

Figure 2.20: Evolution of the RMS lift coefficient with the recirculation length, Re = 150, all geometries, colored by the aspect ratio. Represented regression laws: obtained for regime I (dashed line); and only considering regime II (dotted line).

Overall, it can be concluded that an increase in the recirculation length is associated with a reduction of the fluctuating lift, also noted by Hu & Zhou [78], and consequently the sound emission. The scattering associated with the shape and the regime implies that both factors are highly influenced by how the average flow is organized. Based on the idea that the distance of the vortices to the lift generating surfaces is a fundamental ingredient in the generation of RMS forces, the relationships between C_D', C_L' and the formation length are assessed next.

2.3.2.2 RMS force coefficients vs. formation length

The position of the generation of the vortex, synthesized in the formation length is considered as an indication of how much of the wake energy is going to be converted into aerodynamic fluctuations. This analysis is directly associated with the conclusions of Zielinska [288], who described the relation between the amplitude and position of the maximum global modes with the Reynolds number. A similar conclusion regarding the correlation between the formation length and the aerodynamic efforts fluctuation is also found in [151]. Two exponential laws are proposed:

$$C_D' = \alpha \exp\left(\beta \frac{L_f}{d}\right) \qquad C_L' = \alpha \exp\left(\beta \frac{L_f}{d}\right) \tag{2.3.5}$$

The evolutions of the RMS drag and lift coefficients with the formation length are presented in Figure 2.21 and 2.22, respectively. Once more, it was necessary to separate the two regimes when calculating the regression laws. For the RMS drag coefficient, points that represent flows in regime II are concentrated and biased the fit; for the lift, the behavior cannot be described solely

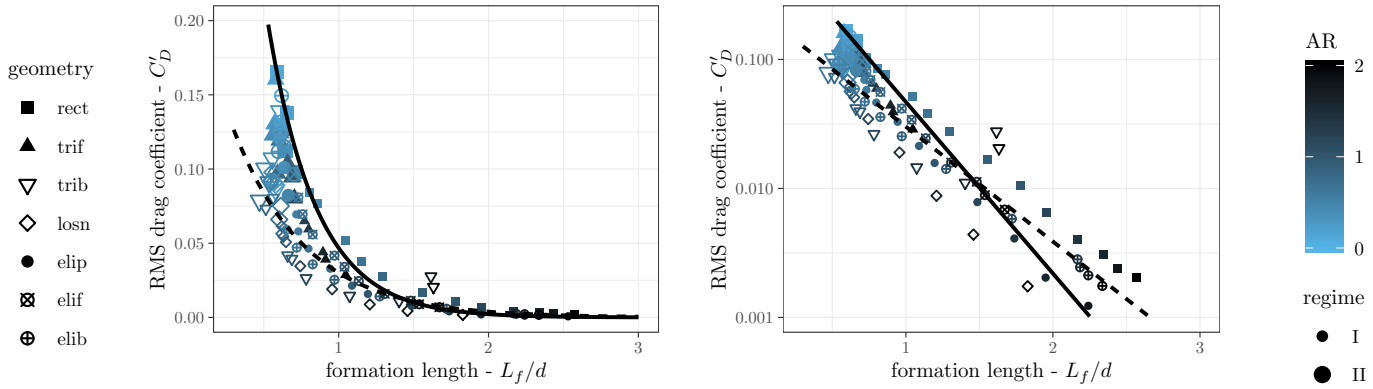

Figure 2.21: Evolution of the RMS drag coefficient with the formation length, all geometries, colored by the aspect ratio (Re = 150); linear scale on the left and lin-log scale on the right. Represented regression laws: obtained for all points (solid line); only considering regime I (dashed line); and only considering regime II (dotted line).

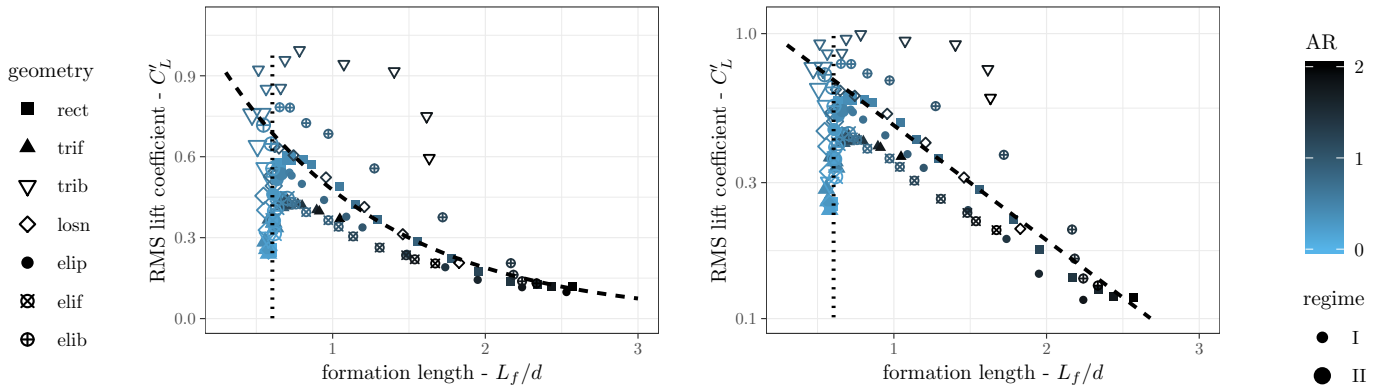

Figure 2.22: Evolution of the RMS lift coefficient with the formation length, all geometries, colored by the aspect ratio (Re = 150); linear scale on the left and lin-log scale on the right. Represented regression laws: only considering regime I (dashed line); and only considering regime II (dotted line).

by the formation length, since all the points corresponding to regime II flows are concentrated at $L_f \sim 0.6$.

Similar to what is presented in Section 2.3.2.1, points are scattered around the global models while geometry based laws fit well (Figure B.2 and B.3). For the points at regime I, following coefficients were obtained: $\alpha = 0.234$ and $\beta = -2.050$ for the drag and $\alpha = 1.205$ and $\beta = -0.928$ for the lift. Note that the exponential decay is twice as large for the drag.

The critical formation length that is associated with regime II can be derived from the presented results. Values considering each geometry, the average and the global model are listed on Table 2.6. This reinforces the conclusion that the second regime is associated with a saturation of the near-wake at $y_1/d = 0.6$, which limits the von Kármán dynamics and is believed to be a function of the Reynolds number.

Although the discontinuity of the trends noted between the two regimes and the offset from the tendency curves being present for all geometries, that difference is more pronounced for the back-pointing shapes (trib and elib). That means that the mechanism of vortex shedding and its translation into force fluctuations is more affected by geometrical features placed further downstream of the body.

The proposed descriptions miss elements for the construction of solid models and further analysis is required, notably using multivariate analysis. Moreover, non-linearities can be noted,

Table 2.6: Critical formation length (L_f/d), Re = 150.

rect	trif	trib	losn	elip	elif	elib	**average**	all*
0.652	0.619	0.543	0.578	0.762	0.641	0.593	**0.605**	0.627

*: issued from the regressions performed for all geometries.

especially for the $C'_L(L_f/d)$ laws, but no simple model that captured that behavior could was found. However, obtained curves formalize the link between the increase of the aerodynamic efforts and the decrease of the formation length (previously stated by Szepessy & Bearman [253], who associated more vigorous vortex shedding with a decrease of L_f) with two shape independent exponential laws.

The dispersion of the points for the RMS lift coefficient law can be explained by the fact that the formation length is a measure in the streamwise direction while the lift is by definition orthogonal to that. According to this principle, a discussion based on observations in the y_2-direction is presented next.

2.3.2.3 RMS lift coefficient vs. vortex displacement

A visual examination of the vortex shedding leads to the observation that the amount of vertical displacement of the vortices from the surface of the body could be associated to the magnitude of the RMS lift coefficient, thus, to the aeolian tone. The quantification of that movement is performed with the analysis of the ω_3 field contour, calculated using bi-linear interpolation.

For several timesteps that compose one period, the point in the iso-line $\omega_3 = 0.1$ (value chosen arbitrarily) that is furthest from the body (largest y_2) in the range $-b/2 \leq y_1 \leq b/2$, defined as y_ω, is stored. For the complete vortex shedding cycle, the difference between the lowest and highest values of y_ω is defined as the flapping amplitude Δy_ω. The symmetry of the bodies allows for the measurement to be performed on the upper and lower sides and the mean value to be considered for the analysis.

An illustration of the lowest and highest points found in a cycle for different rectangular sections is presented in Figure 2.23. As expected, the instantaneous point of max is at $y_1 = b/2$. Tests were also performed using different ranges of streamwise coordinates (expanded shape and complete wake), but the obtained values were sparse and subject to the difference of behavior in the wake, such as the two wake regimes, and were not directly associated to the fluctuations in the surface.

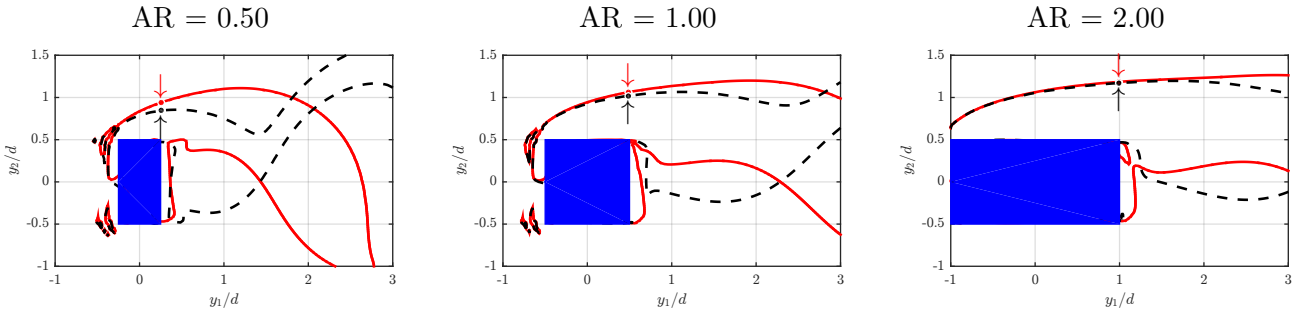

Figure 2.23: Examples of the flapping quantification for a rectangular section (rect) at Re = 150. Solid lines represent the iso-line corresponding to the timestep with maximum y_ω while dashed lines correspond to the flow that has minimum y_ω; arrows are directed to the points of minimal and maximal y_ω.

The correspondence between the 2 quantities is illustrated in Figure 2.24. The relationship between the two variables is presented in Figure 2.25. A least-squares fit is performed with an

imposed crossing at (0,0).

$$C_L' = \alpha \Delta y_\omega \tag{2.3.6}$$

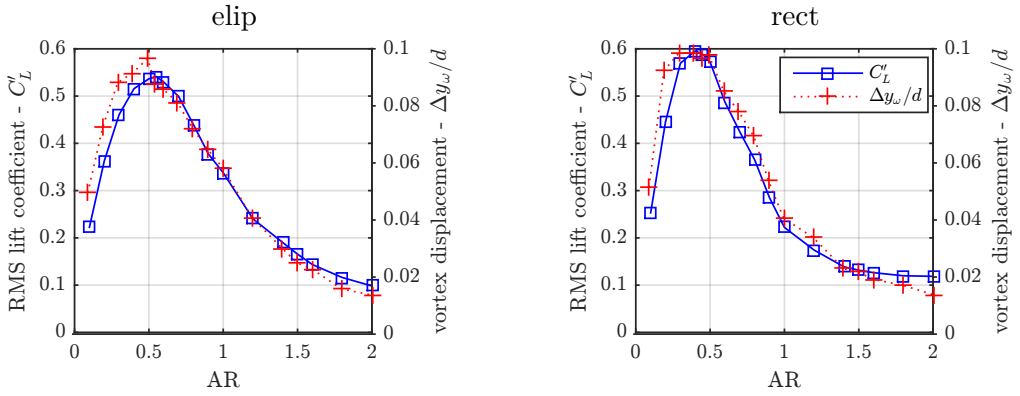

Figure 2.24: Examples of the evolution of the RMS lift coefficient and vortex displacement with the aspect ratio for the elliptical sections (elip, left) and rectangular section (rect, right), Re = 150.

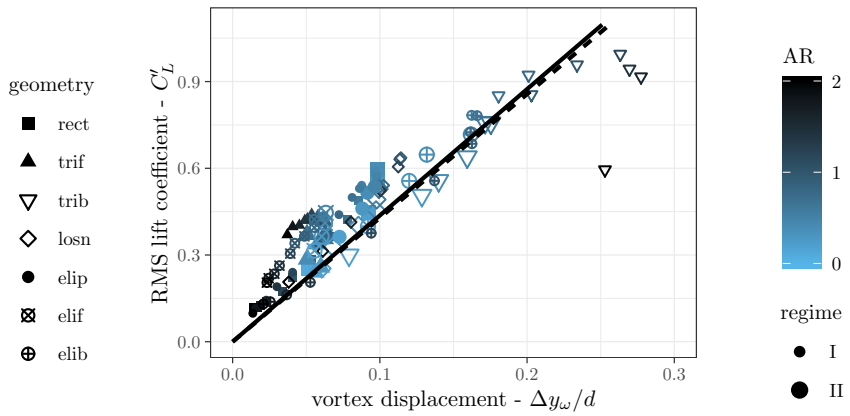

Figure 2.25: Relationship between the RMS lift coefficient and the vortex displacement for all geometries colored by the aspect ratio, Re = 150. Represented regression laws are obtained for all points (solid line) and without the back-pointing triangle, trib (dashed line).

For all the points, the regression law is $C_L' = 4.369\ \Delta y_\omega$ with an adjusted determination coefficient of 0.928. It is notable that the points for the back-pointing triangle (trib) at small aspect ratio are out of the tendency. However, they do not impact the fit, that is found as $C_L' = 4.283 \Delta y_\omega$ when the points of trib are not considered. When each geometry is considered individually, the angular coefficient varies from 3.6 (trib) to 7.1 (elif).

Although it is possible that other curves better represent the trend noted in Figure 2.25, the linear behavior is selected due to the geometry-wise behavior, that is clearly linear (see Figure B.4). Nevertheless, similar relationships are also obtained when considering the average displacement y_ω (not shown), however the curves have discontinuities associated to the two wake regimes.

The fact that the flapping of the vortices can be associated with the fluctuating lift, thus, the aeolian tone, is an important conclusion regarding the dynamics of the flow. Without any information about the shape or the flow regime (the model was also tested with results for the same geometries at different Reynolds number - lower than 150 - and the trend remained consistent), the access to the local movement can provide an estimation of the sound emission. A proper theoretical development to clarify and expand this empirical finding, notably based on the expression of surface force in terms of vorticity [77], is envisaged.

2.3.3 Integral quantities and geometry based relations

Relations based on the integral quantities are more interesting in an application point of view since they are more accessible than flow features, either by experiments or simulations. This section presents relationships that were found between the critical Reynolds number and the aspect ratio, the RMS force coefficients and the aspect ratio, the distance to the critical Reynolds number and the average drag coefficient.

2.3.3.1 Critical Reynolds number vs. aspect ratio

As can be seen on Figure 2.13, there is a clear increase of the critical Reynolds number with the aspect ratio for the tested geometries. Several models were tested (not shown), and the best fit is obtained with an exponential law:

$$\mathrm{Re}_c = \alpha \exp(\beta \mathrm{AR}) \tag{2.3.7}$$

The resulting laws are presented on Figure 2.26, the coefficients (obtained with a least-squares fit) are listed on Tables 2.7 and 2.8, together with the determination coefficient R^2 and the p-value for a normality test [234] of the error. A high p-value ($\gtrsim 0.05$) means that the null hypothesis that the data came from a normally distributed population can not be rejected. For the elliptical section, for example, coefficients are $\alpha = 30.553$ and $\beta = 0.455$, with $R^2 = 0.990$ and normality test p-value = 0.682.

The tested geometries here can be separated in two distinct groups (presented separately on Figure 2.26): I) the ellipse, front-pointing triangle and rectangle (elip, trif and rect), that follow an unique exponential law and converge toward the same value for $\mathrm{AR} \to 0$; II) back-pointing triangle and lozenge (trib and losn), that have a rather constant Re_c up to unitary AR, and an almost identical tendency afterwards.

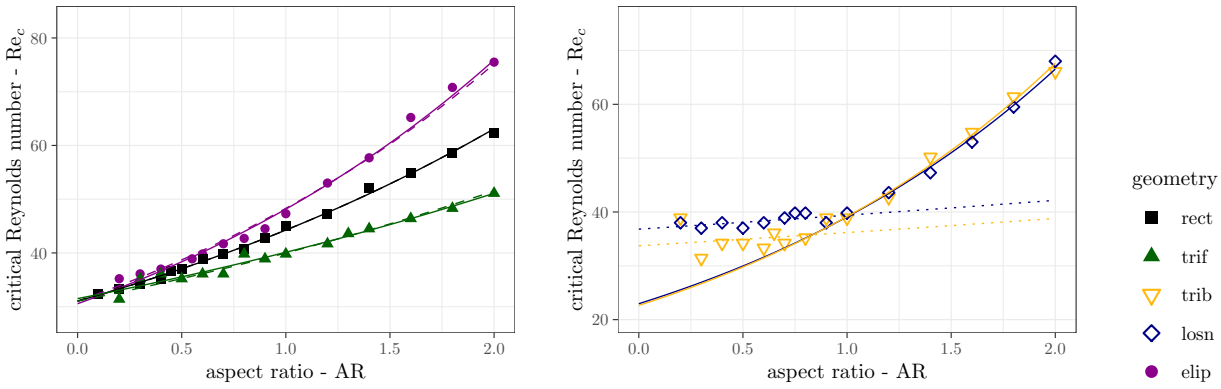

Figure 2.26: Regression laws for the critical Reynolds number as a function of the aspect ratio: for group I (left) solid lines represent the 2 parameters regression while the dashed ones correspond to the laws derived with an imposed $\mathrm{Re}_{c,\mathrm{AR}\to 0}$; for group II (right), dotted lines represent 2 parameters regression fit calculated for $\mathrm{AR} < 1.0$ and solid lines are obtained for $\mathrm{AR} \geq 1.0$.

The congruence of the points and the regression laws at small AR allow the definition of a flat-plate critical Reynolds number ($\mathrm{Re}_{c,\mathrm{AR}\to 0}$). Considering that Equation (2.3.7) is exponential, the coefficient α corresponds to this value ($\mathrm{Re}_c = \alpha$ when $\mathrm{AR} = 0$). That leads to the following reduced model:

$$\frac{\mathrm{Re}_c}{\mathrm{Re}_{c,\mathrm{AR}\to 0}} = \exp(\beta \mathrm{AR}) \tag{2.3.8}$$

The coefficients and statistical quantities for the Re(AR) models in Equations (2.3.7) and (2.3.8) are tabulated on Tables 2.7 and 2.8. Regression model $\mathrm{Re}_c = \alpha + \beta \mathrm{AR}^2$ is, statistically, as

significant as the exponential curve that is proposed. For the elliptical section, for example, the determination coefficient is of 0.99 and the p-value of the normality test is of 0.846. However, the parabolic curve does not capture well the tendency at low Reynolds number (a close to linear increase of Re_c with AR) and is less consistent when taking into account the completeness of the tested shapes.

Table 2.7: Regression law for the critical Reynolds number as a function of the aspect ratio - group I.

	2 parameters regression*			imposing $\mathrm{Re}_{c,\mathrm{AR}\to 0}$ †		
geometry	elip	rect	trif	elip	rect	trif
$\log(\alpha)$	3.419	3.435	3.450		3.435†	
α	30.553	31.041	31.505		31.033†	
β	0.455	0.355	0.242	0.442	0.355	0.254
adjusted R^2	0.990	0.998	0.963	0.997	0.999	0.991
Shapiro-Wilk p-value	0.682	0.608	0.122	0.643	0.606	0.041

*: Equation (2.3.7)

†: regression performed considering a common Re_c at null aspect ratio, Equation (2.3.8), average of the α coefficient obtained for the 3 shapes.

Table 2.8: Regression law for the critical Reynolds number as a function of the aspect ratio - group II. 2 parameters regression - Equation (2.3.7).

	AR < 1		AR ≥ 1	
geometry	losn	trib	losn	trib
$\log(\alpha)$	3.606	3.518	3.134	3.120
α	36.806	33.724	22.959	22.652
β	0.068	0.071	0.532	0.547
adjusted R^2	0.270	-0.081	0.990	0.987
Shapiro-Wilk p-value	0.400	0.520	0.148	0.070

A very small or negative determination coefficient indicates that there is no dependence between the variables. In the case of the back-pointing triangle and lozenge, this represents that the critical Reynolds is independent of the aspect ratio for AR < 1.

Considering the average of the 3 shapes on the first group, the critical Reynolds number for a thin plate (AR → 0) is of 31.03, value that lies within the range of 30-35 proposed by Saha [225] and very close to the value obtained by Thompson et al. [261] of 31.6.

As for the second group, there are 2 distinct behaviors. For AR < 1.0, the obtained critical Reynolds numbers are almost constant and independent of the aspect ratio, fluctuating between 30 and 40. This kind of plateau that exists for the back-pointing triangle and lozenge is a result of their sharp edges that mimic a flat plate. In this sense, the similarity of the dynamics of flow detachment and recirculation results in analogous critical Reynolds numbers. The laws for the two geometries (trib and losn) in the range of bigger aspect ratios (AR ≥ 1.0) are coincidental and reproduce the exponential behavior noted for group I.

The dispersion of points for group II at low aspect ratio may be a result of the limitation in the shape reproduction and associated with employed solver and mesh spatial resolution. The description of the shapes is performed using IBM and a five points stencil finite difference scheme. This means that, for each grid point, 2 neighboring nodes are considered for the

numerical estimation of the derivatives, in each direction. In the case of the two geometries with cusps in their frontal portion, the offsets may be related to the poor description of the flow due to the combination of upstream and downstream parts of the flow in the calculation of the derivatives provoked by the reduced number of solid points in that region. Note that the behavior is, in a smaller scale, also present for the back-pointing triangle (for small AR only) and is more problematic for the lozenge, since the reduction of the nodes in the cusp happens both downstream and upstream of vertexes placed at the maximal cross-section. The author is unaware of literature results that could provide more insight around the validity of current results concerning the back-pointing triangle and lozenge of short aspect ratios (AR < 1.0).

Overall, from Figure 2.26, Tables 2.7 and 2.8, the universal regression is of very good statistical quality. Nevertheless, a comparison between the present law along with the values obtained by Jackson [93], Paul et al. [185] and Thompson et al. [261] is available on Figure 2.27.

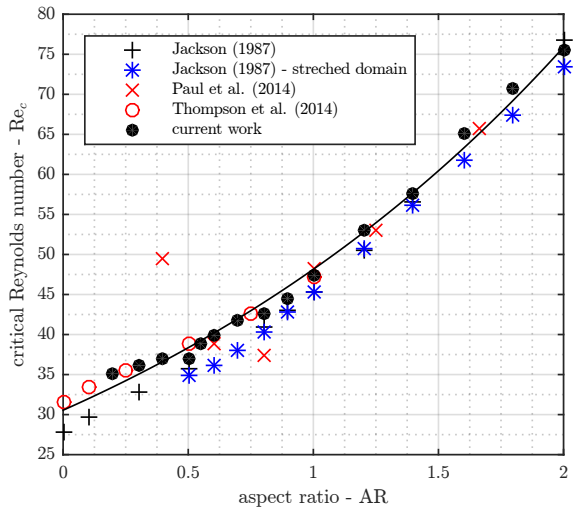

Figure 2.27: Comparison of the evolution of the critical Reynolds number with the aspect ratio, elliptical section, with literature values [93, 185, 261]. Solid line represents the regression law obtained from current data with an imposed $\mathrm{Re}_{c,\mathrm{AR}\to 0}$.

Present results fit well the trend encountered by Jackson [93] and Thompson et al. [261]; values given by Paul et al. [185], converted to the current reference length, are distant from the other sources for AR < 1.0. It is believed that this offset is due to the difference in the numerical setup associated with using the hydraulic diameter as reference for the domain extension, as discussed more deeply in the Appendix C.

2.3.3.1.1 Conclusion The current finding shows quantitatively the correlation between the evolution of the critical Reynolds number with the aspect ratio for different geometries by a single parameter. One important conclusion regards the universality of the tendency. The model is quite robust, and is capable of estimating the critical Reynolds number at a good precision for the tested geometries, which can be useful in the production of bluff body wake models that consider the Re_c or any derived quantity. From the physics point of view, the critical Reynolds number for the flow around the infinitely thin flat plate normal to the flow is obtained. Differences in behavior based on aspect ratio and geometry modifications are discussed in the following section.

As represented visually in the graphs and numerically by the determination values and the results of normality error tests, the exponential relation between the aspect ratio and Re_c seems to be universal. Dependence on the shape resides in the coefficients. The elliptical section is the only considered shape that has no sharp edge, and this geometrical feature is attributed to the observed behavior of having the highest critical Reynolds among the tested cross-sections. The fact that there are no fixed detachment points leaves more space for adaptation of the flow within a steady solution. Also, for the ellipses, the boundary layers remain attached over larger

perimeters, thus, are capable of enhancing diffusion and creating vorticity in the flow, thus, require more energy to transition. On the other hand there is the front-pointing section, which has both detachment and stagnation points fixed and is less dissipative, and also is subjected to a favorable pressure gradient that stabilizes the flow. This is believed to be the reason why the transition is associated with less energetic flows.

2.3.3.2 RMS lift coefficient vs. aspect ratio

2.3.3.2.1 Model synthesis The evolution of the RMS lift coefficient presents, for all geometries, an initial increase followed by a decrease, as discussed in Section 2.2.2.1, and also observed for rectangular sections in previous works at both low [89, 91, 241] and high [227, 240] Reynolds numbers. Such biphasic response is largely discussed in biological sciences and is known as hormesis, defined by a low-dose stimulation and a high-dose inhibition [26]. The universality of such behavior in the response of the flow to an increase of the aspect ratio leads to the proposition of the following relationship:

$$\{C_L'\} = A\{\mathrm{AR}\}_{C_L'}^{B} \exp\left(\frac{\{\mathrm{AR}\}_{C_L'}}{C}\right) \tag{2.3.9}$$

where the operation represented by $\{\bullet\}_q$ is the normalization by the value corresponding to the maximum behavior (maximum q) for that given geometry and flow regime (Re). For example, $\{\mathrm{AR}\}_{C_L'}$ is the aspect ratio divided by the aspect ratio that corresponds to the maximum C_L' at that corresponding Reynolds number. Imposing the point $(\{\mathrm{AR}\}_{C_L'}, \{C_L'\}) = (1,1)$, that is by definition present for all the geometries and flow conditions, the following condition is obtained:

$$C = \frac{1}{-\log(A)} \tag{2.3.10}$$

thus, reducing the model to only 2 parameters: A, related to the magnitude of the curve and the exponential growth; and B, which represents the influence of the available lift-generating-surface (AR) to the resulting C_L'. This formulation is compatible with the considerations concerning the decrease of the surface pressure fluctuation along with an increase of the available surface (with the augmentation of the aspect ratio) presented by Inasawa [89].

The resulting equations are tested for different Reynolds numbers and are presented in Figure 2.28. Results for regimes different from Re = 150 are issued from the procedure to estimate the critical Reynolds numbers [197], so are naturally less numerous. Also, due to the difference in Re_c, some geometries have null C_L' for some of the given Reynolds number and are naturally not presented. Curve coefficients are obtained from a least-squares linear regression and are presented on Table 2.9.

Figure 2.28 shows that the relation is less geometry dependent with the increase of the Reynolds number. This can also be directly associated with the increase of the ε, that is, the farther from the transition, the less the geometry influences the wake when considering a fixed Re. The asymptotic behavior is fully representative of all geometries for AR $\to$ 0 (null C_L'), however, for an increase of the aspect ratio the points deviate from the trend law. It is believed that this is due to the repositioning of detachment point for large bodies (see [176], for instance) for Re $>$ 60, thus, changing into different flow dynamics.

Table 2.9: Regression coefficients of the model of the normalized RMS lift coefficient as a function of the normalized aspect ratio, Equation (2.3.9).

Re	45	60	90	150
A	9.3718	2.9877	2.6879	4.24700
B	2.2678	1.1798	0.9925	1.35423

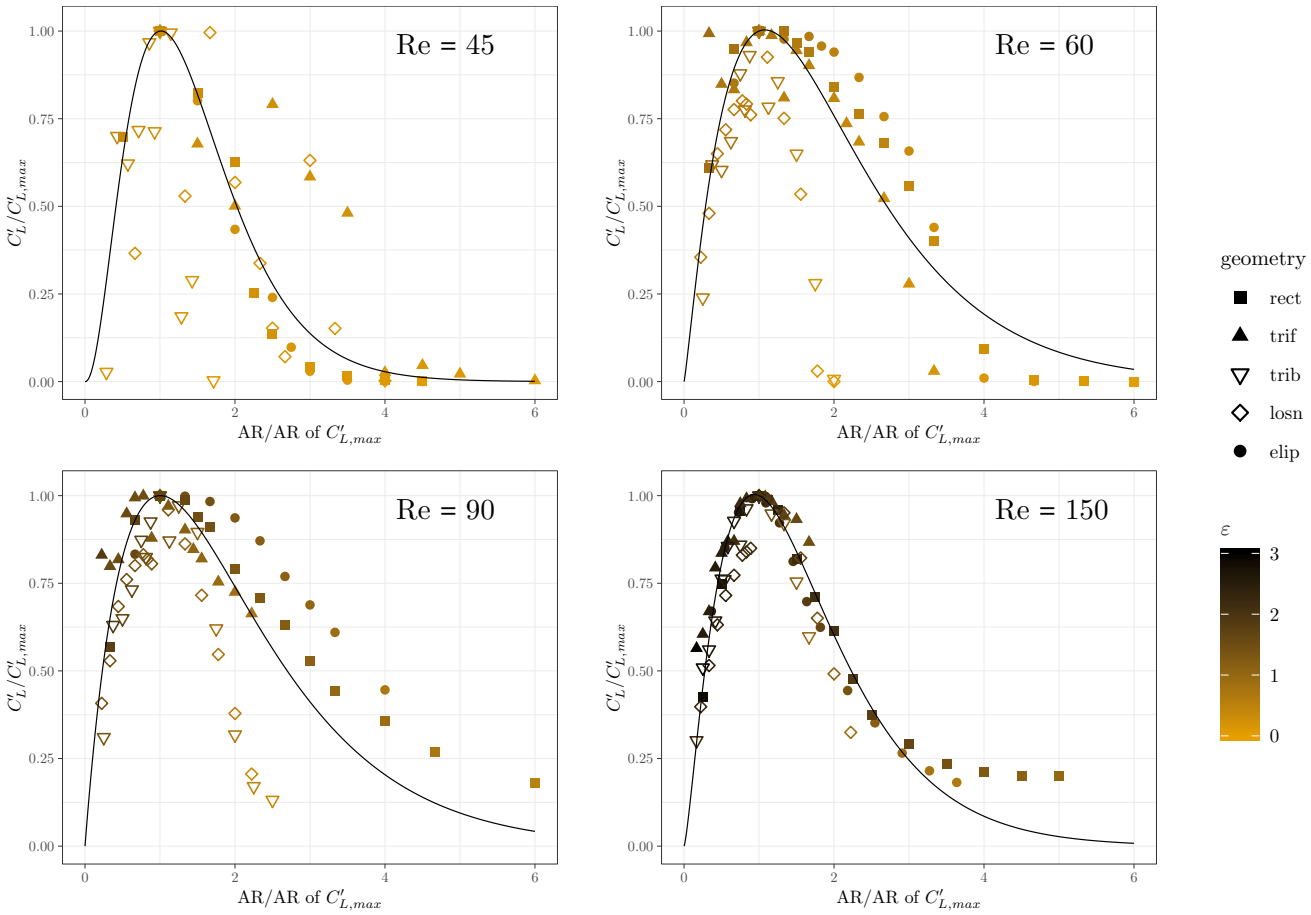

Figure 2.28: Evolution of the RMS lift coefficient with the aspect ratio, both quantities normalized by the levels corresponding to the point of $\max(C'_L)$, multiple Re. Regression curves are as presented in Equation (2.3.9).

While coefficient A is largely modified by Re, B is, for Re > 45, more or less constant and fluctuates around 1. This confirms the distinction between the phenomena that compose the law: the scaling of the lift fluctuation is mainly defined by A and C, thus, it is intrinsically controlled by the incoming flow inertia to viscosity ratio (Re), that can also be interpreted as the amount of incoming energy; on the other hand, the coefficient B, which represents the increase of available surface for the conversion of that wake energy into lift fluctuation, is barely touched.

When reconstructing the original values of RMS lift coefficient and aspect ratio from the corresponding reference values, the following law is derived:

$$C'_L = \alpha \mathrm{AR}^{\beta} \exp\left(-\gamma \mathrm{AR}\right) \tag{2.3.11}$$

with:

$$\alpha = \frac{AC'_{L,max}}{\left(\mathrm{AR}|_{C'_L = C'_{L,max}}\right)^B}\ , \qquad \beta = B\ , \qquad \gamma = \frac{\log(A)}{\mathrm{AR}|_{C'_L = C'_{L,max}}} \tag{2.3.12}$$

The model can either be derived using the coefficients issued from the global regression coefficients A and B and Equation (2.3.12) or calculating new fits for each geometry. Both approaches are performed and the results are listed on Table 2.10 for Re = 150. Regressions are performed for each geometry using the model fitting function nls [12] in R [208]; the values of α, β and γ calculated using Equation (2.3.12) are used as the starting values for the non-linear regression.

Table 2.10: Regression coefficients of the model of the RMS lift coefficient as a function of the aspect ratio, Re = 150 - Equation (2.3.11).

geometry	$AR\|_{C'_L=C'_{L,max}}$	$C'_{L,max}$	universal model*		individual model		
			α	γ	α	β	γ
elip	0.55	0.541	5.1644	1.1420	4.5207	1.2447	2.5548
losn	0.90	0.636	3.1171	0.6979	3.6152	1.6027	1.8299
rect	0.40	0.596	8.7540	1.5702	5.8863	1.1957	3.0869
trib	1.20	0.995	3.3002	0.5234	3.4555	1.4073	1.2965
trif	1.20	0.427	1.4155	0.5234	0.6986	0.6689	0.5331

*: coefficients derived from Equation (2.3.12), $\beta = B = 1.3542$

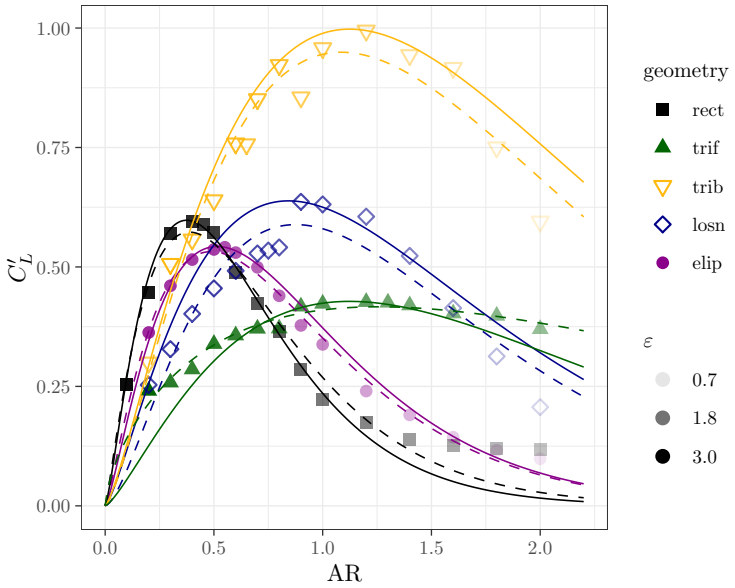

Figure 2.29: Evolution of the RMS lift coefficient with the aspect ratio, Re = 150. Continuous lines correspond to the model using $\beta = B$ (value issued from the regression of all the geometries), hatched line represents the non-linear regression of 3 parameters performed for each geometry.

2.3.3.2.2 Physical insights allowed by the model Both regression models are presented in Figure 2.29 and fit well the original values of $C'_L(\mathrm{AR})$. While the magnitude α is the highest for the rectangular section, the decay is also the strongest, with $\gamma > 3$. The combination of the 2 events results in the rectangular section having its maximum C'_L for the shortest geometry. In the opposite direction is the front-pointing triangular section, which has small α and γ values. Similar of what is seen for the universal model, the scaling coefficients (α and γ) fluctuate more than the coefficient related to the length (β). Thus, while flow modification and change of the capabilities of the obstacle to respond to flow fluctuations cannot be easily separated, it seems that the influence of the geometry to the production of RMS lift is more a matter of the modification of the strength of wake perturbations than the available surface for the generation of the lift.

The fact the β is not exactly 1 and not geometry independent (from 0.7 to 1.6) is an important conclusion in what concerns the geometrical efficiency. The extreme shapes (front-pointing triangle and lozenge) illustrate well the geometrical features that need to be favored when reducing the sound emission: the flow detachment has to be delayed and takes place in regions where pressure fluctuations will not be able to result in lift fluctuations (for example in the form of a sharp edge at the end of the body). However, this statement cannot be considered

individually, since this conclusion regards only the power component of the model. The fact that everything can be scaled differently due to a more or less energetic near-wake (coefficients α and γ) needs to be considered.

The combination of a blockage d and a breadth b defines the velocity gradient that is generated by the body, thus, the strength of the vortex. The geometrical details of the geometry (rectangular, triangular, etc), is mainly going to define how the wake is going to be organized, thus, where vortex shedding is going to take place and consequently the frequency and amplitude of the aerodynamic efforts. In that sense, the use of the Reynolds number based on the macro parameter d is fundamentally correct, since it determines the scale of the flow. However, the nuance of the geometry, the sole source of difference in the integral and topological results, is also a crucial parameter to be considered. One important conclusion that can be drawn from the given regression laws is the universality of the given analysis when considering the aspect ratio.

2.3.3.3 RMS force coefficients vs. distance to the critical Reynolds number

A relationship between the RMS force coefficients and the distance to the critical Reynolds number represented by the parameter ε is examined as well. The lift coefficient is normalized by the aspect ratio so bodies of different breadth are comparable. Following models are proposed:

$$\frac{C_L'}{\mathrm{AR}} = \alpha\varepsilon^{\beta} \qquad\qquad C_D' = \alpha\varepsilon^{\beta} \tag{2.3.13}$$

A polynomial model, based on the formula proposed by Norberg [171] is also considered:

$$\left(\frac{C_L'}{\mathrm{AR}}\right)^2 = \alpha\varepsilon + \beta\varepsilon^2 \tag{2.3.14}$$

In [171], $\alpha = 1/30 \approx 0.033$ and $\beta = 1/90 \approx 0.011$ for circular cylinders. Obtained curves are illustrated in Figure 2.30, regression coefficients are presented on Table 2.11.

Table 2.11: Regression coefficients for normalized RMS, Equation (2.3.9).

		C_L'/AR		C_D'
		$\alpha\varepsilon^{\beta}$	$\sqrt{\alpha\varepsilon + \beta\varepsilon^2}$	$\alpha\varepsilon^{\beta}$
all points	α	0.045	-0.895	0.001
	β	2.678	0.435	3.928
regime I only	α	0.050	-0.406	0.001
	β	2.524	0.233	3.653

Similar to what was obtained for the previously discussed models ($C_L'(L_r/d)$, $C_D'(L_r/d)$ and $C_D'(L_f/d)$), there are some intrinsic deviations from the global laws while more consistent fits are obtained when every geometry is evaluated individually (see Figure B.5 and B.6). Nevertheless, the relation between the fluctuating efforts and ε is evidenced, and can also be taken as universal. The polynomial model is not very representative of a set of multiple geometries.

The rectangle and back-pointing triangle are the sections that deviate the most from the universal regression models. It can be argued that these deviations are associated with a shift in the mechanism of the generation of the fluctuating lift and drag for such kind of geometries for elongated bodies (AR > 1), for which the flow reattaches before reaching the downstream edge.

The given laws naturally lead to the analysis of the ratio between the RMS lift and drag coefficients, illustrated in Figure 2.31.

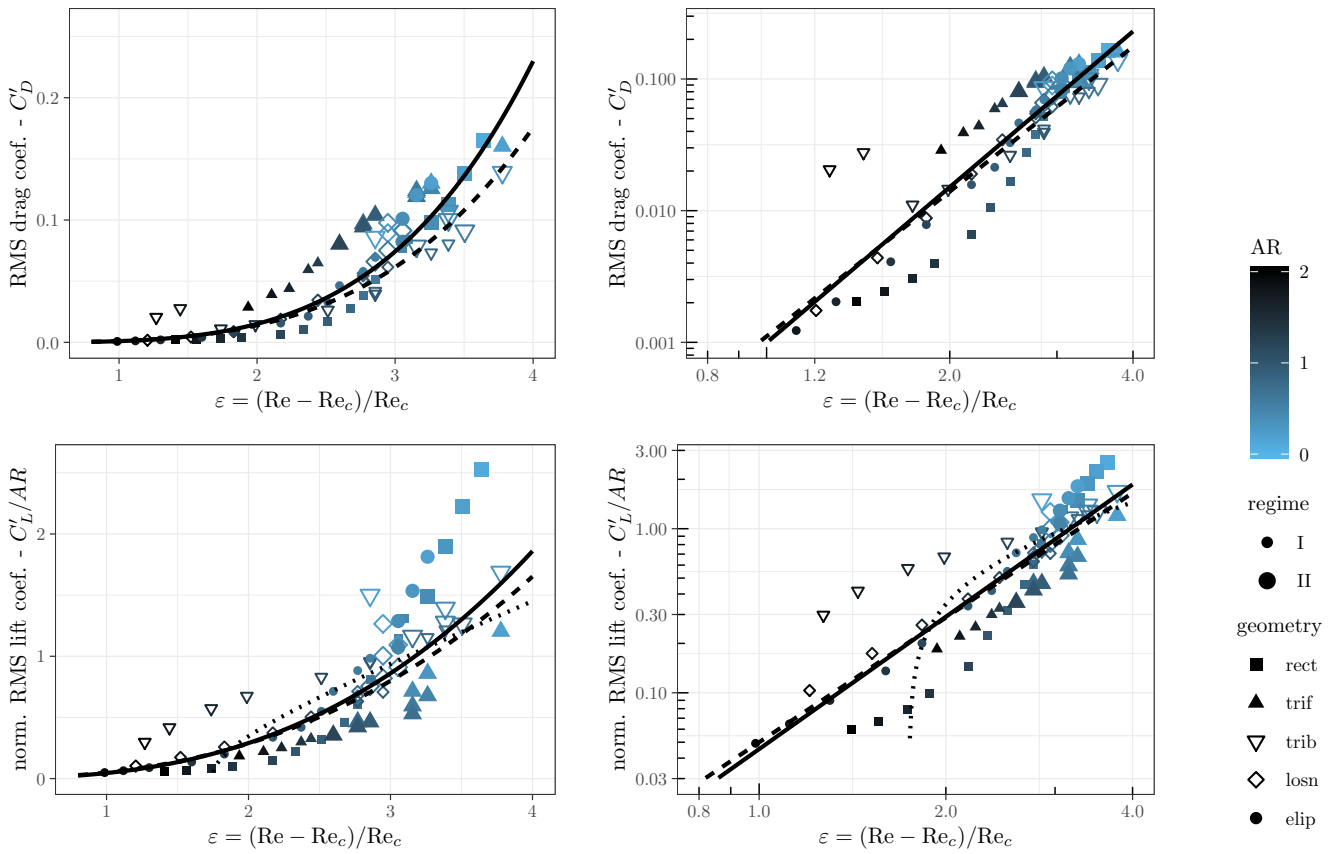

Figure 2.30: Evolution of drag (top) and lift (bottom) RMS force coefficients with ε, linear (left) and log-log (right) scales. Represented regression laws: obtained for all points (solid line); only considering regime I (dashed line); and C'_L model based on the equation proposed by Norberg [171] (dotted lines) calculated for points at regime I.

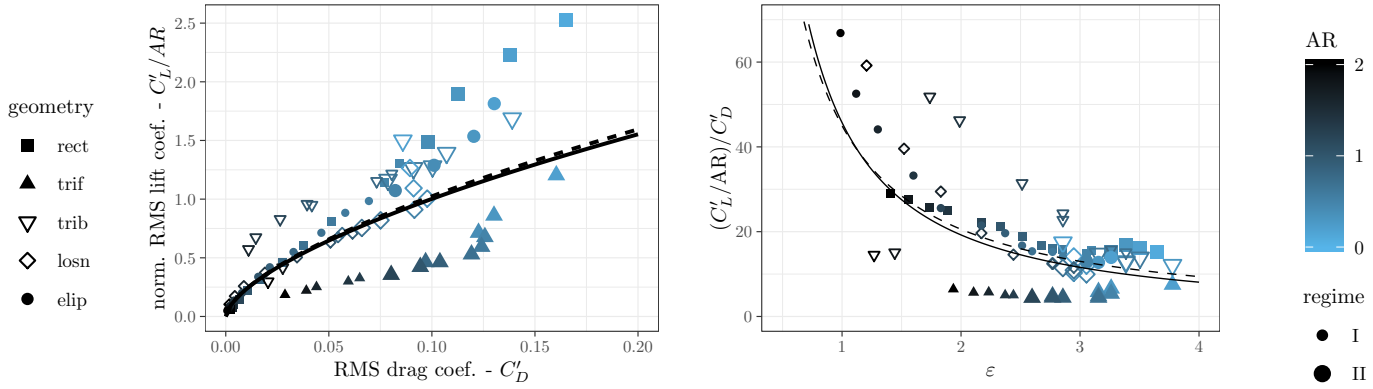

Figure 2.31: Evolution of the normalized RMS lift coefficient with the RMS drag coefficient (left) and the evolution of the lift-to-drag RMS coefficients ratio with ε (right), Re = 150. Represented regression laws: obtained for all points (solid line); and only considering regime I (dashed line).

The dispersion of points in both graphs in Figure 2.31 evidences the influences of the shape and the regime that are less notable in Figure 2.30. The front-pointing triangle has the most continuous behavior, having an almost constant RMS lift-to-drag ratio, while the lozenge and back-pointing triangle range from 10 to 60.

It can also be seen that the bigger ε, the more concentrated are the points, leading to the conclusion that further from the transition there is less influence of the geometry on the levels

of the fluctuating aerodynamic efforts and noise. This could be a biased interpretation due to the fact that large ε values in this work are associated with shorter geometries that are similar in terms of shape (all geometries are converging to a flat plate), thus, less discrepancies between the points is expected.

We may infer that both the drag and lift fluctuation coefficients and the relationship between them can be, partially, associated with the distance to the transition. Even though the points are scattered around the tendency curves, the importance of ε (or any other energy related parameter) as a fundamental ingredient for modeling the phenomenon is noted.

2.3.3.4 RMS lift coefficient vs. mean drag

Empirical laws relating noise and mean drag has been previously proposed by Revell et al. [211]. In an analogous manner, a power relationship between the RMS lift coefficient and the mean drag, Equation (2.3.15), is found in this work. This analysis is only fruitful after normalizing the C_L' by the sectional breadth. This normalization transforms the value of fluctuating lift so it represents with more fidelity the pressure fluctuation on surface.

$$\frac{C_L'}{\mathrm{AR}} = \alpha |C_D|^{\beta} \tag{2.3.15}$$

Points and obtained regression laws considering the complete database and only flows at the regime I are presented in Figure 2.32. Obtained coefficients are $\alpha = 0.0722$ and $\beta = 3.85740$, with adjusted determination coefficient of $R^2 = 0.8863$. When only regime I is considered, coefficients are $\alpha = 0.0661$ and $\beta = 4.210$, with adjusted $R^2 = 0.8819$.

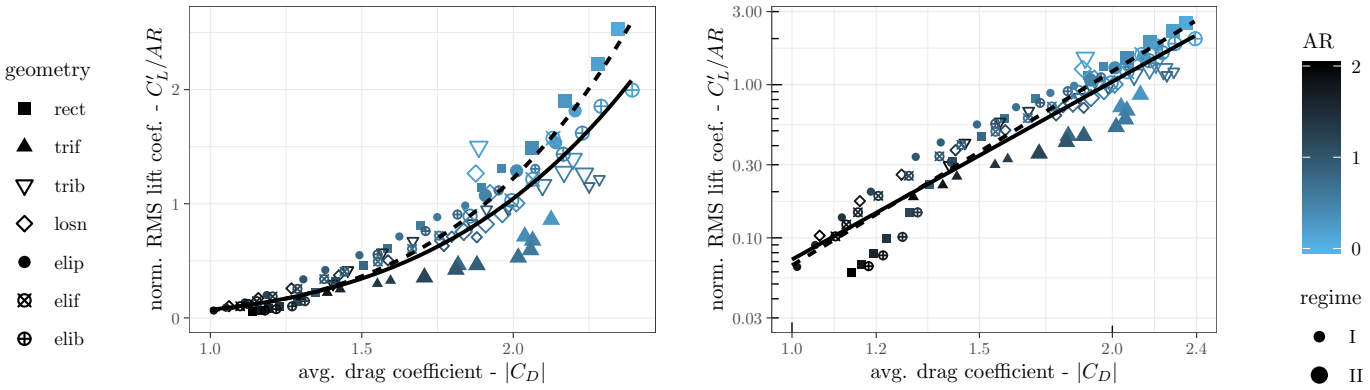

Figure 2.32: Evolution of the normalized RMS lift coefficient with the average drag, Re = 150, all geometries, colored by the aspect ratio; linear scale on the left and log-log scale on the right. Represented regression laws: obtained for all points (solid line); and only considering regime I (dashed line).

This association may be justified from 2 different approaches. From an energetic point of view, we can link the drag coefficient to the amount of energy necessary to the cylinder to move at the given speed in a fluid medium [4]. This energy is disposed in the wake, thus, we may associate a stronger drag to a more energetic wake, that consequently has larger pressure fluctuations at the obstacle's walls, thus, a higher RMS lift coefficient and sound emission. From a wake topology perspective, an increase of the average drag is in fact a decrease of the mean base pressure, that is related to an enhancement of the low-pressure vortices [40], thus, an increase of the RMS lift, the opposite of the effect of the splitter plate initially studied by Roshko [220].

For other Reynolds numbers, the relationship remains consistent, but the fit returns slightly different coefficients. Regression laws obtained using the values issued from the critical Reynolds determination study (Section 2.2.3.1) are presented in Table 2.12. Since the unsteadiness is not present for all points, a threshold of $\varepsilon \geq 0.3$ is used; the regression for all Reynolds numbers considers both wake regimes.

Table 2.12: Regression coefficients of the model of the normalized RMS lift coefficient as a function of the average drag, Equation (2.3.15).

Re	45*	60*	90*	150	all
$\log(\alpha)$	-5.156	-4.549	-3.728	-2.717	-3.231
α	0.006	0.011	0.024	0.066	0.040
β	6.249	6.050	5.177	4.210	4.262

*: for rect, trif, trib, losn and elip, $\varepsilon \geq 0.3$

For an increase of Re there is an increase of the coefficient α and a decrease of the exponent β. Naturally, the disparity between the two coefficients is believed to be due to modifications of the viscous dissipation ratio associated to the change of the Reynolds number. Further investigations must be performed in order to explain that behavior.

The analysis of the laws derived independently for each geometry, Figure B.7, shows that the model underestimates the lift coefficient at the central drag values and overestimate at the extremities. Such behavior is a sign of non-linearities that are not captured by the proposed law. Considering the log-log scale, even though a polynomial model ($\alpha \log(|C_D|)^2 + \beta \log(|C_D|) + \gamma$) results in a better fit, the linear equation is chosen due to its simplicity and overall good representativeness of the relationship.

Recalling that this is an overall tendency, it does not imply that a shape that has a minimal drag will be the one with the smallest RMS lift, notable in the case of aspect ratios that are different than one, but proves that both phenomena (average drag and fluctuating lift) are related at a given Reynolds number and will generally be reduced together. This trend is also reproduced in the shape optimization study presented on Section 3.3.2.2 and on [195].

2.3.4 Synthesis of the empirical laws and concluding remarks

A regression analysis was performed based on the results from aerodynamic simulations of the flow around canonical geometries at low Reynolds. The proposed relations are summarized in Table 2.13. Some comments about the study and the observed behaviors are presented next.

Table 2.13: Summary of discussed models.

#	variables			section	equation
1	RMS lift coefficient	×	recirculation length	2.3.2.1	$C_L' = \alpha + \beta(L_r/d)$
2	RMS drag coefficient	×	formation length	2.3.2.2	$C_D' = \alpha + \exp(\beta L_f/d)$
3	RMS lift coefficient	×	formation length	2.3.2.2	$C_L' = \alpha + \exp(\beta L_f/d)$
4	RMS lift coefficient	×	vortex vertical displacement	2.3.2.3	$C_L' = \alpha \Delta y_\omega$
5	critical Reynolds number	×	aspect ratio	2.3.3.2	$\mathrm{Re_c} = \alpha \exp(\beta \mathrm{AR})$
6	RMS lift coefficient	×	aspect ratio	2.3.3.2	$C_L' = \alpha \mathrm{AR}^\beta \exp(-\gamma \mathrm{AR})$
7	RMS lift coefficient	×	"distance" to transition	2.3.3.3	$C_L'/\mathrm{AR} = \alpha \varepsilon^\beta$
8	RMS drag coefficient	×	"distance" to transition	2.3.3.3	$C_D' = \alpha \varepsilon^\beta$
9	RMS lift coefficient	×	mean drag	2.3.3.4	$C_L'/\mathrm{AR} = \alpha \lvert C_D \rvert^\beta$

Many directions can be taken from the highlighted trends and to expand the empirical laws. For example, a combination of laws # 1 ($C_L' = \alpha + \beta(L_r/d)$) and # 9 ($C_L'/\mathrm{AR} = \alpha|C_D|^\beta$), would generate a function representing the relationship between the mean drag and the recirculation length. Since this work is focused on bluff body noise, many of similar possibilities were not tested.

A global remark concerns, when proposing models based on flow quantities, the necessity to account for the existence of two wake regimes (single and double row of vortices, discussed in Section 2.2.2.2). In about half of the relationships, considering each wake regime independently resulted in quite different regression coefficients.

On all the presented plots the data points corresponding to the low aspect ratio shapes (light blue markers) agglomerate. This is believed to be associated to 2 reasons. First, there is the fact that, particularly with the given geometrical resolution (see Figure 2.2), the differences between the shapes of short AR as seen by the solver are small, represented only by a few number of nodes. Second, the vortex shedding seems to be less influenced by any other geometrical feature when the aspect ratio is reduced, all the shapes being seeing by the flow, at least at the given Reynolds number, as flat plates normal to the incoming particles.

Also, it is found that the distance of average and unsteady flow phenomena from the body grows as the inverse of the RMS force coefficients, thus, aeolian tone levels. The inverse trend is observed when considering the flapping of the vortices on the upper and lower faces of the obstacle (linearly proportional to C_L'). With the increase of the aspect ratio, a mix of contrary effects (increase of the available surface and decrease of the level of surface pressure fluctuations) generates a hormetic response that is found to be universal. When considering the distance from the onset of unsteadiness in the Reynolds number scale, represented by parameter ε, fluctuating efforts are growing with exponents 2.5 and 3.6. The increase of the mean drag coefficient is, on average, accompanied by an increase of the normalized RMS lift coefficient.

The disparity between the increase of the available surface for the establishment of lift fluctuations versus the decrease of proximity of the vortices and of the energy in the wake (with the increase of the critical Reynolds number and decrease of the distance to transition) is the main difficulty when prospecting about the sound efficiency of a given body. Despite being important, the respect of a Reynolds number similitude is not sufficient and actually goes against the principle of placing the different obstacles at an equal energetic scale so that the influence of the geometry alone is analyzed when investigating the sound emission. In the limit of the results presented in this document, ε can be considered a better criterion to represent these energetic effects, thus, without any knowledge about the shape, given an estimation of the RMS force coefficients and aeolian tone level, with the important drawback that the critical Reynolds number must be known.

It must be emphasized that, as stated earlier, there is no implication of causality between the variables. Such assumptions are out of the scope of a regression analysis and demand the use of the flow equations, hypotheses on the physics and an extensive mathematical formalism. However, the highlighted laws have an important role in evidencing the elements that must be considered for the production of simplified wake models from a geometry independent point of view.

In the continuation of the quest to study the shape influence on the noise production, parametric studies of two other shapes are presented next.

2.4 Further parametric studies

The parametric studies performed in this section are inspired by the geometrical features of the triangular section (loudest cross-section). The sharp lateral edges are evaluated in the form of a T-profile and the capacity to deviate the mixing layers is assessed using a trapezium. The use of such non-canonical shapes is meant to enhance the underlying mechanisms of such acoustic efficiency in order to clarify their role in the vortex shedding. This idea is extended in the optimization studies of Chapter 3.

Two parametric studies are presented hereafter: the thickness and the breadth of a T-profile (symmetrical with respect to the streamwise axis) in Section 2.4.1; and the angle of the upper edge of a non-symmetrical trapezium in Section 2.4.2. The numerical setup is the same as in Section 2.1.3, with a fixed blockage and a Reynolds number of Re = 150.

2.4.1 T-profile

Based on the observations reported in the previous sections, a parametric study is performed with T-shaped profiles. The principle is to check if the existence of a sharp edge that generates the flow detachment and the vortex generation, as for in the back-pointing triangle (the loudest shape), is a dominant geometrical feature in what concerns the vortex shedding. The shape is represented in Figure 2.33, the thickness of the profile is defined by the parameter h.

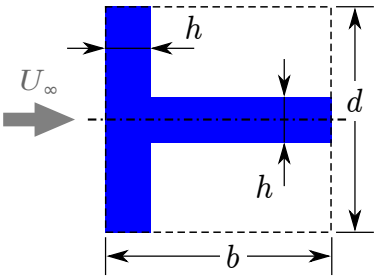

Figure 2.33: Illustration of the T-profile used in the parametric study. Profile of thickness $h/d = 0.2$ is represented.

Two studies are performed: for fixed aspect ratio AR = 1.0, the thickness factor is modified from $h/d = 0.1$ to $h/d = 1.0$ (square); and for a fixed thickness of $h/d = 0.1$, modification of the aspect ratio from 0.2 to 2.0. The results obtained for the two tests are presented next and systematically compared with the back-pointing triangle and the rectangular cross-sections.

2.4.1.1 Aerodynamic behavior of the T-profile

For short sections (small AR), the flow around the profile collapses into the common topology found for all the tested shapes at such aspect ratio, with very strong vortices, small recirculation and formation lengths, and wake mode II. For bigger AR, the aerodynamic fields are quite similar to those of the back-pointing triangle, with two recirculation zones existing right upstream the trailing edge that enhance the opposite sign vortexes that are shed. The transition between the wake modes happens at AR = $0.5 - 0.6$ for thickness of $h/d = 0.1$. Both behaviors are illustrated in Figure 2.34.

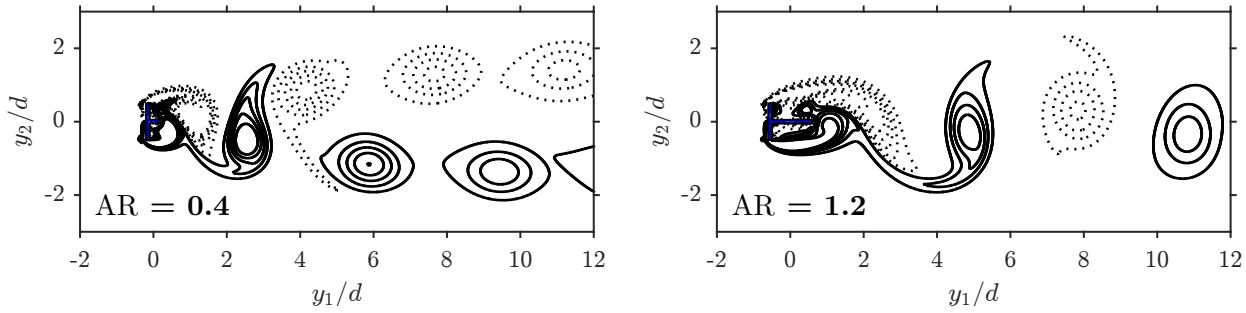

Figure 2.34: Vorticity snapshots for the flow around the T-profile ($h/d = 0.1$), for AR = 0.4 (left) and AR = 1.2 (right), Re = 150. Interval of 0.3 U_∞/d, continuous line for positive and dotted line for negative.

2.4.1.1.1 Multiple aspect ratios The evolution of the aerodynamic quantities with the aspect ratio is presented in Figure 2.35. The similarity with the back-pointing triangle seen in the flow is also present in the aerodynamic coefficients. The values obtained for the integral quantities for the T-profile are even coincidental for a number of aspect ratios, in particular for the quantities that influence noise, that is, the RMS lift coefficient and the vortex shedding Strouhal number.

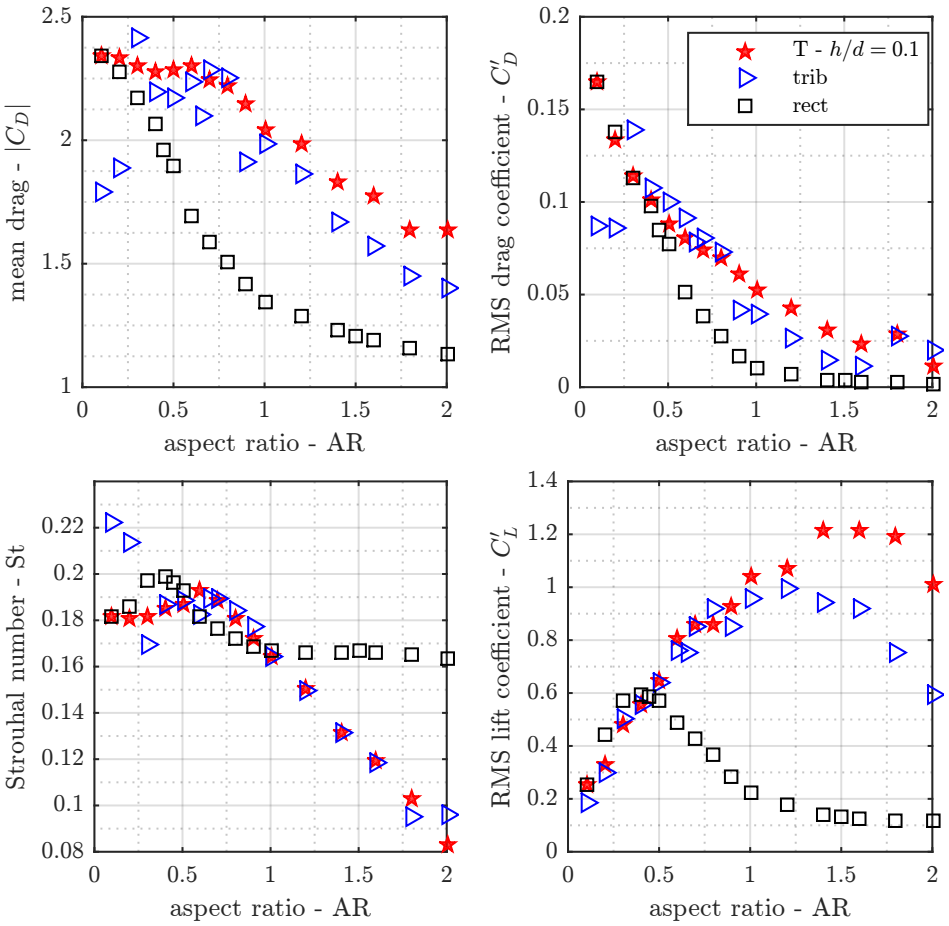

Figure 2.35: Evolution of the mean and RMS drag coefficients, Strouhal number and RMS lift coefficient with the aspect ratio, for the T-profile (h/d = 0.1), back-pointing triangle (trib) and rectangle (rect), Re = 150.

The bi-phasic response of the RMS lift coefficient to an aspect ratio increase, discussed in Section 2.3.3.2, is also present for the T-profile. This contributes to the hypothesis of universality of such behavior and reinforces the relevance of the discussed model.

The fact that the fluctuating lift of the T-profiles even exceeds that of the back-pointing triangle is coherent with the other results presented here. Based on the discussion about the shape influence on the critical Reynolds number in Section 2.2.3.3, one may conclude that the T-profile, such as trib, has an early transition based on the strong discontinuity and low surface for dissipation. Then, from a distance to transition perspective, the wake would be very energetic (high ε) with strong vortices. The main difference from the corresponding triangular cross-section is the fact that there is even less surface for the settlement of energy dissipation, thus, the RMS lift coefficient is even bigger.

2.4.1.1.2 Multiple thickness Results for the case of multiple thickness and unitary aspect ratio are presented on Figure 2.36, with lines representing the corresponding quantities for the back-pointing triangle and the rectangle (square) of the same breadth. There is a clear transition between something close to the back-pointing triangle and the square, apart from the Strouhal number, with no discontinuities.

2.4.2 Trapezium

A trapezium is used in order to evaluate the role of the deviation of the mixing layers in the vortex shedding, similarly to the experimental work performed by Luo et al. [140]. The aspect ratio is fixed as unitary ($b = d$) and a single parameter, the angle of the upper edge, is varied.

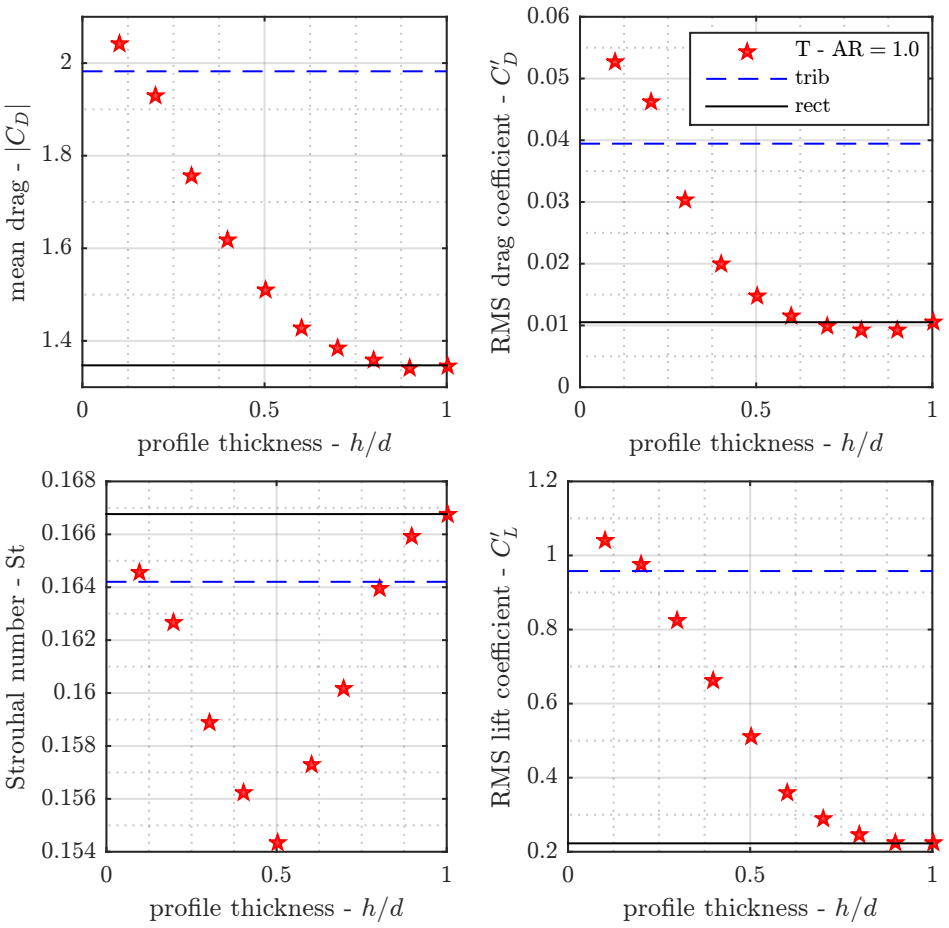

Figure 2.36: Evolution of the mean and RMS drag coefficients, Strouhal number and RMS lift coefficient with the thickness of the T-profile of AR = 1.0. Lines represent the observed values for the back-pointing triangle (trib) and rectangle (rect) of unitary aspect ratio, Re = 150.

As represented on Figure 2.37, a negative angle represents an expanding layer (blockage is increasing in the streamwise direction) and a positive angle the opposite (blockage is decreasing in the streamwise direction); a null angle represents the square cross-section.

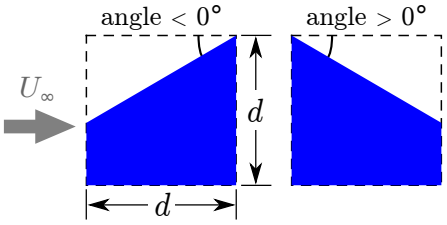

Figure 2.37: Illustration of the trapezium used in the parametric study. Angles of $\pm 30^\circ$ are represented.

The considered range of the angle of the upper edge is bounded by its geometrical limits: from -45° (triangle pointing upstream) to $+45^\circ$ (triangle pointing downstream), every 5 degrees. The flow and the aerodynamic coefficients are discussed next. Values corresponding to the flow around the back and front-pointing triangles are represented as well.

2.4.2.1 Aerodynamic behavior of the asymmetrical trapeziums

The evolution of the aerodynamic coefficients with the angle of the upper edge are presented on Figure 2.38, with the comparison to the front and back-pointing triangles of the same aspect

ratio (trif and trib, AR = 1.0). All the wakes are in regime I (single axis of vortices).

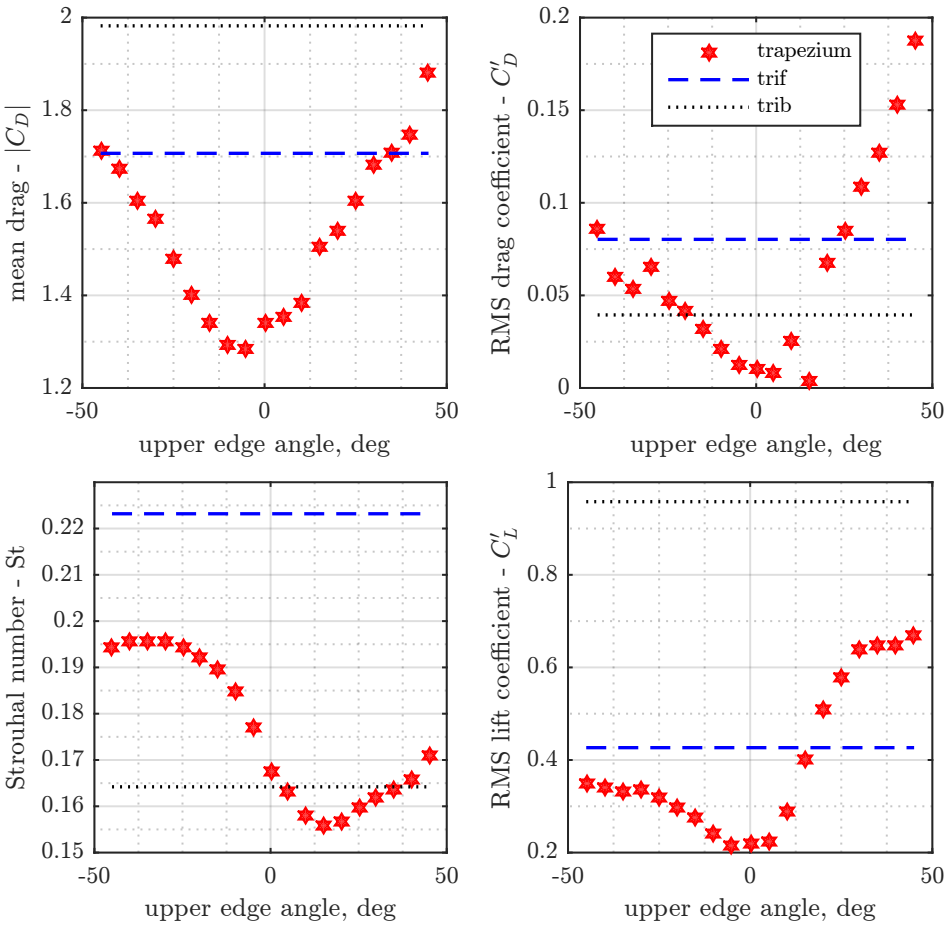

Figure 2.38: Evolution of the mean and RMS drag coefficients, Strouhal number and RMS lift coefficient with the upper angle of the trapezium (AR = 1.0). Lines represent the observed values for the front-pointing triangle (trif, dashed) and the back-pointing triangle (trib, dotted) of unitary aspect ratio, Re = 150.

There is a sort of symmetry around the null angle (square), with an increase of the average drag, RMS drag and lift coefficient. The Strouhal number has a unique behavior, with an increase for all the negative angles and decrease for almost all the positive angles when comparing to 0°. The major difference between the two tendencies is the magnitude.

Despite the gains for the negative angles (increase of the blockage with y_1, expanded mixing layers), the changes in the aerodynamic coefficients are weaker than those obtained with the positive angles.

The analysis of the average and instantaneous flow fields (the latter is illustrated in Figure 2.39) shows that in terms of the vorticity magnitude there is a similar behavior, with the vortices close to the obstacle. Also, both positive and negative inclinations produce wakes which have the axis tilted towards positive y_2. Even so, the main difference is that, for the upper edge at negative angles, this modification simply happens after the end of the geometry, so it does not produce the same effect as for the shapes with positive angle.

Both extrema are louder than the square section ($W_a = 17.43 \times 10^{-5}$ for the trapezium with an edge angle of -45° and $W_a = 5.25 \times 10^{-5}$ for $+45^\circ$, against $W_a = 1.60 \times 10^{-5}$ for the square section). A priori, the asymmetry (present in the trapeziums) is not beneficial to the RMS lift coefficient, thus, beneficial to the noise. The RMS lift coefficient for the angle of $+45^\circ$ is only about half the one of the back-pointing triangle (its symmetrical analogue).

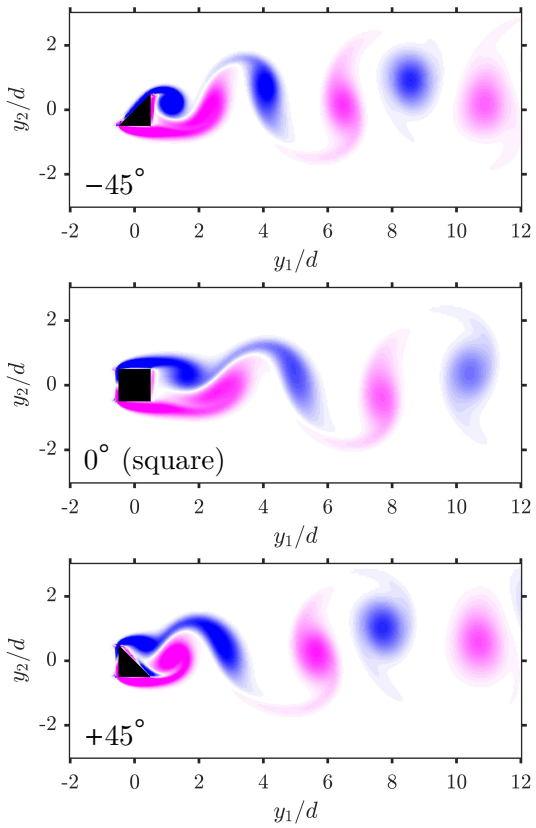

Figure 2.39: Instantaneous vorticity contour for the trapeziums of $+45^\circ$ and -45° and the square section. Vorticity scale is of $\omega_3 = [-3d/U_\infty, +3d/U_\infty]$, same as in Figure 2.6. Re = 150.

2.4.3 Inferences from the parametric studies

In both parametric studies, the behavior is quite similar to what is seem with the triangular sections both in terms of flow (strong vortices, shedding close to the cross-section) and integral quantities (elevated drag and RMS lift coefficient, similar Strouhal number).

The noted behavior leads to the conclusion that, in terms of generation of the perturbation, that is, the production of the conditions for a strong vortex-shedding, the shape is less important once critical features are present. Those features, from the results, are a fast blockage, space for the development of the vortex and small separation between the mixing layers. All these points are found in the T-profile and for the trapeziums with a positive upper edge inclination. They are also present for the trapeziums of negative inclination, however, they do not result in large RMS lift coefficients because there are no walls available to interact with the wake.

Even if not formally tested, the empirical relationships (Section 2.3) that correlate the recirculation and formation lengths, average drag and the RMS lift coefficient seem to be respected. Furthermore, the consistency between the observations issued from the parametric studies and all the other aspects investigated in the chapter are discussed further.

2.5 Discussion of the results and final remarks on cross-section influence on bluff body noise

In order to study of the influence of the geometry in the bluff body noise, two-dimensional, laminar flows at low Reynolds number were simulated for about a hundred different shapes of obstacles, using a DNS solver with an IBM routine for the description of the bodies. Typical von Kármán vortex shedding is present for all the shapes, with the existence of two wake regimes (single and double row of vortices). The second one is associated with low aspect ratio geometries. The transition between the two regimes is marked by a peak of the RMS lift (C_L')

and of the wake frequency (St). A summary of the findings and a discussion about the principal points of the investigations are presented next, with a critical analysis of the performed study and the presentation of possible further steps.

2.5.1 Main conclusions

As a global instability, the von Kármán vortex shedding is fundamentally the same for all the cylinders. Despite the similarities of the wakes, the wall and integral quantities are naturally different due to the change of the form of the obstacles and of the flow excitation. The complexity of the analysis is mostly due to the fact that the shape is at the same time the origin but also the receptor of the modifications it generates in the incoming flow. Despite the size of the challenge, the use of a large set of geometries allowed some general conclusions to be drawn. They are presented next.

Geometries that can be associated to lower levels of noise are those that are capable to dissipate energy before the wake, which is associated with longer recirculation and formation lengths and a low ε. This is achieved for all geometries when increasing the aspect ratio (see Figure 2.5). When comparing the shapes at fixed AR, bodies of increased bluffness (that impose a larger distance between the two shear layers and at the same time have reduced available surface for the production of lift fluctuations downstream of the flow detachment) are the ones that have a lower acoustic efficiency. For the set of tested geometries, the most silent shapes are the front pointing triangle at low aspect ratio ($AR < 0.7$) and the rectangular cylinder at bigger aspect ratios ($AR \geq 0.7$).

On the other hand, the geometrical features that increases the vortex shedding magnitude are a strong "discontinuity" in the fluid, that is, an abrupt blockage of the flow (such as for the rectangle or the back-pointing triangle), and the existence of a place in the wake for the pressure fluctuations caused by the vortices to be transformed into force fluctuations (as encountered in the back-pointing triangle and the T-profile). Though, according to the critical Reynolds analysis in Section 2.2.3.3, following the opposite direction (with a gradual increase of the blockage, such as the obtained with the front-pointing triangle) may not result in a decrease of the noise efficiency. Such geometries have a reduced critical Reynolds number, what would represent, at a fixed Re, a higher energy state.

From the regression laws that were deduced, it was proven that the aerodynamic efforts (mean drag and RMS lift) are correlated with the vortex distance to the trailing edge and the distance to the transition from steady to unsteady flow. Consequently, it seems evident that the main paradigms for the qualification and quantification of the noise production must be based on the vortex strength and location simultaneously. It is also noted that different trends (same functions but different coefficients) are found for the different flow topologies (wake modes I and II, Figure 2.7), evidencing that it is fundamental to consider the flow organization when proposing models that relate the flow quantities.

The correlation between the distance to transition and the amplitude of the efforts may be expanded. As discussed in Section 2.2.3.4, there is a possible link between the Reynolds number at the transition to unsteadiness (Re_c) and the Reynolds number of the transition to 3D flow. This observation could only be made with a large database that expands the vision of these transitions to other shapes than the classical circular and square sections.

2.5.2 Criticism and possible improvements

Many improvements might be performed in this work, notably in terms of a refinement of the post-treatment techniques in order to have access to a larger set of flow variables.

First of all, the absence of wall data due to the use of the IBM formalism impoverishes the analysis. There are no information about the detachment points, the separation between pressure and friction efforts and a precise discrimination between surface effects of interest, such as the base pressure. A methodology used in [145], consisting in the generation of a boundary mesh around the artificial contour (generalized with the use of the CLOVIS algorithm in [216]),

performing the interpolation of the data from the simulated nodes, filtering in the normal and tangential directions and extrapolating to the wall is tried. Despite its good result for some of the geometries, the method was not sufficiently robust for the large set of shapes in the present study, returning, for instance, non-negligible differences between the aerodynamic efforts obtained from the wall quantities and those from the solid elements in the IBM.

Also, this work could benefit from a more refined flow topology analysis. The evolution of the wake, the vortex properties (size, strength, distance), the quantification of circulation are some examples. Such analysis was performed for a small set of cases, but its systematic use is problematic. In addition to the large amount of data that this would generate, there is the intrinsic difficulty in extent of such a database in producing tools that are robust enough to be applied to all the configurations simulated here. One example of the complications is the distinction between the vorticity generated at the walls and the vortex free-rotation vorticity, without the use of arbitrary distance or magnitude thresholds, in order to have a correct comparison between the geometries. On this mater, tests based on the article of Kolář [114] were performed but not developed further.

In addition, the fact that the most the work is performed at a single Reynolds number Re = 150 restricts most of its discussions and conclusions. There is no guarantee that the trends associated with the shape modifications are not limited to such flow regime. Whether possible, a remark around the noted behavior at different Re was presented (for example for the relationship between the RMS lift coefficient and the aspect ratio in Section 2.3.3.2). However, this was not possible for all the results here.

Finally, the proposed laws in Section 2.3 are issued from a regression analysis, that is, only the correlation and not the causality of the flow quantities are studied. The use of analytic developments is necessary to expand the observed trends and further expand the knowledge about the vortex shedding dynamics. Nevertheless, the procedure used to obtain the models is rather archaic and could profit from automatic routines based on machine learning and other advanced techniques of analysis, with a possible extension to a multivariate analysis.

2.5.3 Context of this chapter and perspectives

This part of the work represents a construction and expansion of general knowledge on the shape influence on the noise production of bluff bodies. This chapter is composed of the presentation of the numerical setup, discussions on general trends on the vortex-shedding and conclusions about the geometrical features that are important for the sound production (that leads to the choice of the geometries used in the experimental work).

The performed analysis is mostly based on canonical shapes. Hence, there is a limitation in the range of shapes and geometrical features that were tested, and some interesting phenomena may be missing. In order to expand the range of shapes by focusing on the extreme behaviors in terms of acoustic emission, a shape optimization study is performed and presented next in Chapter 3.

Nevertheless, the extrapolation of these results to high Reynolds number flows, particularly for aeroacoustics applications, is delicate. The cross-section has a fundamental role in the definition of the flow spanwise development, so the use of current values and conclusions, limited to the 2D behavior, may not be directly transposed to an engineering context. A complementary analysis aimed to assess this issue with the use of wind tunnel testing (with measurements of sound emission and of the spanwise distribution of the flow) is presented in Chapter 4.

As recalled several times in the text, the transition dynamics of the instability mode and the distance to transition is a fundamental part of the understanding of vortex shedding dynamics and the influence of the shape on it. The use of a stability study is thus essential for the deepening of such analysis and it is considered in the following steps of the project.

Chapter 3

Extreme behaviors through 2D shape optimization

In the search of understanding the influence of the shape in the aeroacoustic noise generation, one interesting direction is to define geometries that have an extreme behavior. In this case, finding the loudest is of equal interest as finding the quietest cylinder. Based on such shapes, the critical geometrical features and the associated flow characteristics emerge and the analysis may be performed more directly than in the parametric studies carried out in Chapter 2.

To obtain such geometries, an optimization procedure has been implemented for 2D, low Reynolds (Re = 150) flows. It is based on the same numerical setup as in Chapter 2. The absence of the spanwise direction is, as in the previous analysis, a limitation in terms of the range of application of current results and possible direct extrapolations of the findings. Even so, the analysis of the flow response in 2D remains relevant since the dynamics of the vortex shedding and the von Kármán instability is equally present in both 2D, low Reynolds and 3D, high Reynolds regimes. The effect of the third dimension is studied experimentally and presented in Chapter 4.

First, a review of the principles of shape optimization and optimization frameworks found in the literature are presented, with several examples focused on the aerodynamics and/or aeroacoustics (Section 3.1). In, Section 3.2, the optimization method used in this work (Particle Swarm Optimization) is presented, with a detailed discussion about the computational implementation. Optimal shapes and the associated flow topologies are presented next (Section 3.3), for three different shape parametrizations. Finally, a conclusion about the implementation and the physical insights inherited from the optimal shapes close the chapter in Section 3.4. Methods and results from this chapter have also been published in [38] and [195], both articles are partially reproduced here.

3.1 Optimization fundaments and background

An optimization is a mathematical procedure to look for a set of parameters that results in a wanted behavior, that is, for example, the regression coefficients that reduce the error between the measured points and an empirical model, the shape of a beam that is more resistant (yet being light) or the shape of a car that results in a small drag, lift and/or enhanced stability properties. It is employed in all scientific and engineering domains, and is a very complex and diverse subject. The following excerpts are focused on the current application and as such must be considered a small, non-extensive introduction of the subject. Even if restricted, the discussion about the foundations of the optimization routine is a fundamental element in a successful construction of the routine and for validity of the results.

Following sections present a review on the nature and use of the different elements of a shape optimization procedure, and on the shape optimization frameworks found in the literature. The selected optimizer and framework used in this work are introduced and discussed.

3.1.1 Principles of a shape optimization procedure

A shape optimization is composed by 3 fundamental bricks (the global principle is illustrated in Figure 3.1): the shape parametrization defining the relationship between a set of parameters Θ and a shape, the objective/cost function $f(\Theta)$ that, from the shape, returns the quantities that one is aiming to optimize (decrease or increase) and the optimizer, an iterative process that updates the shape parameters based on the previous objective/cost function evaluations.

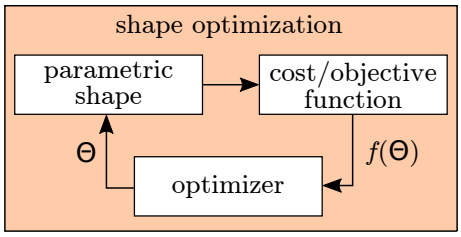

Figure 3.1: Diagram of the base shape optimization framework.

These three elements are discussed further. The optimization elements in this introduction are expanded in Appendix D, where the concepts are further developed and examples of different types of these 3 elements are presented.

3.1.1.1 Shape parametrization

A parametrized shape is a set of equations or geometrical laws that fully define a geometry based on a finite number of parameters. A canonical example of shape parametrization are the 4-digit NACA airfoils, completely defined by 4 variables [1]. Common practices are the use of Bézier curves (Appendix D.1.1) and B-splines (D.1.2) for the construction of the parametric shape due to their geometrical continuity.

The set of constraints (minimum and maximum) for each of the parameters is called the design space. Each dimension of the design space corresponds to a shape parameter. Thus, since the complexity of the problem increases with the number of dimensions that is evaluated, the choices for the parametrization must be performed in a compromise between a desired refinement in the shape control and the feasibility of the optimization.

The nature of the optimization technique limits the optimal shapes to be a function of the geometrical setup and design space, that is, no trend or behavior issued from shapes that can not be reached within the proposed parametrization or that lies outside the design space can be evaluated.

Accordingly to the underlined points, the definition of the parametrization and the design space play a role in the obtained result and must consider the physics of the problem and the scope of the applications of the shape. It is necessary to, simultaneously, allow a shape modification that can have a significant effect in the quantities of interest, while avoiding modifications that are inapplicable or that cannot be correctly predicted by the considered discretization and physical model.

3.1.1.2 Objective/cost function

An objective function or cost function is a function or procedure that has the parametrization parameters as inputs and returns one or a set of quantities of interest, such as the aerodynamic coefficients or the total noise emission in an aeroacoustics application. The terms "objective" and "cost" represent, respectively, cases where you want to maximize and minimize a behavior. Since the minimization and maximization procedures are easily interchangeable procedures just by the application of the inverse to the answer, that is, the maximization of the function g is the minimization of function $1/g$ and vice versa, the two cases are represented in this work by the same symbol f.

There are several options in how the objective function behaves. It can have single or multiple inputs and single or multiple-objectives. Multiple-objective (or multiple criteria) applications are of increased complexity since there must be a compromise between the different outputs, usually conflicting. The definition of a set of solutions that represent a balance between the quantities forms the Pareto's Front [25]. The current study is not focused on any direct application, which would normally require a shape that is aerodynamically and aeroacoustically efficient at the same time, so this work is limited to single objective cases. The shape influence on each of the two aspects (efforts and noise) is analyzed separately, with a focus on the unsteady statistics of the flow and on the cylinder noise efficiency.

For engineering applications, the evaluation of the objective function represents the most expensive part of the calculation, being commonly replaced by a surrogate model when performing the optimization. The surrogate model is obtained from a reduced set of evaluations that compose a database of inputs and outputs that is later modeled using techniques such as interpolation functions or machine learning algorithms.

Also, in what concerns an aerodynamic simulation, the evaluation of the objective function also contemplates the pre-processing (notably, shape and mesh generations), the solution of the equations and the post-processing steps necessary to produce the quantities of interest. In the case of an aeroacoustic analogy, procedure to evaluate the acoustic field increase the complexity and computational cost of each evaluation.

3.1.1.3 Optimizer

The optimizer is the set of equations that control how the shape parameters are updated iteratively and define the optimization routine. In general terms, it consists in guiding the search to follow the direction of a good trend (or to go in the opposite direction a bad trend), based on previous evaluations of the objective/cost function.

There are many options for the optimizer, for instance, they can be based on the partial derivatives of the objective function in terms of the shape parameters, such as the gradient descent optimization, that searches for the location in the design space where the gradient vanishes, which represents a local maximum/minimum. There is also a large range of algorithms that mimic the biological behavior of the species, such as the Darwin's theory of biological evolution or the social behavior of animals, in order to find the most fitting individual or a point of interest in space; they are usually also composed of one or more stochastic steps.

Some examples of the nature based stochastic algorithms are the Genetic Algorithms (GA) [67], Differential Evolution (DE) [246], Ant Colony Optimization (ACO) [47] and Particle Swarm Optimization (PSO) [110]. Reader is invited to check a comparison of methods in [23, 50] and the algorithms of some examples in Appendix D.4.

The gradient based techniques are more adapted to very localized search and to a low number of parameters (due to the necessity of evaluating the derivatives for each dimension of the design space) and the result highly depends on the starting points. On the other hand, the stochastic methods are normally more expensive in terms of objective function evaluations, but more robust and adapted for the exploration of larger design spaces and for the search of a the global optimum.

When performing a shape optimization, not only the elements themselves, but also their organization is important in terms of feasibility and cost of the optimization routine. In this sense, different optimization frameworks found in the literature are presented next.

3.1.2 Review on shape optimization frameworks

By nature, an optimization is based on different evaluations of the objective function. This represents, from a computational point of view, an expensive procedure. Hence, the organization of the optimization procedure (later in this document referred to as optimization framework) revolves around how and how many evaluations of the objective function are going to be performed.

Three different optimization frameworks are introduced next: the base framework, in which there are direct evaluations of the objective function; the adjoint optimization procedure; and the surrogate based framework in which a model of the cost function, previously produced, is used in the optimization as a replacement of the objective function evaluation. Recall that more details about these elements can be found in Appendix D.

3.1.2.1 Base shape optimization framework

The most classical optimization framework is presented in Figure 3.2. From a vector of initial parameters (or family of vectors), $\mathbf{\Theta_0}$, a mesh is built and the solver (in a large sense, representing the procedure from the flow solution to the post-processing steps that result in the aerodynamic or aeroacoustic quantities of interest) is called. The routines in the optimization method (simply referred simply to as "optimizer" in the scheme) update the parameter vectors $\mathbf{\Theta_k}$ in an iterative manner, the shape and mesh are reconstructed and the calculation is performed once more until convergence is achieved. Each iteration implies at least one evaluation of the objective function. Due to the rather large number of evaluations, the application of these methods is normally associated with low-order or low fidelity solutions (panel method, RANS). Examples are limited to the optimization of aerodynamic profiles and wing shapes based on potential flow solvers [72, 75, 268].

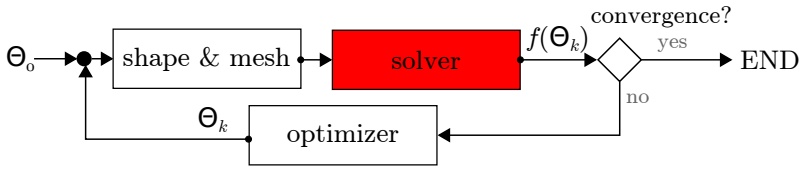

Figure 3.2: Diagram of the base shape optimization framework.

3.1.2.2 Adjoint shape optimization framework

Another possibility for the use of shape optimization for a large number of variables is based on the application of the control theory: the model of the adjoint equations, introduced by Lions [134]. The gradients are obtained from the solution of a single differential equation, and then gradient based optimization routines are applied, see Figure 3.3. Examples of application can be found in [95, 96, 178, 180]. The complexity of this procedure lies in the necessity to define the adjoint equations, that are naturally dependend on the shape parametrization.

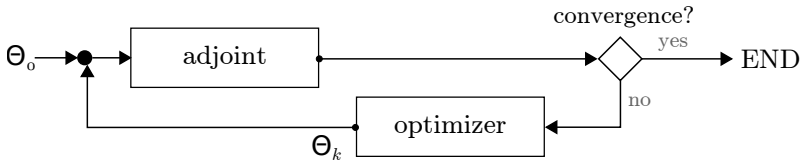

Figure 3.3: Diagram of the adjoint shape optimization framework.

3.1.2.3 Surrogate based shape optimization framework

The use of a surrogate model, also known as metamodel or Response Surface Model (RSM), built from a reduced number of objective function evaluations allows simultaneously to increase the complexity of the problem and the number of iterations of the optimization. As presented in Figure 3.4, an initial vector $\mathbf{\Theta}$ (defined as such to contemplate the totality of different zones and behaviors inside the design space, normally following the principles of the Design of Experiments - DoE) are evaluated producing a matrix of results $f(\mathbf{\Theta})$. The input/output pairs are used for

the definition of a model $\hat{f}(\boldsymbol{\Theta}_k)$ of the objective function. Inside of the optimization routine, the estimation of the objective function is used and there is no reconstruction of the shape and mesh. The quality of the obtained results is completely subjected to the fidelity between the RSM and the objective function.

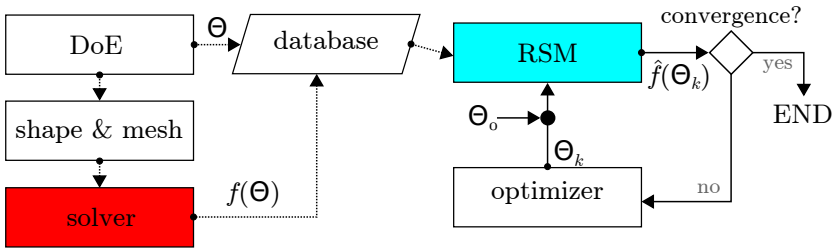

Figure 3.4: Diagram of the surrogate based shape optimization framework.

This approach is found in numerous articles, among them: the minimization of profile noise by Marsden et al. [148]; the optimization framework proposed by Peigin & Epstein [186] applied to a RAE2822 profile; the multidisciplinary optimization (aerodynamics and aeroacoustics) of 4-digit NACA profiles by Jouhaud et al. [103]; shape optimization of high-speed trains performed by Krajnovic [117]; the aerodynamic and aeroacoustic study by Beigmoradi et al. [17] on an extended Ahmed body; the optimization of an air inlet of an aeronautical engine by Naumann et al. [162]; the panhead optimization by Rho et al. [212]; and the multi-objective optimization (drag and noise) of a circular cylinder with a splitter plate by Karthik et al. [107].

An adaptive method of this model is used and consists in performing a supplementary test during the optimization in order to refine the model (Figure 3.5), for example at the regions with a strong gradient of $\hat{f}(\boldsymbol{\Theta}_k)$. Examples can be seen in [103, 223].

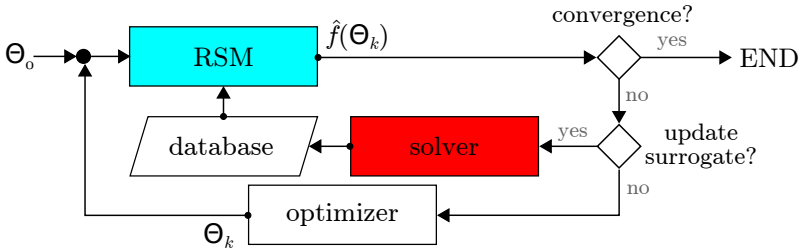

Figure 3.5: Diagram of the adaptive surrogate based shape optimization framework.

The drawback to the use of the surrogate models is the fact that the procedure relies on the correct description of the phenomenon by the RSM in the complete design space. This can be particularly problematic in the case of shapes or regimes submitted to flow transitions, which may simply be undetected or dislocated (attributed to different parameters) in the modeling.

More details on different methods and the principles of the optimization using surrogates can be found in [102] and in the Appendix D.2.

3.1.3 Discussion over the selected optimizer and optimization framework

In order to foreground the geometrical and topological features associated to extreme acoustic efficiency, global optima are searched. As stated earlier, nature based stochastic optimizers are more adapted to global optimization. By its simplicity, straightforward implementation, robustness and good performance [50] and easy parallel implementation, the Particle Swarm Optimization (PSO) is selected. A more expanded discussion about the benefits and drawbacks of the use of the PSO algorithm can be found in [231]. The algorithm and the implementation of the optimization are presented in Section 3.2.

Based on previously discussed points, a natural direction would be to perform a study based on a surrogate model. Although there would be a possible gain in computational efficiency,

an uncertainty concerning the reliability of the response function would be added. Looking for a good refinement of the optimization (the same order of the shape discretization) would demand a large number of previous evaluations in the construction of the surrogate. Due to this objective, the classical shape optimization framework is implemented, without any modeling of the objective function.

A large number of function evaluations is an inherent property of the procedure when using such category of optimizer and framework and is normally avoided in the case of aerodynamic simulations. However, the decision to use these methodologies takes into account the principle of the numerical work in this manuscript to remain in 2D, low Reynolds and low Mach conditions. For such flow regime and numerical setup, the evaluation of the flow is relatively cheap even for a high-fidelity and high-order solver. As discussed in Chapter 2 and in Appendix A, both memory and time consumption have been mitigated to allow carrying out a large number of simulations.

Nevertheless, the use of such optimization routine is made possible by two other elements of the numerical solution. By the use of an IBM formalism, there is no need to perform any remeshing, what can be specially tricky with a diverse set of geometrical features such as sharp leading and trailing edges. The single formula tonal model presented in Chapter 1.2.4 is used for the acoustic evaluation, thus, there are no supplementary steps in the calculations. The combination of the two characteristics lead to a complete evaluation (from shape parameters to aerodynamic/acoustic quantities) within about 2 hours.

3.2 Particle Swarm Optimization (PSO)

3.2.1 Inspiration and concept

Originally proposed by Kennedy & Eberhart [110], the particle swarm optimization is inspired on the behavior of a flock of birds. When the group is looking for food, the communication between the elements of the swarm, that will be called here as agents, makes it easier to find something of interest in the space. The analogy here is related to the search for the minimum (maximum) value of the cost function (objective function) in a limited space, the design space where each parameter is one dimension. An example of the convergence of the swarm is presented on Figure 3.6.

It is considered as a more robust routine than Genetic Algorithm, such as GA, because it relies rather on cooperation than on competition [34, 55], and even the agents that have a poor result contribute to the convergence of the swarm by expanding the knowledge of the design space.

3.2.2 PSO algorithm

The optimization routine is as follows: every agent i is placed at the design space ($\mathbf{\Theta_i}$, arbitrarily distributed) and its velocity vector is initiated ($\theta_\mathbf{i}$, also arbitrary). For each agent, the objective/cost function is evaluated. Based on the obtained fitness values, the best position considering the whole swarm (global best, $\mathbf{p_g}$) and each agent (personal best, $\mathbf{p_i}$) are stored (for the first iteration, the individual best is the agent starting position). For the next iteration, for each element of the swarm, the velocity is recalculated from a weighted sum of: the vector formed between the current agent position in the design space and the global best ($\mathbf{p_g - \Theta_i}$); the current position and the personal best ($\mathbf{p_i - \Theta_i}$); and the previous velocity. In the following iteration, the agents are repositioned based on the updated velocity, the corresponding objective function values are recalculated and the locations of personal and swarm's best result are updated. The optimization continues until a stopping criteria is reached.

The 3 contributions used to update the velocity are weighted by real factors defined, respectively, as the cognitive factor (c_1) that regulates the individual tendency to go back to the position where it found its personal best result, the social factor (c_2) indicating the amount of influence of the vector aiming the global best to each agent position, and the inertial factor (c_w)

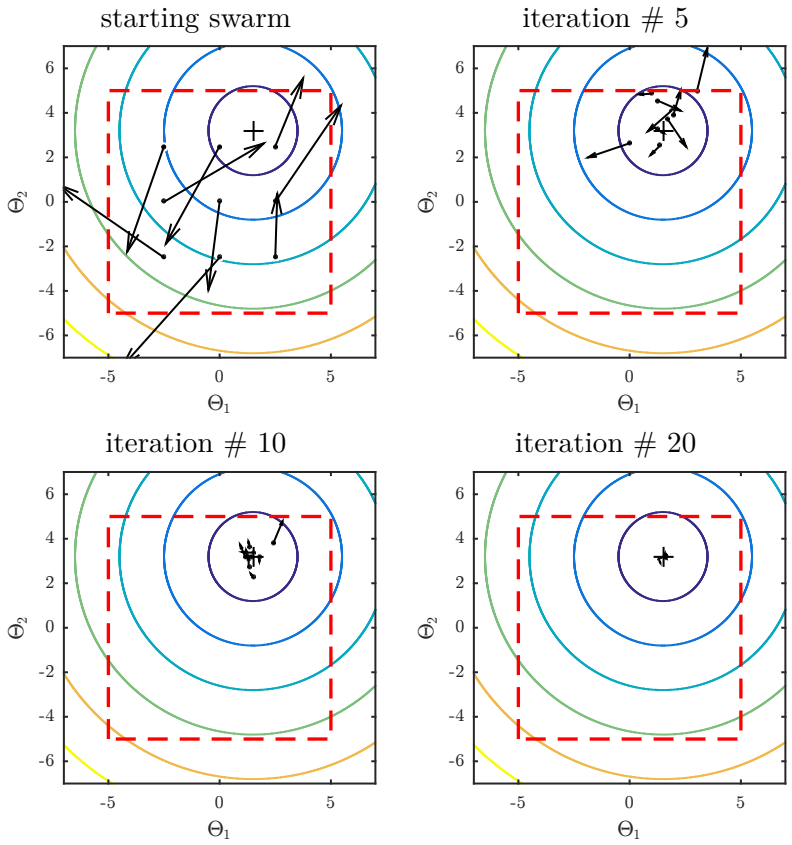

Figure 3.6: Example of the convergence of the swarm (position and velocities) in a PSO routine for a 2D design space with 9 agents starting in a Cartesian grid with random velocities. Contour lines represent the cost function $f = [(\Theta_1 - 1.5)^2 + (\Theta_2 - 3.2)^2]^{1/2}$, cross indicates the global minimum and hashed lines the limits of the design space.

that represents the impulse to remain with the same velocity. For the first two components, randomness is added for each direction in the form of a random coefficient between 0 and 1; it is used to prevent premature convergence [263] by forcing the swarm to explore the design space. The fact that the randomness is applied for every direction independently (not to the vectors) is so that the possible output is not limited to the initial vector direction, leading to a better exploration of the design space by defining a rectangular distribution [34].

The pseudocode of the described PSO implementation is presented on Algorithm 1, where the function rand(a) returns a vector of the same dimension of the design space of random numbers between 0 and a and $\circ$ represents an element-wise multiplication of the vectors.

A decision must be made at the time that a particle gets out of the design space, as illustrated in Figure 3.6. The simplest solution - replacing it at the design space limit - is selected here, other strategies such as mirroring its position or applying an inverse velocity [34] are not used.

The update of the best value may be performed inside the iteration, as illustrated in Algorithm 1, what is known to improve the behavior of the optimizer [34]. For the performed study, this is impossible due to the parallel evaluation of the cost function.

There are different methods to deal with how the swarm communicates [199, 231], called as topologies. For example, it can be defined that each agent updates its global best based in the knowledge of only its neighbors. Separating the swarm into smaller groups of agents enhances the algorithm capabilities to avoid local minima. In this work, all members of the swarm are considered for the definition of the global best and the information is available for every one of them, at all times (the *gbest* topology). The use of different coefficients for independent members of the swarm or the progressive modification of the social and cognitive factor are also possible [34], however both techniques are not implemented here.

Since its introduction, many improvements have been proposed to the method, such as the

Algorithm 1: PSO pseudocode - adapted from [199]

Generate a population Π of n particles, selection of $\mathbf{\Theta_i}$ and $\theta_\mathbf{i}$;
for $\mathbf{\Theta_i} \in \Pi$ **do** $f(\mathbf{\Theta_i})$, $\mathbf{p_i} = \mathbf{\Theta_i}$;
Select the particle with $\max(f(\mathbf{\Theta_i})) \rightarrow \mathbf{p_g}$;
Position and optimal solution: $\mathbf{p_g}$ and $f_{best} = f(\mathbf{p_g})$;
while (convergence = false) & $(t \leq t_{\max})$ **do**
  for $i = 1$ *to* n **do**
    if $f(\mathbf{\Theta_i}) < f(\mathbf{p_i})$ **then**
      update the optimal position $\mathbf{p_i}$
    calculate the velocity: $\theta_\mathbf{i} = \text{rand}(c_1) \circ (\mathbf{p_i} - \mathbf{\Theta_i}) + \text{rand}(c_2) \circ (\mathbf{p_g} - \mathbf{\Theta_i}) + c_w \times \theta_\mathbf{i}$;
    reposition agents: $\mathbf{\Theta_i} = \mathbf{\Theta_i} + \theta_\mathbf{i}$;
    if $f(\mathbf{p_i}) < f_{best}$ **then**
      update the optimal position $\mathbf{p_g}$ and f_{best};
  test convergence;
  new iteration : $t = t + 1$;
return Π optimal

possibility to use different topologies as described on the previous paragraph. The gain offered by such enhancements is found to be small for the current application, consequently, the PSO version used in this work (Algorithm 1) is close to the canonical form [110], the only modification being the use of the inertia component, introduced later by Shi & Eberhart [237]. An extensive discussion about those novelties is available on the previously cited reviews [34, 199, 231].

The control of the optimization behavior, directly associated with the success of the optimization, is closely linked to the swarm properties (its size and initial positioning) and the value of the weighing coefficients used to update the velocity (the cognitive, social and inertia factors). These elements and their influence are discussed next.

3.2.3 Discussion about the optimization settings

As discussed by many authors, choosing the optimization factors is the main difficulty for the use of a meta-heuristic optimizer such as PSO [22, 34, 199].

Despite being a simple algorithm and having a low number of parameters, the PSO behavior remains highly dependent on its settings. It is observed that in terms of the final value, the selection of the parameters is not of great importance, but the convergence to that value, that is, the number of iterations and function evaluations, is itself a direct result of the set of parameters that compose the algorithm.

In its completeness, the PSO algorithm used in this work is fully defined by 5 settings: the number and initial position and velocity of the agents, and the social, cognitive and inertia factors. The definition of these 5 parameters must account for the sensible equilibrium between the number of function evaluations and the reliability of the result. Each of them is discussed next.

3.2.3.1 Swarm size and initial positioning

The size and positioning of the swarm affect the amount of knowledge the agents have of the design space. A natural tendency would be to include the biggest number of agents as possible, however the computational cost limits the number of elements that can be evaluated. The initial positioning (and velocity) can as well define the cost of the optimization. They are discussed next.

3.2.3.1.1 Number of agents in the swarm The size of the swarm can be problematic in the two directions. A small swarm can take too long to converge and have agents trapped in local minima easily; on the other hand, a big swarm, with agents that superpose each other in the

design space, can lead to unnecessary use of computational resources, recalling that each agent represents one cost function evaluation for each iteration. It is more of an empirically defined quantity, based on the complexity of the problem and the size of the design space. Common swarms are found to be of 20 to 50 agents [34, 199].

3.2.3.1.2 Initial position Θ_0 and velocity θ_0 of the agents Even if the technique is designed to be less dependent on the initial conditions, like any other stochastic optimization routine, the starting conditions are important parameters. Though there is a relatively trust in arriving at the global optimum, a preliminary knowledge is needed to mitigate the amount of iterations and objective function evaluations required to achieve convergence.

The initial position and velocity may be random, or respect a given logic. For the initial location, multiple techniques are employed and are intended, at the initial iteration, have a representative sample of the design space. This is analogous to the principles of Design of Experiment (DoE) when using a surrogate model. There is, for instance, the Latin Hypercupe Sampling (LHS). The reader may find further explanation and more examples in Appendix D.

3.2.3.2 Social, cognitive and inertia factors

Three real vectorial factors are used to control the velocity update in each optimization iteration. The update of the agent velocity, as discussed in Section 3.2.2 and presented on Algorithm 1, is illustrated in Figure 3.7. In general terms, with the modification of these 3 parameters, the swarm behavior can be modified. For instance, focus may be placed on local or global search, "fast" (but uncertain) or "slow" (but reliable) convergence. The success of any metaheuristc routine, such as this one, lies in the balance between exploration and exploitation [23].

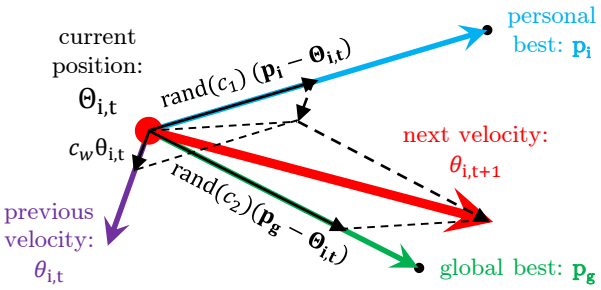

Figure 3.7: Diagram of the velocity update for the PSO at iteration t, 2D design space. The next velocity is a sum of a component of the vector towards the global best, the vector towards the personal best and the previous velocity, weighted by the social, cognitive and inertia factors, respectively. Symbols are defined in Section 3.2.2.

Each parameter is discussed further next.

3.2.3.2.1 Cognitive factor c_1 Defines the importance of the personal best in the search. Controls the amount of exploration, that is, the expansion of the knowledge through the iterations. The response is the inverse of the social factor: when too big, leads to a non converging (even unstable) swarm; if too small, agents are trapped to local minima. Typical values are as well in the range 1.5-2.0 [231].

3.2.3.2.2 Social factor c_2 Defines the importance of the global best in the search. In general terms, it controls the amount of exploitation, that is, the focus given in having a greater knowledge of previously explored regions. If it is too big, the possibility to converge to a local optimum is increased since all agents will be attracted to the first minimum that is found. If it is too small, the swarm may never converge. Typical values are in the range 1.5-2.0 [231].

3.2.3.2.3 Inertia factor c_w Quantifies how much the agent's previous velocity will influence the velocity vector in the next iteration. A small value of the inertia factor (~ 0.4) favors the search of local minima by allowing a very exploitative swarm [199]. The inertia factor is commonly set as $c_w = 0.6$ [231].

3.2.3.3 Selection of factors

Even though convergence can be achieved based on values in the literature, these are mostly adapted for solving hard problems [137]. Since it can lead to a slow, or even impossible convergence, or result in an unstable behavior [137, 263], it is mandatory to perform an analysis of the optimization parameters, notably when dealing with numerically expensive objective/cost functions.

A first (and also second) impetus to "optimize the optimizer" naturally appeared. Being a stochastic process, that is, the results are never the same, it is not a simple task. Also, even if it were feasible, the result would depend on the form of the expensive objective functions that are being studied.

Nevertheless, a study of the performance based on discrete response surfaces is performed for the first parametrization (Section 3.3.1) used in this work. Based on the hypothesis that the behavior is similar for the other cases, the selected factors were the same for all the optimization studies that were performed on this work. Since the result is parametrization-and-quantity-of-interest dependent, the analysis is presented within the discussion about that given parametrization (Section 3.3.1.2) and only the result is presented here. The social and cognitive factors (c_1 and c_2) are set as 1.2 and the inertia factor c_w is defined as 0.6. The number of agents is set to 36-40. For the low dimension design spaces used here (3D to 5D), the relatively large number of agents makes that the initial positioning has only a weak influence on the result or performance. Based on that, the agents are either uniformly distributed in a Cartesian grid or placed using the LHS.

The implementation of the algorithm is discussed next.

3.2.4 Optimization implementation

The optimization is implemented in Python. It seems straighter forward to perform the optimization in the same environment ofas the CFD solver. Moreover, the notable simplicity of the optimization algorithm allows it to be easily implemented in the same language as the solver. However, the use of an interpreted language, that is by definition easy to code and debug, but poor in terms of computational performance, was favored. The framework is them a hybrid, known trend that combines the efficiency of compiled languages and the maneuverability of interpreted languages [39]. There are no major losses in what concerns the use of Python, since the operations that are performed require negligible memory space and processing time, especially compared to the Navier-Stokes calculation.

All optimization logic is performed outside of the CFD routine. The main advantage of such a strategy is that, as intended with non-derivative based optimizations, the complete routine works with the cost function as a blackbox. While also taking advantage of the growing popularity of the Python language, the produced tool may be instantaneously used on other projects as is.

The evaluation of the cost function, in this case, the solution of a CFD problem, is performed by the Fortran code Incompact3d, as in Chapter 2. The principle of the optimization framework is to associate the location of the agents, that is, the values of the parameters for each agent, to the evaluations of the cost function. The proposed association of the Python code with the solver will be presented further, keeping in mind that there is no direct interface between the Python and the Fortran codes (although available using F2Py [190] and/or environment variables).

Initially, a solution based on the build-in multiprocessing package [205], where a pool of workers, each associated with an agent, was created at every iteration. It remains available in the code, but due to the necessity to perform the optimization in a cluster, a MPI based parallelism with a server-managed process was necessary. For that purpose, the Python package

`mpi4py`, that works as an interface for a MPI implementation, is used. It transforms Python types into C types and is able to perform all major MPI operations as a native C or Fortran compiler [39].

The optimizer is implemented with classes for the particle, the swarm and the PSO. All the operations concerning the particle (updating personal best, velocity and position) are implemented as methods in its class. Similarly, the swarm operations (update global best, check convergence) are within its methods, as well as a list of particle instances.

The MPI methods are implemented inside the PSO class so that it is completely independent of the cost function, that is a Python function that is sent as an input to the optimizer method. Only 3 MPI operations are performed: scatter of the swarm, that is, each particle instance is assigned to a process, followed by the evaluation of the cost function in each individual MPI process; a gather call to collect the results; and barriers are present in the code since the iterations may only start after all the particles are finished and the results for the full swarm are available. The implementation is illustrated on Figure 3.8.

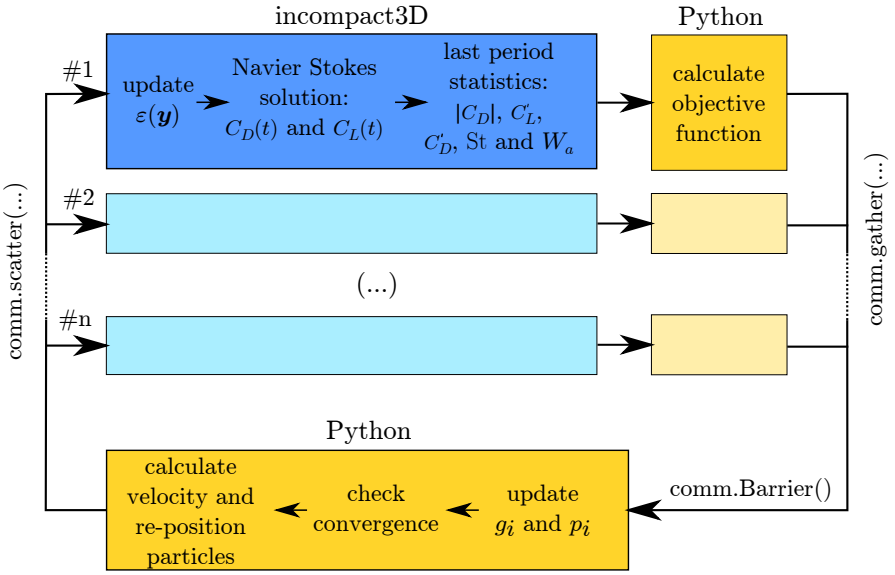

Figure 3.8: Particle Swarm Optimization (PSO) implementation. For a given iteration, the geometrical parameters of the particles are scattered into n MPI processes using `mpi4py` method `scatter`, where comm is the main communicator. After the simulations are completed, data is sent to the main process using the method `gather`, the best local and global positions are updated and the particles are moved if there is not swarm convergence or the maximum number of iterations is not reached.

The capability to continue an optimization run is also implemented. Based on the fact that the process is by definition stochastic and the values of best and current positions and velocities is demanded, the chosen solution was to simulate that the optimization starts from the beginning, but the values of the obtained results and the selected velocity vectors are imposed from the previous run log file until there is no data available.

Two stopping criteria are used in the current implementation. Several convergence criteria were implemented, such as one based on the mean swarm velocity or the convergence of the objective/cost function. For the presented applications, it is chosen to consider that the swarm is converged, thus, stopping the optimization, when the agents are statistically at the same location in the design space. This is evaluated by the sum of the distances between agent number 1 and all other elements of the swarm divided by the swarm size, analogous to a mean distance. When this value is smaller than 0.001, the swarm is considered converged and the optimization stops. The run is also stopped when athe number of iterations of 30 is reached.

Even if the optimization script is completely independent from the cost function, and that the generation of the geometry and the settling of the parameters for the Navier-Stokes solver

are completely independent of the optimization implementation, an interface between the two must be performed to feed the inputs and to retrieve the results of the simulation. The interface between the solver and the optimizer is presented in the next section.

3.2.4.1 Interface with the CFD solver

As stated earlier, the optimization and CFD routines are completely separated, being the CFD executable compiled formerly. The interface is performed via the I/O files, while the input files for the CFD simulations are generated based on dictionaries defined in the Python routine. Analogously, the output files generated by Incompact3d are also read by Python scripts. In order to implement that, the adaptation of the Fortran code for complete control using input files is performed so that all simulation parameters are defined on each run. Some time locks are used to guarantee the existence of these files when calling the executable for the calculation routine. The Incompact3d executable is called using the subprocess module [205]. As a child process of the Python executable, it inherits some commands that are passed to the Python routine.

Several other features concerning the simulation are also implemented, such as data management and control of the simulations (with the ability to restart a case), convergence check, automatic relaunch with smaller timestep in case of divergence and production of post-processing images. Since they are not directly influencing the behavior of the optimizer, the list of features is not further discussed.

The geometries are either implemented directly in the Fortran code, based on parameters passed by text input files, or generated when calling the cost function, being the ϵ matrix (array defining the grid points submitted to the IBM's forcing term) that is passed to the CFD solver. The definition of the solid domains is performed using a point-in-polygon (PIP) routine, based on the "ray to infinity" even-odd test. While there is a tremendous advantage of defining any geometry, care must be taken when analyzing the data since the parameters of the geometry (such as d and b) are completely absent in the Fortran run or not explicitly defined in any I/O file.

Since the shape is discretized into a finite number of rectangular elements based on their coordinates in a Cartesian mesh, small variations on the geometrical parameters do not affect the simulated geometry. For the size element used in the simulations (see Appendix A), the minimum sensitivity is of around 0.001 for all parameters. Therefore, all the inputs are rounded when calling the Navier-Stokes solver (the value is unchanged in the optimization routine). In order to avoid unnecessary calls, if the same set of parameters has been used before in the optimization, the previously calculated value is considered and the simulation is not repeated. At the final iterations, as the swarm converges, the number of actual function evaluations per iteration is highly reduced, specially for a 2D search space.

Though convergence of aerodynamic quantities in time are measured in real-time for each simulation, it was observed that the behaviour is errant when different geometries are compared, leading to premature or retarded simulations stops when the convergence criterion is used. To avoid an excessive number of idle processors in the optimization run, rather than defining a stop criteria, the number of flow cycles is constant for all cases and sufficient for a good convergence ($t = 360d/U_\infty$, up to 50 lift cycles). According to the convergence curve presented on Figure A.5 in Appendix A, a precision of the time solution of the order of 0.010% is reached.

3.2.4.2 Calculation facilities

Part of the implementation and initial testing were performed in the smaller calculators available in the lab `prec5601` and `Calcul2016`, of 16 and 40 cores, respectively. The optimization runs were performed on the local cluster `Thor` of 3760 cores, composed by 188 Intel(R) Xeon(R) CPU E5-2680 v2 @ 2.80GHz computer blades (20 cores per blade). More details on the cluster can be found in [266].

The implementation of the MPI standard was necessary to perform this work in the cluster

architecture. No extensive work has been performed to increase the scalability of the solver in the cluster, even so the running times remain reasonable. About 3 hours are required for the completion of one iteration with 30 particles (2 for a single case) and about 96 hours to complete the optimization.

Now that the optimizer and the objective function computation have been described, the next step in the design of the optimization process is the space of parameters describing how the geometry can vary and how to perform the optimization. Both points are presented next.

3.3 Shape optimizations

The shape optimization needs a parametrization. The optimal shapes are intrinsically a function of the parametrization once the obtained shapes and geometrical features are completely defined by it. The choice of the parametrization is a complex task and must account for the physical phenomenon in evidence. For example, the optimization of aerodynamic profiles must consider smooth curves such as to avoid flow detachments.

With the use of IBM, there is no need to re-mesh after every parameter modification, only to update the solid nodes in the $\epsilon(\mathbf{y})$ array (see Section 2.1.2.2). This allows a greater liberty in terms of the shape parametrization.

Three different parametrizations, aiming to expand the range of geometrical features tested in Chapter 2, are employed:

- shape composed by Bézier curves, presented on Section 3.3.1. Symmetry is imposed, curvature continuity is maintained except at the extremities of the design space;
- sharp-edged polygon, 4 faces, on Section 3.3.2. No constraint on the symmetry; and
- back-facing triangle with a Bézier bump, symmetrical and asymmetrical configurations, Section 3.3.3. This test is based on the study of canonical shapes in Section 2.2 and the results obtained by the two other parametrizations.

In order to be consistent from the aerodynamic point of view, the blocking height d is kept constant. Optimizations are performed at a fixed Reynolds number Re = 150. The numerical setup is the same as in Chapter 2 and discussed in Appendix A.

For each parametrization, the sections are presented as follows: a description of the shape followed by the presentation of the results and a discussion about the optimal forms and the physics of the phenomenon. A study to select parametrization properties that return a consistent result at the smallest number of function evaluations as possible is performed for the first parametrization (Section 3.3.1.2). Recall that, despite the fact that the set of properties that are most efficient is a function of the parametrization, this analysis is performed only once and the same properties are used for the different parametrizations. Also, the behavior of the optimization (convergence of the swarm) is discussed for the first parametric shape.

3.3.1 QCCQBC - 4 Bézier curves

First parametrization is formed by 8 Bézier curves (parametric polygonal continuous curves, more details in Appendix D.1.1), paired in upper and lower parts of the shape (symmetrical) and is called QCCQBC in reference to the order of the Bezier curves that compose the shape (**Q**uadratic **C**ubic **C**ubic **Q**uadratic **B**ézier **C**urves). Bézier curves are used to maintain continuity in the shape contour, thus avoiding detachments. Also, except at the boundaries of the parameter space, second-order continuity is desired so that acceleration of fluid particles is finite.

Moreover, for the first analysis, only symmetric bodies without incidence are considered, avoiding the question of the mean lift, which is null by construction. Finally, although some interesting solutions might be obtained with concave shapes, they were discarded as would form cavities. This would considerably complicate the aeroacoustic problem through possible acoustic feedbacks and whistling, in particular as the Reynolds number is increased. Moreover,

aeroacoustic feedback cannot be reproduced by an incompressible solver. That is why the present parametrization is restricted to convex shapes.

3.3.1.1 QCCQBC parametrization

The obstacle is composed by a combination of 4 Bézier curves denoted as arcs $\hat{A}$, $\widehat{B}$, $\widehat{C}$ and $\widehat{D}$ in Figure 3.9, being $\hat{A}$ and $\widehat{D}$ quadratic curves and $\widehat{B}$ and $\widehat{C}$ cubic curves, mirrored on the horizontal axis. It is circumscribed by a rectangle, represented by the points $M(0,0)$, $N(0,d/2)$, $O(kb,d/2)$, $P(b,d/2)$, $Q(b,0)$ and $R(kb,0)$.

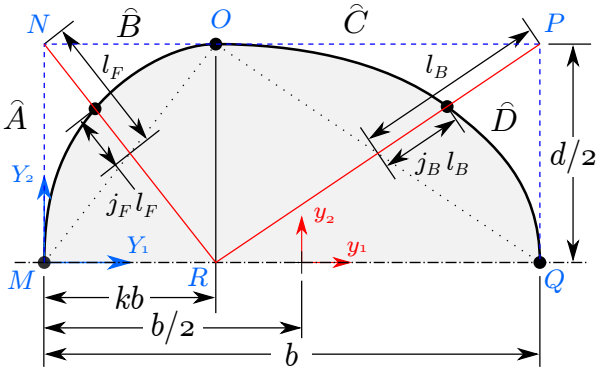

Figure 3.9: Schematic plot of the QCCQBC parametrization, flow from left to right. The shape is convex and circumscribed by the rectangle MNPQ of length b and height $d/2$. The form is completely defined by 5 parameters: b, d, j_F, k and j_B. As d is fixed in this work, the aspect ratio b/d is the only parameter affecting the rectangle. The coordinate system (y_1, y_2) has it origin on the geometrical center of the geometry (the same as in the simulations), while (Y_1, Y_2) is centered on the symmetry axis, at the upstream limit.

The control points are placed so the final geometry shape respects the following geometrical constraints:

1. Breadth b and height $d/2$;
2. Symmetry with respect to the horizontal axis;
3. Tangency to the vertical axes at the beginning (M) and end (Q) of the obstacle
4. Position, tangency and curvature continuities (C^0, C^1 and C^2) at the connections of the 4 curves (for the exception when it's an edge - k, j_B and/or j_F are on their limits);
5. Tangency at the end of arc $\hat{A}$/start of arc $\widehat{B}$ parallel to segment line $\overline{MO}$;
6. Tangency to the horizontal axis at the end of arc $\widehat{B}$/start of arc $\widehat{C}$ - at point O;
7. Infinity curvature radius at the end of arc $\widehat{B}$/start of arc $\widehat{C}$ - at point O;
8. Tangency at the end of arc $\widehat{C}$/start of arc $\widehat{D}$ parallel to segment line $\overline{OQ}$;
9. End of arc $\hat{A}$ placed at the line segment $\overline{NR}$, at a normalized distance of $j_F \in [0, 1]$ from the intersection of $\overline{NR}$ with $\overline{MO}$;
10. End of arc $\widehat{C}$ placed at the line segment $\overline{PR}$, at a normalized distance of $j_B \in [0, 1]$ from the intersection of $\overline{PR}$ with $\overline{OQ}$;

Based on these constraints, the geometry is completely defined by the 5 cited parameters. Parameters j_F and j_B allow the final result vary from a lozenge ($j_F = j_B = 0.0$) to a rectangle ($j_F = j_B = 1.0$) of dimensions b and d. The position of the control points are presented on Table

Table 3.1: Coordinates of the parametrized control points for the QCCQBC geometry.

curve	point	Y_1	Y_2
$\widehat{A}$	0	0	0
	1	0	$j_F d/2$
	2	$(1-j_F)kb/2$	$(1+j_F)d/4$
$\widehat{B}$	0	$Y_{1,A,2}$	$Y_{2,A,2}$
	1	$kb(1-j_F)$	$d/2$
	2	$\begin{cases} 0 & \text{if } j_F = 1.0 \\ kb\left[1-j_F+\frac{3j_F}{(1-j_F)^2}\left(1-\frac{1+j_F}{2}\right)^2\right] & \text{otherwise} \end{cases}$	$d/2$
	3	kb	$d/2$
$\widehat{C}$	0	kb	$d/2$
	1	$\begin{cases} 0 & \text{if } j_B = 1.0 \\ b\left[j_B+k(1-j_B)-\frac{3j_B(1-k)}{(1-j_B)^2}\left(1-\frac{1+j_B}{2}\right)^2\right] & \text{otherwise} \end{cases}$	$d/2$
	2	$b[k+(1-k)j_B]$	$d/2$
	3	$b[k+(1-k)(j_B+1)/2]$	$(1+j_B)d/4$
$\widehat{D}$	0	$Y_{1,C,3}$	$Y_{2,C,3}$
	1	b	$j_B d/2$
	2	b	0

3.1 (where $y_{i,c,p}$ indicates the coordinate on direction i of the control-point number p of curve c).

A first parameter strongly influencing both the mean and unsteady flow is the aspect-ratio AR = b/d. Once it is fixed, this forms a rectangle that circumscribes the body. The next relevant parameter is the position of the maximum cross-section. Here, this is controlled by k, such that the maximum cross-section is at kb. Finally, one may want to adjust the curvature of the front part and the back part separately. For that purpose, two parameters are introduced: j_F and j_B, allowing to change continuously from a lozenge ($j_B = j_F = 0$) to a rectangle ($j_B = j_F = 1.0$).

Accounting for all of these aerodynamic and geometrical constraints, the generic shape used in this optimization study is built from 4 Bézier curves in each hemisphere, two quadratic at the leading and trailing end, and two cubic connected at the main cross-section, as stated earlier. Figure 3.10 illustrates some of the geometries that can be obtained varying k, j_B and j_F. For the sake of completeness, note that half an ellipse is drawn when j_B or j_F equals $\sqrt{2}-1$.

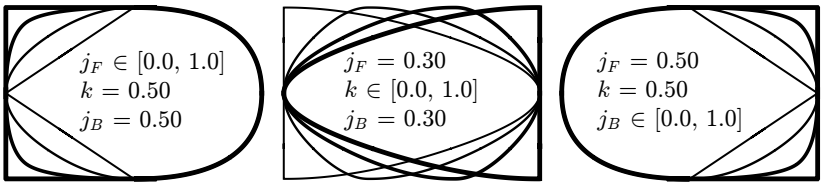

Figure 3.10: Possible shapes for fixed aspect ratio ($b/d = 1.5$) and varying j_F (left), k (center) and j_B (right) between 0 and 1 (thickest curve is for the maximum value of the varying parameter).

3.3.1.2 Selection of the optimization factors

In order to find parameters adapted to the present context (the ones that result in a small number of objective function evaluations/iterations), empirical tests are prepared regarding

response surfaces and performances.

Since the general shape of the objective functions is known, the optimizer's factors can be better defined such as to avoid unnecessary steps of exploration or exploitation. Discrete response surfaces are prepared with the simultaneous variation of 2 among the 4 geometrical parameters, as listed in Table 3.2; the tested points are equally spaced. The production of these surfaces shown in Figure 3.11 is of relatively low time cost, but this kind of analysis is only reasonable for domains with a small number of dimensions. The surfaces are not used for the production of interpolation functions of any kind.

Table 3.2: Discrete response surfaces parameters.

#	1	2	3
b/d	1.00	$[0.25; 1.75]$	$[0.25; 1.75]$
k	0.50	$[0.00; 1.00]$	0.30
j_F	$(0.00; 1.00)$	$\sqrt{2}-1$	$\sqrt{2}-1$
j_B	$(0.00; 1.00)$	$\sqrt{2}-1$	$[0.00; 1.00]$
points	15×15	16×11	16×11

For the evaluated set of geometrical parameters, only one minimum and one maximum are noticed in the tested domain (resembling the surfaces presented by [117] in an aerodynamic optimization). It is assumed that a similar behavior is observed when all the variables are analyzed simultaneously, with zero to a few local minima. The *gbest* topology suits these type of functions and the influence of the settings in the final result is small. Empirical tests are thus performed for known functions with these characteristics, allowing to find settings adapted to the present context. This study is performed with those functions thanks to their cheap evaluation and because of the fact that once the value and the position of the minimum are defined the performance of the optimizer is evaluated based on the expected final result, and the rate of success of the optimization can also be measured.

Performance study From the observed discrete response surfaces, the Michalewicz test function [280] at low dimension is used as test case for the selection of the optimizer parameters. An unimodal version is also proposed, in 2D and 3D. Both functions are presented in Table 3.3. The steepness factor m is set to 10 for the original function so that the tests also contemplate very localized minima. The factor m equals 1 for the modified version.

Table 3.3: Test functions for the definition of the optimization parameters.

Function	Equation	Search space	Global minimum
Michalewicz (m = 10)	$\sum_{i=0}^{D} \sin(x_i)\sin(\frac{ix_i^2}{\pi})^{2m}$	$[0; \pi]^2$	-1.8013 at $[2.20319; 1.57049]$
mod. Michalewicz (m = 1)	$\sum_{i=0}^{D} \sin(x_i)\sin(\frac{x_i^2}{\pi})^{2m}$	$[0; \pi]^2$	-1.6819 at $[2.07169]^2$
mod. Michalewicz (m = 1)	$\sum_{i=0}^{D} \sin(x_i)\sin(\frac{x_i^2}{\pi})^{2m}$	$[0; \pi]^3$	-2.5228 at $[2.07169]^3$

Performance maps are produced with multiple values of the cognitive and the social factors: 19 values of c_1 and c_2 (total of 361 combinations) in (0.0; 2.5); and the inertia factor is maintained fixed at c_w = 0.6.

The chosen optimization is a stochastic technique. Therefore, a total of $N = 10,000$ optimization runs are performed for each pair of values within the set of parameters and the statistics of the obtained distributions are used to represent the influence of the factors. For

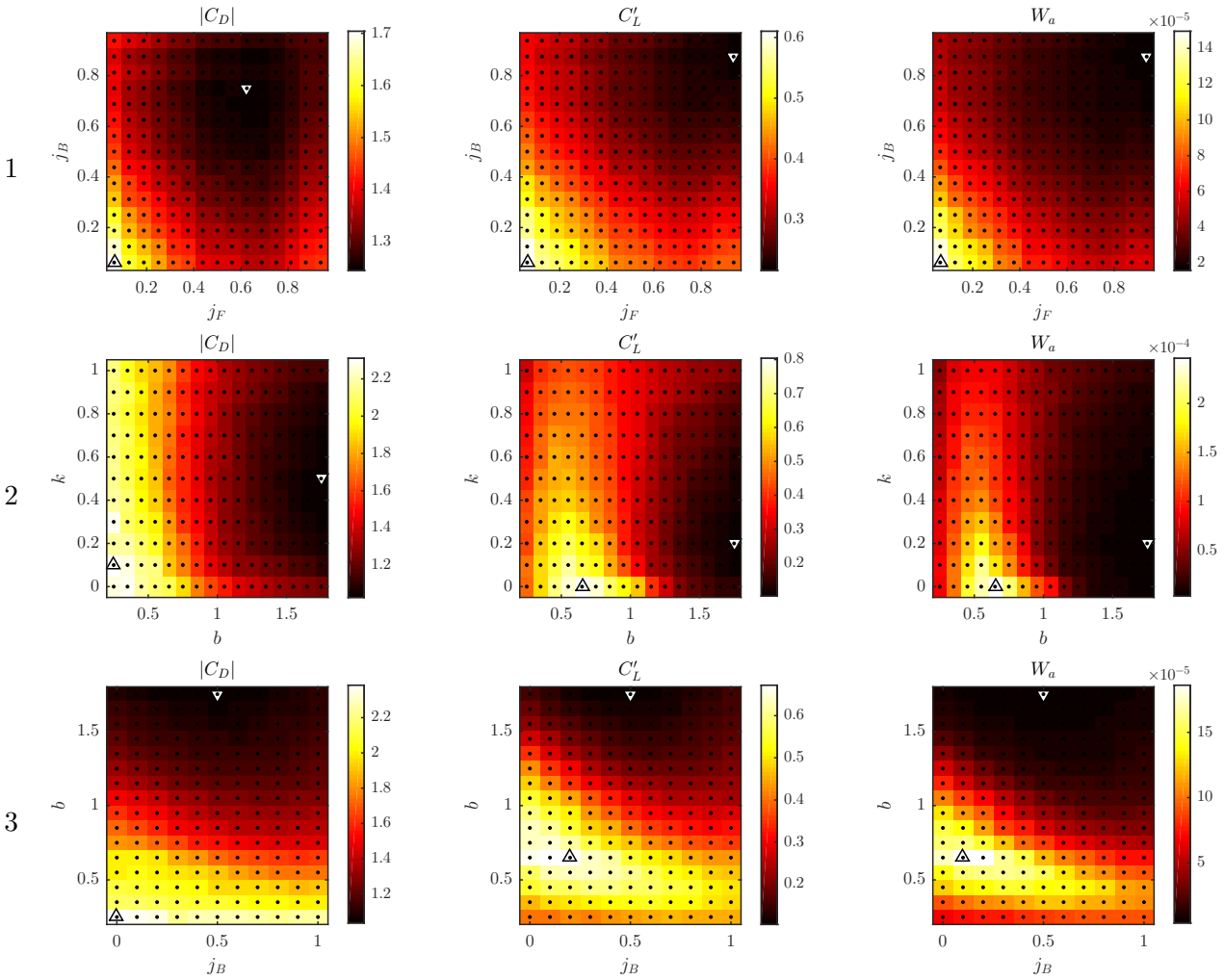

Figure 3.11: Discrete response surfaces for $|C_D|$ (left), C_L' (center) and W_a (right) for the 3 pairs of variables - for every case, the remaining geometrical parameters are fixed. The dots represent the coordinates of the calculated points; the up-pointing triangle is placed at the maximum level and the down-pointing triangle at the minimum.

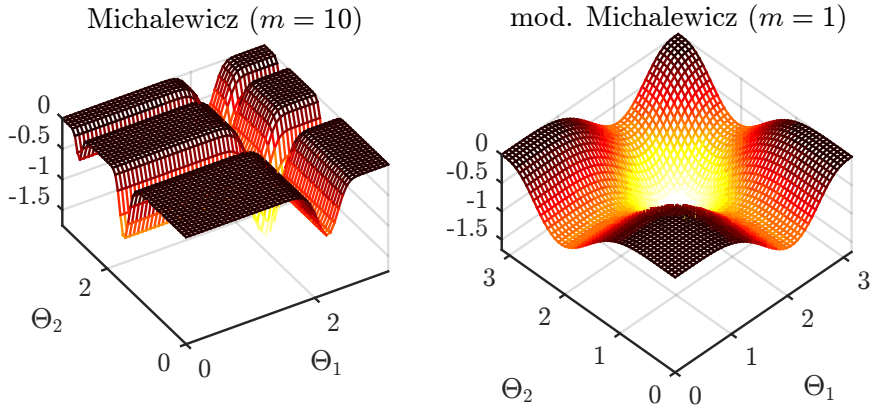

Figure 3.12: Test functions in 2D.

these analyses, a number of 25 (2D) or 27 (3D) particles are used and their initial positioning is a Cartesian mesh of equally spaced nodes (5×5 or $3 \times 3 \times 3$). Since the function optima are known, the optimizations are stopped when the absolute difference between them and the global best is smaller than 0.001. The maximum number of iterations is fixed at $T_{max} = 200$. If the final best is not within the range of precision, the run is considered as a failure. The

total number of iterations is restrictive so a high rate of failure may not be solely caused by a bad choice of parameters. However, for the intended use of the optimization in this work, the selected maximum value is already beyond the desirable number of iterations, in a sense that, a successful but long run is unfeasible.

The results are presented on Figure 3.13 with the average number of function evaluations in the optimization for the total number of runs, and the failure rate (number of runs that did not find the global best divided by N) for every tested pair of parameters. In all 3 configurations, the cognitive factor (c_1) has a low impact on the performance, what is probably due to the topology (every particle has the access to the best result of the complete swarm). A good trade-off between the number of function evaluations and a small failure rate is obtained on the center of the map (about 1200 evaluations for Michalewicz in 2D, 250 for modified Michalewicz in 2D and 450 for modified Michalewicz in 3D). Based on these results, the parameters for the optimization are chosen as $c_w = 0.6$ and $c_1 = c_2 = 1.2$, values within the stability regions proposed in [263] and [137] and fairly consistent even for harder problems than those we are dealing with (such as Michalewicz).

Considering the results for the modified Michalewicz in 3D, the configuration that most resembles the expected objective functions (single minimum, more than 2 dimensions), the number of iterations for achieving the optimum with the selected factors is about 20 (the average number of functions evaluations divided by the number of particles).

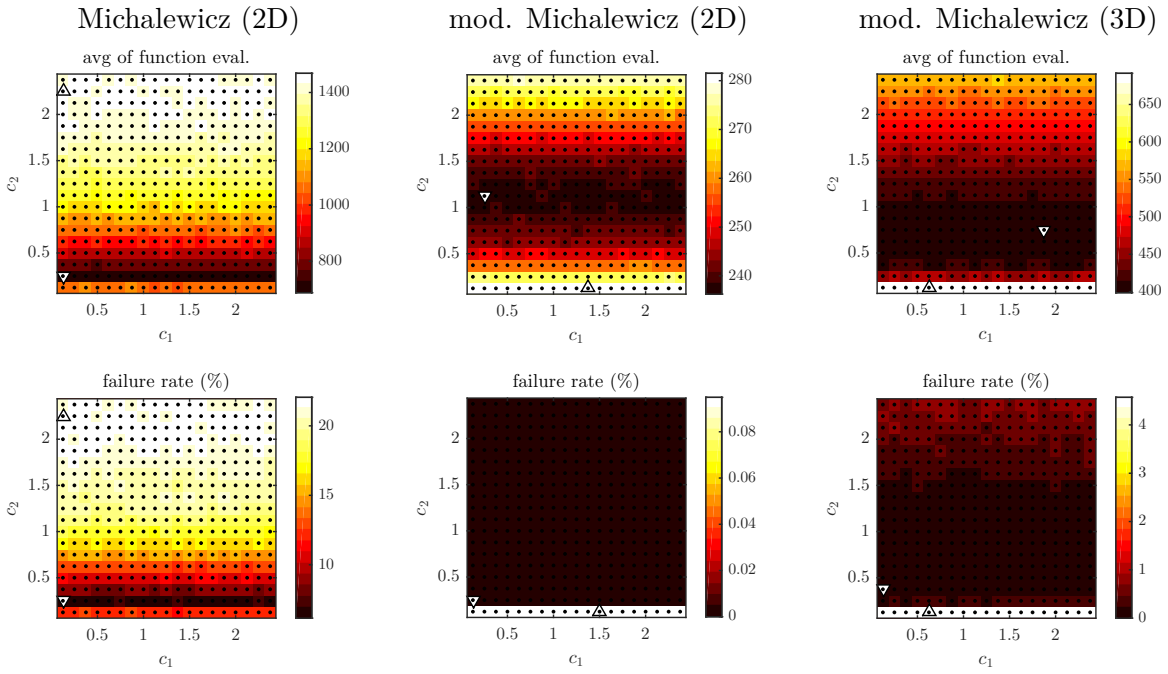

Figure 3.13: Average number of function evaluations (top) and the failure rate (down). The up-pointing triangle is placed at the maximum level and the down-pointing triangle at the minimum.

A similar technique is applied for the study of the number of agents to be selected. For a number of particles from 1 to 40, placed on the search space using a Latin Hypercube Sampling, the same 10,000 runs are evaluated. The obtained evaluations of mean number of function evaluations, normalized number of iterations (mean number of iterations necessary to convergence divided by the max number of iterations) and rate of success (number of runs that converged to the optimal coordinates divided by the total number of runs) are presented on Figure 3.14.

It is noted that, for a good success rate at a tenable number of iterations (less than 30, $T/T_{max} = 0.15$), at least 30 particles must be used. For the modified Michalewicz, above 20 particles, the increase in the number of particles does not affect the success rate. According to this result, the following optimizations are performed with 36 particles.

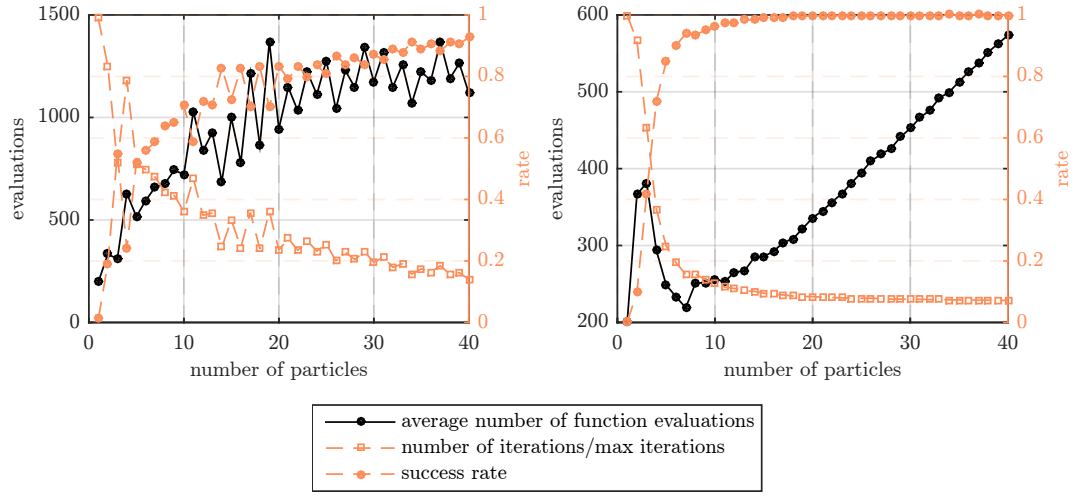

Figure 3.14: Influence of the number of particles for Michalewicz in 2D (left) and modified Michalewicz in 3D (right).

3.3.1.3 Optimal QCCQBC shapes

Several optimizations are performed for a 3D design space (j_F, j_B and k). The aspect ratio is either fixed or constrained to obtain a selected cross-section surface or perimeter. The 2 later properties are calculated via the discrete sum of surface and length elements of each Bézier arc (2000 per arc). As both quantities are monotonic laws of b, the bisection method is applied for each particle in order to obtain the AR that corresponds to the desired surface or contour.

Optimizations were performed in 4D, using AR as a parameter. However, as seen in Section 2.2.2.1, the influence of the length of the obstacle surpasses the remaining geometrical parameters in such a way that all the optimizations are rapidly reduced to 3D, so these runs are not presented here. The swarm converged to the maximum b when minimum drag or acoustic power were aimed.

The search space boundaries are the parameters limits issued from the definition of the geometry, which translates into the design space by $[0;1]^3$. The starting points of the particles are the nodes of an equally distributed rectangular grid of the design space ($4 \times 3 \times 3$ nodes).

Although several other cases were evaluated, only the results for minimum mean drag and acoustic power are presented in details for conciseness. Other results are mentioned in the following sections as a quantitative reference for the detailed cases. The conditions and objectives of those optimizations are summarized in Table 3.4. The breadth of $b = 1.5d$ is chosen to avoid the possible lift fluctuation peaks at reduced aspect ratio, as reported by Inasawa et al. [89] for a rectangular section and largely discussed in Sections 2.2.2.1 and 2.3.3.2. When the length is not fixed, only the shapes that present either the surface or the perimeter of the circular section are considered.

Table 3.4: List of performed optimizations.

AR	min $\lvert C_D \rvert$	min W_a
1.5	# 1	# 4
AR for $S = \pi/4\ d^2$	# 2	# 5
AR for $C = \pi d$	# 3	# 6

The convergence of the swarm is illustrated by Figure 3.15. For all runs, the final best is found before 25 iterations. As it can be seen on the evolution of the mean velocity (mean of the velocity modulus of all the members of the swarm in a specific iteration), the convergence is fast

but there was not enough time for the swarm to reach, in average, the geometrical resolution of the calculation (limited to a variation of 0.001 of any parameter) based on the CFD mesh refinement. However, the small variation of the best result infers that further analysis would not give relevant improvements in the results. The total reduction of the cost function from the initial evaluations is lower than 10%, specially for the mean drag (optimizations 1 to 3), which may be explained by the use of a relatively large number of particles for such reduced number of dimensions. This condition results in a significant knowledge of the design space even at the initial iterations. Running the optimization procedure with a smaller number of particles (12) revealed lower computational time but the solution was affected (slightly higher W_a). That latter feature may also be linked to the topology with full communication between particles.

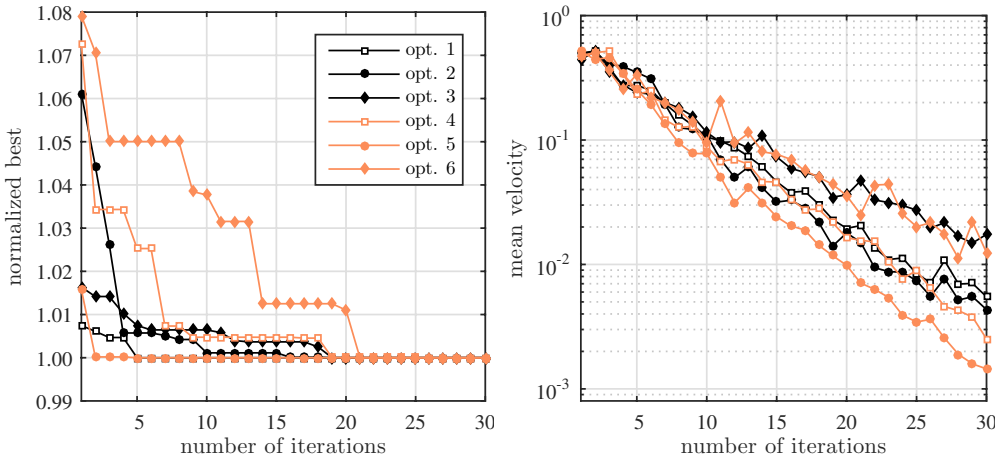

Figure 3.15: Convergence history: evolution of the normalized best (current best result divided by the final best) on the left and evolution of the mean velocity of the swarm (average of the velocity norm of all particles) on the right.

Despite the small gain for the selected objective functions, the advantages of performing the optimization also lies in the achieved precision. The parameters that result in the final best are significantly different from the ones of the initial best (smaller response obtained at the starting positions), as presented by the euclidean distance of those points listed in Table 3.5 (the maximum possible distance is of $\sqrt{3}$). The number of evaluations of the objective function to achieve a similar precision without the use of optimization would be of 1000^3.

Table 3.5: Comparison of initial and final best results.

#	$\frac{\text{initial best}}{\text{final best}}$	distance
1	-1%	0.136
2	-6%	0.424
3	-2%	0.174
4	-7%	0.186
5	-2%	0.473
6	-8%	0.070

The geometrical and aeroacoustic results are discussed in the following sub-sections. Results of simulations of ellipses at similar lengths, reported earlier in Section 2.2.2.1, serve as reference for the optimal results. The obtained optimal shapes and the associated flows are illustrated in Figures 3.16 and 3.17, respectively.

3.3.1.3.1 Minimum drag The corresponding geometrical and aeroacoustic properties of the shapes minimizing the drag are presented in Table 3.6. At a fixed length, there is a small

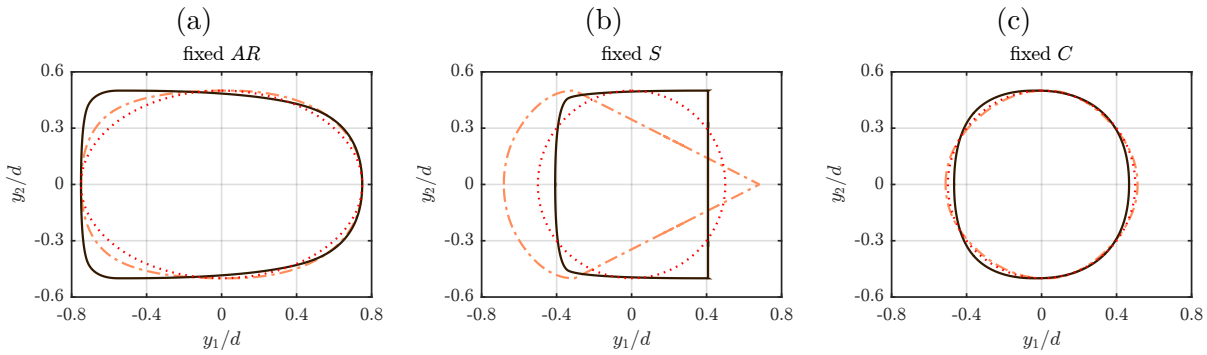

Figure 3.16: Comparison of optimal shapes for minimum drag (dash-dotted lines) and minimum acoustic power (full lines) at fixed aspect ratio (a), fixed surface (b) and fixed contour (c). Dotted lines are representations of ellipses of AR = 1.5 (a) and AR = 1.0 (b and c).

reduction of the mean drag when compared to the elliptical section of the same length (1.3%). There are reductions of 5.9% at equal surface and 0.9% at same total contour when compared to the circular cross-section.

Table 3.6: Geometrical and aeroacoustical quantities for minimum mean drag shapes and elliptical cylinders.

objective	min $\|C_D\|$ fixed AR	min $\|C_D\|$ fixed S	min $\|C_D\|$ fixed C	ellipse (AR = 1.0)	ellipse (AR = 1.5)
j_F	0.561	0.388	0.386	0.414	0.414
j_B	0.475	0.000	0.359	0.414	0.414
k	0.519	0.277	0.526	0.500	0.500
b/d	1.500	1.363	1.024	1.000	1.500
$\|C_D\|$	1.072	1.229	1.296	1.307	1.086
C_L'	0.143	0.327	0.333	0.338	0.166
$C_D', 10^{-1}$	0.025	0.037	0.156	0.157	0.031
St	0.182	0.164	0.191	0.190	0.183
$W_a, 10^{-5}$	0.725	3.434	4.180	4.275	0.986

At a fixed length, the geometry can be interpreted as an inflated circle. Since the perimeter is a very restrictive constraint at fixed d, the obtained result at fixed C is not so different from the circle itself, what can be also noted on the slight variation of the other quantities. Even so, the optimization routine was able to successfully find a geometry with a smaller drag.

For a fixed cross-surface, the smallest drag is obtained with a drop shaped geometry. This result can be justified by two phenomenons: as presented in other studies, the increase of the length is accompanied by a severe drag reduction [89] in this regime, which can only be achieved at constrained S with sharp edges (j_F or j_B close to 0); also, there is a smaller influence of the pressure at the downstream part of the geometry (depression zone after $x = kb$) due to the increased boundary angle, such as in the streamlined bodies, even if the flow separation is still present. In this manner, it is possible that concave surfaces, that are by definition of the parametrization unreachable in our design space, would be able to further reduce the mean drag.

3.3.1.3.2 Minimum acoustic power The corresponding geometrical and aeroacoustic properties of the shapes minimizing the acoustical emission are presented on Table 3.7. At AR = 1.5, the optimized section induces half the sound power of an ellipse of same length, that means -3.0

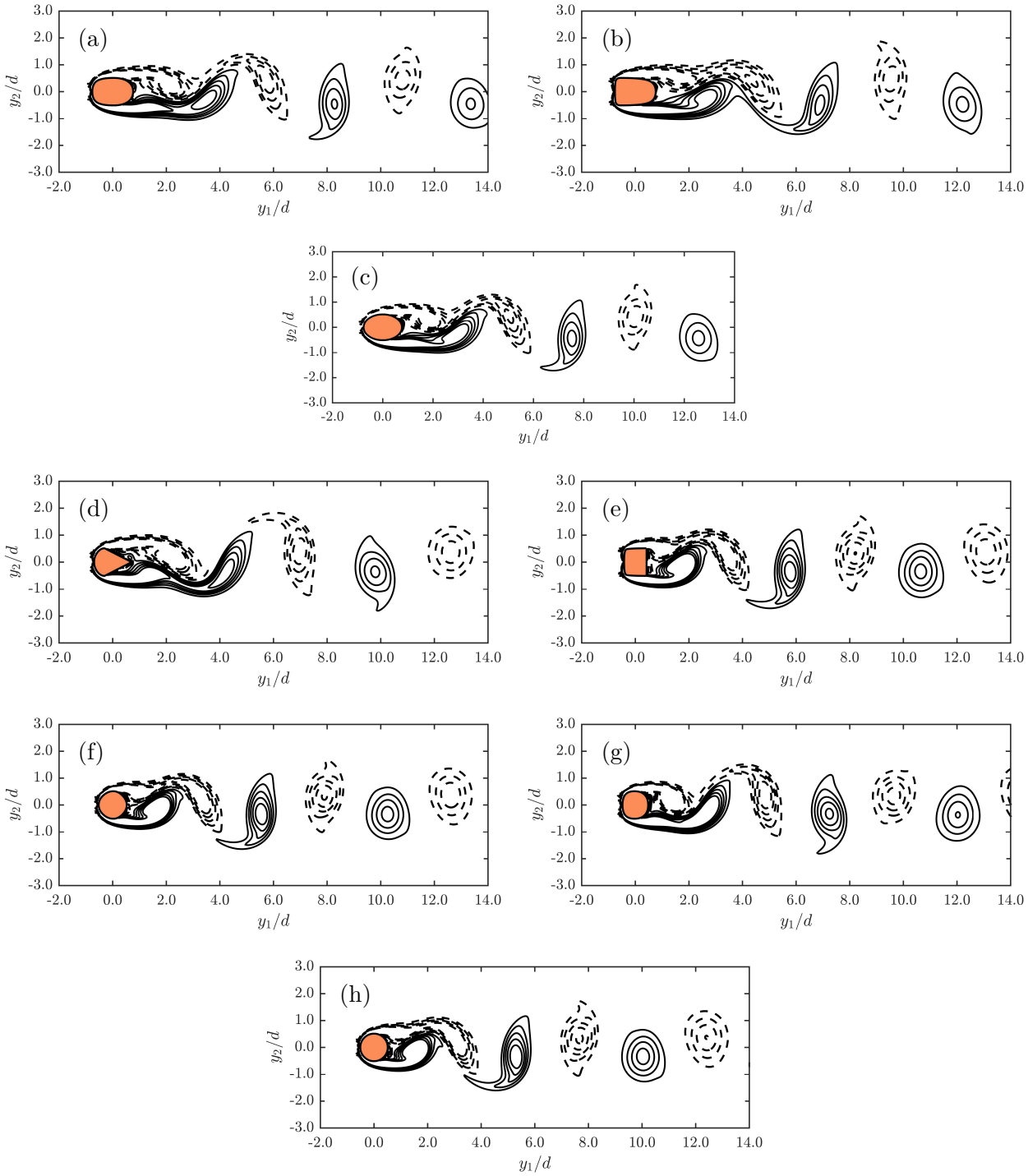

Figure 3.17: Snapshots of instantaneous vorticity for optimized and canonical geometries: optimized geometry for minimum C_D (a) and minimum W_a (b) at fixed length $b/d = 1.5$; optimized geometry for minimum C_D (d) and minimum W_a (e) at fixed cross-section area $S = \pi/4\ d^2$; optimized geometry for minimum C_D (f) and minimum W_a (g) at fixed contour $C = \pi d$; and ellipses of AR = 1.5 (c) and AR = 1.0 (h). The contour intervals are $0.4\ U_\infty/d$ and dashed lines represent negative values.

dB. Performance of the best shapes at fixed surface and contour are of -1.2 and -0.6 dB using the circular section as reference. For the 3 cases, there is an increase in the mean drag with respect to the ellipse, which emphasizes the separation of the two phenomena. A similar dispute between acoustic and drag minimization was also noted by Beigmoradi et al. [17].

Table 3.7: Geometrical and aeroacoustical quantities for minimum acoustic power shapes and elliptical cylinders.

objective	min W_a fixed AR	min W_a fixed S	min W_a fixed C	ellipse (AR = 1.0)	ellipse (AR = 1.5)
j_F	0.656	0.833	0.520	0.414	0.414
j_B	0.603	0.329	0.483	0.414	0.414
k	0.136	1.000	0.465	0.500	0.500
b/d	1.500	0.815	0.933	1.000	1.500
$\lvert C_D \rvert$	1.107	1.377	1.311	1.307	1.086
C_L'	0.120	0.296	0.316	0.338	0.166
$C_D', 10^{-1}$	0.017	0.224	0.154	0.157	0.031
St	0.174	0.185	0.188	0.190	0.183
$W_a, 10^{-5}$	0.492	3.209	3.699	4.275	0.986

For all of the geometries minimizing W_a, there is an increase in the bluffness of the bodies, that is increase of j_B, followed by a slight modification in the topology of the wake. The vortex formation is pushed in the downstream direction when compared to the flow in the presence of ellipses of similar aspect ratio (see Figure 3.17).

It is interesting to point out that the form that minimizes the acoustic efficiency at a fixed aspect ratio is similar to the shape that was obtained in the optimization of the cross-sections of panheads (the device used to connect trains to the electric lines) performed by Ikeda and colleagues [87, 88, 251] and revisited by Rho et al. [212]. Their methodology is completely different from the one use here, with the use of a surrogate model, the variation of the average lift coefficient with the angle of attack as the objective function and at a different flow regime ($\mathrm{Re} > 10^4$). The efficiency of the proposed shape is n in wind-tunnel testings. A comparison of the obtained shapes is presented on Figure 3.18.

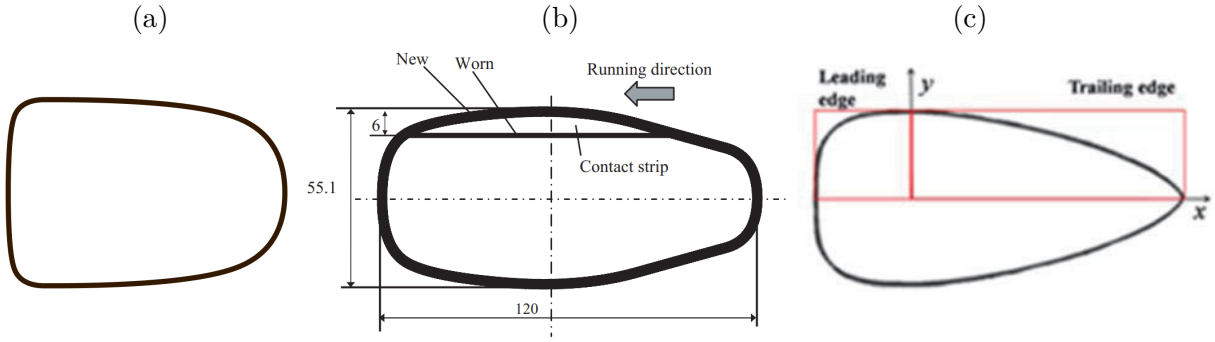

Figure 3.18: Shape with minimal acoustic efficiency in (a) current work, (b) Ikeda et al. [88] and (c) Rho et al. [212]. Despite the difference in methodology and flow regime, similar geometrical features of a bluff leading edge and curved and elongated trailing edge are present. Flow from left to right.

Optimization procedures searching the minimum lift fluctuation (C_L') resulted in very similar geometries. One conclusion is, as expected, that the lift fluctuations are the major component of the acoustic emission at this regime, since it is at least one order higher than the drag

contribution and the one that is most crucially influenced by the shape, notably when compared to the Strouhal.

It is important to note that the chosen reference for all comparisons (the elliptical section), is already fairly optimal if compared to the other possible geometries that reside within the proposed design space and constraints (such as lozenges and triangles). Even so, there are reasonable gains, specially in terms of W_a. In that manner of emphasizing the potential of such routines, optimizations are performed for maximizing $|C_D|$ and W_a, using the inverse of the correspondent quantity as cost function. The ratios between the associated extrema are presented at Table 3.8. The maximum W_a is a backward facing triangle (k = 0, j_B = 0), independently of the constraint. Simultaneously, a cross comparison is performed with the presented values concerning minimum drag and minimum acoustic power.

Table 3.8: Comparison of minimum and maximum results of optimized geometries.

constraint	$\frac{\lvert C_D\rvert(\min W_a)}{\min \lvert C_D\rvert} - 1$	$\frac{W_a(\min \lvert C_D\rvert)}{\min W_a}$	$\frac{\max \lvert C_D\rvert}{\min \lvert C_D\rvert} - 1$	$\frac{\max W_a}{\min W_a}$
fixed AR	3%	1.7 dB	51%	16.5 dB
fixed S	12%	0.3 dB	32%	7.9 dB
fixed C	1%	0.5 dB	40%	9.3 dB

When geometries that minimize different quantities are confronted, their variance response to the shape is once again highlighted. At fixed aspect ratio, for instance, the section that minimizes the drag produces 1.7 dB more noise than the min W_a. For the opposite situation, the ratio between the drag of the shape with min W_a and the minimum drag, a 3% difference in noted. Considering that the human perception can differentiate noise only above a 1 dB difference, one may imply that for the test case configuration, the mean drag optimization may be also sufficient for the acoustic point of view. However, the restrictiveness of the performed study in terms of shape (constrained breadth b and fixed height d) and flow regime confines this conclusion.

The ratios between maximum and minimum behaviors show that even respecting a set of strict continuity and geometrical constraints, the selected geometry can produce up to 8 dB more noise than a optimized version. Since the weight of each aspect is a function of the final application, the importance of this comparison resides in exemplifying the risk of not considering the acoustic aspects on the design process.

3.3.2 Tetragon

The second test shape is a polygonal section, defined by 4 control points positioned at the edges of a circumscribing rectangle. With respect to the parametrization used in Section 3.3.1, the aim is enlarging the varieties of aeroacoustic answers, here enabling non-zero mean lift and a relatively simpler flow topology by fixing detachment at the edges. Similarity with the previous parametrization, triangles and rectangles are in the design space.

For such low order parametric approach a fine control of geometrical characteristics is not possible. This choice is based on the fact that small nuances of the geometry are only of small relevance for the final flow equilibrium in the regime considered, as observed in Section 3.3.1. In that sense, consequent shape modifications are expected in the search of geometries that present extreme aeroacoustic quantities.

3.3.2.1 Tetragon parametrization

The dimensional parameters are the height d and the aspect ratio AR; four non-dimensional parameters, each in [0,1], define the distance of a control point and the origin of its containing edge in the outer rectangle, always in the axis direction: upstream edge ratio (k_u), downstream

edge ratio (k_d), top edge ratio (k_t) and bottom edge ratio (k_b), as illustrated on Figure 3.19, and define a point in the design space $P_4 = (k_u, k_d, k_t, k_b)$ for a selected rectangle (d, AR). Different combinations of these 4 parameters produce triangles, rectangles, lozenges or any other polygonal section with 4 edges. Once the height is fixed for constant blockage ratio, optimizations are performed up-to 5 dimensions.

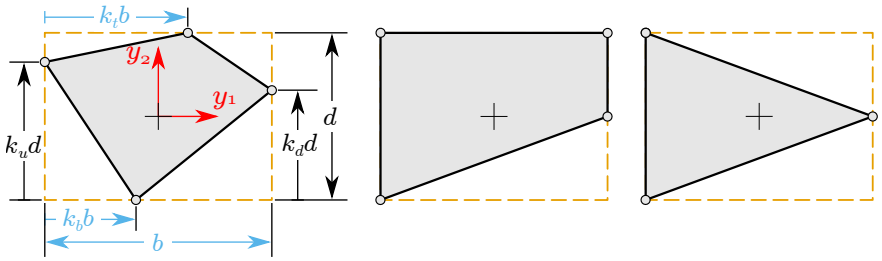

Figure 3.19: Schematic plot of the tetragon parametrization, flow from left to right. The form is completely defined by 6 parameters: b, d, k_u (upstream), k_d (downstream), k_t (top) and k_b (bottom).

Due to the nature of the parametrization, there are at least two points in the design space that produce the same geometry when the shape is mirrored over the y_1 axis, and would produce the same aeroacoustical outcome, only with reverse mean lift, for example, $P_4 = (0.5; 0.3; 0.2; 0.0)$ and $P_4 = (0.5; 0.7; 0.0; 0.2)$. This property guarantees that there are at least 2 global minimums, what is not accounted for in the conception of the optimization routine. The effects of having such characteristics in the response surface is not checked and there is no inspection step to avoid that such duplicates are evaluated twice.

The implemented point-in-polygon (PIP) routine is used to define the elements that are inside the defined polygon.

3.3.2.2 Optimal tentagron shapes

In the search for the mechanisms associated with the tonal noise generated by a flow, shapes that present both the minimum and the maximum values are of interest. Therefore, for different quantities ($|C_D|$, C_L' and W_a), the optimization routine was employed for minimization and maximization (minimizing the inverse). Optimization parameters follow the results obtained in 3.3.1.2.

Besides the use of PSO, a technique that is already more adapted to complex response functions than gradient based optimizers, there are no extra efforts to mitigate the chances to converge to local minima, such as more restraining topologies. For some optimizations performed in this study, there were clear indications that the obtained geometries did not converge to a global minimum, either in terms of the attained value or from the related form. In such cases, the optimization was relaunched from the beginning and the final value was compared to the previous answer; only the values that are considered as global minima or maxima are presented.

Pairs of optimal shapes and their corresponding aerodynamic quantities are listed in Table 3.9, where the cost/objective value are in bold. Graphical representations of the obtained shapes are available in Figure 3.20, while flow and geometry aspects are discussed in the following sections.

As can be seen on the obtained geometrical parameters, at least 2 of the 4 edge ratios were always on the limits of the design space (either 0 or 1). It is observed that, after a few iterations, these final values are already selected and the search is reduced to a 3D or 2D design space. In terms of the optimization procedure, the search for the best response is facilitated, however, it shows that the choice of the parametrization may be poor, once only a part of the variables control the cost function. In terms of the physics of the problem, it means that for a fixed height, the angle of the facing edge is the least significant in both the noise and the mean drag characteristics of an obstacle.

Table 3.9: Optimization results - tetragon.

objective	min $\lvert C_D\rvert^*$	max $\lvert C_D\rvert^*$	min $C_L'^*$	max $C_L'^*$	min $W_a{}^*$	max $W_a{}^*$	min $W_a{}^+$	max $W_a{}^+$
AR	1.000	1.000	1.000	1.000	1.000	1.000	2.000	1.100
k_u	0.113	0.946	0.935	1.000	0.959	1.000	1.000	1.000
k_d	1.000	0.000	0.000	0.275	0.000	0.285	0.111	0.279
k_t	0.000	0.000	1.000	0.000	1.000	0.000	0.956	0.000
k_b	1.000	0.882	0.000	0.242	0.000	0.201	0.000	0.234
$\lvert C_L\rvert$	0.153	1.614	-0.038	0.391	-0.005	0.330	-0.062	0.331
$\lvert C_D\rvert$	**1.274**	**2.259**	1.288	2.258	1.311	2.233	1.127	2.117
C_L'	0.220	0.458	**0.210**	**1.058**	0.211	1.055	0.101	1.066
C_D'	0.017	0.127	0.013	0.201	0.010	0.195	0.002	0.186
St	0.180	0.181	0.174	0.171	0.171	0.172	0.165	0.164
$W_a, 10^{-5}$	1.72	8.60	1.52	40.17	**1.50**	**40.22**	**0.33**	**38.79**

*: fixed AR;

+: AR as a parameter in the optimization, AR $\in [0.5, 2.0]$.

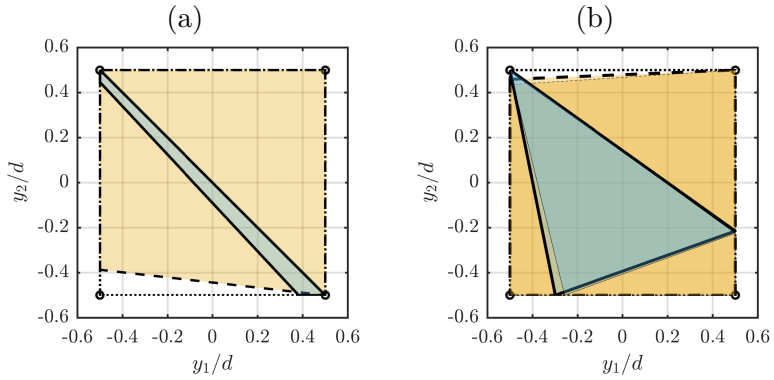

Figure 3.20: Optimal geometry at fixed AR = 1.0, dotted line is the containing rectangle. (a) minimum $\lvert C_D\rvert$ (dashed line) and maximum $\lvert C_D\rvert$ (solid line); (b) minimum C_L' (thick dashed line) and W_a (thin dashed line) and maximum C_L' (thick solid line) and W_a (thin solid line).

Obtained values for rectangles at different lengths are presented in Table 3.10 and serve as a reference for comparison with the optimal sections. Due to the symmetry the mean lift is null (omitted from the table).

Table 3.10: Aerodynamic quantities for a rectangular section.

AR	$\lvert C_D\rvert$	C_L'	C_D'	St	$W_a, 10^{-5}$
0.500	1.895	0.572	0.077	0.193	12.83
1.000	1.347	0.223	0.011	0.167	1.63
2.000	1.138	0.119	0.002	0.164	0.45

3.3.2.2.1 Mean drag The resulting extrema of drag are associated with fairly different geometries. A range of $\Delta\lvert C_D\rvert$ that equals 73% of the drag of the square cylinder is obtained. Although the viscosity effects are not negligible for the selected flow conditions (Sheard at al. [236] presented that 21% of the drag was from the viscous shear tensor for a square cylinder at

the same regime), pressure forces remain the major influence of the drag. From a preliminary analysis, the obtained velocity fields do not vary much, thus viscous efforts are not discussed here. The pressure field for the optimal pair and the square are illustrated on Figure 3.21.

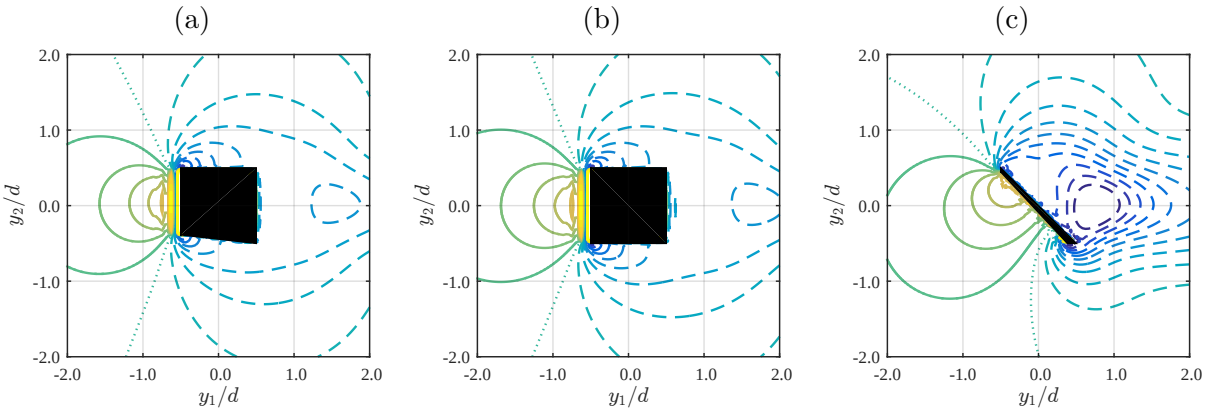

Figure 3.21: Mean pressure field for (a) minimum drag shape, (b) square and (c) maximum drag shape. Pressure coefficient contour, interval of 0.1. Continuous line for positive, dashed line for negative and dotted line for null.

Minimum drag geometry, Figure 3.21.a, is a slightly distorted square, with the bottom edge elevated at the upstream portion. The resulting flow is slightly asymmetrical, and when compared to the rectangle the mean drag is reduced by 5.4%. There is a decrease in the surface submitted to the frontal excess pressure, and since the bottom edge normal has a component in the streamwise direction, the depression on this edge also contributes to the drag reduction.

The biggest drag is encountered for a flat plate like geometry, Figure 3.21.c. The changes in the level of vorticity are small, however, the modification of the vortex disposition in the wake createds an important depression zone downstream of the section that overcomes the pressure reduction on the upstream face. It is known that the drag only increases with the angle of attack of a plate [145, 241], however, at a constrained aspect ratio, this is the biggest angle possible.

For the latter shape, the result is doubted due to the small number of solid points, with some horizontal slices (in the streamwise direction) of the body having only one solid element. The numerical scheme is of order 6, so downstream parts of the flow are being directly influenced by the flow upstream of the obstacle, which is non-physical. To check the consistency of the solution, the simulation is re-run with mesh 4 (see Appendix A), where slices with single or double solid elements only exist in the extreme upper part of the discretized shape. There are no significant changes in the flow, but small variations in the aerodynamic quantities are obtained: -2.6% of mean lift, -9.4% of mean drag, +0.9% of RMS lift and + 21.9% of RMS drag and -0.7% of St. However, especially for the aimed quantity, the original value is of the same order and consistently higher than the minimum, confirming that the optimization result and the numerical setup are reasonable.

3.3.2.2.2 Fluctuating lift and acoustic power As presented in Table 3.9, the minimum/maximum RMS lift and acoustic power are searched independently. As mentioned about their geometrical parameters and aerodynamic results, the obtained geometries are quite similar, see Figure 3.20, and aeroacoustic differences may be considered within the precision of the calculations. Thus only the results for the acoustic power are going to be described in detail. Even if the answer are virtually identical, it is noted that the RMS lift is still better when it is the objective function than when the latter is the acoustic power, and vice versa. Such results constitutes a sign of the success of the optimization procedures.

The similarity of these results corroborates the fact that the transverse fluctuations of the flow, incorporated into the fluctuating lift, are the most important element in the description of the tonal noise of 2D bluff bodies, as discussed on Section 2.2.2.1.1. Based on the equation used

as the acoustic model on this work, remaining variables are the Mach number, C_D' and St. The compressibility effects (Ma) are unchanged between the geometries due the use an incompressible source at fixed flow conditions. The second variable remains one order below the fluctuating lift. Interestingly, when comparing the minimum and the maximum, the increase of C_D' is as twice as large. That means that even if the drag contribution to the noise remains small, it has a wider range and is thus more affected by modifications of the obstacle shape. For the St number, there is a really small variation over the set of geometries evaluated in this study. It can be associated with the fixed height and the limitations regarding geometry modification. Due to these constraints, the width of the wake, which is the main feature to influence its frequency [220], is only moderately modified, keeping St rather unchanged (around 0.17 ± 0.1).

Vorticity snapshots for both minimum and maximum and the rectangle of same aspect ratio (square) are presented at Figure 3.22.

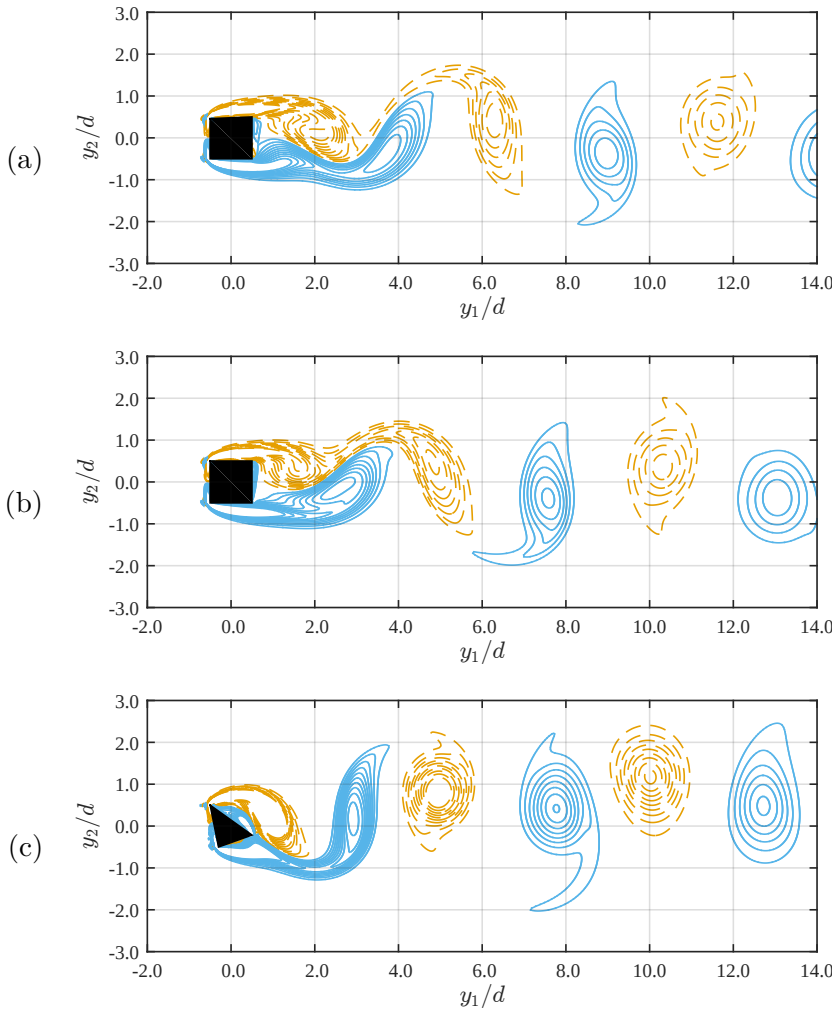

Figure 3.22: Snapshots of vorticity for (a) minimum acoustic power shape, (b) a square and (c) maximum acoustic power shape, interval of 0.3 U_∞/d, continuous line for positive and dashed line for negative; Re = 150.

Similarly to the previous minimizing geometry, the minimum W_a is associated with a deformed square. For this case, the upper edge is lowered at the upstream portion, close to a mirrored version of the previous case. The obtained answer is only -0.37 dB quieter than the square, and is likely to be associated with a small increase of viscous dissipation on the top of the obstacle provoked by the enlargement of the boundary extension, which results in slightly weaker vortices.

The geometry that amplifies the sound power is a back-pointing triangle. The interaction of both mixing layers is increased, which results in shorter recirculation and formations lengths,

and simultaneously stronger vortices, as presented on Figure 3.22.c. The interaction of these structures with the walls of the obstacle causes larger C_D' and C_L', while the Strouhal number is only slightly modified. The wake remains symmetrical, but the symmetry axis is angled towards the upper boundary. This would must certainly modify the directivity of the sound, but the evaluation of this aspect of the acoustic field is not available from the tools used in this work and does not affect the total acoustic power.

Optimizations of the acoustic power at 5 degrees of freedom (DoF) are also performed, for the AR in [0.5; 2.0], and the obtained shapes are illustrated on Figure 3.23.a. As for the previous cases, a deformed rectangle is obtained for minimum W_a, for the longest geometry possible. In this case, the deviation is on the contrary, at the downstream portion of the bottom edge. From the observation of vorticity fields of the shape with minimal noise and the rectangular section of AR = 2.0, it is believed that, at that length, the small modifications in the lateral edge angle are close to insignificant when compared to the effect of the length itself. Further investigations of that influence are performed.

Figure 3.22.b illustrates the obtained acoustic efficiency for all the points evaluated in the 2 optimization runs with the aspect ratio as a parameter and partially reproduces the values obtained for rectangular sections presented at Section 2.2.2.1.1. The association between the aspect ratio and the acoustic power, discussed deeply in Section 2.3.3.1, is reproduced, reinforcing the argument that it is independent of the geometry, thus, a global trend. We may also conclude that the rectangles are already fairly optimal sections in terms of 2D noise production.

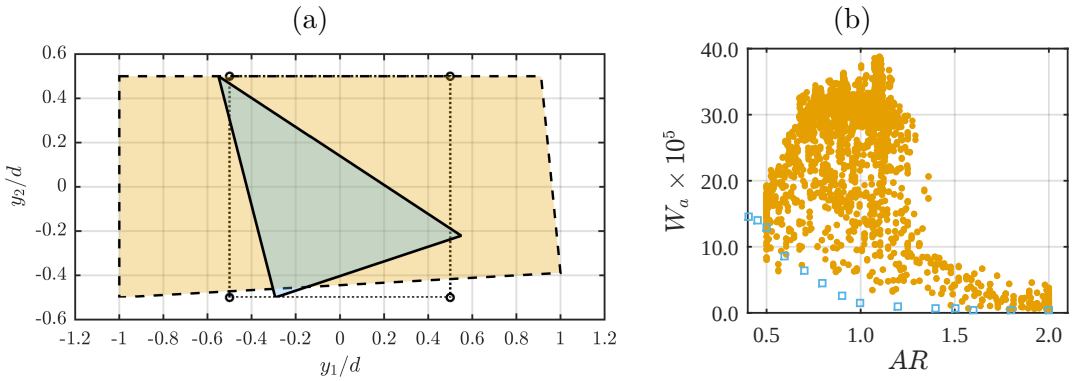

Figure 3.23: Acoustic efficiency for different geometries as a function of their length. Dots include all the geometries evaluated for the 5 DoF optimizations and square makers are for rectangles.

The maximum noise is obtained with another triangle, but not for the minimum aspect ratio. The breadth results from a compromise between flow fluctuations and the available surface to transform these into lift oscillations, similarly to the behavior noted by Inasawa et al. [89] and described in Section 2.3.3.1. It must also be pointed out that the modifications of the aspect ratio were capable of substantially modifying the frequency of the wake, thus, provoking a larger discrimination between the minimum and the maximum noise than what was obtained at fixed AR.

As can be seen on table 3.9, the maximum noise obtained for the 5 DoF optimization ($W_a = 38.79 \times 10^{-5}$) is lower than the value obtained at a fixed length ($W_a = 40.22 \times 10^{-5}$). As clarified previously, some optimizations are believed to converge to local minima, and it was the case for the maximum noise. The same configuration was optimized 3 times, starting in a design space of AR $\in [0.5; 2.0]$ for the aspect ratio for the first two runs and [0.75; 1.25] for the final run, and even so the final result is clearly not the global minimum. The obtained misbehavior contributes to the conclusion that, for every geometry (associated to a specific P_4 coordinate point), there is a unique length that maximizes the noise, in such a way that there are multiple local minimum in the design space. Besides the use of a different swarm topology, a re-setting of the number of particles, total number of iterations and the optimization coefficients could improve the result.

Even for a very limited set of tested geometries at a fixed blockage ratio, globally, a ratio of 2 for the mean drag and a difference of 20 dB for the noise is observed between the extrema. Modifications of the upper and lower edges are the most active in terms of the aerodynamic and aeroacoustic answers. Despite the large range of parameters, all the obtained results originated from similar wakes.

3.3.3 Back-pointing triangle with a bump

The back-pointing triangle is noted as the loudest geometry in Chapter 2 and for both previous parametrizations. In the sense of highlighting the geometrical and topological features that are associated with a tonal noise reduction, the final parametrization focuses in mitigating the noise production of this extreme shape. The principle is adding bumps to the lateral edges of the triangle in order to modify the dynamics of the mixing layers and of the vortex shedding, thus, the noise.

Such principle of adding protuberances to a base shape is found in aeronautics. The deicing boots present in the leading edge of wings and propellers are temporary bumps used to break the ice and restore the aerodynamic behavior of the profile. Even if distant from the current study in both geometrical and regime points of view, there is a possibility that the current results may be of interest for that application of profile's tonal noise.

First, as for the other 2 cases, the parametrization is presented. Optimization results follow, with a discussion on the physics behind the obtained results.

3.3.3.1 Bump parametrization

The shape is derived from the combination of the back-facing triangle (trib) with a bump, as illustrated on Figure 3.24. The base geometry is defined by b and d, while the bump is completely described by 4 parameters: the height of the bump H_b, considering the distance to the bump root; the bump length at its base L_b; the location of the apex of the bump is defined by the coefficient c_b, that controls the relative distance from the start of the bump $c_b \times L_b$; and the absolute position of the bump, defined by the parameter S_b, a ratio that indicates the curvilinear (clockwise if bump is in upper edge, anti-clockwise if in lower edge) distance of start of the bump to the upstream limit inclined edge of the triangle (0 represents a bump starting upstream and 1 represents a bump that finishes downstream). Since the position of the bump is defined such as to have the bump base restricted to the base triangle, changing L_b with a fixed S_b represents a shift in the position as well.

The bump is defined by 2 cubic Bézier curves. The location of those points are expressed in Table 3.11, considering an auxiliary coordinate system (Y_1, Y_2) placed at the start of the bump and with abscissa parallel to the triangle's edge, as illustrated in Figure 3.24.

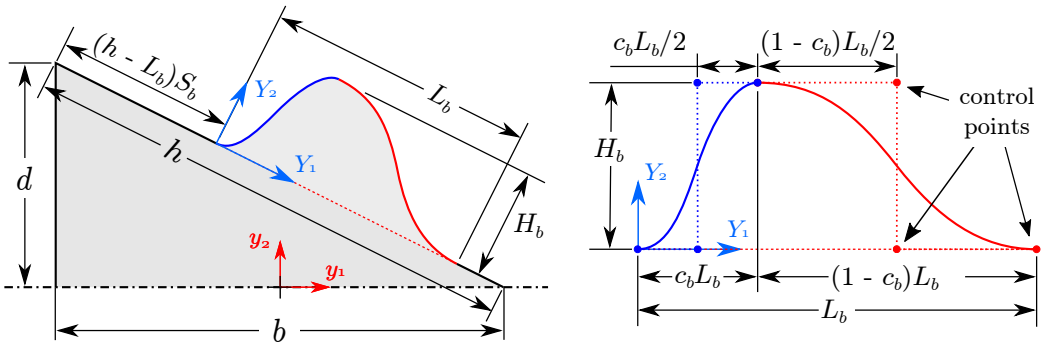

Figure 3.24: Schematic plot of the back-pointing triangle with bump parametrization, flow from left to right. The form is completely defined by 6 parameters: b, d, H_b (height of the bump), L_b (length of the bump), c_b (location of the apex of the bump) and S_b (abscissa placing the bump).

Table 3.11: Coordinates of the parametrized control points for the back-pointing bump.

curve	point	Y_1	Y_2
1	0	0	0
	1	$c_b l_b/2$	0
	2	$c_b L_b/2$	H_b
	3	$c_b L_b$	H_b
2	0	$c_b L_b$	H_b
	1	$(1 + c_b)L_b/2$	H_b
	2	$(1 + c_b)L_b/2$	0
	3	L_b	0

Several examples of the achievable shapes are presented in Figure 3.25. As can be noted on the examples, there is no control on influence of the bump in the global geometrical features of the shape, that is, a given set of parameters may result in geometries that have an effective height and/or length larger than the ones of the base triangle. Even if there is no strict control in the implementation, the design space of the optimizations performed with this parametrization are chosen as to avoid important modifications of effective d and b.

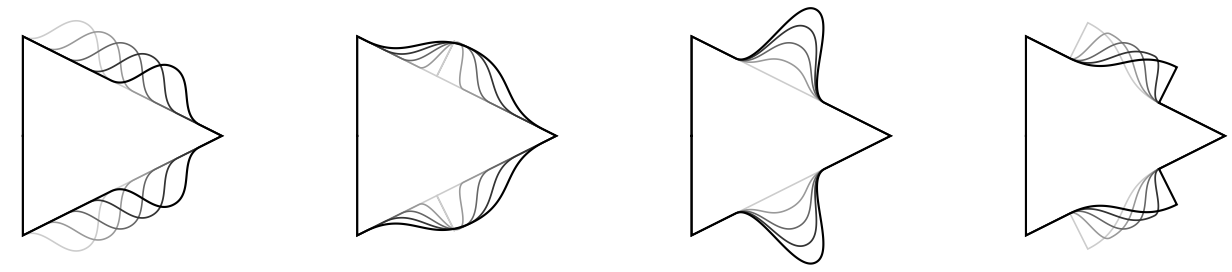

$S_b \in [0.000, 0.800]$ $L_b \in [0.000, 1.000]d$ $H_b \in [0.000, 0.400]d$ $c_b \in [0.000, 1.000]$

Figure 3.25: Sample of the possible shapes that can be generated with the bump parametrization modifying each parameter individually, symmetrical shapes, AR = 1 and flow from the left to the right. When not being modified, parameters are $(S_b, L_b, H_b, c_b) = (0.4, 0.5d, 0.2d, 0.5)$. Shape obtained with the lowest value in represented by thin light gray line, highest for thick black.

The shape parametrization is implemented in the Python framework and the epsilon matrix is defined using a PIP algorithm and later passed as an input to the simulation.

3.3.3.2 Optimal shapes

The optimization is performed for 3 distinct configurations: 1) for minimal RMS lift coefficient, symmetrical bumps; 2) for minimal RMS lift coefficient, asymmetrical bumps (only on upper edge); and 3) for minimal acoustical efficiency, symmetrical bumps. For the 3 cases, the base shape is the back-pointing triangle of aspect ratio AR = 1. The optimization parameters (c_w, c_1 and c_2) are the same as defined in Section 3.3.1.2, 36 particles were used, initially displaced by LHS distribution, for a maximum of 30 iterations. The design space are also the same for all 3 runs: $S_b \in [0.0, 1.0]$, allowing the bump to be placed from the leading to the trailing edge of the base triangle; $L_b \in [0.1, 0.5]d$; $H_b \in [0.0, 0.5]d$, which means that the back-pointing triangle (no bump) is also in the design space); and $c_b \in [0.0, 1.0]$.

The integral quantities associated with the optimal shapes are listed in Table 3.12, values for canonical back-pointing triangle and square are also listed. The flow modification is expressive, as shown in the vorticity snapshots in Figure 3.26. A recirculation is formed in the cavity

encountered between the bumps and the upstream face of the base triangle, creating an artificial wall for the flow. That way, the flow behaves similarly to what is observed around the rectangular sections.

Table 3.12: Optimization results - back-pointing triangle with bump.

objective	min $C_L'^{*}$	min $C_L'^{+}$	min $W_a{}^{*}$	rect	trib
AR			1.000		
S_b	0.785	0.786	1.000	NA	
L_b/d	0.494	0.500	0.500		
H_b/d	0.500	0.500	0.500		
c_b	1.000	1.000	0.900		
$\lvert C_L \rvert$	0.006	0.429	0.006	0.003	0.007
$\lvert C_D \rvert$	1.329	1.582	1.335	1.347	1.982
C_L'	0.174	0.535	0.175	0.223	0.958
C_D'	0.008	0.094	0.007	0.011	0.039
St	0.162	0.155	0.157	0.167	0.164
$W_a, 10^{-5}$	0.97	9.22	0.94	1.63	29.69
effective b	1.104	1.050	1.051	NA	
effective d	1.105	1.024	1.079		
effective AR	1.180	1.000	1.180		

*: symmetrical bumps;

$^{+}$: asymmetrical bumps (only in upper edge).

If compared to the base triangle, there are a reduction of 81% of the RMS lift coefficient for the first optimal shape, 44% for the asymmetrical case. The acoustic efficiency is reduced by 14 dB with the insertion of the bumps that minimize W_a. The average drag coefficient is also reduced for all the 3 cases, being similar to the value obtained for the square section.

The minimum acoustic efficiency is obtained with a shape that has a RMS lift coefficient similar to the one obtained with the shape that minimizes C_L' (0.175 and 0.174, respectively). The reduction the W_a is due to a reduction of the Strouhal number (0.157 and 0.162). This behavior can be justified by the slight increase of the blockage generated by the association of the bump and the recirculation in the produced cavity.

As stated before, the optimal shapes reproduce the wake seen around the rectangular sections, that is, a well defined blockage and an extended dissipation region, as illustrated in Figure 3.27. The presence of the bump increases the distance of the upper and lower boundary layers, notably by the creation of the two recirculation zones (2 for the symmetric case, 1 for the asymmetrical bump), and results in flows that push the vortex shedding donwstream. This is noted on the recirculation lengths that are way larger than what is noted on the base shape and are also larger than what is obtained in rectangular sections of corresponding breadth.

Since there is no control regarding the effective breadth and height of the final shapes (trib + bumps), the shapes total blockage and length are different from the base shape, also listed on Table 3.12. There are no significant changes in d (lower than 5%). For b, there are non-negligible changes, that may as well justify the distance in aerodynamic and acoustic behavior. As stated earlier (Section 2.3.3.2), the increase of the aspect ratio is most probably inducing a reduction of the vortex shedding strength, thus, the bump has a positive effect only by increasing the effective length of the shape.

Is also interesting to point that the asymmetry even still being effective, is not as advantageous as the symmetrical case. This may be justified by the facility of the interaction between the opposite vortexes, that is smaller than the base triangle but bigger than the case of symmetrical bumps.

In conclusion, it is noted that, for the proposed parametrization and design spaces, the

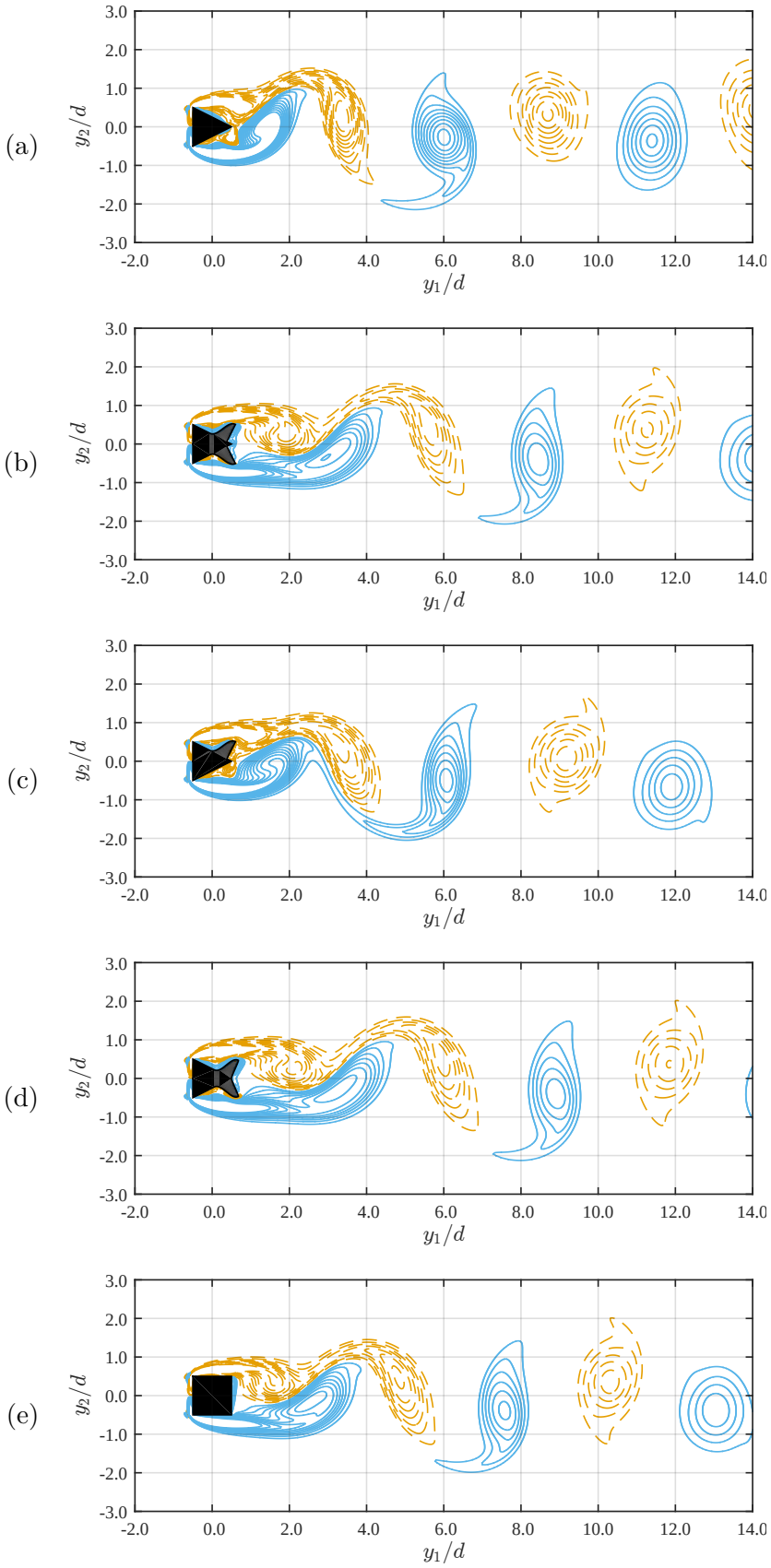

Figure 3.26: Snapshots of vorticity for (a) back-pointing triangle of AR = 1.0, (b) minimum RMS lift coefficient, (c) minimum RMS lift coefficient (asymmetrical bump) and (d) minimum acoustic efficiency, and (e) rectangle of AR = 1.0, interval of 0.3 U_∞/d, continuous line for positive and dashed line for negative; Re = 150.

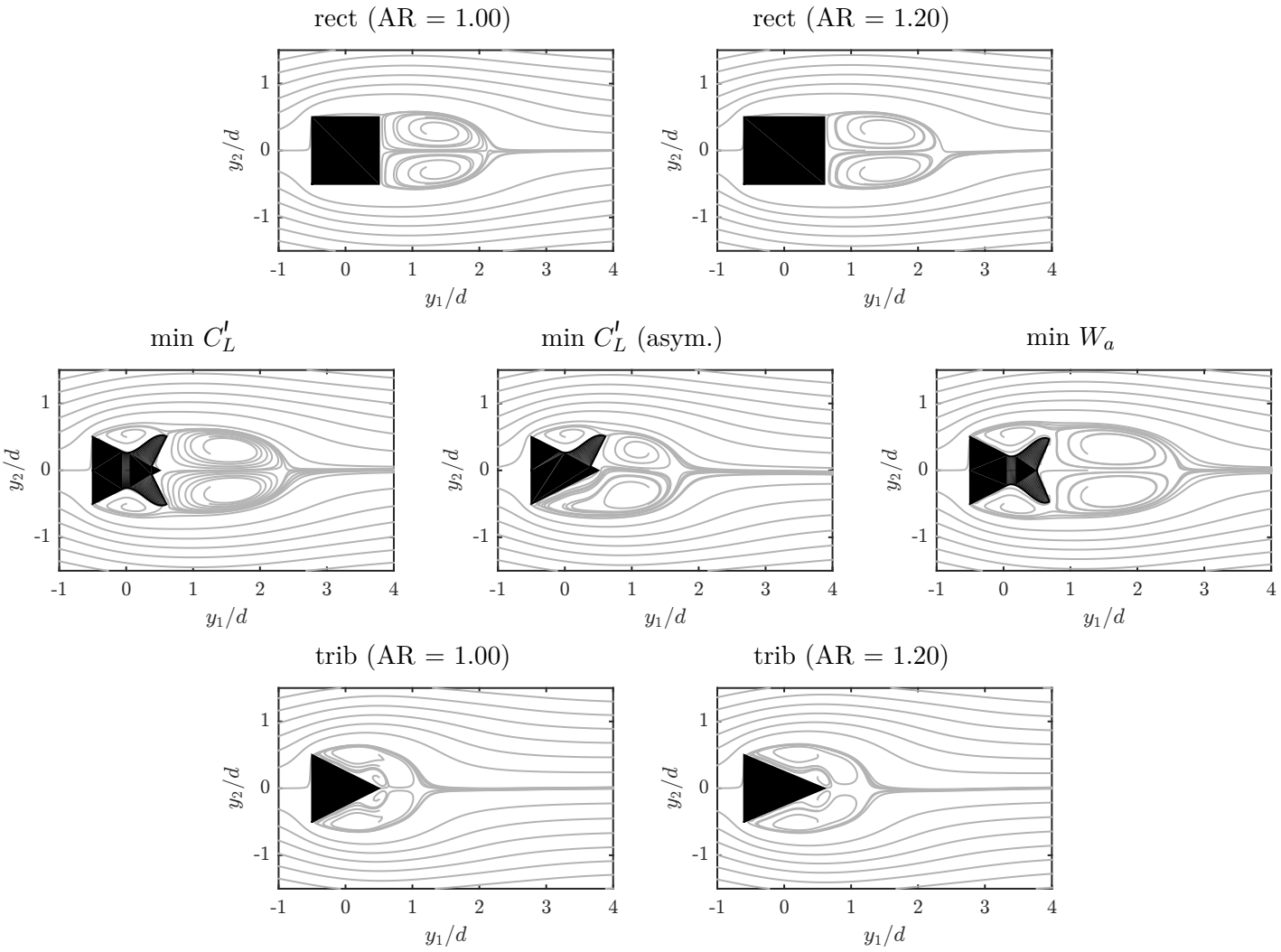

Figure 3.27: Streamlines of the mean flow for rectangular section (top) at multiple AR, the optimized shapes (center) and the back-pointing triangles (bottom) at multiple AR.

major gains proposed by the bumps in terms of shape modification go towards the reproduction of the rectangular section. That is, elongated cross-sections that have an important place for dissipation before the vortex shedding and a well posed separation between the shear layers. Naturally, as discussed on Section 2, those conclusions are only applied to the tone produced by the vortex-shedding and neglect the possible negative outcomes of the created cavity, especially in more energetic flows (larger Re).

3.4 Final discussion and concluding remarks on the aeroacoustic shape optimization

3.4.1 On the pertinence of the proposed implementation

The feasibility of the performed optimization procedure relies fundamentally on the robustness of both the optimizer (PSO) and the IBM. In that way, the management of the tested geometries was possible without direct interference after both optimization and flow simulation settings were defined in careful preliminary studies. Simultaneously, the use of a hybrid acoustic model that is capable of estimating the sound from global flow statistics was an essential component of the proposed framework.

As far as the optimization routine is concerned, the fact that every study performed here returned rather simple and smooth response functions advocates for the use of surrogate mod-

els. It is clear that after knowing the shape of the response function such procedure could be beneficial, however some points must be highlighted concerning the reason of why such kind of response was obtained and the danger of limiting the optimization to a surrogate model.

First, the limitation of the numerical solution to 2D to the laminar regime is believed to provoke such smooth response curves. Rather than implying that this could be an intrinsic characteristic of the current (or any) aeroacoustic problem, one may affirm that the obtained surfaces are strictly limited to the tested configurations.

Imprecisions are inherent to a surrogate model due to the fact that there is an interpolation, also, a poor sampling would return wrong optima. Take for example the curve of the RMS lift coefficient as a function of the aspect ratio. If the values only at low AR (increase with AR) are considered, the deduced curve would be a monotonic increasing law. On the other way, if only the points of AR bigger than the C_L' peak aspect ratio were considered, the obtained surrogate would represent a monotonic decreasing law. In both cases, the physical dispute between the available surface and the strength of the vortex discussed in Chapter 2 would be completely ignored when performing the optimization and most likely would return wrong optima.

3.4.2 Flow and geometrical features associated with extreme noise production

The optimization for minimum RMS lift coefficient and minimum acoustic efficiency returned virtually the same shapes. These results confirm the argument presented in Chapter 2 that the major quantity in terms of shape influence on the tonal noise production is the fluctuating lift.

Despite the noted general trend that associates the average drag and the RMS lift coefficient (see Section 2.3.3.4) there is a dissociation between the cross-sections that have minimal drag and minimal noise, as also noted in the experimental work of Becker et al. [16]. This is notable from the results of the first shape parametrization on Figure 3.16.

It can also be concluded that, in general and based on the later two shape parametrizations, body asymmetry may be associated with an increase of the tonal noise emission. The distance between the mixing layers can be decreased, thus, the interaction of the counter-rotating vortices is increased, causing enhanced vortices and stronger suction, that finally generates larger pressure fluctuations and larger RMS lift coefficients.

As noted in Chapter 2, the back-pointing triangle is, among the tested shapes and forms that could be evaluated with current shape parametrizations, the loudest geometry. This behavior is once more associated to its rather rough transition from upstream to downstream, which represents a relatively early flow transition to unsteadiness, and also plenty of surface for the generation of pressure fluctuations, thus, large C_L'. On the other hand, square and rectangular sections have low efficiency in terms of noise emission.

When the bumps are added, the generation of energy disturbing elements and the overall increase of effective height and length, the dynamics described in the previous paragraph are effectively broken, resulting in non-negligible sound emission reduction. Both the instantaneous and mean flow are, similar to the flow around the rectangular sections. The generated cavity may be problematic in the case of greater Reynolds numbers with the emergence of the Kelvin-Helmholtz instability that is absent in the tested regime.

A look at the shapes with minimal sound emission leads to the conclusion that the key strategy for reducing the vortex shedding strength is to dissipate the wake energy at instances that are different from the vortex shedding. Considering an application where the height d and the flow velocity are fixed (so the Reynolds number), the different shapes immersed into the same flow are going to be at different instances of the flow regime and transitions. A shape that has a later flow transition (such as the long rectangular sections) will eventually be a noise reducing shape due to the fact that for the given Reynolds number of interest, there is less fluctuating energy since the threshold of the unstable mode is higher. For the first parametrization (QCCQBC), at fixed AR, this is achieved by having an abrupt increase of blockage that is combined with a long surface afterwards. This configuration combines a strong energy dissipation on the boundaries with a larger distance between the vortices of opposite

signs.

According to the previous paragraph and as it was observed in the performed studies, in what concerns the fluctuating lift and the acoustic efficiency, the sole parameter that has been proven to be universally capable of reducing the sound emission for the 2D, laminar flow is the sectional breadth.

The conclusions presented here are limited to the flow regime that was tested. This means that, the complete flow development and spanwise distribution of the structures are absent. It has already been established in the literature that the rectangular section is louder than the circular [83, 111], the opposite of what is obtained from the optimizations and in Chapter 2. In order to investigate this disparity and expand the discussion about the physics of the vortex shedding, experimental work is performed and presented next on Chapter 4.

Chapter 4

Experimental study on cross-section influence on flow and noise emission

The influence of the shape in the sound emission is examined experimentally in an anechoic wind-tunnel facility. The investigation of the physical mechanisms of the aeolian tone generation is performed with microphone recordings and streamwise velocity measurements using hot-wire probes. It has the objective of describing and dissecting the acoustical signature of different shapes, complementing the studies reported earlier in the manuscript.

Chapters 2 and 3 present a study of the effects of the shape on bluff body noise emission for a 2D, low Reynolds number flow. It is obtained that the critical geometrical features are a section that is short enough so there is not a lot of dissipation before the wake but wide enough as to have a lift generating surface. The back-pointing triangle section is in both parts of the study the shape that provokes the highest lift fluctuations, thus, the loudest. Since the three dimensionality of the flow is a fundamental brick in the construction of the aeolian tone, the pertinence and extrapolability of those claims are investigated.

While many experimental studies on the sound emission of cylinders can be cited, they are mostly limited to the circular cylinder and do not go deep into the description of the vortex-shedding mechanism. This chapter describes an analysis that follows the principle of the project to apply relatively simple procedures, with the use of well-established measuring and signal processing techniques. The study is based on the analysis of the frequency and amplitudes (total and spectral) of the sound pressure and of the spanwise behavior of the flow (correlation and coherence), with numerous comparisons to literature values and previous discussions on the mater. Such simplicity allows to focus on the details of their application and the physics of the phenomena and to extend the investigation to a wider set of cylinders. In total, about 25 cylinders are considered. The focus is on the circular, square and rectangular cross-sections of aspect ratio 2 and 3, that have been described acoustically and aerodynamically, with measurements of flow spanwise correlation and coherence.

This chapter starts with the description of the experiment in Section 4.1, with the presentation of the facility, the experimental conditions, the tested cylinders and the experimental setup. Section 4.2 contains a description of the wake derived from hot-wire data, with an analysis of the shape influence on the statistical distribution of the velocity signals. This is followed by a discussion about the spanwise correlation and coherence of the circular and rectangular sections in Section 4.3, with the presentation of an algorithm for obtaining the coherence length from noisy data and a discussion about the effect of the shape onto the spanwise flow distribution. After that, in Section 4.4, the acoustic signatures of the different cross-sections are presented and compared. In Section 4.5, the closure of the aerodynamic sound is investigated with the estimation of the RMS lift coefficient, fundamental ingredient in the sound generation, with a correction method. Furthermore, observations concerning the cylinder's length influence on the sound emission are presented and a global empirical formulation for the SPL(ℓ) relationship is proposed. Final remarks and conclusions are presented in Section 4.7.

This work is partially issued from two scientific communications [193, 196].

4.1 Methodology

This part of the study is completely performed in an anechoic wind tunnel, described in Section 4.1.1; the experimental conditions (considered air properties, range of Reynolds and Mach numbers) are presented in Section 4.1.2. Two physical quantities of the flow are measured: the sound pressure and flow velocity. The arrangement of the cylinders, the considered cross-sections and the details about the probes and employed post-treatment techniques are available in Section 4.1.3.

4.1.1 Measurement facilities - BETI acoustic wind-tunnel

The experimental analysis is performed in the anechoic wind-tunnel BETI of Pprime Institute at Poitiers, France, represented in Figure 4.1. It has a closed circuit, with an exit nozzle of section 70 cm × 70 cm, contraction factor of 10:1, maximum velocity of U_∞ = 50 m/s. The anechoic chamber cutoff frequency is of 200 Hz.

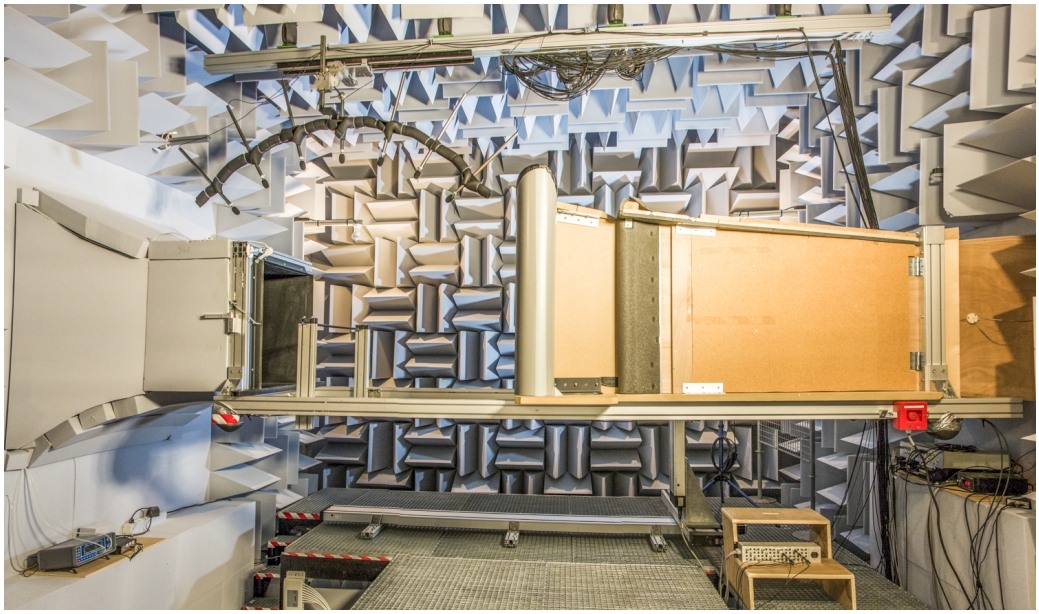

Figure 4.1: Photography of the anechoic chamber of the wind-tunnel BETI of the Pprime Institute, at Poitiers, France.

The original arrangement is a 3/4 open-jet test section with a plate placed at the lower edge of the nozzle, which explains the asymmetrical collector nozzle in Figure 4.1. Such a set-up is ideal for performing experiments with wall mounted obstacles. Some examples, contemporary to this work, are the study of the sound emission of a facing step by Zumu Doli [289] and Beausse et al. [15] and of the three-dimensional description of the aeroacoustic sources of aerodynamic profiles by Zhou et al. [286]. For current experiments, the plate is removed such as to have a full open-jet configuration. Due to flow passing under the collector, its lower wall is extended with an inclined plate (illustrated on Figure 4.2). The effects of that modification were examined in preliminary tests with recordings of the sound emission of the flow around a circular cylinder of diameter d = 14 mm with and without the extension. The global acoustic signature was practically unaffected in terms of levels and spectral distribution of the sound, only a small distortion in the sound directivity is noted, probably due to acoustic reflections. Since the effect is rather marginal, this proposed adaptation of the 3/4 set-up is used for all the current experimental work.

4.1.2 Experimental conditions

Flow velocities in the range of 10 m/s to 40 m/s are used. The turbulence intensity measured at the location of the center of the cylinder with empty test section is of 0.5%. The room

temperature is also measured at each measuring session, with an average temperature oscillating from about 17 to 23 degrees Celsius. For simplicity, air properties are fixed and taken as follows: air density of ρ = 1.225 kg/m^3; sound speed of c = 340 m/s, so the Mach number Ma ranges from 0.03 to 0.12; and air kinematic viscosity of $\nu = 1.5 \times 10^{-5}$ m^2/s, leading to a range of Reynolds numbers from 4,000 to 53,333.

Table 4.1 lists the range of velocities tested in this work and the corresponding Mach numbers. The flow Reynolds numbers, based on the tested cross-section height d, are also presented. The performed measurements are described next.

Table 4.1: Experimental conditions.

U_∞, m/s	10.0	15.0	20.0	25.0	30.0	40.0
Ma	0.03	0.04	0.06	0.07	0.09	0.12
d, mm	Reynolds number - Re, 10^3					
6	4.00	6.00	8.00	10.00	12.00	16.00
8	5.33	8.00	10.67	13.33	16.00	21.33
10	6.67	10.00	13.33	16.67	20.00	26.67
12	8.00	12.00	16.00	20.00	24.00	32.00
14	9.33	14.00	18.67	23.33	28.00	37.33
15	10.00	15.00	20.00	25.00	30.00	40.00
16	10.67	16.00	21.33	26.67	32.00	42.67
20	13.33	20.00	26.67	33.33	40.00	53.33

4.1.3 Measurements setup

The study of the shape influence on the aeroacoustic response of various bluff bodies is performed using static cylinders of multiple cross-sections, without end-plates. A description of the arrangement of the cylinders in the wind tunnel and a list of the studied cross-sections are available on Section 4.1.3.1. Measurements of the sound emission using an array of microphones and of the flow velocity at different positions in the wake using hot-wire anemometry are performed. The experimental set-ups associated with each of these quantities are presented next in Sections 4.1.3.2 and 4.1.3.3, respectively.

4.1.3.1 Cylinder positioning and studied cross-sections

The obstacles are fixed at a streamwise distance of 30 cm from the outlet of the nozzle, at its vertical center. They are supported by two bars at the two axial limits of the cylinder. Considering the region between the supports, the total geometrical length of the cylinder is 86 cm; no end plate or any other technique is applied to minimize the influence of the sides on the flow, thus this is not the actual spanwise extension of the flow aerodynamics. The effective length is considered to be ℓ = 70 cm, the dimension of the nozzle outlet, neglecting the evolution of the lateral mixing layers.

Three different tactics guided the choice of the cylinders:

- a comparison of the sound signature for different cross-sections (circular, square, triangular) with all the other geometrical parameters (such as the length and the aspect ratio) fixed;
- the modification of the aspect ratio, notably inspired by the numerical results in Chapter 2;

- and the measurement of the noise emission of a given cylinder of distinct relative lengths (ℓ/d) by the change of the height d.

A list of the used cylinders is presented on Table 4.2, ordered by the reference length d (cylinders may be at non-zero incidence). Beyond the archival effort, the material of the cylinders is indicated due to the noted influence it may represent on the sound production, as discussed in Sections 4.4.2 and 4.4.4.

Table 4.2: List of experimented cylinders. Number in the parenthesis indicates the angle of incidence when non-null.

d, mm	ℓ/d	material*	cross-section
6	116.67	a	circular
		c	6×16, 6×13
		a, c	6×6
8	87.50	a	circular
		c	6×6 (25.4°), 6×13 (9.3°), 6×16 (7.3°)
		a, c	8×8
10	70.00	a	circular, 10×20
		c	6×13 (19.5°), 6×16 (15.3°)
		a, c	8×8 (17.0°), 10×10
		s	10×5, 10×30, 10×50
		b	10×40
		y	triangle (back-pointing & front-pointing)
12	58.33	a	circular
		s	12×12
14	50.00	a, c	circular
		s	14×14
15	46.67	y	triangle (back-pointing & front-pointing)
16	43.75	a	circular
20	35.00	a	circular

*: a: aluminum, c: carbon fiber, s: steel, b: brass, y: acrylic

While the sound emission is measured for all the cylinders in Table 4.2, the studies of the velocity signals (Section 4.2), spanwise coherence and correlation (Section 4.3) and the estimation of the RMS lift coefficient (Section 4.5) consider only d = 10 mm, circular, square and 2 rectangular (AR = 2 and 3) sections.

4.1.3.2 Acoustic pressure measurements

A 7-microphone array is placed above the cylinder (see illustration on Figure 4.2). The microphones are spaced by 15 degrees, placed at the spanwise center of the cylinder at a distance of r = 1 m (that is 1.42 times the cylinder's length), allowing directivity measurements. The first microphone forms an angle of 45 degrees with the incoming flow and microphone number 4 is at 90°. The sampling frequency is 12.8 kHz for a recording time of 60 seconds. Sound spectra are calculated using the Welch's method, with 8192 points and 90% overlap, leading to a spectral precision of Δf = 1.56Hz. No weighting is applied in the calculation of the sound pressure levels indicated in this work. Decibel levels are calculated as $10\ \log_{10}(\overline{P}^2/{P_{\text{ref}}}^2)$, $\overline{P}^2$ being the averaged auto-spectrum of the acoustic pressure and P_{ref} = 20μPa the reference pressure.

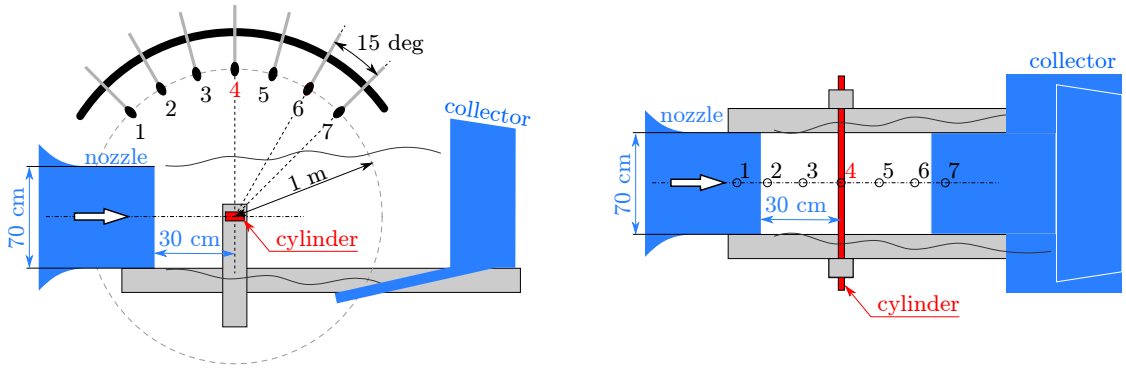

Figure 4.2: Diagram of the experimental setup with the microphone array, side (left) and top (right) views. Arrow indicates the flow direction.

Microphones are calibrated at 1 kHz, 94 decibels. Microphone sensibility is about 40 mV/Pa.

Unless otherwise stated, presented sound spectra were corrected for background noise, based on recordings done without the cylinders. The performed correction accounts only for wind-tunnel noise and does not deal with undesirable aerodynamic effects related to the existing mixing layers, that are considered negligible. Examples of the magnitude of such corrections can be found in [83].

4.1.3.3 Measurements of flow velocity using hot-wire anemometry

Measurements of the streamwise flow velocity are used for the description of the wake. Hot-wire anemometry is performed using Dantec P11 one-dimensional probes and a NI-4472 acquisition plate. All interfaces between the different elements of the measurement chain are coded in LabView.

Since the measurements are based on heat exchange by forced convection, it is impossible to distinguish between a positive or negative velocity. Also, it is not suited for very low velocities, where the natural convection is non-negligible. No correction or treatment are performed for dealing with negative or small velocities, a point that will be discussed when relevant.

The system is re-calibrated before each measuring session and a 4^{th} order polynomial law is used for converting the voltage into velocity. As illustrated on Figure 4.3, values at low speed may be extremely overestimated due to the calibration law. Based on the hot-wire properties and the calibration laws, a minimum of about 5 m/s is proposed.

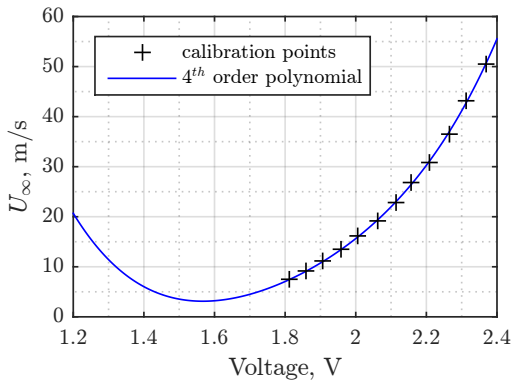

Figure 4.3: Example of the calibration law of the hot-wire measurements.

Measurements with fixed and moving probes are performed. When fixed, the hot-wire is connected to a probe support attached to the upper edge of the nozzle. The moving hot-wire probe is connected to a 3-axis arm via a profiled rod. For measurements at U_∞ = 40 m/s, the

indicated (y_1, y_2) coordinates have less precision, since vibrations of probe support may lead to up to 1 mm of probe displacements.

Two different experimental procedures are applies for the hot-wire measurements (as illustrated by diagrams in Figure 4.4):

- Velocity fields (of velocity magnitude) are obtained via multiple velocity recordings in a Y_1Y_2 plan using the 3-axis robot. The measurement zone starts from the upstream limit of the cylinder section (y_1 = −10, -20 and -30 mm) to y_1 = +30 mm. In y_2, lower limit is the symmetry line of the section (y_2 = 0 mm), and upper limit is y_2 = 15 mm. At the center of the cylinder (y_3 = 0) a grid of Δy_1 = 1 mm and Δy_2 = 2 mm is used, resulting in: 294 acquisition points for the smaller section (AR = 1); 339 for AR = 2; and to 384 for the longest rectangle (AR = 3). Since only the global statistics (average and RMS) are investigated, the acquisition frequency is chosen as 1 kHz and the sampling duration is of 5 seconds. Spanwise consistency of the flow topology is assessed by performing the same procedure at two different plans (y_3 = 150 mm and y_3 = 300 mm), with less points (Δy_1 = 2 mm), composing meshes of 144, 164 and 184 points, from the shortest to longest rectangular section. These fields give access to the main topology of the flow, which is necessary to set the relevant Y_1Y_2 position where the spanwise study shall be conducted.

- Velocity measurements along the spanwise direction are carried out with the same moving hot-wire probe, but now at fixed Y_1Y_2 coordinates. For performing coherence and correlation calculations, a fixed probe is simultaneously recording the velocity values in the spanwise symmetry plans of the cylinder (y_3 = 0 mm). Due to the presence of the supports of the hot-wires, the starting point of the moving probe is at a spanwise distance of Δy_3 = 7mm from the fixed probe. A total of 48 spanwise positions are used, up to y_3 = 300 mm. Aiming at a spectral analysis, a larger acquisition frequency and time of 6.4 kHz and 30 seconds are selected. Considering a spectral peak at a Strouhal number of 0.2, the acquisition time represents a number of at least 6000 cycles of the principal unsteady mode.

For both procedures, the velocity of the probe movement and the time interval between measurements is set as to avoid interference with the preceding measurement and to allow the stabilization of both the flow and the mechanical system. The selected settings are based uniquely on observation and no finer analysis on the influence of those parameters in the measurements is carried out.

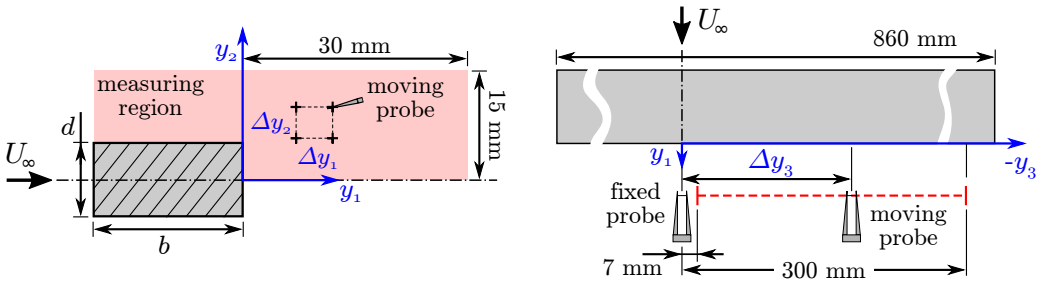

Figure 4.4: Diagrams of the experimental setups for obtaining the mean velocity fields (left) and the spanwise correlation and coherence (right).

4.2 Analysis of streamwise velocity signals

The analysis of velocity signals provides a first hint on the influence of the cross-section shape on the flow dynamics and its acoustic signature. It is restricted to the circular, square and rectangular sections of aspect ratios 2 and 3, d = 10 mm. The focus is on checking the variations of the unsteady aerodynamic behavior in the near-wake due to modification of the shape by

analyzing the velocity signals and their probability distribution function (PDF) at a discrete point (Section 4.2.1). This allows to estimate the turbulence time scale used in the correction method discussed in Section 4.5.2 (Section 4.2.2).

The signals are issued from the spanwise coherence measurements reported in Section 4.3 and are about 0.5 to 1 d away from the center of the cross-section trailing edge. The obtained behaviors are modified when different positions are taken into account. The represented results were chosen due to the consistency with the position used in Section 4.3 and also because they followed the most robust trends.

4.2.1 Normalized signals and PDF

Examination of the fluctuating velocity can highlight some aspects of the vortex shedding. A portion of the normalized velocity signals and the probability density functions (PDF) of the complete recordings are plotted in Figures 4.5 and 4.6. The velocity amplitude is normalized by its RMS value and the time by the period of the vortex shedding cycle $T = 1/f_{\text{peak}}$. For the rectangular section of AR = 2, $\text{St}_{\text{peak}} = 0.08$ is considered.

A similar analysis was performed by Norberg [172], considering surface pressure measurements for a circular cylinder. Current velocity signals are similar in both form and distribution, including the negative skewness and the intermittent low amplitude excitation (the starting point is chosen arbitrarily such as to place the event at the center of the time scale in Figure 4.5 and 4.6), that are associated by Norberg with near-wall vortex dislocations.

It is striking that theses normalized velocity signals are strongly changed by the cross-section shape. The flow around the square section hardly differs from the flow around the circular cylinder, visible in both the signal amplitudes and the probability distribution. For AR = 2, velocity values are more random, as it can be seen by the shape of the PDF, almost identical to a normal distribution, and the existence of two tones is visible in the time evolution with the presence of interchanged peaks of different magnitudes. The longest rectangular section (AR = 3), presents, at both velocities, two clear peaks in its PDF (in a smaller scale, distorted peaks can also be seen for the square and circular sections). Norberg [172] associated that density shape to a sine wave with random noise.

4.2.2 Turbulence time scale

The turbulence time scale defined by Doolan [46] is based on the duration of 10 T of the low amplitude events signalized by Norberg [172]. The same behavior is noted in current results for the circular cylinder. An equal value is assumed for the other cross-sections that are studied, however it is clear that further analysis should be performed for the description and quantification of the phenomenon. Owing to the limitations of the available data, this first approximation is used for the rest of this document.

These observations lead to an initial discussion about the different behaviors due to the modification of the cross-section. The velocity signal footprint is quite similar for both short sections. The transition for AR = 2 that creates the discontinuity of the peak Strouhal number is also associated with an increase in the randomness of the signal. In the other direction, the longest section has a rather clean velocity signal, indicating a flow less affected by turbulence. As a first conclusion, the influence of the shape can be associated with a different state in terms of flow development, working similarly to a modification of the Reynolds number, as discussed in 2.2.3 for the flow in 2D, laminar regime.

4.3 Spanwise behavior of the flow

The difference in sound emission that is noted with the increase of the aspect ratio is commonly associated with an increase of coherence [83, 111], however, no comprehensive study could be found by the author where this aspect is consistently measured and the different cross-sections are confronted. As a fundamental brick of the sound emission [109, 130, 191], the spanwise

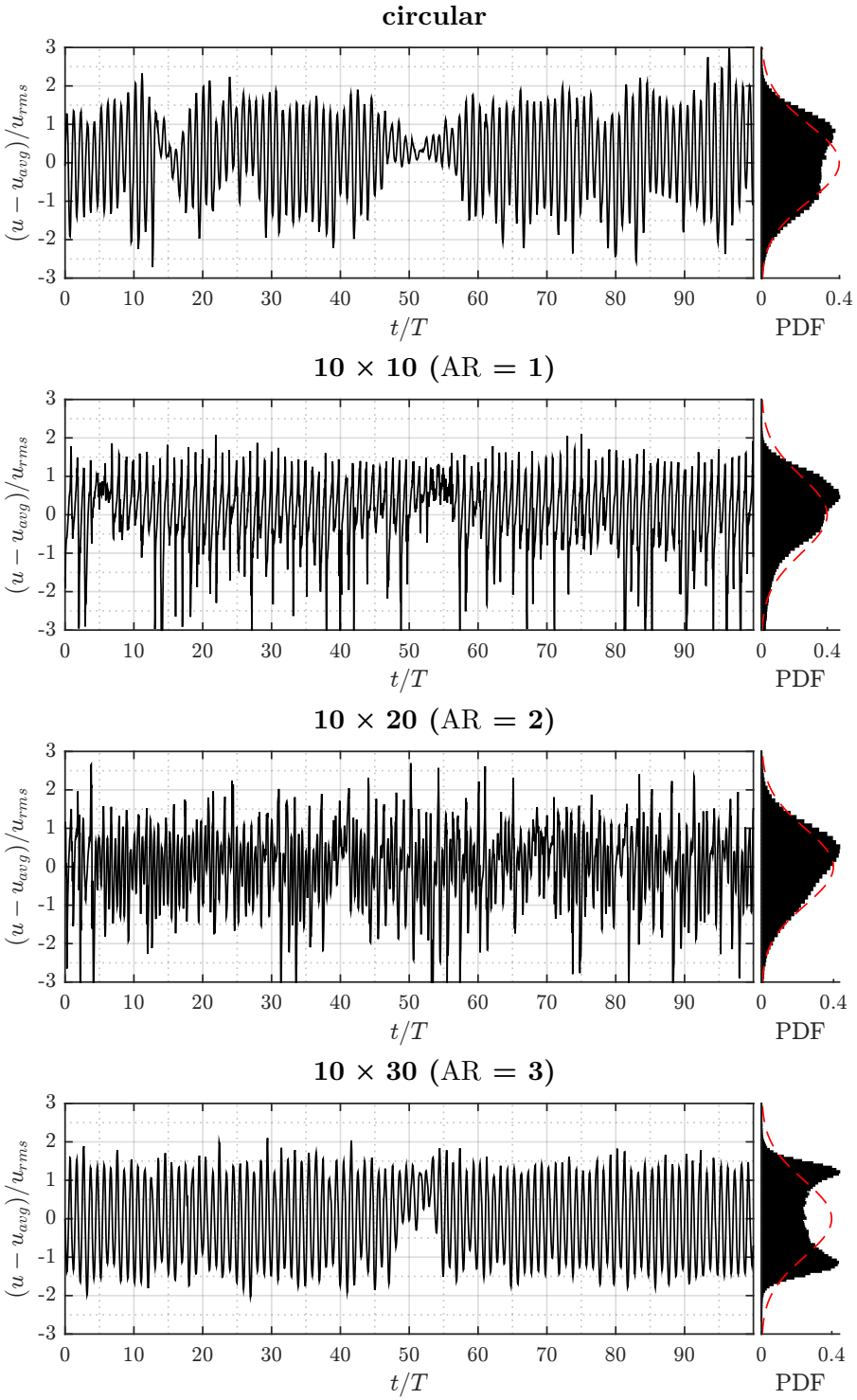

Figure 4.5: Samples of normalized flow velocity for the tested cross-sections near the expansion of the vortex for $U_\infty = 20$ m/s, with the probability density functions (PDF) represented on the right (the hatched line represents the normal distribution).

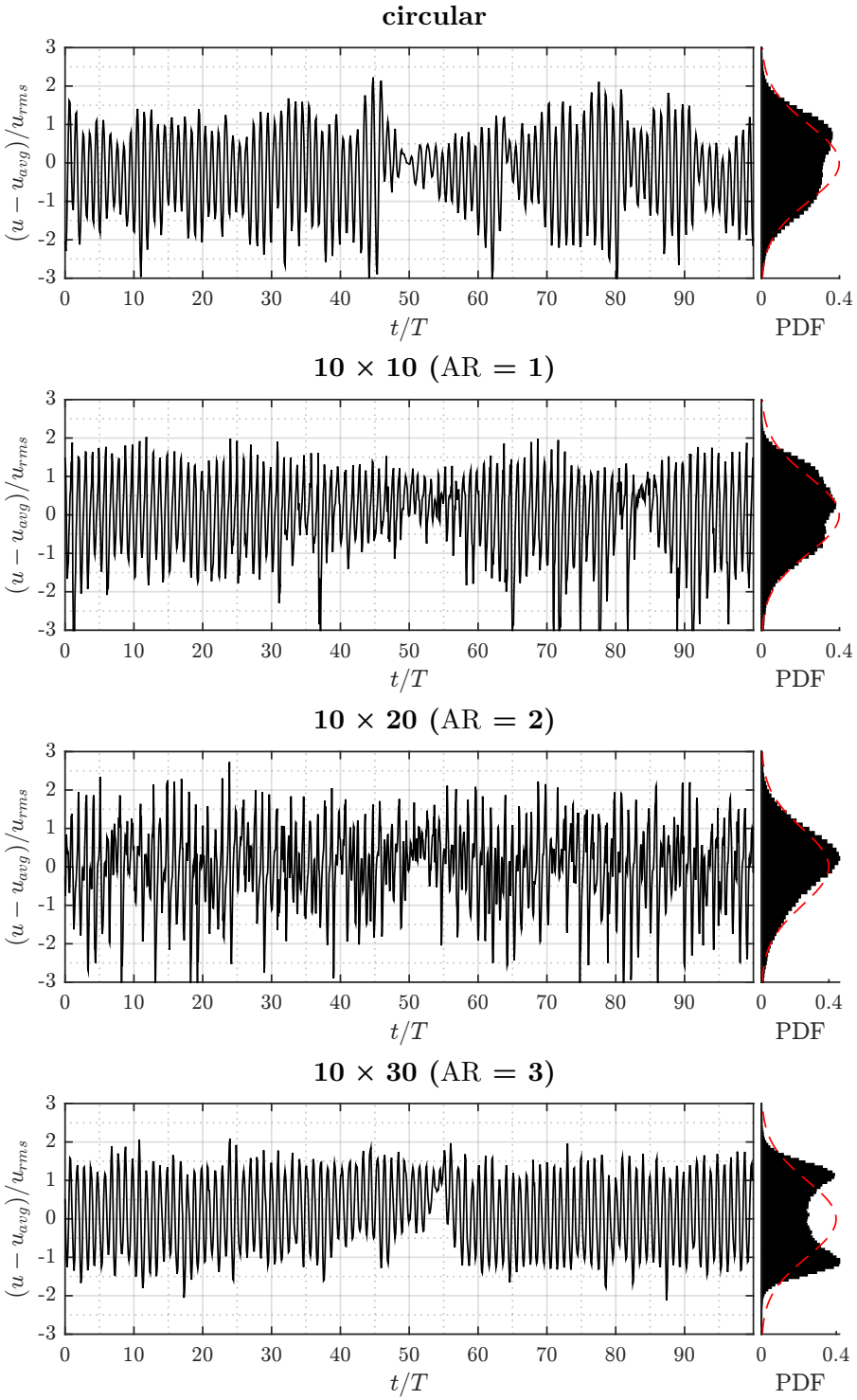

Figure 4.6: Same caption as Figure 4.5, for $U_\infty = 40$ m/s.

distribution of the flow is measured for cylinders of four different cross-sections (d = 10 mm): circular, square and rectangular (of aspect ratios AR = 2 and 3).

For the evaluation of the flow spanwise correlation and coherence, measurements with two hot wire probes are performed. The use of velocity measurements is not ideal, since the correlation of surface pressure is the quantity of interest. This choice of technique is a result of the limitation due to the size of the cylinders (d must be small such as to have a measurable tone and a reasonable Reynolds number) and the capability to perform the study for multiple cross-sections at ease. Even so, it has been proposed by many authors [172, 213] that both quantities lead to similar results. It is also important to note that, even if the observed values for velocity correlation/coherence lengths and pressure lengths may differ, both follow the same trends [49], what may implicate that the use of such estimate is possible when comparing geometries.

Albeit the number of results concerning the measurements of spanwise velocity correlation, no clear identification of the regions where the measurements were performed is available. For defining the positions, flow fields are produced from hot-wire data such as to place the probes at positions that are topologically similar among the different cross-sections (details in Section 4.1.3.3).

Are presented next: the definition of the variables used for the quantification of the flow spanwise distribution (the correlation and coherence lengths, Section 4.3.1); an algorithm developed for the automatic fit of noisy data for the definition of the Gaussian coherence length (Section 4.3.2); the measured average flow fields, spanwise correlations and coherence functions for the tested cross-sections (Section 4.3.3); a global discussion about the influence of the shape on the flow spanwise development (Section 4.3.4); and finally, a summary of the findings and conclusions on Section 4.3.5.

4.3.1 Quantification of the flow spanwise characteristics

Two mathematical procedures are used for the quantitative description of the spanwise behavior of the flow:

- Considering two signals s_i and s_j denoted by the subscripts i and j, recorded simultaneously, that represent a flow quantity at different spanwise locations $y_{3,i}$ and $y_{3,j}$. A spanwise offset is defined, $\Delta y_3 = y_{3,j}$ - $y_{3,i}$, and once normalized by the diameter (or the cylinders height) d, the spanwise distance parameter $\eta = \Delta y_3/d$ is defined. The cross-correlation is a measurement of the linear dependence of those signals, and is calculated by:

$$R_{s,ij} = R_s(\eta) = \frac{\mathrm{cov}(s_i, s_j)}{\sigma_{s_i}\sigma_{s_j}} \tag{4.3.1}$$

  where cov is the covariance of the signals and σ is the standard deviation of each signal. It is a global measurement, where all the modes in the given flow contribute simultaneously.

  A length scale can be derived from the evolution of the correlation. The correlation length Λ_s is defined as the integral of the correlation in the spawnise direction, and may be associated with the average size of the eddies [49]. The one-sided spanwise correlation length is calculated as (being the integral evaluated using the trapezoidal rule in this work):

$$\Lambda_s = \int_0^\infty R_s(\eta)d\eta \tag{4.3.2}$$

  Calculation of a mean correlation value considering a moving subset with overlap of the signals was tested, similarly to logic behind the Welch periodegram. Since the obtained results are very similar to the direct comparison of all the measured data, the complete set of values recorded by the fixed and moving probes are considered simultaneously for the correlation calculation.

- The coherence is another estimator of the linear dependence of two variables. It may be considered as a more complete parameter since it accounts for the spectral properties of both signals. It is calculated as:

$$\Gamma_{s,ij}(\Omega) = \Gamma_s(\eta, \Omega) = \frac{\text{real}(\overline{s}_i \overline{s}_j^*)}{\sqrt{\overline{s}_i^2}\sqrt{\overline{s}_j^2}} \tag{4.3.3}$$

  where $\overline{s}_i$ and $\overline{s}_j$ are the Fourier transforms of the fluctuation of the variables s_i and s_j, and the superscript $*$ indicates the complex conjugate. In order to obtain a more representative spectral distribution, the coherence calculations are based on averaged spectra density, using the same parameters as for the velocity spectra calculation.

  From Equation (4.3.3), at each frequency Ω, one obtains a distribution of $\Gamma_s(\eta)$. Following the work of Casalino et al. [30], the spanwise loss of periodicity represented by the coherence function is believed to follow a Gaussian probability density, thus the following Gaussian model is used (the Laplacian is also tested, but not presented here due to the overall poor fit that was obtained):

$$\Gamma_s(\eta, \omega) = \exp\left(-\frac{\eta^2}{2\ell_g(\Omega)^2}\right) \tag{4.3.4}$$

  where ℓ_g is the Gaussian coherence length estimator (later on referred only as *coherence length*), normalized by the diameter. Note that the coefficient 2 is absent in the model considered by Seo and Moon [233] and Orselli et al. [177], so a factor of $1/\sqrt{2}$ must be applied to the coherence lengths ℓ_g reported by them when comparing results.

Similar to the acoustic analysis (Section 4.1.3.2), the velocity spectra are calculated using the Welch periodogram, with 8192 points and 90% of overlap with an Hamming window. The definition of the main frequency (St_{peak}) is based on these velocity spectra. The flow being eventually slightly distorted at the spanwise ends, in order to avoid having an erroneous Strouhal number but at the same time searching to consider the full spanwise extent of the cylinder, the selected frequencies that correspond to the energy peak for each spanwise location are initially partitioned in 5 bins. Then the final Strouhal (referred here as the peak for each configuration) is the average St of the values that compose the most populous bin. This procedure is particularly important for rectangular cylinders, where modes of similar energy coexist.

For both the correlation and the coherence, a value of 1 represents that the two signals are perfectly correlated. It means that their values at the starting point (the comparison of the signal with itself) are always unitary. Due to the nature of the performed statistical operations, where a coherence value of 0.4 can be obtained even if the correspondence between the signals is negligible (tests with distinct randomly generated signals where capable of returning peaks of coherence up to that value), the use of a model function is fundamental for an objective study and also to compare the spectral distribution of the flow structure between different velocities and geometries. An automatic procedure for calculating the coefficient of such model is presented on the following section.

4.3.2 Coherence length estimation algorithm

4.3.2.1 Motivation

In order to obtain an estimate of the coherence curve, the Gaussian model in Equation 4.3.4 is employed. A linear fit can be used after applying the log function on the two sides of the equation:

$$\log(\Gamma(\eta, \Omega)) = -\alpha\eta^2, \qquad \ell_g(\Omega) = \sqrt{\frac{1}{2\alpha}} \tag{4.3.5}$$

For a given frequency, a simple linear regression returns the corresponding coherence length estimate as part of the angular coefficient α. As the point $\Gamma(\eta = 0) = 1$ is known by construction, the regression may be performed imposing a null intercept term.

Despite this simple logic for calculating the value, a problem arises when a large and diverse set of points is considered, what, in the author's knowledge, was not the case in previous studies. Since both low coherence values and relatively high coherence at distant spanwise locations are non representative of the flow physics and may be associated with noise, it is necessary to consider only the points that qualify the coherence behavior at a given frequency. Also, for values that have noisy and relatively low coherence values at small distances, a maximum of 0.6 for instance, the regression will produce a bad fit due to the distance of those points of the model curve, even if there is a clear tendency.

Techniques of robust linear regression (see Section 2.3.1.2) such as the Theil-Sen estimator [260], were initially tested but the result was not considered universal enough for the present dataset. Therefore, a methodology based on the physics of the problem was developed.

In an initial approach, fixed thresholds for selecting the points to be used for the model fitting were tested. Points were considered based on a maximum spanwise distance to the fixed probe (spatial threshold, $\eta \leq \eta_{\max}$) and/or on a minimum coherence value (coherence threshold, $\Gamma \geq \Gamma_{\min}$). Apart from when there was a direct application of this technique to a subset of points, the results were unsatisfactory for several reasons: 1) due to a large set of different behaviors (configurations or frequencies that vary from very low to very large coherence), a fixed threshold is not universal, that is, either important points are ignored for the description of the coherence decay or an excessive number of distant points with low coherence are considered, which overestimates the coherence length; 2) the definition of the threshold is completely arbitrary and influences the result directly; 3) even if a good fit is obtained, due to the fact that an arbitrary number of points is ignored when performing the fit, the final result is very likely to just ignore the actual decay of coherence.

Rather than the individual analysis of every case, an iterative algorithm is proposed, based on adapting the fit to the available coherence values. A combination of distance and coherence thresholds is employed for the progressive reduction of the set of points that is considered for the fit. The use of an iterative routine rather than applying a quality criterion that evaluates the fit (the determination coefficient, for example) relies on the fact that the curve shape (controlled by the coherence length) and sparsity of the points are not fixed, such that applying a statistical criterion would probably just reduce the number of points to a diminutive value and ignore the tendency of the coherence decay.

4.3.2.2 Algorithm

The proposed algorithm has a single parameter, a coherence level Γ_{lim}. Considering that the points that are farther than the location where $\Gamma(\eta) = \Gamma_{lim}$ are non representative of the physics, they may be ignored. Thus, the spatial threshold $\eta_{\max}$ (the position where the coherence equals Γ_{lim}) is defined as:

$$\eta_{\max} = \sqrt{-2\ell_g^2 \log(\Gamma_{lim})} \tag{4.3.6}$$

The reason for using a distance criterion is that values at smaller distances are likely to representing the physical decay of the coherence, and should not be ignored at the beginning of the analysis. Also, noisy sets of points where a distant value may be higher than Γ_{lim} will tend progressively to small coherence lengths rather than returning an overestimated result that considers points based solely on coherence threshold.

From an initial estimate of ℓ_g (in this work, set as the maximum η location that was measured), a Gaussian law is obtained and $\eta_{\max}$ is calculated. Based on the points that respect the spatial criteria ($\eta \leq \eta_{\max}$), the linear fit is recalculated. Following the new set of points, a new linear regression is performed and the coherence length is updated. The iteration is relaunched,

and the loop is continued until the absolute difference of consecutive ℓ_g values, e, is bigger than the stopping criteria e_{stop}) or the maximum number of iterations ($i_{\max}$) is reached.

Due to the discrete nature of the algorithm, the coherence value may oscillate, meaning that considering or not a set of points close to $\eta_{\max}$ leads L_g to fluctuate between the same 2 values. No correction is performed to modify that behavior. However, to mitigate the influence of such aspect in the final result, if the absolute differences of ℓ_g of two consecutive iterations is the same, which suggests the existence of an oscillation, the algorithm is stopped and the average between the last two calculated coherence lengths is returned. The complete algorithm for a given frequency, with both adjustments, is presented on Algorithm 2.

Algorithm 2: Algorithm for calculating the coherence length

```
Parameters: Γ_lim = 0.4, ε_stop = 0.05, i_max = 1,000;
Initial estimate: ℓ_g = 30d;
Allocating variables: i = 1, ε = ℓ_g;
while e > e_stop & i ≤ i_max do
    store previous value: ℓ_g,0 = ℓ_g;
    store previous difference: e_0 = e;
    calculate η_max - Eq. (4.3.6);
    selecting points: η ≤ η_max;
    if number of points ≤ 2 then
        break
    calculate the linear fit and update ℓ_g - Eq. (4.3.5);
    calculate difference: e = |ℓ_g − ℓ_g,0|;
    if e = e_0 then
        calculate average: ℓ_g = (1/2)(ℓ_g + ℓ_g,0);
        break;
    new iteration : i = i + 1;
return ℓ_g
```

For all the results presented hereafter, the maximum number of iterations is 1,000 and the starting value is fixed as the maximum measured distance ($\ell_g = 30d$), as presented in the example. The stopping criteria is of $0.05d$, and the coherence threshold Γ_{lim} is set as 0.4.

4.3.2.3 Test case with synthetic coherence data

Coherence values are produced numerically, for a coherence length of $\ell_{g,sample} = 6$, which gives a modeled coherence Γ_{sample} when calculated by Equation (4.3.4). Noise is added according to the following equation:

$$\Gamma = \Gamma_{\text{sample}} + 0.04\eta \times noise \tag{4.3.7}$$

where $noise \in [-0.5, 0.5]$ are randomly generated values issued from a uniform distribution. The growing interference using the spanwise distance value as a criterion is applied to reproduce the physics of the problem, while at larger distances, there is no real coherence between the signals, and relatively higher coherence values may be encountered. A correction is performed if they reach the limits ($\Gamma \leq 0$ or $\Gamma \geq 1$).

A graphical representation of the algorithm march is available on Figure 4.7, where the steps of calculating the spatial criterion and recalculating the coherence length are presented independently. The evolution of the error compared to the ℓ_g used to produce the synthetic data is also presented. As we can see, convergence is very fast (with an order of 5 iterations) and the obtained value is 6.09. The oscillatory behavior is also noted on this example, in which the calculation was, on purpose, not stopped, despite of what is implemented in the final algorithm. Note that, for steps 1 and 2, $\eta_{\max}$ is bigger than the location of the farthest coherence value, so all the points are being considered for the linear fit.

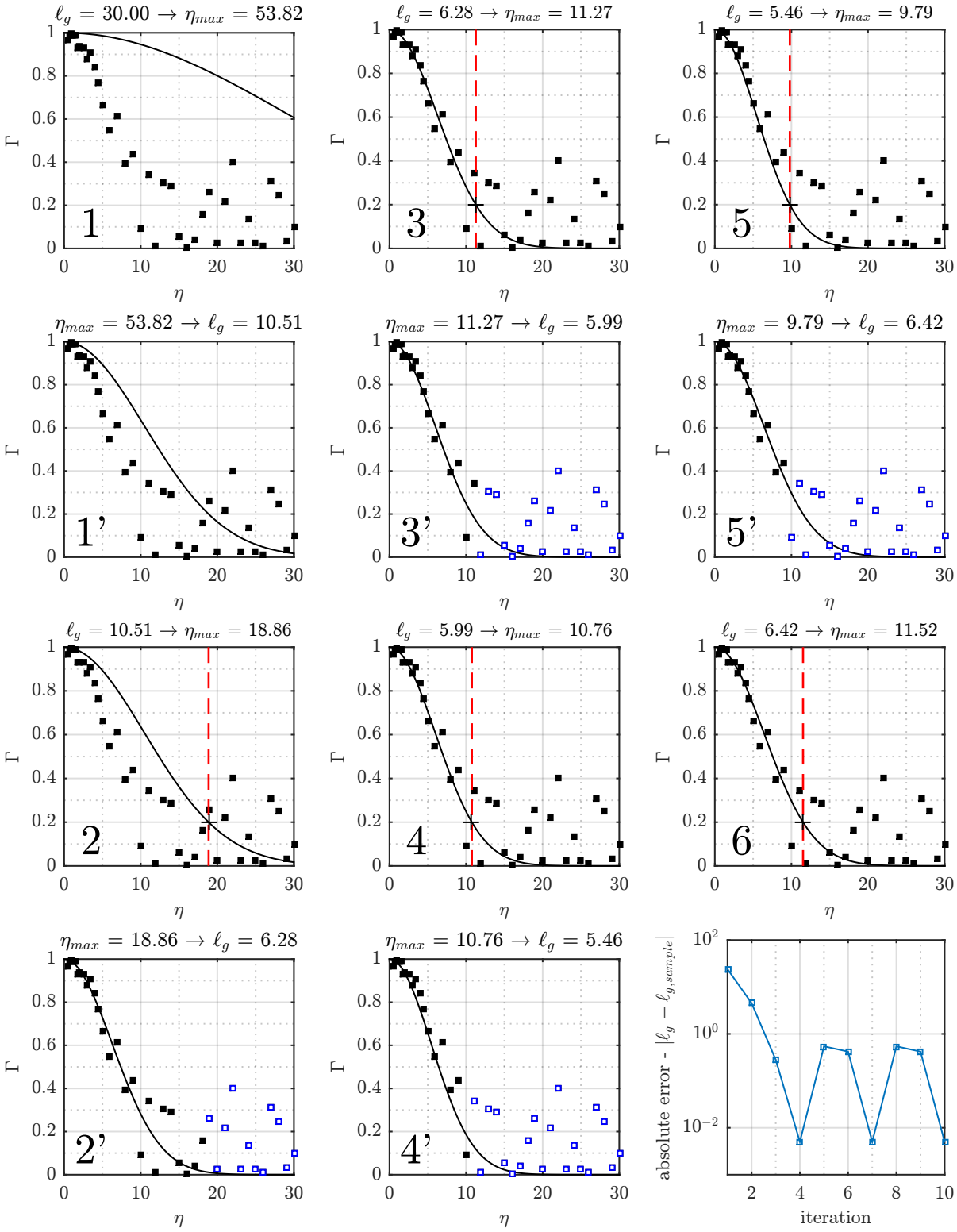

Figure 4.7: Convergence of the algorithm for a sample data, ℓ_g = 6. The solid line represents the obtained curve considering the *in iteration* coherence length value, filled markers are the points that are considered for the linear fit ($\eta < \eta_{\max}$) and empty markers represent points that are ignored due to the spatial masking. Bottom right graph is the evolution of the error, with the synthetic ℓ_g as the reference. Calculations are performed within Γ_{lim} = 0.2.

To illustrate the gain obtained from the use of the proposed algorithm, the same synthetic data is fitted using arbitrary space and coherence thresholds. Results are presented on Figure 4.8. For the first case, only a reduced spanwise extent of 4 is considered (what could also represent an experimental or numerical setup that is short in the spanwise direction), resulting in a slightly overestimated (+15%) ℓ_g of 6.79, once the decay of the coherence is not completely captured. For the other example, the use of a coherence threshold of 0.3 was not capable of removing spurious coherence values at large η, thus a coherence length of ℓ_g = 15.06 is obtained, despite the clear tendency that is observed for the points at $\eta \leq 10$.

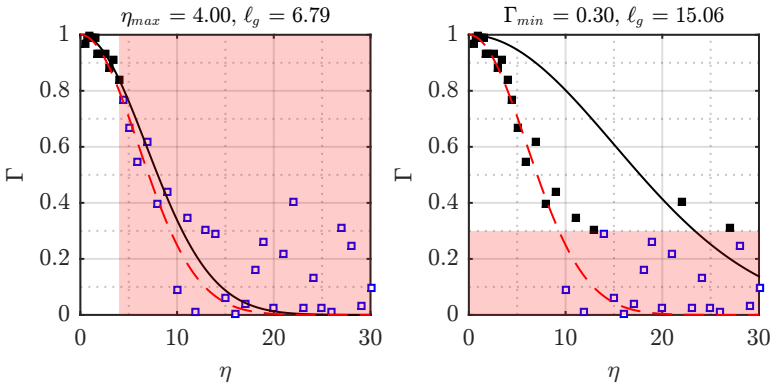

Figure 4.8: Example of obtained results with the use of the algorithm. Filled markers are the points that are considered for the linear fit, empty markers represent points that are unconsidered and the filled regions indicate the zones that are ignored either using distance threshold (left) or a coherence threshold (right). Hashed lines are the sample model, $\ell_{g,sample}$ = 6, and solid lines represent the fitted curve.

For the same data ($\ell_{g,sample}$ = 6) and two other artificial data points ($\ell_{g,sample}$ = 3 and $\ell_{g,sample}$ = 10), a parametric analysis considering the three strategies (the two thresholds and the proposed algorithm) are performed and illustrated on Figure 4.9. Considering the sample points, for all strategies, there is a range where the results are reasonably close to the input value of coherence length, the error for the proposed algorithm being smaller and present only at very low or very high values of Γ_{min}. For a small set of geometries or configurations, a manual procedure of setting the desired values can be performed for all the three cases, as stated earlier, however, this becomes impossible for a large set of (Γ, Ω) points. Moreover, it has been shown that the robustness of the algorithm is not restricted to a single configuration due to its iterative nature, differently from what is noted for the other two techniques that are described.

An intrinsic difficulty to evaluate the precision of the proposed algorithm is the production of a reasonable test data, since the noise has to be high enough to be representative of real measurement, but not so much as to change the global behavior of the curve. This also justifies using $\Gamma(\eta)$ points instead of the generating two noisy signals and later performing the coherence calculation.

The validation on real data is presented in section 4.3.3.1 considering the coherence of a circular cylinder, for which spanwise coherence values of the harmonics are available in the literature.

4.3.3 Measured spanwise correlation and coherence lengths

Measured spanwise correlation, coherence and quantities that are derived from them are presented separately for the circular and rectangular sections, followed by a discussion about the influence of the cross-section onto the spanwise distribution of the flow.

4.3.3.1 Circular cylinder

The aim of the this section is twofold: (i) to validate the experimental experimental setup and post-processing techniques against previous studies of the circular cylinder; (ii) to test and

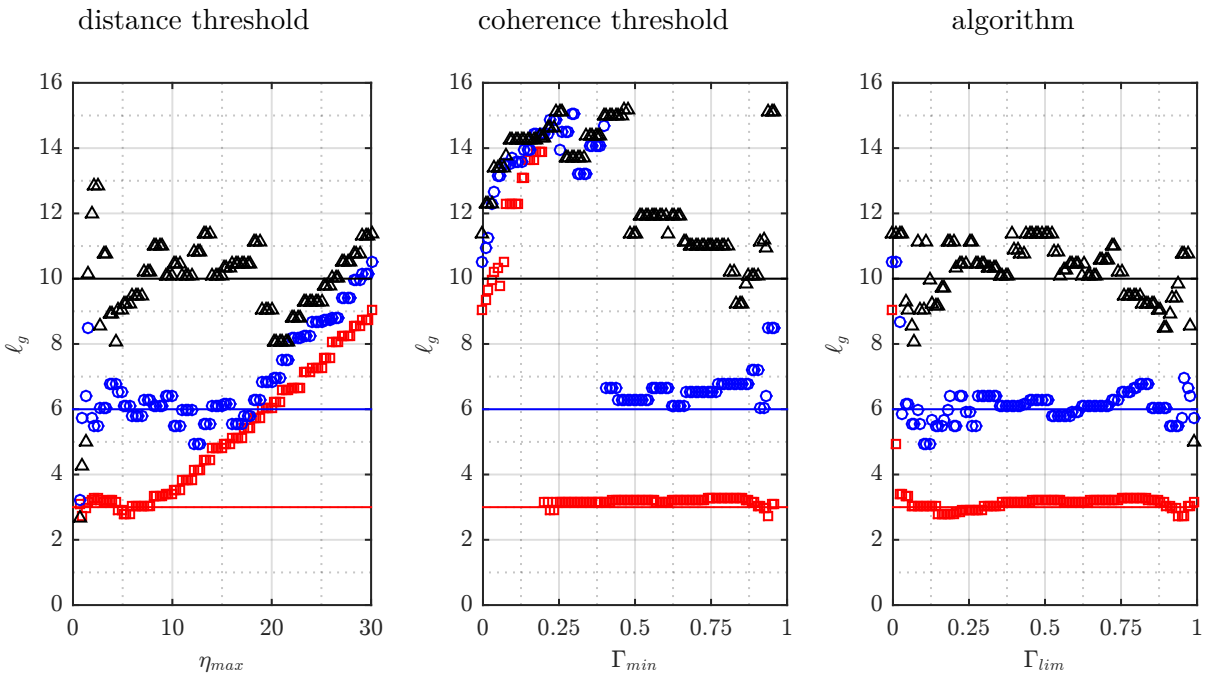

Figure 4.9: Parametric study for the distance threshold method (η_{max}), the coherence threshold method (Γ_{min}) and the proposed algorithm for multiple Γ_{lim} values. Markers represent the obtained coherence lengths for $\ell_{g,sample}$ = 3 (□), $\ell_{g,sample}$ = 6 (○) and $\ell_{g,sample}$ = 10 (△), where $\ell_{g,sample}$ is the value used to create the coherence data, represented by the solid lines.

discuss the present approach at other Reynolds numbers than 22,000.

For the circular section, the review by Ribeiro [213] indicates that the correlation value is relatively independent from the measuring location in the Y_1Y_2 plane once it is above the mixing layer and at a reasonable downstream location to capture more than just the inlet flow. In the present section, the probe is located at $(y_1, y_2) = (+0.0d, +0.9d)$, zero being at the center of the section, consistently with previous works [49, 104, 130, 172].

4.3.3.1.1 Spanwise correlation and coherence The obtained spanwise correlation coefficients are presented in Figure 4.10 along with literature values for multiple Reynolds numbers. With the exception of the data from Casalino & Jacob [30], obtained from surface pressure probes, the referenced values come from similar experimental setups composed by two hot-wire probes. The subscripts u and p are used to represent correlation based on the velocity and pressure, respectively.

The obtained correlation values reproduce well the previously reported behaviors. The fact that the obtained curve reproduces the results of Casalino & Jacob [30] for the surface pressure reinforces the affirmation of Ribeiro [213] (based on the results of Sonneville [244] and retaken by Norberg [172]), concerning the similarity in the behavior of the correlation of surface pressure (R_p) and the correlation of the velocity (R_u). Naturally, and following the argument of the latter author, this could also hold for the spanwise lift correlation, an important quantity when studying vibration and acoustics. Another direct conclusion from the comparison concerns the independence of the correlation value of the Y_1Y_2 location where the measurements are performed, as also noticed by Ribeiro. A further discussion on this matter is presented for the rectangular cylinders on Section 4.3.3.2.

Considering Figure 4.10 there is a decrease in the correlation length with the increase of the Reynolds number for the circular section at low flow velocities. That can be quantitatively seen in Figure 4.11, with the evolution of the integral length scale - Equation (4.3.2) - with the Reynolds number. Once more, the obtained values suit the previously reported data with good precision. We must note that the starting point $(\Delta y_3/d, R_u) = (0, 1)$ is not considered, what

Table 4.3: Description of the spanwise correlation data presented on Figure 4.10

#				quantity	Re
1	▲	current work		R_u	10,000
2	◀	current work		R_u	13,333
3	▶	current work		R_u	16,667
4	○	Moeller (1982)	[156]	R_u	12,500
5	■	current work		R_u	20,000
6	♦	El Baroudi (1960)	[49]	R_u	22,520
7	□	Moeller (1982)	[156]	R_u	20,000
8	+	Casalino & Jacob (2003)	[30]	R_p	22,000
9	●	current work		R_u	26,667
10	×	Moeller (1982)	[156]	R_u	26,000

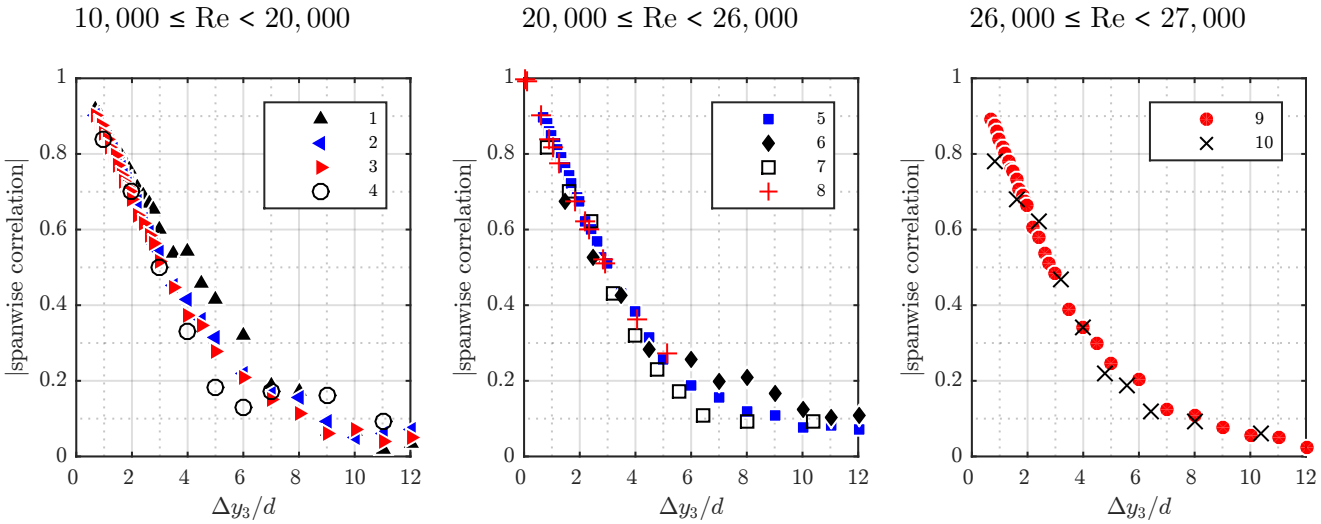

Figure 4.10: Spanwise correlation for the circular cylinder at different Reynolds numbers (description on the data is on Table 4.3).

would result in slightly bigger values of correlation length. The data reported by the earliest study (El Baroudi [49]) exhibit a different behavior as Re increases, which could be due to the use of extrapolated correlation values to estimate the correlation length.

The available coherence data for such type of flow is sparse even for the circular cylinder, the article of Casalino & Jacob [30] being the only one at a similar Reynolds scale (Re = 22,000) that the author is aware of. The data of the spanwise coherence evolution at the peak frequency in Figure 4, page 821 of reference [30], is recovered graphically and a comparison with the current curve is presented on Figure 4.12, as well as the gaussian models and coherence lengths, detailed in the following section. From the values on the reference paper, a linear regression of $log(\Gamma)$ as a function of η^2, null intercept, is applied and a slope coefficient of $\alpha = -0.0321$ is obtained. From Equation 4.3.5, a coherence length of $3.9d$ is then calculated[1]. At other regimes, reported values are $\ell_g = 5.6$ at Reynolds Re = 46,000 [233], and $\ell_g = 4.2$ at Re = 90,000 [177] (note that a factor was applied to their values since they don't consider the factor 2 in their model).

Once more, the similarity between Γ_u and Γ_p contributes to the conclusion that the spanwise distribution of the flow is similar for the velocity and surface pressure fluctuations, thus showing

[1] In the text [30], page 819, $\ell_g = 4.7$ is given: *Data are fitted by a Gaussian* $\exp(-\eta_d^2/2\ell_g^2)$ *function, with* $\ell_g = 4.7$ *for the coherence function, and* $\ell_g = 6.6$ *for the correlation coefficient.*

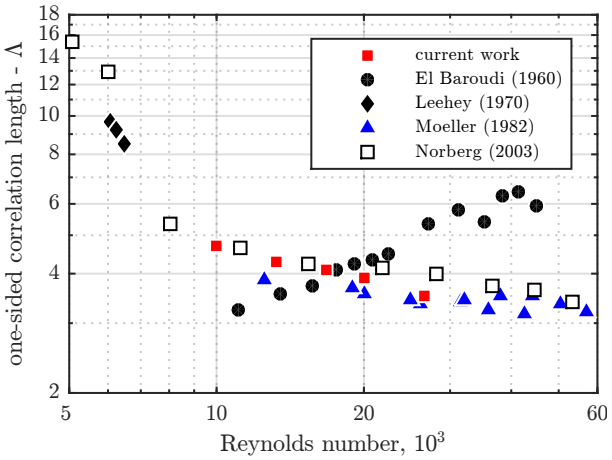

Figure 4.11: Spanwise correlation length for the circular cylinder at different Reynolds numbers [49, 130, 156, 172].

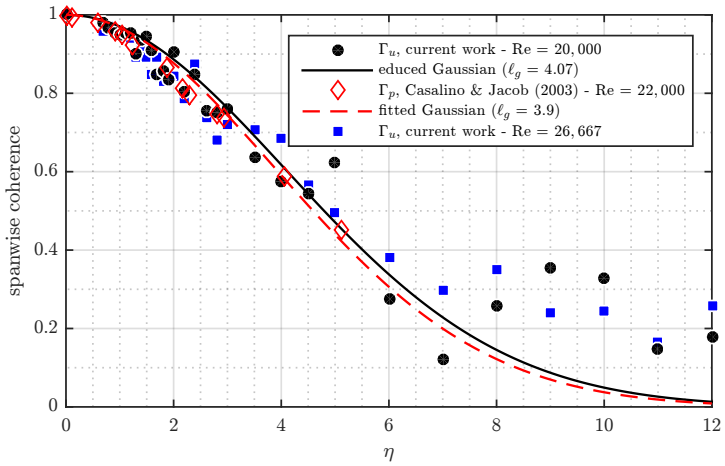

Figure 4.12: Spanwise coherence for the circular cylinder at the peak Strouhal number, comparison with data from Casalino & Jacob [30]. For readability of the figure, the educed Gaussian (leading to $\ell_g = 3.98$) is not plotted for Re = 26,667.

that even in spectral terms, the sole analysis of hot-wire velocity data can be used as an estimator of both pressure and forces spanwise coherence. Since all the data presented in this manuscript correspond to velocity measurements, the subscript u is omitted hereafter and Γ_u is refereed to as Γ.

Is has also been proven that the present experimental setup is capable of producing quality results, even with the absence of end-plates, probably due to the large extent of the cylinder ($86d$), combined with a smaller nozzle extent ($70d$), agreeing with the observations of Humphreys [80] on the independence of the spanwise flow structures from the end conditions. The spanwise consistency of the flow is illustrated by the two following images. Figure 4.13 illustrates the distribution of the deviation of the average total flow velocity, all flow velocities, measuring positions and cross-sections combined. Even for the most disturbed velocity recording (for the square section), mean deviation is below 10% at half of the measuring extension, $y_3 = 15d$.

Figure 4.14 presents a sample of the velocity spectral power density distribution in the spanwise direction, normalized by the inlet velocity. The energy distributions, notably at the principal frequencies, are maintained until about $y_3 = 20d$. Despite maintained global behavior, the observed offsets of the peaks frequency justify the procedure presented in Section 4.3.1 for defining a unique and representative $\mathrm{St}_{\mathrm{peak}}$ number.

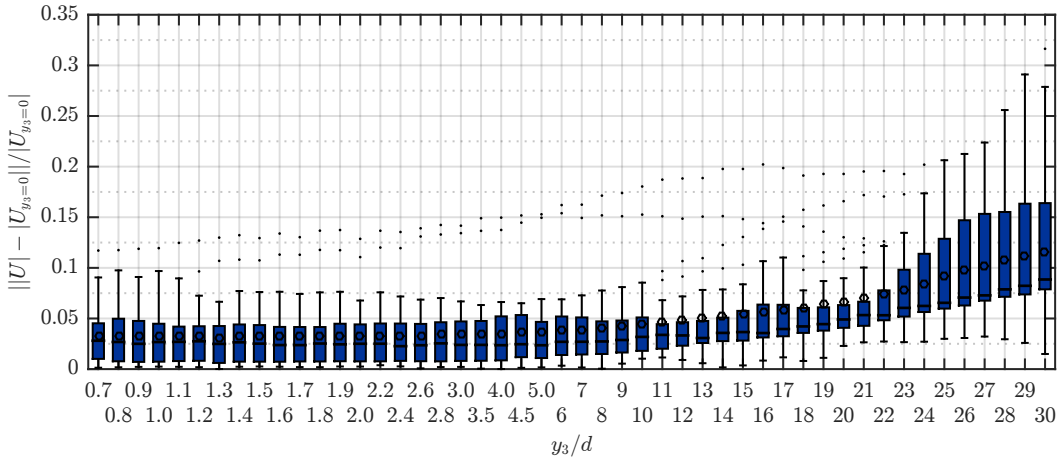

Figure 4.13: Box plot of the deviation of the average flow velocity between the mobile and the fixed hot-wire probes for all the tested cross-sections, positions and flow velocities, where $U_{y_3=0}$ is the mean velocity at the center of the cylinder axis. The box are defined by the first and third quartiles of the velocity deviations at a given position; the interior segment is the median; outer segments are for the limits of the upper and lower quartiles ± 1.5 times the interquartile range, what represents the range of 99.3% of probability in a normal distribution; the circles are the mean value of deviation at each position; and the dots represents the outliers.

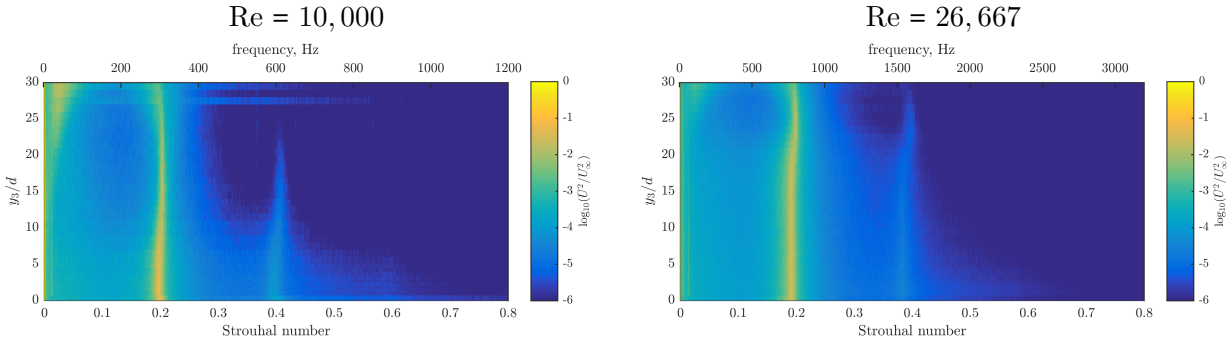

Figure 4.14: Spanwise distribution of the velocity spectral power density for the circular cylinder.

4.3.3.1.2 Spanwise coherence length The algorithm presented in Section 4.3.2.2 is applied to compute the coherence length at all the frequencies. Due to the noisy nature of the data, a Savitzky-Golay smoothing filter (order 1 with a frame size of 9) is used such as to obtain a cleaner graphical representation. The effect of the filter is exemplified on Figure 4.15, and the obtained coherence lengths for the circular cylinder at multiple velocities are presented on Figure 4.16.

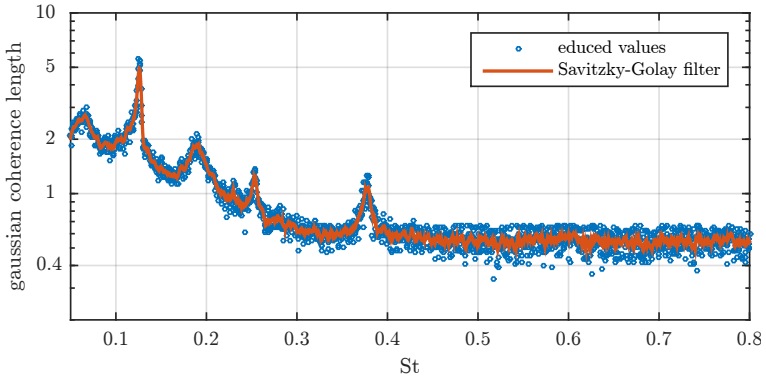

Figure 4.15: Example of the Savitzky-Golay smoothing filter.

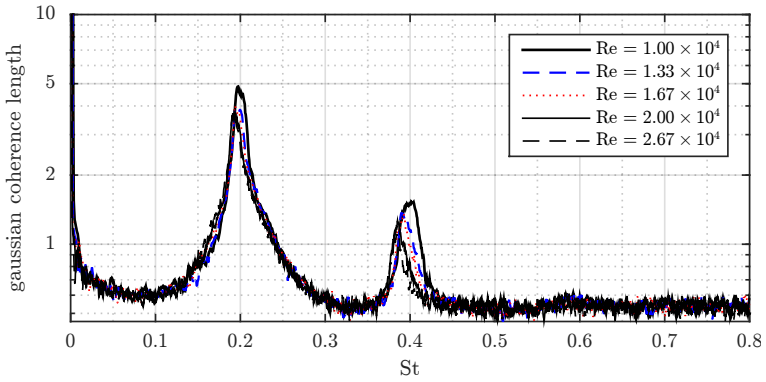

Figure 4.16: Filtered spanwise coherence length for the circular cylinder at different Reynolds numbers.

As expected, higher coherence lengths (associated with an overall higher coherence) are obtained at the frequency of the von Kármán vortex street (around 0.2) and the first 2 harmonics. The Strouhal number corresponding to the main power peak and the coherence length at the main frequency and its harmonics are available on Table E.2 in Appendix E.

In a analogous way to the correlation integral scale, the coherence length grossly decreases with the Reynolds number, what may be associated with the increased transfer of energy to smaller scales and thus, the reduction of the highly coherent structures associated with vortex shedding. Although present, it must be highlighted that at the peak frequency, the obtained difference in the coherence length ℓ_g is virtually nonexistent for Reynolds numbers ranging from 13,333 to 26,667. One can conclude that, for the given regime, contrary to Λ_u which decreases continuously (Figure 4.11), the coherence can be considered as independent of the velocity and that the coherence length equals $\ell_g = 4.0$.

For frequencies that present very low coherence at all spanwise lags, the obtained ℓ_g fluctuates around 0.4 due to the reduction of the procedure to perform a two point linear regression. These values are considered to be nonphysical and, as a consequence of the proposed algorithm, they may be ignored. It is chosen not to impose any treatment on those points at this step of the analysis, since it would be based on a completely arbitrary threshold.

4.3.3.2 Rectangular section cylinders

The same investigation of the spanwise characteristics of the flow is performed for cylinders of rectangular section. In a preliminary study, mean velocity fields are obtained in order to define the positions where to place the probes in the Y_1Y_2 plane for the spanwise analysis. This is followed by a description of the spanwise correlation and coherence for the tested cross-sections.

4.3.3.2.1 Velocity fields Velocity fields are produced with hot-wire measurements for different inflow velocities (U_∞ = 10, 20 and 40 m/s), for the different rectangular sections. Results are presented on Figure 4.17 for the two higher velocities. The contour line $|u|/U_\infty = 1$, calculated using bi-linear interpolation, is also represented.

It is noted that main structures in the flow topology are maintained for all velocities, with a recirculation zone on the upper face of the cylinder. The chosen reference line works as an estimator of the mixing layer position, starting at the upstream edge of the upper face of the section and being expanded downstream due to the evolution of the vortex on the y_2 direction. Despite the similarities, the dimension of the given recirculation is modified simultaneously by the velocity and the aspect ratio AR, the latter parameter being the most important. For the longest rectangle, it appears that the flow is reattached to the upper wall, while for the shorter sections, only the initial dettachment seems to exist.

We must recall that, for the fastest flow, the apparent displacement of the mixing layer in the $+y_2$ direction is probably inflated due to the displacement of the hot wire support in the

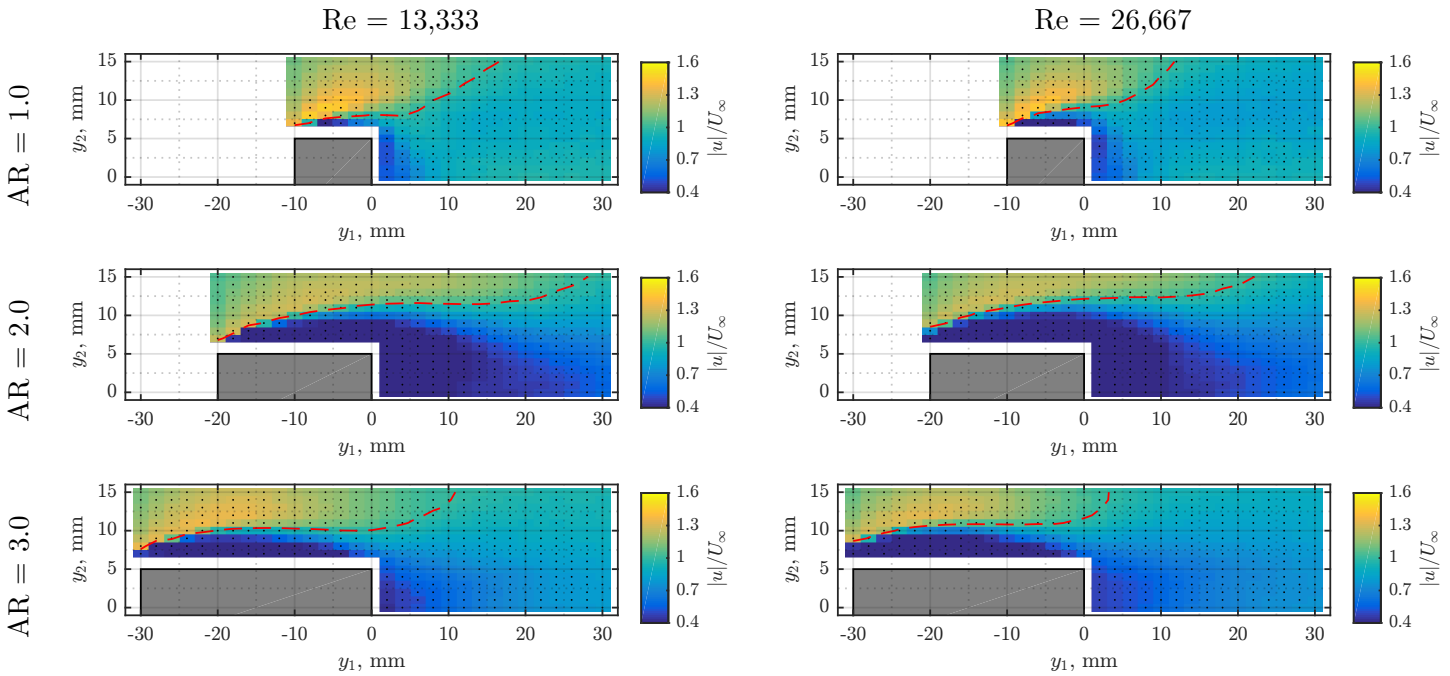

Figure 4.17: Velocity field at the cylinder center for different rectangular sections at different inlet velocities, y_1 axis at the symmetry axis. Dots represent the measuring points and the dashed red line is the iso-contour of the velocity inlet ($|u|/U_\infty = 1$).

opposite direction. No correction is performed since the dislocation value is not known with precision.

Following the remarks performed by Ribeiro [213] concerning the location of the probe in a spanwise analysis, 4 positions are proposed for quantifying the flow behavior in the axial direction:

- P_1: in the wake, fixed location $(y_1, y_2) = (d, 0)$;
- P_2: in the position of maximum mean velocity;
- P_3: in the zone where the reference line is flat, in an analogy of the max y_2 of the mixing layer;
- P_4: in the zone where the curvature of the reference line is maximal, in an analogy of the expansion of the vortex.

Being in the wake, P_1 obviously does not respect the guidelines presented on [213], so it is included mainly to check the consistence of the flow. P_2, being at the position with the highest velocity, is believed to contain a larger quantity of energy. Also, the existence of a minimal speed due to the limitations of the measuring technique, makes a position with larger velocities a safer choice, once the gathered data is farther from this bound, resulting in more representative measurements.

For defining the last two points, the reference line is approximated to a 5 order polynomial. In order to avoid being in the recirculation zone, where it is impossible to perform a proper measurement with a hot-wire, a safety distance (in the Y_1Y_2 plan) of 1 mm normal to the reference line is added. An illustration of the 4 measuring points is presented on Figure 4.18 for a given configuration. It is important to note that, since those values are based on flow topology, they are modified within the section and within the inlet velocity.

All 4 points are considered for the square cylinder; for AR = 2 and AR = 3, only P_2 and P_4 are used. A list of all the positions is given on Appendix E.

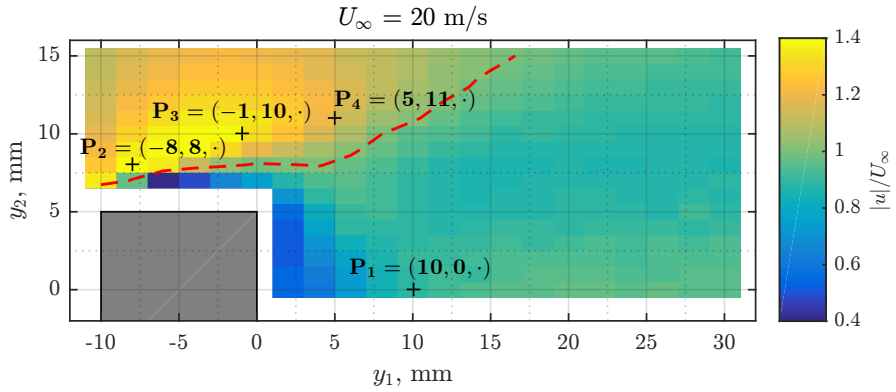

Figure 4.18: Average velocity field and plan coordinates for the spanwise analysis (square cylinder, Re = 13, 333).

4.3.3.2.2 Spanwise correlation and coherence A comparison of the influence of the measurement location is available on Figure 4.19 for the square cylinder. We may note that a consistent result is only observed for P_2, indisputably the most adapted point for the performed analysis, since, by definition, it is the position where the velocity is the highest and thus the measurement is less influenced by the minimum velocity bound imposed by the hot-wire technique and its calibration law. This justifies the observed discrepancy for the other points, notably P_1 that is in a known low speed region for all the tested regimes. With an increase in the inlet velocity, a better result is noted for both P_3 and P_4, contributing to the conclusion that the observed correlation may be highly influenced by the erroneous measurements of low velocities. Due to this fact, the analyses for the other two rectangular sections are not performed for U_∞ = 10 m/s.

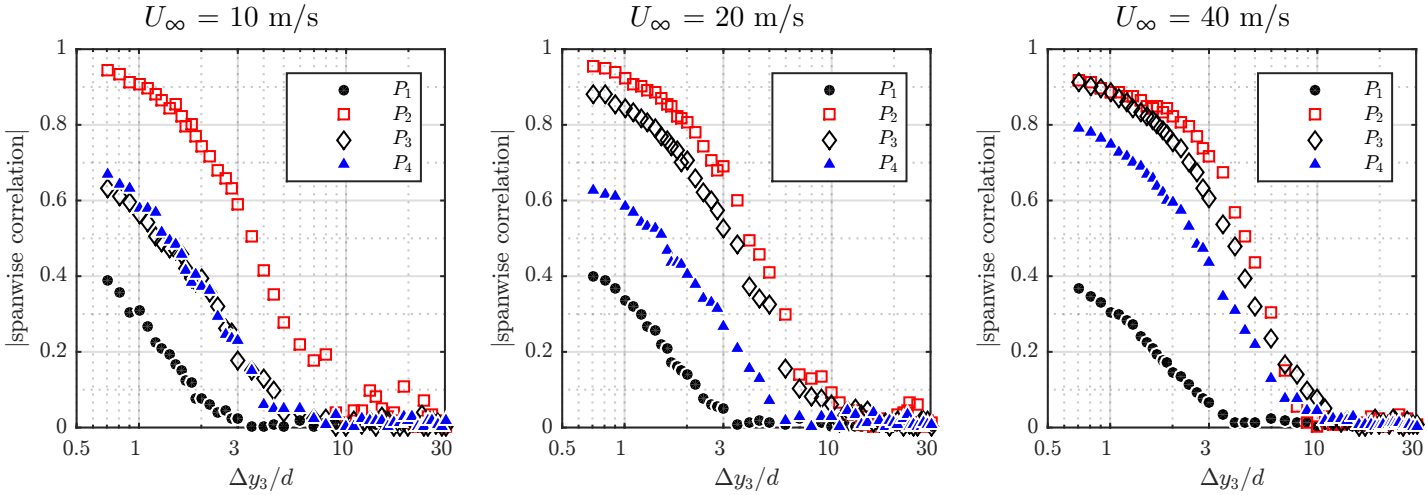

Figure 4.19: Spanwise correlation for the square cylinder at multiple positions and flow velocities.

When comparing the correlation values to the literature, Figure 4.20, considering only P_2, once again the results reproduce well the behavior published previously. It is interesting to note that, differently from the circular section, there is a slight boost in the correlation near central regions (y_3 from about 3 to 10 diameters) with the increase of the velocity, while finally, the results are less influenced by the flow Reynolds number. This behavior may be accounted for by the presence of a sharp edge, that imposes a mean-structure to the flow and makes it less dependent of the Reynolds number [239].

Only P_2 and P_4 are tested for the two additional rectangular sections. The obtained correlation curves are presented on Figures 4.21 and 4.22. Once more, an influence of the probe position and the inlet velocity is noted. However, with exception of P_2 at U_∞ = 20 m/s (Re = 13, 333),

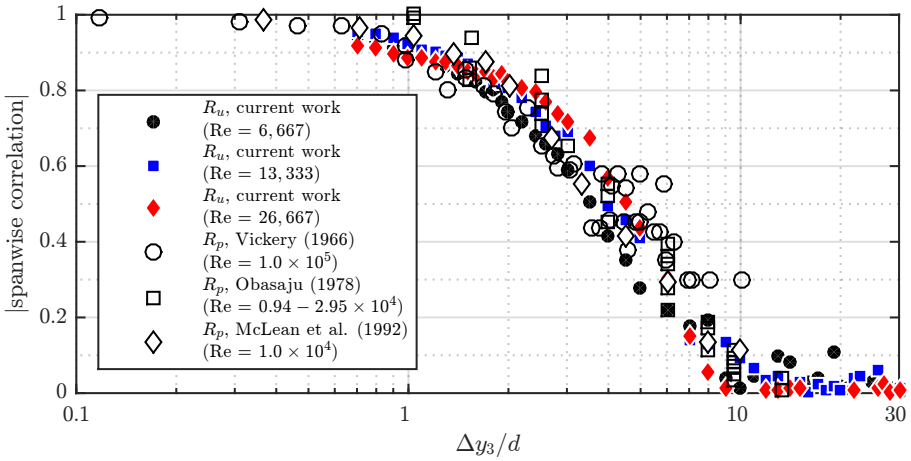

Figure 4.20: Spanwise correlation for the square cylinder at P_2 for multiple velocities, compared to data from the literature [153, 173, 269].

the observed results are only slightly modified by the velocity. Similarly to the square cylinder, the presence of sharp-edges is a key geometrical parameter, that combined with an bigger AR, makes the flow even less influenced by the inertia to viscosity ratio [175].

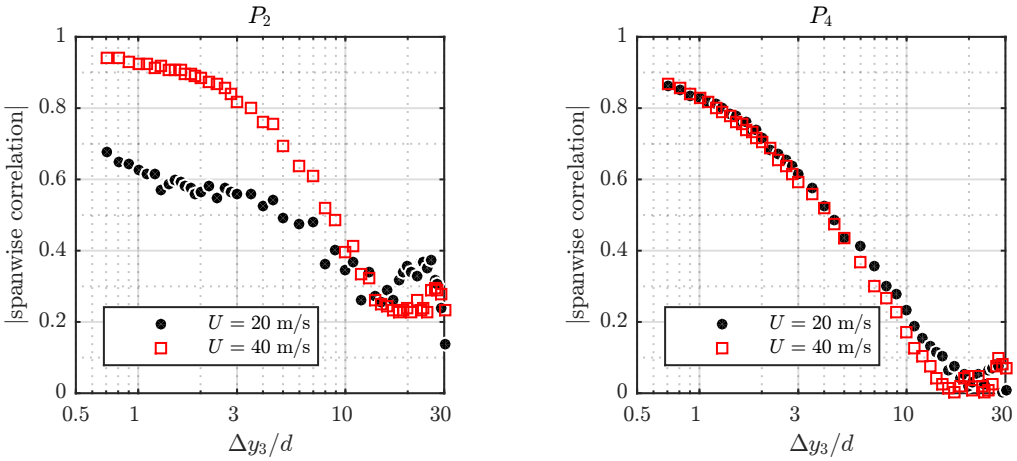

Figure 4.21: Spanwise correlation for the rectangular cylinder (AR = 2) at multiple positions and flow velocities.

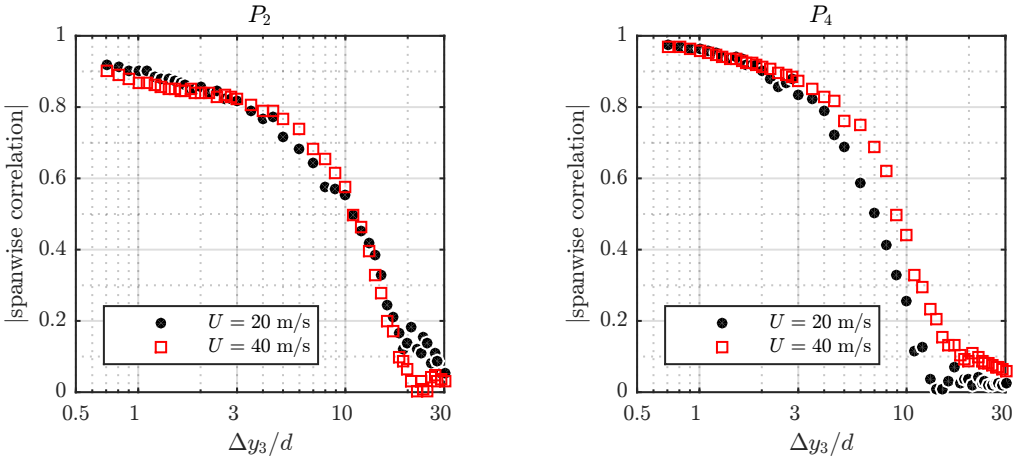

Figure 4.22: Spanwise correlation for the rectangular cylinder (AR = 3) at multiple positions and flow velocities.

The singular behavior observed for the rectangle of AR = 2 may be associated with the flow transitions observed with a modification of the aspect ratio, discussed in many previous works [82, 169, 175, 176, 240]: for small rectangles, the flow detaches at the upstream vertex and does not reattach; with an increase of the sectional width, a new pattern exists where the flow reattaches on the surface and detaches once more at the downstream vertex forming the vortex shedding. A transition region, where the flow is reattached to one of the horizontal edges exists in between these two topologies. Okajima [175] concluded in the analysis of a similar case that a topology such as the one of the latter layout is associated with a widening of the wake, thus, an increase in the Strouhal number.

The aspect ratio effect and the shift of the sectional topology in the Strouhal number are illustrated on Figure 4.23, where the independence of the flow from the Reynolds number is once more reinforced.

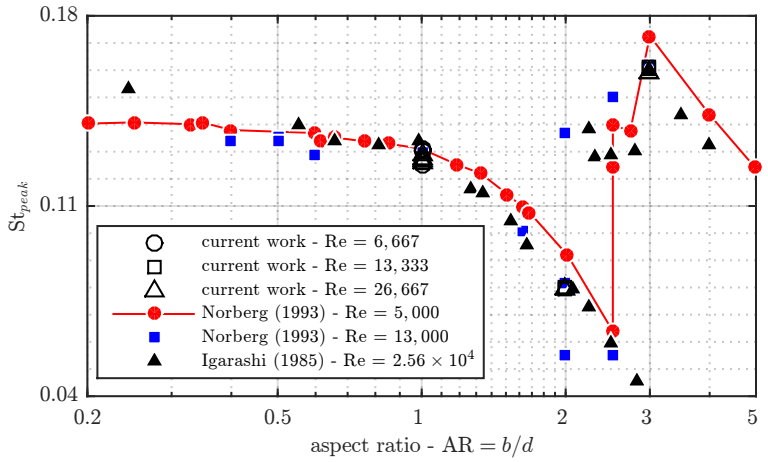

Figure 4.23: Evolution of the Strouhal number as a function of the sectional aspect ratio, with experimental data from [82, 169]. Solid line for visual aid only.

For the current experimental setup, two equally distinguishable peaks at St = 0.08 and St = 0.14 are seen for AR = 2.0, as presented on the spanwise distribution of the velocity spectra on Figure 4.24. Similarly to the behavior noted by Igarashi [82], it was not possible to find a time period when one of the two modes dominates. Hence, we also conclude that both topologies are mixed, in what could be a cycle where flow periodically reattaches to the wall. We clarify that even if two peaks are present, only a single Strouhal value (the most energetic one) is represented for each measurement on Figure 4.23.

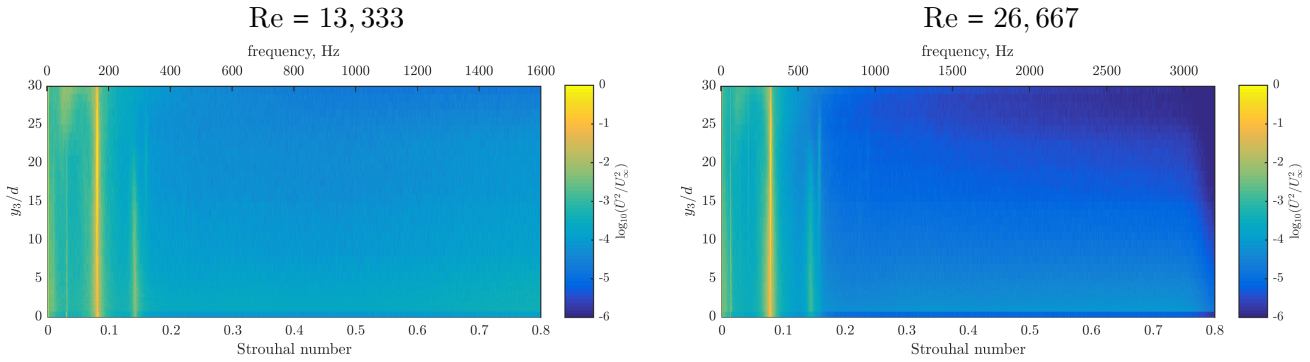

Figure 4.24: Spanwise distribution of the velocity spectral power density for the rectangular cylinder (AR = 2) at P_2.

The previous studies referenced here place the limit between the two topologies at AR > 2.8, and indicated a transition at 2.3 ≤ AR ≤ 2.8. Since the relation of shear layers and boundaries follows a complex mechanism, the Reynolds number [175] and small differences of the inlet

turbulent intensity between the experiments [161, 175] could be one of the reasons that shifted the transition to take place at a shorter section. The same reasoning justifies the variations in the response obtained for the same section at two velocities.

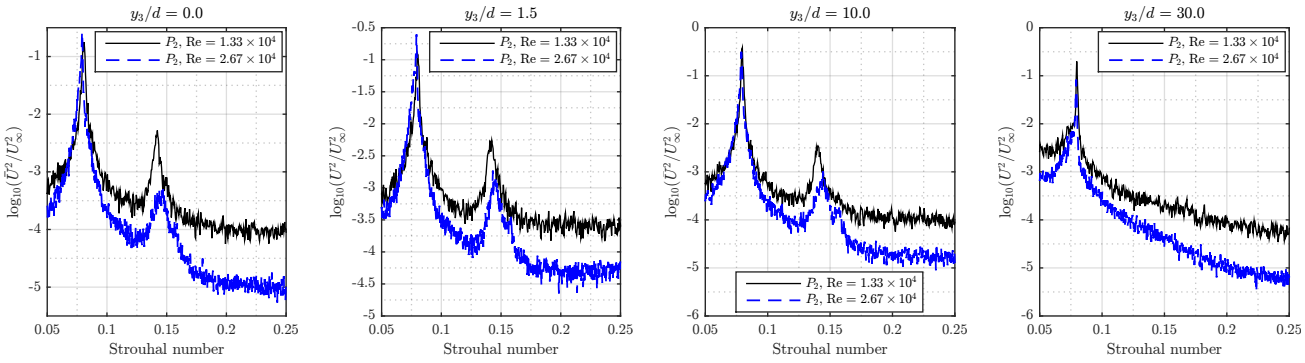

Figure 4.25: Comparison of the velocity spectra for the rectangular cylinder (AR = 2) at P_2 for different spanwise coordinates.

Another observation emerges from the analysis of the velocity spectra presented on Figure 4.24. At the farthest locations, the peak at St = 0.14 (associated with the re-attaching pattern) disappears completely. Being the most energetic mode, St = 0.08 may be the most robust one and less perturbed by the end conditions and possible distortions provoked by the presence of the measuring gear.

For AR = 3, there is a single highly energetic frequency, see Figure 4.26, as described in the literature to be associated to the re-attached flow, as also seen in velocity fields on Figure 4.17. It is important to note that, in spectral terms, the flow spanwise distribution for the tested rectangular cross-sections was even more constant than for the circular section, which allows to conclude that presence of end-plates is even more dispensable in those cases.

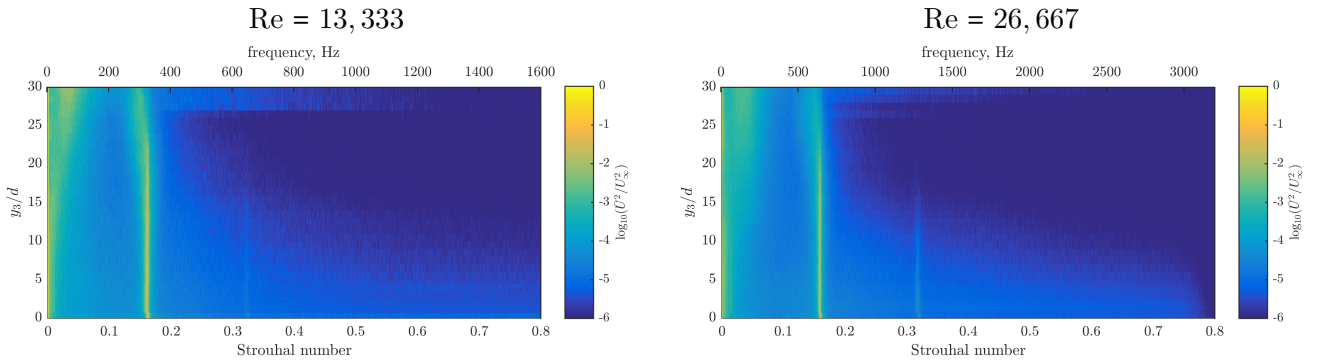

Figure 4.26: Spanwise distribution of the velocity spectral power density for the rectangular cylinder (AR = 3) at P_2.

In terms of coherence, similar, though worth discussing conclusions are performed. Starting with the square section, we see at the $\Gamma(\eta, \Omega)$ representations on Figure 4.27 that in the main regions (at St = 0.127 and the first 2 harmonics) a high coherence level is obtained even for P_1. The increase of overall coherence for P_2, along with the appearance of intermediary modes, is believed to be due to its reduced distance to the wall (3 mm), so that the impossibility to have a precise measurement at low speed and the influence of the hot-wire on the flow dynamics are possibly non negligible. Despite the presented discrepancies, we may conclude that the key aspects in the flow spanwise distributions are equally visible for the 4 tested points, the graphical representations of the coherence obtained at P_3 and P_4 being almost identical. The same behavior is also observed at the other flow velocities that are tested (not shown).

For the rectangular section with an aspect ratio of 2 (Figure 4.28), high coherence levels are associated with the two modes described previously, one at St = 0.08 and the other at St = 0.14.

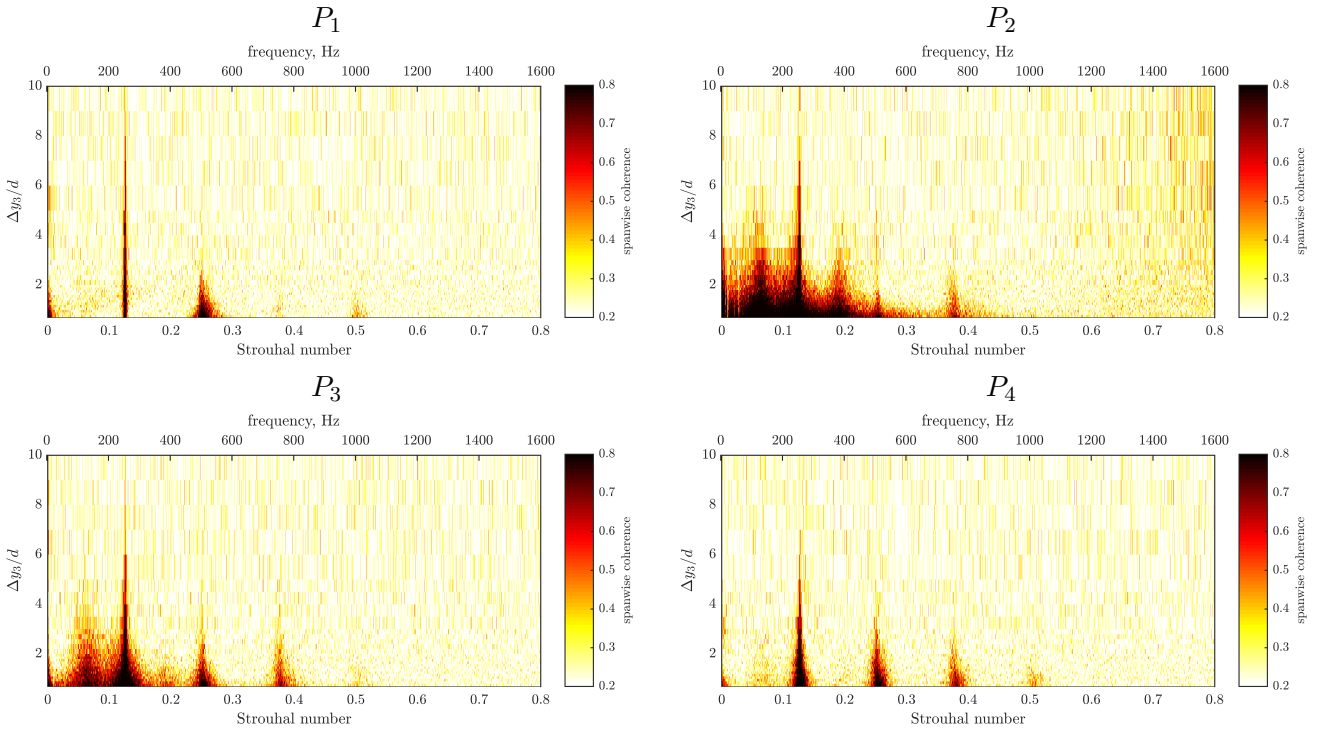

Figure 4.27: Spanwise coherence of the velocity around the square section (AR = 1) at different positions, Re = 13, 333.

For AR = 3, high values of Γ are found around St = 0.16 and also around St = 0.32, the first harmonic. For these geometries, the high coherence at low to zero frequency may be associated with the reduced strength of the unsteady mode encountered with longer sections [240], so the calculated values are more influenced by the uniformity of the mean velocity.

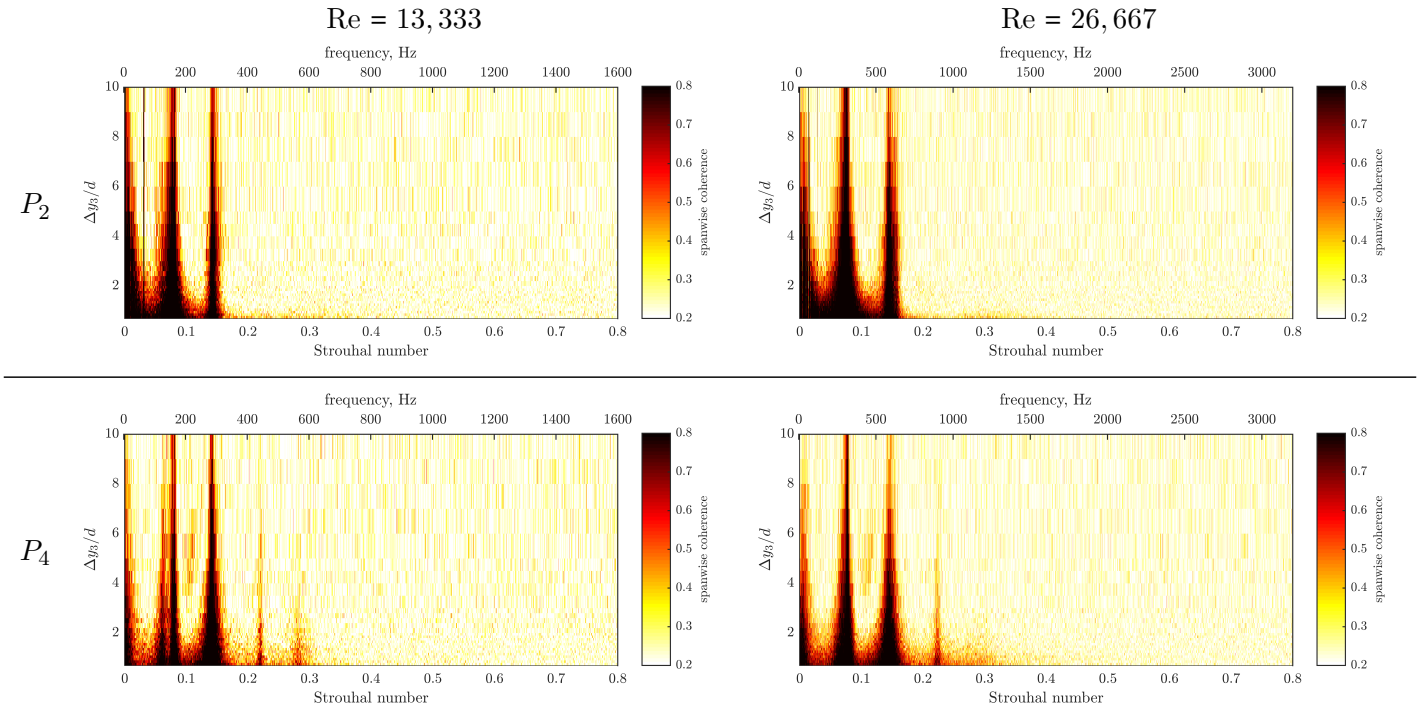

Figure 4.28: Spanwise coherence of the velocity around the rectangular section AR = 2 at different positions and Reynolds numbers.

In global terms, what is seen is that, as for the correlation, the coherence distribution is

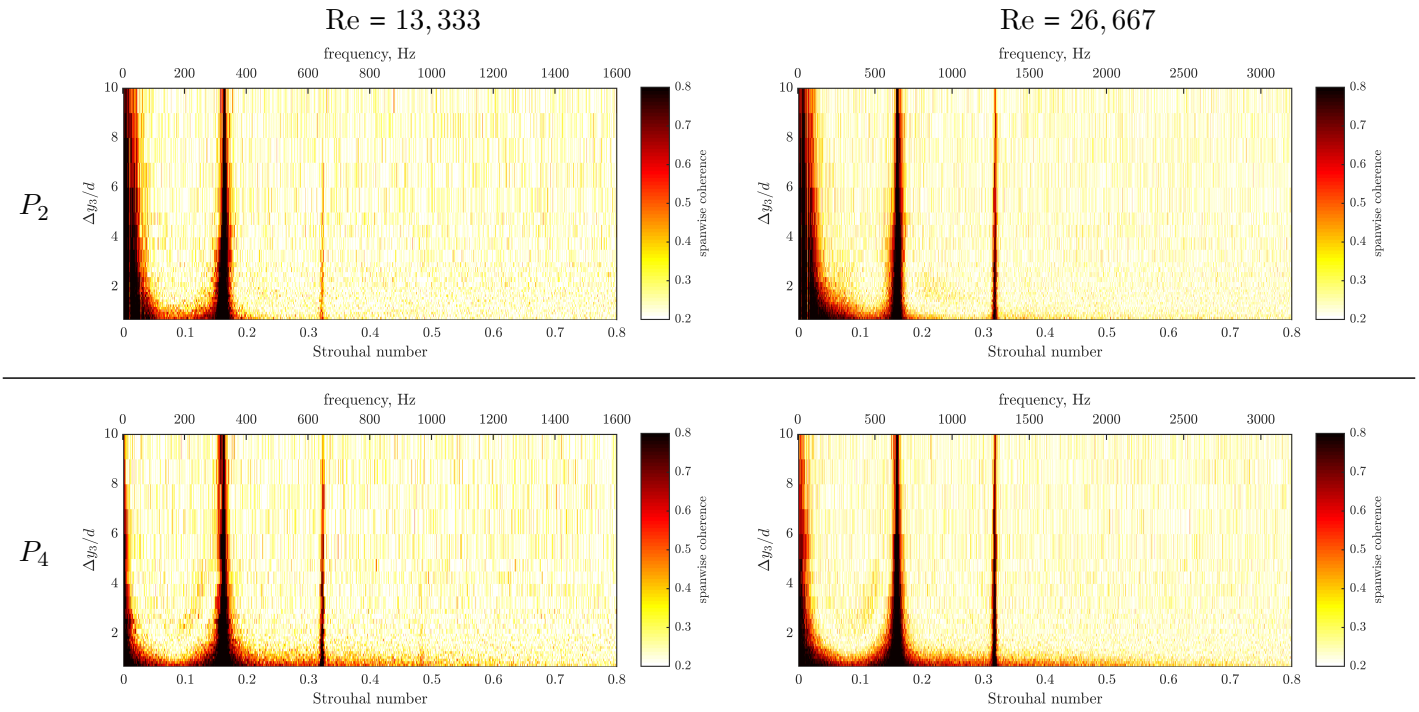

Figure 4.29: Spanwise coherence of the velocity around the rectangular section AR = 3 at different positions and Reynolds numbers.

also maintained for the different measuring positions and velocities. Despite the similarity, key aspects regarding the flow, such as the double mode for AR = 2, are not noticed when only the correlation is calculated. Also, considering the study with the square section, the coherence is more robust in terms of the influence of the sectional position and even surpasses the limitations of the hot-wire anemometry technique employed in this work. The natural conclusion regarding both affirmations is that the coherence is simultaneously a more robust and more reliable quantity than the correlation when analyzing the spanwise distribution of such kind of flow.

4.3.3.2.3 Spanwise coherence length The coherence length is calculated for the rectangular sections using the algorithm presented in Section 4.3.2.2.

As a first step, the influence of the measuring position is assessed from the results obtained for the square section, presented on Figure 4.30. Note that the curves are smoothed, like those presented for the circular section (see Section 4.3.3.1.2).

The results are similar to what is observed in the brute coherence values distribution. At the peak frequencies, there is a strong similarity for the values obtained at all the points. P_2 has a richer frequency distribution, considered here as a probable collateral effect of the presence of the hot-wire in the flow. Interestingly, for P_1, even though it is placed in the wake and has a poor response in terms of spanwise correlation, the coherence length values are also aligned with the other points. The fact that the results at different positions tend to better converge at the highest flow velocity contributes to the argument that the observed deviations may be more an influence of the hot-wire technique than of the position in the flow itself.

Figure 4.31 proposes a closer look at the coherence length calculated at the vortex shedding frequency and its harmonics. The values are presented in Appendix E. For the square section, considering all measurements positions, the average coherence length at the vortex shedding frequency are of $\ell_g = 2.64$ (Re = 6, 667), $\ell_g = 4.73$ (Re = 13, 333) and $\ell_g = 5.40$ (Re = 26, 667). The apparent increase in the values may be unreal and due to the difficulty of measuring low flow speeds. It may also be noted that apart from the measurements at $U_\infty = 10$ m/s and not in sensitive regions, that is, considering only P_3 and P_4, the result is barely influenced by the

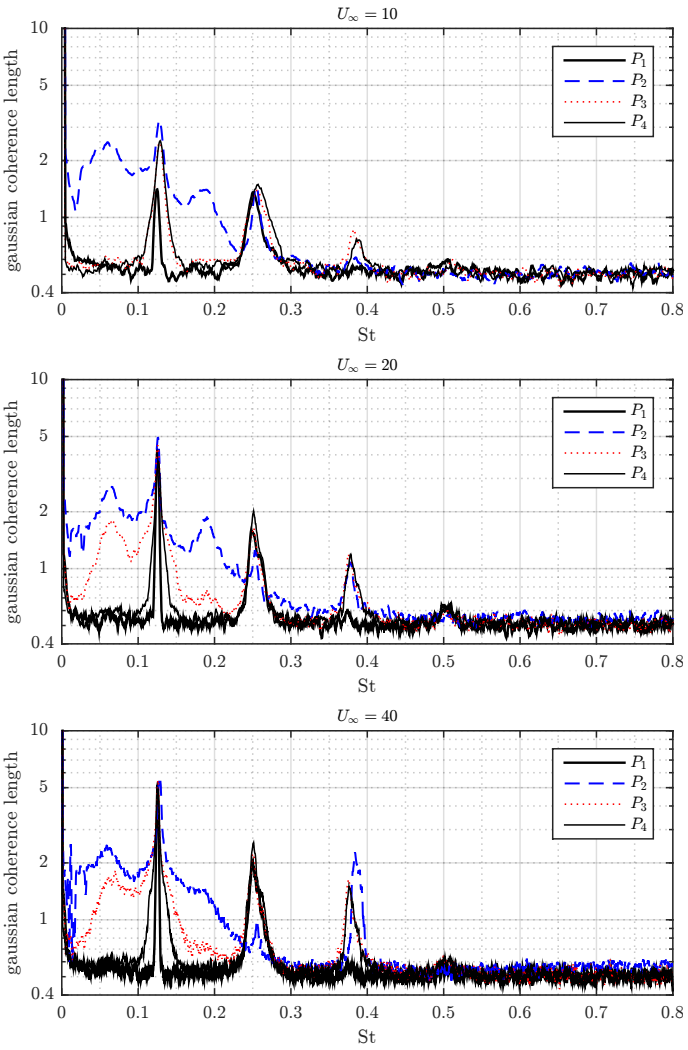

Figure 4.30: Filtered spanwise coherence length for square cylinder (AR = 1) at different probe positions and flow velocities.

Reynolds number. Consequently, the value of ℓ_g = 5.0 is considered a good approximation for the coherence length of the square section in the examined Reynolds number range.

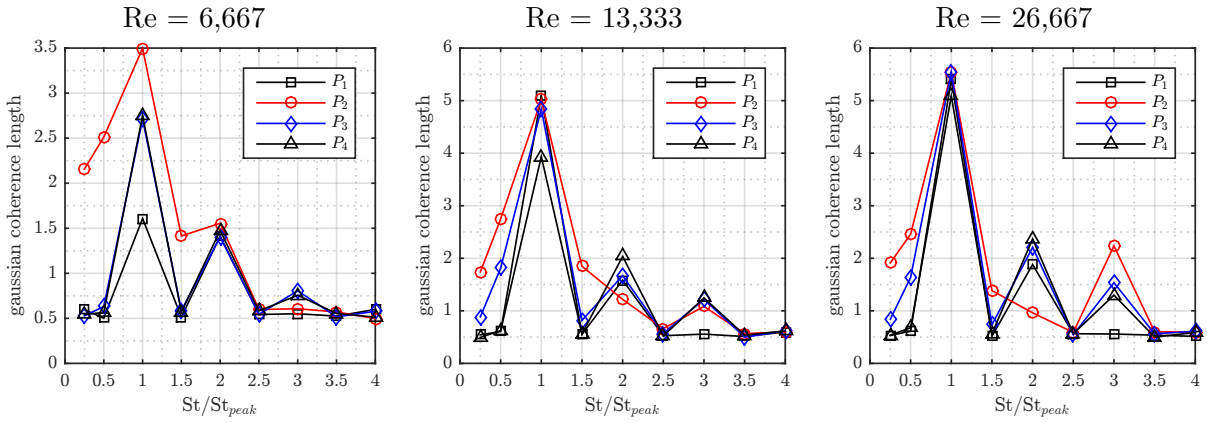

Figure 4.31: Close up view of spanwise coherence lengths at St$_{peak}$ and its harmonics for the square section at multiple Reynolds numbers.

Next, the coherence length values for the other rectangular cross-sections are presented on Figure 4.32. Overseeing the already discussed results for the square section at P_2, strong simi-

larity is noted for the three rectangular sections. At the von Kármán frequency, the coherence length varies from about 5 to 20 times d, and half of that is observed for the first harmonic; it is also interesting to see that some small structures of higher St (at the harmonics) are only seen with the probe at P_4, that is, with the hot-wire most distant from the solid boundaries. No explanation could be found for the sharp peaks at very low St (St ≤ 0.03) present for AR = 2.0.

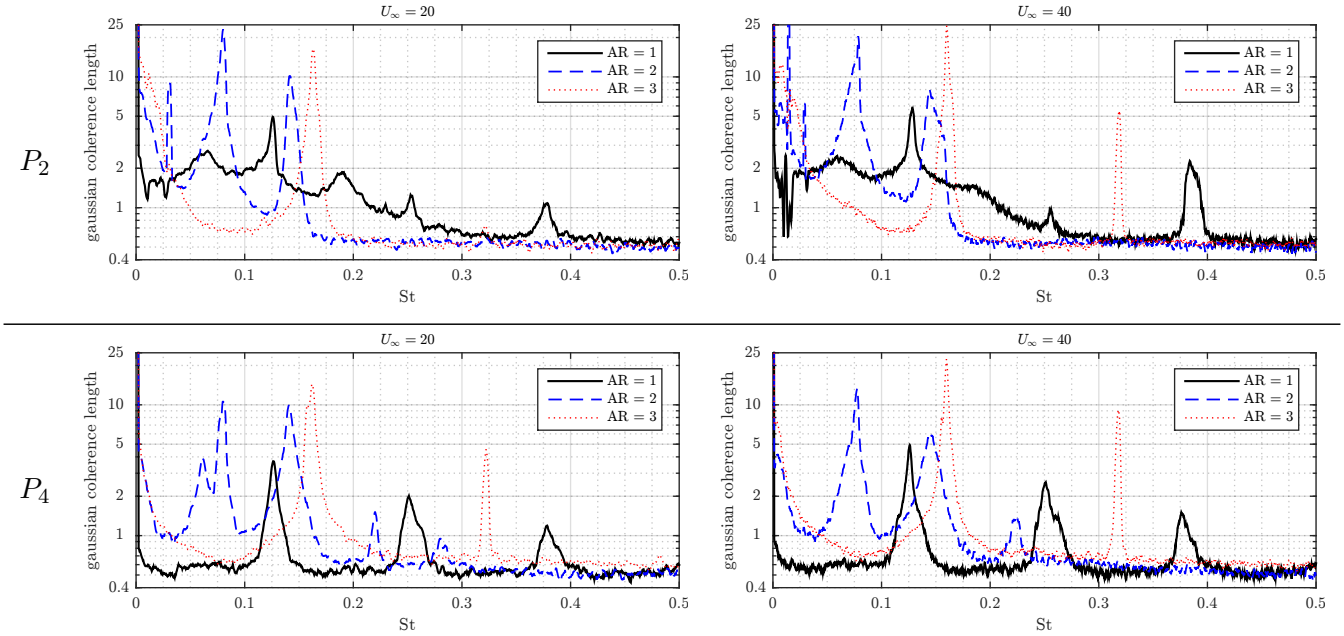

Figure 4.32: Filtered spanwise coherence length for rectangular cylinders at different positions and flow velocities.

For the intermediary rectangle (AR = 2.0), very large coherence lengths (10-20) are present at both detachment modes described in previous section, at St = 0.08 and St = 0.14. For P_4, values of ℓ_g close to one are also seen for some of the harmonics of both frequencies. The completely detached mode not only dominates in energy (Figure 4.25), but also in dimension, being associated with the longest structure for all measuring points and velocities. Globally, the coherence lengths are all above 10. Motivated by the high value of ℓ_g, a closer look at the $\Gamma(\eta)$ points for the peak frequency is presented on Figure 4.33.

As we can see, the Gaussian model, and consequently the estimated coherence length, represents extremely well the coherence decay for the cylinder with rectangular sections of AR = 1 and AR = 3. A singular behavior is observed for AR = 2, where coherence levels fluctuate around 0.7 for $y_3 > 10d$ and the fit is not as good as for the others.

In subsequent tests, it is observed that the proposed algorithm is capable of fitting a curve that captures well the points at smaller y_3 when the coherence parameter is set to $\Gamma_{\text{lim}} = 0.6$, as can be seen on Figure 4.34. Nevertheless, it is clear that either the Gaussian model does not represent the spanwise evolution of the coherence for that given section or the data is too noisy (probably due to the disturbance to the flow stability introduced by the presence of the hot-wires) to provide a quality model. So, based on the behavior noted for other geometries and the fact that the loss of coherence at larges distances is expected even in the case of a fully 2D flow due to the end of the cylinder, we can only imply that the detached mode in the flow around the rectangle of AR = 2 is actually two-dimensional, noting that, for the other mode (St = 0.14), the obtained coherence is smaller. Further experiments with a finer control of the end conditions and eventually end-plates should be performed to confirm this.

The average coherence lengths considering all measuring points at the peak frequency are $\ell_g = 19.14$ and $\ell_g = 19.16$, for $U_\infty = 20$ m/s and $U_\infty = 40$ m/s, respectively.

A closer, but not the same, conclusion is drawn about the two-dimensionality for the rectangle of AR = 3, where for a half cylinder of 35 cm, the obtained one-side coherence at the peak frequency is on average 17.07 at Re = 13,333 and 24.58 at Re = 26,667 (Figure 4.32). This means

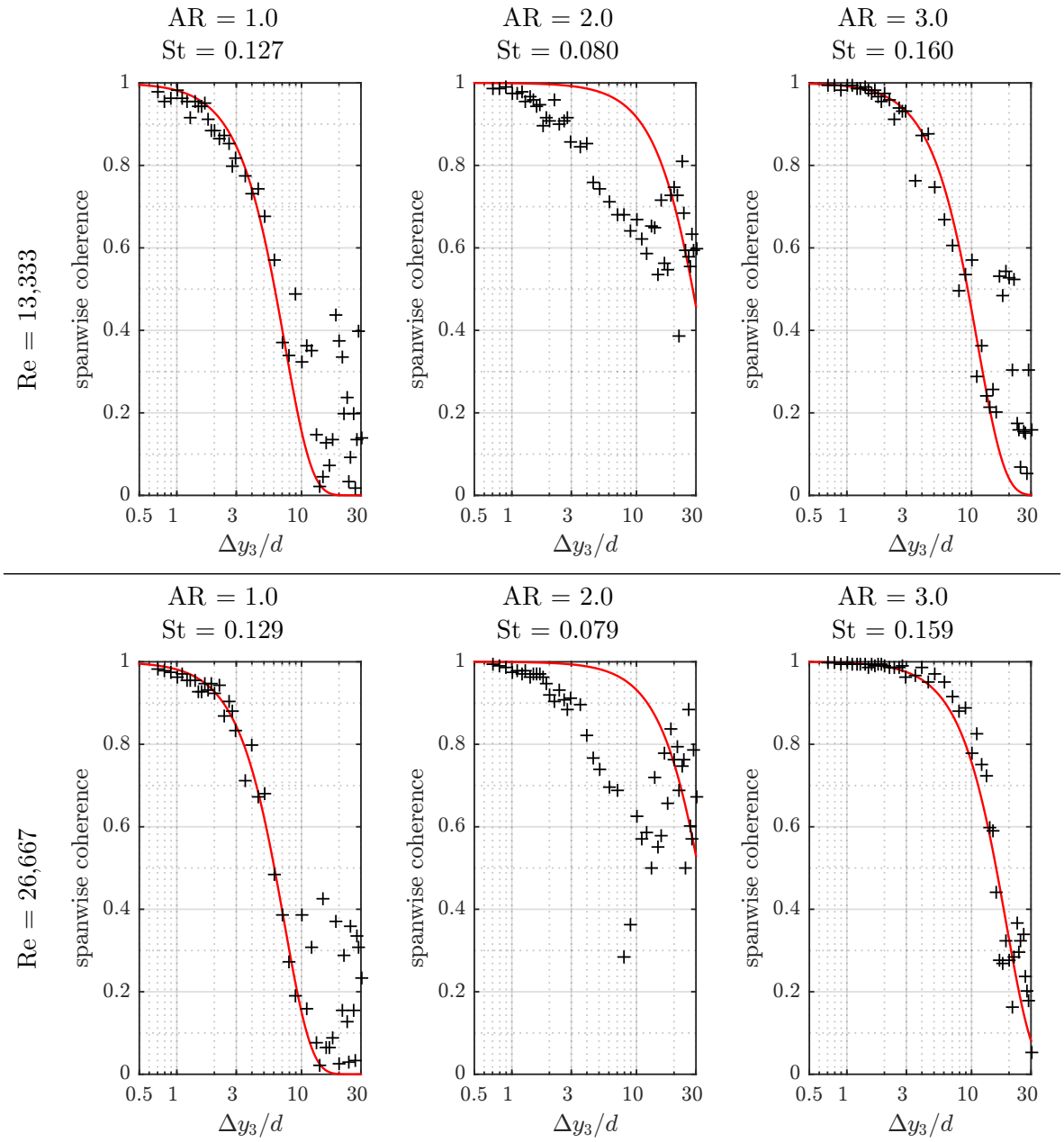

Figure 4.33: Spanwise coherence evolution at the peak frequency for multiple geometries and Reynolds numbers at P_2. The crosses (+) represent the calculated coherence and the continuous line is the educed Gaussian model.

that, along the full spanwise extent of the cylinder, there are only 2 or 3 portions oscillating out of phase.

4.3.4 Influence of cross-section on spanwise behavior

There is a clear distinction between the behavior noted for circular and sharp-edged sections. While in the first case, the flow deforms in the spanwise direction due to the excess of energy, the geometries formed by cuspid vertex lay in a more fixed flow topology imposed by the detachment zone [239]. The only available modification concerns the size and position of those recirculations, as observed for the rectangular section of AR = 2.

Despite the difference, as it is shown on Figure 4.35 that the values obtained at the vortex shedding frequency for the square and circular section are quite similar. For the two other rectangular prisms, a way larger ℓ_g is obtained. As a preliminary analysis, one may conclude

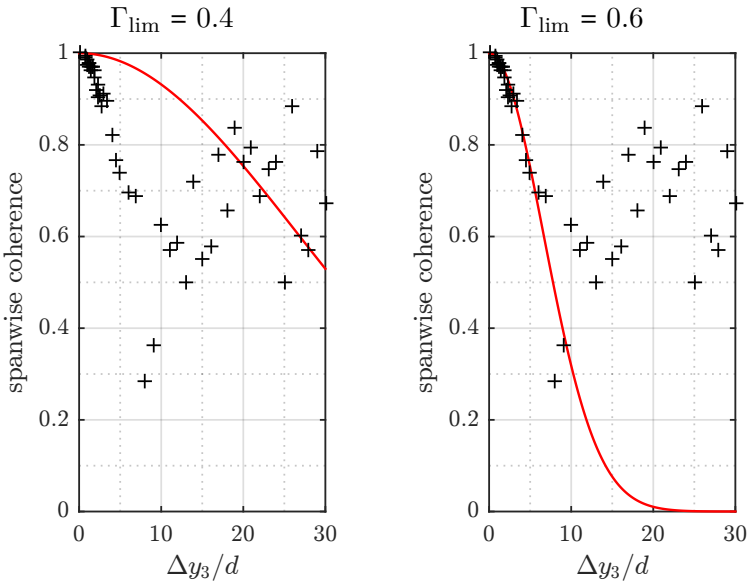

Figure 4.34: Spanwise coherence gaussian models at the peak frequency (St = 0.079) for AR = 2.0 at P_2, Re = 26,667, with different Γ_{lim}. The crosses (+) represent the calculated coherence and the continuous line is the educed Gaussian model, returning ℓ_g = 26.61 (left) and ℓ_g = 6.61 (right).

that, at this regime, changing the aspect ratio of the cross-section has more impact on the flow than changing the geometrical paradigm itself.

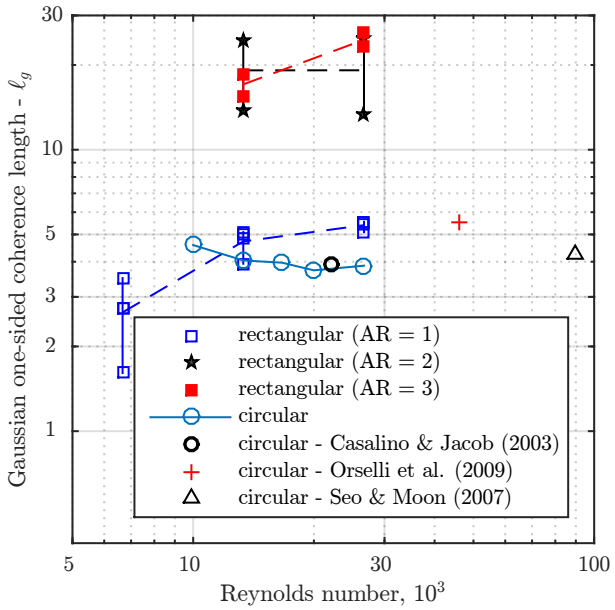

Figure 4.35: Evolution of spanwise coherence gaussian length at the peak frequency for all tested configurations, with data from the literature [30, 177, 233]. Hashed lines connect the average values obtained in the different locations used at each configuration.

On one hand, the strength of the vortices is smaller when the width of the section is increased [240]. On the other hand, the spanwise correlation and coherence lengths are increased. The available data cannot aliment a complete discussion about the relationship between the two phenomena, so only an initial discussion is proposed. In a simple extrapolation exercise, if we imagine a very long rectangular section with the same height d, it is simple to agree that the sectional height is clearly not the ideal dimension to quantify the inertia to viscosity ratio for the given flow. However, for both short and long cross-sections, there are Reynolds numbers

associated with flow transitions, notably the transition from steady to unsteady flow (onset of vortex shedding) and transition to three-dimensionality. The author believes that once we think in terms of the distance of the current Reynolds number to the marks of flow transition (as discussed in Section 2.2.3 for the laminar flow), the comparison of different geometries becomes fairer, since the flow velocity is selected based on giving the flow around different geometries a similar energy quantity in terms of what overpasses the necessary amount to set the flow topology in place.

When we look at the quality of the data, we may also note that the results obtained with the rectangular prisms are seemingly more influenced by the position of the probe than those obtained with the circular cylinder (even if only one Y_1Y_2 location is used for the circular section, the values are well correlated with previously reported data). The fact that, for the rectangular sections, the peaks of velocity spectra and coherence length are not as broad as the ones for the circular cylinder could imply that turbulence development is delayed for the tested sharp-edged sections. Thus, the author suspects that the presence of the hot wire is more disturbing to the flow equilibrium for the latter geometries.

4.3.5 Recapitulation of results and conclusions

An experimental campaign was performed to evaluate the spanwise correlation and coherence of flow around cylinders with different cross-sections. Using of hot-wire anemometry, velocity fields, correlation and coherence evolution were measured for circular and rectangular prisms. An algorithm for the calculation of the coherence length in the case of heterogeneous and noisy data is proposed. Tests concerning the effect of the velocity (Reynolds number varies from 6×10^3 to 26×10^3) and the sectional position of the probe in the results were performed.

As indicated in the literature [213] and once more confirmed herein, for the circular cylinder, the obtained result of correlation and coherence is considered independent of the measuring location, as long as the chosen position is not in the wake or in a free-stream region. This hypothesis is tested for the square cylinder for multiple flow velocities, and the results are very similar, specially when we disconsider measurements that where probably affected by the measurement technique limitations. Also, even though a more consequent study about the relationship of surface pressure and velocity spanwise coherence remains necessary, it is observed that even for the coherence, the use of velocity data is capable of reproducing the values derived from wall pressure measurements [30] (in the case of a circular cylinder).

Present correlation and coherence values reproduce well those of the literature, even without the presence of end-plates. For the circular section the average coherence length at the vortex shedding frequency is of about 4.0 diameters; for the square section, ℓ_g fluctuates around 5.0. For the widest rectangular sections, higher values are obtained: ℓ_g = 19.1 and 19.2 for AR = 2.0 and ℓ_g = 17.1 and 24.6 for AR = 3, at Re = 13, 333 and 26,667, respectively. Considering that the maximum measured spanwise distance was of $30d$ and that no end-plate was used, for AR = 2 at the first speed, the vortex shedding may be considered virtually 2D.

The Reynolds number small dependence of the flow around sharp-edged sections is noted, especially at the vortex shedding frequency, however an important point regarding the influence of Re must be highlighted. The Reynolds number is intrinsically associated with the dynamics of flow detachment, and as we were able to see in this section, even if one detachment point is imposed, the sectional topology may be able to adapt itself as is seen for the rectangular cylinder of AR = 2. In this way, any extrapolation of these results to other regimes may not reproduce the flow physics.

The use of the proposed algorithm allowed the production of continuous $\ell_g(\mathrm{St})$ curves, that could be of interest in many fields. The data was noisy for all the tested configurations, which justifies the implementation of such routine. Even if it seems evident, it must be stated that for performing a consistent coherence estimation one must have data up to a spanwise distance at least as long as the expected coherence length, once an under quantification of the spanwise extent of the flow would easily provoke two opposite effects: to mask highly correlated sections and frequencies and to overestimate some values due to not capturing the full coherence decay.

When correlation and coherence are compared, it is clear that the coherence is a more robust estimator, keeping a constant tendency even when there are limitations in the measurements. The correlation was found to not only be more influenced by the measuring location, but also to probably underestimate the size of the structures. A comparison regarding the obtained correlation and coherence lengths at the peak frequency is presented on Figure 4.36. The correlation will on average, return half of the value that is obtained from the coherence Gaussian model. More conclusions should be performed with further experiments and simulations to verify which estimator (coherence or correlation) is closer to represent the spanwise flow distribution with a direct look of the flow structures.

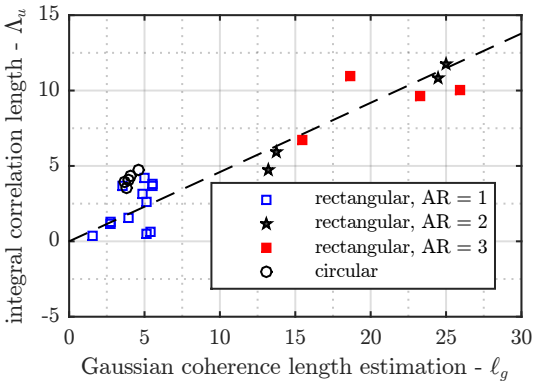

Figure 4.36: Comparison of the correlation length and the Gaussian coherence length estimation.

Measured differences in the spanwise flow development are in accordance with the discussion concerning the distance to flow transition observed in Section 2.2.3.4. The widest cross-sections, associated with higher critical Reynolds number, are found to be less developed in terms of the flow transition (more sinusoidal signals, larger coherence lengths). That is, flow around sections that transition sooner from steady to unsteady flow in the Reynolds number scale present flow streamwise (as seen in Section 4.2) and spanwise characteristics that are analogous to what is observed for the circular cylinder at a lower Reynolds number.

The aspect ratio was found to be a geometrical feature that has an enormous effect on the modification of the spanwise coherence of the flow, a similar importance is found in 2D (Section 2.2.2.1). To confirm the universality of that trend, such as proposed for the laminar flow, tests with different sections and of different aspect ratios, such as ellipsoids or triangles, should be performed. As presented in Table 4.2, triangular cylinders are also part of this study, however, due to bending of the cylinder (further discussed in Section 4.4.4.1, the coherence length is not measured.

From an aeroacoustic point of view, it is now necessary to evaluate the acoustic signature of those geometries. The recorded acoustic signals are presented next in Section 4.4 (for current shapes, Section 4.4.3).

4.4 Measurements of acoustic emission of cylinders with different cross-sections

This section reports the measurements of the acoustic emission of a set of 34 cylinders (described in Table 4.2), combining the different cross-sections, sizes, orientations and materials. Issues regarding the structural response of the beams are discussed. The effect of the shape change in the sound signature is evaluated in the spectrum, directivity diagrams and sound pressure level evolution. In Appendix E, the peak Strouhal number and the peak (PSPL), band (BSPL) and overall (OASPL) sound pressure levels, described in this Section, are listed for all the tested cylinders, central microphone (middle of the cylinder's axis, 1 m normal to the flow).

First, the different noise criteria (overall, band and peak) used in the work are described and illustrated in Section 4.4.1. Second, the experiments performed with carbon fiber cylinders

are described on Section 4.4.2, with a short explanation of the effect of resonance and edge rounding on the sound emission. Third, in Section 4.4.3, the sound emission of the cylinders that have been described in detail in previous sections (the circular, square and rectangular - AR = 2 and 3 - cylinders of d = 10 mm) are presented, differences and similarities are highlighted. Forth, results for the triangular cylinders are presented in Section 4.4.4, including a disclaimer concerning the structural response of the beams. Finally, in Section 4.4.5, a global comment about the similarities and disparities associated with the different cross-sections are presented.

Naturally, more focus is given to the cases that have also been examined by the hot-wire anemometry.

4.4.1 Test of different noise criteria

Different noise criteria present in the literature are tested before performing the comparison between the different geometries. The following criteria, illustrated on Figure 4.37, are considered: the peak sound pressure level; the integral of the sound power spectral desnity (PSD) around the peak using a frequency based range ($f_{\text{peak}} \pm 20$ Hz) and a Strouhal based range ($f_{\text{peak}} \pm 10\%$ of St_{peak}); integral of the PSD considering the frequency range whose lower and upper limits correspond to SPL levels that are some decibels down from the peak SPL value, above the threshold and for the complete range, as performed by Hutcheson & Brooks [81] with -10 dB and Haramoto et al. [73] with -3 dB; and the complete spectrum, raw signal and subtracted by the background noise (recording without the cylinder). The tests consider data from the measurements with the carbon fiber cylinders presented in Section 4.4.2.

Three examples of what is obtained with the 7 methodologies are presented on Figure 4.38 with the evolution of the SPL for three square sections of different size. It is obvious, especially when the trends are evaluated, that there are only 3 groups of responses: the peak (lower levels), the integral of a band around the peak (independent if the range is derived from the frequency or the level) and the integral of the complete spectrum (only an offset with the subtraction of the background noise).

From these observations, the following criteria are chosen for the description of the sound production of the cylinders and used in the rest of this manuscript: the sound pressure level at the tone frequency (PSPL); the overall sound pressure level (OASPL), calculated by the integral of the power density over all frequencies; and the band sound pressure level (BSPL) calculated by the integral of the sound pressure density in the range delimited by the peak minus 10 decibels.

In addition to the presented criteria for the full spectrum (integral for the complete spectra from 0 to 6400 Hz), two other procedures were tested for the calculation of the overall sound pressure level: integral for $f > 80$ Hz; and $f \in [100, 1000]$ Hz, same procedure used by King & Pfizenmaier [111]. As the results from these two procedures are barely modified, notably no remarkable effect on the velocity exponents is obtained, the components at low frequency and high frequencies are, as expected, negligible. Thus, to avoid setting arbitrary thresholds, the levels obtained from the complete spectra ($f \in [0, 6400]$ Hz) are used in the present study.

4.4.2 Preliminary study: carbon rectangular sections at incidence

An initial experimental campaign was performed inspired by the observations at low Reynolds, 2D in Chapter 2. Aiming at observing the effect of the aspect ratio, available square and rectangles models in carbon fiber were used. Three different blockages (d = 6, 8 and 10 mm) were obtained by changing the incidence of the cylinders.

Tested cross-sections and incidences are presented on Table 4.4; two aluminum cylinders are also tested. The measurement of the angles is initially performed using an angle meter of precision 0.1° aligned to one of the faces of the cross-section. On further analysis, where the angle is fixed at 0°, a cell phone with an angle meter app is used. Note that the indicated range represents the difference in inclination between the two extremities of the cylinder.

The obtained noise emission hierarchy is different from the expected 2D results (not shown). Naturally, there is the three dimensional effect, absent in the simulations. Nevertheless, there are

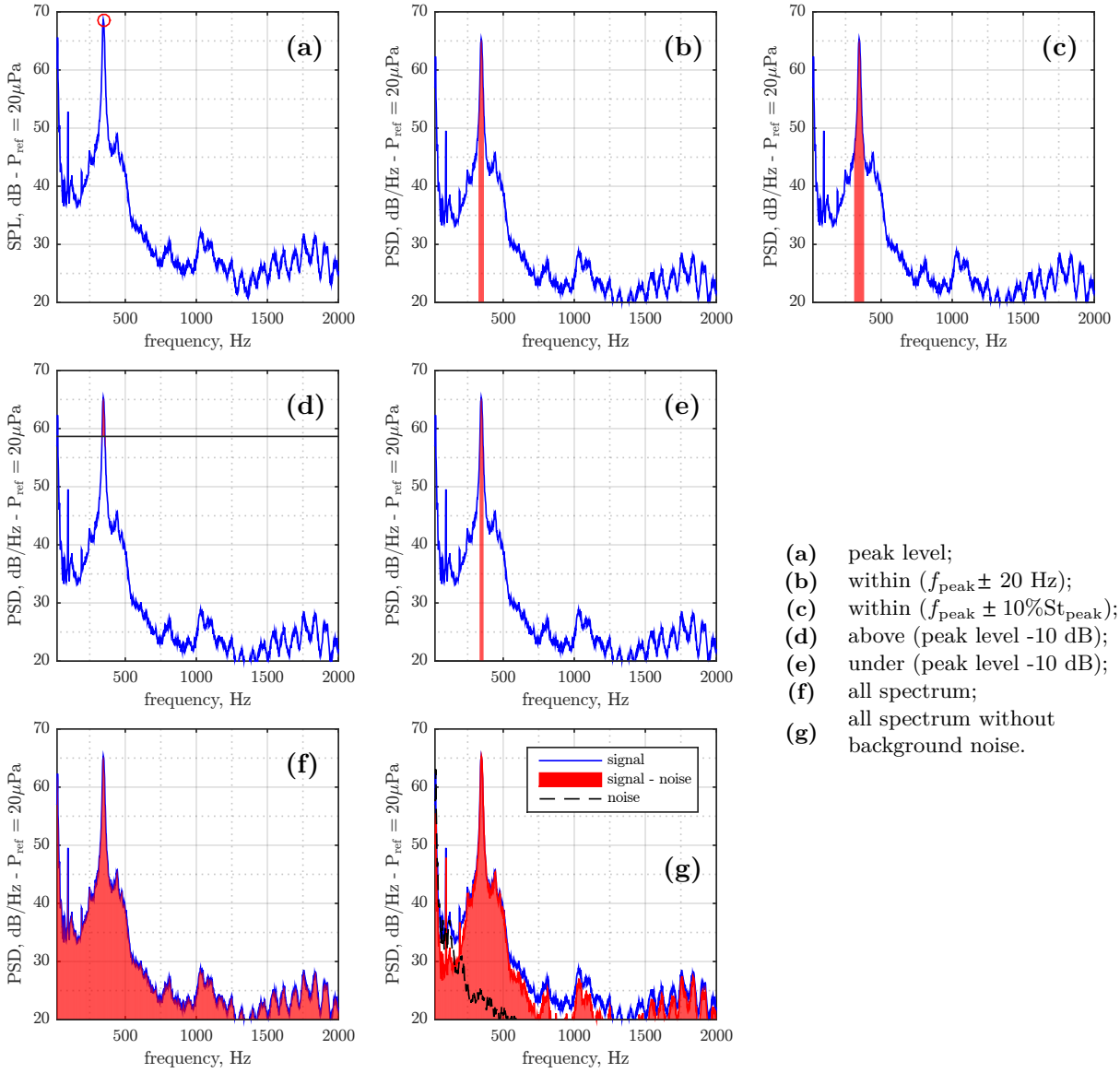

Figure 4.37: Illustration of the tested noise criteria for a sample configuration (square section, carbon fiber, d = 8 mm, U_∞ = 20 m/s, Re = 10, 256), central microphone.

Table 4.4: Angle of attack of the tested configurations on the preliminary study with carbon fiber cylinders. Empty cells indicate configurations that were not tested.

cross-section	material*	d = 6 mm	d = 8 mm	d = 10 mm
6 × 6	c	$0.0 \pm 0.1^\circ$	$25.4 \pm 0.1^\circ$	
6 × 16	c	$0.0 \pm 0.4^\circ$	$7.3 \pm 0.2^\circ$	$15.3 \pm 0.1^\circ$
6 × 13	c	$0.0 \pm 0.1^\circ$	$9.3 \pm 0.3^\circ$	$19.5 \pm 0.2^\circ$
8 × 8	a		$0.0 \pm 0.3^\circ$	$17.0 \pm 0.1^\circ$
	c		$0.0 \pm 0.1^\circ$	$17.1 \pm 0.1^\circ$
10 × 10	a			$0.1 \pm 0.3^\circ$
	c			$0.1 \pm 0.2^\circ$

*: a: aluminum, c: carbon fiber.

differences that disregard the deficiencies of the simulations: these can be seen when comparing the responses of the carbon fiber and aluminum cylinders for the same cross-section, as illustrated

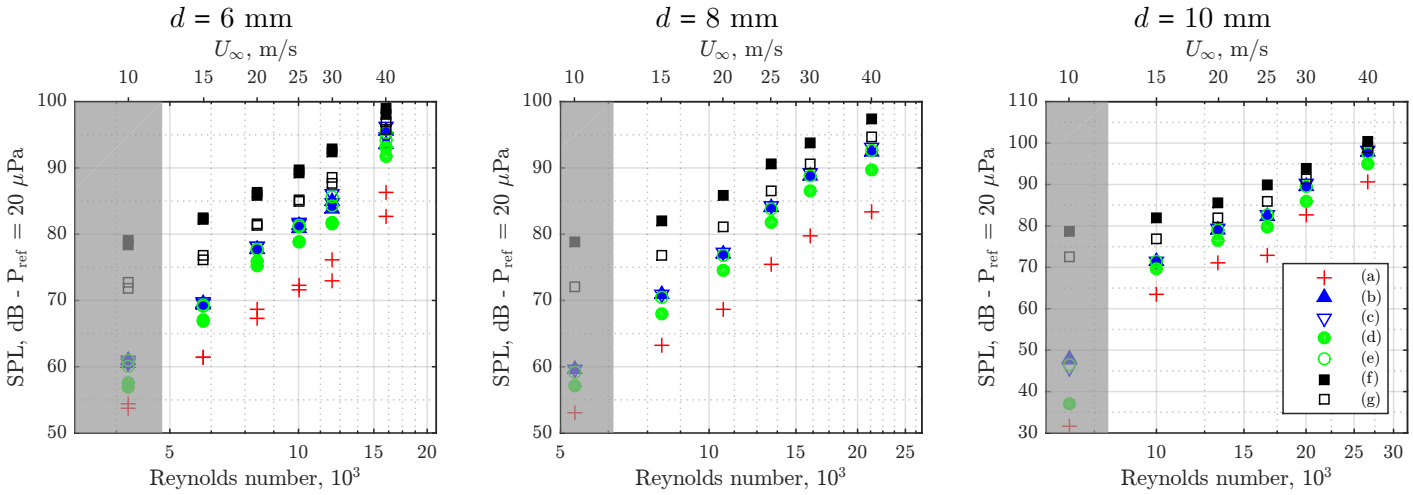

Figure 4.38: Evolution of the sound pressure levels of the central microphone for different carbon fiber square section (d from 6 to 10 mm) considering the multiple noise criteria. Legend correspond to the different criteria as presented in Figure 4.37.

by the sound spectra on Figure 4.39.

For instance, there is a change in the tonal frequency, noted more easily when looking at the first harmonic, and a modification of the levels, consistently higher for the carbon fiber of d = 10 mm and consistently lower for the carbon fiber cylinder at d = 8 mm, when compared to aluminum cylinder of equal dimension. Two possible origins of such variations are found and discussed further: the rounding of the cross-section and the resonance of the carbon fiber cylinders.

4.4.2.1 Resonance of the carbon fiber cylinders

Resonance between the hydrodynamic excitation and the structural mode was noted several times for the carbon cylinders. Resonances were spotted by the modification of the wind tunnel velocity assisted by a real-time short-term Fourier transform of the microphone signals. For the tested range of velocities, 1 or 2 resonances could be found for the square sections, many more for the rectangular sections at incidence. For instance, for the rectangular section 6×13 at 7 degrees, resonance was obtained at 4, 6, 8, 10, 12, 14 and 16 m/s. An example of the measured sound emission at a resonance frequency is presented on Figure 4.40.

On Figure 4.39, traits of and incoming resonance can be seen for the square section of side d = 8 mm at U_∞ = 15 m/s. On the measurement, resonance was found to exist at U_∞ = 15.74 m/s.

4.4.2.2 On the influence of rounding in the sound emission

The rounding of the edges of the carbon cylinders could be noticed when maneuvering the materials. A closer look using photos of the cross-sections, see Figure 4.41, proved that there is a significant rounding in the carbon fiber cylinders that were tested.

Rudimentary visual analysis of the photos lead to an estimation of a radius of 0.67 mm. This represents a ratio of about 12% percent of the side of the square section of side d = 8 mm and 8% for the square cylinder of side d = 10 mm.

In previous works in the literature [29, 256], it is reported that the rounding has an important effect in the RMS lift coefficient of cylinders with square cross-sections, as illustrated on Figure 4.42. Depending on the radius-to-edge ratio, a reduction of about 80% of C_L' is found for a null angle of attack.

Presented points evidenced the problem to use the carbon fiber cylinders for the analysis of the bluff bodies noise. The modifications in the aeroacoustic response due to the rounding of

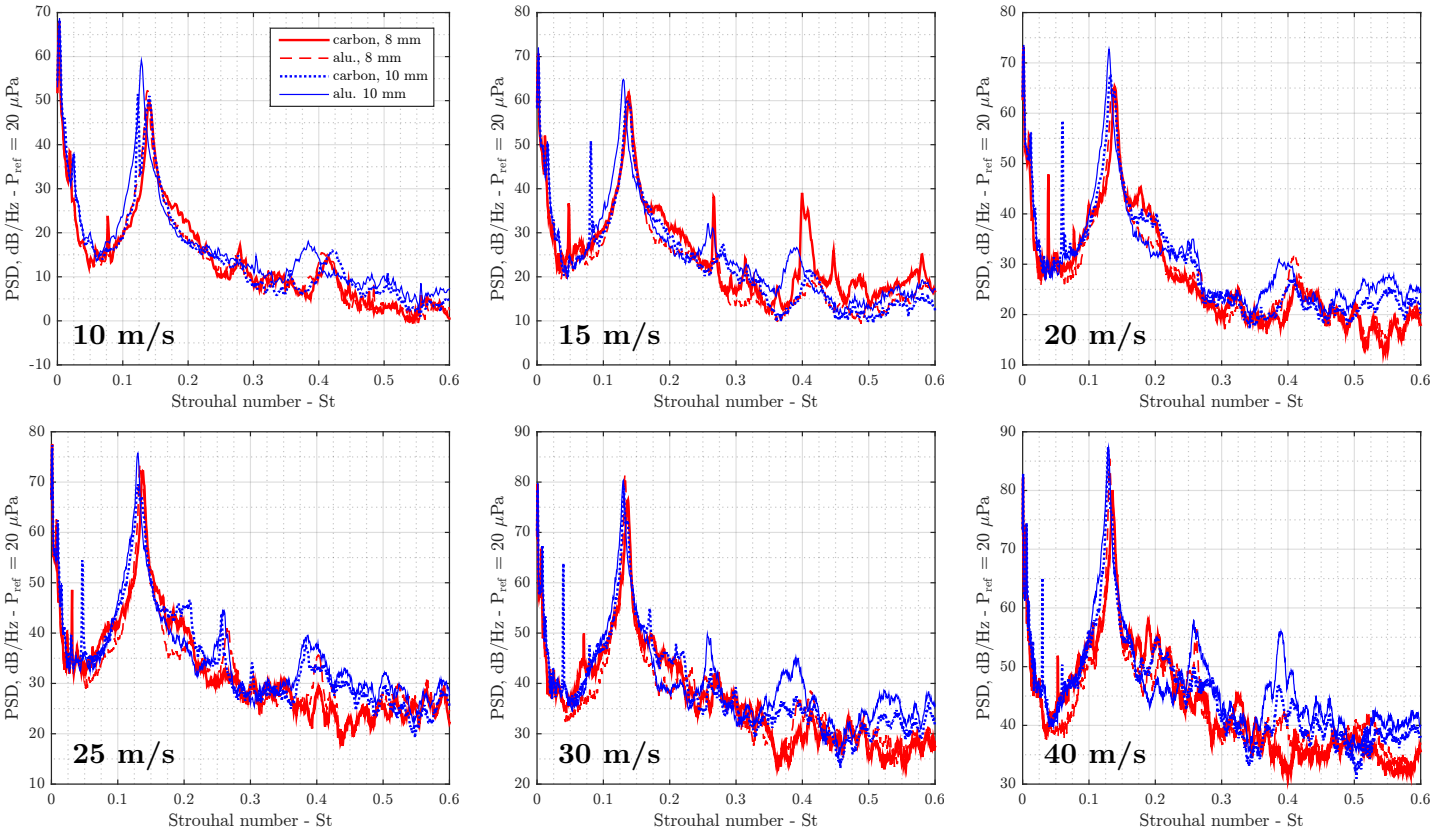

Figure 4.39: Sound spectra for the aluminium and carbon square cylinders of different height (d of 8 mm and 10 mm, zero angle of attack), at different flow velocities. Microphone at 90 deg of the flow.

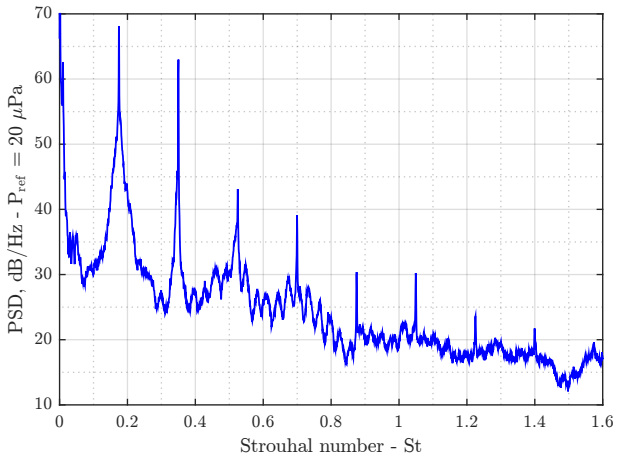

Figure 4.40: Example of sound emission obtained at a resonance. Cylinder of section 6×6 mm with an angle of 25.4° (blockage of d = 8 mm), incoming flow at U_{∞} = 19.18 m/s.

the edges and the structural response of the rods compromise the analysis. Consequently, the results obtained with carbon fiber cylinders are not further discussed in this manuscript.

4.4.3 Circular section and rectangular sections of aspect ratio 1, 2 and 3

Apart from the circular section, the description of the sound emission around square and rectangular cylinders are the most recurrent cases in the bluff body aeroacoustics literature [83, 111, 174]. Not only it is a canonical geometry with diverse discussion on academics, rectangular cylinders are a fundamental element in engineering and architectural designs. Measured

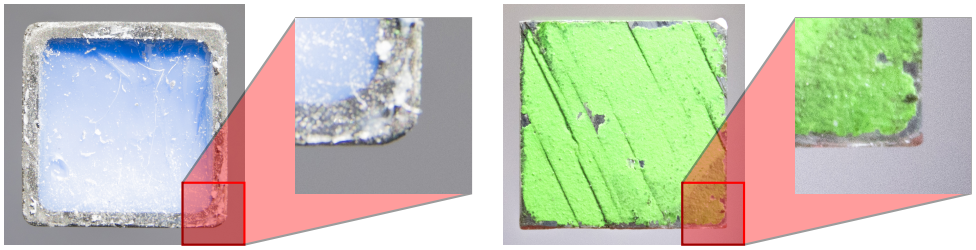

Figure 4.41: Photographies of the edges of the cross-section of the tested cylinders of d = 10 mm in carbon fiber (left) and aluminum (right).

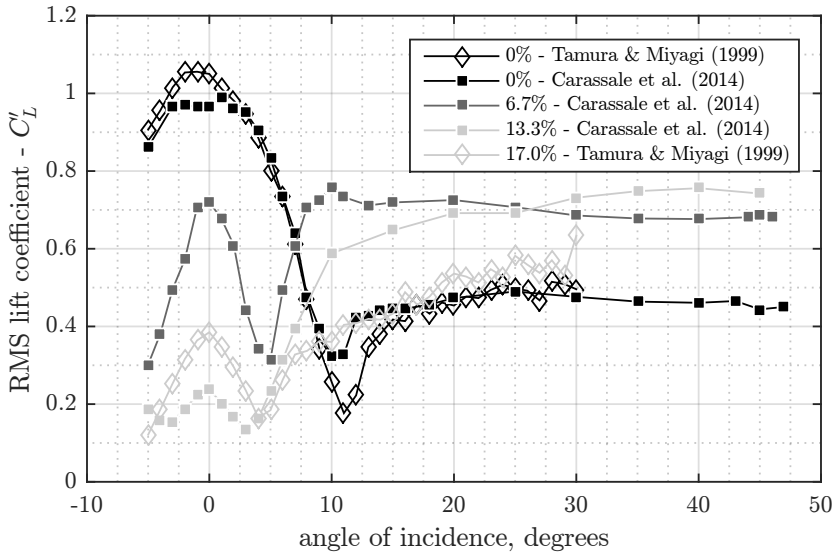

Figure 4.42: Evolution of the RMS lift coefficient of the square cylinder with the angle of incidence, multiple rounding categorized by the radius-to-edge ratio. Data from: Tamura & Miyagi [256], flow at Re = 30×10^3; and Carassale et al. [29], for a Reynolds number range of Re = $27 - 37 \times 10^3$.

sound spectra (Section 4.4.3.1 and 4.4.3.2), directivity (Section 4.4.3.3) and sound pressure level exponents with flow velocity (Section 4.4.3.4) are presented next for circular and rectangular cylinders of aspect ratio 1 (square), 2 and 3. The circular cylinder is used as reference and for checking the consistency of the experimental setup.

This analysis of the sound signature of those shapes must be considered together with the study of the flow streamwise behavior in Section 4.2 and the estimation of the RMS lift coefficient and discussion over the closure of the bluff body noise in Section 4.5.

4.4.3.1 Validation - Circular cylinder

A comparison of the obtained noise spectra with literature data is performed for the circular cylinder and presented in Figure 4.43. There is a constant offset between the experiments for the sound pressure levels (Figure 4.43a). The observed behavior is a consequence of different experimental conditions (cylinder's length and diameter and flow velocity and Mach number), and experimental setup, notably the presence of end-plates at the nozzle extremities in the works used as reference [30, 73]), and observed similitude in the levels are just coincidence. In terms of frequency content, considering the difference of the spectral distribution to the peak level (Figure 4.43b), the similarity of the curves is shown. The values around the first peak are slightly lower than those observed in previous works, what may be associated to the slightly smaller Reynolds number. The prominence of 30 dB of the fundamental mode, as well as the

shape of the curve at the first 2 harmonics are comparable in all studies.

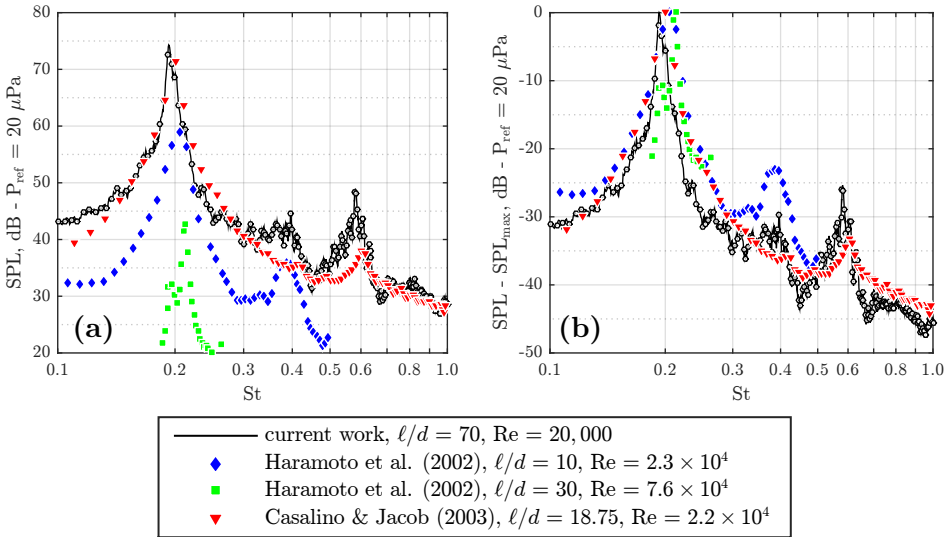

Figure 4.43: Spectral distribution of the sound pressure level (a) and relative sound pressure level (b) of the emission of the circular cylinder. Current work data are not corrected for background noise and circle markers are added every 12.5 Hz for visual aid. Comparison with data from the literature [30, 73].

One-third octave scaled levels for the sound emission of circular cylinders are presented further on this document, Figure 4.63. Once again, the difference of cylinders' length (ℓ/d) and flow velocities provokes the offsets for both the level and the frequency. However, the shape of the curves is quite similar to previously reported results [83, 250], especially in what concerns the prominence of the sound contribution at the peak frequency compared to the other frequency bands.

The acoustic signatures of the different cross-sections are compared next by analyzing the sound pressure spectra, the width of the spectral band around the peak, the sound directivity and the exponent of the sound pressure dependency to the inlet velocity. A table containing the peak frequencies and sound levels (peak, overall and band) is present in the Appendix E.

4.4.3.2 Sound spectra

4.4.3.2.1 Peak frequencies and peak levels First, sound spectra are presented in Figure 4.44 for the multiple flow velocities that are tested, for the central microphone (90° of the incoming flow). As noted in previous works, the square is louder than the circular section [83, 111, 158]. At the peak frequency, the current hierarchy is observed: circular cylinder < rectangular cylinder of aspect ratio 2 < square cylinder < rectangular cylinder of aspect ratio 3. The prominence of the first and second harmonics follow the same hierarchy, that is less noticeable for the circular cylinder and easily remarked for the widest rectangular section. For all the geometries, the peak Strouhal number (listed in Appendix E) is rather unmodified with the flow velocity.

For U_∞ = 10 m/s, the tone associated with the vortex shedding is under the anechoic chamber cut-off frequency of 200 Hz for all geometries, thus this is not considered for most of the analysis performed in this work. Due to a reduced peak Strouhal number, this is also the case for most velocities for the rectangle of AR = 2.0, thus results for that section are not as reliable as what is obtained for the other geometries.

Two peaks for AR = 2, at St ≈ 0.08 and St ≈ 0.14 are due to the existence of two vortex shedding modes for that given geometry. The first and most energetic one is associated with the flow separation at the upstream vertex, similarly to what happens for the square section, while the later corresponds to the vortex shedding happening at a downstream position due to the

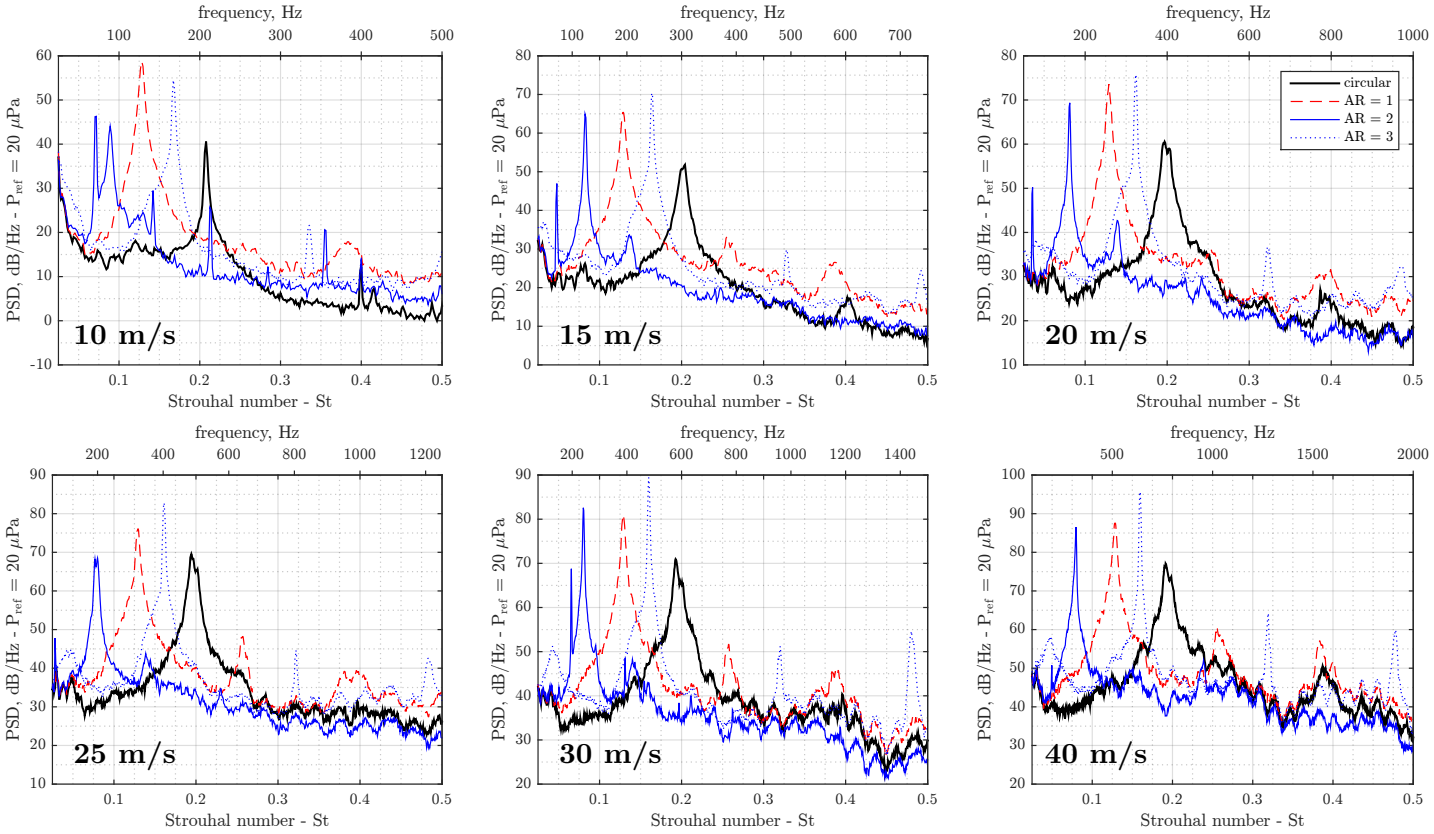

Figure 4.44: Sound spectra for the circular, square and rectangular cylinders (AR = 2.0 and 3.0) at different flow velocities, microphone at 90 degrees of the flow.

reattachment of the flow on the upper and lower faces of the prism, as observed for the rectangle of AR = 3. This transition creates a discontinuity on the St × AR curve and is present in several works in the literature, such as [169, 175, 240]. From the analysis of the velocity field spectra performed in Section 4.3.3.2, the two modes are believed to coexist. The origin of the narrow peak on the left of the vortex shedding one is unknown.

4.4.3.2.2 Peak width Differences regarding the width of the peaks can also be seen in Figure 4.44. Considering the definition of the pressure level band (frequency range for which the level is greater than peak level - 10 dB), evolution of the obtained peak widths are illustrated in Figure 4.45. Except for the lowest velocity, the peak is almost of constant size for the circular cylinder, fluctuating around $\Delta St = 0.017$. For the rectangular sections, the band size decreases with the Reynolds number. The high width for AR = 2.0 at U_∞ = 25 m/s is associated with the merge of two peaks.

The noted trend is an indication that the evolution of the flow is different regarding the shape of the geometries and the presence of sharp edges. For the circular cylinder, there is no significant change in the shape of the spectrum, implying that the experimented flow regime is well established at the tested range. For the rectangular sections, a change in the velocity is more capable of modifying the sound spectrum, and peaks are narrower at larger Reynolds number. This results is the opposite of what could be deduced from classical turbulence development deduction, and shows that the difference of cross-section is an important factor in the behavior of the flow and the cylinder aeroacoustical response.

4.4.3.3 Directivity

The sound directivity is illustrated in Figure 4.46 with the difference between the level for each microphone and the level of the central one (90°), considering the peak sound pressure level.

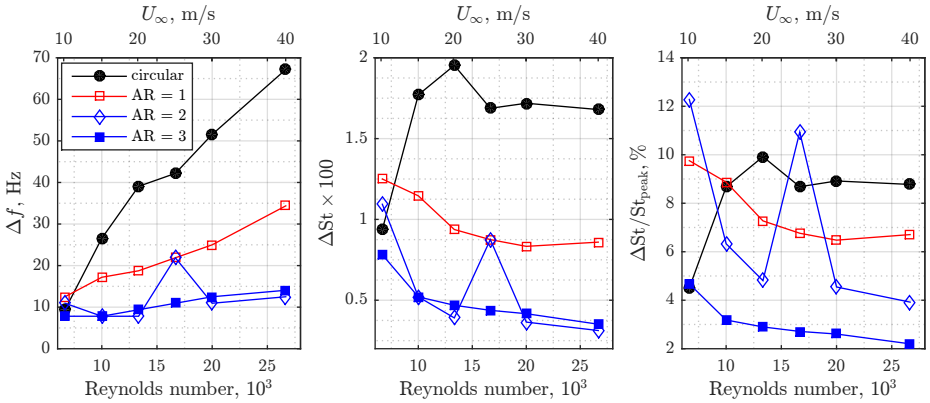

Figure 4.45: Evolution of peak width for multiple cross-sections considering the frequency range delimited under 10 dB of the peak frequency: in frequency (left), in St (center) and percentage of the St_{peak}.

For the first microphones, the dipole shape is relatively respected; for microphones after 90°, measured pressure levels are higher than expected. This result is believed to be due to the flow, which can freely expand, what may perturb the pressure fluctuations that are captured by the microphones downstream 90°, and to sound waves reflections, notably at the convergent.

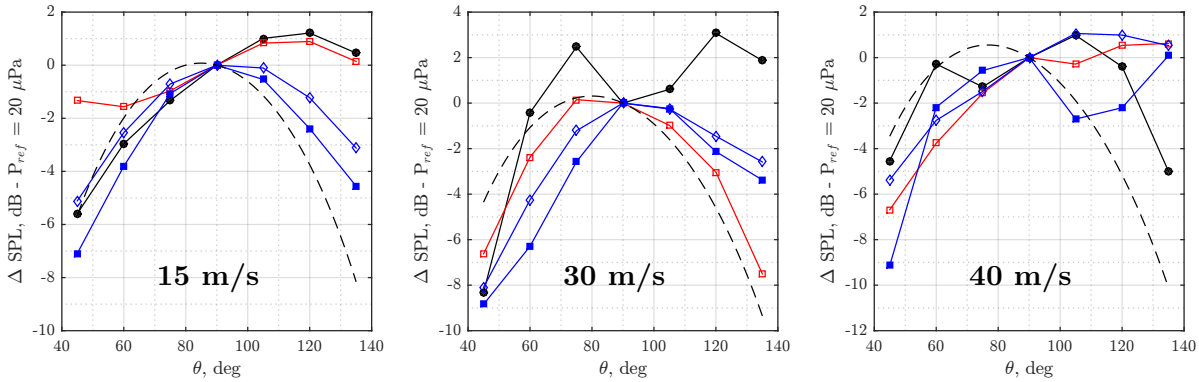

Figure 4.46: Sound directivity for all tested cross-sections at different flow velocities, peak sound pressure levels, same legend as in Figure 4.45. Hatched line represents the analytical dipole corrected by the flow [81].

4.4.3.4 Sound level velocity exponent

The sound pressure level evolution with the velocity is presented in Figure 4.47, for the four cross-sections and the microphone at 90°. The peak value (PSPL) and the full spectrum (OASPL, integral of the power spectral density from 0 to 6400 Hz) are selected and the least-squares linear regression law is presented. For both criteria and all sections the levels evolve exponentially with an exponent close to 6 (6.0 for the circular cylinder, 5.1 for the square cross-section, 5.4 for the rectangle of AR = 2.0 and 6.2 for AR = 3.0), as deduced by Curle [37], evidencing the dipolar and compact nature of the emissions. Tests without the background correction returned the same exponents. For wider rectangles, the compactness of the section may not be respected, resulting in an exponent different from 6, as discussed by [135] when examining the sound emission of a rectangular section of aspect ratio 7. Once more, values at U_∞ = 10 m/s slightly deviate from the tendency, for example for AR = 2, and spoil the regression line when considered. Thus, the corresponding velocity exponents and curves presented on Figure 4.47 do not consider the measures at that flow velocity.

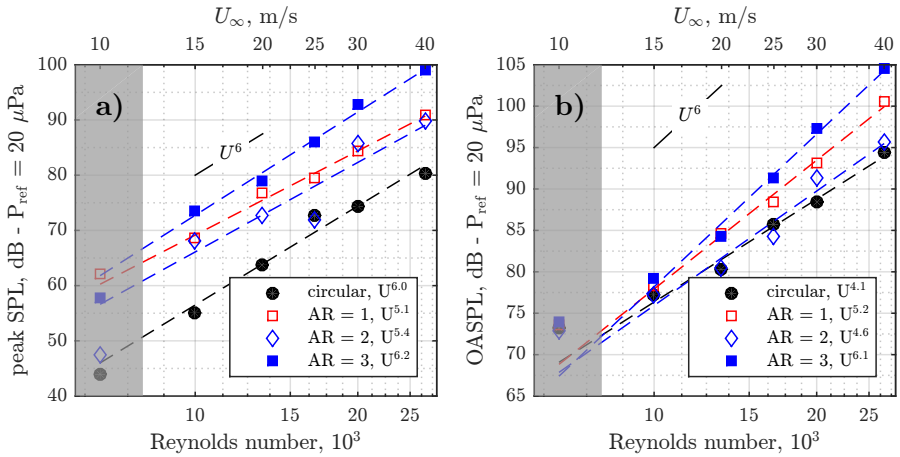

Figure 4.47: Evolution of the sound pressure level for the circular and rectangular cross-sections as a function of the flow velocity for: (a) level at the peak frequency; and (b) the integral of power spectral density (0 - 6400 Hz, OASPL). The points corresponding to U_∞ = 10 m/s are not considered when calculating the regression laws that are displayed.

4.4.4 Sound emission of cylinder of triangular cross-sections and comparison to square and circular cylinders

Sound emission is also examined for cylinders with triangular cross-sections, influenced by the extreme behavior that is found in 2D, noticed in the study of several cross-sections at low Reynolds number, available in Chapter 2 and reinforced by the optimization studies reported in Chapter 3. For the wind tunnel testing, the size of the cylinders is limited due to the frequency cut-off of the anechoic chamber (the produced aeolian tone must be above 200 Hz, so the height d must not be too large) and by, from an aerodynamic point of view, the necessity to have small blockage test section and to remain at an interesting Reynolds number range (out of the drag crisis, that is, before the boundary layer transition), thus limiting the use of cylinders with large d. To conclude, d must be around 10 mm, value that represents most of the different cross-sections presented herein. Also, as discussed on Section 4.4.2.2, the edges must be sharp such as to have an experiment that is consistent with the targeted shape.

For such set of conditions, only acrylic cylinders where found available on the marked. Purchased beams have equilateral triangles (AR = 1.0) of sides d = 5, 10 and 15 mm as cross-sections. Considering the setup presented earlier (Section 4.1.3.2) with a cylinder of fixed span of ℓ = 700 mm, they represent three distinct effective lengths: ℓ/d = 140.0, 70.0 and 46.7, respectively. Measurements consider, for each cylinder, two orientations: wedge pointing downstream and wedge pointing upstream. The notation used in Chapters 2 and 3 is employed: "trib" for back-pointing triangle and "trif" for front-pointing triangle. The angle of incidence of the profiles are measured for only one of the ends using a cellphone and an angle meter app, as presented in Section 4.4.2.

Expecting a poor structural resistance of the cylinders, a mechanism to apply tension to the cylinder, thus increasing its resistance to the bending provoked by the aerodynamic load, was built. After preliminary testings, the system is found unsuccessful, probably due to non-linear behavior of the material in terms of the response to the structural load.

Even if the comparison to the other cylinders, virtually undeformed, may not be fair and that the bending could play a significant influence on the flow and acoustic emission, the results are still reported due to its scientific relevance: the author is unaware of measurements of sound emission of cylinders with triangular sections, specially of such long span. Exception is made for the smallest cylinder (d = 5 mm) which could not maintain its straightness even in the absence of flow, that was not tested.

In following section (4.4.4.1), the beam's deformation is exemplified and discussed further. Next, the measured sound spectra, directivity and flow velocity exponents are presented, always

comparing to the results of the circular and square cylinders introduced earlier. A discussion around the observed sound signature of the flow around triangular cylinders (Section 4.4.4.3) concludes this section.

4.4.4.1 Deformation of the triangular cylinders

After noticing the deformation, a camera was installed in the anechoic chamber, under the cylinder, to allow an estimation of the amplitude of the bending, as can be seen on Figure 4.48. The camera is controlled remotely; photos are taken for the base condition (no flow) and all the velocities of interest (U_∞ = 10 to 40 m/s), sound pressure measurements are performed after in the original setup (no camera).

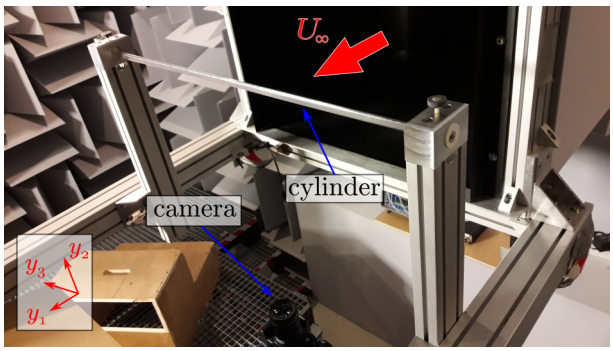

Figure 4.48: Setup for the photo of the deformation of the cylinders with triangular sections.

An example of the obtained deformations is presented on Figure 4.49. Note that for an easier visualization of the effect, the most extreme case, that is, the cylinder with less resistance to bending (d = 10 mm) in the most aerodynamically demanding orientation (back-pointing) is presented. At U_∞ = 40 m/s, the streamwise deformation of the center of the cylinder (y_3 = 0) is of at least one d. Even if the deformations are not as severe for the other configurations, they remain non negligible and can be seen by the naked eye.

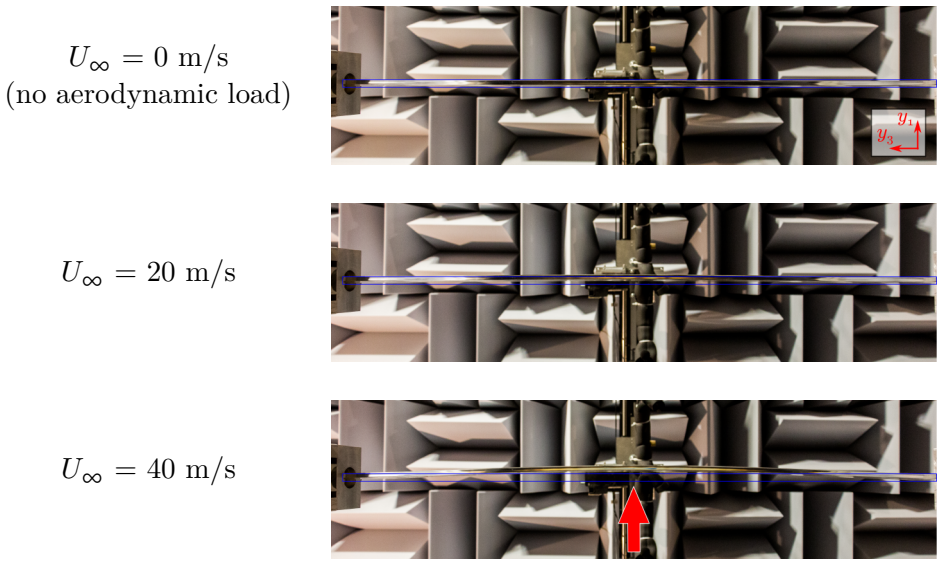

Figure 4.49: Example of the deformation of the cylinder with triangular section (d = 10 mm, back-pointing), bottom view. Arrow indicates the flow direction.

As expected, the cylinder with d = 15 mm is less deformed. The use of different heights change two aspects of the flow: the relative length of the cylinder and the Reynolds number. Even if the modifications are not so extreme for both aspects, a direct comparison between different

sized cylinders is not recommended. However, since they may represent different geometries due to the bending, the acoustic signature of both cylinders (d = 10 mm and d = 15 mm) are discussed further. Comparison is performed with the square and circular cylinders that are similar (d = 10 mm and 14 are used).

4.4.4.2 Evolution of the sound with flow velocity and sound spectra

The evolution of the sound pressure levels for the 4 cross-sections are presented on Figure 4.50; the exponents of the velocity term are as well presented (without considering the lowest flow velocity because the tone was at a frequency lower than the wind tunnel cut-off frequency). The following hierarchy is found: trif < circle < trib < square. The offsets between levels are augmented with the increase of the flow velocity, what may be associated with the change of flow dynamics within the increase of the Reynolds number.

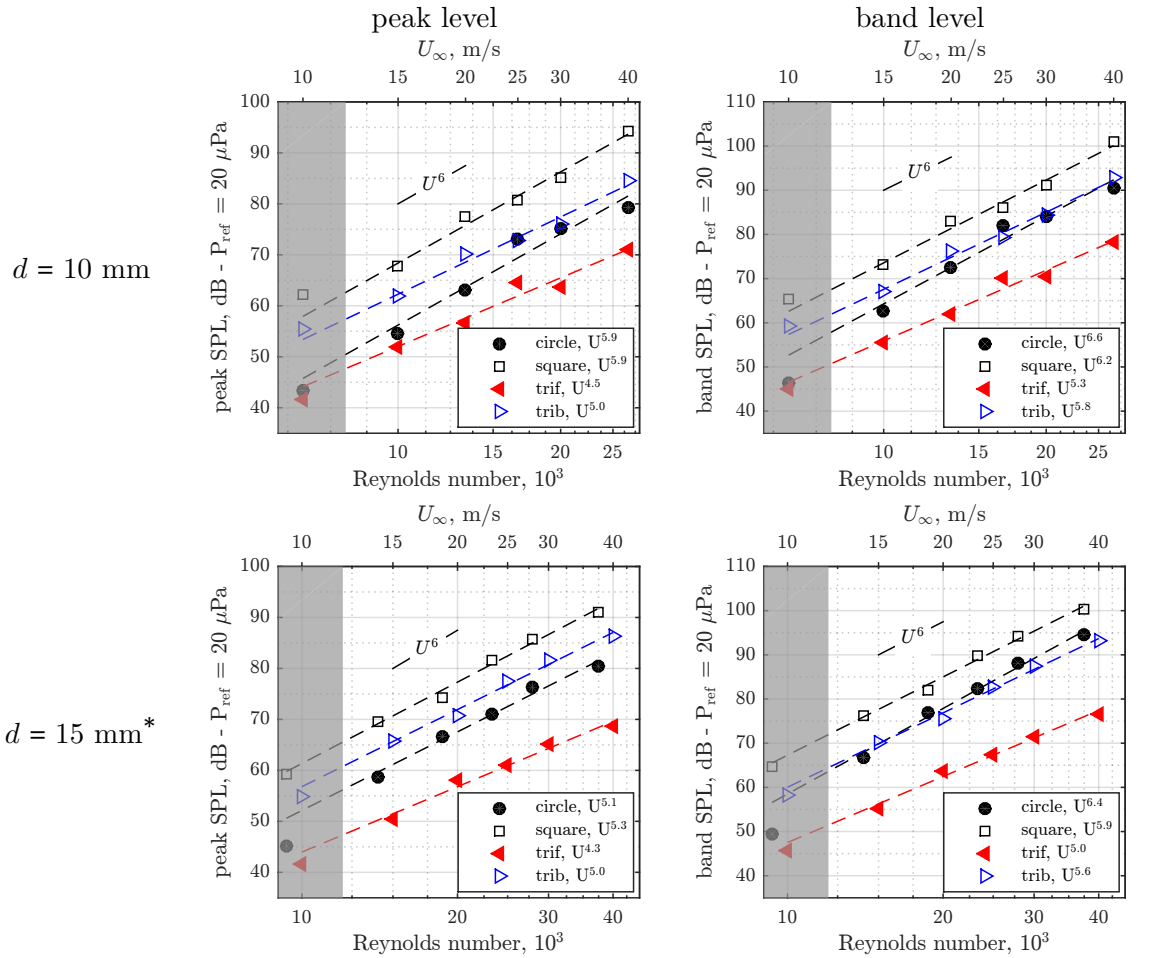

*: d = 14 mm for square and circular, 15 for the triangular sections.

Figure 4.50: Evolution of the sound pressure level for the circular, square and triangular cross-sections as a function of the flow velocity for: level at the peak frequency, on the left; and the integral of power spectral density around the peak (peak level - 10 dB), on the right. The points corresponding to U_∞ = 10 m/s are not considered when calculating the regression laws that are displayed.

The exponents are, for d = 10 mm, significantly distant from the theoretical value of 6. As discussed earlier, the beam deformation is quite pronounced at that situation, what may interfere with the sound emission. Even so, the dipolar and compact nature of the emissions are confirmed.

Figure 4.51 presents the sound spectra for some of the tested flow velocities, central microphone. Two pairs are formed based on the vortex shedding of emission levels. The front-pointing

triangle (trif) is quite similar to the circular section, with vortex shedding Strouhal number of around 0.2; the sound spectra for the back-pointing triangle (trib), are quite similar to the acoustic signature of the square section, with a tone at around $St_{peak} = 0.14$. Note that the similarity is more marked for the lower flow speeds, which are more reliable since the bending is weaker.

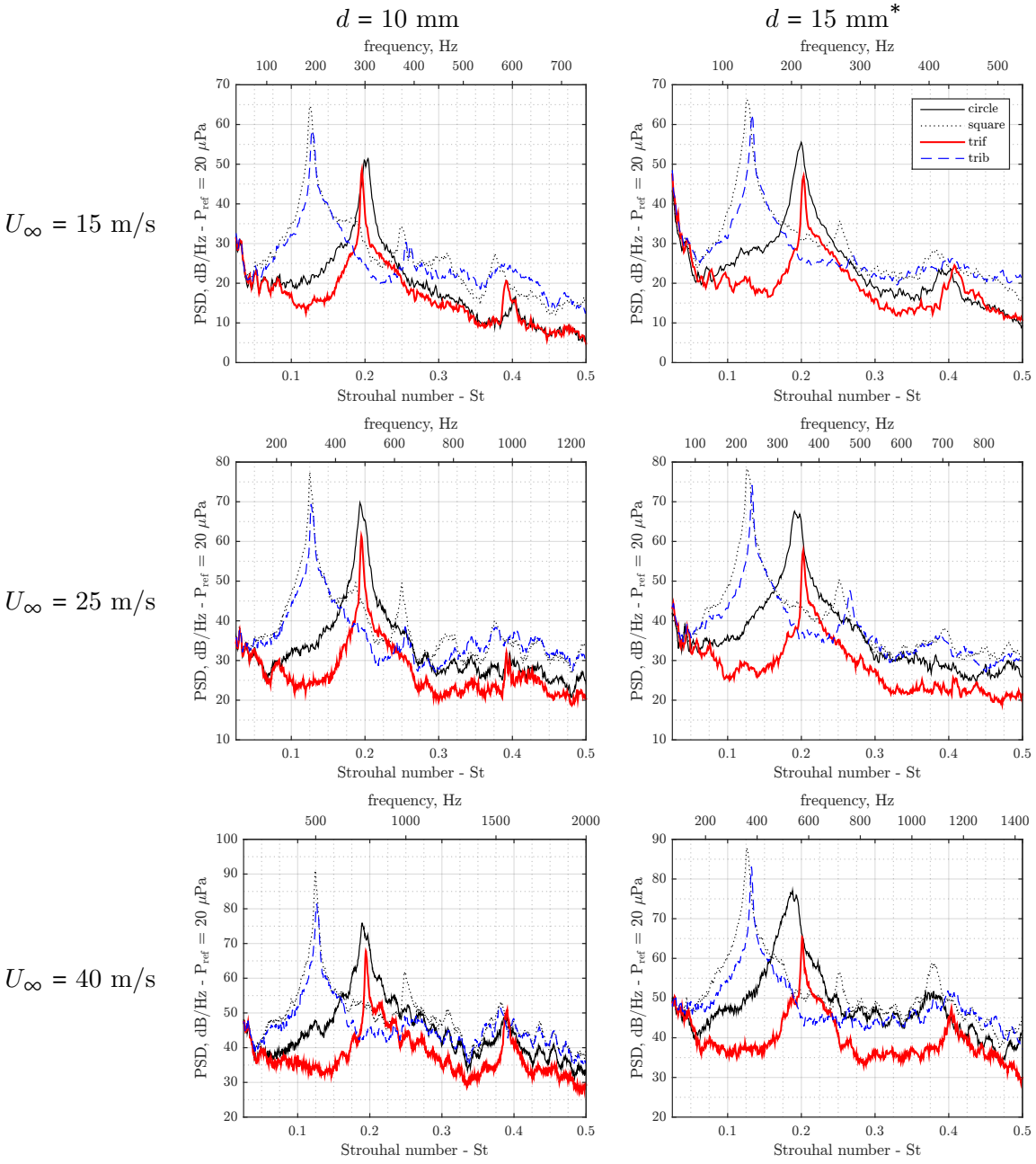

*: d = 14 mm for square and circular, 15 for the triangular sections.

Figure 4.51: Sound spectra for the square, circular, front-pointing (trif) and back-pointing (trib) cylinders, at for some of the tested flow velocities, microphone at 90 degrees of the flow.

This similarity may be explained by the nature of the vortex shedding and the dynamics of the boundaries. Both the circular and the front-pointing triangle are expected (it cannot be affirmed since it was not measured) to have detachment points that are at further downstream portions of the shape. For trib, it is fixed at the edges. Opposite behavior is expected for the square and for the trib cross-sections, with a detachment at the upstream limit of the shapes. This represents, for the two pairs, a difference in the wake width, thus, difference in the vortex shedding frequency [220]. Similarities in the vortex shedding frequency are presented by the

values on Table 4.5.

Table 4.5: Vortex shedding Strouhal number (St_{peak}) for the triangular, square and circular sections, d = 10 mm.

U_∞, m/s	trib	rect	elip	trif
10	0.131	0.128	0.211	0.200
15	0.128	0.125	0.204	0.196
20	0.127	0.125	0.197	0.196
25	0.127	0.125	0.193	0.195
30	0.127	0.124	0.192	0.196
40	0.127	0.125	0.189	0.195

For all the tested velocities and sizes, the back-pointing triangle (trib) is the loudest triangular cylinder. This result is compatible with the studies at 2D (Section 2.2) and the fluctuating effort hierarchy reported by Iungo & Buresti [92] when studying wall mounted triangular cylinders of small aspect ratios ($\ell/d \leq 3.0$), Re = 1.2×10^5. They reported that the standard deviation of the cross-flow force fluctuations (C_L') for the back-pointing triangle cylinder is about twice the one with the front-pointing triangular section. Nonetheless, none of them is louder them the square and circular section as expected in the 2D study.

Despite the differences in flow regime that may explain the difference, there is also the three-dimensionality of the flow. The sound is fundamentally associated with a force fluctuation and a measurement of the flow de-correlation [109, 191]. When measuring only the sound emission, a louder bluff body may either be a result of very strong fluctuating efforts or a weak C_L' but very correlated in the spanwise direction. Neither one of the two quantities are available for the triangular cylinders with the performed experiment. Reader is invited to check Sections 4.3 and 4.5, where this aspect is studied for other cross-sections. Due to the bending of the cylinders and its resulting difficulty to measure the spanwise distribution of the flow, this analysis was not performed for the triangular cylinders.

Nevertheless, it is possible to hypothesize around the origins of such behavior. Considering the differences in the Re for achieving flow transition studied in Section 2.2.3, if the principle is extrapolated for current Reynolds number and to three-dimensional flow structures, it is expected that the flow transitions will arrive sooner in the Reynolds number scale for the front and back-pointing triangles (both shapes have lower Re_c than the square and the circular cross-sections). Consequently, in terms of the de-phasing of the spanwise vortexes, it can be taken as more perturbed (less phased, smaller coherence length), so, less noisy than expected in 2D, low Reynolds. When comparing the two triangles, the availability of the surface for receiving the pressure fluctuations in the wake in form of RMS lift coefficient, thus noise, is also noted in the experiments. The presence of walls interacting with the vortex shedding is bigger for the back-pointing triangle, the noisiest triangle in this experiment.

4.4.4.3 Concluding remarks on the sound emission of cylinders with triangular cross-sections

The analysis of the measurements of the sound emission produced by the flow around triangular sections is delicate. Due to a poor structural resistance of the acrylic, the tested cylinders bend with the flow. Nevertheless, some interesting aspects of the sound emission arise and have the merit to be discussed.

The back-pointing triangle (trib) has a spectral acoustic signature that is very close to the square section (both in terms of the frequencies of the tones and their magnitudes). On the other way, the front-pointing triangle (trif) is very close to the circular cylinder. These similarities are partially in agreement with what is seen at low Reynolds number, 2D flow, where trib

is pointed as the loudest cross-sections. While the resemblances can be associated with the effective blockage defined by the boundary layers inward or outward tendencies [140, 220], the distinctions seem to be in accordance with the trend seen at low Re. It is believed that the flow around triangular sections follows a faster routine of wake transitions, thus, will produce, at a given Reynolds number, a more de-phased (thus less noisy) vortex shedding. Quantification of such behavior was not possible due to the deformation of the beam. For the back-pointing triangle, the deformation seems to play a role on reducing the noise.

4.4.5 Conclusion about shape influence from acoustical measurements

It is noted that the modification of the cross-sections results in remarkable changes on the sound spectrum features and sound pressure levels. Even so, in terms of the tonal character and the evolution with the flow velocity, all tested sections have a dipolar trait and respect Curle's analogy despite the disturbances on the velocity exponents and directivity patterns, also noted in literature values [83, 111].

Change from circular to any other cross-section of the same aspect ratio (AR = 1) represent a reduction in the Strouhal number and a decrease of the width of the aeolian tones in the spectra. These changes can be minimal, but they are present for all shapes tested here. This conclusion is biased by the limited number of observations and lack of diversity in the set of shapes that were analyzed, all convex and with sharp edges, however, this contributes to the argument that the extra degree of freedom for the establishment of the flow in the case of a curved wall, that is, the non predefined dettachement point, may be associated with a stronger freedom to dissipate energy in both the axial plan and axial direction. This results in more common vortex dislocations (thus, wider tone [46]). Both phenomena construct a very de-phased flow, that is, quieter vortex shedding.

The only shape that was quieter than the circular cylinder was consistently the front-pointing triangle. The author believes that this may be associated with the a sooner de-phasing of the spanwise vortexes in the Reynolds number scale (in analogy to a sonner transition from steady to unsteady flow) and the deformation of the beam, what forces a de-correlation and could provoke the modification of the shape of the tone on Figure 4.51.

Considering the central microphone, the evolution of the overall sound pressure levels with the aspect ratio of the rectangular sections is presented on Figure 4.52. Plotted values are centered at the linear average of the difference between the OASPL for the rectangle and the square section (ΔOASPL = OASPL(AR) − OASPL(AR = 1.0)) calculated for each flow velocities, error bars representing the limits of minimal and maximal difference. Supplementary testing with AR = 0.5, 4.0 and 5.0 are as well presented.

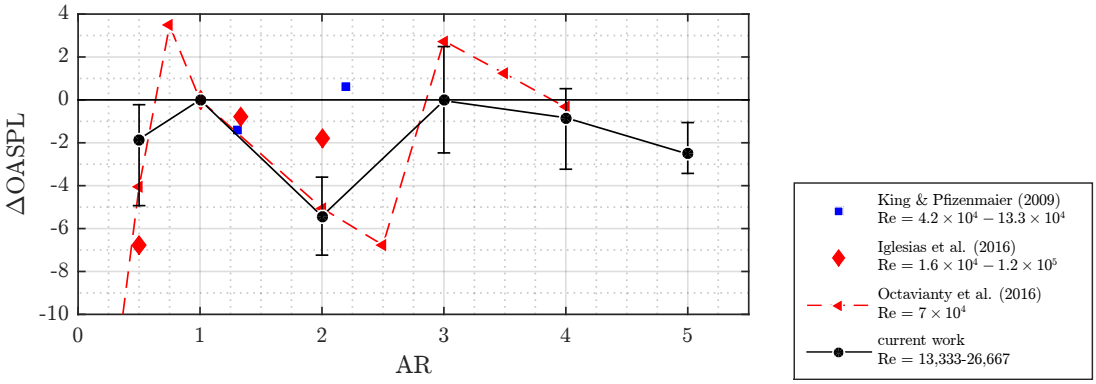

Figure 4.52: Evolution of overall SPL with aspect ratio, difference to the level obtained for the square section [83, 111, 174].

The behavior noted here is the same than presented in articles in the literature: a decrease from the square to AR = 2 and an increase from AR = 2 to AR = 3; the circular cylinder is, for all velocities, the quietest shape. Octavianty et al. [174] associated the shape of the curve OASPL

versus AR to the modification of the peak Strouhal number, noting the similarity between the two curves. Same conclusion was not possible with current data.

The discussed points are solely derived from the observation of the sound pressure spectra. Such description contributes humbly to the understand of the bluff body sound production mechanisms since it does not present the origins of the observed differences. Further discussion on the origins of those disparities is made possible by the combination of the microphone's data with the spanwise flow distribution measurements, reported in Section 4.3, and is presented next.

4.5 Bluff body noise closure and estimation of the RMS lift coefficient

Working from the outside in, the influence of body shape and flow velocity on the acoustic field and on the spanwise coherence have been described in Sections 4.4 and 4.3, respectively. Further understanding of the influence of shape on the noise generation mechanism requires the analysis of the missing quantity in the Curle-Phillips formalism, that is the lift fluctuation, see Equation (1.2.32) and Figure 4.53. This section is limited to the shapes within the spanwise characteristics of the flow have been described length, that is, the circular section, square and rectangular sections of aspect ratios 2 and 3.

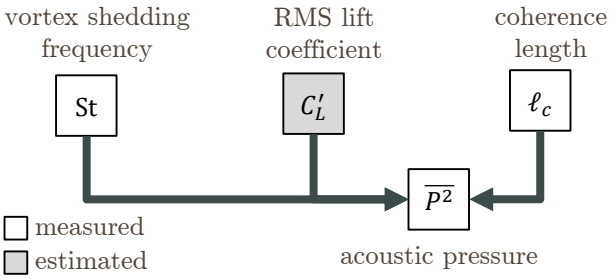

Figure 4.53: Diagram representing the ingredients of the bluff body noise.

Ideally, the lift fluctuation should be measured in the same experimental conditions. A sectional lift could be extracted from an array of wall pressure probes. However, this misses the spanwise behavior and causes severe settling issues. In particular, each rod of cross-section must be instrumented. Otherwise, the total lift may be obtained by aerodynamic balance, but then the spanwise distribution is integrated, and sectional behavior insight is prevented. Here, the sectional lift is educed by searching for a value that, when joined to the measured spanwise coherence in Curle-Phillips formalism, would best approach the measured acoustic spectrum.

This estimation is presented as follows: first, a procedure to compute an artificial acoustic spectrum from a given sectional lift signal is described Section 4.5.1, with a sensitivity study that is conducted in order to remove bias from the parameter's settings. Second, the procedure used to find the RMS lift coefficient that best fits the acoustic spectrum is identified on Section 4.5.2, along with the obtained the result. Third, the shape influence on each of the aeolian tone's ingredients are discussed, with a recall of the results described in Section 4.4.3 and 4.3.3. Forth, the estimated RMS lift coefficients are contraposed to the literature values, Section 4.5.4. Finally, a conclusion, Section 4.5.5, closes this section.

4.5.1 Acoustic spectrum reproduction method

The methodology to obtain the acoustic spectrum from the RMS lift and drag coefficients, based on Seo & Moon [233] and Doolan [46], is presented on Figure 4.54. It consists in considering a segment of cylinder that is fully phased and is submitted to a given amplitude of fluctuating aerodynamic efforts. For one segment, the peak is spread based on the behavior of the flow in

tha wake, and the sound emission is calculated further. Finally, the sum of the contributions of a given number of equal but de-phased segments is performed, resulting in the final sound pressure level. Each substep is discussed further.

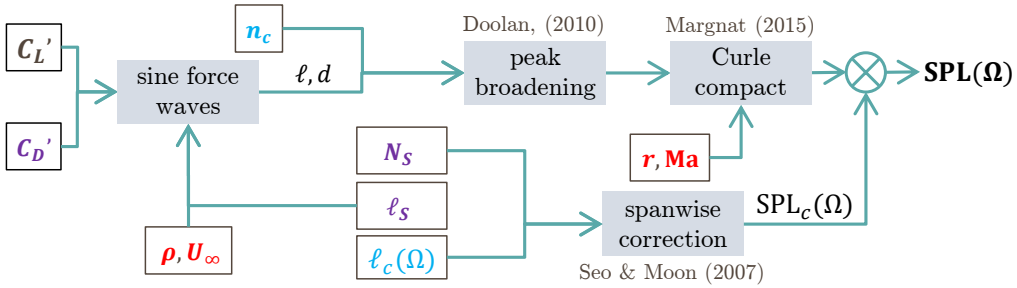

Figure 4.54: Diagram representing the methodology used to produce an artificial sound pressure spectrum from the RMS lift and drag coefficients. Intermediary steps are described in [46, 145, 233].

4.5.1.1 Force model

Perfect sinusoidal signals are considered for the lift L and the drag D of a segment length L_s, with amplitudes defined by the RMS force coefficients C_D' and C_L':

$$\begin{aligned} D &= (C_D'\sqrt{2})(1/2\ \rho U_\infty^2 d\ell_s)\ \sin(2\Omega_p t + \pi/2) \\ L &= (C_L'\sqrt{2})(1/2\ \rho U_\infty^2 d\ell_s)\ \sin(\Omega_p t) \end{aligned} \tag{4.5.1}$$

where $\Omega_p = 2\pi f_{\text{peak}}$ and t is the time. The modeled time sampling reproduces the duration and sampling used in the experiments.

4.5.1.2 Peak broadening representation

For the association of the long-span behavior quantified experimentally with the sectional behavior, the procedure proposed by Doolan [46] is considered. Based on Curle's analogy, only the aerodynamic efforts are associated with the noise emission of the cylinder's section. The first step consists in applying a statistical correction for representing the natural random phasing that distributes the energy around the peak of each tone present in the sectional aerodynamic efforts (issued from a 2D simulation). The peak broadening is represented by an exponential decay, resulting in a modified 2D force vector $F_T(t)$, defined as:

$$F_T(t) \approx \alpha\ \cos(\Omega t)\ \exp\left(-\sqrt{\frac{t}{4\tau_c}}\right) \tag{4.5.2}$$

where α is a real coefficient used to guarantee the energetic correspondence between original and modified force signals, Ω represents the fundamental frequency at each dimension, t is the time and τ_c is a turbulence time scale associated with the spreading of the peak. The turbulence time scale is represented as a multiple of the vortex shedding time scale, using the factor n_c, such as $\tau_c = n_c/f_{\text{peak}}$. As discussed by Doolan [46], $n_c = 1.25T$ is the equivalent of a disturbance of duration 10 T as the ones observed in Section 4.2.2.

4.5.1.3 Application of Curle's formula and long-span correction

After the peak broadening step, Curle's analogy is applied in the spectral domain in 2D compact formulation, that is, for the microphone at 90°:

$$\overline{P}(r,\Omega) \approx \frac{\iota\Omega}{4c} H_1^{(2)}\left(\frac{\Omega r}{c}\right)\overline{L}(\omega) \tag{4.5.3}$$

where $H_1^{(2)}$ is the Hankel function of second kind, order 1 and $\overline{L}$ is the Fourier transform of the lift L, corrected using Equation (4.5.1). See [145] for more details. The observer distance is $r = 1$ m, considering the wind-tunnel conditions.

The next step consists in correcting the sound level due to the spanwise extent of the cylinder using the procedure proposed by Seo and Moon [233], introduced in Section 1.2.3.4. For the extrapolation, the length ℓ_s, taken as completely correlated, must be chosen. The total sound is then taken as a sum of the contribution of each segment, considering the dephasing present in the long-span using the coherence length ℓ_c, a dimension associated with the correlation portion of the flow at each frequency. The following equation presents the correction level SPL_c that must be added to compensate the span effect on the spectrum obtained with the modified force (Equation (4.5.2)):

$$\mathrm{SPL}_c(\Omega) = 10\,\log_{10}\left\{\sum_{i=1}^{N_s}\sum_{j=1}^{N_s}\exp\left[-(i-j)^2\left(\frac{\ell_s}{\ell_c(\Omega)}\right)^2\right]\right\} \tag{4.5.4}$$

where N_s is the number of segments, such as $\ell = N_s\ell_s$. Continuous spectral evolution of the coherence length $\ell_c(\Omega)$ are fitted from the measured data (Section 4.3.3), procedure and curves are presented on Appendix F.

It does not account for the retarded time, so emission of very large cylinders may be overestimated. Also, the level correction accounting for the modification of the peak Strouhal values between the long cylinder and the experiment/simulation with short span cylinder, present in previous works [30, 177] and also used by Doolan [46], is not considered in this contribution.

Once all parameters are well posed, a sensitivity study, presented next, is performed in order to evaluate the influence of each parameter on the sound spectrum estimation, thus on the eduction of the RMS lift coefficient.

4.5.1.4 Sensitivity study

4.5.1.4.1 Presentation The influence of the number of segments N_s, the sectional aerodynamic efforts and the turbulence time scale τ_c, represented by the number of periods of vortex shedding n_c ($\tau_c = n_c/\mathrm{f_{peak}}$), and the coherence length (calculated by the function $\ell_c(\mathrm{St})$) are tested for a fixed cylinder length of $\ell = 70d$. A simple factor is applied for each of these variables and the spectrum estimation is done. In order to vary the coherence length, the peak scaling parameter m_i in Equation (F.1.1) is the only parameter that is modified.

When other parameters are tested, one takes:

- $N_s = 140$ (segment length of $\ell_s = 0.5d$);
- $C_L' = C_{L,\mathrm{Norberg}}' = 0.4728$, issued from the empirical law presented by Norberg [172];
- $C_D' = C_L'/10$ as a first approximation;
- $n_c = 1.25$;
- $\ell_c = \ell_g$ as determined by Equation (F.1.2) for the circular cylinder at $U_\infty = 30$ m/s ($\mathrm{Re} = 20,000$).

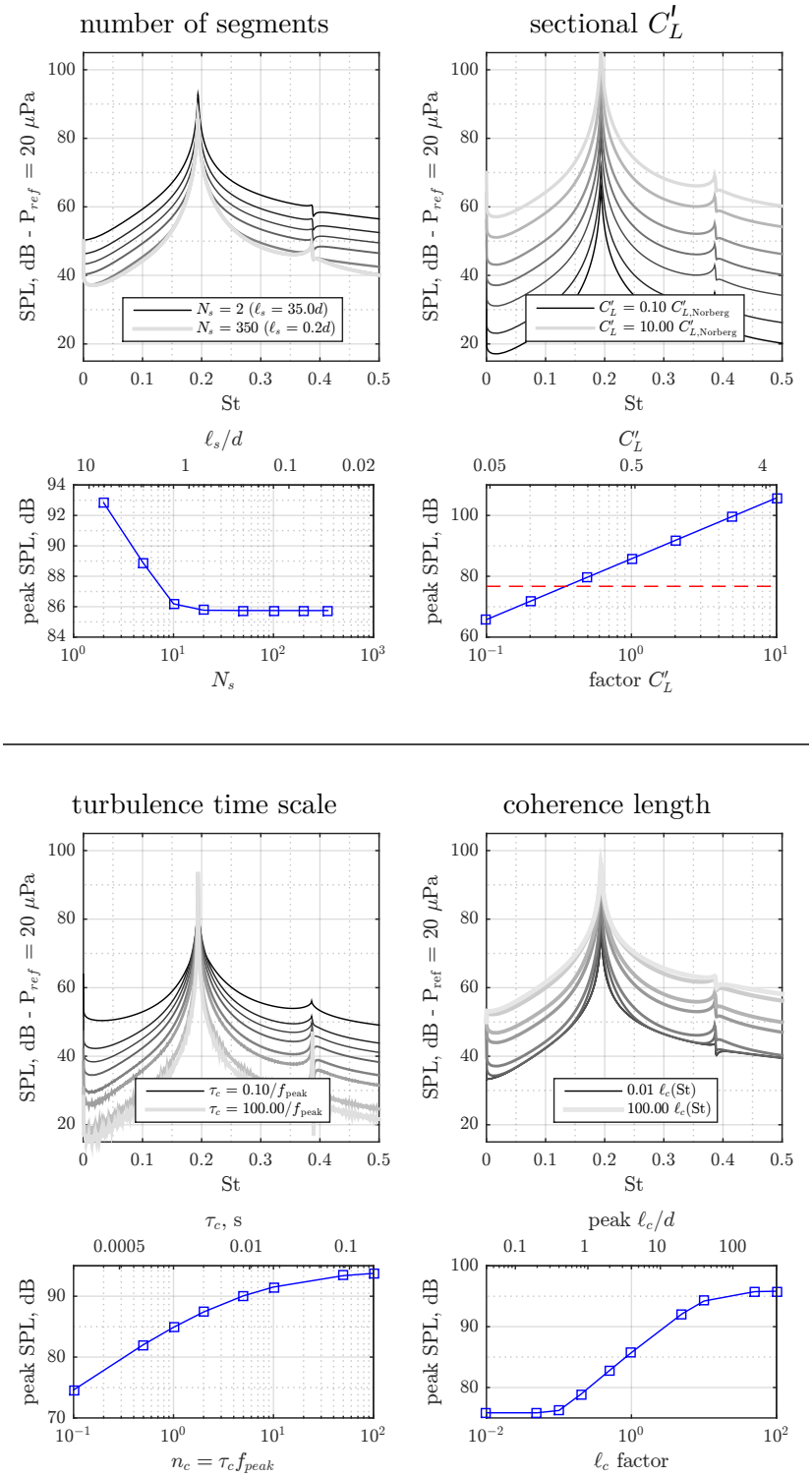

Figure 4.55: Sensitivity study of the acoustic spectrum reproduction method. Influence on spectrum (top) and peak levels (bottom). Parameters are the number of segments N_s, the sectional fluctuating lift C_L', the turbulence time scale τ_c and the coherence length (function $\ell_c(\mathrm{St})$ with different scale parameters); increase of the quantity is represented with the thickness of the line. Study is performed with data for the circular cylinder at Re = 20,000; when not being analyzed, values are: $N_s = 140$, $C_L' = 0.4728$ [172], $n_c = 1.25$ [46] and $\ell_c(\mathrm{St}) = \ell_g$ with coefficients as listed on Table F.1. Hatched line represents the sound level obtained in the experiment.

4.5.1.4.2 Results Spectral and peak behaviors are presented on Figure 4.55.

In what concerns the number of segments/segment length, convergence is well defined. Values are extremely overestimated for long segments/small N_s once the calculation imply that a big subsection is completely in phase and producing noise corresponding to the sectional fluctuating coefficient. With the increase of N_s, levels are reduced for the complete spectrum. For the main peak, converged values are obtained after 10 segments. A change in the aerodynamic efforts represents a uniform offset of the sound levels for the complete spectrum; as expected the exponent for the fluctuating lift is 2. As proposed and illustrated by Doolan [46], the turbulence time scale τ_c controls the sharpness of the spectral distribution, thus, is also highly influential on the peak level and shape of curve. The evolution of sound with the coherence length produces as well a global level offset, also presented by Seo and Moon [233] and the simplified equations, with an exponent of 1. The two highlighted exponents agree with the simplified model in Equation (1.2.32). This result is consistent once the two procedures were derived from Curle's analogy and made the same assumptions (far-field, acoustically and geometrically compact source).

Based on the given analysis, the segment length is chosen as $\ell_s = 0.5d$ ($N_s = 140$). Although this spanwise distance was not evaluated in the coherence experiment, it is believed that for distance of half of that given length (comparing the extremities to the center of the segment) the coherence is close to one, independently of the frequency. In other words, the hypothesis is that a segment of that size is completely correlated in terms of fluctuating efforts and sound emission. The conversion factor based on the spanwise correlation, described by West & Apelt [273] and others, that links the sectional C_L' to the RMS lift coefficient of finite length cylinders serves as a quantitative criteria to justify this choice. This factor is calculated from the correlation of velocity signals [196] considering a segment of $2d$, imposing a symmetrical correlation distribution. Obtained results are higher than 0.9.

As intrinsically associated with the flow physics, later 3 varied parameters (actually, inputs) are case dependent and highly influential on the final spectra. Used values are presented next along the results of the application of the correction method.

4.5.2 Lift eduction and artificial spectra

The principle of the lift eduction routine is to build an artificial sound pressure spectrum from an estimation of the RMS lift coefficient, as described on Section 4.5.2, and using an optimization routine to find the value of C_L' that represents the best the measured sound spectrum. The procedure is illustrated on Figure 4.56.

More refined optimization techniques presented in Chapter 3 and Appendix D could be used. Once the problem is quite simple with only 2 dimensions and a cheap cost function, the Nelder-Mead Simplex optimization [163] is used. The cost function is the sum of the squares of the difference between the artificial and the measured sound pressure level, considering a frequency range ΔSt:

$$\text{cost function} = \sum_{\Omega \in \Delta\text{St}} \left[\text{SPL}(\Omega) - \text{SPL}_{\text{exp}}(\Omega)\right]^2 \tag{4.5.5}$$

The same procedure is used to fit the continuous coherence length function, see Appendix F, only without the use of the penalization factor at the peak.

This procedure does not aim at estimating fluctuating efforts based on the acoustic emission. It is used as a complement of the analysis performed for the coherence length in the characterization of the cross-section influence on the flow and the acoustic emission. The analysis is here limited to 20 and 40 m/s, velocities that have been used for the spanwise coherence measurements for all the geometries.

Based on previous section, one takes $\ell_s = 0.5d$, $\ell_c = \ell_g(\text{St})$ (measured). From Section 4.2.2, an estimate of the turbulence characteristic time can be obtained, being the intermittent behavior on the velocity signals for the other sections quite similar to what is seen for the circular cylinder. Thus, the value $n_c = 1.25$, the as used by Doolan [46], what corresponds to a near-wall

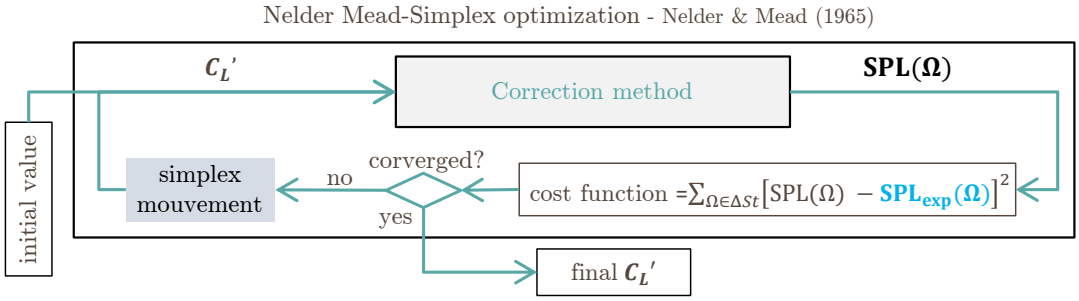

Figure 4.56: Diagram representing the methodology used to produce estimate the RMS lift coefficient from the minimization of the error between the modeled spectrum and the measures spectra. The "Correction Method" box is as presented on Section 4.5.2 and Figure 4.54.

dislocation time of 10 T [172]. C_L' is them educed by minimizing the error between artificially and measured acoustic spectra at each velocity for each cross-section.

4.5.2.1 Definition of lift coefficient

There are two possibilities to define the lift coefficient in this case. Either the frontal surface is considered, that is, the reference area is defined as the product of the height d and the length of the prism ℓ, or the streamwise surface is used, $b \times \ell$ (for the circular and the square section both definitions return the same value since $d = b$). They are calculated as follows:

$$C'_{L,d} = \frac{L'}{\frac{1}{2}\rho U_\infty^2 d\ell} \qquad C'_{L,b} = \frac{L'}{\frac{1}{2}\rho U_\infty^2 b\ell} \tag{4.5.6}$$

where L' is the RMS lift. Each coefficient can be applied in a different context. $C'_{L,d}$ may be directly compared to the drag and also considers the reference length for the wake. It can be considered as an engineering approach once the same analysis is performed for the whole group of geometries with a fixed reference, so the relation between the efforts can be direct among the set of different configurations, and interest quantities such as mechanical load or noise production are clearly stated. On the other hand, $C'_{L,b}$ is not based on a fixed reference, and direct comparison of the fluctuating lift is not possible only regarding the coefficients. The interest remains in its association with the pressure fluctuation, since the effective surface that products the lift is taken as reference, thus it is called here a physics oriented coefficient. The authors recommend the lift coefficient to be explicitly defined in future publications, especially in the case of different sectional breadth.

Since the main objective in this work is the comparison of the sectional influence, first definition ($C'_{L,d}$) is used, as can be seen in Equation (4.5.1). When not explicitly defined, C'_L is used as a synonym of $C'_{L,d}$.

4.5.2.2 Searching for best acoustic spectrum fit

An optimization is done for the eduction of the forces RMS coefficients, applying the same techniques used for the determination of the coefficients of the $\ell_g(\mathrm{St})$ functions (Appendix F). For this case, there is no penalization for the peak and the error is the square value of the difference of the sound pressure levels in decibels. Ideally, analysis should be performed using two parameters: C'_L and C'_D. Due to its small influence on the final result and in employed Curle's formalism [145] for the microphone at 90°, the fluctuating drag coefficient is not considered as a variable in the optimization and its value is fixed as $C'_D = C'_L/10$.

For the calculation of the fit, different Strouhal ranges are considered, in order to favor the reproduction of different parts of the spectrum. Obtained artificial spectra are presented on Figures 4.57 and 4.58 for the 4 tested sections, where each continuous lines corresponds to a

different band considered in the error function. The lowest limit is associated to optimization accounting only for the fundamental peak ($0.5\ \mathrm{St_{peak}} < \mathrm{St} < 1.5\ \mathrm{St_{peak}}$). When a broader range is selected, a higher level appears such as to add energy to the first harmonic and neighboring frequencies. Maximum value for the optimal C_L' presented on figures correspond to the error function being calculated for $0.5\ \mathrm{St_{peak}} < \mathrm{St} < 3.5\ \mathrm{St_{peak}}$ (note that for the circular cylinder at $U_\infty = 40$ m/s, all the measured sound spectrum above the peak is considered since the limit is St = 0.6).

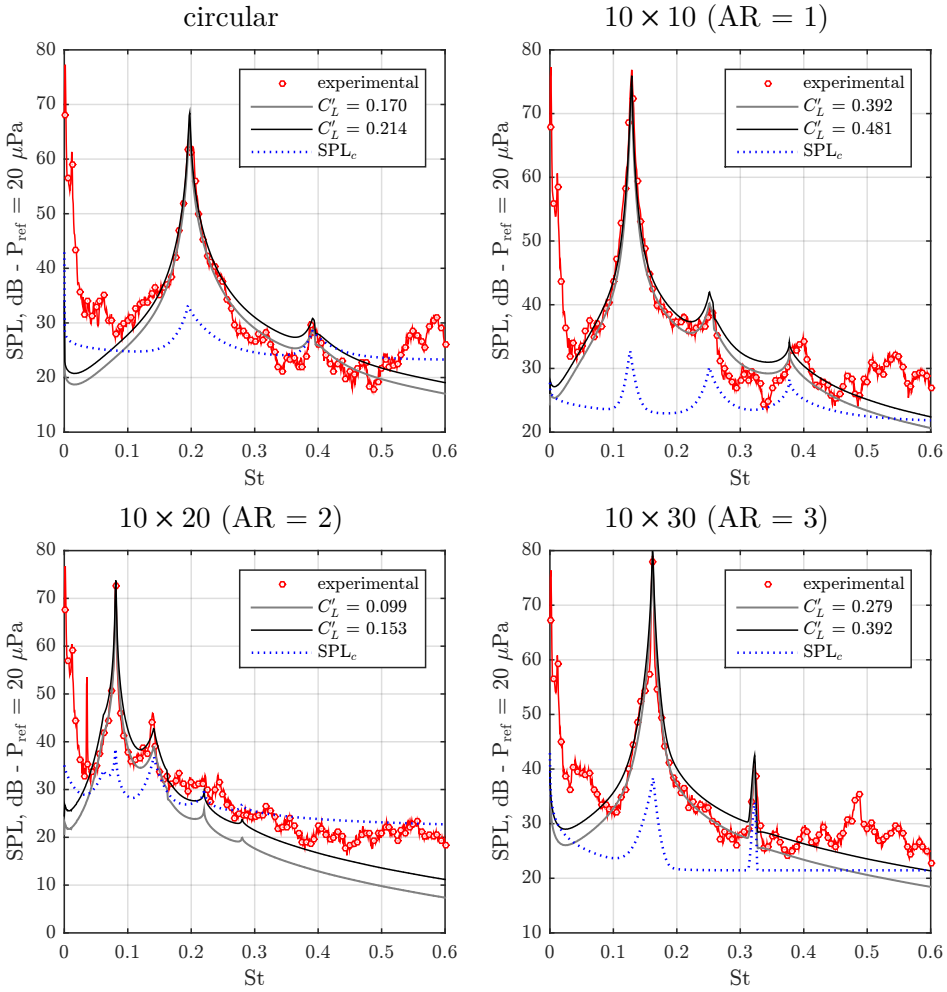

Figure 4.57: Experimental and optimal artificial sound spectra (solid lines) for $U_\infty = 20$ m/s. The turbulent time scale is fixed, with $n_c = 1.25$ (see Section 4.2.2), and $\ell_c(\mathrm{St}) = \ell_g$ is calculated with the coefficients as listed on Table F.1. Circle markers are added to the experimental curve at every 12.5 Hz for visual aid, and the dotted line represents the spanwise correction level $\mathrm{SPL_c}$ (see Equation (4.5.4)).

The current procedure reproduces extremely well the sound spectra found in the experiments, notably for the principal peak. This fact is fundamentally determined by the definition of C_L' that forces a good fit. However, the time decay and spectral correction levels defined by $\ell_c(\mathrm{St})$ and τ_c, fixed in the optimization, are in accordance and may be considered as a good estimate of the physics.

4.5.2.3 Discussion of the procedure and comparison to literature data

On Table 4.6, fluctuating lift and drag coefficients obtained in the optimization of the spectra are listed along with literature values. Since the hypothesis considered for the application of the correction algorithm is that the fundamental segment is small and completely correlated, the obtained RMS force coefficients correspond to sectional values.

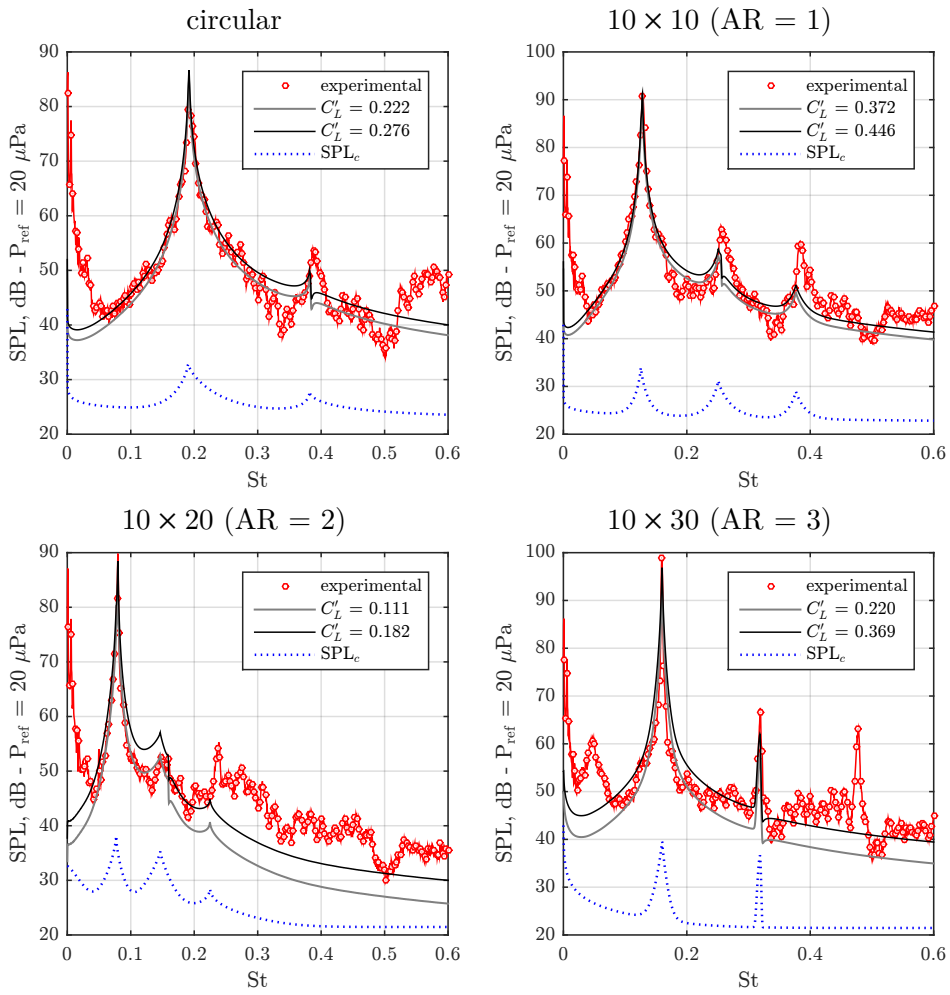

Figure 4.58: Same caption as Figure 4.57, for $U_\infty = 40$ m/s.

Table 4.6: Aerodynamic RMS lift coefficient in the literature and optimal values obtained from the fit of the sound spectra.

section	Re, 10^3		literature	optimal
circular	1.3 2.7	[171]	0.446 0.484	0.170-0.214 0.222-0.276
10 × 10 (AR = 1)	1.3 2.7	[227, 264]	1.15-1.71†	0.392-0.481 0.372-0.446
10 × 20 (AR = 2)	1.3 2.7	[209, 227, 240, 255]	0.83-1.36†	0.099-0.153 0.111-0.182
10 × 30 (AR = 3)	1.3 2.7	[209, 227, 240, 255]	0.35-0.57†	0.279-0.392 0.220-0.369

†: literature values of fluctuating efforts for rectangular sections are not given for the section.

The force coefficients are within the same order of what is available in the literature, however their magnitude is about 4 times smaller. Several factors could explain the discrepancy and are discussed next:

- From the purely acoustic point of view, **compactness and far-field hypothesis** present

in theoretical formulation are not always strictly respected in the current work. Even if the natural tendency would be an increase of the level, what would result in a higher estimate of the RMS lift coefficient, it remains an unknown and may spoils the result. The differences in the retarded time of the segments are not accounted in the spanwise correction formulation proposed by Seo & Moon [233]. Applying this correction could represent a necessity of increased segment sound levels, that is, bigger C_L', such as to reproduce the sound levels that are recorded, as can be deduced from formulation presented by Perot et al. [206] that considered this time delay.

- The fluctuating lift for the circular section is explicitly given as sectional [172]. The authors could not find information about the rectangular sections that stated clearly to correspond to **sectional values**, represented by a measurement segment of reduced spanwise extension. Presented C_L' are the normalization of the efforts over the whole cylinder, that is, only a division of the total fluctuation lift by a reference surface ($\ell \times d$ or $\ell \times b$). In this case, the information available in the coherence length is actually present twice, and values of C_L' are miss-evaluated.

- There is a remarkable scatter in fluctuating coefficients data, especially scarce in experimental procedures. The fluctuating efforts are influenced by wind-tunnel conditions such as the incoming turbulence intensity [153, 161, 273]. Also, the tendency observed in the literature is to reinforce the 2D behavior of the flow by running simulations for very short cylinders and/or using end plates. Such choices artificially increase C_L', described numerically [65, 159] and experimentally [20, 104, 253], where a length of at least $20d$ is recommended for the circular section to prevent **confinement**. Considering that the coherence length is bigger for the other cross-sections studied in this work, it is implied that an even larger span is necessary to avoid the influence of the end conditions. Initially, Szepessy [253] attributed the increase of fluctuating lift to an increase of spanwise correlation. Current results (Section 4.3.3) show that the spanwise correlation is rather similar to what is observed with end-plates when comparing to pressure coherence measurements performed by Casalino & Jacob [30] for the circular cylinder. In that sense, it is believed that the modification of the efforts due to end plates is rather associated with the increase of strength of the vortex and an increase in the perfect de-phasing from the upper and lower parts of the flow, later proposed by Szepessy [252]. This could also justify why the sound levels obtained by Casalino & Jacob are similar to the current results with a cylinder that is of 1/3 of the current span. Even the results of Norberg [172], that clearly highlights the effects of end plates, may not be adapted for the present range (ℓ/d = 26 with supporting plates), as discussed in an earlier work [170].

- Values on the table for the rectangular sections are not at the same **Reynolds number**. However, the difference is considered to be small due to the observed independence of the flow around rectangular sections in this regime, as mentioned previously in this document. This is noted for the square section in the review by Bai & Alam [10] and for rectangular sections of aspect ratios 1/3 and 3 in the article by Yang & Mason[279] and other works [153], it is also evidenced in the values presented in the graph of C_L' versus the aspect ratio of the section at several Reynolds numbers, Figure 4.61, that is discussed further.

- The **time scale parameter** τ_c is grossly set and could not be determined with certainty for the different geometries in study. Also, the fact that the fit is good is not a sufficient criteria. In preliminary tests it was noted that multiple combinations of C_L' and n_c values can result in fits of similar quality. Further analysis was performed with the optimization of the n_c value considering a fixed C_L', selected as the average value from the range listed in Table 4.6. Naturally the shape of the spectra is well respected, since it is the value that is minimized, however, results were unsuccessful with exaggerated values of n_c (from 5 to 170) and sound pressure levels at the vortex shedding frequency were consistently overestimated. Only reasonable result was obtained for the rectangle of AR = 3.0, with n_c

between 1.7 and 7.3, but in accordance to the other results, peak level is overestimated of the order of 5 dB. The conclusion is that n_c = 1.25 can be considered as a representative value, however there is an intrinsically imprecision associated with this value, thus, an imprecision exists for educed lift coefficient values.

- The effort model considered for Curle's analogy inside the algorithm are taken as **pure tones**. This means that all the energy is concentrated in f_{peak} and its first harmonic. Experimental and 3D simulations have a more distributed energy in the efforts spectra (for example, [166, 230] and [112, 153] for the circular and square cylinders, respectively), specially the neighborhood of the peaks. When compared to the tonal C_L' level, the only way of achieving the same magnitude at the peaks (which are the only points that influence the artificial sound spectra) would be to increase the total energy. Consequently, the optimal C_L' values are underestimated for not having a spectrally distributed energy and should be considered as pure tone analogous values.

4.5.3 How Reynolds number, shape, sectional lift and spanwise topology combine

4.5.3.1 Geometry ranking

The obtained hierarchies for flow and noise quantities are synthesized next, for the sound level (equally maintained for peak, band or overall), coherence length (considering the peak) and fluctuating lift (issued from the correction method, for a perfect sine wave):

$$\begin{array}{rccccccc} \text{SPL:} & \text{circular} & < & \text{AR} = 2.0 & < & \text{square} & < & \text{AR} = 3.0 \\ \ell_g\text{:} & \text{circular} & \lesssim & \text{square} & < & \text{AR} = 2.0 & \simeq & \text{AR} = 3.0 \\ C_L'\text{:} & \text{AR} = 2.0 & < & \text{circular} & < & \text{AR} = 3.0 & < & \text{square} \end{array}$$

It appears that there is no direct association between the 3 hierarchies, although the extrema (circular and AR = 3) are reproduced in both SPL and ℓ_g. It must be recalled that the time scale τ_c is considered the same for all cases.

As predicted by King & Pfizenmaier [111], the square prism has a coherence length larger than the circular section. However, the difference in the sound emission is also due to a modification of the wall pressure fluctuations, represented by the increase of the RMS lift coefficient. Current results reinforce partially the statement of Iglesias [83], that implied that the difference in sound emission of the rectangular sections comes from an increase of the coherence length. Even tough there is a prominent variation of the ℓ_g, it is as important as the difference of the C_L' when square and other rectangular sections are compared. A computation of the contribution of each variable based on the model in Equation (1.2.32) was tried. The results were not capable to fully described the difference noted in the wind-tunnel, and may indicate that the model is too reducing or that some of the hypothesis may not be fully respected.

4.5.3.2 Sectional lift fluctuations and spanwise coherence length

It is possible to conceive that the sectional lift coefficient grows in the inverse direction of the coherence. A relationship is presented in Figure 4.59, considering the peak coherence length returned from the continuous coherence length functions and the center of the range of fluctuating lift coefficients issued from the optimizations of spectra, along with a regression law. The correction and fitting procedure is also performed for the other velocities tested for the circular section that were not discussed in the previous session (U_∞ = 15, 25 and 30 m/s). Error bars are set as $0.7d$ for the coherence length and the limits for the $C_{L,b}'$. Note that the used coefficients are based on the breadth of the geometry.

Obtained least-squares fit regression laws (determination coefficient of $R^2 = 0.63$) are the following:

$$\ell_g(\text{St}_{\text{peak}}) = 1.41(C_{L,b}')^{-0.93} \qquad C_{L,b}' = 0.64\ \ell_g(\text{St}_{\text{peak}})^{-0.68} \tag{4.5.7}$$

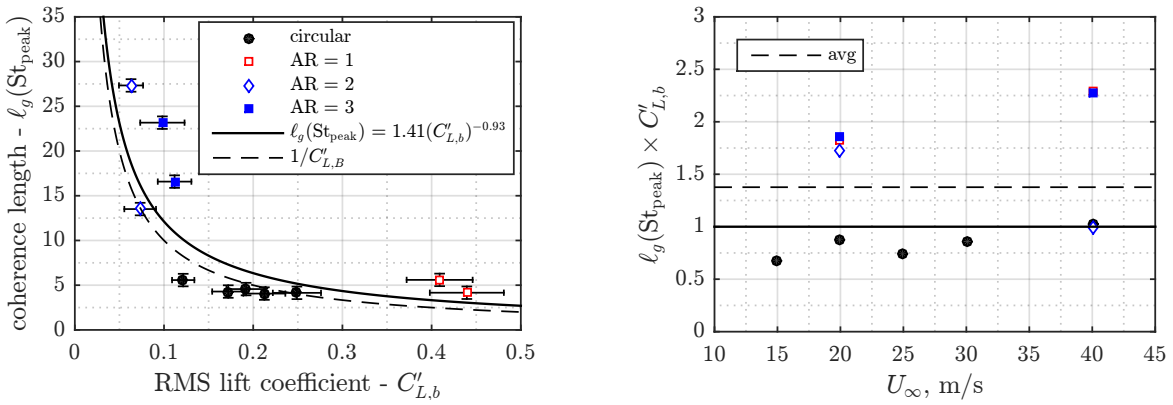

Figure 4.59: Comparison of the coherence length at the peak frequency $\ell_g(\mathrm{St_{peak}})$ and the b based RMS lift coefficient $C'_{L,b}$ (left) and the evolution of their product with the flow speed (right).

Since the method used to obtain the estimations of the fluctuating lift coefficient involves the coherence length as an input, the result may be biased. Even so, and despite the impreciseness in the determination of C'_L, this result seems to be physically consistent. That is: a cross-section with an important pressure fluctuation (large $C'_{L,b}$) will most likely generate a spanwise flow distribution that is as well uncorrelated (small ℓ_g). The same comparison is not successful when the engineering coefficient $C'_{L,d}$ is considered, since the lift is directly modified by the available streamwise surface and does not correspond only to the vortex strength and associated pressure fluctuations.

Even if preliminary, a link between the sectional and axial behavior has thus been unearthed. Further analysis concerning the shape influence on the sectional behavior are presented next.

4.5.4 Further analysis of the sectional behavior

4.5.4.1 Reynolds number dependence for the circular cylinder

Figure 4.60 presents the evolution with the Reynolds number of the observed estimation of C'_L for the circular cylinder and literature values; a length of $\ell/d = 0$ indicates a sectional coefficient, obtained either from the movement of a short segment or from wall pressure captors distributed around the section. Current results are represented by markers at the limits of the range of optimal values, illustrated in Figures 4.57 and 4.58, and lines that connect the center of those ranges. Coefficients deduced from the application of Equation (1.2.32) (without the use of the near wake correction term) with the quantities associated to the vortex shedding frequencies are as well presented, that is:

$$C_L'^2 = \frac{\overline{P}^2{}_{\mathrm{peak}} 16 c^2 r^2}{\rho^2 U_\infty^6 \mathrm{St_{peak}}^2 \ell \ell_g(\mathrm{St_{peak}}) d} = \frac{\overline{P}^2{}_{\mathrm{peak}}}{\rho^2 U_\infty^4} \frac{16 \mathrm{Ma}^2}{\mathrm{St_{peak}}^2} \frac{r^2}{\ell \ell_g(\mathrm{St_{peak}}) d} \tag{4.5.8}$$

In Figure 4.60 current values are about 3 times smaller than what is observed in the literature. Many factors influence that difference, as listed on Section 4.5.2.3. As stated earlier, the objective of the present lift eduction is not to measure the lift coefficient from the noise emission, but rather compare between different cross-sections the perfectly sinusoidal lift and drag fluctuations that would generate an equivalent sound emission. Even if the amplitudes are underestimated, the increase of C'_L with the Reynolds number present in published values is well reproduced in current results, what can be directly associated with the reduction of coherence length discussed in Section 4.3.3.1. The fact that the values derived from Equation (1.2.32) are smaller is attributed to the absence of the correction associated with the distribution of the energy around the spectra peak, what is accounted with the τ_c time scale. Furthermore, we may conclude that if the

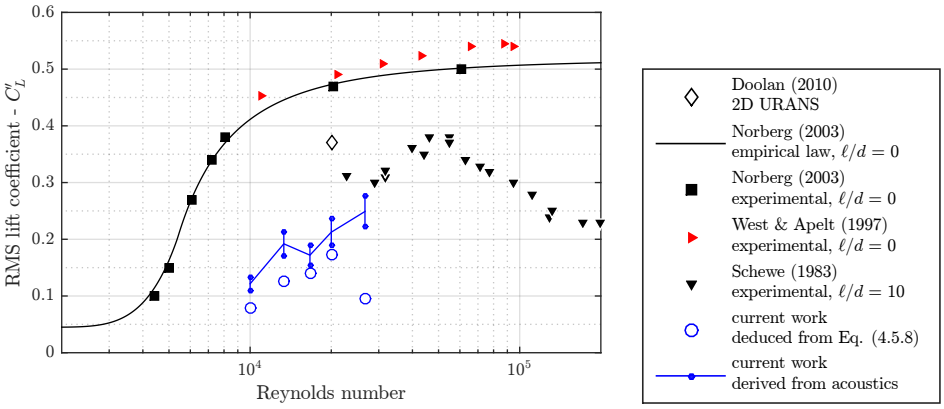

Figure 4.60: Comparison of currently estimated circular cylinder RMS lift coefficients with literature values at different Reynolds numbers [46, 172, 230, 273].

spanwise energy distribution is removed (it is going to be applied later in the correction), the corresponding C'_L values that would produce the same acoustic energy are significantly smaller.

In that sense, the success of the first test case presented by Doolan [46] with an overestimated C'_L is attributed to performing the validation with an also overestimated sound emission data from Casalino & Jacob [30]. Their sound pressure levels are quite similar to the new results introduced here, Figure 4.43, even if the current cylinder is more than 3 times longer and flow velocity is higher. This similarity is believed to be the effect of the end plates. The used coherence length of $5d$ is also overestimated, as discussed in Section 4.3.3.1.

4.5.4.2 Influence of aspect ratio for rectangular cylinders

4.5.4.2.1 General trends For the rectangular section, the literature and current C'_L values are presented in Figure 4.61. Low (left) and high (right) Reynolds number values are considered. Similarly to what is employed on previous plots, current results are represented by markers at the optimal values issued from the optimization and lines connect the central position for each aspect ratio. Note that only one experimental study could be found and that all the cited works use very small extent in the spanwise direction.

The evolution of the fluctuating lift consists of an increase until a maximum C'_L at around AR = 0.6, and a decrease for longer geometries. The "golden ratio" of 0.6 has been discussed in several previous works, notably the references of Figure 4.61. This bi-phased behavior of the $C'_L \times$ AR curve is common for all geometries as discussed in Section 2.2.2.1, with the analysis of the flow around other shapes such as ellipses and triangles. After the breadth has a significant number of diameters, there is a slight recovery, in a somehow oscillating curve that may be associated with the position where the vortex are generated. Similar shape is present in all plots, except for low Reynolds number when considering the breadth as the reference length. This traduces the fact that at lower Reynolds number, the available surface is a main factor in the creation of the lift fluctuation and the pressure tends to infinity with the decrease of b. The behavior is different at high Reynolds number, where the short sections are associated with small $C'_{L,b}$. This may be due to a loss of coherence associated with the small available surface in the streamwise direction. Even if the detachment point is fixed, the vorticity generating region is rather small and more subjected to vortex dislocations and three dimensional developments. This correlates to the discussion about the inverse relationship that is noted between the sectional efforts and the spanwise coherence.

4.5.4.2.2 Magnitudes It may be noted that the educed values for C'_L are close to literature for the rectangular section of AR = 3, what may be related to two factors. First, the coherence length is really high, what represents an almost two-dimensional flow. In this case, a true sectional C'_L, measured for a reduced section, would be close to the same as a total cylinder

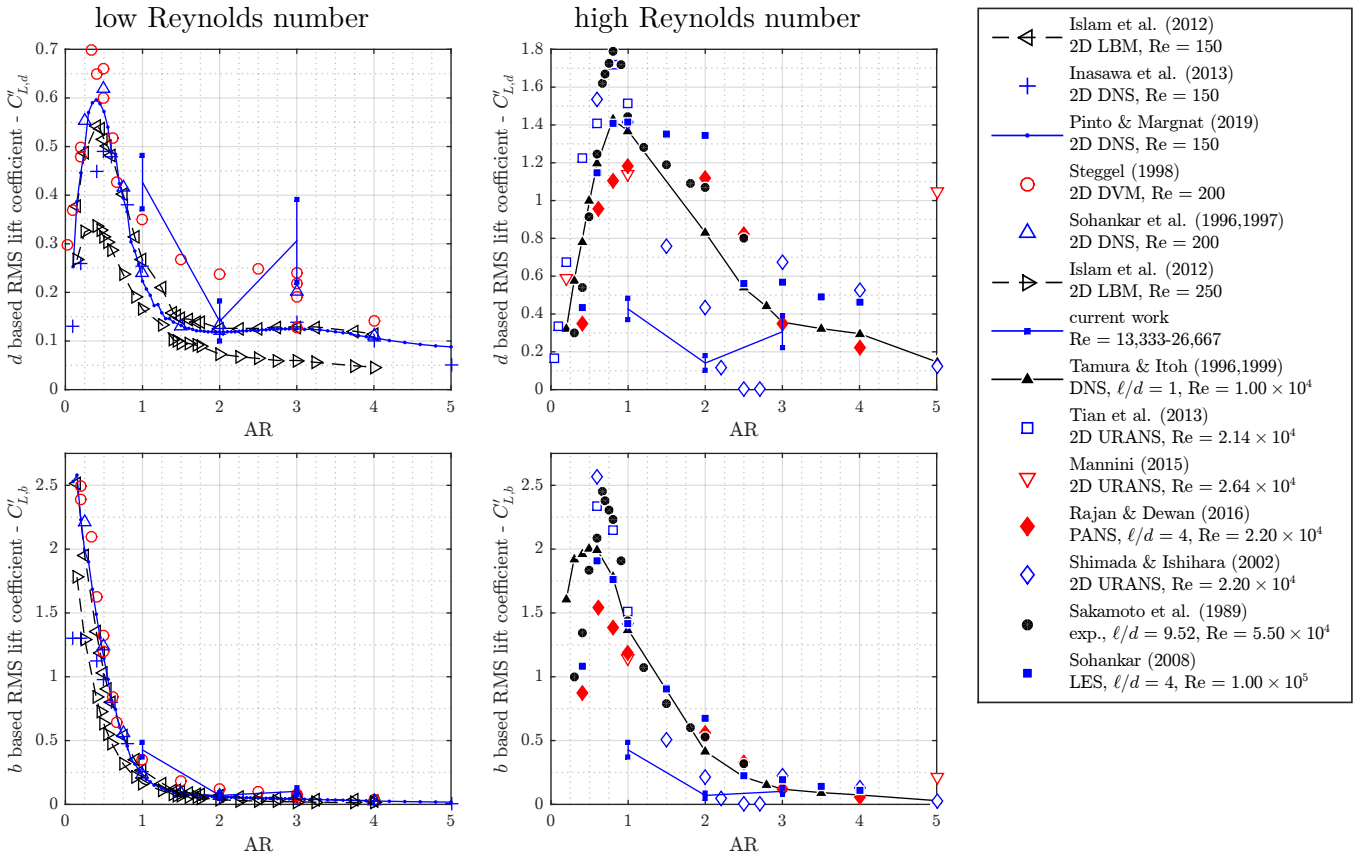

Figure 4.61: Comparison of currently estimated rectangular cylinder d based and b based RMS lift coefficients with literature values at low [89, 91, 241, 243, 245] and high Reynolds numbers [143, 209, 227, 238, 240, 255, 256, 262].

force coefficient normalized by ℓ. Secondly, as can be noted on the velocity signals in Figure 4.5 and 4.6, the fluctuating lift for that geometry is more of a pure tone, so that an estimation of the perfect sine wave lift and drag in the statistical correction is close to the reality of the flow.

It can also be inferred that, per available lifting surface, the longer geometries undergo less pressure fluctuations, as presented on the graph for $C'_{L,b}$. However, that effect is surpassed by the increase of the available surface and of the coherence, thus giving an increase of the sound emission, exactly in the opposite direction of what is noted on the sectional behavior. We may also imply from current results that the behavior noted in the OASPL vs AR graph (Figure 4.52) is not due to the modification of the Strouhal, as discussed by Octavianty et al. [174], but rather to a combined increase of ℓ_g and $C'_{L,d}$. Naturally, all three quantities are intrinsically related and a clear description of their relationship should need a greater database and a refined physical modeling.

Another important conclusion concerns the fact that the obtained C'_L are relatively close to those obtained by low Reynolds number simulations. The current procedure implies that the transition from a short to long geometry is possible, meaning that an homogeneity in the axial dimension is assumed. Also, the correction of the tonal efforts implies that most of the low amplitude features of the aerodynamic efforts spectra can be neglected and that the peak neighborhood is correctly represented by an exponential decay. In short, given these hypotheses and current results, the procedure allows a connection between the 2D low Reynolds number (tonal) to 3D flows: the transition from low to high Reynolds number is condensed in the τ_c correction, and the transition from 2D to 3D in the coherence length. This is particularly consistent in the case of rectangular sections, where the flow is rather Reynolds number independent for an important range of velocities.

4.5.5 Conclusions

The statistical analysis and correction procedures for the spanwise influence on cylinder's airframe noise proposed by several authors [30, 46, 206, 233] is successfully applied to different cross-sections, leading to estimations of the RMS lift coefficient considering the aerodynamic effort as two perfect sinusoidal waves.

Despite the good fit that is observed in the modeled sound spectra, the educed fluctuating lift coefficients are smaller than what is present in the literature. Although that behavior was expected due to the simplification of the efforts into clean sinusoids and the difficulty associated with measuring fluctuating aerodynamic efforts, it may indicate a deficiency in the applied technique. In all likelihood, the not so strict respect of the far-field and compact conditions would not produce such important errors. Furthermore, the spanwise statistical correction method used in this work is a reformulation of the classical equations derived by Curle [37] and Phillips [191]. To the authors knowledge, until this day no simultaneous measurement of all the ingredients (C_L', spanwise coherence and sound emission) has been performed. It is thus necessary, as hoped by Lighthill [133], to perform a systematic test of such physical and mathematical reasoning. The work of Leehey & Hanson [130] is the only one the author could find that performed something similar to that. However they were using a vibrating cylinder at a low Reynolds number range (4,000 to 6,450) and performed the calculations with the correlation length, that is found to be lower than the coherence length (see Section 4.3.5). Similarly, the validity of the procedure to correct the sound emission by sum of segments, that was used to educe the sectional lift in this article, has to be further checked both theoretically and experimentally, as far as fair comparison between shapes is targeted.

As implied by previous works [83, 111] and discussed in Section 4.3, sharp-edged sections are more coherent. However, the difference in coherence alone does not justify the offset found in the acoustical signature of each prism. Performed analysis shows that they are not only more coherent but also have greater sectional RMS lift coefficient. Current results also indicate that the spanwise coherence length is inversely proportional to the breadth based fluctuating lift, such that the acoustic emission is more influenced by the modifications of the pressure fluctuations and the available surface than by the spanwise characteristic of the flow, not forgetting that the latter is a result of the first two.

As discussed the description and comparison of the sound signatures of the different beams in Section 4.4, the rectangular sections have an aeroacoustic response that is similar to the circular cylinder at lower Reynolds number. This contributes to the argument that the shape modification may be seen as a change of the status of the flow in terms of its energetic state and the relative distance to transitions between the different topologies. This is directly related to the discussion at low Reynolds number in Section 2.2.3.4.

Nevertheless, the similarities between then flow response to an increase of the aspect ratio at low and high Reynolds number indicates that the mechanisms of vortex shedding and bluff body noise is open to a geometrical based description. However, it must be stated that this conclusion is made from the analysis of rectangular sections, with sharp edges. Even if the trend is proven to be global in 2D, laminar flow (see Section 2.2.2.1) its existence in 3D and at other flow regimes may be exclusive to such category of cross-section. Thus, firm conclusions demand analysis with other geometries.

The link between the 2D and 3D behaviors naturally concerns the de-phasing. But once the 3D effects are also a consequence of the axial extent of the cylinder, an analysis of the evolution of the sound pressure level with the length of the cylinder is as well necessary. This point is investigated on following section, with the description of new measurements and the proposition of empirical laws.

4.6 Influence of the length of the cylinder on sound emission

A study on the relationship between the aeroacoustic response of the flow and the cylinder's length is performed. This analysis originates in the difficulty to compare current measurements

with literature values due to its multiple and correlated parameters, as discussed on Section 4.4.3.1.

The influence of the length was directly studied by King & Pfizenmaier [111], Moreau & Doolan [158] (for wall mounted cylinders) and Karthik et al. [106]. In the observations of these authors, the aeroacoustic response of a cylindrical body is separated in three distinct regions. For a span lower than 10 diameters ("short" cylinder), flow is highly influenced by end-effects (three-dimensional flow topology marked by tip and/or joint vortices) the aeolian tone level is rather unchanged by the increase of the cylinder's length. From ℓ/d = 10 to about 25, there is a remarkable rise of the sound pressure levels and also an increase of the vortex shedding Strouhal number. Also, there is a linear behavior in the log-log plot of the SPL with ℓ/d, that is, the sound intensity follows an exponential growth with the increment of the length of the cylinder. This region, defined here as "medium", marks the path through the establishment of the vortex shedding as the main phenomenon of the wake. For extended cylinders (ℓ/d > 25 30, "long"), the vortex shedding properties, notably the vortex shedding frequency, are established and, in terms of the von Kármán instability, the cylinder may be considered infinite.

A cylinder is considered long by King & Pfizenmaier [111] when it is larger than 25 diameters, length above which the Strouhal number is fixed. For Karthik et al. [106], this value is 20 when based on response of the vortex shedding Strouhal number to ℓ/d, however, when analyzing the flow spanwise coherence (discussed in Section 4.3), a threshold of 30 diameters is proposed. In terms of the flow aerodynamics, King & Pfizenmaier [111] acknowledged that a ℓ/d of about 45 seems to be necessary for the end effects to be insignificant. The influence of the span, albeit still noticeable, is no longer a dominant factor in establishing the values of the acoustical parameters.

4.6.1 Performed experiments

The experimental setup and flow conditions are the same as presented on Sections 4.1.2 and 4.1.3.2, with flow from 10 to 40 m/s. The change of the relative length of the cylinders is achieved by modifying the diameter: ℓ is fixed in 700 mm and d varies from 6 to 20 mm, what results in a range of ℓ/d from 35 to 117. Measurements contemplate square and circular cross-sections; all the cylinders are made of aluminum, with the exception of the square prism of dimension d = 14 mm that is made of steel. The complete list of flow regimes and considered cylinders is presented on Table 4.7.

Table 4.7: Considered cylinders and flow conditions.

d, mm	20	16	14	12	10	8	6
Re, 10^3	13.3-53.3	10.67-42.67	9.33-37.33	8.00-32.00	6.67-26.67	5.33-21.33	4.00-16.00
ℓ/d	35.00	43.75	50.00	58.33	70.00	87.50	116.67
circular section	✓	✓	✓	✓	✓	✓	✓
square section			✓	✓	✓	✓	✓

Some of these configurations have been tested before current study and the results are present on previous parts of the manuscript. Since there are 6 months between the measurements, these shapes are tested again to safeguard the comparisons to eventual environmental and setup changes. No remarkable difference is observed between the experiments that were performed at the two different times, thus, previous results complement this analysis, enriching the results from a statistical point of view.

Naturally, the direct comparison of the different measures is not possible. A scaling aimed to isolate the effect of the length in the sound emission is proposed and discussed next.

4.6.2 Scaling law for the comparison of sound measurements

Considering the deduction by Fujita [57], derived from the developments of Curle [37] and Philips [191], the RMS value of the acoustic pressure fluctuation may be estimated as (see Section 1.2.3.2,

near-field contribution is taken as 1):

$$\overline{P}^2(r) = \frac{\rho^2 U_\infty^6 \mathrm{St}^2 \ell \ell_c C_L'^2}{16 c^2 r^2} \tag{4.6.1}$$

In order to allow the comparison between different measurements, notable from the literature, a scaling based in Equation 4.6.1 is implemented. First, the sound attenuation is accounted by the product of the square of the normalized distance r/d, as proposed by King and Pfizenmaier [111]. The RMS pressure is then multiplied by all the physical quantities associated with the incoming flow present in the right side of the equation ($1/\rho^2$, $1/U_\infty^6$ - as done in [158] - and c^2), reducing to the non-dimensional scaled sound pressure (SSP):

$$\mathrm{SSP} = \overline{P}^2 \left(\frac{r}{d}\right)^2 \frac{c^2}{\rho^2 U_\infty^6} \tag{4.6.2}$$

The same approach is applied when scaling with overall, peak or band values (defined on Section 4.4.1), using the pressure issued from the following transformation:

$$\overline{P}^2 = P_{\mathrm{ref}}^2 \; 10^{SPL/10} \tag{4.6.3}$$

The effect of the proposed correction is exemplified next.

4.6.2.1 Effect of the scaling for the circular cylinder spectra

A comparison of the obtained scaled sound pressure spectrum with literature values is presented on Figure 4.62. There is a constant offset between the sound pressure levels (a) and scaled pressure (b). The observed behavior is a consequence of the differences in the experimental setup, notably the presence of end-plates at the nozzle extremities in the works used as reference [30, 73] and due to the modification of the cylinder's span ℓ, matter discussed later on this section. In the case of experiments performed in same configuration, data from Haramoto et al. [73], the scaling was able to correct the hierarchy between the cylinders of ℓ/d = 10 and 30.

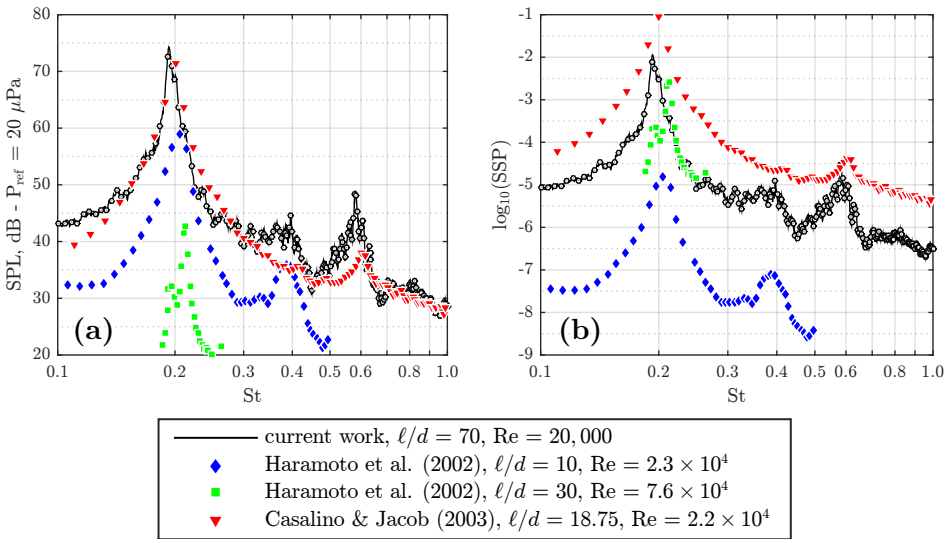

Figure 4.62: Spectral distribution of the sound pressure level (a) and scaled sound pressure (b) of the sound emission of the circular cylinder. Current work data are not corrected for background noise and circle markers are added at every 12.5 Hz. Comparison with data from the literature [30, 73].

One-third octave scaled levels are presented in Figure 4.63. Once again, the difference of the length of the cylinders (ℓ/d) and the flow Reynolds number provoke the offsets for both the level and the frequency. However, the scaling reduces the offset between the curves representing

current data measured at different flow velocities. The hierarchy of the magnitudes between the different cases is in accordance with their respective cylinder's length and is maintained after the scaling.

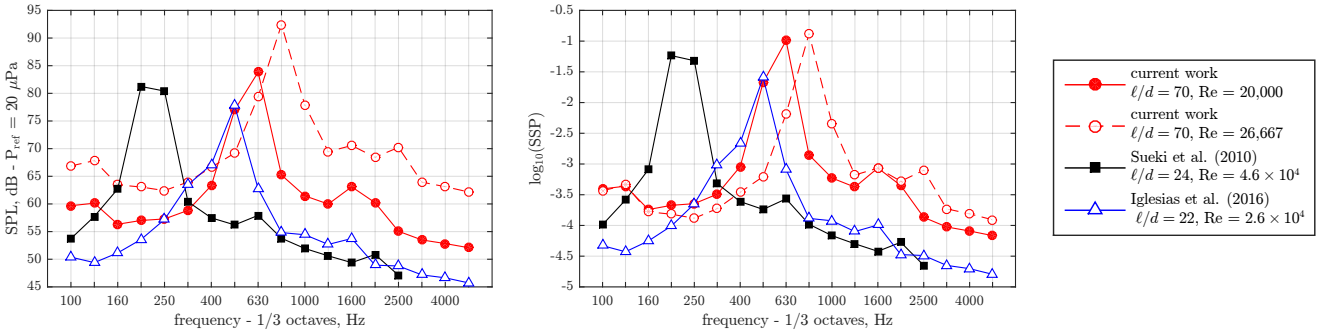

Figure 4.63: Effect of the scaling on 1/3 of octave sound pressure spectra for the circular cylinder, d = 10 mm at Re = 20,000 and Re = 26,667 and data from the literature [83, 250].

4.6.3 Literature review on data for the sound emission of the circular cylinder

In order to assess the influence of the length on the noise emission of long circular cylinders, data is collected from several works in the literature, see Table 4.8, and the evolution of the noise emission as a function of ℓ/d is presented in Figure 4.65 for all the noise criteria used on this work (OASPL, PSPL and BSPL) and multiple experimental and numerical setups. When not tabulated, data is acquired digitally from the presented graphs using a script that scales the values based on the axis, the impreciseness of the procedure is considered way lower than the resulting values.

Once flow velocity, cylinder diameter and microphone position vary between works, a direct comparison is inconclusive, thus both sound pressure level and the scale sound pressure introduced in Equation 4.6.2, are illustrated. Note that the selected limits for the plots of scaled sound pressure correspond to the same values used in the SPL plots considering the current experimental setup (r = 1 m, d = 10 mm) and a flow of 20 m/s, so the effect of the scaling is visible. For performing the scaling, air properties are defined arbitrarily when not clearly stated, same goes for the flow velocity, when necessary deduced from the given Reynolds number and the diameter, using an usual viscosity value.

Different experimental setups are present on the literature and were classified as follows (illustrated in Figure 4.64): closed (C) setup, defined by the presence of end-plates directly connected to both of the wind tunnel nozzle, being the plates acoustically invisible or not, where 2 boundary layers are present, such as for Fujita [57]; open (O) setup, that is, when there are no end-plates and the cylinder surpasses the flow section in both ends, each one associated to one mixing layer, such as the current work and Iglesias et al. [83]; and the finite (F) setup, for cylinders that have one [111] or the two [106] free-ends. Wall-mounted geometries [158] are placed on this category as well. Other numerical results are also used for comparison, but once the used boundaries (2D simulation, symmetric or periodic) are not representative of any of the previously cited configurations, they are categorized as none (N).

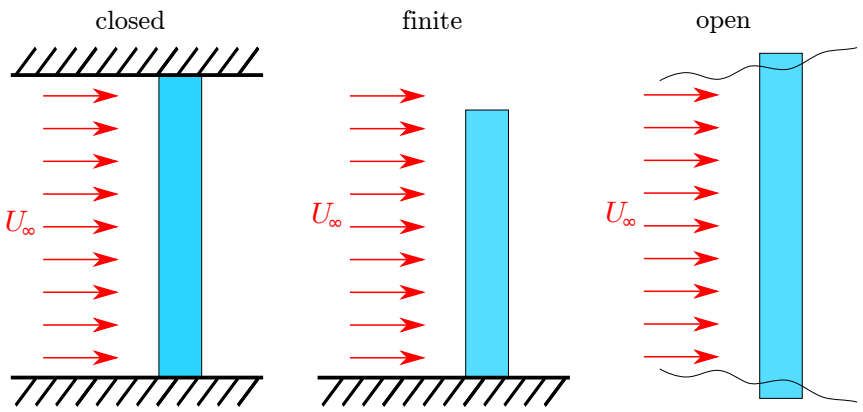

Figure 4.64: Illustration of the different experimental configurations.

Table 4.8: Literature data for circular cylinder sound production (chronological order).

#			reference	setup*	c, m/s	ρ, kg/m^3	r, m	d, mm	U_∞, m/s	Re	ℓ/d
1	[109]	◁	Keefe (1961), experimental	O	335.28	1.2266	3.81	4.7625	14.66-48.55	$4.6\times10^4 - 15.4\times10^4$	32
2	[130]	☆	Leehey & Hansons (1970), experimental	O	†	‡	1.000	3.91	15.3-24.7	4000-6450	97.40
3	[53]	●	Fink et al. (1976), experimental	C	†	‡	2.25	51	31-125	$1.05\times10^5 - 2.58\times10^5$	15.43
4	[210]	▽	Revell et al. (1977), experimental	O	†	‡	2.438	19.05	70.08	8.90×10^4	25.3
5	[85]	◀	Iida et al. (1996), experimental	C	†	‡	1.000	40	3.75-52.5	$1\times10^4 - 1.4\times10^5$	12.5
6	[35]	*	Cox et al. (1998), 2D URANS - fully correlated	C	340.0	‡	2.438	19.05	68.00	90,000	5-26.3
7	[73]	♦	Haramoto et al. (2002), experimental	C	†	‡	1	10-30	11.4-39.1	2.3×10^4	10-30
8	[30]	▼	Casalino & Jacob (2003), experimental	C	340.0	1.225	1.380	16	20	22,000	18.75
9	[177]	■	Orselli et al. (2009), 2D URANS - fully correlated	N	†	‡	2.430	19	71.05	90,000	2.5-25.3
10	[177]	▶	Orselli et al. (2009), 3D LES - corrected	N	†	‡	2.430	19	71.05	90,000	25.3
11	[111]	+	King & Pfizenmaier (2009), experimental	F	343.3	‡	1.4	20	32-69	$4.24\times10^4 - 9.14\times10^4$	2-35
12	[250]	★	Sueki et al. (2010), experimental	C	†	‡	2.000	25-45	27.7	$4.6\times10^4 - 8.3\times10^4$	13.33-24
13	[57]	▼	Fujita (2010), experimental	C	†	‡	1.000	20	13.5	18,000	10
14	[57]	●	Fujita (2010), experimental	C	†	‡	1.000	267	14-110	$2.5\times10^5 - 2\times10^6$	11.24
15	[81]	▲	Hutcheson & Brooks (2012), experimental	C	†	‡	1.980	2.4-25.4	24.0-58.3	$3.8\times10^3 - 10^5$	36-384
16	[158]	·	Moreau & Doolan (2013), exp. - wall-mounted	F	†	‡	0.515	6	25-35	$1.0\times10^4 - 1.4\times10^4$	1.6-22.6
17	[83]	○	Iglesias et al. (2016), experimental	O	†	‡	1.4	12	20-50	$1.64\times10^4 - 4.11\times10^4$	22
18	[61]	♦	Geyer & Sarradj (2016), experimental	C	†	‡	0.5	30	8.18-53.52	$16.2\times10^4 - 106\times10^4$	9.33
19	[18]	×	Bensow & Liefvendahl (2016), 3D LES + FW-H	F	345	‡	1	12	50	41100	5
20	[106]	×	Karthik et al. (2018), 3D LES + FW-H	F	343.3	1.184	1.400	20	64	84,770	3-35
21	[9]	■	Arcondoulis & Liu (2018), experimental	C	†	‡	1	40-60	20-40	$0.5\times10^5 - 1.6\times10^5$	6.67-10
22		□	current work, experimental	O	340.0	1.225	1	6-20	10-40	4,000 – 53,333	35-116.67

*: experimental setup (**O**pen, **C**losed, **F**inite and **N**one);

†,‡: undefined values, arbitrarily selected by the current author as $c = 340$ m/s and $\rho = 1.225$ kg/m^3, respectively.

The current sound pressure levels, even considering the cylinder in carbon fiber (not shown), are in the same range of literature values, for the three criteria that are used. This means that even if the conditions of compactness and far-field are not always strictly respected, the influence of current microphone position remains negligible or at least at the same level of the deviations observed in previous works. For the scaled values, the data points are closer attesting the physical pertinence of the proposed scaling. Also, a trend associating the increase of SSP with the length of the cylinder is noted in the multiple plots.

4.6.3.1 On the dispersion of the data

Naturally, the data is still scattered even after the scaling, what is justified by two reasons. First, components of the flow emission, notably the fluctuating lift and the coherence length (present in Equation 4.6.1), are influenced by the flow inertia to viscosity ratio synthesized by the Reynolds number, as expressed, for example, by the data and the empirical laws of $C_L'(\mathrm{Re})$ and $\ell_g(\mathrm{Re})$ proposed by Norberg [172] and Iida et al. [86], respectively. Thus, for a same length, different flow velocities result in different sound levels even if the corrections associated to the change in the Mach number and the acoustic efficiency (U_∞^6) are performed. Secondly, the experimental setup and end conditions taken in the numerical calculation are an indistinguishable factor. The two points are discussed next.

A minor effect (not discussed further) is due to the fact that the velocity exponent is not strictly 6, as supposed in the scaling.

4.6.3.1.1 Correction using empirical laws for the Reynolds number dependent quantities Even after the normalization by the physical quantities of the incoming flow, other elements remain in the formulation, that is, the Strouhal number, the coherence length and the RMS lift coefficient, all shape (ℓ) and Reynolds dependent quantities.

In order to isolate only the effect of the length in the magnitude of the sound emission, a correction of the scaled sound pressure is performed using the RMS lift coefficient empirical law proposed by Norberg [172]. It is composed by 7 equations, each one of them regarding a different flow regimes. It ranges from $\mathrm{Re} = 47$ to 3.4×10^5; values corresponding to flows that are superior to the upper limit are considered to have the RMS lift coefficient of the biggest value contemplated by the empirical law, that is $C_L' = 0.1446$ for $\mathrm{Re} = 3.4 \times 10^5$. A sample of the considered values and the global effect of the transformation is available in Figure 4.66, where the data for the overall sound pressure levels, experiments performed with the finite and open configurations, are presented.

In general, the correction by the division of the square of the RMS lift coefficient represents a multiplication of the SSP by a factor of 5.5726 (value issued from the regression curve represented in Figure 4.66). For most of the points considered in this work, the modification is rather small due to the fact that most of them lies in a plateau of $C_L' \approx 0.5$ (Reynolds number of about 10^4 to 10^5). However, the correction has an influence in the analysis due to the current results, that were performed at a Reynolds number range ($5 \times 10^3 - 10^4$) that presents a significant variation of the amplitude of the RMS lift coefficient. This conclusion is extended for the measurements performed at velocities higher than the discussed plateau, where there is a drop in C_L'.

In what concerns the coherence length, the sole empirical relationship that could be found by the author is the proportionality law proposed by Iida et al. [86]. Note that in their work, the coherence length is defined by the integral of the coherence in the spanwise direction. They propose that ℓ_c is proportional to $\mathrm{Re}^{-0.5}$. A direct use of such law is not possible due the different definition of the coherence length, also, this relationship is considered problematic due to the dispersion of the points for flows at high Reynolds number, as can be seen on Figure 13 of the cited article.

The Strouhal number is as well modified by the Reynolds number. However, due to its small variation considering the studied range (from $\mathrm{St} \approx 0.19$ to 0.21 [172], Figure 1) and its dependency to the length of the cylinder for $\ell/d < 30$ (discussed on the introduction of current section), no transformation is performed.

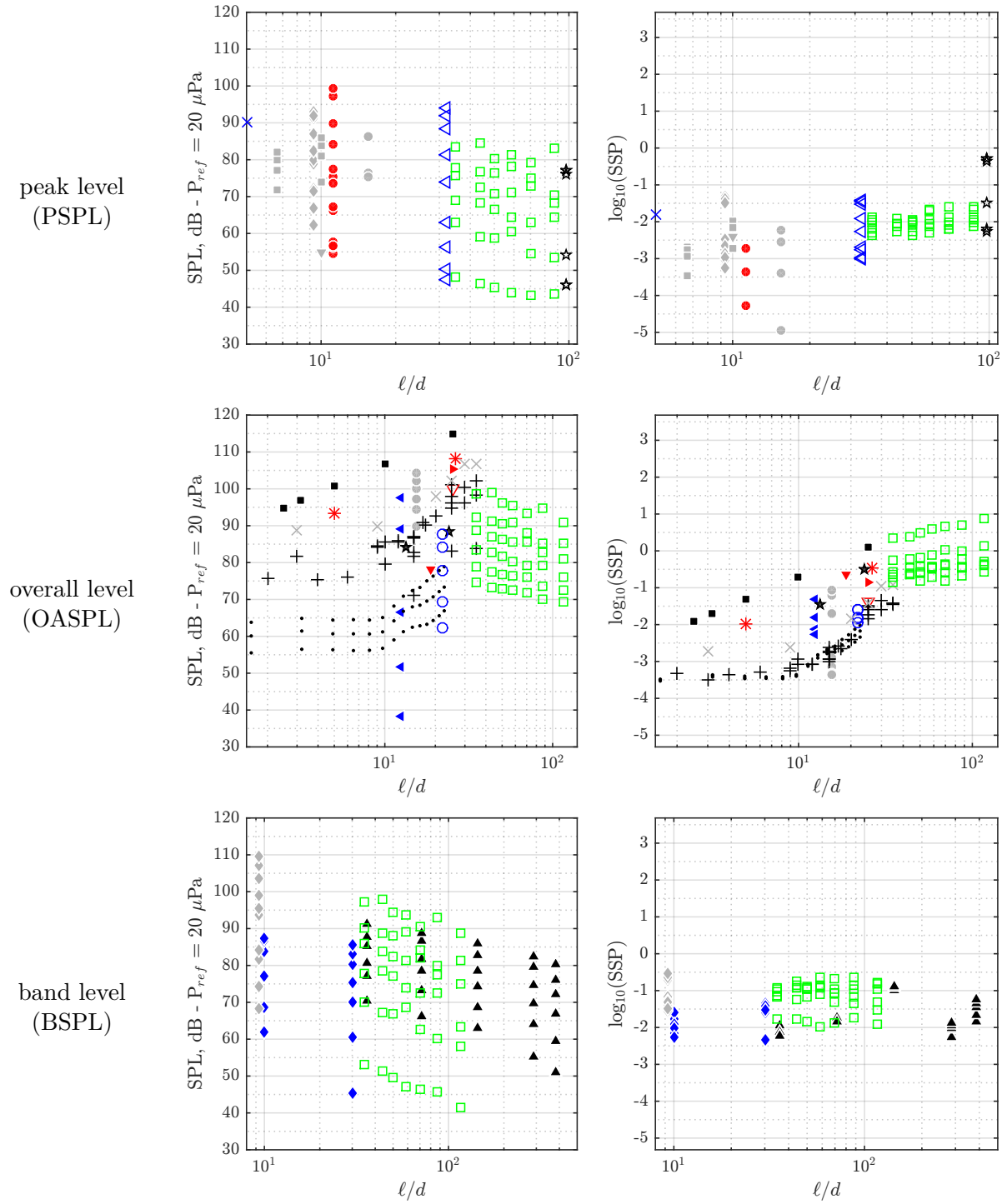

Figure 4.65: Peak, overall and band sound pressure levels (SPL, left) and corresponding scaled sound pressure (SSP, right) for circular cylinder on the literature (details concerning the flow conditions and parameters used in the scaling are present on Table 4.8). **Closed**: ● Fink et al. (1976) [53], ◀ Iida et al. (1996) [85], ◆ Haramoto et al. (2002) [73], ▼ Casalino & Jacob (2003) [30], ★ Sueki et al. (2010) [250], Fujita (2010) [57] - ▼ d = 20 mm, Re = 18,000 and ● d = 0.297 m, multiple Reynolds (some points are not shown in the SSP plot), ▲ Hutcheson & Brooks (2012) [81]; **Open**: ◁ Keefe (1961) [109], ☆ Leehey & Hansons (1970) [130], ▽ Revell et al. (1977) [210], ○ Iglesias et al. (2016) [83], ◆ Geyer & Sarradj (2016) [61], ■ Arcondoulis & Liu (2018) [9], □ current work; **Finite**: + King & Pfizenmaier (2009) [111], · Moreau & Doolan (2013) [158], × Bensow & Liefvendahl (2016) [18], × Karthik et al. (2018) [106]; and **None** (numerical results that do not reproduce the boundaries existing in the experiments): ∗ Cox et al. (1996) [35], Orselli et al. (2009) [177] - ■ 2D fully correlated and ▶ 3D simulation.

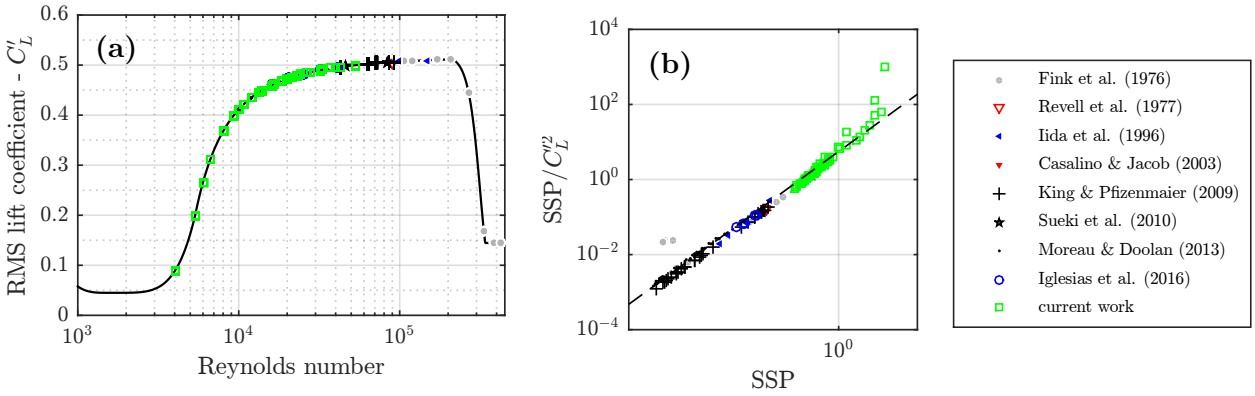

Figure 4.66: Effect of the RMS lift coefficient in the scaled sound pressure magnitude: (a) estimated RMS lift coefficient for the current and literature values based on the set of empirical laws proposed by Norberg [172] (continuous line); and (b) the corrected SSP versus SSP, hatched line represents the regression law $5.5726\ \mathrm{SSP}^{1.0174}$, least-squares fit.

In conclusion, the RMS lift coefficient correction is the only transformation applied for the analysis of the tendencies. The distinction in response issued from the differences in the experimental setup is discussed further, based on the values divided by C'^2_L.

4.6.3.1.2 Difference in terms of the experimental setup The scaled sound pressure values for the OASPL, all wind tunnel configurations, are presented in Figure 4.67, with and without the RMS lift coefficient correction discussed in Section 4.6.3.1.1. As discussed previously, apart from current results and analysis at very high Reynolds number values, the graphs are rather unchanged with the division by C'^2_L.

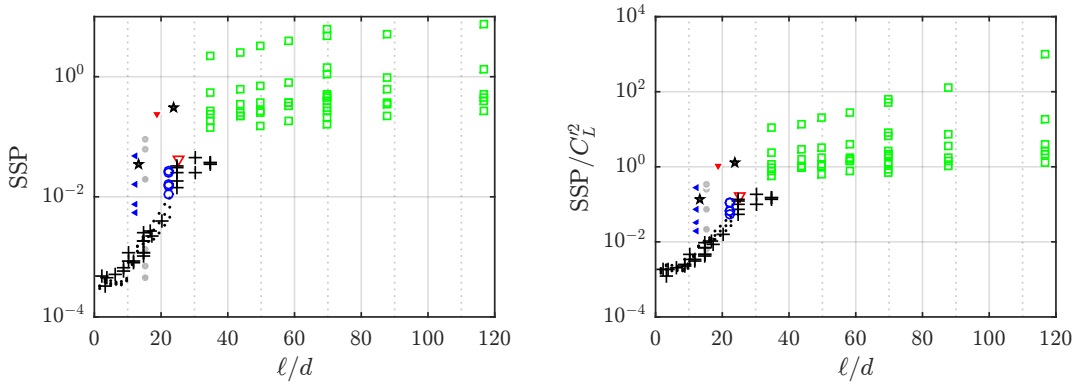

Figure 4.67: Scaled sound pressure from the OASPL, without (left) and with (right) the correction by the square of the RMS lift coefficient. Symbols are as presented on Figure 4.65.

Part of the dispersion of the points remain even after the correction by C'^2_L. However, it is possible to cluster the data between measurements in closed (filled markers) and open/finite (empty markers) setups, being the experiments performed in the first setup (at ℓ/d of about 20, SSP/C'^2_L between 10^{-2} and 1) systematically louder. According to Szepessy [252] and as already discussed in Section 4.5.2.3, end plates are responsible for an increase in the fluctuating aerodynamic efforts, probably by imposing a perfect dephasing between the vortex shedding happening on the upper and lower segments of the cylinder. Consequently, the lift amplitudes are more elevated than in the case of free cylinders. Such phenomenon of the modification of the flow by the use of end-plates is referred by King & Pfizenmaier [111] as a stabilization effect. In the case of short cylinders ($\ell/d < 10$), the increase in the aeolian tone is issued by the elimination of the vortex at the free-end, as showed by Becker et al. [16], what harmonizes and strengths the von Kármán vortex shedding. By adding walls to the limits of the cylinder, it is

also possible that acoustic effects such as reflections or even reverberation are created. They would artificially (in the sense that is not related to the flow or the vortex shedding) increase the sound levels.

Though, even if the totality of values, obtained from the multiple experimental setups, are considered, a global relationship between the sound pressure levels and the length of the cylinders is evident. Next, the trends are quantified in a regression analysis and empirical laws are proposed.

4.6.4 Empirical laws for the evolution of the scaled sound pressure with the length

The relationship between the sound pressure levels and the length of the cylinders are quantitatively described in a regression analysis. In Section 2.3.1, the concepts of regression analysis and model selection have been discussed in the context of the study of empirical laws relating the flow quantities of laminar 2D simulations.

The distinguishable trends in the SPL(ℓ) plot are discussed. Further next, empirical laws are presented. Initially, local power laws considering different ranges of ℓ/d are considered. At a second time, a sigmoid curve is fitted for the continuous representation of the relationship SSP(ℓ/d).

Data from numerical works, represented in Figure 4.65, are not considered in the regressions. The experimental configuration within the data were acquired (closed, finite or open) is as well taken into account.

4.6.4.1 Different trends in the sound emission vs length graph

From the current and gathered values, the three trends discussed earlier are evident (see Figure 4.68), with short ($\ell/d < 10$, sound emission unchanged by the length), medium ($10 \leq \ell/d < 30$, exponential growth of the sound emission with the length) and long ($\ell/d \geq 30$, small gain of sound emission with the length).

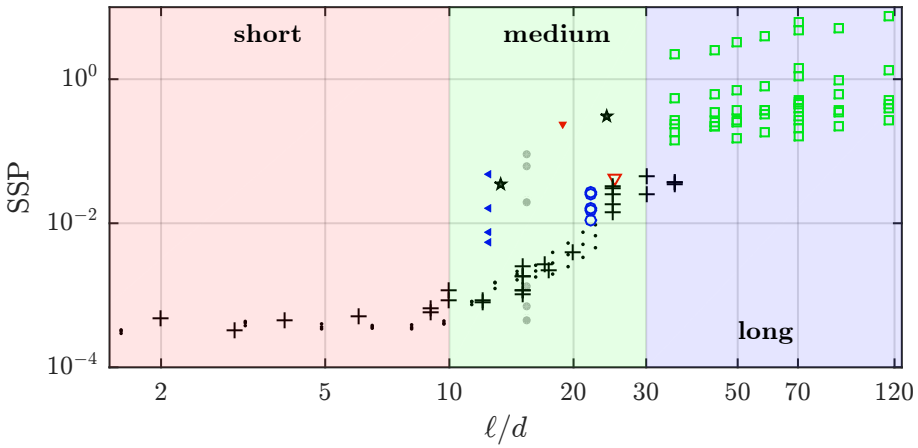

Figure 4.68: Different trends of the sound emission of the circular cylinder with the evolution of the length. Symbols are as presented on Figure 4.65.

The fact that the long cylinders do not follow the trend for medium cylinders is rather unexpected. Controversially, this saturation is seen in [35] and reappears in [48, 177], when modeling long cylinders by interposing the source terms issued from 2D simulations, fully correlated cylinders. It is also argued by Perot et al. [206], when proposing a method for modeling the sound emission of long cylinders that accounted for the retarded time. Results are reproduced in Figure 4.69. There is a well marked exponential increase of the sound emission until about 50 diameters. Beyond 100 diameters that behavior is changed and the levels fluctuate around 112

dB. This stagnation of the increase of the OASPL is justified by the interference between the different spanwise stations of the cylinder, made possible by the offsets of the time the sound waves need to they reach the observer.

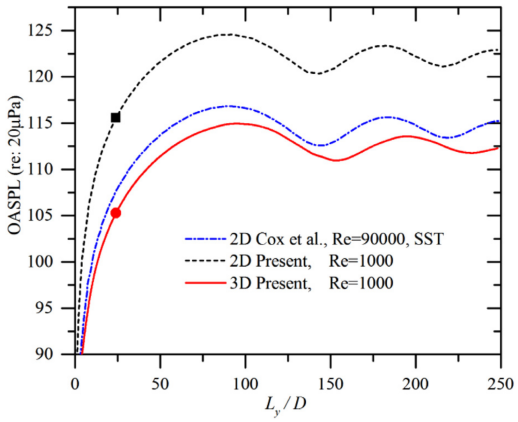

Figure 4.69: Evolution of the overall sound pressure level with the length of the cylinder, completely phased. Reproduced from [48] with data from [35].

The current points do not represent established or fluctuating levels, but a smaller decrease. There is the possibility that the available data may not be enough to clarify the transition, with the necessity to more data points between 30 and 50 and after 120 diameters. Also, the natural flow de-phasing may act as a contributor or destroyer of the interferences originated in spanwise direction. Even so, the different trends are well marked, thus, a qualitative analysis based on curve regressions is performed and presented next.

4.6.4.2 Local regression curves - power laws

A regression analysis is performed considering the 3 regions discussed in Section 4.6.4.1 individually and also for the cylinders that are not short ($\ell/d > 10$). Following the principles of the many formulations derived from the Curle's analogy, the power law is used for the representation of the data:

$$\mathrm{SSP} = \alpha(\ell/d)^{\beta} \tag{4.6.4}$$

For short cylinders, the exponential laws is slightly better (adjusted R^2 of 0.27 instead of 0.21). The sound pressure levels for such small bodies are almost constant and independent of the length, also, at such magnitudes of the determination coefficient, not much can be concluded on the goodness-of-fit of any of the models. Consequently, for consistency with the other trends, the power law is selected for all the ranges of ℓ/d and it is the only model presented here.

Analysis is performed for both the scaled sound pressure SSP and its version normalized by the square of the RMS lift coefficient $\mathrm{SSP}/C_L'(\mathrm{Re})^2$, so that the effect of comparing experiments at different Reynolds numbers is mitigated. Nevertheless, other aspects must be considered when performing the regression in what concerns the use of current data, discussed next.

4.6.4.2.1 Vortex shedding frequency and Reynolds number thresholds Two different conditions justify the dispersion of the current experiments and must be taken into account when performing the regressions:

- Due to the limited anechoic properties of the wind tunnel, some of the sound pressure measurements obtained for the lowest flow velocities ($U_\infty = 10 - 15$ m/s) and/or the biggest cylinders ($d = 16 - 20$ mm) may not be considered once they present vortex shedding frequencies and/or a great part of the tone under the cut-off frequency of 200 Hz (for instance,

f_{peak} = 208 Hz for d = 10 mm and f_{peak} = 148 Hz for d = 14 mm at U_∞ = 10 m/s). Consequently, a threshold of vortex shedding frequency of 250 Hz (margin of 50 Hz so that all the emerged noise associated to the aeolian tone is above 200 Hz) is considered;

- Similar conclusion can be performed in what concern the flow regime. As noted in Figure 4.66, for $10^3 < \mathrm{Re} < 10^4$ there is a change in the flow behavior associated to the shear layer transition [276]. This is accounted in the correction by the square of the RMS lift coefficient discussed in Section 4.6.3.1.1, however, the eventual modifications on the spanwise decorrelation (described by the coherence length ℓ_c) can not be corrected. Finally, a threshold of $\mathrm{Re} \geq 10^4$ is proposed.

In summary, when analyzing the current results, one must consider three possibilities: with and without the correction by the RMS lift coefficient; with and without the tone frequency threshold; and with and without the Reynolds number threshold. This may introduce a bias into the analysis, so all the combinations (8 possibilities) are tested. Also, the influence of measured values is identified by performing the regression with (indicated by the word "all") and without current values. Following those principles, the regression study for each noise criteria (overall, peak and band), analyzed separately, is presented next.

4.6.4.2.2 Regression laws for the OASPL data Regressions of the scaled sound pressure based on OASPL from literature and current experiments are presented in Figure 4.70, considering both SSP and SSP$/C_L'^2$. Analysis is focused on each sub-range discussed in Section 4.6.4.1, each curve is discussed next.

Short and medium cylinders The current experiments are performed with cylinders that are over 30 diameters long, thus, they do not appear in the analysis of short and medium cylinders. The number of observations is n = 26 for the short cylinders and n = 46 for the medium cylinders. The least-square fit coefficients and the adjusted determination coefficient are presented in Table 4.9 for the SSP and SSP$/C_L'^2$ laws. As presented in Figure 4.66, the correction by the RMS lift coefficient does not change the distribution of the points due to the similarities in terms of flow regimes for all the data in the literature. Thus, the two laws are only linearly scaled with a factor of, on average, 0.17 and the exponents β are practically the same.

Table 4.9: Regression laws for the sound emission of short and medium cylinders - Equation (4.6.4).

	range	α	β	adj. R^2
SSP	$\ell/d \leq 10$	2.846×10^{-4}	0.247	0.214
	$10 < \ell/d < 30$	1.612×10^{-8}	4.307	0.832
SSP$/C_L'^2$	$\ell/d \leq 10$	1.461×10^{-3}	0.215	0.247
	$10 < \ell/d < 30$	1.096×10^{-7}	4.177	0.840

For the short cylinders, the exponent is very small (around 0.2), and the determination coefficient is as well reduced. This behavior is in accordance with the fact that the vortex shedding is not the main topological features of those flows, highly perturbed by the extremities of the cylinders, ends of joints. An exponent of about 4.2 is found for the medium cylinders, with a considerable determination coefficient of 0.84.

Long cylinders For the total of 8 datasets that result from the combination of corrections and thresholds, there are three subgroups: considering only the new data; only the literature values; and both sources. For $\ell/d \geq 30$, the set of literature data points is too small and too

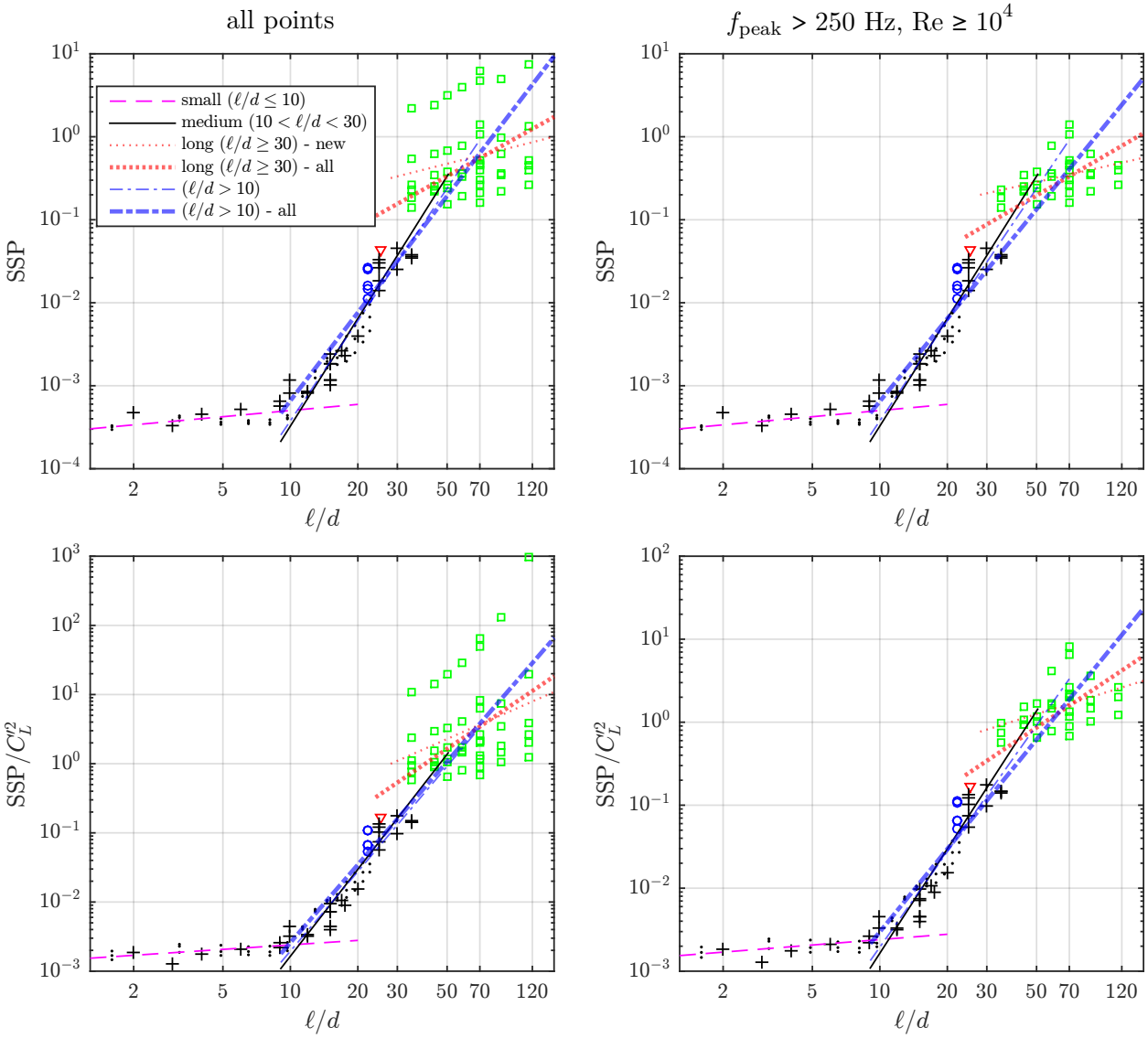

Figure 4.70: Regression laws of the scaled sound pressure from the OASPL as a function of the cylinder's length, log-log scales. Without (upper) and with (lower) the correction by the square of the RMS lift coefficient and without (left) and with (right) the exclusion of points based on the tone frequency and Reynolds number thresholds. Symbols are as presented on Figure 4.65.

concentrated to give a representative law ($n = 5$, only 2 different lengths) so not considered separately. Consequently, the analysis is reduced to only the last 2 subgroups, referred as "new" (only current data) and "all" (current + literature data). The regression results for both subgroups and considering the complete and reduced dataframes (with frequency and Reynolds limits) are listed in Table 4.10. For conciseness, not all possibilities are presented or described, focusing on the effects of the $C_L'^2$ correction and the full filtering (frequency and Reynolds number).

As it can be seen in Figure 4.70, there is a considerable change on the regression law when considering both current and previous data. The latter has lower magnitudes than what can be expected by an extrapolation of the current values to shorter cylinders. This difference pushes the average to lower values at ℓ/d around 35 diameters, which results in a larger exponent. For the SSP law, the exponent changes from 0.68 to 1.50, without correction, and from 0.61 to 1.57 when applying the frequency and Reynolds number thresholds. The α coefficient is reduced in order to follow the trend associated with an augmented slope. Similar effect is noted for the SSP/$C_L'^2$ curves.

In general, using the correction by the RMS lift coefficient increases the exponents. As dis-

Table 4.10: Regression laws for the sound emission of long cylinders ($\ell/d \geq 30$) - Equation (4.6.4).

	set	min f_{peak}	min Re	α	β	adj. R^2
SSP	new	0	0	3.27×10^{-2}	0.683	0.034
	all	0	0	9.46×10^{-4}	1.500	0.194
	new	250	10,000	2.58×10^{-2}	0.613	0.120
	all	250	10,000	4.16×10^{-4}	1.573	0.413
SSP/$C_L'^2$	new	0	0	8.63×10^{-2}	1.435	0.095
	all	0	0	3.01×10^{-4}	2.199	0.239
	new	250	10,000	4.62×10^{-2}	0.843	0.170
	all	250	10,000	7.32×10^{-4}	1.808	0.447

cussed in Section 4.6.3.1.1, for some of the Reynolds number experimented in the current study, the C_L' is quite different from the majority of the observations considered here. When performing the correction, the scaled sound pressure levels are increased relatively to the literature values and a slope of the order of the medium cylinders can be detected visually for the loudest points (corresponding to the low flow velocities). For the new data without the f_{peak} and Re filtering, for example, the exponents are 0.68 and 1.43 for SSP and SSP/$C_L'^2$, respectively.

When the filtered data frame is taken into account ($f_{\text{peak}} > 250, \text{Re} \geq 1000$), there is a decrease of the exponent, associated with the absence of the points that have its magnitude enlarged by the $C_L'^2$ correction. Those points are associated to an incertitude regarding the spanwise distribution of the flow.

In conclusion, there is a non negligible difference between the regression curves issued from the different combinations of dataframes. The simultaneous use of new and literature data does not reproduce well the trend that is noted for longer cylinders. It is preferred to consider the laws from the "new" data points as the curves with more physical accuracy. There must be further analysis to confirm the trend, but there seems to be a coherence in the stagnation of the sound emission associated with the acoustic interference (point discussed further with the analysis of the other two noise criteria - peak and band - in Section 4.6.4.2.3). Also, the use of the filtered values seems the most reasonable procedure.

Based on the previous paragraph, it is concluded that the sound emission for long cylinders ($\ell/d \geq 30$) evolves with the cylinder's length with an exponent of about 0.7 (average between the SSP and SSP/$C_L'^2$ laws). This exponent quantifies the discontinuity observed when going from the medium ($\beta = 4.2$) to the long cylinders. The act to consider both groups simultaneously in a regression will mask that difference. Even so, a statistically representative analysis to quantify a global trend is performed for the "not short" cylinders, that is, ℓ longer than 10 diameters, and it is presented next.

Cylinders longer than 10 diameters The transition between "short" and "medium" cylinders at $\ell/d = 10$ is well marked in the graphs and has been discussed in the literature [111, 158]. However, the transition between the medium and long cylinders, taken at $\ell/d = 30$ is not as clear, and it is fundamentally visible only with current data. To consider the possibility that there is not a well posed change in trends, analysis is also performed for the complete set of "not short" cylinders, that is, $\ell/d > 10$. Similar to the analysis for the long cylinders, only a part of the regression are discussed and presented in Table 4.11. The filtering is only applied for new data, so only two possibilities are considered for the literature values: with and without the $C_L'^2$ correction.

Naturally, the exponent obtained with the literature dataset is not that different from the value presented for the medium cylinders in Section 4.6.4.2.2 - 4.0 and 4.2, respectively. Only 5

Table 4.11: Regression laws for the sound emission of "not short" cylinders ($\ell/d > 10$) - Equation (4.6.4).

	set	min f_{peak}	min Re	α	β	adj. R^2
SSP		0	0	3.72×10^{-8}	4.006	0.864
	all	0	0	1.95×10^{-7}	3.529	0.826
	all	250	10,000	3.17×10^{-7}	3.311	0.893
SSP/$C_L'^2$		0	0	2.92×10^{-7}	3.824	0.864
	all	0	0	4.64×10^{-7}	3.746	0.812
	all	250	10,000	1.44×10^{-6}	3.315	0.900

points with ℓ/d bigger than 30 had been found in the literature for open and finite configurations and they follow the trend of the smaller cylinders. Also as expected, the addition of current data reduces the exponent (to about 3.5), since its points follow a quite smaller slope. The improvement of the determination coefficients is mostly due to the expansion of the range of cylinder lengths, naturally increasing the sum of totals. Same conclusions as those of the previous section can be performed regarding the influence of the $C_L'^2$ correction and of the filtering.

Statistically, for cylinders with a spanwise extent larger than 10 diameters, the sound emission amplitude is associated with the length with an exponent 3.3.

4.6.4.2.3 Analysis of the evolution of band and peak levels Data for peak and band values are rather scarce, as can be seen in Figure 4.71. Current data is filtered for the tone frequency and the Reynolds number ($f_{\text{peak}} > 250$ and $\text{Re} \geq 10,000$). Due to the reduced quantity of points at the range of small cylinders ($\ell/d > 10$), this range is not considered in the regression analysis. Also, the overall reduced number of observations demands that the analysis is performed combining open/finite and close experimental setups such as to allow a meaningful statistical study. Even if the points and curves are very scattered, some interesting conclusions may be derived from them.

With the 33 points issued from current experiments, a total of $n = 70$ observations are available when considering the band levels. The data from Haromoto [73] considers a band formed under the peak level minus 3 dB and not peak minus 10 dB like on the current work and in Hutcheson & Brooks [81] and Geyer & Sarradj [61]. Also, due to the reduced number of data points for small and medium cylinders, analysis is restricted to $\ell > 10$ and $\ell/d \geq 30$. Data is way more scattered than for the overall level, specially for the points of very small diameter ($\ell/d > 100$). A growth trend can be noted, more clear for the SSP/$C_L'^2$ plot, even so, the levels are more or less constant. The determination coefficients are diminutive (order of 0.01), factor that indicates that the response variable (the scaled sound pressure) is independent from the explanatory variable (cylinders length). This contributes to the observations around a stagnation of the level.

Similar conclusions are issued from the regression of the SSP derived from peak sound pressure levels. The observations performed in closed configurations (filled symbols, from [9, 53, 57, 61]) are overestimated when compared to the other data points (including current work). Also, for a fixed ℓ/d, that is, a given cylinder at different flow velocities, they are very spread what denotes an important deviation from the velocity exponent 6. The exponents for the medium range are 8 and 14, completely incompatible with the physics. Nevertheless, for long cylinders, literature and new data ($n = 48$), the exponents are 1.3 and 2.3 for SSP and SSP/$C_L'^2$, respectively. Even if numerically distant, the trend is similar to what is observed for the data issued from the overall sound pressure levels discussed in Section 4.6.4.2.2. Similarity also present in the regression for ($\ell/d > 10$), with β around 3 4.

It is evident that the analysis for the band and peak levels is quantitatively irrelevant due to

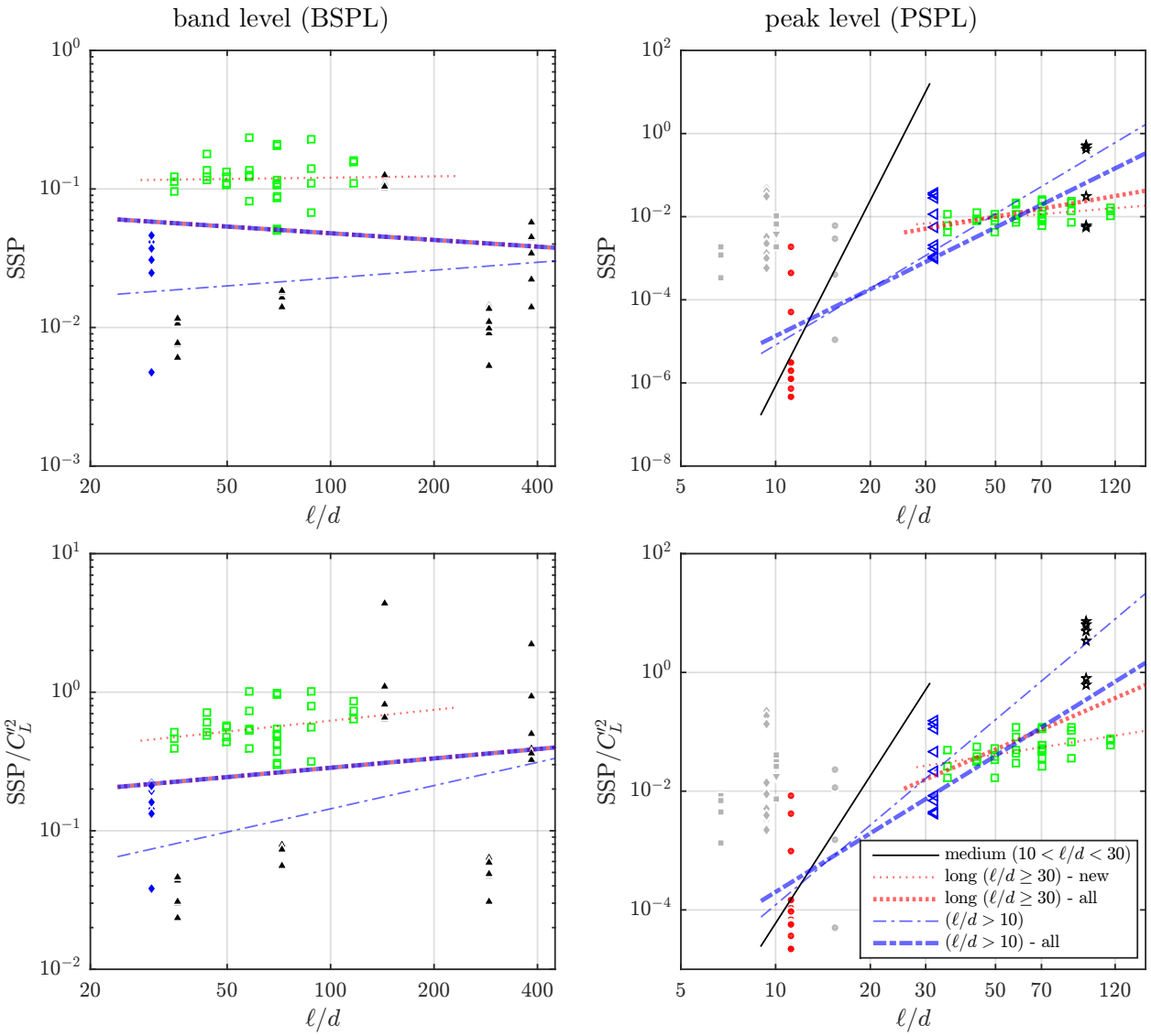

Figure 4.71: Regression laws of the scaled sound pressure from the band (BSPL, left) and peak (PSPL, right) levels as a function of the cylinder's length, log-log scales. Without (upper) and with (lower) the correction by the square of the RMS lift coefficient. Current data points are filtered based on the tone frequency and Reynolds number thresholds. Symbols are as presented on Figure 4.65.

the poor distribution of the explanatory variables (only a few lengths). However, three relevant aspects are reinforced by the analysis. First, the difference between closed and open/finite configurations is attested, clearly noted in the graphs for the SSP derived from band levels. Second, the argument of a stagnation of the amplitude of the sound emission for longer cylinders ($\ell/d > 100$) is also reinforced. Finally, the trends observed at the different ranges of length on the regressions of the OASPL values are corroborated by the analysis of the peak level values.

4.6.4.3 Global regression model - sigmoid curve

In addition to considering the different ranges and exploring the associated trends, a global regression model is proposed. The change in exponent represents an evolving gradient. The response to an increase of the cylinder's length starts with a fixed value, an expressive increase and a saturation, defined by an asymptotic maximum. This behavior, known as a sigmoidal function, is present in the binary regression models [52], that are aimed to reproduce a binary response (from 0 - "no" or "false" to 1 - "yes" or "true"). Commonly used in many domains where

there are qualitative variables (for instance, blood pressure status: high blood pressure, not high blood pressure [120]) and in neural networks [52, 120]. The principle is to estimate the evolution of the probability of being in one of the two states according to the explanatory variables.

Analogously, for the study of the acoustic emission of cylindrical bodies herein, the starting state corresponds to a flow condition that is not dominated by the von Kármán vortex shedding (thus, less noisy) and the final state is the flow fully defined in terms of its spanwise distribution, being limited to the acoustic interference associated to long cylinders.

The logistic model (also known as logit model), is considered:

$$Y = \frac{\alpha \exp(X)}{1 + \exp(X)} = \frac{\alpha}{\exp(-X) + 1} \tag{4.6.5}$$

where α is a real constant. In their most popular applications, the coefficient α is taken as 1 so the binary response (0 to 1) is represented. The explanatory and response variables are initially taken as the logarithm of the physical quantities, respectively $X = \beta \log(\ell/d) + \gamma$, $Y = \log(\mathrm{SSP})$, β and γ are also real constants. By the reciprocity that exists between the logarithmic and the exponential function, $a^b = \exp(b \log(a))$, the length ℓ/d may be evaluated directly after some mathematical development. For an easier regression, starting state is defined as 0, so a reference SSP is proposed. Also, the base of the analysis is set as 10, the standard in acoustic studies. Finally, the following model is proposed:

$$\log_{10}(\mathrm{SSP}) = \frac{\alpha}{1 + \beta(\ell/d)^{-\gamma}} + \log_{10}(\mathrm{SSP}_{\mathrm{ref}}) \tag{4.6.6}$$

Different from the previous case, this model is non-linear. Thus, the regressions are performed using the model fitting function `nls` [12] in `R` [208], the same environment employed in the regression analysis in Chapter 2, discussed in Section 2.3.1.3. The starting values for the non-linear regression are defined from manual testing of the proposed function.

Based on the previously presented discussion around the use of all of the measured values and its difference to the rest of the data, the analysis is limited to the filtered dataset ($f_{\mathrm{peak}} > 250$Hz and $\mathrm{Re} \geq 10,000$), uncorrected and corrected by the RMS lift coefficient (not shown). The obtained fit is presented in Figure 4.72. The different data sources are not represented on the graph, please refer to Figures 4.65 and 4.70.

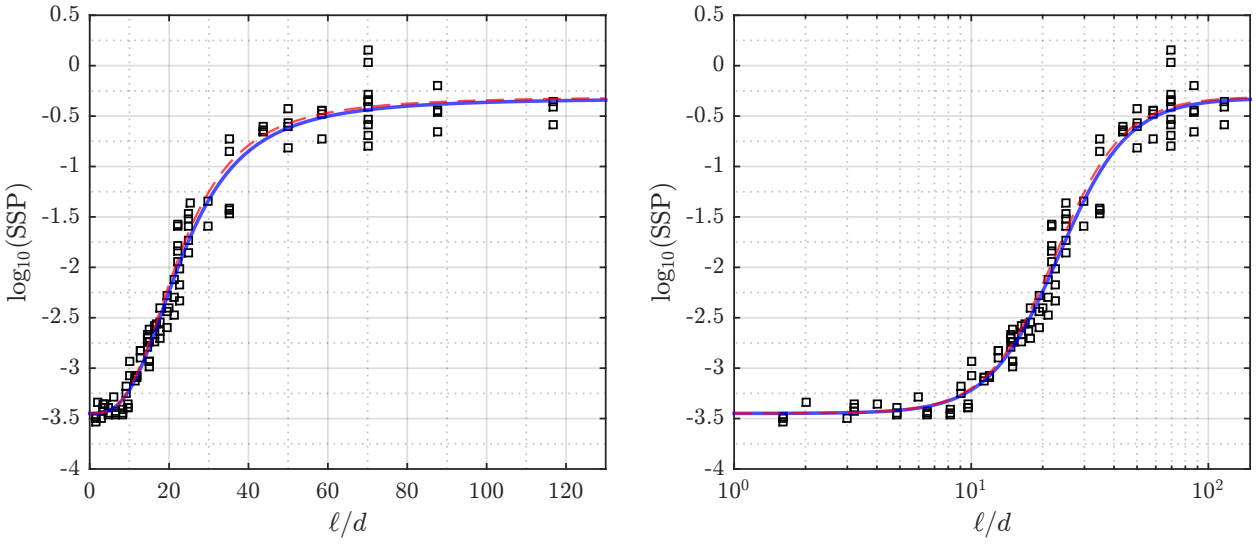

Figure 4.72: Regression laws of the scaled sound pressure from the overall sound pressure level (OASPL) as a function of the cylinder's length, lin-log (left) and log-log (right) scales, circular cylinder; continuous line represented the curve obtained using all the coefficients issued from the regression and the hatched line considers $\alpha = \pi$ and $\gamma = 3$.

The regression coefficients are listed in Table 4.12. The coefficients are barely unchanged when the corrected scaled sound pressure ($\mathrm{SSP}/C_L'^2$) is considered (α from 3.12 to 3.15 and β

from 2.97 to 2.80). An approximation to $\alpha = \pi$ and $\gamma = 3$ can also be performed, without any major losses in the quality of the representation of the relationship, as presented in Figure 4.72.

Table 4.12: Regression laws for the sound emission of circular cylinders, all lengths - Equation (4.6.6).

	α	β	γ	$\mathrm{SSP}_{\mathrm{ref}}$
SSP	3.127	1.163×10^{4}	2.970	3.558×10^{-4}
$\mathrm{SSP}/C_L'^2$	3.159	7.283×10^{3}	2.799	1.694×10^{-3}

The two asymptotes are presented in Table 4.13. The inferior asymptote seems off (non-null sound emission for a cylinder of length 0). As discussed earlier, at the range of the short cylinders ($\ell/d < 10$), the vortex shedding is not the major feature in the wake. Consequently, it is complicated to contemplate that change in sound generation mechanisms in a single, continuous curve. Nevertheless, this behavior of the regression curve is a result of the constant sound emission levels noted for the short cylinders reported in the literature, measured for cylinders that were at least $1.6d$ long. For a more refined description of the asymptotic behavior, it would be necessary to consider more data points at $\ell/d < 2$.

When the cylinders length tends to infinity, the SSP saturates at 0.476 (for instance, this represents a sound pressure level of about 80 dB for a cylinder of diameter $d = 15$ mm for a flow of $U_\infty = 10$ m/s and 100 dB for the same cylinder at $U_\infty = 40$ m/s. This behavior is considered physical, once it is in accordance with the increase of the retarded time and interference between the sound waves generated at different spanwise stations of the cylinder and the increase of the rates of attenuation of the pressure fluctuations prior to arrive at the observer, as discussed in Section 4.6.4.1. A comparison with similar modeling of the length effect laws found in the literature is conducted next.

Table 4.13: Asymptotes for the global regression law.

			SPL^*		
ℓ/d	$\log_{10}(\mathrm{SSP})$	SSP	10 m/s	20 m/s	40 m/s
0	-3.449	3.559×10^{-4}	34.1	52.2	70.3
∞	-0.322	4.762×10^{-1}	65.4	83.5	101.5

*: example of sound pressure level considering $d = 15$ mm, $r = 1$ m ($r/d = 66.7$), $c = 340$ m/s and $\rho = 1.225$ kg/m^3.

4.6.4.4 Synthesis and comparison to correction methods

4.6.4.4.1 Proposed models and comparison of the local and global curves From the multiple possibilities in terms of considering literature and/or new data, filtered or unfiltered values, and the correction by the square of the RMS lift coefficient, the following set of equations are proposed as the most coherent representation of the foregrounded experimental trends:

$$\mathrm{SSP} = \begin{cases} 2.846 \times 10^{-4} (\ell/d)^{0.245} & \text{for } \ell/d < 11.12 \\ 1.612 \times 10^{-8} (\ell/d)^{4.307} & \text{for } 11.12 \leq \ell/d \leq 47.85 \\ 2.585 \times 10^{-2} (\ell/d)^{0.613} & \text{for } \ell/d > 47.85 \end{cases} \tag{4.6.7}$$

Note that the ranges are modified such as to force the transitions to appear at the intersections between the curves (at $\ell/d = 11.12$ for the transition from short to medium cylinders and at $\ell/d = 47.85$ for medium to long) avoiding the gaps in the level calculation if one considers

the original limits of 10 and 30 diameters (see the intersections in Figure 4.73). An underlying physical meaning lies in the trend limits based on the curves intersections. For the upper bound of the small cylinders, the number of diameters is approximately equal to the equivalent to 3 times the coherence length at the vortex shedding frequency (Section 4.3.3.1.2), as noted by Moreau et al. [158] when pointing a similar number of flow cells for the change in trend. For the definition of a long cylinder, the number of coherence lengths is of more than 10 times the coherence length, also, it is in accordance with the length of 45 diameters necessary to fully mitigate the end-effects on the cylinder flow, proposed by King & Pfizenmaier [111].

For the global sigmoidal curve, following equation and coefficients are proposed:

$$\log_{10}(\mathrm{SSP}) = \frac{3.127}{1 + 11,633.18(\ell/d)^{-2.970}} + \log_{10}(\mathrm{SSP}_{\mathrm{ref}}) \tag{4.6.8}$$

The two different approach (local and global) regression result in 2 curves that have distinct asymptotic behaviors. As can be seen in Figure 4.73, the major features of the two curves are very similar, notable for medium cylinder ($10 < \ell/d < 30$). However, for small cylinders, the power law converges to a null sound emission while the sigmoidal function converges to a fixed value. The opposite is noted when ℓ/d is very large: the sigmoidal curve stagnates and the power law maintains its rate of increases.

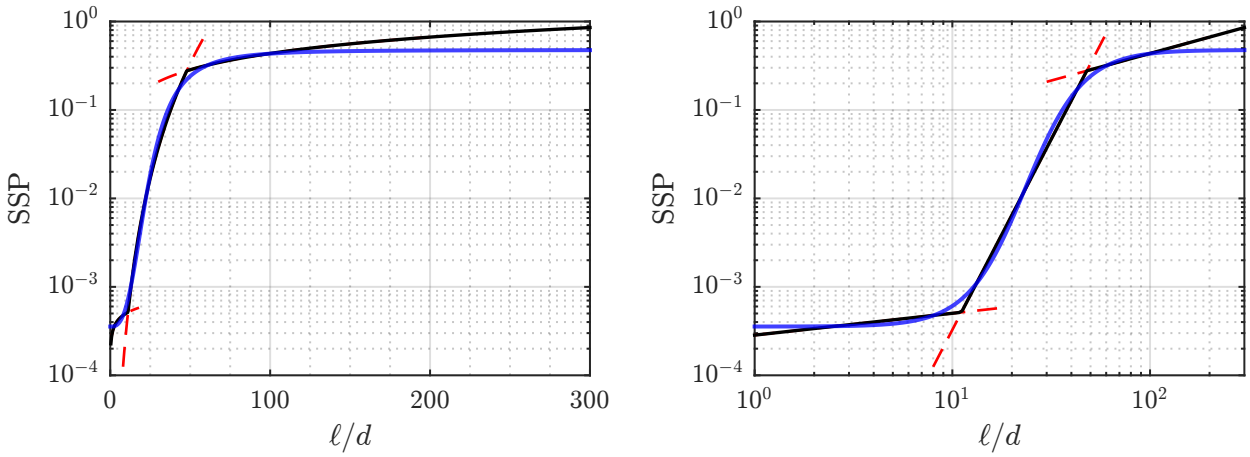

Figure 4.73: Comparison between the power and sigmoidal regression laws of the scaled sound pressure, lin-log (left) and log-log (right) scales.

Nevertheless, both curves may be of interest. The power law is a simplified formulation that can be seen as an engineering approximation. The effect for long cylinders can be biased due to the limitation of datapoints for ℓ/d bigger than 100, even so, it remains statistically meaningful for the available data. On the other hand, the sigmoidal curve is of complex interpretation, but has a physically consistent behavior for longer cylinders. Furthermore, found empirical models are compatible with formulations presented in the literature while give supplementary insights over the physics, as can be seen on next section.

4.6.4.4.2 Literature correction methods Correction methods to get the sound emission of a long-span cylinder from a short simulated segment are defined in the literature from the necessity to extrapolate the results from extremely cheaper simulations, with some successful applications [46, 177], as discussed in Section 4.5.1. The current laws are then compared to the works of Kato et al. [108], Perot et al. [206] and Seo & Moon [233], who derived algorithms based on Curle's analogy.

Considering a segment of cylinder of length ℓ_s, the total sound emission of a longer cylinder of length $\ell = N_s\ell_s$ is modeled as the sum of the contribution of N_s segments. The correction account for the phase lag between different sections of the cylinder is derived using the hypothesis of statistical homogeneity in the spanwise direction, that means, it is assumed that every section

has the exact same spectral noise emission and there is only a phase lag between the sections, being that phase lag a Gaussian distribution [30]. From that procedure, the coherence length $\ell_c(\Omega)$ is defined as a shape parameter of the Gaussian, where Ω represents the frequency. The used definitions for the coherence length in the two works of Kato et al. and Seo & Moon are different, for simplicity they are here referred equally as ℓ_c. Reader is invited to check the cited references for the exact definition.

The proposed sound pressure levels that must be added to the segment sound emission are:

$$\Delta\text{SPL}_{\text{Kato}} = \begin{cases} 10\ \log_{10}(N_s) & \text{if } \ell_c \leq \ell_s \\ 20\ \log_{10}(\ell_c/\ell_s) + 10\ \log_{10}(\ell/\ell_c) & \text{if } \ell_s \leq \ell_c \leq \ell \\ 20\ \log_{10}(N_s) & \text{if } \ell \leq \ell_c \end{cases} \tag{4.6.9}$$

$$\Delta\text{SPL}_{\text{Perot}} = 10\ \log_{10}\left(\frac{\arctan(\ell/r) - \arctan(\ell_s/r)}{\arctan(\ell_s/r)}\right) \tag{4.6.10}$$

$$\Delta\text{SPL}(\Omega)_{\text{Seo}} = 10\ \log_{10}\left\{\sum_{i=1}^{N_s}\sum_{i=1}^{N_s}\exp\left[-(i-j)^2\left(\frac{\ell_s}{\ell_c(\Omega)}\right)^2\right]\right\} \tag{4.6.11}$$

Seo & Moon et al. [233] also present an engineering approximation, quite similar to Kato et al. [108] correction level:

$$\Delta\text{SPL}_{\text{Seo}} = \begin{cases} 10\ \log_{10}(N_s), & \text{if } \ell_c/\ell_s \leq \sqrt{\pi} \\ 20\ \log_{10}(\ell_c/\ell_s) + 10\ \log_{10}(\sqrt{\pi}N_s) & \text{if } 1/\sqrt{\pi} < \ell_c/\ell_s < N_s/\sqrt{\pi} \\ 20\ \log_{10}(N_s) & \text{if } \ell_c/\ell_s \geq N_s/\sqrt{\pi} \end{cases} \tag{4.6.12}$$

4.6.4.4.3 Present correction methods In an analogous way, a correction factor is proposed from the empirical laws that are found to represent the sound emission as a function of the length. Considering the noise produced by two cylinders of the same diameter, in the same air conditions and submitted to the same flow speed, of spans ℓ_1/d and ℓ_2/d and associated RMS sound pressure values $\overline{P}_1^2$ and $\overline{P}_2^2$, the ratio between the noise emissions deduced from the power (pwr) law is (once the different cylinders may not be on the same range, the subscripts 1 and 2 are added to the coefficients):

$$\frac{\text{SSP}_2}{\text{SSP}_1} = \frac{\overline{P}_2^2}{\overline{P}_1^2} = \frac{\alpha_2(\ell_2/d)^{\beta_2}}{\alpha_1(\ell_1/d)^{\beta_1}} \tag{4.6.13}$$

After applying the transformation to decibels, the following correction is obtained:

$$\Delta\text{SPL}_{\text{pwr}} = 10\left[(\log_{10}(\alpha_2/\alpha_1) + \beta_2\log_{10}(\ell_2) - \beta_1\log_{10}(\ell_1)\right] \tag{4.6.14}$$

where $\Delta\text{SPL} = \text{SPL}_2 - \text{SPL}_1$ is the difference between the level obtained for the two cylinders. Note that, when the two cylinders are in the same range ($\alpha_1 = \alpha_2$ and $\beta_1 = \beta_2 = \beta$), the equations is simplified to $10\beta\ \log_{10}(\ell_2/\ell_1)$. That is, the empirical law equals part of the models from Kato et al. [108] and Seo & Moon [233] if $\beta = 2$.

Same procedure is applied for the sigmoidal regression model (sig), deriving the following equation:

$$\Delta\text{SPL}_{\text{sig}} = 10\ \log_{10}\left(\frac{\text{SSP}_2}{\text{SSP}_1}\right) = 10\ \alpha\left[\frac{1}{1+\beta(\ell_2/d)^{-\gamma}} - \frac{1}{1+\beta(\ell_1/d)^{-\gamma}}\right] \tag{4.6.15}$$

4.6.4.4.4 Comparison to the literature A comparison of the corresponding correction level for the five methods, Equations (4.6.11), to (4.6.15), is presented in Figure 4.74, for different values of the ratio ℓ_c/ℓ_s, for a segment always shorter than the coherence length. In an analogous manner of the literature algorithms, empirical correction levels are calculated considering a short

cylinder of length $\ell_1 = \ell_s$ and a long cylinder of length $\ell_2 = \ell$. The calculations are performed for $\ell_c = 4d$ (Section 4.3.3.1.2), what corresponds to the ℓ_c at the vortex shedding frequency. The coefficients used in Equation (4.6.14) are the values presented in Equation (4.6.7). One of the microphones distances used in this work ($r = 50d$) is considered to calculate $\Delta\text{SPL}_{\text{Perot}}$.

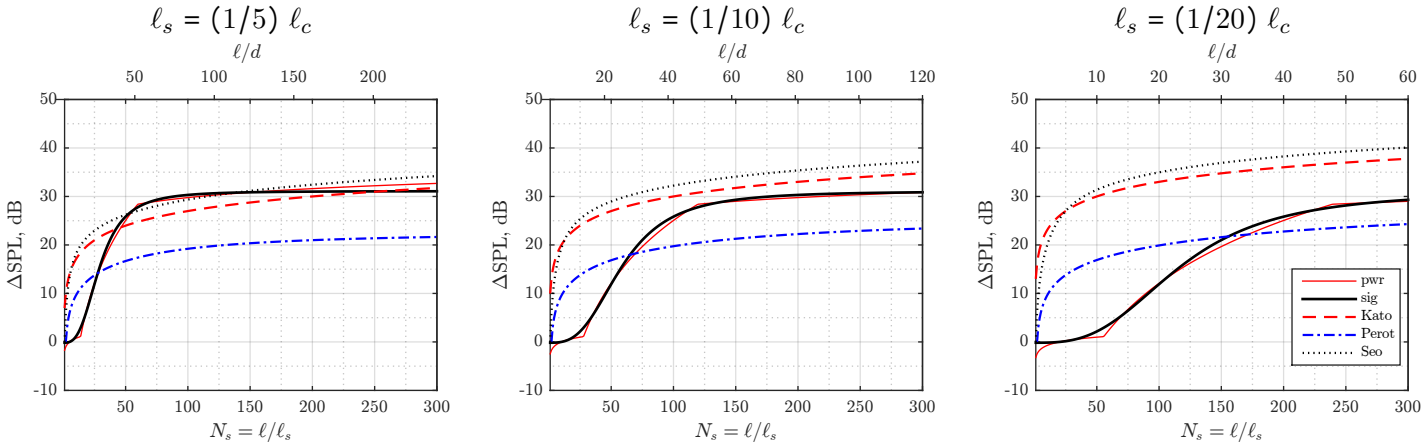

Figure 4.74: Evolution of the correction level with cylinder length for different methodologies [108, 206, 233] and current empirical laws.

Like in Figure 4.73, the behavior of the correction levels issued from the power and sigmoidal curves are similar. Discrepancy arises for longer cylinders (number of segments) due to the symptotic behavior of the sigmoidal law. All the literature correction factors curves follow some form of a power law and have very similar shapes. Formulations proposed by Kato et al. [108] and Seo & Moon [233] are quite similar, for all the tested range of number of segments; the shape of the curve proposed by Pérot et al. [206] is similar to the latter two but with lower amplitudes, thus, shifted in the ordinate axis.

For a small number of segments/short cylinder, current laws propose a way smaller correction level. For example, for a short-span cylinder of $\ell_s = (1/20)\ell_c = 0.20d$ and a long-span cylinder of $\ell = 20d$ ($N_s = 100$), current laws propose a ΔSPL of about 10 dB, while this value is of about 35 dB for the formulations proposed by Kato and Seo and 20 dB for Perot. This discrepancy is provoked by the fact that the empirical law is derived from experimental data. For such range of lengths, the hypothesis of spanwise homogeneity encountered in the analytic correction formulations is not respected.

In the long term ($\ell > 50$), the current and previous formulations propose a similar trend, going for an asymptote or a steady growth. However, the difference in terms of magnitude is marked, current formulation reaches to about 31.1 dB, while the others go to 40 (Kato and Seo) and 25 (Perot). Also, only two curves (Perot and sig) have an horizontal asymptote, the two which account for the change in the retarded time.

It must also be stated that the use of the empirical functions described here may not be adapted for the correction of sound emission of measurements/simulations of smaller cylinders. The regression analysis is performed considering the sound emission of open/finite cylinders, that is, with no reinforcement of three-dimensionality and notable influences of end effects if $\ell/d < 30$. This is not the case for most of the experiments and simulations, where numerical or practical artifices are used to simulate a different end-condition. For example, a simulation of a very short cylinder ($\ell/d = 2$, for instance) with free-slip or symmetrical boundaries does not, from an aerodynamic point of view, equal an experiment or simulation of such cylinder with one or two open ends.

In conclusion, the 5 curves have similar shape; for long spans, literature models have a lower estimate. Despite the resemblance of the curves, the differences in the beginning and on the asymptotic behavior and values foreground that there are some of the possible misconceptions in the hypothesis used to propose the correction methods. Furthermore, it is possible that the saturation is misrepresented due to the limitation of the current data to cylinders shorter than

120 diameters, point that must be further investigated with the evaluation of the sound emission of very long cylinders in an open/finite configuration.

4.6.5 Observed behavior for the square cylinder

Apart from the circular section, reports of the sound emission of the square section were the only that could be found in the literature for 3D flows and at similar Reynolds number. Three of the four sources have also reported values for the circular section, with the same experimental setup and flow conditions presented in Table 4.8. Though, the height of the cross-sections is not the same: 30 mm for King & Pfizenmaier [111], 10 mm for Moreau et al. [158] and 16 mm for Iglesias et al. [83]. Sole new reference is the article by Becker et al. [16], that used a finite, wall mounted square cylinder of height d = 20 mm and a length of ℓ = 120 mm (ℓ/d = 6). Flow velocity is of U_∞ = 30 m/s and the observer is at r = 0.71 m of the cylinder (standard quantities were used for ρ and c). Note that Hutcheson & Brooks [81] also performed experiments with square cylinders, but their results are not considered here due to the use of a closed configuration.

Experiments performed on this work expand the database, as can be seen in Figure 4.75. Similar experiments were also performed for triangular sections (described in 4.4.4), but since there are only 2 different lengths, a description of the evolution of the sound emission levels with ℓ/d is not reliable.

Similarly to the behavior discussed for the circular section, the scaling is effective and reduces the dispersion of the data-points. The trends are as well similar to what has been discussed on Section 4.6.4.1, with the existence of 3 regions (short, medium and long): a continuous sound emission for $\ell/d < 7$ (limit based on the discussion on [158]), a well marked slope for $7 \leq \ell/d \leq 30$ and a small variation/stagnated evolution for $\ell/d > 30$.

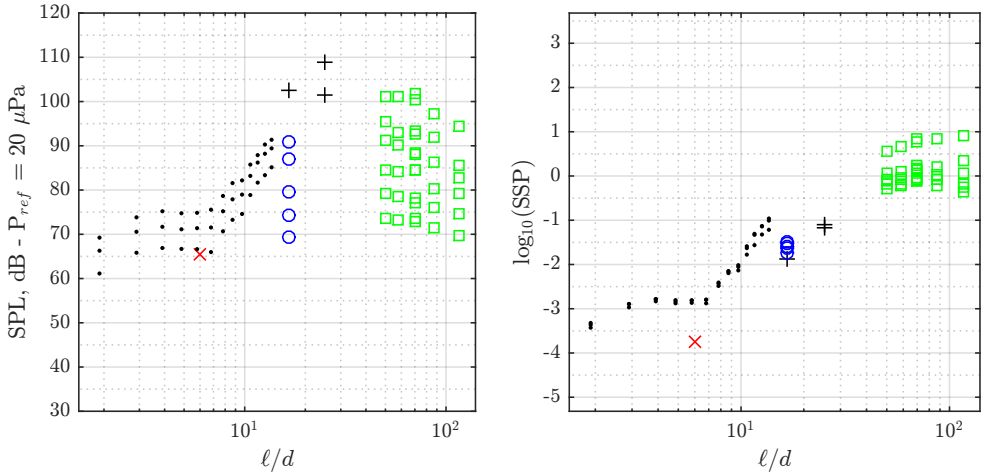

Figure 4.75: Peak, overall and band sound pressure levels (SPL, left) and corresponding scaled sound pressure (not corrected SSP, right) for square cylinder on the literature (details concerning the flow conditions and parameters used in the scaling are present on Table 4.8). **Open**: ∘ Iglesias et al. (2016) [83], □ current work; **Finite**: × Becker et al. (2008) [16], + King & Pfizenmaier (2009) [111], · Moreau & Doolan (2013) [158]

Analysis by region, even if they are visible on the graphs, is very problematic due to the reduced number of points. When considering all the "not short" cylinders, for the threshold of $\ell/d > 7$, an exponent of 2 is obtained for the power law.

The global sigmoidal model in Equation (4.6.6) is used. Fit considers the database filtered by the vortex shedding frequency and flow Reynolds number ($f_{\text{peak}} > 250$ Hz and $\text{Re} > 10^4$). The resulting curve is presented in Figure 4.76, along with the regression law obtained for the circular section. The coefficients are listed in Table 4.14 (no correction by the C_L' lift coefficient is performed due to the incapacity to find any empirical laws that could represent the evolution of the RMS lift coefficient of square cylinders).

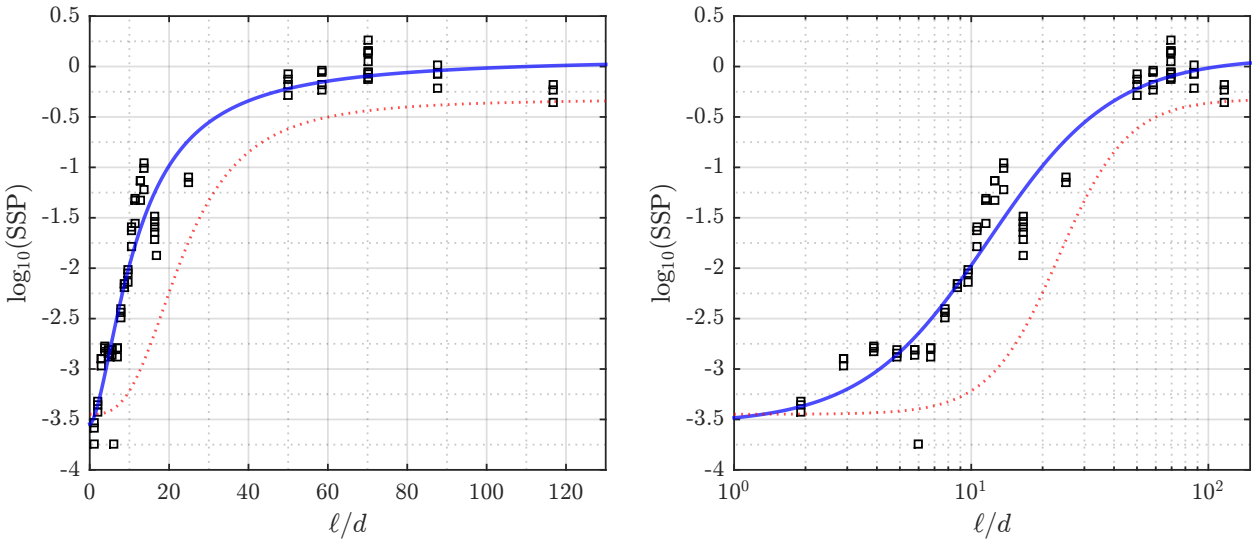

Figure 4.76: Regression laws of the scaled sound pressure from the overall sound pressure level (OASPL) as a function of the cylinder's length, lin-log (left) and log-log (right) scales. Data-points and continuous line are for the square cylinder while the dotted lines is the empirical law obtained for the circular cylinders.

Table 4.14: Sigmoïd law coefficients for the sound emission of the square cylinder, all lengths - Equation (4.6.6).

	α	β	γ	$\mathrm{SSP}_{\mathrm{ref}}$
SSP	3.636	5.761×10^{1}	1.643	2.843×10^{-4}

Visually, other reasonable curves seem to exist, specially when ignoring the outliers. However, similar coefficients are obtained when they are filtered (regression performed without the values for $\ell/d < 3$ and the point with lowest SSP at $\ell/d = 6$ - data from Becker et al. [16]). From a statistical point of view, this remains the most consistent fit. Once the database is not extensive ($n = 76$) and there are important gaps in the observations (no data points for ℓ/d between 25 and 50), no further conclusions can be performed.

While the curves for the two cross-sections are very similar, theirs distinctions synthesize the differences in flow and sound signature of the two cylinders. Considering the empirical sigmoidal laws, for all cylinder lengths, the vortex shedding produced around a square section is louder than the flow generated by circular cylinder. It is also noted that the transitions between the different ranges (flow dominated by end conditions, evolving vortex shedding and saturation) happen sooner in the spanwise length scale for the square cylinder. The exponent γ is smaller for the square section, what represents a slower transition. This may be associated with the presence of sharp edges that fix the detachment points.

4.6.6 Conclusions regarding the length effect

The evolution of the aeolian tone level with the span of the cylinder was investigated. New experimental results and literature data are used. In order to compare the levels, a scaling formulation based on Curle's formalism is proposed. This scaling can successfully bring together the data from different flow conditions and cylinder dimensions leaving the length of the cylinder ℓ/d as the sole explanatory variables of the sound magnitude. Reynolds number dependent quantities (the Strouhal number, the RMS lift coefficient and the coherence length) play a negligible role, specially when only flows at an established regime ($10^4 \geq \mathrm{Re} \geq 2 \times 10^5$) are considered.

Data is classified in 4 categories regarding the experimental setup (open, close, finite and none

for simulations). Open and finite setups are observed to give quite similar absolute levels. Closed setups, where flow is limited by end-plates, are consistently louder but have similar spectra than those obtained in non restricted ends and are shown to follow a resembling behavior in what concerns the evolution of the noise emission with the length.

In terms of the sound emission, three distinct trends are noted: short ($\ell/d < 12$), medium ($12 \geq \ell/d \geq 50$) and long cylinder ($\ell/d > 50$), the first two already discussed in the literature [111, 158]. While there is no gain associated with the increase of ℓ/d for the first range of lengths, an asymptotic behavior is observed for the longest cylinders, that is, the sound stagnates due to the acoustic interference of different spanwise stations [35, 206]. The central range is a transition between the two zones, happening with a slope of 3 in the log-log scale. Power and sigmoidal models were derived for the description of the local and global, respectively, description of those behaviors. Such relationship between the length and the sound emission is present for both circular and square cylinders.

When compared to analytic descriptions of the length influence on noise, the behavior is similar but deviates for both short and long ranges. The segmentation based formulations in the literature do not account for the flow development that influences the short and medium cylinders and the acoustic phenomenon that limits the level of the long cylinders. A theoretical and deeper experimental investigation of the mechanism described by the sigmoidal law (notably accounting for intermediary ℓ/d) is demanded.

In face of the observed change of trends derived from spanwise aerodynamic and acoustic mechanisms, it is recommended to work at the stagnation region ($\ell/d > 50$) when the study is directed to the description of the physics of the vortex shedding and the associated noise emission. That way, in an analogy to a numerical study, the flow is known to be independent of the domain, fully established. Also, as noted on current analysis, the use of a short but closed cylinder may produce overestimated sound levels magnitudes, condition which can be problematic in application oriented studies.

4.7 Final discussion of the experimental study

The sound generation of flows around elongated bluff bodies was examined experimentally in an anechoic wind-tunnel. Measurements of acoustic signature with an array of microphones allowed the examination of acoustic pressure spectra, sound pressure levels, directivity patterns and the exponent of the velocity in the evolution of the sound magnitudes for a set of diverse cylinders and flow velocities. By the use of hot-wire anemometry, the spanwise characteristics of the flow around a sub-set of the cylinders were also examined.

An algorithm is proposed for the fit of a Gaussian curve that correlates the spanwise distance to the coherence for the estimation of the coherence length, one of the ingredients of the aeolian tone. Obtained results are similar to data from surface pressure taps. New data explicit and quantify the modifications in flow topology due to a change of cross-section, being the flow around the rectangular cylinders of aspect ratio 2 and 3 practically 2D at the tested regimes. The latter two have both streamwise and spanwise attribute that are analogous to the circular cylinder at a lower Reynolds number.

A compact, dipolar acoustical behavior is observed for all the tested cylinders. On general, the square and rectangular cross-sections have the loudest acoustic responses, with very sharp tones. Cylinders with triangular sections have acoustic signatures very similar to the circular and square cylinders. Attention must be given for not using low resistance rods and beams, that on this works were subjected to fluid-structure resonance and bending. Also, rounding of the edge alters the acoustics significantly.

Combination of the sound emission and coherence length measurements allowed the estimation of the RMS lift coefficient of some of the cylinders. Artificial spectra were constructed based on a reconstruction of the emission of long span cylinders from small, fully correlated segments. The fluctuating efforts are obtained using the minimization of the error between the measured and artificial sound pressure spectra. Resulting values are only rough in terms of magnitude,

however, the trends are reproduced. Similarity is noted between the high and low Reynolds number flow response to the increase of the aspect ratio of the rectangular cross-section.

When the effect of the length in the sound pressure levels is isolated, three trends are evidenced: no expressive growth for small cylinders ($\ell/d < 12$); an increase with exponent 3 for medium cylinder ($12 \geq \ell/d \geq 50$); and a stagnated level for long cylinders ($\ell/d > 50$). Power laws and a sigmoidal curve fit the data-points for both square and circular cross-sections. The effect of the end conditions and spanwise flow elements is highlighted by the existence of these 3 behaviors and by the difference noted between experiments performed in a closed (flow is limited by end-plates) and free or finite (at least one free-end) arrangements.

Next, description of the global conclusions and observations issued from the experimental results are presented, followed by a discussion on some of the aspects of this work that are open to improvement. After that, further questions concerning the phenomenology associated to the aeolian tone and perspectives are presented.

4.7.1 General remarks on the phenomenon

The experimental analysis serves both as a complement and a contrast to the 2D laminar flow analysis in Chapters 2 and 3. The triangular cylinders were not the loudest, in opposition to what was described in the 2D study, however, the effect of the aspect ratio on the RMS lift coefficients is reproduced in 3D for the rectangular sections. Despite the decrease of the C_L', the sound emission increases due to the changes in the spanwise behavior of the flow. The investigation of the shape influence on the flow spanwise de-correlation, encapsulated in the coherence length ℓ_c, actually corroborates to the results in 2D. The cross-sections that produce very energetic flows (elevated C_L', W_a) at low Reynolds number will tend to be very perturbed and de-correlated at higher Reynolds number, thus, less noisy.

Nevertheless, the importance of the 3D topology in the magnitude of the sound emission is also explicited when analyzing the evolution of the sound pressure level with the increase of the length of the cylinder. The flow evolution with ℓ/d, normally absent in span correction formulations, must be accounted for performing precise predictions.

One interesting result is that the sound production hierarchy between the geometries (for instance, circular $<$ AR = 2 $<$ square $<$ AR = 3) is held for all the Reynolds numbers tested in this experiment. One logical conclusion would be that, for a given velocity range where there is not a known transition, as the one used in this work, there is, a priori, no necessity to perform a Reynolds number dependency study when confronting sound production of different geometries.

While the use of end-plates is highly advocated for the reduction of end conditions interference in flow, its influence is responsible for forced increase of the aerodynamic efforts. In the case of small and medium cylinders ($\ell/d \leq 50$), the end-plates impose a more organized flow, thus, more energetic vortex shedding. This may be reasonable in the sense of exploring the dynamics of a virtually infinite cylinders in smaller facilities, even so, this choice may be problematic in terms of the description of the phenomenon, strongly influenced by the spanwise extent of the flow, as numerically described in [65, 99], and when aiming at an engineering application due to the overestimation of the acoustic emission. For long cylinders ($\ell/d > 50$), the author believes that the end-plates are more influential than the presence of open ends and must be avoided.

In that direction, it is fundamental that, in the continuous effort of understanding unsteady fluid dynamics and describing bluff body flows, for more quality experimental measurements of RMS force coefficients to be performed, accounting for the several parameters that influence the final result such as the turbulence intensity and the length of the cylinder.

In terms of strategies of reducing airframe noise and structural vibrations, current results lead to the following 2-step proposition: (i) increase the breadth of the cross-section such as to reduce the flow fluctuations and the strength of the vortex (decrease of $C_{L,b}'$, as is observed in low Reynolds 2D simulation); (ii) add flow spanwise decorrelation devices, such as surface protrusions and shrouds [282], in order to compensate for the increase of the coherence. Since the tonal trait will be increased, this may not be fully advantageous, also due to the increase of available surface (illustrated by the curve of $C_{L,d}'$, Figure 4.61). This logic must be seen as a

general direction rather than a guaranteed procedure.

4.7.2 Criticism and possible improvements

Despite the overall good results and alignment to the behaviors noted in the literature, some methodological and technical improvements could be performed for the current experimental setup and aspects of the data treatment. Most of those points would be present in a thesis completely focused on the experimental work.

The influence of the size and the inclination of the plate used for adapting the 3/4 configuration to an open jet one must be further described, in both aerodynamic and acoustic aspects. Nevertheless, the same analysis should be performed for the distance of the cylinder to the nozzle, taken as 30 cm. The distance of the microphones to the axis of the prism, taken as r = 1 m, could have been increased such as to guarantee that the far-field condition is fully respected for the complete set of tested cylinders and flow velocities. Also, the analysis would benefit from a more strict definition of the effective length, considered as the size of the nozzle ℓ = 70 cm. Spanwise measurements of the average streamwise flow are limited to 30 cm, not reaching to the lateral mixing layers that delimit the aerodynamic ℓ/d.

This work could benefit from a more rigorous description over the flow topology and the distinctions on turbulent development with the different cross-sections. Due to the primary interest in the sound production, the measurements focused on the description of the spanwise distribution of the flow. Though the description is successful in terms of discerning the differences between the elements that have a role in the sound emission, a deeper discussion over the dimensions and distances on the wake (the recirculation and formation lengths, for instance) and the energetic state of the turbulent scales could lead to deeper or different insights. It is as well reinforced that the coherence length measurements should have been performed for more than only 4 of the cylinders.

Distortions of the hot-wire results due to the poor description of low speed flow are shown to be relatively small. However, the full picture is not available due to the wrong description of some zones, for instance, boundary layers and the recirculations. More refined techniques, such as PIV or LDV, must be employed for a complete description of the flow.

From a data treatment point of view, considering other correction formulations for the RMS lift coefficient estimation study, notable the one by Perot et al. [206] which accounts for the retarded time changes could improve the results.

Finally, test should have been performed with end-plates, strongly criticized in this manuscript. Since no experiments are performed with the same setup, but with end plates, it is impossible to quantify the effect of the latter on current flow condition. These results could provide a stronger argument or even deny some of the performed claims, largely built on arguments and data issued from the literature.

4.7.3 Open questions and perspectives

The simultaneous accordance and distinction between the sound emission in 2D, laminar and 3D, turbulent flows indicate that there is an intrinsic connection between the 2 regimes, naturally associated with the shape of the cross-section. Such relationship, preliminarily discussed in Section 2.2.3.4 (2D to 3D transition Reynolds number) and also discussed in the analysis in Section 4.5.3.2 (sectional lift estimation), should be further investigated.

A more developed description of the different trends of the evolution of the sound levels with the length of the cylinders, reported in Section 4.6, should be performed. For instance, there is no clear explanation for the obtained power law exponents of 4 (for medium cylinders) and 3 ($\ell/d > 10$) and the coefficients of the sigmoidal law. A possibility is to perform the analytic description of the noted trends from Curle's formalism of cylinders sound emission combined with a more complex spanwise description of the flow.

In terms of experimental procedures, different methodologies to visualize the spanwise distribution of the flow could be evaluated. For example, the use smoke visualization or of wall

threads [80]. For its simplicity, such procedures could be performed easily for a large set of cylinders, thus, providing a vast complementary material for the description of the shape influence on the flow and, consequently, on the sound emission.

All the herein proposed analysis are focused on a better description of the flow. Ultimately, they can be complemented by a stability study, envisaged next. Analysis of the modes and frequencies of both the Y_1Y_2 plan and spanwise are planned, using experimental data to scale the amplitudes.

Chapter 5

Conclusion and perspectives

A numerical and experimental study of the sound generated by the flow around cylindrical bodies was performed for the investigation of the shape influence on bluff body aerodynamics and sound generation. Simulations were performed in 2D, low Reynolds and laminar flow using a DNS solver and an IBM formalism. The acoustic response is estimated using a single formula derived from Curle's analogy. Statistical tools are used for description and analysis of the numerical results. Shapes with extreme aeroacoustic signature were investigated using an optimization routine (PSO) with different parametrizations. The experiments were performed in an anechoic wind tunnel at Reynolds number of order of thousands, with measurements of the flow velocity signature, the spanwise correlation and the coherence using hot-wire anemometry probes and the sound emission was measured using an array of microphones. Despite this important disparity in regimes of these two analyses, the universality of the phenomenon of vortex shedding allows the conclusions derived from each methodology to be contrasted, thus, complementing each other.

The observation of the behavior of canonical geometries in Chapter 2, leads to the general conclusion that, for a 2D flow, less noise is associated with a shape that dissipates more energy upstream of the wake. This argument is both derived from and supported by the behavior noted when increasing the aspect ratio of the geometries. In a larger sense, the increase of bluffness, that is, the enlargement of the blockage, also seems to be capable of reducing the sound emission. From the analysis of the critical Reynolds number of the transition from steady to unsteady flow, it is also evidenced that there is a correlation between the distance to transition (in terms of flow Reynolds number and the necessary value for having an established vortex shedding) and the amplitude of the aerodynamic efforts.

Similar conclusions were observed in the shape optimization study reported on Chapter 3. At the considered flow regime (Re = 150), the changes in the acoustic efficiency are directly associated with variations of the magnitude of the RMS lift coefficient, being not only the major quantity but also the one that is the most susceptible to changes when modifying the shape. It was also noted that adding asymmetries to the body, supposedly associated with an increase of the interaction between the upper and lower mixing layers. In general, as discussed in Chapter 2, the noise reducing aerodynamic features are the presence of an abrupt increase of blockage associated with an extended length and curved, thus, increasing the dissipation of energy before the wake. The principle is summarized on Figure 5.1.

Nonetheless, those observations neglect the spanwise distribution of the flow, a major ingredient of the noise emission, and proven to be regime dependent when performing the experiments, as discussed in Chapter 3. In the wind tunnel testing, the vortex shedding generated downstream of rectangular sections (AR = 2 and 3) were practically two dimensional. This is one of the reasons why those are the loudest sections in the performed study, nevertheless, an estimation of the surface RMS lift coefficient indicated that there is also a significant change in the force coefficients when thinking about those sections.

In terms of the experimental setup, the compilation and analysis of literature data and new measurements showed that the acoustic response to an increase of the length of the cylinder follows different trends based on ℓ/d (short, medium and long). Also, the difference in response

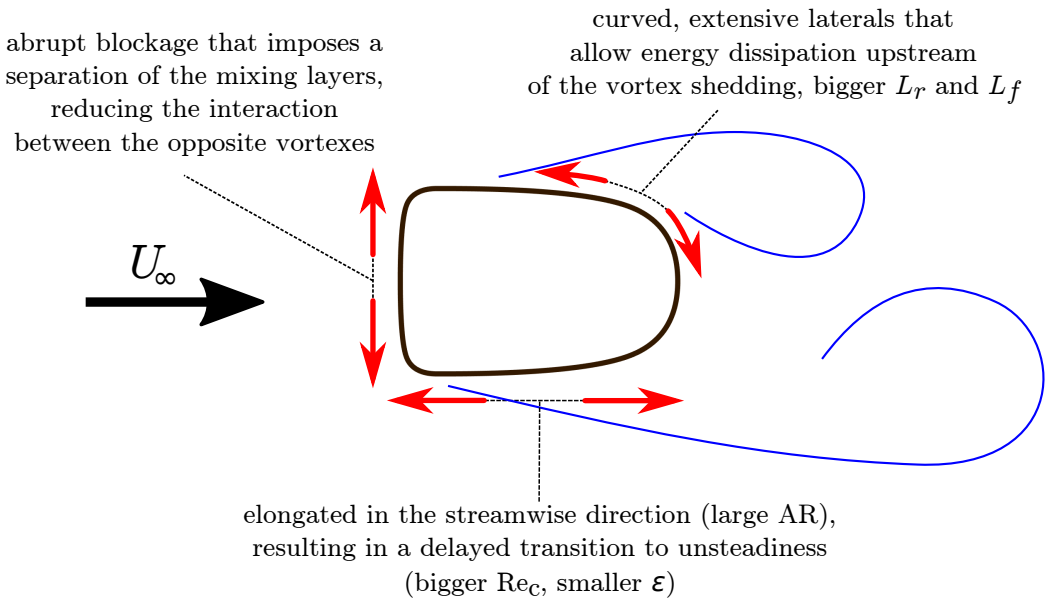

Figure 5.1: Summary of the geometrical features that reduce the sound emission at laminar, 2D, low Reynolds flow based on current results. Naturally, all the discussed points contribute with each other and produce simultaneous effects, thus they must not be considered individually.

based on the end conditions is also noted, the closed configuration (end-plates on both ends) being consistently louder.

Next, the principal conclusions of the document are condensed, with the presentation of some propositions that emerged from current results and suggestions for further development of the project.

5.1 On the influence of the cross-section in studied 2D and 3D flows

In 2D (in both the study of canonical shapes and in the shape optimizations) the back-pointing triangle is the loudest geometry while the rectangular sections are close to the quietest. In the experiments, the rectangular sections (square and AR = 3) are the loudest while the front-pointing triangle is the quietest cross-section, being very similar to the circular cylinder in terms of both tone frequencies and magnitudes. The disparity between the 2D and 3D results lies on the spanwise mechanisms, thus extremely influenced by the cross-section.

The flow's three-dimensionality is a result of vorticity dynamics [154], thus, alimented by the 2D behavior (spanwise vortices). Following that principle, the influence of the section plays a fundamental role in the definition of both the energetic state of the wake, condensed in the RMS lift coefficient, and the flow topology, synthesized by the coherence length. The intrinsic relationship between the two is due to the dynamics of the transition to 3D following the same principle of the transition to 2D: the larger velocity gradients in the wake the sooner the transition will take place (short cross-section, shapes that have smaller dissipation at the walls); the larger the vorticity gradients in the wake are, more developed the streamwise vortex will be, thus, more turbulent and less coherent. The interest in this analysis resides in the dispute between the two phenomena when thinking in the design of acoustically efficient cross-sections (efficient in the sense of low noise). When searching a reduced sectional fluctuation, the result will be a flow strongly correlated in the spanwise direction, thus, noisy and tonal. On the other hand, the highly perturbed sectional behavior is highly energetic and even if strongly de-phased has a state that is possibly also very loud.

Globally, for both laminar and developed flows, when one consider an incoming fluid that has

a fixed amount of energy, represented by a given d-based Reynolds number and equal blockage, the shape that produces less noise is the one that is capable of dissipating the energy before the vortex shedding. When there is no spanwise direction for that dissipation, this can only take place on the plan and is associated with bluffer and longer geometries. When the spanwise direction is added, the results are different even if following the same dynamics.

Despite the differences in the hierarchy of the sections, a conclusion that regards both flow regimes that were investigated is that the aspect ratio is proven to be a major component in both flow dynamics and acoustic efficiency. In a design point of view, this geometrical feature has been noted to overcome any other feature, affecting both tonal and broadband sound emissions, the spectral distribution and the sound pressure levels of the acoustic pressure. If we think in an application point of view, note that a change of the yaw angle of the cylinder represents a sectional increase of AR, noted by Wang et al. [272] to mitigate the vortex shedding of a circular cylinder.

All of the measured flow quantities indicate the widest rectangular sections as having an aeroacoustic signature that represents something that is analogous to a circular cylinder at lower Reynolds number: sharp tones and a strong spanwise coherence. As evoked several times in the manuscript, this indicates that the modification of the cross-section may be associated with a change in the Reynolds scale, leading to a proposition by the author on how to investigate bluff body flows, further discussed next.

5.2 An energetic view of shape influence on bluff body flow and noise

Rather than a description formalism, looking at flow quantities for every geometry and trying to make a deduction on the flow dynamics based on the flow behavior around a given shape, an energetic and transition based approach is proposed.

Consider the wake strength as a result of the amount of energy that reaches at the wake, downstream of the obstacle. The aerodynamic and aeroacoustic performance of a given cylinder can be associated with how and how much energy it is capable to dissipate. The Reynolds number performs a similar quantification by indicating the rate of viscous dissipation, however, since it only considers a single dimension of the body, it is not adapted to compare different geometries.

The current results show that different geometries behave similarly but at different Reynolds number. This implies that it may be possible to, imagining the cross-section shape to work analogously to a forcing term, to deduced a supplementary description that would allow a direct comparison of the effect of the geometry. A preliminary tip for building such type of analysis is the relative position of the flow in terms of its evolution in the Reynolds scale. As illustrated in Figure 5.2, where the ranges of the current study are evidenced, when analyzing the different shapes on the same flow regime, one is looking at different stages of the flow development. For instance, at Re = 150, value used in most of the simulations, the flow around the square cross-section is closer to the steady to unsteady transition than the flow around the circular cylinder but farther than for the triangular one. The effect of the relative distance to transition is specially visible on the 2D simulations at low Reynolds number, where small changes in the absolute value of Re represent a significant change in flow topology and the relative distance to the transitions, as discussed in Chapter 2, specially in Section 2.2.3.

The proposed concept is to think on the geometry of the cross-section not in terms of the absolute Reynolds number, but as a scale between transitions, as tried with the ε criterion. Following such principle, it is believed that there is a clear association between the geometries with low fluctuating lift/noise in 2D and a high noise production in 3D. Once at a given fixed Reynolds number, those geometries that have a less disturbed flow in 2D, that is, are generally close to the transition, will also present a similar behavior when analyzing the transition to 3D. In practical terms, at a fixed Reynolds number, the obtained 3D flow will be of higher spanwise coherence (associated with a subcritical regime, where the ramification of flow structures in

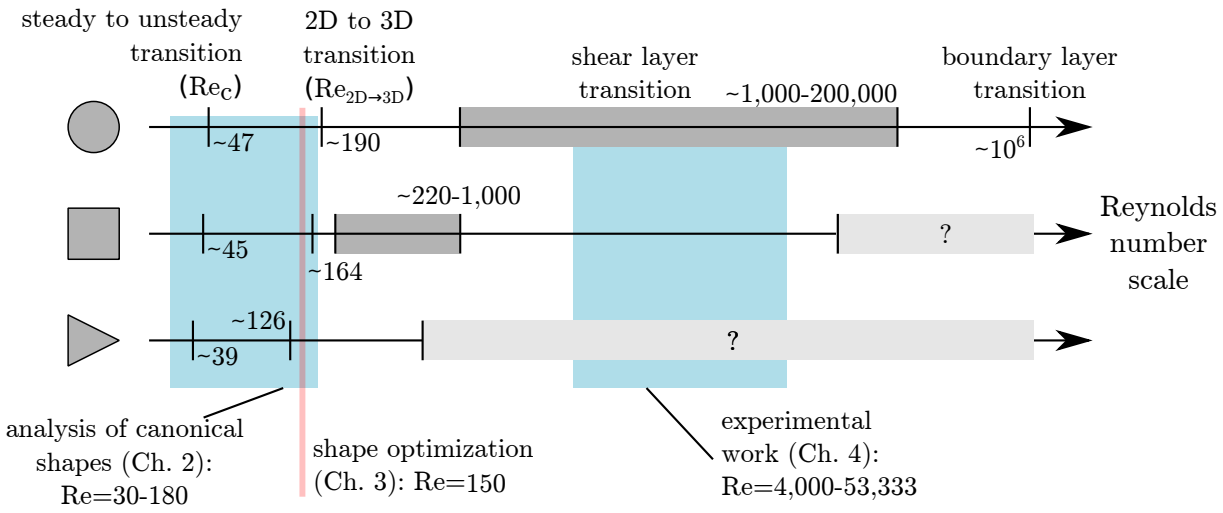

Figure 5.2: Flow development of different cross-sections. The Reynolds number for the flow transitions are from [10, 276].

smaller bodies is not the major phenomena).

This explain the disparity between the results in 2D and 3D in terms of sound efficiency hierarchy, discussed in Section 5.1. While it is preferable to trigger a later transition in 2D, where a more energetic threshold for transition would directly result in a smaller amount of energy for flow fluctuation, thus, smaller acoustic power, in 3D, this represents a flow that is less disturbed in the spanwise direction, what generally results in louder configurations. The result of the combination of the two effects represents a dispute between the sectional lift and the spanwise flow distribution. For the rectangular sections, while the section forces are rather small, the spanwise coherence is elevated, resulting in more noise even if, for the section, the flow topology presents small magnitude of fluctuation of the aerodynamic efforts.

A more formal and quantitative description of the concept is needed, with a probably definition of a new adimensional number or the definition of a different characteristic length to represent each problem. Despite the premature state of the proposal, these observations can also be of interest of the industry by giving insights under the modifications that must be applied in order to mitigate the vortex shedding and the sound production. By predicting or simulating the behavior in 2D, an engineer may advance or delay the flow development such as to modify the behavior at the operational range. In conclusion, the principal benefit of such approach is to be able to apply the knowledge that exists for the circular section in any cross-section, and need not perform the same three hundred years of work for each geometrical modification.

5.3 Final comments and perspectives

Some major trends in the shape influence on bluff body flow and sound emission have been presented at two distinct flow regimes. A very rich database was produced, with ten of thousands of simulations and hundreds measurements for a diverse set of geometries.

The main handicaps of the numerical work that was performed (working in 2D, low Reynolds), surprisingly, contributed to many of the performed conclusions. With a simulation in 2D, close to the onset of the von Kármán instability, the influence of the shape in the flow dynamics is more evident. The dispersion provoked by the spanwise flow development and the associated difficulties in simulating flow around a cylinder are not present, aspects which allowed further look at the basis of the flow and the nuances of the shape modification.

Once different global relationships and several geometries have been studied, it would be beneficial to focus on specific trends and refine the analysis. For instance, the base of the spanwise analysis on this work concerns firmaments of the aerodynamic coherence structures analysis and

is supported by quantities such as the correlation and coherence and its corresponding lengths. The dynamics of the flow may not be fully described by those approaches, specially in regards of the spectral behavior at the spanwise direction.

A possible direction would be to consider the evolution with the Reynolds number of the flows around the square and triangular sections using more refined experimental techniques such as optical measurements techniques (PIV or LDV), combined with the numerical estimation of those flows at the same or at similar regimes. In terms of future simulations, it must be emphasized the importance to perform a complete and rigorous domain convergence study. As discussed on this document, there are non-negligible aerodynamic and acoustic differences due to imposing a behavior at the limits of the cylinder or by simulating/testing short cylinders. A methodical quantification of such influence on the sound emission, without the use of span correction laws, would also be advantageous.

Also, the use of different techniques for the flow visualization is encouraged to depict the effect of the shape in both flow and noise.

The relation of the cross-section in the 2D to 3D transition must be further analyzed, both in statistical and formal methods. It would be interesting to evaluate if the effect of the transition is qualitatively similar to the transition to unsteadiness. The use of stability analysis, both for the 2D laminar flow and for the spanwise flow distribution is an interesting tool for the further distinction between the shapes and a mean to outline the origin of the noted differences. The use of such techniques is envisaged next.

In what concerns the behavior in 2D, it would be as well possible, via theoretical work, to derive and/or formalize the obtained empirical laws that are presented on Section 2.3. Envisaging to separate the shape influence on modification of the flow and on the walls capability to scatter sound, an analysis of the acoustic scattering of each individual cross-section could be conducted, based on the work of Gloerfelt et al. [66], including the concept of tailored Green's function, with a later effort to try to correlate those values with flow integral and topological values produced on current work.

Another interesting possibility of the current results, distant from the over cited applications into the physical description of the phenomena and on the transportation industry, is the application of the provided knowledge on the bluff body noise production for the proposition and design of musical instruments. The tonal behavior of the wide cross-sections is of extreme cleanliness and can be easily expanded to the creation of tones and accords in a completely different and fun application.

Appendix A

Convergence study and validation of the numerical setup

This appendix is dedicated to present the convergence study and validation of the numerical setup. Even though the simulations parameters are not always the same in different moments of the numerical analysis, notably the Reynolds number, the principal characteristics of the numerical setup, that is, number and physical duration of the timesteps, mesh refinement and dimensions of the numerical domain, are based in what is presented on this section.

Analysis is performed at Reynolds number of Re = 150. The small Re is mandatory so the physics of the problem can be reproduced in a 2D simulation, however, for the wide range of geometries that are considered in the manuscript, there are no warranties that the flow is always well described without the third dimension (as discussed in Chapter 4). For this regime, both drag and lift are close to sinusoidal signals, so the flow periods are defined from consecutive lift peaks. The final simulated period statistics (C_D, C_L', C_D' and St) are used for the analysis presented on this section.

The numerical setup is as follows. Uniform velocity is set inflow, while a convection condition is set outflow; lateral boundaries are defined with free slip condition. Mesh is uniform in flow direction and stretched [124] in transverse direction, with grid points concentrated in the center. Flow initial condition is uniform and equals inlet velocity, $u_1 = U_\infty$ and $u_2 = 0$, for the complete domain including the solid elements. No disturbance is added, once the transient from the IBM elements are sufficient to give onset to the flow periodicity. A scheme of the domain is presented in Figure A.1. Lateral boundaries are fixed at $20d$ for a blockage ratio of 5%, based on [242].

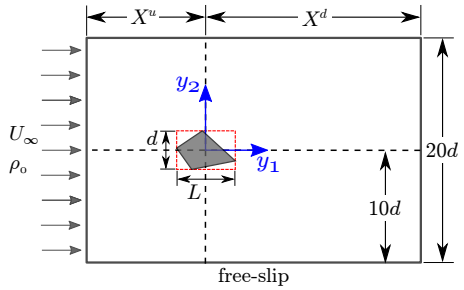

Figure A.1: Scheme of numerical domain.

Convergence studies and validation graphs are presented next.

A.1 Convergence study

Domain and mesh independence tests are performed for both upstream and downstream distances of the vertical boundaries (X^u and X^d, respectively) and element size (number of grid elements). Not only to quantify the consistency of the numerical setup, this study is also aimed

at reducing both memory and time requirements for the use of the DNS simulations such as to allow the production of a wide database of results and to performed an stochastic optimization that requires the evaluation of thousands of cases, while correctly representing the physics of the problem.

The tests are performed with an symmetrical shape of height d and length $2d$, composed by half ellipse at the leading edge ($y_1 \leq -0.1b$) and two second degree polynomials on trailing edge, enabling C^1 and C^2 continuities with the ellipse. The solid domain is the set of grid points that are inside the selected closed contour, defined by ones on the $\epsilon(\mathbf{y})$ matrix. The use of a non-canonical geometry for this step is justified by the intended use of its conclusions, once there is no restriction of the type of geometry that are studied in this work, notably in the optimizations.

A.1.1 Domain convergence

The domain analysis is performed for different streamwise extensions, with a variable number of grid points to maintain the elements' size constant. The number of mesh points in both transverse and flow direction is chosen as a multiple of small prime factors + 1 for a better performance of the spectral solution of the Poisson equation [56], consequently, they are the parameters that defined the selected test distances. Mesh elements are of size $(\Delta y_1, \Delta y_2) = (1.953, 1.125) \times d/100$ at $y_2 = 0$, and timestep duration is of $\Delta t = 0.0042 d/U_\infty$, with a Courant number of CFL = 0.21; calculation stops at 40,000 timesteps ($t = 170 \times d/U_\infty$).

Simulations are performed for asynchronous variations of X^u and X^d, being the complementary distance fixed at an arbitrary level issued from previous testing. These evaluations are based on the hypothesis that the effect of the modification of a boundary location is independent of the position of the other for the chosen complementaries ($X^u = 12d$ and $X^d = 18d$). Results are presented in Figure A.2 for the variables of interest.

Asymptotic curves are obtained for both X^u and X^d, similarly to the results for circular section by Posdziech and Grundmann [201]. Simultaneously, it is observed that an increase in those two reduces the levels of fluctuating lift and drag. The order is not similar for mean drag and Strouhal number: they are monotonically increasing for X^u and monotonically decreasing for X^d. According to this tendency, variations of the actual boundaries distances from the section edges caused by the modifications of the length of the geometries in the optimization procedures are always advantageous, once they are smaller than the value used in the convergence tests ($b \leq 2d$).

Inflow distance has more influence in the flow response due to the modification of upstream conditions in the presence of the obstacle, even at large X^u. The obtained curves confirm that the selected fixed value for the complementary distance are coherent in terms of flow physics.

For a precision of about 1%, the selected values for the final domain are $X^u = 11d$ and $X^d = 14.31d$, what represents a mesh of 1297×513 grid points. Simulations are performed for the selected domain and the final result is compared to the extrema of the domain study, as presented in Table A.1.

Table A.1: Aerodynamic quantities' errors between the final domain and the most extended boundaries.

case	X^u/d	X^d/d	$\Delta\lvert C_D\rvert$	$\Delta C_L'$	$\Delta C_D'$	ΔSt
X^u max	22.0	18.0	-3.2%	-1.2%	-13.5%	-0.8%
X^d max	12.0	33.0	-1.1%	-0.5%	-10.4%	-0.4%

Final domain has higher level for all quantities, as indicated in Figure A.2, albeit the discrepancies are relatively small. The fluctuating drag has an elevated offset (order of 10%) provoked

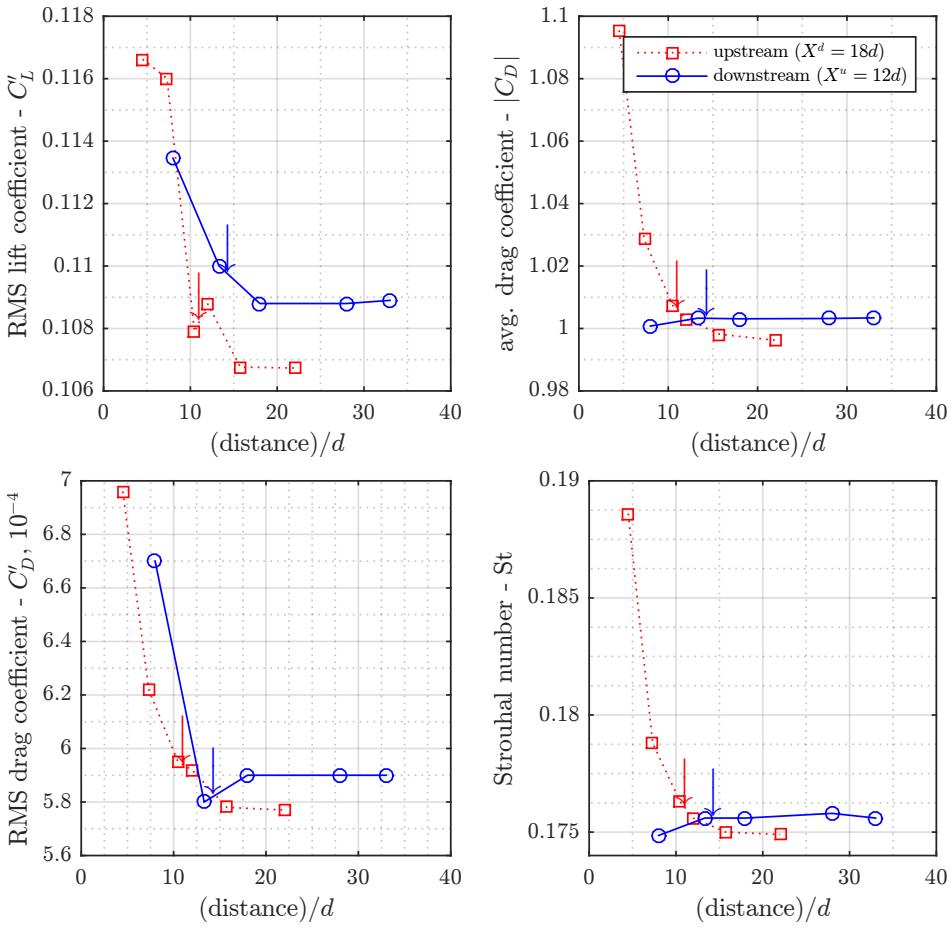

Figure A.2: Influence of domain's upstream and downstream distances on RMS lift coefficient, average drag coefficient, RMS drag coefficient and Strouhal number. Arrows point to the selected configurations.

by its low order O(-4) and thus has a insignificant influence in the aeroacoustical result. Once the domain is defined, further steps are performed for reducing the calculation time.

A.1.2 Mesh convergence

When comparing the element size, the ratio between number of elements in streamwise and spanwise directions is maintained, thus, the elements are isotropically contracted or expanded. A total of 5 meshes are tested, being number 4 the mesh used on the domain study and number 5 the most refined. The timestep physical duration is modified to guarantee numerical convergence, and the number of timesteps is chosen to achieve at least $225 \times d/U_\infty$ of physical time, within which the comparisons are performed. Figure A.3 presents the results for the quantities of interest.

There is a maximum offset of 1.2% for C'_L and 3.3% for $|C_D|$, when compared to the most refined grid. There is a 8.5% deviation for C'_D and 0.4% for the Strouhal number. The small impact of the mesh refinement can be associated with the flow regime, because once the Reynolds number is small, the flow presents very large boundary layers that are less influenced by small oscillations in the solid elements size and position. Observed fluctuations may be associated with the modifications of the dynamic of the solid domain by the consistent change in the number of solid points, once the finite difference scheme is unchanged and there are no interpolations on the obstacle wall.

Following the behavior of the global coefficients, a similarly good result is also obtained when spanwise velocity profiles are compared, as showed in Figure A.4. The mean and RMS velocity profiles at $y_1 = 0$ of the last 2 simulated periods are presented for meshes 2 and 5.

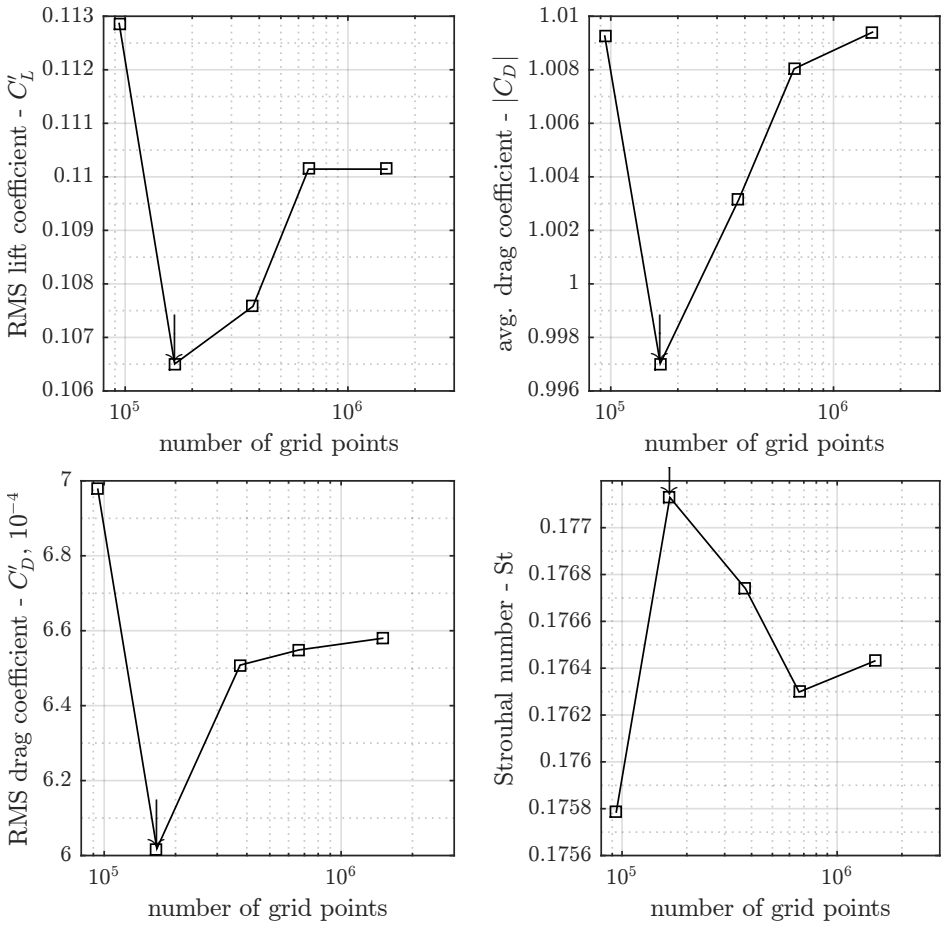

Figure A.3: Influence of mesh refinement in RMS lift coefficient, average drag coefficient, RMS drag coefficient and Strouhal number. Arrows point to the selected configuration.

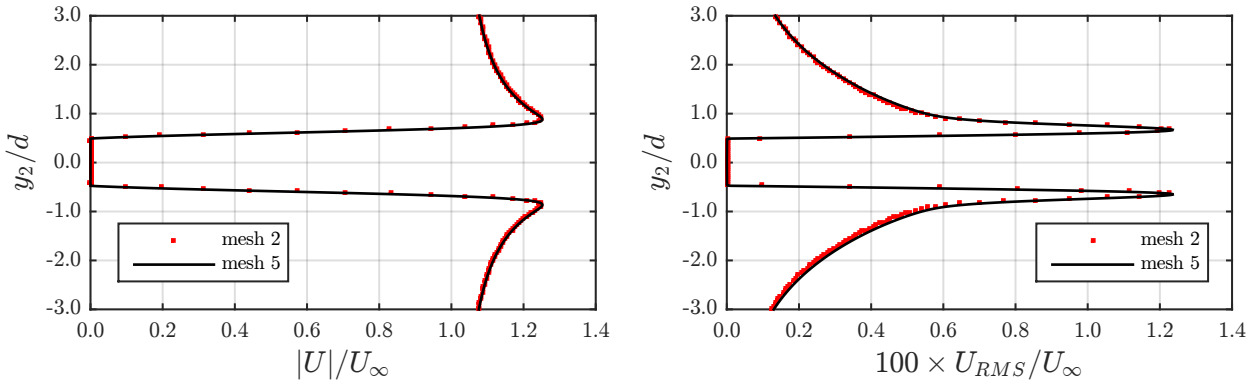

Figure A.4: Influence of mesh refinement in mean (left) and RMS (rigth) velocity profiles at $y_1 = 0$.

Profile comparisons at upstream ($y_1 = -5d$) and downstream ($y_1 = +5d$ and $y_1 = +10d$) positions are performed similarly to the analysis executed at the central spanwise axis ($y_1 = 0$). Considering all 4 profiles, there are a maximum deviation of 1% for the mean velocity and of $8 \times 10^{-3} \times U_\infty$ for RMS velocity profiles.

In a search for a compromise between time consumption and physical representativeness, mesh number 2 is selected. For the chosen space discretization, there are about 25 elements by diameter in y_1 and 50 in y_2. There is a slight loss in accuracy, however, for an equal flow time and CPU conditions, calculation time is reduced to 2.5% of the one obtained with mesh number 5. For 50,000 timesteps, an average CPU time of 2 hours is needed for a single simulation.

Though similar accuracy could be obtained with even coarser meshes, the corresponding geometrical precision would be reduced leading to the fact that relatively large modifications of shape parameters would be irrelevant for the solver. The consistency of the optimization depends on the fact that variations of the theoretical geometry are well represented in the solver, even if the difference in the aeroacoustic answer is not significant, respecting the physics of the cost function.

A.1.3 Time convergence

Once the domain and the mesh are fixed, further analysis must be performed to check in time convergence. Figure A.5 illustrates drag evolution and the convergence of the period aerodynamic quantities, based on the relative error of the 10 points moving average. A convergence of 0.01% is observed for the quantities of interest at $t = 300 \times d/U_\infty$. The Strouhal number does not oscillate after $t = 150 \times d/U_\infty$, what can be explained by the limits in the technique used for determining it (inverse of a lift period, maximum precision being the duration of a timestep), and obtained errors after that time are either null or of the order of the machine precision.

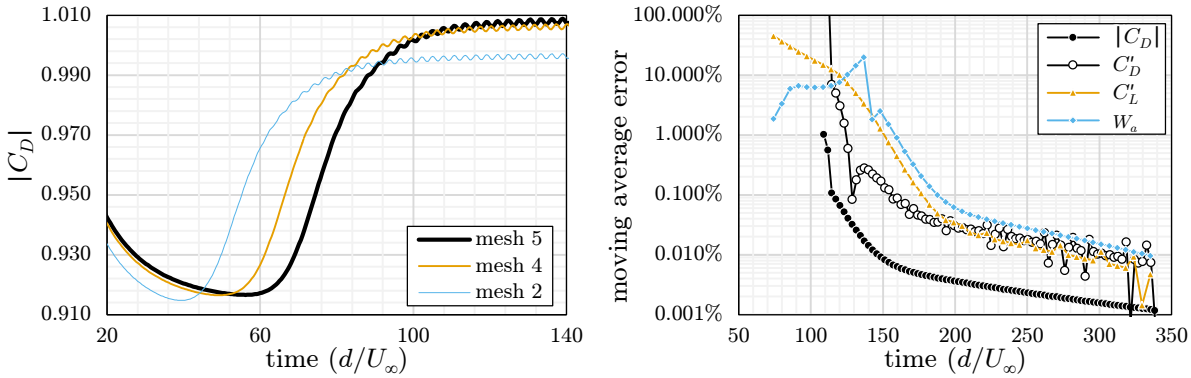

Figure A.5: Time evolution of drag coefficient for different meshes (left) and time convergence of mean drag, fluctuating drag and lift and acoustic power for the final domain, with mesh 4 (right).

Convergence in time is also regarded for the different meshing configurations from the previous studies. Apart from differences in time required for the settlement of the periodic wake structure, as noted on Figure A.5, there is no significant variation of convergence errors or convergence time as a function of either the domain size or the discretization level.

A.2 Validation

Based on mesh and domain independence studies, final domain ($X^u, X^d = 11d, 14.31d$) meshes 2 (grid of 649×257 points) and 4 (1297×513) are used for a validation procedure against literature values for 40,000 timesteps ($t = 288 \times d/U_\infty$). Simulations are performed with canonical geometries of different breadths and Reynolds numbers. Average flow statistics (Strouhal number, average and RMS drag coefficient, RMS lift coefficient) and topological quantities (recirculation length) are considered.

Since this works concerns both a change in regime and in the shape, validation is presented considering two different analysis. First (Section A.2.1), for the circular cylinder at different Reynolds numbers. As a canonical fluid mechanics problem, it is largely discussed in the literature by both experimental and numerical means. At the given low regimes such as the ones that are simulated here, numerical values correspond to the major number of contributions.

Second, see Section A.2.2, comparison is also performed in terms of geometrical modifications such as to guarantee that the given setup behaves correctly when geometrical features are modified. This is achieved by considering the evolution of the aerodynamic quantities of the

flow around rectangular cross-sections with the change of the aspect ratio at Re = 150; only simulation results could be found at that given regime.

A.2.1 Different flow regimes: Circular section, multiple Reynolds numbers

Comparison of currently obtained values and data from the literature for the circular cross-section at multiple Reynolds number are presented next. Following quantities are considered: Strouhal number (Figure A.6), RMS lift coefficient (Figure A.7), average drag coefficient (Figure A.8) and recirculation length (Figure A.9).

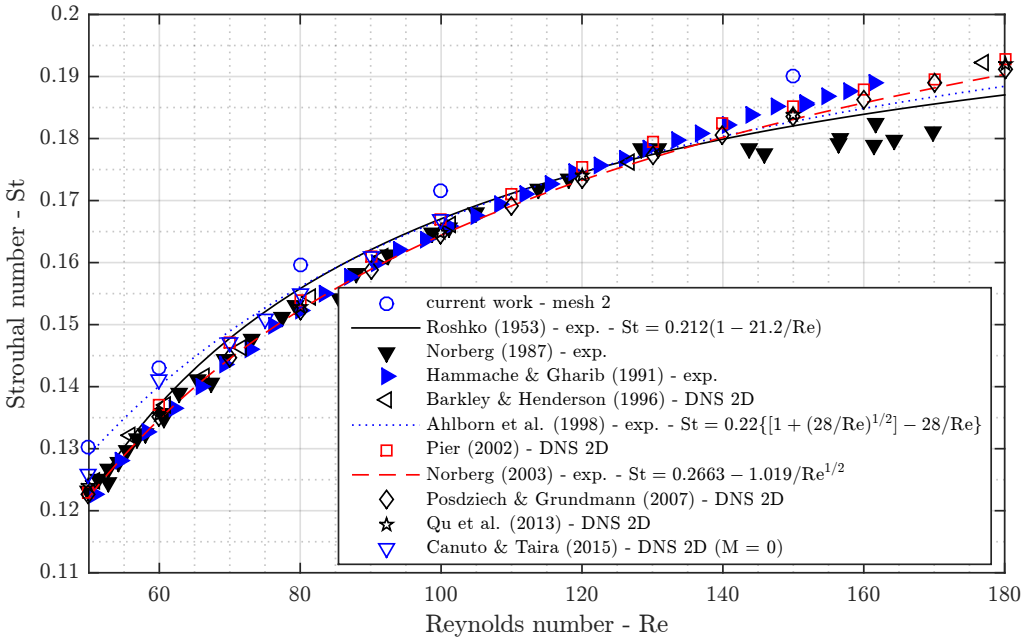

Figure A.6: Evolution of the Strouhal number with the Reynolds number for the circular cylinder (elip, AR = 1.0). Comparison of current results with experimental/empirical laws [3, 71, 168, 172, 218] and numerical [11, 27, 192, 201, 207] values present in the literature.

Values lies within reported results for all the tested quantities. The trends are correctly reproduced in all curves, specially for the unsteady statistics (St and C_L') that are the key values in an aeroacoustical study. It is important to recall that an elevated Strouhal number is a known phenomenon for 2D simulations due to the absence of energy dispersion in the spanwise direction and has been reported by other authors [30].

A.2.2 Different shapes: rectangular section, multiple aspect ratios

Results of the evolution of aerodynamic quantities with the modification of the aspect ratio of rectangular sections at Re = 150 for 2 different meshes (mesh 2 and 4, the latter being more refined) are presented. The comparisons are based on the numerical works of Islam et al. [91] and Inasawa [89]. Considered quantities are the Strouhal number, RMS lift coefficient, RMS drag coefficient, average drag coefficient and recirculation lenght; all graphs are presented in Figure A.2.2.

Once more there is a good resemblance between current results and literature values for all graphs, with some offsets but a exact reproduction of trends. Differences observed in the Strouhal graph (Figure A.2.2.a) are believed to be provoked by the effect of compressiblity, unaccounted in the in current incompressible simulation. There seems to be a gain in precision when refining the mesh (going from mesh 2 to mesh 4), however, the benefit is considered marginal when accounting for the increase of computational cost.

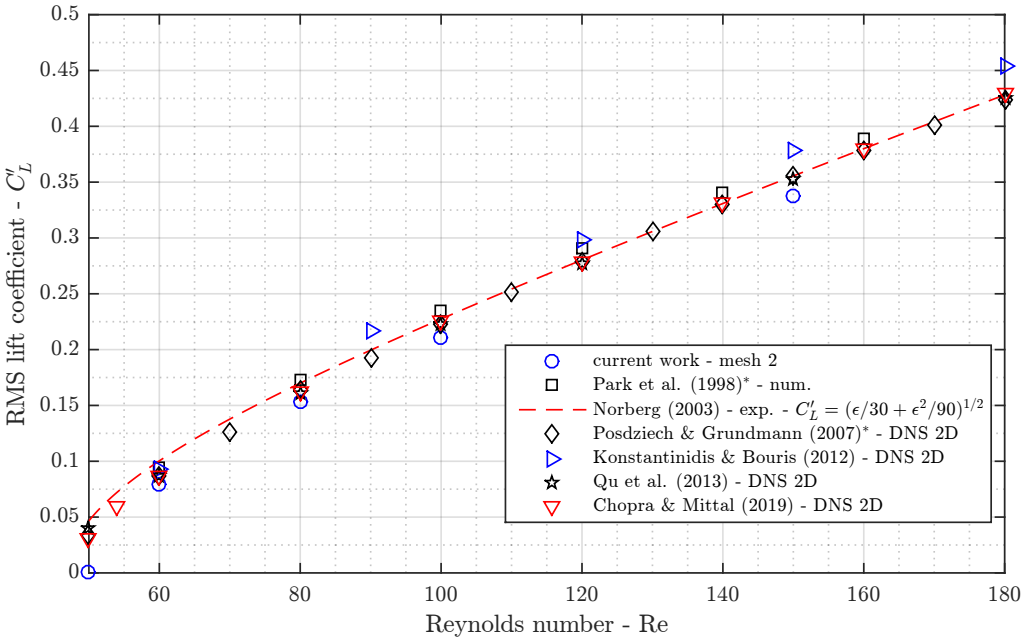

*: obtained considering lift as a perfect sine wave $C'_L = C_{L,max}/\sqrt{2}$.

Figure A.7: Evolution of the RMS lift coefficient with the Reynolds number for the circular cylinder (elip, AR = 1.0). Comparison of current results with experimental/empirical laws [172] and numerical [33, 115, 181, 201, 207] values present in the literature.

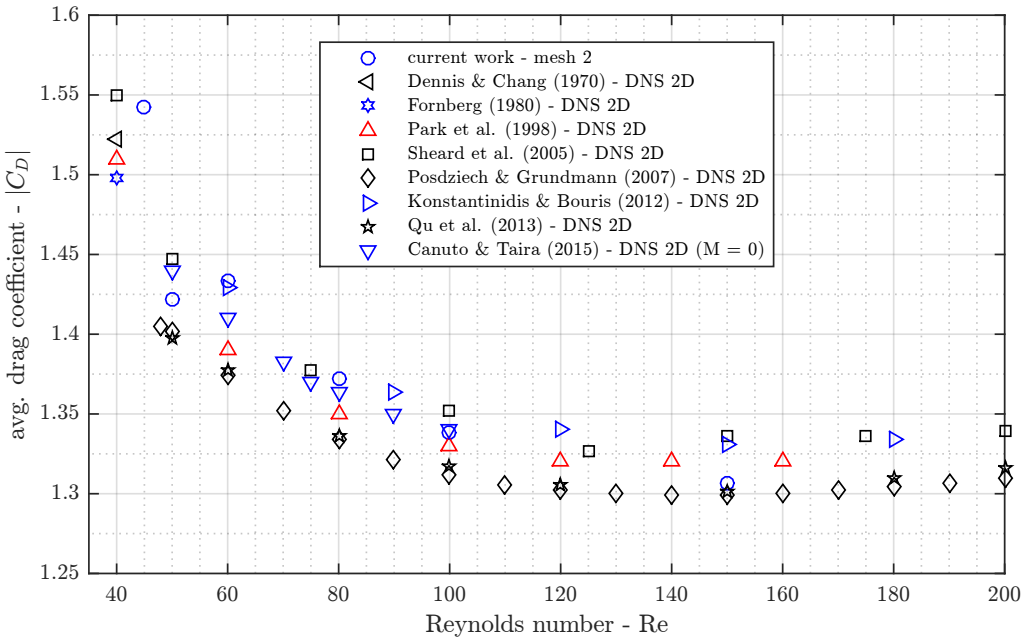

Figure A.8: Evolution of the average drag coefficient with the Reynolds number for the circular cylinder (elip, AR = 1.0). Comparison of current results with numerical [33, 45, 115, 181, 201, 207] values present in the literature.

A.2.3 Conclusion

Current numerical setup is compared to literature data for a single shape at different flow regimes (multiple Reynolds numbers) and different geometries at the same flow conditions. For both analysis, a positive offset between current results and literature tendency is present in almost all points for the set of tested quantities. The elevated levels are a result of the choices made in the convergence studies, where a shorter and coarser mesh is shown to result in overestimated aerodynamic quantities.

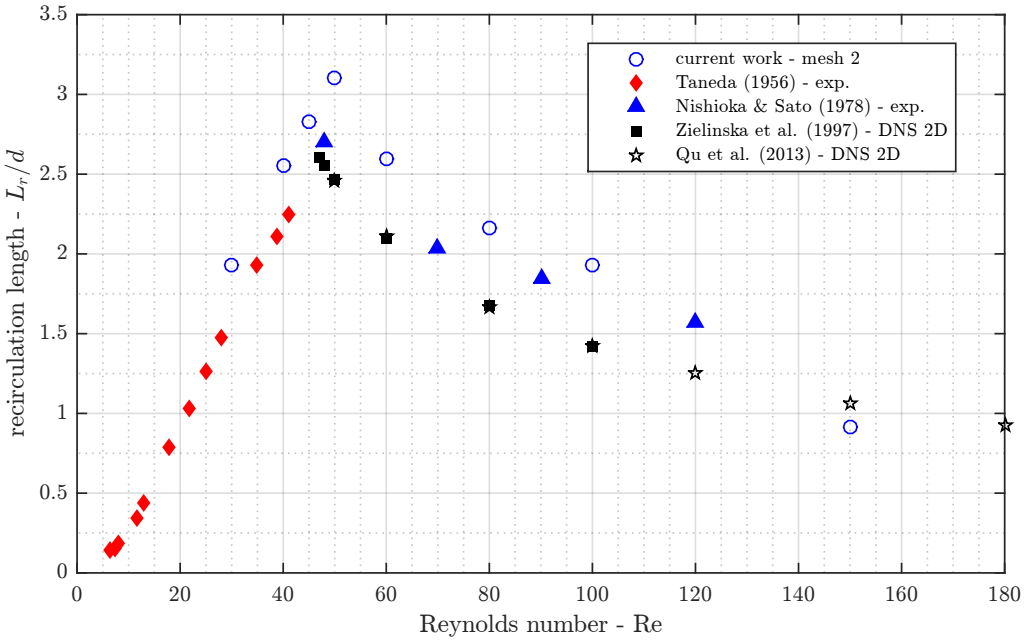

Figure A.9: Evolution of the recirculation length with the Reynolds number for the circular cylinder (elip, AR = 1.0). Comparison of current results with experimental/empirical laws [167, 258] and numerical [207, 287] values present in the literature.

Despite the limited precision for the characterization of individual cases, the trends are maintained and there is a global good fit when confronted to literature data. This characteristic is considered sufficient once the objective of the present study is quantifying the effect of the shape in the flow and noise emission and not to perform a refined description of a single shape.

In summary, considering the performed study and settings, mesh 2 is considered validated. All the obtained results are avowedly slightly over estimated at the order of 1 to 5%. However, even with the limited accuracy that is obtained, these small oscillations are negligible when confronted to the elevated variation provoked by geometrical changes. This is specially pertinent when considering the extreme behaviors present in the shape optimization studies (see Chapter 3).

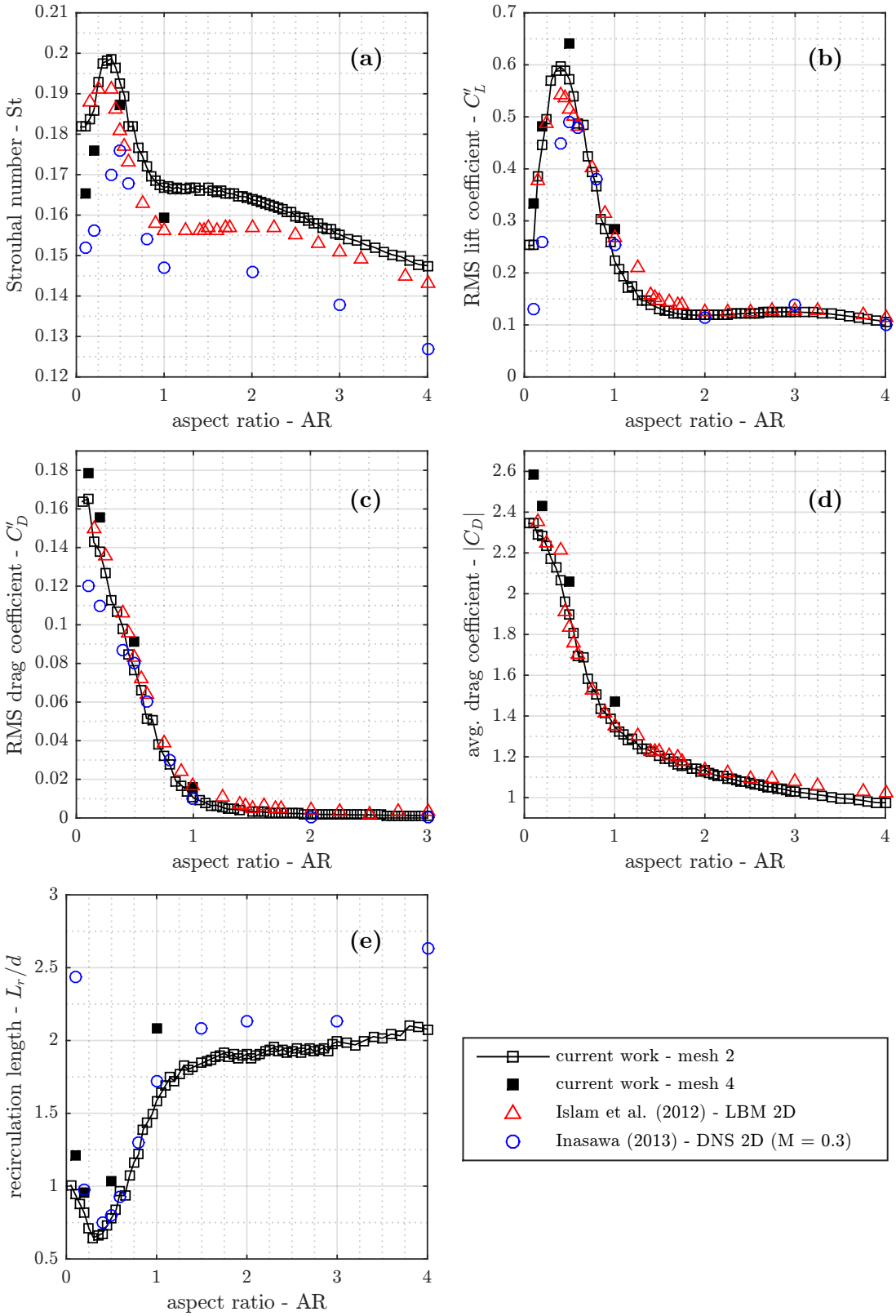

Figure A.10: Evolution of the Strouhal number (a), RMS lift coefficient (b), RMS drag coefficient (c), average drag coefficient (d) and recirculation length (e) with the aspect ratio for the rectangular cylinder (rect, Re = 150). Comparison of current results with numerical [89, 91] values present in the literature.

Appendix B

Empirical laws for individual geometries

Multiple empirical laws relating flow and geometrical quantities are presented in Section 2.3 for the tested canonical shapes; a synthesis of the obtained laws is available in Table 2.13. As stated earlier, the analysis by geometry is often associated with a better fit. Also, the definition of the functions is performed emphasizing a good representation of the trends by geometry.

On this appendix, graphs that illustrate the points and regression curves derived for each individual geometries (same paradigm, different aspect ratios) are presented. Since some of the individual curves are already present in the main text, not all laws figure here, the presented curves are listed next.

Table B.1: List of presented models.

variables			figure	equation
RMS lift coefficient	×	recirculation length	B.1	$C_L' = \alpha + \beta(L_r/d)$
RMS drag coefficient	×	formation length	B.2	$C_D' = \alpha + \exp(\beta L_f/d)$
RMS lift coefficient	×	formation length	B.3	$C_L' = \alpha + \exp(\beta L_f/d)$
RMS lift coefficient	×	vortex vertical displacement	B.4	$C_L' = \alpha\Delta y_\omega$
RMS lift coefficient	×	"distance" to transition	B.5	$C_L'/\mathrm{AR} = \alpha\varepsilon^\beta$
RMS drag coefficient	×	"distance" to transition	B.6	$C_D' = \alpha\varepsilon^\beta$
RMS lift coefficient	×	mean drag	B.7	$C_L'/\mathrm{AR} = \alpha\lvert C_D\rvert^\beta$

B.1 Flow topology based relations

RMS lift coefficient vs. recirculation length

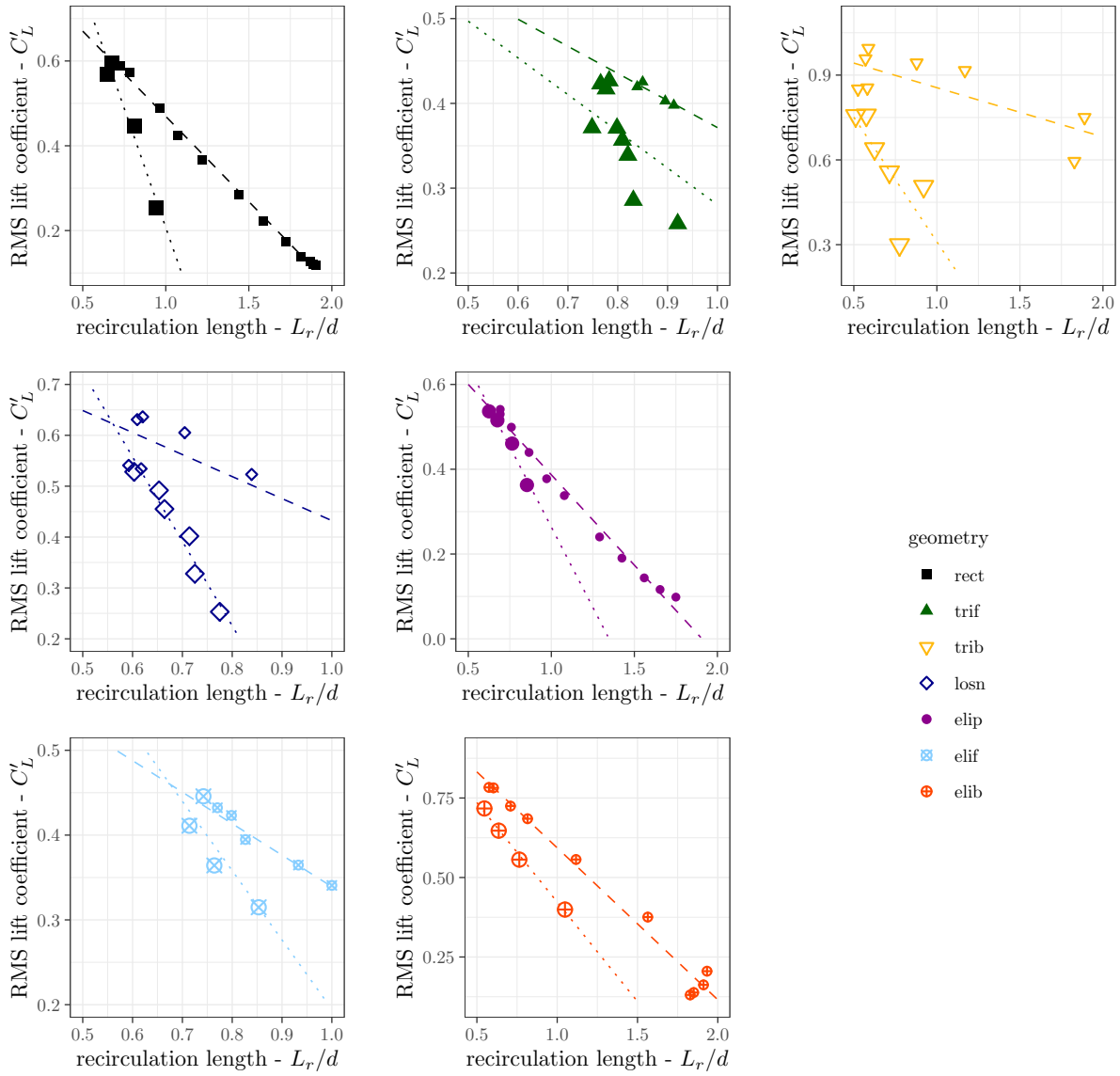

Figure B.1: Regression laws for the RMS lift coefficient as a function of the recirculation length (lin-lin scale); dashed line for regime I and dotted line for regime II.

RMS drag coefficient vs. formation length

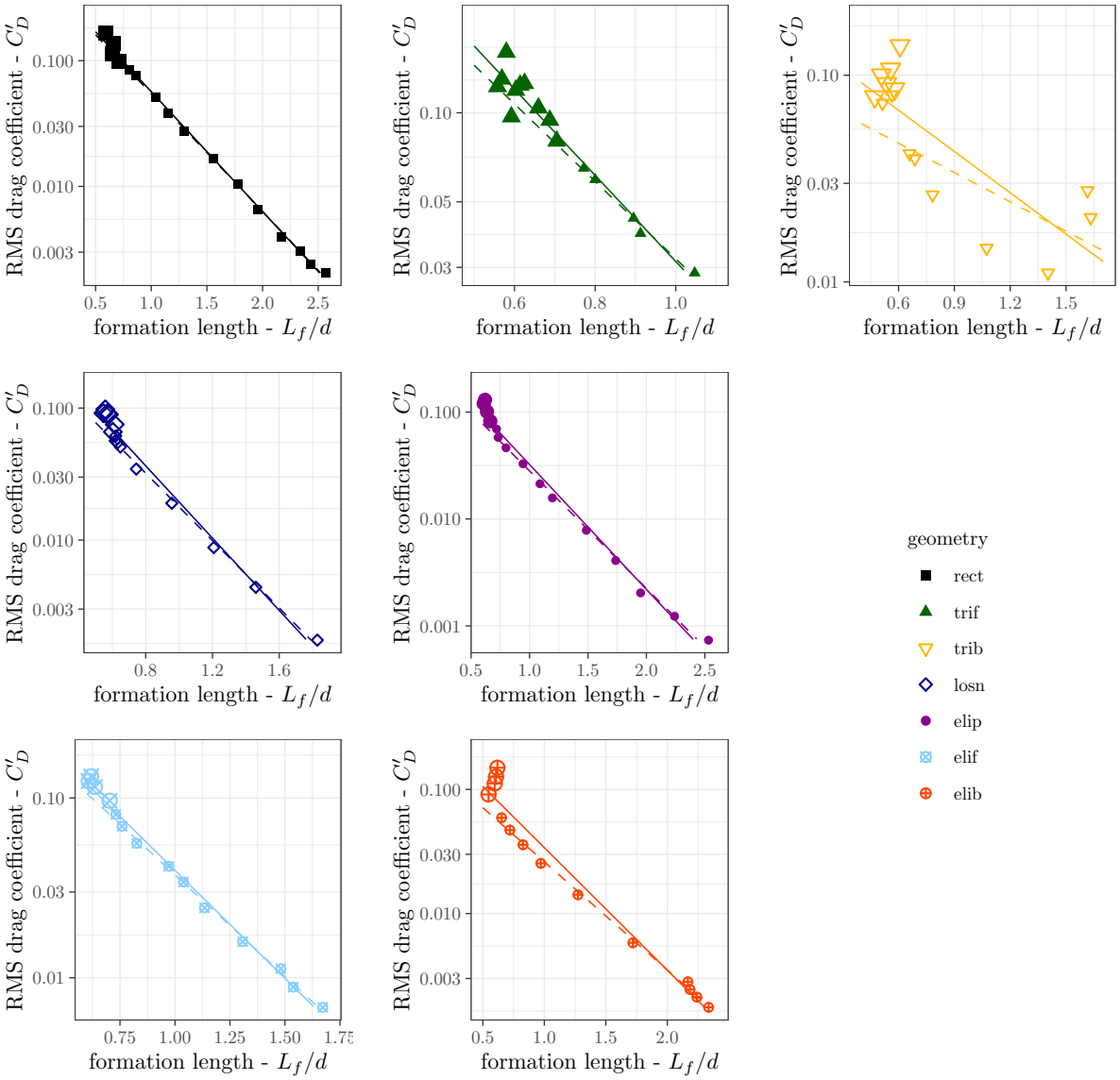

Figure B.2: Regression laws for the RMS lift coefficient as a function of the formation length (lin-log scale); dashed line for regime I and dotted line for regime II.

RMS lift coefficient vs. formation length

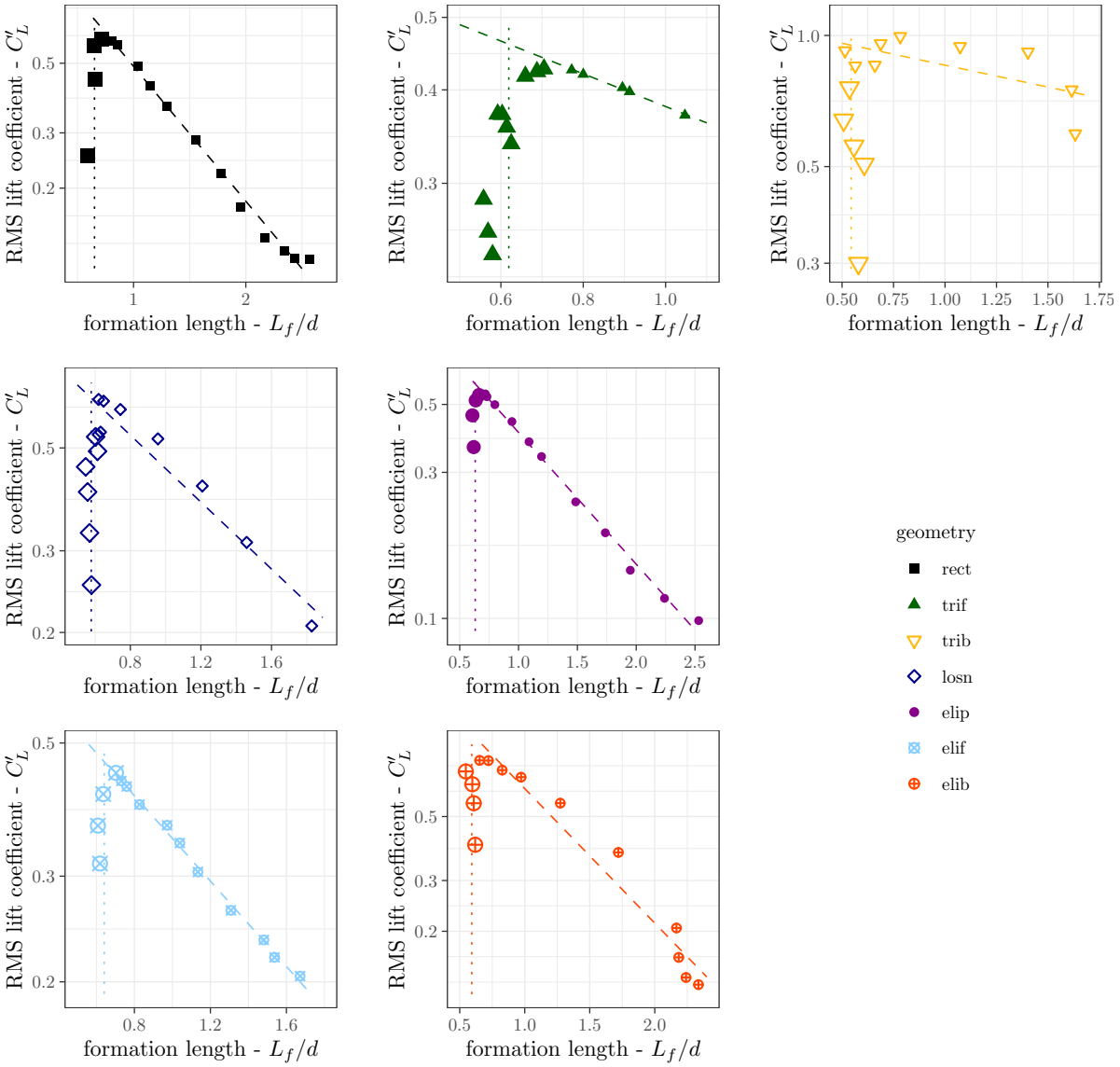

Figure B.3: Regression laws for the RMS drag coefficient as a function of the formation length (lin-log scale); dashed line for regime I and dotted line for regime II.

RMS lift coefficient vs. vortex displacement

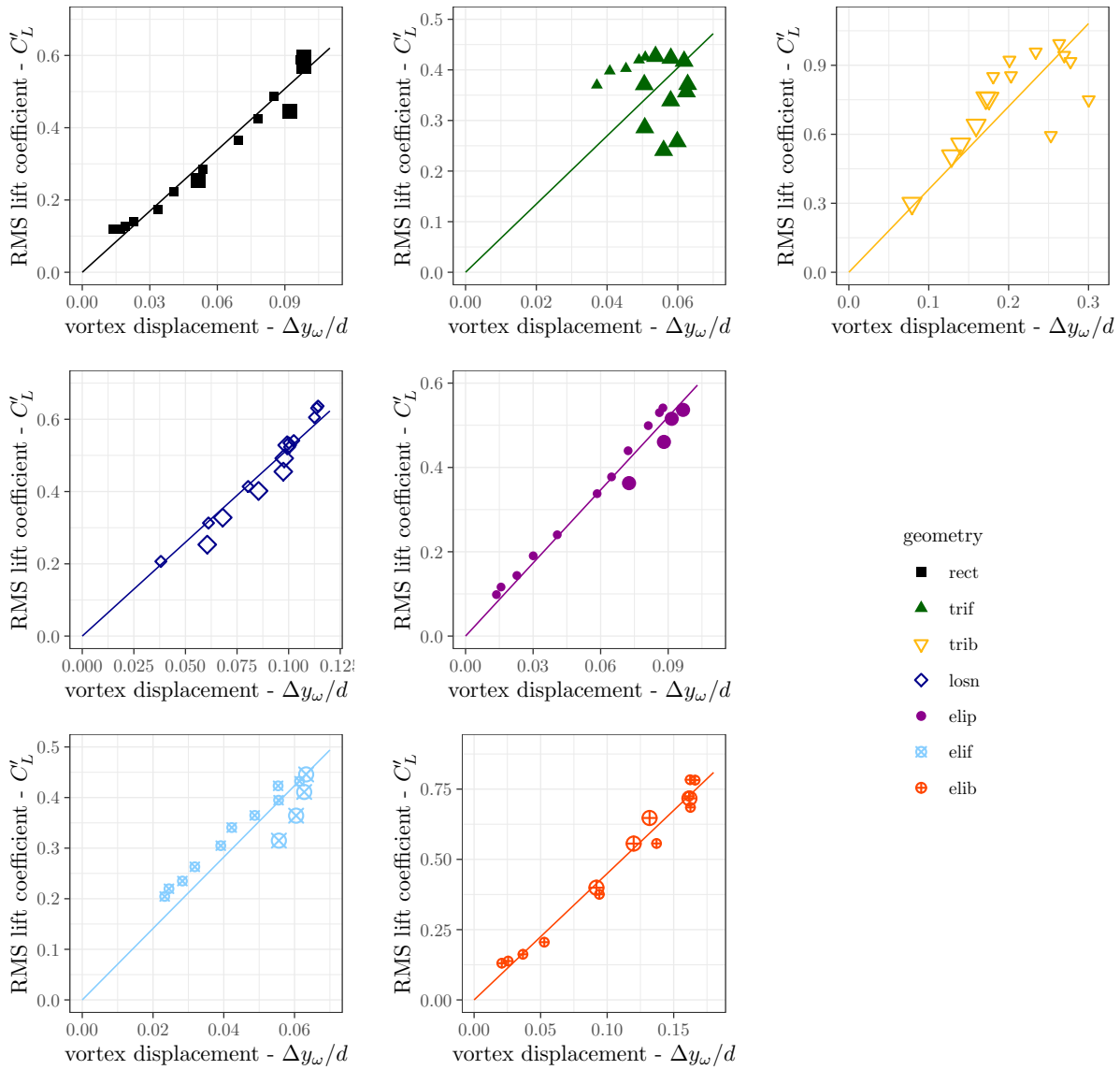

Figure B.4: Regression laws for the RMS lift coefficient as a function of the vortex vertical displacement Δy_ω (lin-lin scale).

B.2 Integral quantities and geometry based relations

RMS lift coefficient vs. distance to the critical Reynolds number

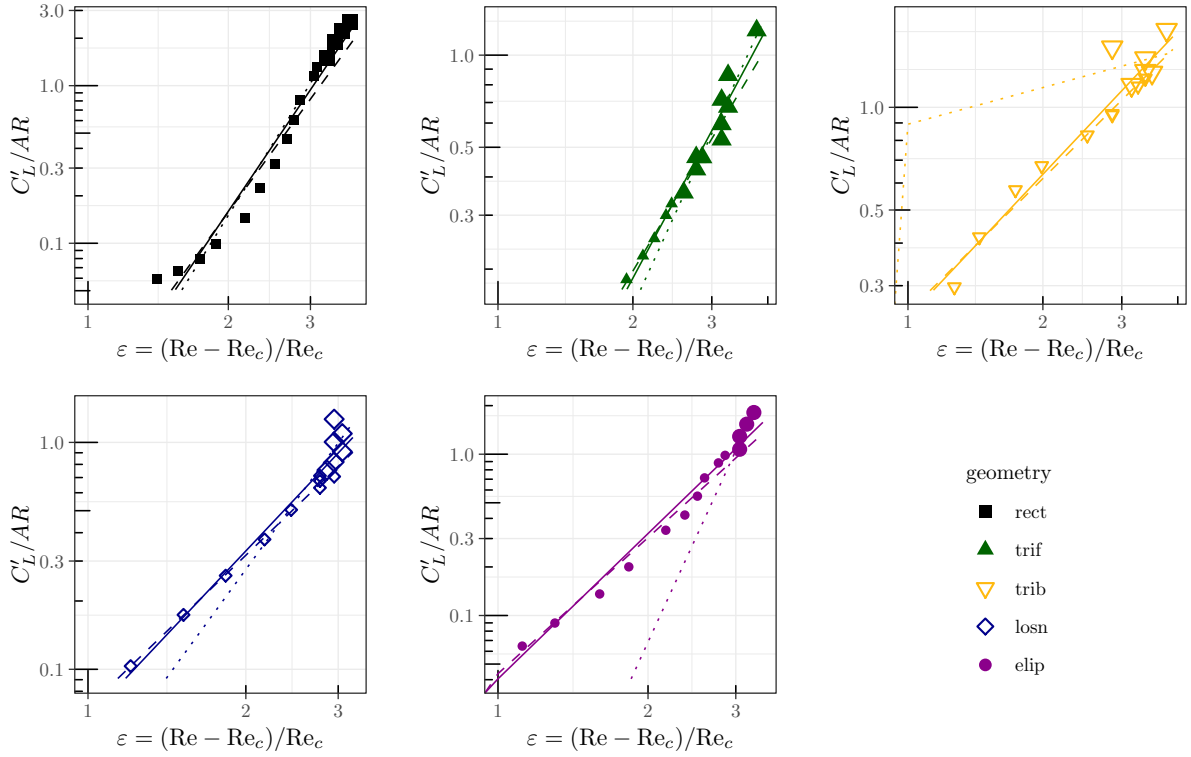

Figure B.5: Regression laws for the normalized RMS lift coefficient as a function of ε (log-log scale); solid line for all points, dashed line for regime I and dotted line for regime II.

RMS drag coefficient vs. distance to the critical Reynolds number

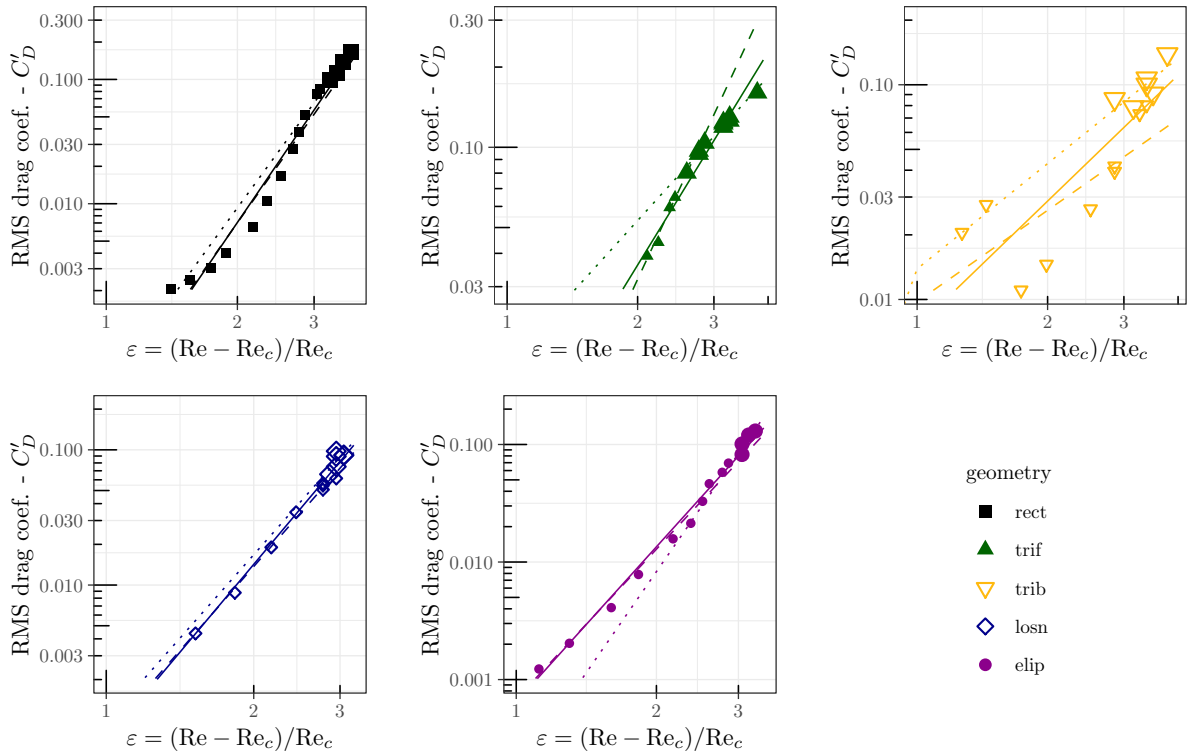

Figure B.6: Regression laws for the RMS drag coefficient as a function of ε (log-log scale); solid line for all points, dashed line for regime I and dotted line for regime II.

RMS lift coefficient vs. mean drag

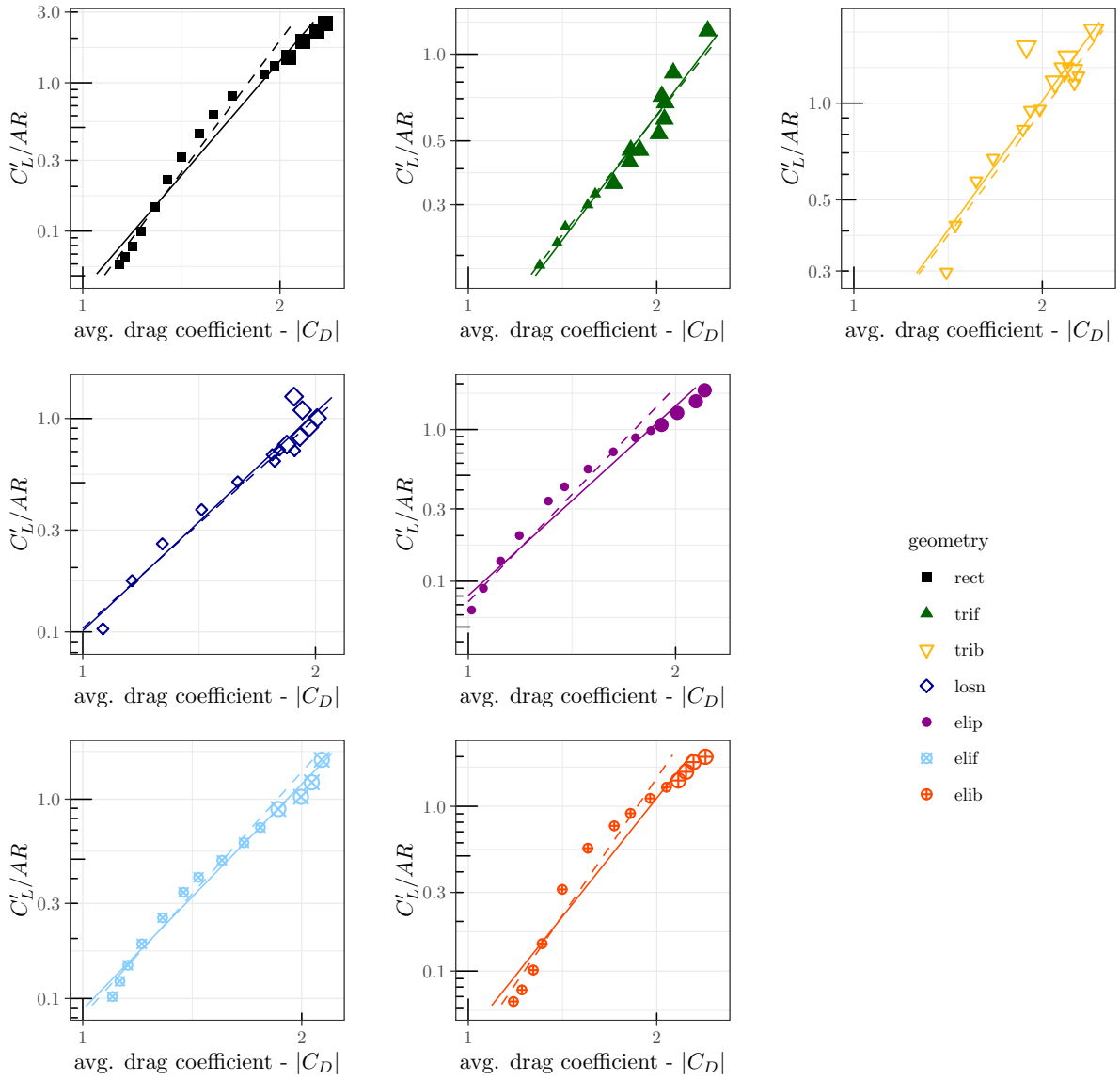

Figure B.7: Regression laws for the normalized RMS lift coefficient as a function of the average drag (log-log scale); solid line for all points and dashed line for regime I.

Appendix C

Comparison with the empirical law of Paul et al. (2014) for the critical Reynolds

The regression law for the evolution of the critical Reynolds with the aspect ratio (Section 2.3.3.1) is compared to the function proposed by Paul et al. [185] for elliptical sections. Since its use a different reference for the definition of the Reynolds number (the hydraulic diameter), a transformation was necessary. Both the conversion and the comparison are presented next.

C.1 Transformation

In order to analyze the results and the tendency law proposed by Paul et al. [185], a transformation of the presented values is necessary since the used reference length is the hydraulic diameter of the ellipse. Consider Re_{d_H} as the Reynolds number that uses the hydraulic diameter $d_H = 4S/P$ as the reference length, where S is the surface P is the perimeter of the ellipse; major axis and minor axis a and b, respectively. Independently of the orientation, the hydraulic diameter is defined as:

$$d_H = \frac{4(\pi ab)}{4aE(e)} = \frac{\pi b}{E(e)} \tag{C.1.1}$$

where E is the complete elliptic integral of second kind and $e = \sqrt{1-(b/a)^2}$ is the ellipse eccentricity. For a circle, $e = 0$ and $E(e) = \pi/2$; for AR $\to 0$, $e = 1$ and $E(e) = 1$. The relationship between the Reynolds numbers defined by the height d and by the hydraulic length d_h for the same flow velocity and viscosity is:

$$\mathrm{Re} = \mathrm{Re}_{d_H}\frac{d}{d_H} = \mathrm{Re}_{d_H}E(e)\frac{d}{\pi b} \tag{C.1.2}$$

According to the current definition of the aspect ratio, the ellipse's axis can either be $a = d/2$ and $b = \mathrm{AR}d/2$ ($\mathrm{AR} \leq 1$) or $a = \mathrm{AR}d/2$ and $b = d/2$ ($\mathrm{AR} > 1$). Thus, two equations are defined:

$$\mathrm{Re} = \begin{cases} \frac{2E(e)}{\pi AR}\mathrm{Re}_{d_H}, & \text{if AR} \leq 1 \\ \frac{2E(e)}{\pi}\mathrm{Re}_{d_H}, & \text{if AR} > 1 \end{cases} \tag{C.1.3}$$

The law relating the critical Reynolds number to the axis ratio (b/a) and the angle of attack of elliptical cylinders given by Paul et al. [185] is:

$$\mathrm{Re}_{d_H,c} = 43.513\ (b/a)^{(-1.920\lambda^2+3.197\lambda-1.023)} \tag{C.1.4}$$

where λ is the ratio between the angle of attack and $\pi/2$. Considering the shorter ellipses normal to the flow (AR $\leq$ 1, λ = 1, b/a = AR) and the longer geometries parallel to the flow (AR > 1, λ = 0, $b/a = 1/AR$), the following relationships arise:

$$\mathrm{Re}_{d_H,c} = \begin{cases} 43.513\ (b/a)^{+0.254} = 43.513\ \mathrm{AR}^{+0.254}, & \text{if AR} \leq 1 \\ 43.513\ (b/a)^{-1.023} = 43.513\ \mathrm{AR}^{+1.023}, & \text{if AR} > 1 \end{cases} \tag{C.1.5}$$

Replacing the Reynolds number conversion term from Equation C.1.3 into Equation C.1.5, the final equations are obtained:

$$\mathrm{Re}_c = \begin{cases} 27.7012\ E(e)\mathrm{AR}^{-0.746}, & \text{if AR} \leq 1 \\ 27.7012\ E(e)\mathrm{AR}^{+1.023}, & \text{if AR} > 1 \end{cases} \tag{C.1.6}$$

C.2 Comparison to the law proposed in this work

The current relation and law represented by Equation C.1.6 are illustrated in Figure C.1.

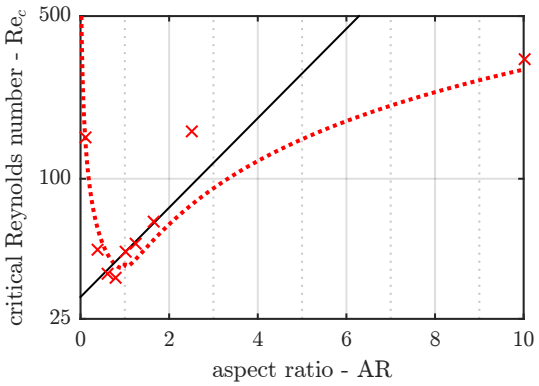

Figure C.1: Comparison of the laws for the evolution of the critical Reynolds number with the aspect ratio, elliptical section. Solid line represents the current exponential fit with an imposed $\mathrm{Re}_{c,\mathrm{AR}\to 0}$ and dotted line represents the law proposed by Paul et al. [185].

The model proposed by Paul et al. [185] is asymptotically inconsistent once it supposes that the flow around thin plates (AR $\to$ 0) has an infinite critical Reynolds number. This behavior is believed to arise from 2 issues. First, employing the hydraulic diameter as the reference length for the definition of the domain can result in a large flow blockage, what is problematic when defining the critical Reynolds number as pointed by Jackson[93] and Patil & Tiwari [183]. For example, considering the ellipse of axis-ratio (minor axis divided by the major axis) 0.1 and angle of attack of 90 degrees (in this work, ellipse of AR = 0.10), the hydraulic diameter in this configuration is of 0.1557 d (see Equation C.1.1), being d taken as the height of the geometry as illustrated in Figure 2.1. In Paul et al. [185], the domain goes from $-8d_H \leq y_2 \leq +8d_H$, what represents a domain of $-1.25d \leq y_2 \leq +1.25d$ and a blockage factor of 40%. In such conditions, the flow is extremely influenced by the lateral boundaries and there is an increase in the critical Reynolds number. So, at low aspect ratio, the data and regression law capture the influence of the increase of the blockage rather than the modification of the geometry.

Secondly, there is the consideration of the transition criteria used by Paul et al. [185], which supposes that the behavior is linear and constant even close to Re_c. This is believed to be more influential at larger aspect ratios, AR > 2, and could justify why the Re_c values are lower than the present exponential law tendency. Those points biased the relationship proposed by Paul et al. [185] and result in an underestimation of the critical Reynolds number at 1 < AR < 2 even if the obtained values at that range are similar to current and literature values, as observed in Figure 2.27.

Present Re_c(AR) models lead to an infinite critical Reynolds number with the increase of the aspect ratio (for an infinitely long flat plate parallel to the flow). The existence of a vortex

shedding is uncertain for long plates, and a different category of flow, fundamentally defined by boundary layer effects, exists. That behavior is physically plausible, however, more data are necessary to confirm that and the consistency of the extrapolation of the proposed model to extended bodies (AR > 2).

Appendix D

Review on shape optimization elements

This appendix is dedicated to some concepts and techniques used in the shape optimization. It is a complement and extension of the introduction presented in Section 3.1. It is recommended for the reader who is interested in performing an shape optimization study.

In Section D.1, different methods for defining a parametric shape are presented. Next, in Section D.2, response surface models, used as estimations of the are discussed, with a description of both the definition of the sampling and the interpolation methods. Furthermore, the adjoint equation method is introduced in Section D.3. Gradient and evolutionary optimizes (Gradient Algorithm and Differential Evolution) close the appendix in Section D.4.

D.1 Shape parametrization

The design of aerodynamic and aeroacoustic efficient shapes imposes the use of complex geometries, derived from complex equations of multiple inputs and continuity constraints. The use of a parametric shape is fundamental to make the optimization realizable with the limitation of the number of parameters and for a better clarity of the results and definition of the constraints.

This section is dedicated to the presentation of 3 examples of parametric curves. The equations are generalized, and the concepts may be applied as well in 2D or 3D, and the combination of the curves may also generates surface and volumes [162, 277]. This discussion is based on the work of Patrikalakis & Maekawa [184], reference to look for more details on the properties of those curves.

D.1.1 Bézier curve

A Bézier curve is a parametric curve based on the Bernstein polynomial that uses the position of control points:

$$\mathbf{r}(t) = \sum_{i=0}^{n} \mathbf{p}_i B_{i,b}(t), \qquad 0 \leq t \leq 1. \tag{D.1.1}$$

$$B_{i,n}(t) = \frac{n!}{i!(n-i)!}(1-t)^{n-i}t^i, \qquad i = 0, ..., n. \tag{D.1.2}$$

where $\mathbf{p}_i$ are the n control points (y_1, y_2) and $B_{i,n}(t)$ are the Bernstein polynomials.

A major advantage of this kind of curve for the use in aerodynamic and aeroacoustic contexts is the possibility to obtain any desirable level of continuity by an appropriate choice of the order. More details about the properties of these curves are also available in [184].

D.1.2 B-spline curve

A B-spline (Basic Spline) is a combination of control points $\mathbf{p}_i$ and polynomial functions, $N_{i,k}(t)$, of order $k-1$ (degree k) and of continuity of at least equal to C^{2-k} in the knot. An array of increasing knots ($T = (t_0, t_1, ..., t_{n+k})$ with $t_i > t_{i-1}$) must be defined, in which are defined the following curve (Boor algorithm):

$$\mathbf{r}(t) = \sum_{i=0}^{n} \mathbf{p}_i N_{i,k}(t), \quad n \geq k-1, \quad t \in [t_{k-1}, t_{n+1}]. \tag{D.1.3}$$

The number of control points (n) must be equal or superior to the order of the functions. A Bézier curve of order k is an B-spline without an internal knot and $n = k-1$:

$$\mathbf{T} = (\underbrace{t_0, t_1, ..., t_{k-1}}_{k \text{ repeated nodes}}, \underbrace{t_{n+1}, ..., t_{n+k}}_{k \text{ repeated nodes}}), \tag{D.1.4}$$

The advantage of this type of curve is the possibility to modify the geometry locally while keeping the order of the equation reduced.

D.1.3 NURBS

A NURBS (**N**on-**U**niform **R**ational **B**-**S**pline) is a generalization of the B-Spline, which already is a generalization of the Bézier curve. Definition:

$$\mathbf{r}(t) = \frac{\sum_{i=0}^{n} w_i \mathbf{p}_i N_{i,k}(t)}{\sum_{i=0}^{n} w_i N_{i,k}(t)}, \tag{D.1.5}$$

where $w_i > 0$ are the weighting factors and $N_{i,k}(u)$ are a base functions, analogous to the one presented in the B-spline equation (D.1.3). If the factors w_i are constant and equal to 1, the NURBS becomes a B-spline. If the number of control points equals the order of the curve $(k-1)$, it becomes a rational Bézier curve.

D.1.4 Use of parametric curves

In the context of an aerodynamic/aeroacoustic optimization, the geometry is associated to a mesh for the resolution of the flow equations and the evaluation of the objective function. For each modification on the shape of the body, an update of the mesh must be performed, keeping the quality of the mesh elements.

One of the techniques to solve the issues associated with the change of the geometry is the use of the control points of the parametric curves for the definition of the mesh [162], as presented in Figure D.1.

As signaled by Naumann et al. [162], the displacement of the nodes may be performed by 2 different categories of algorithms: the methods based on the connective of the mesh, like for example the spring analogy, under which every point has an elasticity and the solution of a equation for the equilibrium of "forces" for the new mesh [43, 277] and the schemes of point to point with the interpolation of the displacements of the boundary elements, which can, for example, take account of the distance between those points by mean of radial basis functions (RBF) [42].

With the use of a Immersed Boundary Method, the redefinition of the position of the mesh elements is not necessary, once the solid domain is composed by the global discretization. The shape is modified by the simple update of the list of nodes/cells submitted to a non-null forcing term.

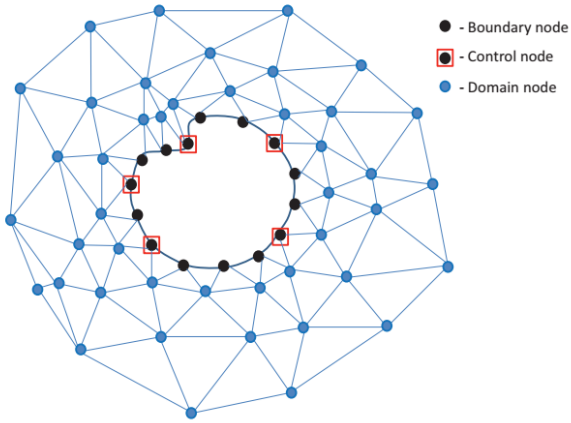

Figure D.1: Definition of the control nodes, the boundary nodes and the domain nodes for a non-structured mesh (reproduced from [162]).

D.2 Reponse Surface Models

For optimization problems with computationally expensive objective/cost functions, the optimization routines may be performed with a model of the function, also called surrogate model, interpolated from a predefined number of points. after the model is defined, the gradient based or evolutionary algorithms may be used without major use of CPU hours.

For the construction of the model, it is necessary to capture the behavior of the function on the full extent of the design space. For that, a series of conventions and techniques are proposed, called as Design of Experiment (DoE) that present the techniques to define the position where to perform the calculations.

This section is composed by the presentation of three DoE and three interpolation methods used for the creation of the surrogate model. A complete discussion over the use of surrogates in global optimization may be found in [102].

D.2.1 Design of Experiments (DoE)

The definition of a model of the objective function, independently of the method that is used, demands a number of complete evaluations of the objective function. Many methods are used for defining the set of points more adapted for the composition of that database that will define the surrogate, some of them are presented next.

D.2.1.1 Factorial plan

With the admissible set of study defined by the dimension D, a discretization of N levels is performed for each parameter, producing a Cartesian mesh of the domain. The combination of all the options (the intersections of the mesh) are tested (example for $D = 2$ in Figure D.2).

One of the weakness of this method is the elevated number of cost function evaluations, once the number of testing points is equal to the order of discretization elevated by the number of parameters (N^D). However, depending on the refinement, all the possibilities in the domain are contemplated in the composition of the model.

D.2.1.2 Latin Hypercube Sampling (LHS)

The major concern when constructing the database for the production of the surrogate is that all the different zones of the domain are represented. The Latin Hypercube Sampling (LHS), introduced by McKay [152], proposes the sampling of the domain with a part of the elements of the factorial plan. As described in [148] and [162], for the definition of N vectors, one need to split each dimension of the D dimensional domain into $N - 1$ sections, creating $(N - 1)^D$ cells

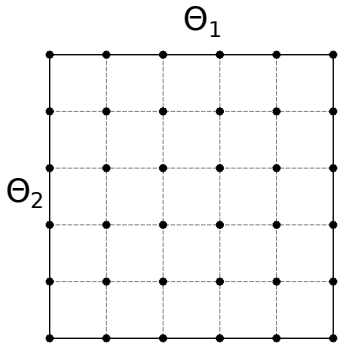

Figure D.2: Factorial plan. Each point represents on parameters vector (Θ_1, Θ_2) for the evaluation of the cost function.

and N^D nodes. Each element of the vector is defined by the random selection one of those nodes, banning the use of the corresponding parameter values on the definition of following vectors. This procedure must be repeated until all the N vectors are fully defined. One example of the application of the method in a 2D domain is illustrated on Figure D.3.

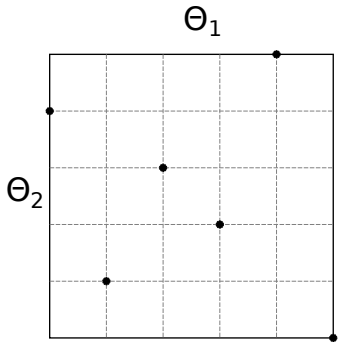

Figure D.3: Example of the Latin Hypercube Sampling (LHS) with a 2D domain.

D.2.1.3 Taguchi plan

The Taguchi method is a general procedure for quality and production. One of the aspects of this technique is the definition of an experiments plan. As presented by Beigmoradi et al. [17], the Taguchi plan consists in the evaluation of the parameters and the decision of the number of levels that will exist in the evaluation. An orthogonal table - fraction of the factorial plan, that is, that presents the simultaneous variation of all the factors in order to reduce the number of evaluations - is produced with the levels as a function of the number of tests that are chosen (rows in the table).

For every experiment (row), each factor (column), must be in the defined level (cell). Figure D.4 contains an example for 4 experimentation, with 3 parameters and 2 levels (1 or 2).

In the figure, only 4 simulations are performed instead of 8 (2^3). In their optimization study, Beigmoradi et al. [17] employed a L25 Taguchi plan (25 experiments), with 4 parameters and 5 levels.

D.2.2 Interpolation methods

D.2.2.1 Polynomial response surface

The polynomial response model, proposed by Box in 1951 [24], defines the response surface as an arbitrary polynomial law of the design space parameters. The quadratic model used by Tang

	Level		
#	Θ_1	Θ_2	Θ_3
1	1	1	1
2	1	2	1
3	2	1	1
4	2	2	1

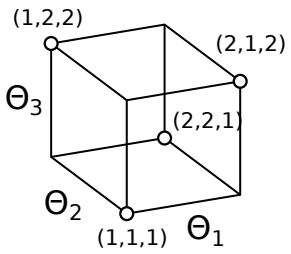

Figure D.4: Taguchi plan for a three-dimensional domain, with 2 levels.

[259] is presented next.

Be Θ_j one of the variables of the optimization problem. For n_s evaluated points, $\Theta_j(p)$ with $p = 1$ to n_s, the result ($f^{(p)}$) is supposed to be represented by:

$$f^{(p)} = \alpha_0 + \sum_{1 \leqslant j \leqslant n_v} + \alpha_j \Theta_j^{(p)} + \sum_{1 \leqslant j \leqslant k \leqslant n_v} \alpha_{(n_v - 1 + j + k)} \Theta_j^{(p)} \Theta_k^{(p)}, \tag{D.2.1}$$

where α_0, α_j and $\alpha_{(n_v-1+j+k)}$ are the n_t coefficients of the model, with $n_t = (n_v + 1)(n_v + 2)/2$. In matrix notation, for the p-th experiment:

$$f^{(p)} = \mathbf{A}^T \mathbf{\Theta}^{(p)}, \tag{D.2.2}$$

being $\mathbf{A}$ the vector of coefficients and $\mathbf{\Theta}^{(p)}$ the vector of parameters:

$$\begin{aligned} \mathbf{A} &= [\alpha_0, \alpha_1, ..., \alpha_{n_t - 1}] \\ \mathbf{\Theta}^{(p)} &= [1, \Theta_1^{(p)}, \Theta_2^{(p)}, ..., \Theta_{n_v}^{(p)}, (\Theta_1^{(p)})^2, \Theta_1^{(p)} \Theta_2^{(p)}, ..., (\Theta_1^{(p)})^2] \end{aligned} \tag{D.2.3}$$

The interpolated response vector $\hat{f}$ for an input $\mathbf{\Theta}$ is defined as:

$$\hat{f} = \hat{\mathbf{A}}^T \mathbf{\Theta} \tag{D.2.4}$$

The coefficients may be defined by a lest-squares model:

$$\hat{\mathbf{A}} = (\mathbf{X}^T \mathbf{X})^{-1} \mathbf{X}^T \mathbf{Y} \tag{D.2.5}$$

with $\mathbf{X}$ and $\mathbf{Y}$ being the arrays built from the evaluated points:

$$\mathbf{X} = \begin{bmatrix} 1 & \Theta_1^{(1)} & \Theta_2^{(1)} & \cdots & (\Theta_{n_v}^{(1)})^2 \\ \vdots & \vdots & \vdots & \ddots & \vdots \\ 1 & \Theta_1^{(n_s)} & \Theta_2^{(n_s)} & \cdots & (\Theta_{n_v}^{(n_s)})^2 \end{bmatrix} \qquad \mathbf{Y} = [f^{(1)}, f^{(2)}, ..., f^{(n_s)}] \tag{D.2.6}$$

One must take account that, for this solution, the number of evaluations (n_s) must be at least as big as the number of coefficients ($n_v \leq n_s$). For example, for an optimization of 3 parameters, the number of evaluations for the definition of the polynomial model must be of at least 10 points.

The coefficients may also be obtained by running an optimization routine to minimize the error, as used in [259] and discussed on Section 2.3.1.2.

D.2.2.2 Kriging

Kriging consists in defining the linear interpolation of the evaluated points that minimizes the variance of the error estimation [103, 148]. The estimated value is a result of an weighted average of the known values. It was introduced by Krige in 1951 for the study of spatial distribution of minerals [118]. The equations presented next are issued from the work of Lophaven et al. [139].

Be $\mathbf{f}(\mathbf{\Theta})$ a solution of the problem to be optimized with the parameter vector $\mathbf{\Theta}$, which are tested for the predefined $\mathbf{\Theta_i}$ points. The Kringing regression model is based on a linear estimation of the following form:

$$\hat{\mathbf{f}}(\mathbf{\Theta}) = \Gamma^T(\mathbf{\Theta})\mathbf{f_p} \tag{D.2.7}$$

where $\Gamma(\mathbf{\Theta})$ is a vector of coefficients associated with each known point, that behave as control points; and $\mathbf{f_p}$ is the array of known solutions $\mathbf{f_p} = \{\mathbf{f}(\mathbf{\Theta_1}), ..., \mathbf{f}(\mathbf{\Theta_i}), ..., \mathbf{f}(\mathbf{\Theta_n})\}^T$.

The definition of the coefficients is based on 2 hypothesis on the properties of the real function $\mathbf{f}(\mathbf{\Theta})$: isotropic and stationary (the covariance is only a function of the distance between the estimation point $\mathbf{\Theta}$ and the known points $\mathbf{\Theta_i}$); and without bias (the sum of the coefficients $\gamma(\mathbf{x})$ equals 1). The coefficients are defined for a minimal variance of the error (difference between the calculated and estimated f). From mathematical manipulations and the use of the Lagrange multiplier, the regression function is reduced to:

$$\hat{\mathbf{f}}(\mathbf{x}) = \mathbf{f}(\mathbf{\Theta})^T\beta^* + c(\mathbf{\Theta})^T\gamma^*, \tag{D.2.8}$$

where β^* and γ^* are $n \times m$ real coefficient matrices and $c(\mathbf{\Theta}) = [\mathcal{C}(\mathbf{\Theta}, \mathbf{\Theta_1}), ..., \mathcal{C}(\mathbf{\Theta}, \mathbf{\Theta_n})]$ is the vector of correlations, described later. The least-squares solution is:

$$\beta^* = (R^T C^{-1} R)^{-1} R^T C^{-1} \mathbf{f_p} \tag{D.2.9a}$$

$$\gamma^* = C^{-1}(\mathbf{f_p} - R\beta^*) \tag{D.2.9b}$$

with C and R the correlation and regression matrices, respectively, defined as:

$$C_{i,j} = \mathcal{C}(\mathbf{\Theta_i}, \mathbf{\Theta_j}), \quad i, j = 1, ..., n$$
$$R_{i,j} = \mathcal{R}_j(\mathbf{\Theta_i}), \quad i = 1, ..., n \; j = 1, ..., d, .$$

where $\mathcal{C}(\mathbf{\Theta}, \mathbf{\Theta_i})$ is the correlations between the vector $\mathbf{\Theta}$ and the tested point $\mathbf{\Theta_i}$ and $\mathcal{R}_j(\mathbf{\Theta})$ is the regression model (constant, linear, quadratic, etc).

The closure of the estimator lies in the selection of the regression ($\mathcal{R}_j(\mathbf{\Theta_i})$) and correlation ($\mathcal{C}(\mathbf{\Theta}, \mathbf{\Theta_i})$) models. They can be defined from a measured behavior of the statistical distribution of the function of be defined by arbitrary theoretical laws.

Jouhaud et al. [103] used the exponential correlation model, where the parameter θ_j is a coefficient that defines the "strength" of the correlation between the vectors $\mathbf{w_j}$ and $\mathbf{\Theta_j}$ (constant for the isotropic model), and the constant regression model:

$$\mathcal{C}_j(\mathbf{w}, \mathbf{\Theta}), = \prod_{j=1}^{d} \exp(-\theta_j(w_j - \Theta_j)^2) \qquad \mathcal{R}_j(\mathbf{\Theta_i}) = 1$$

D.2.2.3 Artificial Neural Networks (ANN)

Artificial Neural Networks (ANN) are defined as the combination of connected multiple data treatment units that work similar to the human neurons. Each element applies a transformation to the input and from the connection of several neurons, one or multiple outputs are generated.

From pairs of tested inputs and outputs ($\mathbf{\Theta_i}$, $\mathbf{f}(\mathbf{\Theta_i})$) experimented according to a predefined sampling, the laws for each neuron (coefficients of the transformation function) are defined in the learning period, the only expensive step of this method. A major advantage of this technique is the capacity to reproduce non-linear behaviors that can exist in the cost/objective function.

One of the main difficulties of the methodology is the definition of the number and the distribution of the neurons. In studies of the shape optimization for aerodynamics, Giannakoglou [62], used a Radial Basis Function Network (RBFN), Figure D.5, and Beigmoradi et al. [17] adopted a feedforward network, composed by three layers of 12, 6 and 1 neuron with a tangent-sigmoid transfer function. It is also fundamental to select a robust design of experiments so that

the ANN estimates the cost function correctly and remains reproducing its behavior correctly for the different set of inputs that are used.

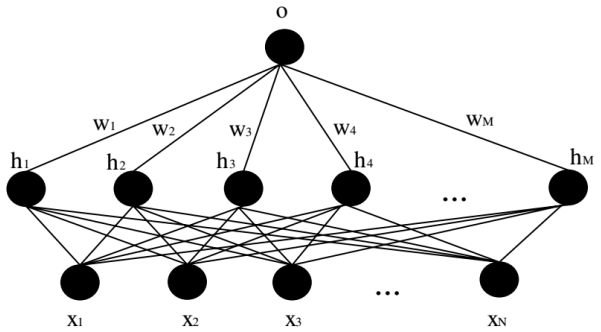

Figure D.5: Radial basis function network (reproduced from [63]).

D.3 Adjoint equations

The evaluation of the gradients of the objective/cost function for a continuous response is made by the evaluation of at least one supplementary point per parameter (two if the estimation considers a first order centered scheme). With a significant number of variables, the application of gradient based optimization routines is not practicable. The method of adjoint equations overcomes this limitation be defining the gradient evaluation such as to be independent of the number of variables.

Following the development presented by Vassberg & Jamenson [267], consider the cost function I. For an aerodynamic application, it can be represented as the function of flow parameters (w) and the geometry parameters ($\mathbf{\Theta}$):

$$f = f(w, \mathbf{\Theta}) \tag{D.3.1}$$

A change in the geometry parameters provokes a change in the cost function that may be described as:

$$\delta f = \frac{\partial f}{\partial w}^T \delta w + \frac{\partial f}{\partial \mathbf{\Theta}}^T \delta \mathbf{\Theta} \tag{D.3.2}$$

The cancellation of the gradient ($\delta f = 0$) is a necessary condition to obtain a local minimum. In order to have a gradient calculation that is independent of the number of variables ($\partial f / \partial w$), the component δw must be null. The application of the control theorem proposed by Jameson allows to evaluation Equation (D.3.2) without solving the Navier-Stokes equations for the considered flow.

From a Lagrange variable based development, the gradient is reduced to:

$$\mathcal{G} = \frac{\partial f}{\partial \mathbf{\Theta}}^T - \psi^T \left[\frac{\partial R}{\partial \mathbf{\Theta}} \right] \tag{D.3.3}$$

where R is the equation that describes the dependence between the flow and geometry parameters. This way, the gradients are defined by the solution of another differential equation, for all the shape variables simultaneously, and the solution of the flow equations is no longer necessary

Therefore, the optimization of the objective function may be performed with a gradient based even if the number of parameters is elevated. The difficulty of the methodology lies in the definition of the f and R functions and the solution of the new differential equation.

D.4 Optimizer

Numerous optimization methods exist. The principle of techniques employed in the context of aerodynamics/aeroacoustics shape optimizations are described next: gradient based optimizers on Section D.4.1, commonly used with low fidelity or adjoint solvers; and the meta-heuristic optimizers (Section D.4.2) that mimic the biological dynamics, normally associated with the use of response surfaces.

D.4.1 Gradient based

Consider the gradient and the Hessian matrix of an objective/cost function $f(\mathbf{\Theta})$ [96]:

$$g_i(\mathbf{\Theta}) = \frac{\partial f}{\partial \Theta_i} \qquad H_{i,j}(\mathbf{\Theta}) = \frac{\partial^2 f}{\partial \Theta_i \partial \Theta_j} \tag{D.4.1}$$

The optimization consists in defining the point in the design space where function's gradient is null, $g(\mathbf{\Theta}) = 0$.

A gradient descent algorithm presuppose a successive reduction of the function value by the iterative update of the parameters' vector $\mathbf{\Theta_k}$, in the inverse sense of the increase of the objective function, as presented in Algorithm 3, α_k being the step and $\mathbf{d_k}$ the descent direction.

Algorithm 3: Pseudocode of the gradient based optimization method, adapted from [64].

```
define an initial vector: Θ_0;
while (convergence = false) do
    calculate the descent direction: d_k;
    update parameters' vector : Θ_{k+1} = Θ_k + α_k d_k;
    k = k + 1;
    test convergence;
return optimal Θ_k
```

For gradient based optimization, the convergence is extremely influenced by the initial position and there are no mechanisms to differentiate a global from a local optimum.

Different techniques consider different methods and models for obtaining the descent direction. Next, three of them are presented.

D.4.1.1 Gradient descent

The descent direction is the opposite of the gradient:

$$\mathbf{\Theta_{k+1}} = \mathbf{\Theta_k} - \mathbf{g_k}\alpha_k \tag{D.4.2}$$

D.4.1.2 Newton method

The descent direction is the opposite of inverse the Hessian matrix (second derivative of the objective function):

$$\mathbf{\Theta_{k+1}} = \mathbf{\Theta_k} - H^{-1}\alpha_\mathbf{k} \tag{D.4.3}$$

As the definition of the Hessian matrix is numerically expensive, quasi-newton models where there H matrix are estimated are widespread. One example is presented as follows.

D.4.1.3 Broyden-Fletcher-Goldfarb-Shanno method (BFGS)

This method employs the inverse of an estimated Hessian matrix, A, as the descent direction:

$$\mathbf{\Theta_{k+1}} = \mathbf{\Theta_k} - A^{-1}\mathbf{g}(\mathbf{\Theta_k}) \tag{D.4.4}$$

A definition is as well iterative, from the previous estimate and the variation of the parameters' and gradient vectors $\mathbf{\Theta}$ and $\mathbf{g(\Theta)}$:

$$A_{k+1} = A_k - \frac{A_k(\Delta\mathbf{\Theta_k})^T A_k}{\Delta\mathbf{\Theta_k} A_k \Delta\mathbf{\Theta_k}} + \frac{\Delta\mathbf{g_k}(\Delta\mathbf{g_k})^T}{\Delta\mathbf{g_k}\Delta\mathbf{\Theta_k}} \tag{D.4.5}$$

with:

$$\Delta\mathbf{\Theta_k} = \mathbf{\Theta_{k+1}} - \mathbf{\Theta_k} \qquad \Delta\mathbf{g_k} = \mathbf{g(\Theta_{k+1})} - \mathbf{g(\Theta_k)} \tag{D.4.6}$$

D.4.2 Evolutionary Algorithms

Evolutionary algorithms are the stochastic algorithms that reproduce the evolution mechanism an/or the social behavior of animals [50]. The limitations of the use of classical optimization techniques when facing complex problems (elevated number of parameters, non-linearities) and the impossibility to guarantee a global minimum make the use of evolutionary algorithms very popular for the shape optimization studies, notably in aerodynamic and aeroacoustics (for instance, [62, 94, 141, 271]). The elevated number of cost function evaluations, inherent of this category of optimizers, may be mitigated by the use of a surrogate model, presented in D.2.

Among the numerous optimizers that can be found in the literature, 2 are presented on this appendix: the Genetic Algorithm (GA) and the Differential Evolution (DE). Recalling that multiple versions of each technique exist, current presentation focus on the canonical versions, where the major elements of the procedures are noted. The Particle Swarm Optimization (PSO), as the technique used in the manuscript, is presented on the main text (Section 3.2).

D.4.2.1 Genetic Algorithm (GA)

The Genetic Algorithm employs the concept of the "survival of the fittest" from the Darwinian evolutionary theory to select the subjects that are more adapt for the environement. The procedure is presented next.

A population of initial vectors, P, is build randomly. Each vector, $\mathbf{\Theta_i}$, is analogous to a chromosome composed by different genes (the parameters). This set of vectors constitutes the first generation.

For each vector, the fitness (the objective function or the inverse of the cost function) is calculated. Afterwards, one of the following diversification operations is performed: a *crossover* (combination of the genes of the best chromosomes for the generation of an offspring); or a *mutation* (random modification of a chromosome, reducing the risk of stagnation of the population). The objective function is evaluated for the new chromosome, if the obtained fitness value is higher than for a member of the previous generation, the new gene replaces the "weakest" element in the new generation.

The calculation is iterative and considers a predefined number of generations or stopping criteria; convergence of a considerable number of chromosomes to an unique solution is one example of stopping criterion. The pseudocode is presented in Algorithm 4.

An elevated number of generations and a numerous population favors the discover of the optimal solution, however, amplify the number of objective/cost function evaluation and the associated computational cost. The rates of mutation and crossover are key parameters of the methodology [50].

D.4.2.2 Differential Evolution (DE)

Proposed by Storn & Price [246], the differential evolution is also based on the application of the evolutionary principle in a population. The method is defined by three fundamental steps: *mutation*, *crossover* and *selection*.

Algorithm 4: Pseudocode of the GA algorithm, adapted from [50].

```
Create a random population P with NP chromosomes;
for Θ_i ∈ P do fitness(Θ_i);
while (convergence = false) & (ge ≤ nbGenerations) do
    selecting operation (crossover or mutation);
    if crossover then
        random selection of two chromosomes: Θ_a and Θ_b;
        generation of an offspring: Θ_c = crossover(Θ_a, Θ_b);
    else if mutation then
        random selection of a chromosome: Θ_i;
        generation of an offspring: Θ_c = mutate(Θ_i)
    calculation of the fitness of Θ_c;
    if fitness(Θ_c) > min(fitness(Θ_i)) ∀ Θ_i ∈ P then
        replace Θ_i with lowest fitness by Θ_c
    test convergence;
    new generation : ge = ge + 1;
return optimalP
```

For a problem with N parameters, and a population of NP agents (matrix of NP parameters' vectors), generated randomly, the ge-th generation is defined as:

$$\mathbf{\Theta_{i,ge}}, \quad i = 1, 2, ..., NP \tag{D.4.7}$$

The first step, *mutation*, consists in the generation of a new family of vectors from the different between pairs of vectors of the previous generation, that is:

$$\mathbf{v_{i,ge+1}} = \mathbf{\Theta_{r_1,ge}} + F \cdot (\mathbf{\Theta_{r_2,ge}} - \mathbf{\Theta_{r_3,ge}}) \tag{D.4.8}$$

where r_1, r_2, r_3 $(1, 2, ..., NP)$ are random indexes and $F \in [0, 2]$ is a real constant, parameter which defines the "strength" of the mutation. The increase of the diversity of the family of vectors is performed by the *crossover* operation. A test vector $\mathbf{u} = [u_{ji}]$ is generated by:

$$u_{ji,ge+1} = \begin{cases} v_{ji,ge+1} & \text{if } (randb(j) \leq CR) \text{ or } j = rnbr(i) \\ \Theta_{ji,ge} & \text{if } (randb(j) > CR) \text{ and } j \neq rnbr(i) \end{cases} \quad j = 1, 2, ..., D. \tag{D.4.9}$$

with $randb(j)$ being the j-th evaluation of a random number function between 0 and 1, and $rnbr(i)$ is a random index.

The cost function (inverse of the objective function for the maximization problem) of the test vector $f(\mathbf{u_i}, ge + 1)$ is evaluated. If the test vector results in a value of f that is smaller than the lowest value in the population, $u_{ji,ge+1}$ replaces the "weaker" agent and is maintained for the next iteration. The algorithm is presented next.

Algorithm 5: Pseudocode of the DE algorithm, adapted from [246].

Generate a random population P of NP agents;
while *(convergence = false) & (ge ≤ nbGenerations)* **do**
  for $i = 1$ *to* NP **do**
    selecting 3 agents randomly ($\mathbf{\Theta_a}$, $\mathbf{\Theta_b}$, $\mathbf{\Theta_c}$);
    mutation: $\mathbf{v} = \mathbf{\Theta_a} + F(\mathbf{\Theta_b}, \mathbf{\Theta_c})$;
    combination of the vectors: $\mathbf{u} = crossover(\mathbf{v}, \mathbf{\Theta})$;
    selection: **if** $f(\mathbf{u}) < f(\mathbf{\Theta_i})$ **then**
      replace $\mathbf{\Theta_i}$ by $\mathbf{u}$
  test convergence;
  new generation : $ge = ge + 1$;
return *optimal* P

Appendix E

Experimental results database

For documentation purposes in the case of future works on this project and envisaging to offer validation data for the community, experimental results are listed on this appendix. For the spanwise flow measurements, the positions of the hot-wire probes and the obtained correlation and coherence length are presented. For the latter, the values are listed only for the first 3 harmonics; a different description is available in Appendix F, where the coefficient for continuous $\ell_g(\mathrm{St})$ laws are presented. Integral acoustic quantities (peak frequency and levels) is presented for the considered cylinders. Some configurations have been tested more than once but only the latest result is reported.

E.1 Spanwise correlation and coherence

E.1.1 Location of the measuring points of spaniwse coherence and correlation

The coordinate system starts at the center of the downstream face of the cylinder's cross-section. Spanwise measurements at P_1, fixed at $(y_1, y_2) = (1.0d, 0)$ for all velocities, and P_3 are used with the square section only. For the circular cylinder, all measurements are performed at $(y_1, y_2) = (0.0d, 0.9d)$, with the origin $(0, 0)$ defined as the further downstream point of the section.

Table E.1: Measuring coordinates in the Y_1Y_2 plan (in terms of the height d) for rectangular sections.

AR	P_2	P_3	P_4
Re = $6,667$ (U_∞ = 10 m/s)			
1.0	(-0.6d, 0.0d)	(0.1d, 0.9d)	(0.4d, 0.9d)
Re = $13,333$ (U_∞ = 20 m/s)			
1.0	(-0.8d, 0.8d)	(-1.0d, 1.0d)	(0.5d, 1.1d)
2.0	(-0.8d, 1.2d)	(1.1d, 1.4d)	(2.6d, 1.6d)
3.0	(-2.2d, 1.1d)	(-3.0d, 1.2d)	(0.6d, 1.4d)
Re = $26,667$ (U_∞ = 40 m/s)			
1.0	(-1.0d, 0.7d)	(-1.0d, 1.1d)	(0.5d, 1.2d)
2.0	(-1.2d, 1.2d)	(0.6d, 1.4d)	(2.1d, 1.7d)
3.0	(-2.2d, 1.2d)	(-1.3d, 1.3d)	(-1.0d, 1.4d)

E.1.2 Correlation and coherence lengths for harmonics

Correlation and coherence length at harmonics of the principal mode are presented for the tested configurations. Both values are normalized by the section diameter/height d. Values of ℓ_g correspond to calculations with algorithm presented in Section 4.3.2, with $\Gamma_{\text{lim}} = 0.4$.

Selecting the coherence length at exactly St = St_{peak} and its harmonics result in highly underestimated ℓ_g, once points are noisy and the peak frequencies are slightly different from the values observed in the velocity spectra. In order to define a single value, a procedure was performed: 1) the peak frequency (or one of the harmonics) is selected based on the St_{peak} selected from the velocity spectra; 2) a region ΔSt of $\pm$ 12 points neighboring St_{peak} is used to select the peak value; 3) the maximum coherence length available at this region is defined as the $\ell_{g,max}$ for the given mode; 4) for a given frequency, the length estimator ℓ_g is defined as the average between the set of values limited by the 2 points neighboring the selected $\ell_{g,max}$ at both directions (before and after the peak) while the error estimator, $\Delta\ell_g$, is the standard deviation. The elements used in the procedure are illustrated in Figure E.1, along with the filter used to represent the graphs.

Due to the use of values at the two sides of the slopes when performing the smoothing, the peak values are lowered, what justifies the difference between the values listed here and what can be deduced from the coherence length at the graphs in the text. The listed ℓ_g values, being the mean around the peak, are also lower than $\ell_{g,max}$, so the upper limit of the estimation ($\ell_g + \Delta\ell_g$) is observed in some cases.

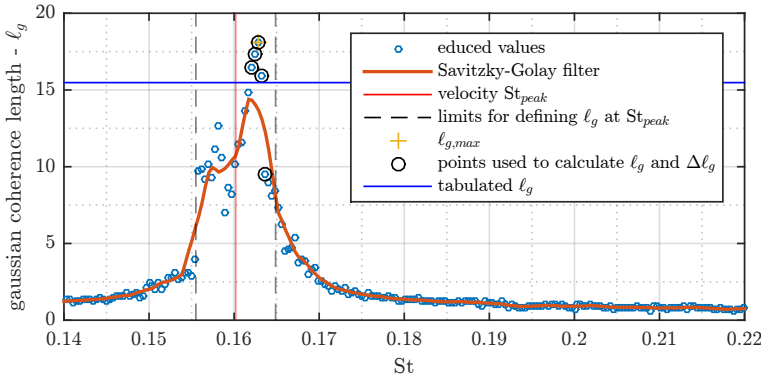

Figure E.1: Example of selection of the Gaussian coherence length at peak frequency (for rectangular of AR = 3.0, P_4, at U_∞ = 20 m/s).

As the coherence lengths are presented for harmonics of the most energetic frequency, intermediary peaks that may exist are not listed here so other relatively higher values of ℓ_g may exist; the reader is invited to check Figures 4.16, 4.30 and 4.32.

Table E.2: Correlation and coherence lengths for the tested configurations.

section	P_i	Re, 10^3	$\mathrm{St}_{\mathrm{peak}}$	$\Delta\mathrm{St}$	$\ell_g \pm \Delta\ell_g$ (St)			Λ_u
					$1.0 \times \mathrm{St}_{\mathrm{peak}}$	$2.0 \times \mathrm{St}_{\mathrm{peak}}$	$3.0 \times \mathrm{St}_{\mathrm{peak}}$	
10×10	1	6.7	0.125	0.019	1.61 ± 0.34 (0.123)	1.41 ± 0.08 (0.251)	0.55 ± 0.07 (0.370)	0.33
	2		0.131		3.50 ± 0.14 (0.128)	1.56 ± 0.14 (0.254)	0.61 ± 0.07 (0.384)	3.68
	3		0.130		2.71 ± 0.42 (0.129)	1.40 ± 0.09 (0.256)	0.81 ± 0.04 (0.384)	1.26
	4		0.130		2.75 ± 0.21 (0.129)	1.48 ± 0.09 (0.254)	0.76 ± 0.10 (0.388)	1.16
	1	13.3	0.126	0.009	5.10 ± 0.46 (0.126)	1.58 ± 0.13 (0.249)	0.56 ± 0.06 (0.378)	0.53
	2		0.127		5.02 ± 0.47 (0.125)	1.22 ± 0.15 (0.254)	1.08 ± 0.16 (0.380)	4.17
	3		0.127		4.84 ± 0.64 (0.126)	1.67 ± 0.08 (0.251)	1.22 ± 0.13 (0.378)	3.13
	4		0.127		3.93 ± 0.28 (0.126)	2.04 ± 0.21 (0.251)	1.25 ± 0.07 (0.378)	1.49
	1	26.7	0.126	0.005	5.40 ± 0.55 (0.126)	1.88 ± 0.19 (0.252)	0.56 ± 0.07 (0.377)	0.59
	2		0.129		5.54 ± 0.66 (0.129)	0.96 ± 0.11 (0.256)	2.24 ± 0.17 (0.384)	3.70
	3		0.127		5.54 ± 0.32 (0.126)	2.21 ± 0.17 (0.251)	1.54 ± 0.10 (0.378)	3.75
	4		0.127		5.09 ± 0.59 (0.126)	2.37 ± 0.03 (0.252)	1.30 ± 0.07 (0.379)	2.59
10×20	2	13.3	0.080	0.009	24.50 ± 3.68 (0.081)	0.99 ± 0.12 (0.156)	0.55 ± 0.04 (0.237)	10.86
	4		0.080		13.79 ± 4.59 (0.081)	1.88 ± 0.12 (0.155)	0.64 ± 0.03 (0.239)	5.92
	2	26.7	0.079	0.005	25.06 ± 2.10 (0.079)	3.56 ± 0.37 (0.156)	0.55 ± 0.09 (0.236)	11.79
	4		0.080		13.26 ± 0.84 (0.078)	2.37 ± 0.23 (0.157)	0.72 ± 0.08 (0.241)	4.78
10×30	2	13.3	0.161	0.009	18.66 ± 1.29 (0.163)	0.75 ± 0.08 (0.322)	0.51 ± 0.06 (0.487)	10.94
	4		0.160		15.48 ± 3.42 (0.163)	5.04 ± 0.63 (0.323)	0.71 ± 0.06 (0.482)	6.75
	2	26.7	0.159	0.005	25.94 ± 1.59 (0.160)	5.14 ± 1.36 (0.319)	0.62 ± 0.06 (0.477)	10.02
	4		0.159		23.23 ± 1.23 (0.160)	8.88 ± 1.17 (0.319)	0.63 ± 0.05 (0.476)	9.69
circular	-	10.0	0.197	0.012	4.58 ± 0.84 (0.203)	1.51 ± 0.18 (0.396)	0.61 ± 0.05 (0.586)	4.70
	-	13.3	0.196	0.009	4.04 ± 0.30 (0.195)	1.38 ± 0.08 (0.391)	0.58 ± 0.10 (0.589)	4.28
	-	16.7	0.194	0.008	3.97 ± 0.23 (0.193)	1.30 ± 0.10 (0.391)	0.55 ± 0.09 (0.580)	4.10
	-	20.0	0.192	0.006	3.73 ± 0.33 (0.193)	1.29 ± 0.13 (0.386)	0.55 ± 0.08 (0.577)	3.92
	-	26.7	0.192	0.005	3.87 ± 0.26 (0.190)	1.04 ± 0.12 (0.382)	0.56 ± 0.07 (0.575)	3.51

E.2 Acoustic measurements

The vortex shedding frequency (f_{peak}) and the corresponding Strouhal number (St_{peak}), the flow Reynolds number (Re) and the peak, overall and band sound pressure levels (PSPL, OASPL and BSPL, respectively, as defined in Section 4.4.1) are listed for the cross-sections tested on wind-tunnel. The cross-sections are illustrated within 1:1 scale and the cylinder's material is also indicated. Data is organized by the blocking length d, the characteristic length of the problem, and presented as follows:

- d = 6 mm: Table E.3;
- d = 8 mm: Table E.4;
- d = 10 mm: Table E.5;
- d > 10 mm: Tables E.6 (circular section) and E.7 (non-circular section).

Table E.3: Peak frequencies and acoustic pressure levels for cylinders with blockage d = 6 mm, ℓ/d = 116.67, central microphone. Flow from left to right, reference pressure P_{ref} = 20μPa.

cross-section		U_∞, m/s	Re, 10^3	St_{peak}	f_{peak}, Hz	PSPL, dB	OASPL, dB	BSPL, dB
 circular d = 6 mm	aluminum	10	4.0	0.211	352	46.0	71.7	43.3
		15	6.0	0.205	513	54.1	74.8	60.3
		20	8.0	0.201	670	60.1	78.2	64.9
		25	10.0	0.198	825	65.7	83.3	77.1
		30	12.0	0.197	986	70.5	87.4	83.6
		40	16.0	0.194	1291	78.9	93.2	90.9
 square 6×6 mm	aluminum	10	4.0	0.137	228	55.1	72.0	60.2
		15	6.0	0.138	345	62.1	77.0	69.3
		20	8.0	0.138	459	69.9	81.5	78.0
		25	10.0	0.138	575	72.8	84.9	81.3
		30	12.0	0.137	686	74.9	88.0	84.4
		40	16.0	0.137	911	85.9	96.6	95.0
	carbon fiber	10	4.0	0.140	233	54.3	71.8	60.2
		15	6.0	0.140	350	61.3	76.1	69.1
		20	8.0	0.138	459	68.7	81.3	77.7
		25	10.0	0.137	572	72.2	85.0	81.1
		30	12.0	0.137	684	73.0	87.8	84.3
		40	16.0	0.135	902	82.7	95.8	94.2
 rectangle 6×13 mm	carbon fiber	10	4.0	0.216	359	60.1	73.0	63.7
		15	6.0	0.218	545	71.8	79.3	76.9
		20	8.0	0.217	722	77.1	84.1	82.6
		25	10.0	0.216	902	78.5	86.6	84.6
		30	12.0	0.213	1067	82.1	91.1	89.8
		40	16.0	0.209	1395	89.6	97.8	97.0
 rectangle 6×16 mm	carbon fiber	10	4.0	0.202	338	51.8	71.7	57.4
		15	6.0	0.204	511	70.3	78.5	75.1
		20	8.0	0.203	677	68.6	79.9	75.2
		25	10.0	0.202	842	73.6	85.3	81.3
		30	12.0	0.201	1006	80.6	90.6	88.8
		40	16.0	0.200	1336	82.6	94.9	93.1

Table E.4: Peak frequencies and acoustic pressure levels for cylinders with blockage d = 8 mm, ℓ/d = 87.50, central microphone. If non-null, angle of incidence indicated between parenthesis. Flow from left to right, reference pressure P_{ref} = 20μPa.

cross-section		U_∞, m/s	Re, 10^3	St_{peak}	f_{peak}, Hz	PSPL, dB	OASPL, dB	BSPL, dB
 circular d = 8 mm	aluminum	10	5.3	0.210	263	46.1	71.2	46.7
		15	8.0	0.203	381	53.7	74.7	61.1
		20	10.7	0.198	494	64.5	80.2	73.6
		25	13.3	0.194	605	68.4	83.6	78.4
		30	16.0	0.191	717	70.5	86.2	81.1
		40	21.3	0.189	945	83.2	95.6	93.9
 square 8×8 mm	aluminum	10	5.3	0.136	170	55.2	72.4	60.6
		15	8.0	0.133	248	65.8	76.9	72.2
		20	10.7	0.131	328	70.3	81.4	77.5
		25	13.3	0.131	408	78.2	87.4	84.8
		30	16.0	0.130	488	84.6	92.9	91.7
		40	21.3	0.130	648	89.7	98.1	96.8
	carbon fiber	10	5.3	0.141	177	53.0	72.1	59.2
		15	8.0	0.139	261	63.1	76.9	70.6
		20	10.7	0.138	345	68.6	81.1	76.9
		25	13.3	0.137	427	75.4	86.6	83.9
		30	16.0	0.137	513	79.7	90.7	88.8
		40	21.3	0.135	675	83.4	94.7	92.6
 square 6×6 mm (25.4°)	carbon fiber	10	5.3	0.183	228	51.3	72.0	57.0
		15	8.0	0.178	334	57.0	75.9	64.7
		20	10.7	0.177	442	64.4	79.7	74.1
		25	13.3	0.177	555	67.6	83.3	76.5
		30	16.0	0.176	659	71.9	86.9	82.0
		40	21.3	0.174	870	79.1	93.3	90.1
 rectangle 6×13 mm (9.3°)	carbon fiber	10	5.3	0.181	227	44.6	71.3	48.5
		15	8.0	0.175	328	53.9	75.5	58.2
		20	10.7	0.174	436	59.0	78.9	67.2
		25	13.3	0.177	553	65.7	82.6	65.3
		30	16.0	0.176	659	71.6	85.3	71.3
		40	21.3	0.178	892	77.5	89.4	74.3
 rectangle 6×16 mm (7.3°)	carbon fiber	10	5.3	0.210	263	44.3	71.4	49.4
		15	8.0	0.213	400	54.5	75.3	59.9
		20	10.7	0.209	523	59.2	78.8	67.8
		25	13.3	0.207	648	89.5	90.7	90.0
		30	16.0	0.209	783	71.5	86.2	78.2
		40	21.3	0.222	1109	77.2	93.5	91.0

Table E.5: Peak frequencies and acoustic pressure levels for cylinders with blockage d = 10 mm, ℓ/d = 70.00, central microphone. If non-null, angle of incidence indicated between parenthesis. Flow from left to right, reference pressure P_{ref} = 20μPa.

cross-section		U_∞, m/s	Re, 10^3	St_{peak}	f_{peak}, Hz	PSPL, dB	OASPL, dB	BSPL, dB
 rectangle 10×5 mm	steel	10	6.7	0.136	136	54.4	72.0	59.9
		15	10.0	0.132	198	64.8	76.3	71.1
		20	13.3	0.133	266	76.1	83.4	81.4
		25	16.7	0.133	333	79.0	87.7	85.7
		30	20.0	0.131	394	82.8	91.5	89.7
		40	26.7	0.130	519	84.6	96.8	95.6
 square 10×10 mm	aluminum	10	6.7	0.128	128	62.2	72.9	65.2
		15	10.0	0.125	188	67.9	77.2	73.3
		20	13.3	0.125	250	77.5	84.5	83.0
		25	16.7	0.125	313	80.7	87.9	86.2
		30	20.0	0.124	373	85.3	92.6	91.2
		40	26.7	0.125	498	94.3	101.7	101.0
	carbon fiber	10	6.7	0.122	122	54.8	72.7	55.4
		15	10.0	0.135	203	63.5	76.9	71.3
		20	13.3	0.132	264	70.9	82.1	79.0
		25	16.7	0.130	325	72.8	85.8	82.5
		30	20.0	0.130	389	82.5	91.2	89.7
		40	26.7	0.129	514	90.7	98.9	97.6
 rectangle 10×20 mm	aluminum	10	6.7	0.091	91	52.1	72.6	53.3
		15	10.0	0.082	123	62.3	75.1	64.6
		20	13.3	0.081	163	65.5	78.5	68.4
		25	16.7	0.077	192	68.4	82.6	74.6
		30	20.0	0.080	241	83.4	89.0	86.7
		40	26.7	0.079	317	88.7	94.5	92.4
 rectangle 10×30 mm	steel	10	6.7	0.169	169	57.7	72.4	60.1
		15	10.0	0.163	244	71.7	78.0	74.4
		20	13.3	0.161	322	77.7	83.3	81.0
		25	16.7	0.160	400	83.7	89.0	87.5
		30	20.0	0.159	477	88.4	95.0	94.2
		40	26.7	0.159	634	92.7	99.2	98.4
 rectangle 10×40 mm	brass	10	6.7	0.142	142	58.7	72.4	60.0
		15	10.0	0.136	205	68.6	77.1	71.4
		20	13.3	0.136	272	79.4	83.9	81.8
		25	16.7	0.136	339	82.9	87.9	86.3
		30	20.0	0.135	406	88.4	93.1	91.8
		40	26.7	0.135	539	92.9	98.5	97.1
 rectangle 10×50 mm	steel	10	6.7	0.116	116	45.2	71.0	49.5
		15	10.0	0.111	167	62.8	75.5	66.4
		20	13.3	0.111	222	75.4	81.3	78.5
		25	16.7	0.111	277	81.2	86.8	84.9
		30	20.0	0.110	331	84.2	90.2	88.3
		40	26.7	0.111	442	93.3	98.3	97.4

Table E.5: Continued

cross-section		U_∞, m/s	Re, 10^3	$\mathrm{St}_{\mathrm{peak}}$	f_{peak}, Hz	PSPL, dB	OASPL, dB	BSPL, dB
 circular d = 10 mm	aluminum	10	6.7	0.211	211	45.1	71.9	46.4
		15	10.0	0.204	306	54.7	76.0	62.7
		20	13.3	0.197	394	63.0	79.1	72.5
		25	16.7	0.193	483	73.0	85.5	82.2
		30	20.0	0.192	577	75.1	88.0	84.1
		40	26.7	0.189	758	79.1	93.2	90.7
 square 8×8 mm (17.0°)	aluminum	10	6.7	0.188	188	48.2	72.4	53.6
		15	10.0	0.184	277	59.6	76.1	66.2
		20	13.3	0.181	363	65.2	79.7	73.5
		25	16.7	0.179	448	71.6	84.7	80.5
		30	20.0	0.178	533	71.4	87.1	82.3
		40	26.7	0.179	714	77.2	91.5	87.7
	carbon	10	6.7	0.181	181	48.3	71.2	54.4
		15	10.0	0.182	273	58.5	75.9	66.5
		20	13.3	0.181	363	65.0	80.0	73.6
		25	16.7	0.180	450	71.0	84.9	80.7
		30	20.0	0.178	533	71.4	87.1	82.9
		40	26.7	0.178	713	77.2	92.2	87.7
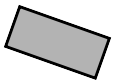 rectangle 6×13 mm (19.5°)	carbon	10	6.7	0.173	173	48.4	71.5	53.5
		15	10.0	0.173	259	59.1	75.8	66.9
		20	13.3	0.172	344	63.3	79.4	72.7
		25	16.7	0.173	433	70.5	84.6	80.2
		30	20.0	0.171	514	74.2	87.7	84.0
		40	26.7	0.173	694	77.5	92.0	88.1
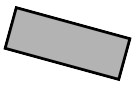 rectangle 6×16 mm (15.3°)	carbon fiber	10	6.7	0.192	192	44.4	71.2	46.8
		15	10.0	0.191	286	53.9	76.2	59.3
		20	13.3	0.189	378	58.8	79.1	66.4
		25	16.7	0.189	472	66.1	82.7	74.2
		30	20.0	0.189	566	70.7	85.3	75.2
		40	26.7	0.188	752	77.8	90.0	77.0
 front-pointing triangle d = 10 mm	acrylic	10	6.7	0.200	200	45.6	70.9	44.9
		15	10.0	0.196	294	53.3	74.6	55.5
		20	13.3	0.196	392	60.6	78.9	61.8
		25	16.7	0.195	488	66.1	82.8	70.2
		30	20.0	0.196	588	69.9	85.5	69.5
		40	26.7	0.195	778	77.0	88.7	77.3
 back-pointing triangle d = 10 mm	acrylic	10	6.7	0.131	131	55.5	71.7	59.3
		15	10.0	0.128	192	61.9	75.6	67.2
		20	13.3	0.127	255	70.2	80.4	76.3
		25	16.7	0.127	317	72.7	84.1	79.4
		30	20.0	0.127	380	75.9	88.0	84.3
		40	26.7	0.127	506	84.7	94.9	92.9

Table E.6: Peak frequencies and acoustic pressure levels for circular cylinders with blockage $d > 10$ mm, multiple ℓ/d, central microphone. Flow from left to right, reference pressure $P_{ref} = 20\mu$Pa.

cross-section			U_∞, m/s	Re, 10^3	St_{peak}	f_{peak}, Hz	PSPL, dB	OASPL, dB	BSPL, dB
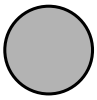	circular d = 12 mm ℓ/d = 58.33	aluminum	10	8.0	0.208	173	45.2	71.9	46.1
			15	12.0	0.196	245	60.7	75.5	67.8
			20	16.0	0.193	322	64.3	79.5	73.1
			25	20.0	0.193	402	71.0	85.0	80.7
			30	24.0	0.191	477	78.2	90.2	88.2
			40	32.0	0.188	625	81.5	94.8	93.0
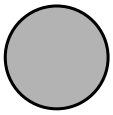	circular d = 14 mm ℓ/d = 50.00	aluminum	10	9.3	0.206	147	46.0	71.6	47.9
			15	14.0	0.200	214	58.8	75.5	65.4
			20	18.7	0.191	273	66.7	80.3	75.6
			25	23.3	0.191	341	70.9	84.7	80.8
			30	28.0	0.190	406	76.3	89.1	86.5
			40	37.3	0.188	538	80.3	94.6	93.0
		carbon	10	9.3	0.206	147	55.1	76.1	48.9
			20	18.7	0.195	278	69.3	82.7	75.4
			30	28.0	0.190	406	79.2	90.8	86.4
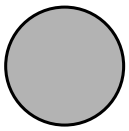	circular d = 16 mm ℓ/d = 43.75	aluminum	10	10.7	0.208	130	46.5	71.1	49.5
			15	16.0	0.198	186	59.2	75.6	65.3
			20	21.3	0.198	247	68.3	80.6	76.5
			25	26.7	0.190	297	72.5	85.0	81.7
			30	32.0	0.188	352	76.8	89.3	86.6
			40	42.7	0.187	467	84.6	96.8	95.8
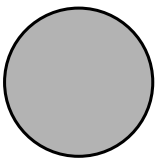	circular d = 20 mm ℓ/d = 35.00	aluminum	10	13.3	0.206	103	48.0	71.6	50.3
			15	20.0	0.200	150	62.9	76.0	67.1
			20	26.7	0.197	197	69.1	80.4	74.9
			25	33.3	0.196	245	75.7	85.7	82.9
			30	40.0	0.194	291	77.8	89.5	87.3
			40	53.3	0.192	384	83.5	95.8	94.1

Table E.7: Peak frequencies and acoustic pressure levels for non-circular cylinders with blockage $d > 10$ mm, multiple ℓ/d, central microphone. Flow from left to right, reference pressure $P_{ref} = 20\mu Pa$.

cross-section			U_∞, m/s	Re, 10^3	St_{peak}	f_{peak}, Hz	PSPL, dB	OASPL, dB	BSPL, dB
	square 12×12 mm $\ell/d = 58.33$	aluminum	10	8.0	0.128	106	60.9	72.4	64.4
			15	12.0	0.125	156	69.2	77.6	73.7
			20	16.0	0.126	209	76.1	83.3	81.5
			25	20.0	0.125	261	82.0	89.5	88.1
			30	24.0	0.126	314	83.5	92.2	90.7
			40	32.0	0.126	419	91.9	100.3	99.4
	square 14×14 mm $\ell/d = 50.00$	steel	10	9.3	0.129	92	59.3	72.2	63.3
			15	14.0	0.125	134	69.5	77.9	74.6
			20	18.7	0.127	181	74.4	82.9	80.7
			25	23.3	0.126	225	81.6	89.7	88.3
			30	28.0	0.126	270	85.8	94.0	92.8
			40	37.3	0.126	361	91.1	99.8	98.9
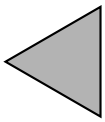	front-pointing triangle $d = 15$ mm $\ell/d = 46.67$	acrylic	10	10.0	0.206	138	46.2	70.8	43.5
			15	15.0	0.203	203	53.4	75.4	53.2
			20	20.0	0.203	270	60.5	79.3	61.8
			25	25.0	0.203	338	66.1	81.7	65.0
			30	30.0	0.202	405	71.0	85.1	69.3
			40	40.0	0.201	536	76.7	88.8	73.1
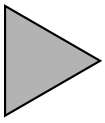	back-pointing triangle $d = 15$ mm $\ell/d = 46.67$	acrylic	10	10.0	0.136	91	54.9	71.7	56.5
			15	15.0	0.133	133	65.9	75.4	68.5
			20	20.0	0.134	178	70.8	79.7	73.9
			25	25.0	0.133	222	77.5	85.0	81.0
			30	30.0	0.133	266	81.7	88.8	85.6
			40	40.0	0.132	353	86.4	94.0	91.5

Appendix F

Continuous coherence length laws

Rather than selecting a single coherence length, or correcting only the principal mode ($\mathrm{St}_{\mathrm{peak}}$) and its harmonics, and applying an arbitrary correction for the rest of the spectrum, as performed by Orselli et al. [177] and [46], the complete spectrum of coherence length is used to perform the sound emission magnitude correction in Section 4.5.2. The use of a regression function rather than interpolating the values for the frequencies of interest is justified by two reasons. Firstly, noisy character of the ℓ_g values would lead to imprecise values, notably at the peaks. Secondly, the algorithm used for the calculation of ℓ_g returns a minimum value of $\ell_g \leq 0.6$ that is non-physical [196], of the same order that those obtained at the first point ($\eta = 0.6$) used to measured the coherence length.

F.1 Formulation

Visual analysis of Figures 4.16, 4.30 and 4.32 indicates that each peak and its associated slope may be represented by exponential laws, centered at the peak frequency. The following equation, based on asymmetric Laplacian, is introduced for a given peak i:

$$l_g^i(\mathrm{St}) = m_i \exp\{-[(\mathrm{St} - p_i)\psi_i s\kappa_i^s]^{\varepsilon_i}\} \tag{F.1.1}$$

where m_i is an amplitude parameter, ψ_i is a shape parameter defining the broadness of the peak (smaller the value of ψ_i, broader the peak), p_i is the location parameter indicating the peak location, κ_i is the asymmetry parameter (skew is positive for $\kappa_i < 1$ and negative for $\kappa_i > 1$, symmetrical if unitary), s is the sign function of $(\mathrm{St} - p_i)$, and ε_i is a decay parameter: $\varepsilon_i = 1$ returns the Laplacian shape (pointed peak) while $\varepsilon_i = 2$ returns a Gaussian-like decay. The final curve is the sum of each contribution, a continuous law of ℓ_g:

$$\ell_g(\mathrm{St}) = \sum_{i=1}^{N} l_g^i(\mathrm{St}) \tag{F.1.2}$$

F.2 Identification of the model parameters

Initially, the equation parameters p_i and m_i are set as the Strouhal and L_g values at each peak, respectively. The rest of the parameters are set arbitrarily as $\psi_i = 10$, $\kappa_i = 1$ and $\varepsilon_i = 1$, returning a symmetric Laplacian shape. With these values, a Nelder-Mead Simplex optimization [163] is performed individually for each peak, correcting the parameters of the function (for simplicity, the peak location p_i is fixed by hand). Only points at the frequency range delimited by the half distance between the neighboring peaks and that returned ℓ_g above $0.7d$ are considered. This restriction is in accordance with the limitation of the algorithm, evoked earlier, and of the experimental procedure, since the measurements start at that given spanwise distance so that no coherence length under that quantity is captured correctly.

The cost function is the square sum of the difference obtained between the model - Equation (F.2.1) - and the measured coherence lengths with a penalization factor of 50 at the peak value. In order to obtain a corrected magnitude after summing all the contributions, the optimizations are performed sequentially, that is, the cost function considers the contribution of the previously optimized peaks. So, for the peak number k, we have:

$$\text{error}_\text{k} = \sum_{j \in \text{NB}} \left[\ell_{g,j} - \sum_{i=1}^{k-1} l_g^i(\text{St}_\text{j}) \right]^2 + 49 \left[\ell_{g,j_\text{peak}} - \sum_{i=1}^{k-1} l_g^i(p_k) \right]^2 \tag{F.2.1}$$

where NB represents the subs-set of indexes of frequencies that neighbor each peak and j_peak the index of the frequency that is closest to the max peak location p_k.

Also, in order to correctly reproduce the behavior close to null frequency, an artificial peak at St = 0.002 is defined. For some cases, the threshold of minimum frequency is adapted to facilitate the convergence. A sample of the quality of the models is represented in Figure F.1. Better fit is observed for the circular cylinder, nevertheless the results are quite reasonable for the rectangular sections.

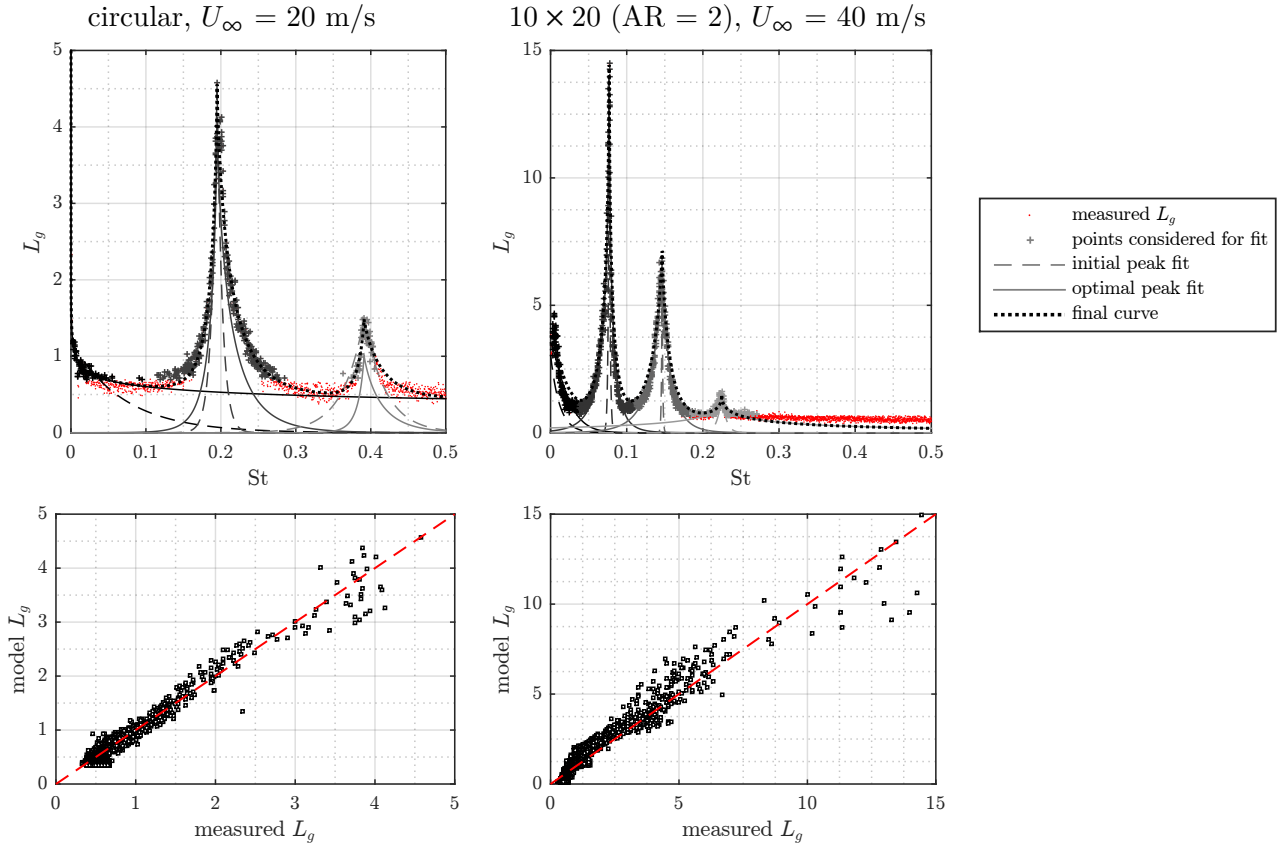

Figure F.1: Examples of the fit for the circular (left) and rectangular section, AR = 2.0 (right).

F.3 Coherence length functions

Coefficients for the continuous coherence length functions, presented in Section F.1, are listed in Tables F.1 and F.2, for the circular and rectangular cross-sections, respectively. First peak (i = 1) corresponds to the artificial peak added at St = 0.005 used to account for the coherence at very-low/null frequency. Corresponding plots are given in Figures F.4, F.2 and F.3.

Table F.1: Coefficients for the coherence function $\ell_g(\mathrm{St})$, circular section.

	i	1	2	3	4	5	6
15 m/s	m_i	6.04×10^{12}	5.697	1.504	-	-	-
	κ_i	6.61×10^{47}	1.163	0.690	-	-	-
	ψ_i	2.35×10^{49}	82.958	45.828	-	-	-
	ε_i	0.015	0.636	1.051	-	-	-
	p_i	0.000	0.203	0.396	-	-	-
20 m/s	m_i	8.80×10^{5}	4.042	1.015	-	-	-
	κ_i	3.57×10^{43}	0.694	0.611	-	-	-
	ψ_i	6.26×10^{44}	77.553	69.643	-	-	-
	ε_i	0.013	0.763	0.874	-	-	-
	p_i	0.000	0.195	0.391	-	-	-
25 m/s	m_i	5.26×10^{7}	3.828	1.112	-	-	-
	κ_i	1.69×10^{50}	0.679	1.098	-	-	-
	ψ_i	1.48×10^{51}	72.584	74.403	-	-	-
	ε_i	0.013	0.718	0.623	-	-	-
	p_i	0.000	0.193	0.393	-	-	-
30 m/s	m_i	1.81×10^{7}	3.626	0.956	-	-	-
	κ_i	2.83×10^{50}	0.804	0.942	-	-	-
	ψ_i	3.59×10^{52}	65.937	65.578	-	-	-
	ε_i	0.012	0.749	0.583	-	-	-
	p_i	0.000	0.193	0.386	-	-	-
40 m/s	m_i	7.90×10^{6}	3.624	0.741	-	-	-
	κ_i	7.55×10^{54}	0.709	0.560	-	-	-
	ψ_i	2.39×10^{55}	73.514	65.187	-	-	-
	ε_i	0.011	0.688	0.543	-	-	-
	p_i	0.000	0.190	0.382	-	-	-

Table F.2: Coefficients for the coherence function $\ell_g(\mathrm{St})$, rectangular sections.

	i	1	2	3	4	5	6
				10×10 (AR = 1)			
20 m/s	m_i	1.21×10^{0}	3.787	1.900	1.056	-	-
	κ_i	1.26×10^{0}	0.949	0.804	0.733	-	-
	ψ_i	8.20×10^{0}	190.246	103.504	66.736	-	-
	ε_i	0.239	0.920	0.778	0.538	-	-
	p_i	0.000	0.126	0.251	0.377	-	-
40 m/s	m_i	3.86×10^{2}	5.334	2.405	1.208	-	-
	κ_i	3.81×10^{17}	0.961	0.865	0.903	-	-
	ψ_i	5.43×10^{17}	255.806	117.963	113.276	-	-
	ε_i	0.024	0.674	0.747	0.864	-	-
	p_i	0.000	0.126	0.251	0.377	-	-
				10×20 (AR = 2)			
20 m/s	m_i	6.31×10^{0}	3.819	41.971	11.031	2.008	1.625
	κ_i	2.76×10^{0}	0.935	1.229	0.965	1.286	0.594
	ψ_i	3.54×10^{1}	90.949	4727.229	144.747	125.171	234.401
	ε_i	0.737	0.887	0.314	0.765	0.347	0.116
	p_i	0.000	0.062	0.081	0.141	0.220	0.280
40 m/s	m_i	3.53×10^{0}	14.542	6.787	1.570	-	-
	κ_i	6.52×10^{-1}	1.221	1.153	0.962	-	-
	ψ_i	6.40×10^{1}	214.602	84.837	29.328	-	-
	ε_i	1.291	0.645	0.826	0.386	-	-
	p_i	0.000	0.077	0.146	0.225	-	-
				10×30 (AR = 3)			
20 m/s	m_i	4.00×10^{4}	17.876	5.218	-	-	-
	κ_i	1.31×10^{8}	1.441	1.589	-	-	-
	ψ_i	2.44×10^{8}	252.929	416.854	-	-	-
	ε_i	0.068	0.766	1.398	-	-	-
	p_i	0.000	0.163	0.323	-	-	-
40 m/s	m_i	9.51×10^{11}	24.308	9.953	-	-	-
	κ_i	5.32×10^{27}	1.160	1.476	-	-	-
	ψ_i	2.10×10^{30}	358.578	454.424	-	-	-
	ε_i	0.025	0.747	1.620	-	-	-
	p_i	0.000	0.160	0.319	-	-	-

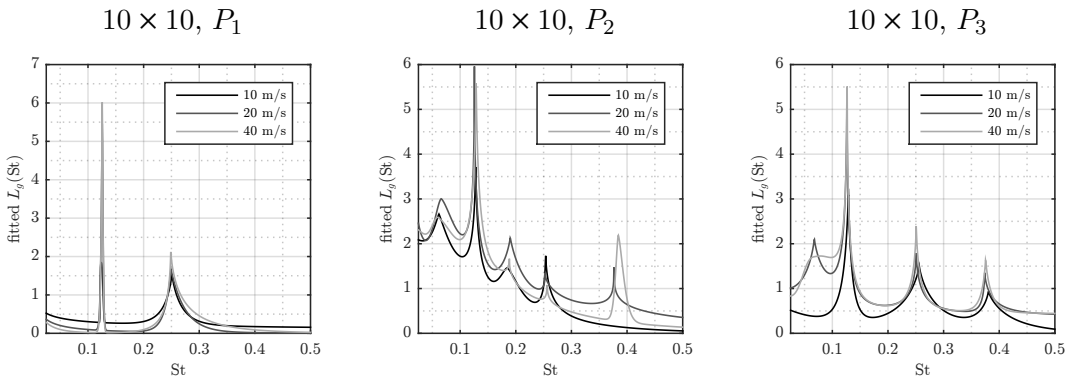

Figure F.2: Regression laws $\ell_g(\mathrm{St})$ for the square section at multiple velocities, P_1 to P_3.

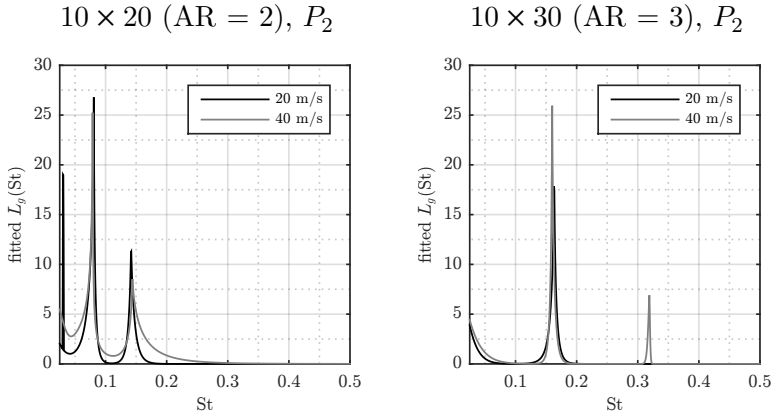

Figure F.3: Regression laws $\ell_g(\mathrm{St})$ for the rectangular sections (AR = 2 and AR = 3) at multiple velocities, P_2.

F.4 Influence of shape and velocity

A sample of the comparison of the obtained fits for all the tested section at different flow velocities is presented in Figure F.4. Remaining curves are presented on appendix.

The results are extremely similar, even when modifying the flow velocity, specially in the peaks. This is in accordance with the small Reynolds number dependence at the studied regime noted by previous authors [10, 239] and reinforces the validity of using velocity data for such measurement [172, 213]. Nevertheless, the sectional position selected for the measurement has more influences the shape of the curve between the peaks. From the multiple points that are used to define the spanwise flow distribution for the rectangular sections (4 for square and 2 for AR = 2 and AR = 3), the relations obtained with P_4 are selected for the use on the RMS lift coefficient estimation in Section 4.5.2. Being the most distant from the surfaces, thus to the limitations of the measuring procedure (difficulty to measure very small velocities) and less likely to be intrusive, those values are believed to be the most representative of the flow spanwise distribution.

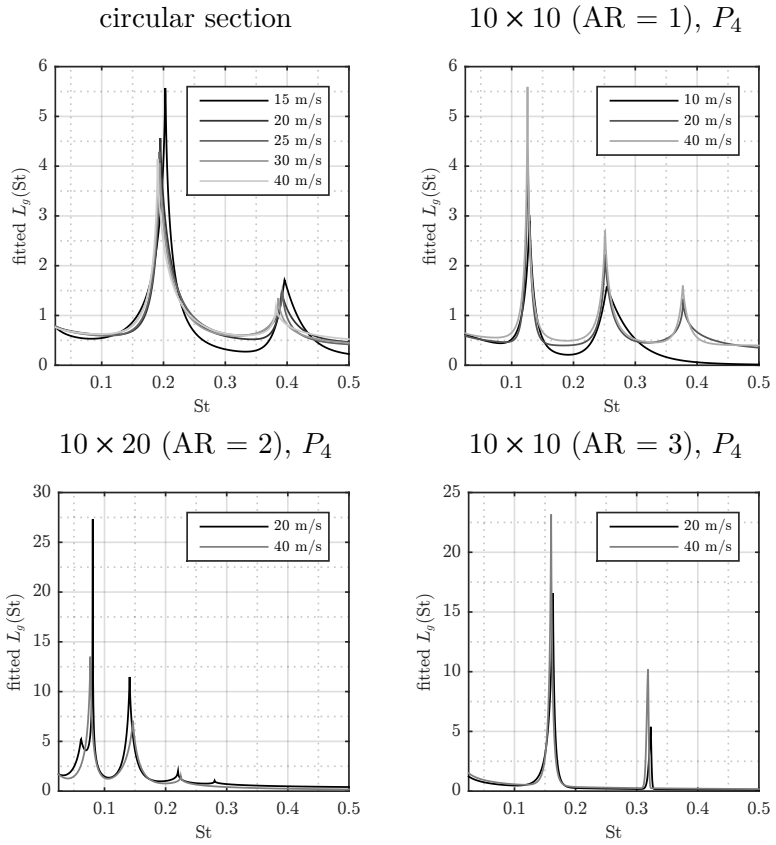

Figure F.4: Regression laws $\ell_g(\mathrm{St})$ for the the tested cross-sections, multiple velocities.

Bibliography

[1] Abbott, I. H., Von Doenhoff, A. E., and Stivers Jr, L. (1945). Summary of airfoil data. techreport NACA Technical Report 824, National Advisory Committee for Aeronautics, Langley Aeronautical Lab.; Langley Field, VA, United State.

[2] Abernathy, F. H. and Kronauer, R. E. (1962). The formation of vortex streets. *Journal of Fluid Mechanics*, 13(1):1–20.

[3] Ahlborn, B., Lefrançois, M., and King, D. H. (1998). The clockwork of vortex shedding. *Physics Essays*, 11:144.

[4] Ahlborn, B., Seto, M. L., and Noack, B. R. (2002). On drag, strouhal number and vortex-street structure. *Fluid Dynamics Research*, 30(6):379 – 399.

[5] Alomar, A., Angland, D., and Zhang, X. (2012). Experimental study of noise emitted by circular cylinders with large roughness. In *18th AIAA/CEAS Aeroacoustics Conference (33rd AIAA Aeroacoustics Conference)*.

[6] Amiet, R. K. (1975). Acoustic radiation from an airfoil in a turbulent stream. *Journal of Sound and Vibration*, 41(4):407 – 420.

[7] Aoki, M. and Ishihara, K. (1999). Study on prediction of aerodynamic sound radiated from various cylinders: Effect of cross-section on aeolian tones. *Transactions of the Japan Society of Mechanical Engineers Series B*, 65(636):2748–2754.

[8] Arafa, N. and Mohany, A. (2019). Wake structures and acoustic resonance excitation of a single finned cylinder in cross-flow. *Journal of Fluids and Structures*, 86:70 – 93.

[9] Arcondoulis, E. and Liu, Y. (2018). The effect of porosity on the porous coated cylinder diameter. In *Proceedings of ACOUSTICS*, volume 7.

[10] Bai, H. and Alam, M. M. (2018). Dependence of square cylinder wake on Reynolds number. *Physics of Fluids*, 30(1):015102.

[11] Barkley, D. and Henderson, R. D. (1996). Three-dimensional Floquet stability analysis of the wake of a circular cylinder. *Journal of Fluid Mechanics*, 322:215–241.

[12] Bates, D. M. and Chambers, J. M. (1992). Nonlinear models. In *Statistical Models in S*. Wadsworth & Brooks/Cole.

[13] Bates, D. M. and Watts, D. G. (2008). *Nonlinear Regression: Iterative Estimation and Linear Approximations*, chapter 2, pages 32–66. John Wiley & Sons, Ltd.

[14] Bearman, P. W. (1966). On vortex street wakes. techreport, National Advisory Committee for Aeronautics.

[15] Beausse, Y., Valeau, V., Brizzi, L.-E., and Margnat, F. (2019). Étude expérimentale dans le domaine temporel des mécanismes de production du bruit aéroacoustique produit par l'interaction d'un corps et d'un écoulement. In *Book of Abstracts - Journées des Doctorants de l'Institut PPRIME (JDD2019)*.

[16] Becker, S., Hahn, C., Kaltenbacher, M., and Lerch, R. (2008). Flow-induced sound of wall-mounted cylinders with different geometries. *AIAA Journal*, 46(9):2265–2281.

[17] Beigmoradi, S., Hajabdollahi, H., and Ramezani, A. (2014). Multi-objective aero acoustic optimization of rear end in a simplified car model by using hybrid Robust Parameter Design, Artificial Neural Networks and Genetic Algorithm methods. *Computers & Fluids*, 90:123 – 132.

[18] Bensow, R. and Liefvendahl, M. (2016). An acoustic analogy and scale-resolving flow simulation methodology for the prediction of propeller radiated noise. In *31st Symposium on Naval Hydrodynamics, September 11th-16th, Monterey, California.*

[19] Bessis, R. (2014). *Analyse expérimentale des contribution aérodynamiques à la transmission acoustique dans un véhicule.* PhD thesis, Université de Poitiers.

[20] Blackburn, H. M. and Melbourne, W. H. (1996). The effect of free-stream turbulence on sectional lift forces on a circular cylinder. *Journal of Fluid Mechanics*, 306:267–292.

[21] Bonamy, C. (2007). *Analyse expérimentale de l'aérodynamique proche paroi et modélisation du bruit de bord de fuite d'un profil d'aile en écoulement subsonique.* PhD thesis, Université de Poitiers.

[22] Bonyadi, M. R. and Michalewicz, Z. (2017). Particle Swarm Optimization for single objective continuous space problems: A review. *Evolutionary Computation*, 25(1):1–54. PMID: 26953883.

[23] Boussaïd, I., Lepagnot, J., and Siarry, P. (2013). A survey on optimization metaheuristics. *Information Sciences*, 237:82 – 117. Prediction, Control and Diagnosis using Advanced Neural Computations.

[24] Box, G. E. P. and Wilson, K. B. (1951). On the experimental attainment of optimum conditions. *Journal of the Royal Statistical Society. Series B (Methodological)*, 13(1):1–45.

[25] Branke, J., Branke, J., Deb, K., Miettinen, K., and Slowiński, R. (2008). *Multiobjective optimization: Interactive and evolutionary approaches*, volume 5252. Springer.

[26] Calabrese, E. J. and Baldwin, L. A. (2002). Defining hormesis. *Human & Experimental Toxicology*, 21(2):91–97. PMID: 12102503.

[27] Canuto, D. and Taira, K. (2015). Two-dimensional compressible viscous flow around a circular cylinder. *Journal of Fluid Mechanics*, 785:349–371.

[28] Cao, S., Ozono, S., Tamura, Y., Ge, Y., and Kikugawa, H. (2010). Numerical simulation of Reynolds number effects on velocity shear flow around a circular cylinder. *Journal of Fluids and Structures*, 26(5):685 – 702.

[29] Carassale, L., Freda, A., and Marrè-Brunenghi, M. (2014). Experimental investigation on the aerodynamic behavior of square cylinders with rounded corners. *Journal of Fluids and Structures*, 44:195 – 204.

[30] Casalino, D. and Jacob, M. (2003). Prediction of aerodynamic sound from circular rods via spanwise statistical modelling. *Journal of Sound and Vibration*, 262(4):815 – 844.

[31] Cheng, M. and Liu, G. (2000). Effects of afterbody shape on flow around prismatic cylinders. *Journal of Wind Engineering and Industrial Aerodynamics*, 84(2):181 – 196.

[32] Chomaz, J.-M. (2005). Global instabilities in spatially developing flows: Non-Normality and Nonlinearity. *Annual Review of Fluid Mechanics*, 37(1):357–392.

[33] Chopra, G. and Mittal, S. (2019). Drag coefficient and formation length at the onset of vortex shedding. *Physics of Fluids*, 31(1):013601.

[34] Clerc, M. (2006). *Particle Swarm Optimization*. ISTE.

[35] Cox, J. S., Brentner, K. S., and Rumsey, C. L. (1998). Computation of vortex shedding and radiated sound for a circular cylinder: Subcritical to transcritical reynolds numbers. *Theoretical and Computational Fluid Dynamics*, 12(4):233–253.

[36] Crighton, D. G. (1991). Airframe noise. In Hubbard, H. H., editor, *Aeroacoustics of Flight Vehicles: Theory and Practice. Volume 1: Noise Sources*. NASA.

[37] Curle, N. (1955). The influence of solid boundaries upon aerodynamic sound. *Proceedings of the Royal Society of London A: Mathematical, Physical and Engineering Sciences*, 231(1187):505–514.

[38] da Silva Pinto, W. J. G. and Margnat, F. (2019). A shape optimization procedure for cylinders aeolian tone. *Computers & Fluids*, 182:37 – 51.

[39] Dalcín, L., Paz, R., Storti, M., and D'Elía, J. (2008). MPI for Python: Performance improvements and MPI-2 extensions. *Journal of Parallel and Distributed Computing*, 68(5):655 – 662.

[40] Darekar, R. M. and Sherwin, S. J. (2001). Flow past a square-section cylinder with a wavy stagnation face. *Journal of Fluid Mechanics*, 426:263–295.

[41] De, K. A. and Dalal, A. (2006). Numerical simulation of unconfined flow past a triangular cylinder. *International Journal for Numerical Methods in Fluids*, 52(7):801–821.

[42] de Boer, A., van der Schoot, M., and Bijl, H. (2007). Mesh deformation based on radial basis function interpolation. *Computers & Structures*, 85(11–14):784 – 795. Fourth MIT Conference on Computational Fluid and Solid Mechanics.

[43] Degand, C. and Farhat, C. (2002). A three-dimensional torsional spring analogy method for unstructured dynamic meshes. *Computers & Structures*, 80(3–4):305 – 316.

[44] Demartino, C. and Ricciardelli, F. (2017). Aerodynamics of nominally circular cylinders: A review of experimental results for Civil Engineering applications. *Engineering Structures*, 137:76 – 114.

[45] Dennis, S. C. R. and Chang, G.-Z. (1970). Numerical solutions for steady flow past a circular cylinder at Reynolds numbers up to 100. *Journal of Fluid Mechanics*, 42(3):471–489.

[46] Doolan, C. J. (2010). Computational bluff body aerodynamic noise prediction using a statistical approach. *Applied Acoustics*, 71(12):1194 – 1203.

[47] Dorigo, M., Maniezzo, V., and Colorni, A. (1996). Ant system: Optimization by a colony of cooperating agents. *Trans. Sys. Man Cyber. Part B*, 26(1):29–41.

[48] Du, L. and Sun, X. (2019). Noise reduction by feedback rotary oscillation of a three-dimensional circular cylinder. *Journal of Fluids and Structures*, 84:421 – 439.

[49] El Baroudi, M. Y. (1960). Measurement of two-point correlations of velocity near a circular cylinder shedding a Karman vortex street. Technical report, University of Toronto.

[50] Elbeltagi, E., Hegazy, T., and Grierson, D. (2005). Comparison among five evolutionary-based optimization algorithms. *Advanced Engineering Informatics*, 19(1):43 – 53.

[51] Fage, A., Johansen, F. C., and Lamb, H. (1927). On the flow of air behind an inclined flat plate of infinite span. *Proceedings of the Royal Society of London. Series A, Containing Papers of a Mathematical and Physical Character*, 116(773):170–197.

[52] Fahrmeir, L., Kneib, T., Lang, S., et al. (2013). *Regression - Models, Methods and Applications*. Springer-Verlag Berlin Heidelberg.

[53] Fink, M. R., Schlinker, R. H., and Amiet, R. K. (1976). Prediction of rotating-blade vortex noise from noise of nonrotating blades. Technical report, National Aeronautics & Space Administration.

[54] Fischer, J. (2014). *Identification de sources aéroacoustiques au voisinage de corps non profilés par formation de voies fréquentielle et temporelle*. PhD thesis, Université de Poitiers.

[55] Fourie, P. and Groenwold, A. (2002). The particle swarm optimization algorithm in size and shape optimization. *Structural and Multidisciplinary Optimization*, 23(4):259–267.

[56] Frigo, M. and Johnson, S. G. (2005). The design and implementation of FFTW3. *Proceedings of the IEEE*, 93(2):216–231. Special issue on "Program Generation, Optimization, and Platform Adaptation".

[57] Fujita, H. (2010). The characteristics of the aeolian tone radiated from two-dimensional cylinders. *Fluid Dynamics Research*, 42(1):015002.

[58] Gerrard, J. H. (1966). The mechanics of the formation region of vortices behind bluff bodies. *Journal of Fluid Mechanics*, 25(2):401–413.

[59] Gerrard, J. H. (1978). The wakes of cylindrical bluff bodies at low Reynolds number. *Philosophical Transactions of the Royal Society of London. Series A, Mathematical and Physical Sciences*, 288(1354):351–382.

[60] Geyer, T., Sarradj, E., and Fritzsche, C. (2010). Measurement of the noise generation at the trailing edge of porous airfoils. *Experiments in Fluids*, 48(2):291–308.

[61] Geyer, T. F. and Sarradj, E. (2016). Circular cylinders with soft porous cover for flow noise reduction. *Experiments in Fluids*, 57(3):30.

[62] Giannakoglou, K. C. (2002). Design of optimal aerodynamic shapes using stochastic optimization methods and computational intelligence. *Progress in Aerospace Sciences*, 38:43–76.

[63] Giannakoglou, K. C., Papadimitriou, D. I., and Kampolis, I. C. (2006). Aerodynamic shape design using evolutionary algorithms and new gradient-assisted metamodels. *Computer Methods in Applied Mechanics and Engineering*, 195(44-47):6312–6329.

[64] Gilbert, J. C. (2013). *Fragments d'Optimisation Différentiable - Théorie et Algorithmes*. INRIA.

[65] Gioria, R., Meneghini, J., Aranha, J., Barbeiro, I., and Carmo, B. (2011). Effect of the domain spanwise periodic length on the flow around a circular cylinder. *Journal of Fluids and Structures*, 27(5):792 – 797. IUTAM Symposium on Bluff Body Wakes and Vortex-Induced Vibrations (BBVIV-6).

[66] Gloerfelt, X., Pérot, F., Bailly, C., and Juvé, D. (2005). Flow-induced cylinder noise formulated as a diffraction problem for low Mach numbers. *Journal of Sound and Vibration*, 287(1):129 – 151.

[67] Goldberg, D. E. (1989). *Genetic Algorithms in Search, Optimization and Machine Learning*. Addison-Wesley Longman Publishing Co., Inc., Boston, MA, USA, 1st edition.

[68] Goldstein, D., Handler, R., and Sirovich, L. (1993). Modeling a no-slip flow boundary with an external force field. *Journal of Computational Physics*, 105(2):354 – 366.

[69] Goldstein, M. E. (1974). Aeroacoustics. Technical Report NASA-SP-346, National Aeronautics & Space Administration.

[70] Griffin, O. M. (1980). Universal similarity in the wakes of stationary and vibrating bluff structures. In CERMAK, J., editor, *Wind Engineering*, pages 607 – 617. Pergamon.

[71] Hammache, M. and Gharib, M. (1991). An experimental study of the parallel and oblique vortex shedding from circular cylinders. *Journal of Fluid Mechanics*, 232:567–590.

[72] Haney, H. P. and Johnson, R. R. (1980). Application of to the design of wings with specified pressure distributions. Contractor Report 3238 3238, NASA.

[73] Haramoto, Y., Matsuzaki, K., Munekata, M., and Ohba, H. (2002). Emitted sound from inclined circular cylinder and three-dimensional flow structure in wake. *The Twelfth International Offshore and Polar Engineering Conference*.

[74] Helfer, M. and Busch, J. (1992). Contribution of aerodynamic noise sources to interior and exterior vehicle noise. In *Tagungsband des DGLR-Workshop "Aeroacoustics of Cars", Emmeloord (NL), 16.-17.11.1992*.

[75] Hicks, R. M. and Szelazek, C. A. (1978). Airfoil design by numerical optimization using a minicomputer. Technical Memorandum 78502, NASA.

[76] Howe, M. S. (1975). Contributions to the theory of aerodynamic sound, with application to excess jet noise and the theory of the flute. *Journal of Fluid Mechanics*, 71(4):625–673.

[77] Howe, M. S. (2002). *Theory of Vortex Sound*, chapter 4, page 82–113. Cambridge Texts in Applied Mathematics. Cambridge University Press.

[78] Hu, J. C. and Zhou, Y. (2008). Aerodynamic characteristics of asymmetric bluff bodies. *Journal of Fluids Engineering*, 131(1):011206–011206–9.

[79] Huerre, P. and Monkewitz, P. A. (1990). Local and global instabilities in spatially developing flows. *Annual Review of Fluid Mechanics*, 22(1):473–537.

[80] Humphreys, J. S. (1960). On a circular cylinder in a steady wind at transition Reynolds numbers. *Journal of Fluid Mechanics*, 9(4):603–612.

[81] Hutcheson, F. V. and Brooks, T. F. (2012). Noise radiation from single and multiple rod configurations. *International Journal of Aeroacoustics*, 11(3-4):291–333.

[82] Igarashi, T. (1985). Characteristics of the flow around rectangular cylinders : The case of the angle of attack 0 deg. *Bulletin of JSME*, 28(242):1690–1696.

[83] Iglesias, E. L., Thompson, D., and Smith, M. (2016). Experimental study of the aerodynamic noise radiated by cylinders with different cross-sections and yaw angles. *Journal of Sound and Vibration*, 361:108 – 129.

[84] Iglesias, E. L., Thompson, D., and Smith, M. (2017). Component-based model to predict aerodynamic noise from high-speed train pantographs. *Journal of Sound and Vibration*, 394:280 – 305.

[85] Iida, A., Fujita, H., Kato, C., and Otaguro, T. (1996). Experimental investigation of the generation mechanism of aerodynamic noise: 2nd report, on correlation between surface pressure fluctuation and aerodynamic sound radiated from a circular cylinder (in japanese). *Transactions of the Japan Society of Mechanical Engineers Series B*, 62(604):4160–4167.

[86] Iida, A., Fujita, H., Kato, C., and Takano, Y. (1995). Experimental investigation of the generation mechanism of aerodynamic noise: 1st report, on a coherent structure of surface pressure fluctuation on a circular cylinder (in japanese). *Transactions of the Japan Society of Mechanical Engineers Series B*, 61(592):4371–4378.

[87] Ikeda, M., Mitsumoji, T., Sueki, T., and Takaishi, T. (2010). Aerodynamic noise reduction in pantographs by shape-smoothing of the panhead and its support and by use of porous material in surface coverings. *Quarterly Report of RTRI*, 51(4):220–226.

[88] Ikeda, M., Suzuki, M., and Yoshida, K. (2006). Study on optimization of panhead shape possessing low noise and stable aerodynamic characteristics. *Quarterly Report of RTRI*, 47(2):72–77.

[89] Inasawa, A., Asai, M., and Nakano, T. (2013). Sound generation in the flow behind a rectangular cylinder of various aspect ratios at low Mach numbers. *Computers & Fluids*, 82(Supplement C):148 – 157.

[90] Inoue, O. and Hatakeyama, N. (2002). Sound generation by a two-dimensional circular cylinder in a uniform flow. *Journal of Fluid Mechanics*, 471:285–314.

[91] Islam, S. U., Zhou, C. Y., Shah, A., and Xie, P. (2012). Numerical simulation of flow past rectangular cylinders with different aspect ratios using the incompressible lattice Boltzmann method. *Journal of Mechanical Science and Technology*, 26(4):1027–1041.

[92] Iungo, G. and Buresti, G. (2009). Experimental investigation on the aerodynamic loads and wake flow features of low aspect-ratio triangular prisms at different wind directions. *Journal of Fluids and Structures*, 25(7):1119 – 1135.

[93] Jackson, C. P. (1987). A finite-element study of the onset of vortex shedding in flow past variously shaped bodies. *Journal of Fluid Mechanics*, 182:23–45.

[94] Jahangirian, A. and Shahrokhi, A. (2011). Aerodynamic shape optimization using efficient evolutionary algorithms and unstructured CFD solver. *Computers & Fluids*, 46(1):270 – 276. 10th ICFD Conference Series on Numerical Methods for Fluid Dynamics (ICFD 2010).

[95] Jameson, A. (1988). Aerodynamic design via control theory. *Journal of Scientific Computing*, 3(3).

[96] Jameson, A. (1995). Gradient based optimization methods. Technical Report MAE Technical Report No. 2057, Princeton University.

[97] Jiang, C., Fischer, J. R., Moreau, D., and Doolan, C. J. (2019). Experimental investigation of novel porous-serrated treatments on airfoil trailing edge noise reduction. In *25th AIAA/CEAS Aeroacoustics Conference*, Aeroacoustics Conferences. American Institute of Aeronautics and Astronautics.

[98] Jiang, H. and Cheng, L. (2018). Hydrodynamic characteristics of flow past a square cylinder at moderate Reynolds numbers. *Physics of Fluids*, 30(10):104107.

[99] Jiang, H., Cheng, L., and An, H. (2017). On numerical aspects of simulating flow past a circular cylinder. *International Journal for Numerical Methods in Fluids*, 85(2):113–132.

[100] Jiang, H., Cheng, L., Draper, S., An, H., and Tong, F. (2016). Three-dimensional direct numerical simulation of wake transitions of a circular cylinder. *Journal of Fluid Mechanics*, 801:353–391.

[101] Johnson, S. A., Thompson, M. C., and Hourigan, K. (2004). Predicted low frequency structures in the wake of elliptical cylinders. *European Journal of Mechanics - B/Fluids*, 23(1):229 – 239. Bluff Body Wakes and Vortex-Induced Vibrations.

[102] Jones, D. R. (2001). A taxonomy of global optimization methods based on response surfaces. *Journal of Global Optimization*, 21(4):345–383.

[103] Jouhaud, J.-C., Sagaut, P., Montagnac, M., and Laurenceau, J. (2007). A surrogate-model based multidisciplinary shape optimization method with application to a 2D subsonic airfoil. *Computers & Fluids*, 36(520–529).

[104] Kacker, S. C., Pennington, B., and Hill, R. S. (1974). Fluctuating lift coefficient for a circular cylinder in cross flows. *Journal of Mechanical Engineering Science*, 16(4):215–224.

[105] Kamps, L., Geyer, T. F., Sarradj, E., and Brücker, C. (2017). Vortex shedding noise of a cylinder with hairy flaps. *Journal of Sound and Vibration*, 388:69 – 84.

[106] Karthik, K., Vengadesan, S., and Bhattacharyya, S. K. (2018a). Prediction of flow induced sound generated by cross flow past finite length circular cylinders. *The Journal of the Acoustical Society of America*, 143(1):260–270.

[107] Karthik, K., Vishnu, M., Vengadesan, S., and Bhattacharyya, S. (2018b). Optimization of bluff bodies for aerodynamic drag and sound reduction using CFD analysis. *Journal of Wind Engineering and Industrial Aerodynamics*, 174:133 – 140.

[108] Kato, C., Iida, A., Takano, Y., Fujita, H., and Ikegawa, M. (1993). Numerical prediction of aerodynamic noise radiated from low Mach number turbulent wake. In *31st Aerospace Sciences Meeting*, Aerospace Sciences Meetings. American Institute of Aeronautics and Astronautics.

[109] Keefe (1961). An investigation of the fluctuating forces acting on a stationary circular cylinder in a subsonic stream and of the associated soud field (UTIA REPORT NO. 76). Technical report, Institute of Aerophysics, University of Toronto (UTIA).

[110] Kennedy, J. and Eberhart, R. (1995). Particle swarm optimization. In *Neural Networks, 1995. Proceedings., IEEE International Conference on*, volume 4, pages 1942–1948 vol.4.

[111] King, F. and Pfizenmaier, E. (2009). An experimental study of sound generated by flows around cylinders of different cross-section. *Journal of Sound and Vibration*, 328(3):318 – 337.

[112] Knisely, C. (1990). Strouhal numbers of rectangular cylinders at incidence: A review and new data. *Journal of Fluids and Structures*, 4(4):371 – 393.

[113] Koch, W. (1985). Local instability characteristics and frequency determination of self-excited wake flows. *Journal of Sound and Vibration*, 99(1):53 – 83.

[114] Kolář, V. (2007). Vortex identification: New requirements and limitations. *International Journal of Heat and Fluid Flow*, 28(4):638 – 652. Including Special Issue of Conference on Modelling Fluid Flow (CMFF'06), Budapest.

[115] Konstantinidis, E. and Bouris, D. (2012). Bluff body aerodynamics and wake control. In Lerner, J. C. and Boldes, U., editors, *Applied Aerodynamics*, chapter 4. IntechOpen, Rijeka.

[116] Kozlov, A. V. and Thomas, F. O. (2011). Bluff-body flow control via two types of dielectric barrier discharge plasma actuation. *AIAA Journal*, 49(9):1919–1931.

[117] Krajnovic, S. (2009). Shape optimization of high-speed trains for improved aerodynamic performance. In *Proceedings of the Institution of Mechanical Engineers, Part F: Journal of Rail and Rapid Transit*, pages 439–452.

[118] Krige, D. G. (1951). A Statistical Approach to Some Basic Mine Valuation Problems on the Witwatersrand. *Journal of the Chemical, Metallurgical and Mining Society of South Africa*, 52(6):119–139.

[119] Kumar, B. and Mittal, S. (2006). Prediction of the critical Reynolds number for flow past a circular cylinder. *Computer Methods in Applied Mechanics and Engineering*, 195(44):6046 – 6058.

[120] Kutner, M., Nachtsheim, C., Neter, J., and Li, W. (2005). *Applied Linear Statistical Models*. McGrwa-Hill international edition. McGraw-Hill/Irwin, 5th edition.

[121] Kármán, T. v. (1911). Ueber den Mechanismus des Widerstandes, den ein bewegter Körper in einer Flüssigkeit erfährt. *Nachrichten von der Gesellschaft der Wissenschaften zu Göttingen, Mathematisch-Physikalische Klasse*, pages 509–517.

[122] Lai, M.-C. and Peskin, C. S. (2000). An immersed boundary method with formal second-order accuracy and reduced numerical viscosity. *Journal of Computational Physics*, 160(2):705 – 719.

[123] Laizet, S. (2005). *Développement d'un code de calcul combinant des schémas de haute précision avec une méthode de frontières immergées pour la simulation des mouvements tourbillonnaires en aval d'un bord de fuite*. PhD thesis, Université de Poitiers.

[124] Laizet, S. and Lamballais, E. (2009). High-order compact schemes for incompressible flows: A simple and efficient method with quasi-spectral accuracy. *J. Comput. Phys.*, 228(16):5989–6015.

[125] Lamballais, É. and Silvestrini, J. H. (2002). Direct numerical simulation of interactions between a mixing layer and a wake around a cylinder. *Journal of Turbulence*, 3:N28.

[126] Lardeau, S. (2001). *Simulation numérique directe du contrôle d'écoulements cisaillés libres par injection de fluide*. PhD thesis, Université de Poitiers.

[127] Largeau, J.-F. (2004). *Analyse expérimentale de la dynamique et du rayonnement acoustique d'un écoulement de marche montante*. PhD thesis, Université de Poitiers.

[128] Lazure, H., Morinière, V., Laumonier, J., and Philippon, L. (2016). Sifflement aérodynamique d'un rétroviseur. In *13ème Congrès Français d'Acoustique (CFA16 - Le Mans)*.

[129] Lee, C. (2003). Stability characteristics of the virtual boundary method in three-dimensional applications. *Journal of Computational Physics*, 184(2):559 – 591.

[130] Leehey, P. and Hanson, C. (1970). Aeolian tones associated with resonant vibration. *Journal of Sound and Vibration*, 13(4):465 – 483.

[131] Liao, C.-C., Chang, Y.-W., Lin, C.-A., and McDonough, J. (2010). Simulating flows with moving rigid boundary using immersed-boundary method. *Computers & Fluids*, 39(1):152 – 167.

[132] Lighthill, M. J. (1952). On sound generated aerodynamically i. General theory. *Proceedings of the Royal Society of London A: Mathematical, Physical and Engineering Sciences*, 211(1107):564–587.

[133] Lighthill, M. J. (1962). The Bakerian Lecture, 1961 Sound generated aerodynamically. *Proceedings of the Royal Society of London. Series A. Mathematical and Physical Sciences*, 267(1329):147–182.

[134] Lions, J. L. (1971). *Optimal Control of Systems Governed by Partial Differential Equations*. Springer, New York.

[135] Liow, Y., Tan, B., Thompson, M., and Hourigan, K. (2006). Sound generated in laminar flow past a two-dimensional rectangular cylinder. *Journal of Sound and Vibration*, 295(1):407 – 427.

[136] Liu, H., Wei, J., and Qu, Z. (2012). Prediction of aerodynamic noise reduction by using open-cell metal foam. *Journal of Sound and Vibration*, 331(7):1483 – 1497.

[137] Liu, Q. (2015). Order-2 stability analysis of particle swarm optimization. *Evolutionary computation*, 23(2):187–216.

[138] Liu, Z. and Kopp, G. A. (2011). High-resolution vortex particle simulations of flows around rectangular cylinders. *Computers & Fluids*, 40(1):2 – 11.

[139] Lophaven, S. N., Nielsen, H. B., and Sondergaard, J. (2002). DACE: A MATLAB Kriging toolbox version 2.0. techreport IMM-TR-2002-12, Technical University of Denmark, Copenhagen.

[140] Luo, S., Yazdani, M., Chew, Y., and Lee, T. (1994). Effects of incidence and afterbody shape on flow past bluff cylinders. *Journal of Wind Engineering and Industrial Aerodynamics*, 53(3):375 – 399.

[141] Madavan, N. (2004). On improving efficiency of differential evolution for aerodynamic shape optimization applications. In *10th AIAA/ISSMO Multidisciplinary Analysis and Optimization Conference*.

[142] Majumdar, S., Iaccarino, G., and Durbin, P. (2001). RANS solvers with adaptive structured boundary non-conforming grids. *Annual Research Briefs—2001*, pages 353–366.

[143] Mannini, C. (2015). Applicability of URANS and DES simulations of flow past rectangular cylinders and bridge sections. *Computation*, 3(3):479–508.

[144] Margnat, F. (2005). *Méthode numérique hybride pour l'étude du rayonnement acoustique d'écoulements turbulents pariétaux*. PhD thesis, Université de Poitiers.

[145] Margnat, F. (2015). Hybrid prediction of the aerodynamic noise radiated by a rectangular cylinder at incidence. *Computers & Fluids*, 109:13 – 26.

[146] Margnat, F. and da Silva Pinto, W. J. G. (2018). Contribution à l'optimisation de forme pour le bruit d'origine aérodynamique. In *14ème Congrès Français d'Acoustique (CFA18 - Le Havre)*.

[147] Margnat, F. and Morinière, V. (2009). Behavior of an immersed boundary method in unsteady flows over sharp-edged bodies. *Computers and Fluids*, 38(6):1065–1079.

[148] Marsden, A. L., Wang, M., Dennis, J. E., and Moin, P. (2004). Optimal aeroacoustic shape design using the surrogate management framework. *Optimization and Engineering*, 5(2):235–262.

[149] Massarotti, M. R. and Wolf, W. R. (2018). Aeroacoustic analysis of automotive roof crossbars through on-track acoustic measurements. *Applied Acoustics*, 142:95 – 105.

[150] Mathis, C., Provansal, M., and Boyer, L. (1984). The Benard-Von Karman instability: an experimental study near the threshold. *J. Physique Lett.*, 45(10):483–491.

[151] McClure, J. and Yarusevych, S. (2016). Surface and wake pressure fluctuations of a cylinder in transitional flow regime. In *18th International Symposium on the Application of Laser and Imaging Techniques to Fluid Mechanics, Lisbon*.

[152] McKay, M. D., Beckman, R. J., and Conover, W. J. (1979). A comparison of three methods for selecting values of input variables in the analysis of output from a computer code. *Technometrics*, 21(2):239–245.

[153] McLean, I. and Gartshore, I. (1992). Spanwise correlations of pressure on a rigid square section cylinder. *Journal of Wind Engineering and Industrial Aerodynamics*, 41(1):797 – 808.

[154] Meiburg, E. and Lasheras, J. C. (1988). Experimental and numerical investigation of the three-dimensional transition in plane wakes. *Journal of Fluid Mechanics*, 190:1–37.

[155] Mittal, R. and Iaccarino, G. (2005). Immersed Boundary Methods. *Annual Review of Fluid Mechanics*, 37(1):239–261.

[156] Moeller, M. J. (1982). *Measurement of unsteady forces on a circular cylinder in cross flow at subcritical Reynolds numbers*. PhD thesis, Massachusetts Institute of Technology, Department of Ocean Engineering.

[157] Moon, Y. J. (2013). Sound of fluids at low Mach numbers. *European Journal of Mechanics - B/Fluids*, 40:50 – 63. Fascinating Fluid Mechanics: 100-Year Anniversary of the Institute of Aerodynamics, RWTH Aachen University.

[158] Moreau, D. J. and Doolan, C. J. (2013). Flow-induced sound of wall-mounted finite length cylinders. *AIAA Journal*, 51(10):2493–2502.

[159] Mueller, A. (2012). *Large Eddy Simulation of cross-flow around a square rod at incidence with application to tonal noise prediction*. PhD thesis, University of Twente, Netherlands.

[160] Nakato, S., Kimura, K., Fujino, Y., and Ogawa, T. (2001). Aerodynamic sound from rectangular cylinders at incidence. In *Bluff bodjjy (Fundamental Study)*, number 89, pages 129–156. Wind Engineers, JAWE.

[161] Namiranian, F. and Gartshore, I. (1988). Direct measurements of oscillating lift on a rigid square section cylinder in a turbulent stream. *Journal of Wind Engineering and Industrial Aerodynamics*, 28(1):209 – 218.

[162] Naumann, D., Evans, B., Walton, S., and Hassan, O. (2016). A novel implementation of computational aerodynamic shape optimisation using Modified Cuckoo Search. *Applied Mathematical Modelling*, 40(7–8):4543 – 4559.

[163] Nelder, J. A. and Mead, R. (1965). A simplex method for function minimization. *The Computer Journal*, 7(4):308–313.

[164] Ng, Z. Y., Vo, T., Hussam, W. K., and Sheard, G. J. (2016). Two-dimensional wake dynamics behind cylinders with triangular cross-section under incidence angle variation. *Journal of Fluids and Structures*, 63:302 – 324.

[165] Ng, Z. Y., Vo, T., and Sheard, G. J. (2018). Stability of the wakes of cylinders with triangular cross-sections. *Journal of Fluid Mechanics*, 844:721–745.

[166] Nishimura, H. and Taniike, Y. (2001). Aerodynamic characteristics of fluctuating forces on a circular cylinder. *Journal of Wind Engineering and Industrial Aerodynamics*, 89(7):713 – 723. 10th International Conference on Wind Engineering.

[167] Nishioka, M. and Sato, H. (1978). Mechanism of determination of the shedding frequency of vortices behind a cylinder at low Reynolds numbers. *Journal of Fluid Mechanics*, 89(1):49–60.

[168] Norberg, C. (1987). Effects of Reynolds number and a low-intensity freestream turbulence on the flow around a circular cylinder. Technical Report 2, Dept. Applied Thermodynamics and Fluid Mechanics, Chalmers University of Technology, Gothenburg, Sweden.

[169] Norberg, C. (1993). Flow around rectangular cylinders: Pressure forces and wake frequencies. *Journal of Wind Engineering and Industrial Aerodynamics*, 49(1):187 – 196.

[170] Norberg, C. (1994). An experimental investigation of the flow around a circular cylinder: influence of aspect ratio. *Journal of Fluid Mechanics*, 258:287–316.

[171] Norberg, C. (2001). Flow around a circular cylinder: aspects of fluctuating lift. *Journal of Fluids and Structures*, 15(3):459 – 469.

[172] Norberg, C. (2003). Fluctuating lift on a circular cylinder: review and new measurements. *Journal of Fluids and Structures*, 17(1):57 – 96.

[173] Obasaju, E. D. (1978). *Pressure fluctuations on stationary and oscillating square section cylinders*. PhD thesis, Imperial College London.

[174] Octavianty, R., Asai, M., and Inasawa, A. (2016). Experimental study on vortex shedding and sound radiation from a rectangular cylinder at low Mach numbers. *Transactions of the Japan Society for Aeronautical and Space Sciences*, 59(5):261–268.

[175] Okajima, A. (1982). Strouhal numbers of rectangular cylinders. *Journal of Fluid Mechanics*, 123:379–398.

[176] Okajima, A., Nagahisa, T., and Rokugoh, A. (1990). A numerical analysis of flow around rectangular cylinders. *JSME international journal. Ser. 2, Fluids engineering, heat transfer, power, combustion, thermophysical properties*, 33(4):702–711.

[177] Orselli, R., Meneghini, J., and Saltara, F. (2009). Two and three-dimensional simulation of sound generated by flow around a circular cylinder. In *15th AIAA/CEAS Aeroacoustics Conference (30th AIAA Aeroacoustics Conference)*, Aeroacoustics Conferences. American Institute of Aeronautics and Astronautics.

[178] Othmer, C. (2014). Adjoint methods for car aerodynamics. *Journal of Mathematics in Industry*, 4(1):6.

[179] Padois, T. (2011). *Localisation de source acoustique en soufflerie anéchoïque par deux techniques d'antennerie : formation de voies et retournement temporel numérique*. PhD thesis, Université de Poitiers.

[180] Papoutsis-Kiachagias, E., Magoulas, N., Mueller, J., Othmer, C., and Giannakoglou, K. (2015). Noise reduction in car aerodynamics using a surrogate objective function and the continuous adjoint method with wall functions. *Computers & Fluids*, 122:223 – 232.

[181] Park, J., Kwon, K., and Choi, H. (1998). Numerical solutions of flow past a circular cylinder at Reynolds numbers up to 160. *KSME International Journal*, 12(6):1200–1205.

[182] Parnaudeau, P. (2004). *Etude numérique d'un écoulement cisaillé turbulent complexe à basse vitesse : application à la protection rapprochée*. PhD thesis, Université de Poitiers.

[183] Patil, P. P. and Tiwari, S. (2008). Effect of blockage ratio on wake transition for flow past square cylinder. *Fluid Dynamics Research*, 40(11-12):753–778.

[184] Patrikalakis, N. M. and Maekawa, T. (2002). *Shape Interrogation for Computer Aided Design and Manufacturing*. Springer-Verlag Berlin Heidelberg, 1 edition.

[185] Paul, I., Prakash, K. A., and Vengadesan, S. (2014). Onset of laminar separation and vortex shedding in flow past unconfined elliptic cylinders. *Physics of Fluids*, 26(2):023601.

[186] Peigin, S. and Epstein, B. (2004). Robust optimization of 2D airfoils driven by full Navier–Stokes computations. *Computers & Fluids*, 33(9):1175–1200.

[187] Perry, A. E., Chong, M. S., and Lim, T. T. (1982). The vortex-shedding process behind two-dimensional bluff bodies. *Journal of Fluid Mechanics*, 116:77–90.

[188] Peskin, C. S. (1972). *Flow patterns around heart valves: a digital computer method for solving the equations of motion*. PhD thesis, Albert Einstein College of Medicine, Yeshiva University.

[189] Peskin, C. S. (2002). The immersed boundary method. *Acta Numerica*, 11:479–517.

[190] Peterson, P. (2009). F2PY: a tool for connecting Fortran and Python programs. *Int. J. Comput. Sci. Eng.*, 4(4):296–305.

[191] Phillips, O. M. (1956). The intensity of aeolian tones. *Journal of Fluid Mechanics*, 1(6):607–624.

[192] Pier, B. (2002). On the frequency selection of finite-amplitude vortex shedding in the cylinder wake. *Journal of Fluid Mechanics*, 458:407–417.

[193] Pinto, W. J., Margnat, F., and Gervais, Y. (2019a). Effect of cross-section on flow three-dimensionality for prismatic bodies and the associated noise emission. In *25th AIAA/CEAS Aeroacoustics Conference*, Aeroacoustics Conferences. American Institute of Aeronautics and Astronautics.

[194] Pinto, W. J., Margnat, F., and Gervais, Y. (2019b). Influence of cross-section on the aeolian tone: a numerical study in the laminar regime. In *25th AIAA/CEAS Aeroacoustics Conference*, Aeroacoustics Conferences. American Institute of Aeronautics and Astronautics.

[195] Pinto, W. J. G. S. and Margnat, F. (2018). Shape optimisation for the noise induced by the flow over compact bluff bodies. In *International Conference on Computational Fluid Dynamics (ICCFD10), July 9th-13th, Barcelona, Spain.*

[196] Pinto, W. J. G. S. and Margnat, F. (2019a). Experimental study of the influence of cross section shape on spanwise coherence length in flow around cylinders. *under consideration for publication.*

[197] Pinto, W. J. G. S. and Margnat, F. (2019b). Influence of bluff body sectional breadth and shape on the onset of flow unsteadiness. *submitted to Physics of Fluids.*

[198] Pinto, W. J. G. S. and Margnat, F. (2019c). Shape optimisation for the noise induced by the flow over compact bluff bodies. *submitted to Computer & Fluids - ICCFD special issue.*

[199] Poli, R., Kennedy, J., and Blackwell, T. (2007). Particle swarm optimization. *Swarm Intelligence*, 1(1):33–57.

[200] Porteous, R., Moreau, D. J., and Doolan, C. J. (2014). A review of flow-induced noise from finite wall-mounted cylinders. *Journal of Fluids and Structures*, 51:240 – 254.

[201] Posdziech, O. and Grundmann, R. (2007). A systematic approach to the numerical calculation of fundamental quantities of the two-dimensional flow over a circular cylinder. *Journal of Fluids and Structures*, 23(3):479 – 499.

[202] Powell, A. (1964). Theory of Vortex Sound. *The Journal of the Acoustical Society of America*, 36(1):177–195.

[203] Prhashanna, A., Sahu, A. K., and Chhabra, R. (2011). Flow of power-law fluids past an equilateral triangular cylinder: Momentum and heat transfer characteristics. *International Journal of Thermal Sciences*, 50(10):2027 – 2041.

[204] Provansal, M., Mathis, C., and Boyer, L. (1987). Bénard-von Kármán instability: transient and forced regimes. *Journal of Fluid Mechanics*, 182:1–22.

[205] Python (2016). *The Python Standard Library.* Python Software Foundation.

[206] Pérot, F., Gloerfelt, X., Bailly, C., Auger, J.-M., and Giardi, H. (2003). Numerical prediction of the noise radiated by a cylinder. In *9th AIAA/CEAS Aeroacoustics Conference and Exhibit*, Aeroacoustics Conferences. American Institute of Aeronautics and Astronautics.

[207] Qu, L., Norberg, C., Davidson, L., Peng, S.-H., and Wang, F. (2013). Quantitative numerical analysis of flow past a circular cylinder at Reynolds number between 50 and 200. *Journal of Fluids and Structures*, 39(Supplement C):347 – 370.

[208] R Core Team (2017). *R: A Language and Environment for Statistical Computing*. R Foundation for Statistical Computing, Vienna, Austria.

[209] Ranjan, P. and Dewan, A. (2016). Effect of side ratio on fluid flow and heat transfer from rectangular cylinders using the PANS method. *International Journal of Heat and Fluid Flow*, 61:309 – 322.

[210] Revell, J. D., Prydz, R. A., and Hays, A. P. (1977). Experimental study of airframe noise vs. drag relationship for circular cylinders. Technical Report Final Report for NASA Contract NAS1-14403, Lockeed Report 28074.

[211] Revell, J. D., Prydz, R. A., and Hays, A. P. (1978). Experimental study of aerodynamic noise vs drag relationships for circular cylinders. *AIAA Journal*, 16(9):889–897.

[212] Rho, J.-H., Jeong, S., and Kim, K. (2016). Optimal shape of blunt device for high speed vehicle. *International Journal of Aeronautical and Space Sciences*, 17(3):285–295.

[213] Ribeiro, J. L. D. (1992). Fluctuating lift and its spanwise correlation on a circular cylinder in a smooth and in a turbulent flow: a critical review. *Journal of Wind Engineering and Industrial Aerodynamics*, 40(2):179 – 198.

[214] Ritz, C. and Streibig, J. C. (2008). *Nonlinear Regression with R*. Use R! Springer-Verlag New York, 1 edition.

[215] Robichaux, J., Balachandar, S., and Vanka, S. P. (1999). Three-dimensional Floquet instability of the wake of square cylinder. *Physics of Fluids*, 11(3):560–578.

[216] Roget, B., Sitaraman, J., Lakshminarayan, V., and Wissink, A. (2018). Prismatic mesh generation using minimum distance fields. In *International Conference on Computational Fluid Dynamics (ICCFD10), July 9th-13th, Barcelona, Spain*.

[217] Rokugou, A., Kiwata, T., Okajima, A., Kimura, S., and Yamamoto, H. (2008). Numerical analysis of aerodynamic sound radiated from rectangular cylinder. *Journal of Wind Engineering and Industrial Aerodynamics*, 96(10):2203 – 2216. 4th International Symposium on Computational Wind Engineering (CWE2006).

[218] Roshko, A. (1953). On the development of turbulent wakes from vortex streets. techreport, National Advisory Committee for Aeronautics.

[219] Roshko, A. (1954). On the drag and shedding frequency of two-dimensional bluff bodies. Technical report, National Advisory Committee for Aeronautics.

[220] Roshko, A. (1955). On the wake and drag of bluff bodies. *Journal of the Aeronautical Sciences*, 22(2):124–132.

[221] Roshko, A. (1961). Experiments on the flow past a circular cylinder at very high Reynolds number. *Journal of Fluid Mechanics*, 10(3):345–356.

[222] Roshko, A. (1993). Perspectives on bluff body aerodynamics. *Journal of Wind Engineering and Industrial Aerodynamics*, 49(1):79 – 100.

[223] Rumpfkeil, M. P. and Beran, P. (2018). Multi-fidelity surrogate models for flutter database generation. In *International Conference on Computational Fluid Dynamics (ICCFD10), July 9th-13th, Barcelona, Spain*.

[224] Saffman, P. G. and Schatzman, J. C. (1982). An inviscid model for the vortex-street wake. *Journal of Fluid Mechanics*, 122:467–486.

[225] Saha, A. K. (2007). Far-wake characteristics of two-dimensional flow past a normal flat plate. *Physics of Fluids*, 19(12):128110.

[226] Saha, A. K., Muralidhar, K., and Biswas, G. (2000). Transition and chaos in two-dimensional flow past a square cylinder. *Journal of Engineering Mechanics*, 126(5):523–532.

[227] Sakamoto, H., Haniu, H., and Kobayashi, Y. (1989). Fluctuating forces acting on rectangular cylinders in uniform flow: On rectangular cylinders with fully separated flow. *Transactions of the Japan Society of Mechanical Engineers Series B*, 55(516):2310–2317.

[228] Samion, S. R. L., Ali, M. S. M., Abu, A., Doolan, C. J., and Porteous, R. Z.-Y. (2016). Aerodynamic sound from a square cylinder with a downstream wedge. *Aerospace Science and Technology*, 53(Supplement C):85 – 94.

[229] Schaefer, J. W. and Eskinazi, S. (1959). An analysis of the vortex street generated in a viscous fluid. *Journal of Fluid Mechanics*, 6(2):241–260.

[230] Schewe, G. (1983). On the force fluctuations acting on a circular cylinder in crossflow from subcritical up to transcritical reynolds numbers. *Journal of Fluid Mechanics*, 133:265–285.

[231] Schmitt, B. (2015). *Convergence Analysis for Particle Swarm Optimization*. FAU Forschungen : Reihe B. Medizin, Naturwissenschaften, Technik. FAU University Press.

[232] Schumm, M., Berger, E., and Monkewitz, P. A. (1994). Self-excited oscillations in the wake of two-dimensional bluff bodies and their control. *Journal of Fluid Mechanics*, 271:17–53.

[233] Seo, J. H. and Moon, Y. J. (2007). Aerodynamic noise prediction for long-span bodies. *Journal of Sound and Vibration*, 306(3):564 – 579.

[234] Shapiro, S. S. and Wilk, M. B. (1965). An analysis of variance test for normality (complete samples). *Biometrika*, 52(3-4):591–611.

[235] Sheard, G. J., Fitzgerald, M. J., and Ryan, K. (2009). Cylinders with square cross-section: wake instabilities with incidence angle variation. *Journal of Fluid Mechanics*, 630:43–69.

[236] Sheard, G. J., Hourigan, K., and Thompson, M. C. (2005). Computations of the drag coefficients for low-Reynolds-number flow past rings. *Journal of Fluid Mechanics*, 526:257–275.

[237] Shi, Y. and Eberhart, R. (1998). A modified particle swarm optimizer. In *Evolutionary Computation Proceedings, 1998. IEEE World Congress on Computational Intelligence., The 1998 IEEE International Conference on*, pages 69–73. IEEE.

[238] Shimada, K. and Ishihara, T. (2002). Application of a modified k-epsilon model to the prediction of aerodynamic characteristics of rectangular cross-section cylinders. *Journal of Fluids and Structures*, 16(4):465 – 485.

[239] Sohankar, A. (2006). Flow over a bluff body from moderate to high Reynolds numbers using large eddy simulation. *Computers & Fluids*, 35(10):1154 – 1168.

[240] Sohankar, A. (2008). Large eddy simulation of flow past rectangular-section cylinders: Side ratio effects. *Journal of Wind Engineering and Industrial Aerodynamics*, 96(5):640 – 655.

[241] Sohankar, A., Norberg, C., and Davidson, L. (1996). A numerical study of unsteady two-dimensional flow around rectangular cylinders at incidence. Technical Report Internal Report Nr. 96/25, Departement of Thermo and Fluid Dynamics, Chalmers University of Technology.

[242] Sohankar, A., Norberg, C., and Davidson, L. (1998). Low-Reynolds-number flow around a square cylinder at incidence: study of blockage, onset of vortex shedding and outlet boundary condition. *International Journal for Numerical Methods in Fluids*, 26(1):39–56.

[243] Sohankar, A., Norbergb, C., and Davidson, L. (1997). Numerical simulation of unsteady low-Reynolds number flow around rectangular cylinders at incidence. *Journal of Wind Engineering and Industrial Aerodynamics*, 69-71:189 – 201. Proceedings of the 3rd International Colloqium on Bluff Body Aerodynamics and Applications.

[244] Sonneville, P. (1976). *Étude de la structure tridimensionnelle des écoulements autour d'un cylindre circulaire*. PhD thesis, Université Pierre et Marie Curie.

[245] Steggel, N. (1998). *A Numerical Investigation of the Flow Around Rectangular Cylinders*. PhD thesis, University of Surrey.

[246] Storn, R. and Price, K. (1997). Differential evolution – a simple and efficient heuristic for global optimization over continuous spaces. *Journal of Global Optimization*, 11(4):341–359.

[247] Strouhal, V. (1878). Ueber eine besondere Art der Tonerregung. *Annalen der Physik*, 241(10):216–251.

[248] Strykowski, P. J. (1986). *The Control of Absolutely and Convectively Unstable Shear Flows*. PhD thesis, Yale University.

[249] Strykowski, P. J. and Sreenivasan, K. R. (1990). On the formation and suppression of vortex 'shedding' at low Reynolds numbers. *Journal of Fluid Mechanics*, 218:71–107.

[250] Sueki, T., Takaishi, T., Ikeda, M., and Arai, N. (2010). Application of porous material to reduce aerodynamic sound from bluff bodies. *Fluid Dynamics Research*, 42(1):015004.

[251] Suzuki, M., Ikeda, M., and Yoshida, K. (2008). Study on numerical optimization of cross-sectional panhead shape for high-speed train. *Journal of Mechanical Systems for Transportation and Logistics*, 1(1):100–110.

[252] Szepessy (1993). On the control of circular cylinder flow by end plates. *European Journal of Mechanics*, 12(2):217–244.

[253] Szepessy, S. and Bearman, P. W. (1992). Aspect ratio and end plate effects on vortex shedding from a circular cylinder. *Journal of Fluid Mechanics*, 234:191–217.

[254] Talotte, C. (2000). Aerodynamic noise: A critical survey. *Journal of Sound and Vibration*, 231(3):549 – 562.

[255] Tamura, T. and Itoh, Y. (1996). Aerodynamic characteristics and flow structures around a rectangular cylinder with a section of various depth/breadth ratios (in japanese). *Journal of Structural and Construction Engineering (Transactions of AIJ)*, 61(486):153–162.

[256] Tamura, T. and Miyagi, T. (1999). The effect of turbulence on aerodynamic forces on a square cylinder with various corner shapes. *Journal of Wind Engineering and Industrial Aerodynamics*, 83(1):135 – 145.

[257] Tan, X.-m., Xie, P.-p., Yang, Z.-g., and Gao, J.-y. (2019). Adaptability of turbulence models for pantograph aerodynamic noise simulation. *Shock and Vibration*, 2019:20.

[258] Taneda, S. (1956). Experimental investigation of the wakes behind cylinders and plates at low Reynolds numbers. *Journal of the Physical Society of Japan*, 11(3):302–307.

[259] Tang, Z., Periaux, J., Bugeda, G., and Onate, E. (2009). Lift maximization with uncertainties for the optimization of high lift devices using multi-criterion evolutionary algorithms. In *2009 IEEE Congress on Evolutionary Computation*, pages 2324–2331.

[260] Theil, H. (1992). *A Rank-Invariant Method of Linear and Polynomial Regression Analysis*, pages 345–381. Springer Netherlands.

[261] Thompson, M. C., Radi, A., Rao, A., Sheridan, J., and Hourigan, K. (2014). Low-Reynolds-number wakes of elliptical cylinders: from the circular cylinder to the normal flat plate. *Journal of Fluid Mechanics*, 751:570–600.

[262] Tian, X., Ong, M. C., Yang, J., and Myrhaug, D. (2013). Unsteady RANS simulations of flow around rectangular cylinders with different aspect ratios. *Ocean Engineering*, 58:208 – 216.

[263] Trelea, I. C. (2003). The particle swarm optimization algorithm: convergence analysis and parameter selection. *Information Processing Letters*, 85(6):317 – 325.

[264] Trias, F., Gorobets, A., and Oliva, A. (2015). Turbulent flow around a square cylinder at Reynolds number 22,000: A DNS study. *Computers & Fluids*, 123:87 – 98.

[265] Uffinger, T., Ali, I., and Becker, S. (2013). Experimental and numerical investigations of the flow around three different wall-mounted cylinder geometries of finite length. *Journal of Wind Engineering and Industrial Aerodynamics*, 119:13 – 27.

[266] Université de Poitiers (2019). Mésocentre SPIN Calcul. `https://forge.univ-poitiers.fr/projects/mesocentre-spin-git/wiki`. [Online; accessed 21-June-2019].

[267] Vassberg, J. C. and Jameson, A. (2002). Aerodynamic shape optimisation of a Reno race plane. *International Journal of Vehicle Design*, 28(4).

[268] Vicini, A. and Quagliarella, D. (1998). Airfoil and wing design through hybrid optimization strategies. In *16th AIAA Applied Aerodynamics Conference*.

[269] Vickery, B. J. (1966). Fluctuating lift and drag on a long cylinder of square cross-section in a smooth and in a turbulent stream. *Journal of Fluid Mechanics*, 25(3):481–494.

[270] Vijaybabu, T., Anirudh, K., and Dhinakaran, S. (2018). LBM simulation of unsteady flow and heat transfer from a diamond-shaped porous cylinder. *International Journal of Heat and Mass Transfer*, 120:267 – 283.

[271] Vytla, V. V. S., Huang, P., and Penmetsa, R. (2010). Multi-objective aerodynamic shape optimization of high speed train nose using adaptive surrogate model. In *28th AIAA Applied Aerodynamics Conference*.

[272] Wang, R., Cheng, S., and Ting, D. S.-K. (2019). Effect of yaw angle on flow structure and cross-flow force around a circular cylinder. *Physics of Fluids*, 31(1):014107.

[273] West, G. and Apelt, C. (1997). Fluctuating lift and drag forces on finite lengths of a circular cylinder in the subcritical reynolds number range. *Journal of Fluids and Structures*, 11(2):135 – 158.

[274] Wickham, H. (2016). *ggplot2: Elegant Graphics for Data Analysis*. Springer-Verlag New York.

[275] Williams, J. E. F. and Hawkings, D. L. (1969). Sound generation by turbulence and surfaces in arbitrary motion. *Philosophical Transactions of the Royal Society of London. Series A, Mathematical and Physical Sciences*, 264(1151):321–342.

[276] Williamson, C. H. K. (1996). Vortex dynamics in the cylinder wake. *Annual Review of Fluid Mechanics*, 28(1):477–539.

[277] Xu, S., Jahn, W., and Müller, J.-D. (2014). CAD-based shape optimisation with CFD using a discrete adjoint. *International Journal for Numerical Methods in Fluids*, 74(3):153–168.

[278] Xu, S. J., Zhang, W. G., Gan, L., Li, M. G., and Zhou, Y. (2017). Experimental study of flow around polygonal cylinders. *Journal of Fluid Mechanics*, 812:251–278.

[279] Yang, T. and Mason, M. S. (2019). Aerodynamic characteristics of rectangular cylinders in steady and accelerating wind flow. *Journal of Fluids and Structures*, 90:246 – 262.

[280] Yang, X.-S. (2010). *Engineering Optimization: An Introduction with Metaheuristic Applications*, chapter Test problems in optimization. John Wiley & Sons.

[281] Yoon, D.-H., Yang, K.-S., and Choi, C.-B. (2010). Flow past a square cylinder with an angle of incidence. *Physics of Fluids*, 22(4):043603.

[282] Zdravkovich, M. (1981). Review and classification of various aerodynamic and hydrodynamic means for suppressing vortex shedding. *Journal of Wind Engineering and Industrial Aerodynamics*, 7(2):145 – 189.

[283] Zdravkovich, M. (1997). *Flow Around Circular Cylinders: Volume I: Fundamentals*. OUP Oxford.

[284] Zdravkovich, M. M. (1969). Smoke observations of the formation of a Kármán vortex street. *Journal of Fluid Mechanics*, 37(3):491–496.

[285] Zebib, A. (1987). Stability of viscous flow past a circular cylinder. *Journal of Engineering Mathematics*, 21(2):155–165.

[286] Zhou, Y., Valeau, V., Marchiano, R., Marx, D., and Prax, C. (2019). Inverse methods for experimental aeroacoustic source identification by using massive microphone arrays. In *Book of Abstracts - Journées des Doctorants de l'Institut PPRIME (JDD2019)*.

[287] Zielinska, B. J. A., Goujon-Durand, S., Dušek, J., and Wesfreid, J. E. (1997). Strongly nonlinear effect in unstable wakes. *Phys. Rev. Lett.*, 79:3893–3896.

[288] Zielinska, B. J. A. and Wesfreid, J. E. (1995). On the spatial structure of global modes in wake flow. *Physics of Fluids*, 7(6):1418–1424.

[289] Zumu Doli, C. (2018). *Transmission des fluctuations de bruit aéroacoustique dans un modèle d'habitacle automobile générées par un écoulement instationnaire : étude en soufflerie*. PhD thesis, École Nationale Supérieure d'Ingénieurs de Poitiers - ENSIP.

Contents (detailed)

Résumé

L'influence de la forme de cylindres longs sur leur rayonnement acoustique en écoulement est étudiée. Des simulations bidimensionnelles (2D) sont réalisées à bas nombre de Reynolds ($\mathrm{Re} = 20 - 200$), à l'aide du code de calcul direct (DNS) incompressible incompact3D au moyen d'une méthode de frontière immergée (IBM). Une formule dérivée de l'équation de Curle pour un cylindre compact permet la quantification de l'émission acoustique en 2D. En soufflerie anéchoïque, la signature acoustique d'une trentaine de géométries est mesurée, $\mathrm{Re} = 4,000 - 53,000$; l'anémométrie par fil chaud est utilisée pour la description des propriétés axiales de l'écoulement. L'avant corps et l'allongement (AR) sont les plus importantes propriétés géométriques tant pour l'écoulement que pour le rayonnement acoustique en 2D. Les géométries allongées sont généralement les plus silencieuses car les tourbillons sont moins intenses et repoussés vers l'aval et l'apparition de l'instationnarité est retardée. De leur côté, les résultats expérimentaux montrent que les géométries allongées sont les plus bruyantes, ce qui est à l'opposé des conclusions précédentes. Ceci est justifié par une augmentation significative de la cohérence de l'écoulement en envergure pour les AR les plus longs, presque complètement en phase, donc plus efficace acoustiquement. Globalement, cela implique que les géométries dont l'écoulement 2D est faiblement perturbé, marqué par un déclenchement plus tardif de l'instationnarité (Reynolds critique plus élevé), sont aussi plus organisées en 3D aux Re des mesures. La relation sous-jacente entre les transitions successives vers la turbulence nécessite une étude approfondie.

Mots clés : sifflement éolien, bruit de cylindre, aéroacoustique, écoulement d'obstacle, sillage de Von Karman, Simulation Numérique Directe, optimisation de forme, cohérence

Abstract

The influence of the shape on the sound emission of cylindrical bluff-bodies is studied. Simulations are performed in two-dimensions (2D) at low-Reynolds number ($\mathrm{Re} = 20 - 200$), with the incompressible direct Navier-Stokes (DNS) solver incompact3D, using the Immersed Boundary Method (IBM) formalism; the acoustic emission is evaluated by a single formula derived from Curle's equation for compact cylinders. In anechoic wind tunnel, the acoustic signature is measured for about 30 geometries, $\mathrm{Re} = 4,000 - 53,000$; hot-wire measurements of the spanwise flow characteristics are performed for a subset of the tested cylinders. The influence of both the shape of the upstream portion of the geometry and the breadth-to-height ratio (AR) are proved to be major features in terms of both the flow and its acoustic emission in 2D. By reducing the strength of the vortices and pushing them downstream and affecting the mechanics of the von Kármán instability (delaying the transition to unsteadiness), stretched shapes (with higher AR) are generally quieter. From the experiments, it is found that the geometries of biggest AR are the loudest, contraposing the results obtained in 2D. The disparity is justified by a significant increase of the spanwise coherence associated with the larger AR's, practically fully-phased, thus more acoustically efficient. Globally, it is implied that geometries which have weakly perturbed flow in 2D, marked by a later transition to unsteadiness (larger critical Reynolds number), are also more organized in 3D, high-Reynolds number regimes. The underlying relationship between low and high-Reynolds number transitions must be further investigated.

Keywords: aeolian tone, cylinder noise, aeroacoustics, bluff-body flow, von Kármán wake, Direct Numerical Simulation, shape optimization, coherence